UNIVERZITA PALACKÉHO V OLOMOUCI
Přírodovědecká fakulta
Katedra anorganické chemie

Komplexy vybraných přechodných kovů s makrocyklickými ligandy

HABILITAČNÍ PRÁCE

RNDr. Bohuslav Drahoš, Ph.D.

Olomouc 2020

Obsah:

1. Úvod

Neobvyklá kombinace fyzikálních vlastností molekulárních materiálů je v posledních letech příčinou renesance magnetochemie a molekulárního magnetismu, což dokládá velké množství nedávno publikovaných přehledových článků v této oblasti výzkumu.[1,2,3,4,5,6,7,8,9,10,11] Tyto sloučeniny mají zajímavé magnetické chování, které například zahrnuje magnetické uspořádání s kritickou teplotou (T_c) překračující pokojovou teplotu, kvantové efekty pozorované pro jednotlivé molekuly/řetězce nebo přepínání magnetického/spinového stavu změnou teploty, tlaku nebo osvětlením.[12,13,14] Tyto pozoruhodné vlastnosti jsou příčinou vzniku mnoha revolučních aplikací, jako jsou vysokokapacitní paměťová média, spintronika, kvantové počítače, molekulární přepínače atd.[3,4] Velká část těchto materiálů je založena na koordinačních sloučeninách, a proto v tomto ohledu představuje koordinační chemie velmi důležitý a nenahraditelný nástroj k dosažení významného pokroku v této vědní oblasti.

Využití makrocyklických ligandů se v této souvislosti jeví jako velice zajímavý a slibný způsob, jakým lze připravovat komplexní sloučeniny se zajímavými magnetickými vlastnostmi, neboť tyto speciální ligandy často umožňují dosažení méně běžných koordinačních čísel nebo geometrií. Proto makrocyklické ligandy ve svých komplexech představují univerzální stavební prvky/bloky, které umožňují řadu rozličných způsobů přípravy různých typů komplexních sloučenin: a) výměna koligandů (typické pro lineární/necyklické ligandy) monodentátních = tvoří se jednojaderné komplexy, bidentátních = tvoří se dvoj- nebo vícejaderné komplexy, b) snadná modifikace makrocyklického skeletu (donorové atomy, velikost makrocyklické kavity) ve smyslu i) změny rigidity ligandu, ii) ladění bazicity resp. donor-akceptorových vlastností ligandu (např. pomocí různých pendantních ramen), iii) poskytující silnějších mezimolekulové interakce (modifikace různými funkčními skupinami), (iv) propojení ligandu s jinými molekulami, které mají další zajímavé vlastnostmi (multifunkční materiály). Tuto koordinační a chemickou flexibilitu makrocyklických ligandů lze považovat za vynikající výchozí bod pro návrh nových systémů na bázi komplexních sloučenin kovů s požadovanými magnetickými vlastnostmi.

Z nepřeberného množství magneticky aktivních látek bude pozornost v této habilitační práci věnována především tzv. jednomolekulovým magnetům (z angl. Single-Molecule Magnets, SMMs),[15,16] jevu tzv. spinového křížení (z angl. Spin Crossover, SCO)[17] a jejich případného spojování do podoby multifunkčních magnetických materiálů. Tato habilitační práce je koncipována jako soubor uveřejněných vědeckých publikací (Příloha P1–P11) doplněných komentářem. V úvodních kapitolách 2, 3 a 4 jsou vysvětleny základní pojmy

potřebné pro orientaci v problematice molekulového magnetismu, kapitola 5 se zabývá nejběžnějšími metodami přípravy azamakrocyklických ligandů a v kapitole 6 a 7 je nastíněn současný stav poznání ve vybraných oblastech molekulového magnetismu, konkrétně je uveden přehled doposud studovaných komplexních sloučenin s makrocyklickými ligandy, které vykazující SCO nebo které jsou SMMs a mají méně běžné koordinační číslo sedm. Dále jsou již v práci diskutovány výsledky z vědeckých publikací v rámci tří kapitol rozdělených podle strukturního typu studovaných sloučenin a povahy jejich magnetických vlastností, případně způsobu ladění jejich magnetické anizotropie. V kapitole 8 (přílohy P1–P4) jsou popisovány vlastnosti komplexů se stěžejním ligandem **15-pyN$_3$O$_2$** (3,12,18-triaaza-6,9-dioxabicyklo[12.3.1]oktadeka-1(18),14,16-trien), v kapitole 9 (přílohy P5–P8) jsou diskutovány vlastnosti komplexů s třemi strukturními deriváty ligandu **15-pyN$_3$O$_2$** a kapitola 10 (přílohy P9–P11) se zabývá železnatými komplexy s pyridinovým derivátem cyklamu (1,4,8,11-tetraazacyklotetradekan) vykazující SCO a syntézou ligandů a případně jejich železnatých komplexů s potenciálním využitím v multifunkčních magnetických materiálech. V poslední kapitole jsou stručně shrnuty dosažené výsledky a obecné závěry.

2. Magnetická anizotropie – klíč k tajemství jednomolekulových magnetů

Z nepřeberného množství magneticky aktivních sloučenin je pozornost této práce primárně zaměřena na tzv. jednomolekulové magnety (SMMs).[15,16] Tyto sloučeniny se pod blokovací teplotou (T_B) vyznačující velmi pomalou relaxací magnetizace a magnetickou hysterezí čistě molekulárního původu. Proto se u nich nepozoruje žádné uspořádání na dlouhou vzdálenost typické pro klasické magnetické materiály, na druhou stranu u nich lze pozorovat kvantové efekty (kvantové tunelování magnetizace – z angl. Quantum Tunelling of Magnetization, QTM) nebo přepínání magnetického/spinového stavu pomocí změny teploty, tlaku nebo osvětlením.[1,2,12,13,15,16] V posledních desetiletích byla vědecká pozornost věnována zkoumání těchto sloučenin z důvodu jejich potenciálních aplikací v nanozařízeních pro informační technologie (vysokokapacitní paměťové nosiče, procesování kvantové informace, organizace SMMs na površích), úzce propojených se spintronikou, magnetickými senzory nebo biologickými spinovými systémy.[2,16,18] Po chemické stránce jsou SMMs založeny na sloučeninách s radikály nebo na různých komplexních sloučeninách d- a f-kovů (organická „obálka" většinou obklopuje „kovové" centrum). Fyzikální vlastnosti SMMs mohou být během jejich syntézy významně ovlivňovány cílenou strukturní modifikací použitých ligandů, což může představovat molekulární přístup výroby takových nanomagnetů.

SMMs jsou obvykle charakterizovány tzv. energetickou bariérou U_{eff} pro změnu orientace magnetického momentu (překlopení/reorientace vektoru magnetizace) (Obr. 1), která souvisí s velkou hodnotou magnetické anizotropie, což je preferenční orientace magnetického momentu ve specifickém směru (magnetická odezva vzorku je závislá na jeho orientaci vůči vnějšímu magnetickému poli). Pro sloučeniny přechodných kovů je magnetická anizotropie obvykle popisována ve smyslu tzv. štěpení v nulovém magnetickém poli (z angl. Zero-Field Splitting, ZFS), které v systémech s celkovým spinem $S > \frac{1}{2}$ způsobuje odstranění mikrostavové degenerace multipletu (2S+1), tj. rozštěpení energetických hladin iontů kovů v nulovém magnetickém poli. ZFS je způsobeno elektronovými vlastnostmi molekuly, především spin-spinovou a spin-orbitální interakcí, které jsou zásadním způsobem závislé na druhu a symetrii koordinační sféry molekuly (především vnitřní, ale i vnější). ZFS se popisuje pomocí axiálního parametru štěpení v nulovém poli (D) a rombického parametru štěpení v nulovém poli (E), pro které platí $|D| \geq 3E \geq 0$. Pokud je $D < 0$, jedná se magnetickou anizotropii typu lehké osy (axiální, z angl. easy-axis), pokud je ovšem $D > 0$, jedná se magnetickou anizotropii typu lehké roviny (rombickou, z angl. easy-plane). ZFS se projevuje především při nízkých teplotách (pozoruje se pokles efektivního magnetického momentu μ_{eff}/μ_B resp. součinu molární magnetické susceptibility a teploty $\chi_m T$), když se kT sníží pod hodnotu odpovídající rozštěpení energetických hladin a dochází tak k jejich nerovnoměrnému obsazování (zvyšuje se populace základního stavu). Energetickou bariéru U_{eff} lze pro d-kovy definovat jako $U_{eff} = |D|S^2$ nebo $U_{eff} = |D|(S^2 - \frac{1}{4})$ pro celočíselný nebo poločíselný základní spinový stav S.[15] Velikost nezávisí na znaménku, ale jak je znázorněno v levé části Obr. 1, pouze záporná hodnota vede reálně ke vzniku energetické bariéry pro přechod mezi stavy s nejnižší energií (pro $D < 0$ $M_s = +S$ a $M_s = -S$, pro $D > 0$ $M_s = 0$).
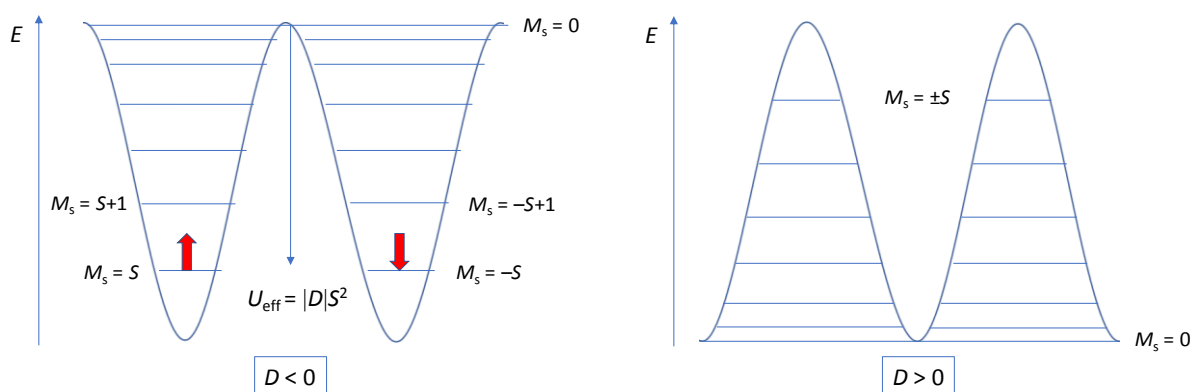
Obrázek 1 Schématické znázornění diagramu energetických hladin v případě záporné (*vlevo*) a kladné (*vpravo*) hodnoty axiálního parametru štěpení v nulovém poli D ilustrující energetickou bariéru U_{eff} překlopení magnetického momentu částice.

V rané fázi výzkumu SMMs byly provedeny rozsáhlé studie na polynukleárních komplexech 3d kovů (např. komplex označovaný jako Mn_{12} – první pozorovaný SMM)[19] za účelem porozumění chování těchto sloučenin. Následně byly studovány smíšené systémy 3d–4f,[20,21,22] vícejaderné a později především jednojaderné 4f komplexy (obvykle obsahující Dy^{III}),[16,23,24] tj. mononukleární SMMs nebo tzv. jedno iontové magnety (z angl. Single-Ion Magnets, SIMs).[25] V poslední době byl vědecký zájem soustředěn především na mononukleární komplexy 3d kovů, známé také jako 3d-SIMs nebo mononukleární 3d-SMMs.[3,4,7,8,9] Třetí skupinou molekulových magnetů jsou jednořetězcové magnety (z angl. Single-Chain Magnets, SCMs)[26] založené na vícejaderných lineárních komplexech, které tvoří více či méně izolované magnetické řetězce. V těchto materiálech je nutné, aby mezi sousedními nositeli spinu s velkou magnetickou anizotropií existovaly slabé feromagnetické nebo antiferomagnetické výměnné interakce.

Protože byla magnetická hystereze SMMs pozorována pouze při velmi nízkých teplotách, což značně omezuje technickou využitelnost SMMs v reálných aplikacích, bylo vynaloženo velké úsilí, aby se zvýšila T_B obvykle pomocí zvýšení energetické bariéry U_{eff}. V prvním kroku byl co nejvíce navýšen celkový spin S základního stavu molekuly tak, že byly syntetizovány velké polynukleární komplexy.[27] Ukázalo se však, že to není celkový spin S základního stavu, ale spíše magnetická anizotropie (hodnota parametru D), která má pro zvyšování energetické bariéry U_{eff} zásadní roli.[28] Proto byla pozornost raději zaměřena na mononukleární komplexy 3d kovů, pro které lze magnetickou anizotropii modulovat racionálním designem ligandů. Značný pokrok ve výzkumu mononukleárních SMMs obsahujících různé přechodné kovy v různých oxidačních stavech (např. Mn^{III}, $Fe^{I/II/III}$, $Co^{I/II/III}$, $Ni^{I/II}$ nebo Re^{IV}) a v různých koordinačních geometriích (koordinační čísla v rozsahu 2–8) byl jasně dokumentován rostoucím počtem připravených sloučenin popsaných ve velkém počtu publikací a přehledných článků.[3,4,6,7,8,9] Asi největší studovanou skupinu v tomto směru představují komplexy Co^{II},[6,7] u kterých byla pozorována pomalá relaxace magnetizace i přesto, že pro ně byly zjištěny kladné hodnoty parametru D. Takové chování může být vysvětleno v případě velké rombicity (E/D se blíží maximální hodnotě 1/3) změnou magnetické anizotropie z typu lehká rovina na typ lehká osa[29] nebo jiným typem relaxačního mechanismu než je teplotně aktivovaný Orbachův relaxační proces , pro který se uvažuje U_{eff} (bližší popis v následující kapitole).[30]

Před třemi lety bylo dosaženo významného pokroku díky objevu vysoké T_B = 60 K (U_{eff} = 1837 K)[31] pro dysprosocenium a dnes nejvyšší T_B dokonce překonala teplotu kapalného dusíku v dalším metalocenu s Dy^{III} (T_B = 80 K, U_{eff} = 1541 cm^{-1}).[32]

V rozrůstající se skupině SMMs není motiv makrocyklických ligandů tak častý ve srovnání s ligandy s otevřeným/acyklickým řetězcem (malé bidentátní nebo tridentátní ligandy typu acetáty, oxaláty, acetylacetonáty, *N*-heterocykly jako jsou bipyridin nebo fenantrolin, nebo vícedentátní aminy, Schiffovy báze atd.).[33] Například větší makrocykly byly úspěšně použity při syntéze SMMs na bázi Ln^{III} obsahujících ionty kovů 3d (Cu^{II}, Zn^{II} atd.) a 4f (Tb^{III}, Dy^{III}, Er^{III}),[34] protože komplexy s lanthanoidy mívají mnohem větší hodnoty U_{eff} v důsledku jejich velké spinové multiplicity a velké magnetické anizotropie základního stavu. I přesto celá tato skupina zahrnuje mnoho sloučenin, pokud vezmeme v úvahu možnou strukturní modifikaci ligandu a rozmanitost možných komplexovatelných iontů kovů, a dále se rozrůstá (v kapitole 7 budou blíže diskutovány makrocyklické ligandy poskytující komplexy s koordinačním číslem 7).
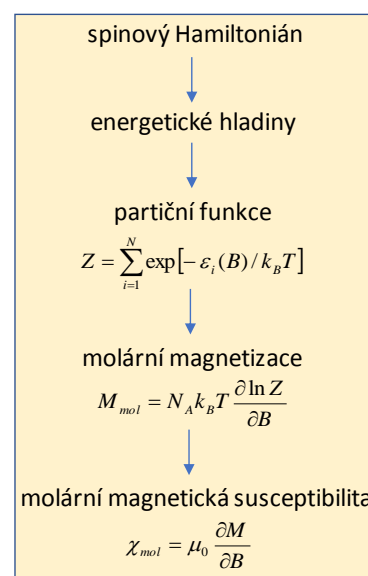
3. Magnetická měření

Základem interpretace magnetických vlastností je znalost informace o tom, jak reaguje vnější magnetické pole s magnetickými momenty komplexních sloučenin. Pro základní charakterizaci je nutné provést následující měření: (i) teplotní závislost molární magnetické susceptibility (χ_m) v konstantním magnetickém poli – DC (z angl. direct current) data, často doplněné o závislost magnetizace na rostoucím magnetickém poli, (ii) teplotní a frekvenční závislost magnetické susceptibility ve střídavém magnetickém poli – AC (z angl. alternating current) data. Výše uvedená měření bývají prováděna na moderních SQUID (z angl. Superconducting Quantum Interference Device) magnetometrech s vysokou citlivostí pracující od teploty 1.9 K a do magnetických polí až 7 T, případně pomocí VSM (z angl. Vibrating Sample Magnetometer) magnetometrů.

3.1. *Analýza magnetických DC dat*

Všeobecný postup při interpretaci magnetických DC dat je znázorněn na Obr. 2, kdy jsou pomocí aparátu kvantové chemie a statistické termodynamiky aplikovány různé zjednodušené modely, které umožňují popsat vlastnosti základního energetického stavu molekuly a interpretovat její magnetické vlastnosti.

Při zpracování naměřených dat se používá metody efektivního spinového Hamiltoniánu, který má různý tvar

spinový Hamiltonián

↓

energetické hladiny

↓

partiční funkce

$$Z = \sum_{i=1}^{N} \exp\left[-\varepsilon_i(B)/k_B T\right]$$

↓

molární magnetizace

$$M_{mol} = N_A k_B T \frac{\partial \ln Z}{\partial B}$$

↓

molární magnetická susceptibilita

$$\chi_{mol} = \mu_0 \frac{\partial M}{\partial B}$$

Obrázek 2 Znázornění postupu zpracování magnetických DC dat

podle typu studovaného systému. Nejpoužívanější modely pro jednojaderný komplex (H^{mono}),
dvojjaderný komplex (H^{di}) a polymerní řetězec (H^{1D}) jsou uvedeny níže:

$$\hat{H}^{\text{mono}} = D\left(\hat{S}_z^2 - \hat{S}^2/3\right) + E\left(\hat{S}_x^2 - \hat{S}_y^2\right) + \mu_B B g \hat{S}_a - zj\left\langle \hat{S}_a \right\rangle \hat{S}_a \tag{1}$$

$$\hat{H}^{\text{di}} = -J\left(\vec{S}_1 \cdot \vec{S}_2\right) + \sum_{i=1}^{2} D_i\left(\hat{S}_{i,z}^2 - \hat{S}_i^2/3\right) + E_i\left(\hat{S}_{i,x}^2 - \hat{S}_{i,y}^2\right) + \mu_B B g_i \hat{S}_{i,a} \tag{2}$$

$$\hat{H}^{\text{1D}} = -J\left(\vec{S}_1 \cdot \vec{S}_N\right) - \sum_{i=1}^{K-1} J\left(\vec{S}_i \cdot \vec{S}_{i+1}\right) + \sum_{i=1}^{K} D_i\left(\hat{S}_{i,z}^2 - \hat{S}_i^2/3\right) + E_i\left(\hat{S}_{i,x}^2 - \hat{S}_{i,y}^2\right) + \mu_B B g_i \hat{S}_{i,a} \tag{3}$$

kde D je axiální a E je rombický parametr štěpení v nulovém poli (členy obsahující tyto
parametry popisují magnetickou anizotropii pomocí ZFS a bývají označovány jako H^{ZFS}), $\hat{S}^2$
je operátor velikosti spinu, $\hat{S}$ je operátor projekce spinu ve směru osy x ($\hat{S}_x$), y ($\hat{S}_y$), z ($\hat{S}_z$) nebo
ve směru vnějšího magnetického pole a ($\hat{S}_a$), $\mu_B B g \hat{S}_a$ je člen popisující Zeemanovo štěpení
v magnetickém poli, člen obsahující zj reprezentuje korekci na molekulové pole (modeluje
nespecifické slabé intermolekulární magnetické interakce)[35] a $<S_a>$ představuje teplotní
průměr projekce spinu molekuly do směru a magnetického pole definovaného pomocí
polárních souřadnic jako $B_a = B\cdot(\sin\theta\cos\varphi, \sin\theta\sin\varphi, \cos\theta)$, v neposlední řadě J je konstanta
izotropní magnetické výměny (členy obsahující tento parametr popisují izotropní
magnetickou interakci mezi dvěma/více magnetickými centry zprostředkovanou chemickými
vazbami případně přes prostor).

Molární magnetizace ve směru magnetického pole a může být potom vypočítána
v případě použití korekce na molekulové pole pomocí rovnice (4), nebo v případě absence
této korekce pomocí rovnice (5)

$$M_a = -N_A \frac{\sum_i \left(\sum_k \sum_l C_{ik}^+ (Z_a)_{kl} C_{li} \right) \exp(-\varepsilon_{a,i}/kT)}{\sum_i \exp(-\varepsilon_{a,i}/kT)} \tag{4}$$

$$M_a = N_A kT \frac{d\ln Z}{dB} \tag{5}$$

kde v rovnici (4) je Z_a maticový element Zeemanova členu pro směr magnetického pole a
a C jsou vlastní vektory získané diagonalizací kompletní matice spinového Hamiltoniánu, a
v rovnici (5) je Z tzv. partiční funkce.

Celková molární magnetizace práškového vzorku je spočítána jako integrál všech různých
orientací:

$$M_{mol} = 1/4\pi \int_0^{2\pi} \int_0^{2\pi} M_a \sin\theta d\theta d\varphi \tag{6}$$

Teplotní i polová závislost jsou analyzovány souběžně, aby bylo dosaženo lepších výsledků.

3.2. Analýza magnetických AC dat

Měření střídavé magnetické susceptibility (magnetická AC data) je jedním z nejdůležitějších měření, které mohou potvrdit chování látky jako SMM, samozřejmě kromě změření magnetické hystereze. Signál střídavé molární magnetické susceptibility v sobě obsahuje fázovou (reálnou, χ_{real}) a mimofázovou (imaginární, χ_{imag}) složku a je měřen jako funkce teploty a jako funkce frekvence oscilujícího magnetického pole (AC frekvence) v (ne)nulovém statickém magnetickém (DC) poli (Obr. 3 *vlevo*). Přítomnost nenulové
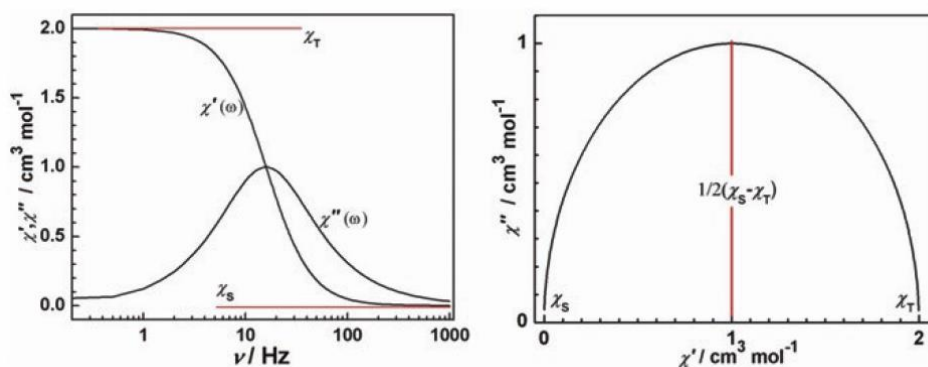
Obrázek 3 *Vlevo*: Reálná (χ_{real}) a imaginární (χ_{imag}) komponenta střídavé magnetické susceptibility jako funkce frekvence (ν) střídavého magnetického pole společně s indikací izotermické (χ_T) a adiabatické (χ_S) susceptibility. *Vpravo*: Argandův nebo Cole-Cole diagram jednoho relaxačního procesu charakterizovaného jediným relaxačním časem. Obrázek převzat z literatury.[24]

mimofázové složky bývá považována za důkaz SMM chování. Pokud je magnetický systém charakterizovatelný jedním relaxačním procesem popsaným jediným relaxačním časem $\tau = \omega^{-1} = 1/(2\pi\nu)$, bývá v Argandově diagramu (Cole-Cole diagram, závislost χ_{imag} na χ_{real}, Obr. 3 *vpravo*) pozorován půlkruh a matematicky může být systém popsán pomocí tzv. Debyeova modelu:

$$\chi_{ac}(\omega) = \chi_S + \frac{\chi_T - \chi_S}{1 + i\omega\tau} \tag{7}$$

který zavádí tzv. izotermální (χ_T) a adiabatickou (χ_S) susceptibilitu (Obr. 3), pomocí kterých je možné definovat fázovou i mimofázovou složku následujícím způsobem:

$$\chi_{real} = \chi_S + \frac{\chi_T - \chi_S}{1 + (\omega\tau)^2} \tag{8}$$

11

$$\chi_{imag} = \omega\tau \frac{\chi_T - \chi_S}{1 + (\omega\tau)^2} \tag{9}$$

Nicméně ve většině magnetických vzorků není relaxační proces charakterizován pouze jediným relaxačním časem, ale dochází k distribuci relaxačních časů a rovnice (7) může být přepsána do obecnějšího tvaru:

$$\chi_{ac}(\omega) = \chi_S + \frac{\chi_T - \chi_S}{1 + (i\omega\tau)^{1-\alpha}} \tag{10}$$

kde α představuje parametr distribuce relaxačních časů (dosahuje hodnot od 0 do 1, čím je větší, tím širší je distribuce časů).

Pro popis složitých relaxačních procesů v SMMs byly využity různé teorie relaxace – např. QTM nebo teorie spin-mřížkové relaxace. Druhá zmíněná teorie vychází z předpokladu, že spinový systém (paramagnetický ion) vyměňuje energii s vibrující mřížkou prostřednictvím fononů, a proto bývá relaxační čas často modelován pomocí níže uvedené rovnice:

$$\tau^{-1} = AH^m T + CT^n + \tau_0^{-1} \exp(-U_{eff}/kT) \tag{11}$$

kde parametry A, C a τ_0 jsou konstanty a první člen odpovídá jednofononovému přímému relaxačnímu procesu (H je intenzita aplikovaného vnějšího DC pole, $m = 4$ nebo 2 pro Kramersovy nebo ne-Kramersovy dublety), druhý člen odpovídá dvojfononovému Ramanovu relaxačnímu procesu zahrnující virtuální excitovaný stav (teoreticky $n = 7$ nebo 9 pro ne-Kramersovy nebo Kramersovy dublety, prakticky pozorované přijatelné hodnoty jsou $n \geq 4$) a třetí člen odpovídá dvojfononovému Orbachovu relaxačnímu mechanismu zahrnujícímu reálný excitovaný stav. Orbachův relaxační mechanismu uvažuje energetickou bariéru U_{eff}, diskutovanou výše, která bývá tak často zmiňována v souvislosti s SMMs. Z rovnice (11) ovšem vyplývá, že U_{eff} popisuje pouze jeden z možných relaxačních dějů a proto (i) existuje celá řada systémů s vysokou hodnotou U_{eff}, které ovšem nevykazují pomalou relaxaci magnetizace, protože ostatní relaxační mechanismy (přímý, Ramanův nebo QTM) výrazně urychlují proces relaxace magnetizace a snižují reálnou anizotropní bariéru, což může být omezeno modulací ligandového pole ve snaze o zvýšení axiální anizotropie, aplikací nenulového statického DC pole nebo tzv. magnetickým zředěním, (ii) existuje pomalá relaxace magnetizace v případě Co^{II} komplexů s kladným parametrem D (systém relaxuje pomocí přímého a Ramanova mechanismu).

4. Spinové křížení neboli spin crossover

Fenomén spinového křížení neboli spin crossover (SCO)[17] je jedním z nejpozoruhodnějších příkladů molekulární bistability, která může být chápána jako monomolekulární reakce mezi nízkospinovým (z angl. low-spin (LS)) a vysokospinovým (z angl. high-spin (HS)) izomerem především oktaedrických komplexů obsahujících centrální ion kovu s elektronovou konfigurací valenční vrstvy $3d^4$–$3d^7$ (na Obr. 4 ilustrováno pro železnatý komplex). Taková změna spinového stavu může být vyvolána určitými chemickými (efektu ligandů nebo rozpouštědla) a fyzikálními podněty jako jsou např. změna teploty, světelné ozářením (z angl. Light-Induced Excited Spin-State Trapping, LIESST),[36] změna vnějšího tlaku nebo magnetického pole.[12] Přechod elektronu(ů) z nevazebných t_{2g} orbitalů (LS stav) do protivazebných e_g orbitalů (HS stav) je doprovázen prodloužením vazebných vzdálenosti kov-ligand (Obr. 4). Taková objemová expanze moduluje mezimolekulové interakce a dává vznik tzv. kooperativnímu efektu,[17] který je odpovědný za strmost a kompletnost přechodu z LS do HS konfigurace (primárně pozorovaný v pevném stavu), jenž je obvykle doprovázen teplotní hysterezí.
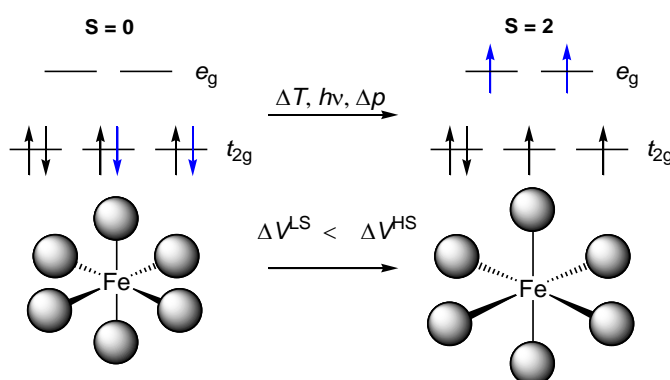
Obrázek 4 Změna elektronové konfigurace při přechodu z LS do HS stavu komplexu s centrálním atomem s elektronovou konfigurací d^6 (např. Fe^{II}) společně s expanzí objemu koordinačního polyedru.

Pro praktické využití sloučenin s SCO je potřeba: a) aby byl přechod strmý a měl kritickou teplotou přechodu ($T_{1/2}$, $x_{HS} = x_{LS} = 0.5$) okolo laboratorní teploty s širokou teplotní hysterezi (asi 50 K), b) aby byla změna měřené vlastnosti dostatečná (např. magnetický moment, barva) pro rozlišení mezi LS a HS stavem, c) aby byla dostatečná chemická stabilita materiálu a přechod byl dostatečně stabilní během následných opakujících se teplotních cyklů.[17,37] Když jsou tyto podmínky splněny, lze sloučeniny s SCO využít v mnoha pozoruhodných aplikacích včetně miniaturizace součástek používaných při konstrukci elektronických zařízení, jako jsou velkokapacitní paměti (na molekulární úrovni), molekulární přepínače nebo nízkoenergetické displeje (termochromismus).[17,38,39] Dnešní pokrok ve vývoji takových zařízení může být ilustrován na rychlém rozvoji v oblastech koordinačních nanočástic s SCO efektem nebo tenkých filmů.[4,40] Kromě toho, nejdůležitějším trendem v oblasti aplikací SCO se stal dizajn a výzkum nových hybridních funkčních materiálů[41]

kombinujících synergickým způsobem SCO s další zajímavou vlastností (magnetický kaplink, vlastnost kapalných krystalů, interakce „host-guest", nelineární optika, elektrická vodivost nebo luminiscence).[42] Na druhou stranu bylo nedávno publikováno, že spinový přechod pro Fe(II) komplex může být v roztoku vyvolán také chemickým činidlem.[43] Taková spinová odezva systému na přítomnost konkrétní chemické látky přináší velmi perspektivní aplikace, například detekci enzymů nebo enzymatických drah.

# 5. Syntéza makrocyklických ligandů

Makrocyklický ligand je definován jako sloučenina s devítičlenným nebo vícečlenným kruhem/cyklem (včetně heteroatomů), který v sobě obsahuje alespoň tři donorové atomy.[44] Do této skupiny patří celá řada strukturně odlišných sloučenin typu crownethery, porfyriny, ftalokyaniny, kryptandy, katenany a případně další sloučeniny spadající do oblasti makromolekulární a supramolekulární chemie.[45] Tato práce je ovšem zaměřena na azamakrocykly (makrocyklické ligandy obsahující dusíkové atomy), ve kterých mohou být některé atomu dusíku zaměněny za atomy kyslíku nebo síry.

Azamakrocyklické ligandy[46] se nejčastěji připravují pomocí tzv. templátové syntézy[47] nebo pomocí reakcí využívajících různé protektivní skupiny, především tedy Richman-Atkinsovu syntézu[48] (Obr. 5).

Schopnost iontů kovů ovlivňovat průběh organických reakcí byla známa již od 60. let. 20. století a její konkrétní podoba byla formulována jako tzv. efekt templátujícího kovu, který může být buď kinetický nebo termodynamický.[45] Kinetický efekt znamená, že iont kovu se koordinuje na reaktant(y) a vytvoří s ním(nimi) komplex o takové geometrii, která umožňuje/usnadňuje průběh následných reakcí vedoucí k takovému produktu, který by bez přítomnosti iontu kovu nevznikal. Kinetický efekt tedy ovlivňuje mechanismus reakce (dochází k aktivaci molekuly pomocí koordinace iontu kovu), kterým většinou vznikají cyklické produkty. Tento efekt byl především pozorován při reakcích, kdy dochází k uzavření cyklus v původním chelatovaném prekurzoru. Na druhou stranu termodynamický efekt znamená, že iont kovu se preferenčně koordinuje na jeden z více rovnovážných produktů reakce, a tím posunuje rovnováhu ve prospěch tohoto většinou cyklického produktu. V případě syntéz azamakrocyklů se jako templátujících iontů nejčastěji využívá Ni^{2+} a Cu^{2+}, nicméně bylo použito i Mn^{2+}, Fe^{2+}, Mg^{2+}, Zn^{2+}, Ba^{2+}, Pb^{2+} a dalších.[49] Faktorů, na kterých závisí, jaký vznikne výsledný produkt, je několik – elektronové (zařazení reaktantů mezi tvrdé a měkké kyseliny a báze, donor-akceptorové vlastnosti reaktantů obecně) a geometrické

faktory (rigidita reaktantů, meziproduktů apod.) ovlivňující stabilitu vznikajícího komplexu, chelátový efekt, makrocyklický efekt atd.[45,47]

Templátové reakce, z pohledu jejich mechanismu, nejčastěji zahrnují substituční alkylační reakce, kondenzace za vniku Schiffovy báze (iminy), Mannichovy kondenzační reakce, samokondenzace nitrilů případně tvorbu samouspořádáním (z angl. self-assembly).[45] Příkladem vzniku Schiffovy báze na templátujícím iontu je na Obr. 5 popsaná syntéza ligandu **15-pyN₃O₂**, který je stěžejním ligandem pro tuto habilitační práci.[50]
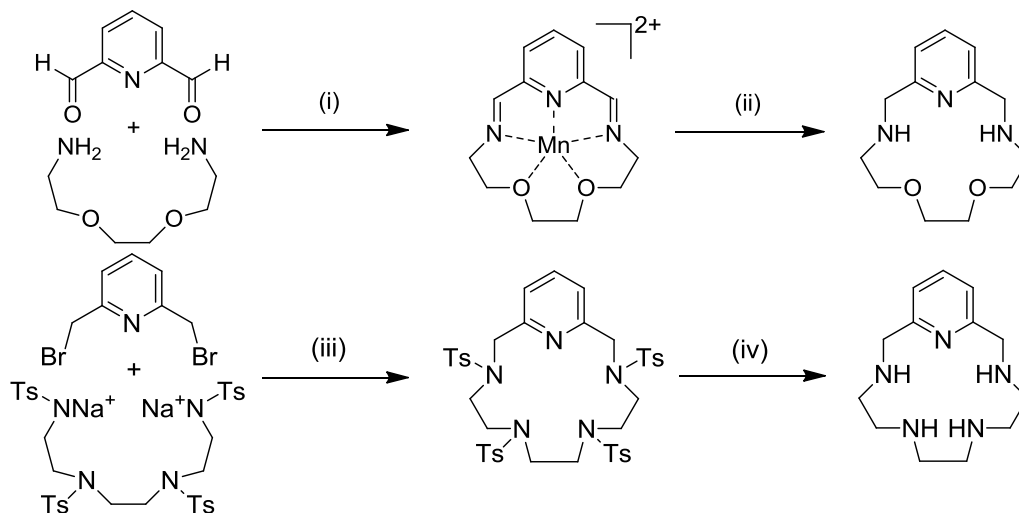
Obrázek 5 *Nahoře*: Příklad templátové syntézy ligandu **15-pyN₃O₂** diskutovaného dále v textu. (i) MnCl₂, MeOH, 60 °C, 2 h; (ii) 1. NaBH₄; 2. H₂O/O₂. *Dole:* Příklad Richman-Atkinsovy syntézy použité pro přípravu ligandu **15-pyN₅**: (iii) DMF, 130 °C, 16h; (iv) 96% H₂SO₄, 100 °C, 24h.[50]

Richman-Atkinsova syntéza využívá reakci halogenidu s bis(sulfonamidovou) solí ve vysokém zředění (Obr. 5). Amin se běžné chrání pomocí různých sulfonových skupin (*p*-toluensulfonyl = tosyl (Ts), methylsulfonyl = mesyl (Ms), *o*- nebo *p*-nitrobenzensulfonyl = nosyl (Ns), 5-dimethylamino-1-naftalensulfonyl = dansyl (Dns)) za vzniku sulfonamidu, protože tyto poměrně objemné chránící skupiny podporují v podmínkách velkého zředění vznik makrocyklického produktu oproti acyklickému polymeru. Následně byl tento postup modifikován tak, že byl halogenid nahrazen estersulfonovou skupinu (OTs, OMs) a bis(sulfonamidová) sůl byla generována *in situ* přídavkem báze (nejčastěji bezvodým K₂CO₃), což poskytlo vyšší výtěžky cyklických produktů.[46,51] Touto metodou byly připraveny 9–24členné makrocykly s 3–7 heteroatomy bez použití templátujícího iontu kovu,[46] ovšem odstranění chránících skupin, především potom tosylové skupiny, vyžaduje poměrně drastické reakční podmínky (typicky koncentrovaná H₂SO₄ za teploty 160–180 °C),[52] které mohou způsobit až štěpení a degradaci cyklu.

Kromě studovaného ligandu **15-pyN₃O₂** byla výše popsanými syntetickými metodami připravena také celá řada ligandů diskutovaných v následujících kapitolách (např. základní a nejdůležitější makrocykly jako tacn, cyklen a cyklam, viz Obr. 6).

6. Komplexní sloučeniny vykazující SCO

Makrocyklické ligandy byly použity v komplexech s SCO již od začátku výzkumu v této oblasti. Nejvíce byly zkoumány komplexy Fe^{II}, ale značná pozornost byla také věnována komplexům Fe^{III}, Mn^{III} nebo Co^{II}. Knižní trilogie v „Topics in Current Chemistry" o fenoménu SCO komplexně shrnula vývoj v této oblasti až do roku 2004.[17] V poslední době bylo publikováno také několik přehledových článků a knih popisujících SCO komplexy nejen makrocyklických ligandů.[2,39,53] Stručné shrnutí dříve studovaných komplexů je uvedeno níže.

6.1. Fe^{II} komplexy

Nejznámější Fe^{II} komplexy s makrocyklickými ligandy vykazující SCO mají v pevném stavu spíše postupný tepelný spinový přechod, který je podobný přechodům běžně pozorovaným spíše v roztocích (značí nízkou kooperativitu). Spinové stavy těchto systémů jsou primárně určovány silou ligandového pole vytvořeného první koordinační sférou ligandu, která úzce koreluje s hodnotou teploty přechodu $T_{1/2}$. Silně bazické alifatické aminy jsou lepšími σ-donory a obvykle tvoří HS komplexy ve srovnání s heterocyklickými aminy (π-akceptory), které často poskytují LS nebo SCO komplexy. Proto většina SCO komplexů s Fe^{II} zahrnuje polydentátní ligandy kombinující jak *N*-heterocyklické, tak alifatické aminové skupiny, zejména pyridin je preferovaná skupina přítomná téměř v 90 % systémů z oblasti SCO.

Více než třináctičlenné tetradentátní tetraazamakrocykly se koordinují na ion kovu v rámci ekvatoriální roviny (konfigurace *trans*) a SCO komplexy byly připraveny s jedním izomerem hexamethylcyklamu **A1** (Obr. 6) studovaným Bushem a spolupracovníky[54] a s dvakrát záporně nabitou N4 makrocyklickou Schiffovou bází **A3** ($T_{1/2}$ se mění se substituentem R1-R3 = H, Me nebo karboxylát).[55] Na rozdíl od výše uvedeného byla u koordinujících se 12-členných tetraazacyklů pozorována *cis* geometrie v SCO komplexech s **A2a–A2c**.[17,53] Další známou třídou N4 ligandů jsou porfyriny a ftalocyaniny, které tvoří velkou skupinu různých komplexů, jejichž popis je však nad rámec toto krátkého shrnutí. Pentadentátní ligand **A4a** s jedním SCN⁻ poskytly Fe^{II} komplex v LS stavu, když byl NH proton nahrazen benzylovou skupinou (**A4b**),[17] vznikal již SCO komplex. Zajímavé vlastnosti byly nalezeny pro komplexy Schiffových bází **15-pydienN₃O₂** a **15-pydienN₅** s koordinačním
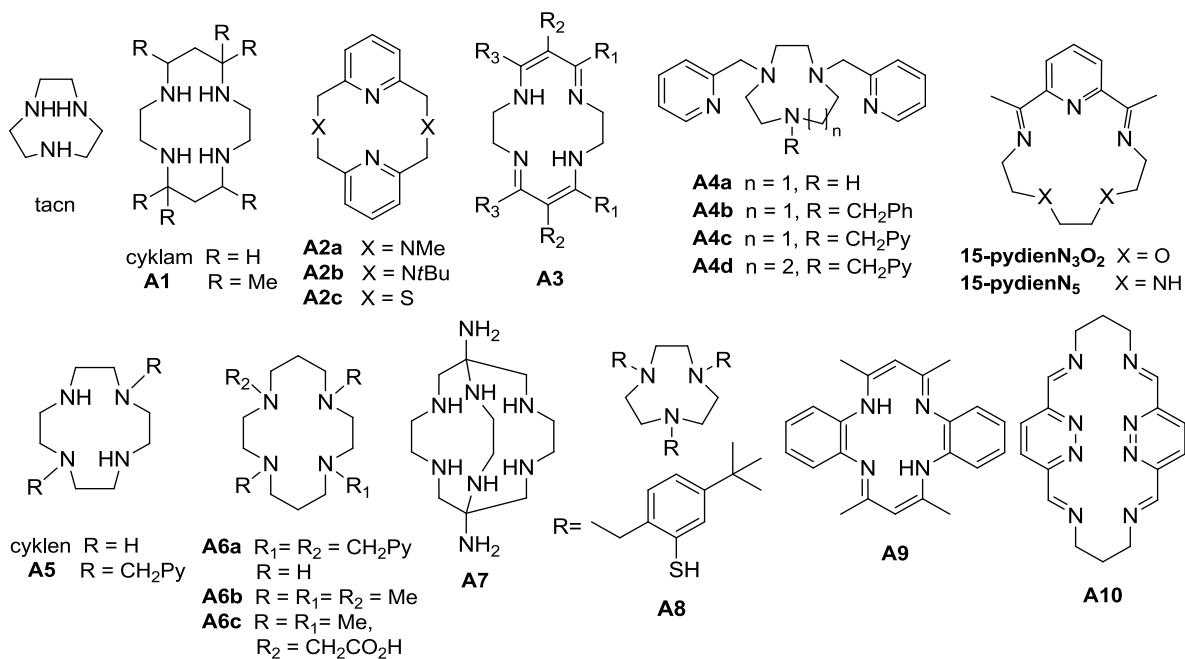
Obrázek 6 Strukturní vzorce dříve studovaných makrocyklických ligandů v SCO komplexech přechodných kovů.

číslem sedm a se dvěma kyanidovými ionty v axiálních polohách. Oba studované komplexy [Fe(**15-pydienN₃O₂**)(CN)₂].H₂O[56,] a [Fe(**15-pydienN₅**)(CN)₂].H₂O[57] vykazovaly SCO efekt spojený navíc se změnou spinového stavu indukovanou světelným ozářením ($T_{(LIESST)}$ = 135 K pro první zmiňovaný komplex, $T_{(LIESST)}$ = 105 K pro druhý komplex) zapříčiněnou disociací jedné vazby mezi atomem Fe a atomem kyslíku/dusíku z etherové/aminové funkční skupiny v LS formě s koordinačním číslem šest.[58,59] Hexadentátní ligandy jsou většinou odvozeny od menších makrocyklů (tacn, cyklen, cyklam, Obr. 6) modifikovaných různými pendantními rameny. Silné ligandové pole způsobené **A4c**[60] v LS komplexech bylo sníženo expanzí makrocyklického kruhu o jednu přidanou CH₂ skupinu v **A4d**, se kterým vznikal SCO komplexu ($T_{1/2}$ = 282 K v roztoku propionitrilu).[61] Dalšího způsobu jemného ladění intenzity ligandového pole bylo dosaženo zavedením methylové skupiny (sterický efekt) do polohy 6 jednoho z pyridinových ramen.[17] Nedávno byly zkoumány deriváty cyklenu (**A5**) a cyklamu (**A6a**) modifikované 2-pyridylmethylovým ramenem v protějších polohách, avšak pouze komplex cyklamového derivátu vykazoval SCO přechod ($T_{1/2}$ ~ 150 K).[2,62,63] Unikátní řada klecových ligandů (**A7**) umožňující enkapsulaci Fe[II] byla vyvinuta Martinem et al. (spinový přechod pozorován pouze v roztoku).[64] Zatím není známo, že by existovaly SCO komplexy s více než hexadentátními makrocyklickými ligandy.

6.2. Fe^{III} komplexy

Existuje pouze několik příkladů Fe^{III} komplexů s makrocyklickými ligandy, které vykazují SCO. Pro [Fe(cyklam)Br$_2$](ClO$_4$) byly pozorovány dvě sady EPR signálů jejichž relativní intenzity závisely na teplotně (Cl$^-$ i SCN$^-$ koligandy vytvářely LS komplex).[65] Přechod $S = 1/2 \leftrightarrow S = 3/2$ (dokumentováno EPR a ^{57}Fe Mössbauerovými spektry) byl pozorován pro Fe^{III} komplex (deformovaná tetragonální pyramida) tetra-*N*-methylovaného cyklamu (**A6b**) s NO v apikální poloze.[66] Dále bylo zjištěno, že komplex s tri-*N*-methylovaným cyklamem s jedním acetátovým pendantním ramenem (**A6c**) a s koordinovaným azidovým aniontem prochází neúplným spinovým přechodem (60% vzorku zůstává HS stavu).[67] Zajímavým příkladem byl Fe^{III} komplex s deprotonizovaným ligandem **A8**, který obsahoval FeN$_3$S$_3$ chromofor a u kterého byl pozorovaný postupný a nekompletní SCO ani při 500 K.[68]

6.3. Komplexy ostatních iontů kovů

Jedním příkladem SCO komplexu s jinými ionty kovů je manganitý komplex obsahující porfyrinovou jednotku,[69] který v pevném stavu podléhá postupnému SCO při teplotě klesající pod teplotu laboratorní. Druhým příkladem je nitrosylový manganitý komplex s **A9** (H$_2$tmtaa = dibenzotetramethyltetraaza[14]anulen) s neúplným neobvyklým přechodem $S = 2 \leftrightarrow S = 0$ ($T_{1/2}$ = 213 K).[70] Začlenění můstkujících pyridazinových jednotek poskytlo planární ligand **A10** tvořící dvojjaderný systém s Co^{II}. Komplex s SCN$^-$ a MeCN jako axiálními ligandy prochází neúplným pozvolným spinovým přechodem s antiferomagnetickou výměnnou magnetickou interakcí.[71] Podobným neúplným postupným spinovým přechodům podléhala také série kobaltnatých komplexů s ligandy **A2a** (obsahující navíc koligand 3,5-di-*terc*-butyl-1,2-dioxolen nebo dva koligandy SCN$^-$) a **A2b** (dva koligandy SCN$^-$).[53]

7. Magnetické vlastnosti komplexů s koordinačním číslem sedm

7.1. Komplexy přechodných kovů s koordinačním číslem sedm

Velká skupina mononukleárních 3d-SMMs sestává většinou z komplexů s nižšími koordinačními čísly (v rozmezí mezi 2–6, nejčastěji ovšem 4 a 5),[8] a proto komplexy s koordinačním číslem 7 představují relativně malou, ale o to více zajímavou skupinu sloučenin.[72] Počet takových sloučenin nicméně rychle roste, a proto jsou dále uvedeny pouze nejnovější výsledky. Komplexy s koordinačním číslem 7 a pentagonálně bipyramidální geometrií byly ve většině případů studovány s následujícími ionty kovů: Mn^{II}, Fe^{II}, Co^{II}, Ni^{II},[73] a nejnověji také s Mo$^{III/IV}$,[74,75] nebo Cr^{III},[76] a s následujícími ligandy typu

polyaminů/polyoxaaminů nebo Schiffových bází s necyklickou, např. **B1**[77,78,79,80] nebo makrocyklickou strukturou, např. **15-pydienN₃O₂**,[73] **15-pydienN₅** (Obr. 6),[73] **B2**,[81] **B3**,[82] **B4**[83] a **B5**[84] (Obr. 7). Nikelnaté a železnaté komplexy jsou většinou charakteristické svou velkou magnetickou anizotropií typu lehké osy ($D < 0$) a u některých jednojaderných komplexů byla dokonce pozorována pomalá relaxace magnetizace, např. [Fe(H₂**B1a**)Cl₂][79] a [Fe(H₂**B1c**)Cl₂].[80] Oproti tomu kobaltnaté komplexy představují největší a asi nejvíce prozkoumanou skupinu komplexů s koordinačním číslem 7 a jsou charakteristické vysokou mírou magnetické anizotropie typu lehké roviny ($D > 0$). Navzdory kladné hodnotě parametru D, která dle teorie neumožňuje vznik energetické bariéry U_{eff} a nedovoluje pomalou relaxaci magnetizace, mnoho kobaltnatých komplexů ovšem takovou relaxaci vykazuje a chovají se jako SMMs, např. [Co(**15-pydienN₅**)(H₂O)₂]Cl₂,[85] [Co(H₂**B1a**)(H₂O)NO₃]NO₃,[85,86] [Co(**B1a**)(imidazole)₂],[85] [Co(H₂**B1a**)(NCS)₂],[87] [Co(**B1a**)(H₂O)₂],[87] [Co(**B4**)(X)₂]$^{2+/0}$ (X = H₂O, CN⁻, NCS⁻, SPh⁻),[83] [Co(**15-pydienN₃O₂**)(CH₃CN)₂](BPh₄)₂.[88]
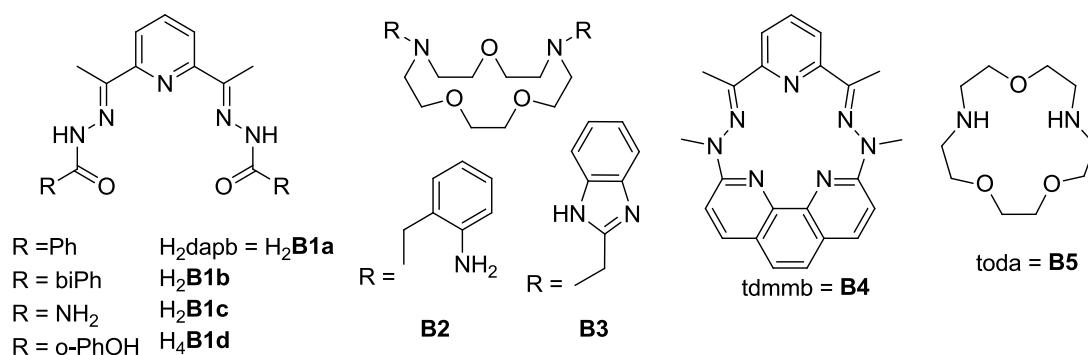
Obrázek 7 Strukturní vzorce dříve studovaných acyklických/makrocyklických ligandů v komplexech s koordinačním číslem 7.

Pozorování pomalé relaxace magnetizace pro Kramersovy ionty s dominantní anizotropií typu lehké roviny, jako je právě Co²⁺, vysvětlili E. Ruiz, F. Luis a spolupracovníci v roce 2014[30] a navrhli několik mechanismů pro proces relaxace magnetizace (přímý, Orbachův, Ramanův nebo kvantové tunelování magnetizace – QTM, viz kapitola 3.2).[3] Míra příspěvku každého mechanismu k celkovému relaxačnímu procesu je stále otázkou debat a zůstává otevřenou výzvou pro magnetochemiky, kteří se snaží nalézt odpověď s pomocí sofistikovaných technik, jako je např. infračervená spektroskopie v proměnlivém magnetickém poli nebo HF-EPR (z angl. High-Frequency Electron Paramagnetic Resonance).[89] U těchto Co^II komplexů byla pozorována pomalá relaxace magnetizace pouze v přítomnosti malého vnějšího magnetického (DC) pole, které muselo být aplikováno za účelem potlačení QTM, a proto se tyto sloučeniny nazývají polem indukované SMMs.

Jak bylo dříve publikováno, ve snaze o vylepšení vlastností SMMs může být magnetická anizotropie úspěšně laděna pomocí adekvátních („na míru") změn elektronové struktury centrálního atomu kovu způsobené výměnou donorových atomů ligandu a/nebo změnou koordinačních čísel a geometrie komplexu. Tento přístup byl úspěšně použit v pseudotetraedrických komplexech $[Co^{II}(A)_2I_2]$ (A = chinolin, PPh$_3$, AsPh$_3$)[90] a $[Co^{II}(APh)_4]^{2-}$ (A = O, S, Se),[91] $[Co(L_1)_2X_2]$ (L$_1$ = tetramethylthiomočovina, X = Cl$^-$, Br$^-$, I$^-$)[92] nebo trigonálně-bipyramidální komplexech $[Co^{II}(NS_3^{tBu})X]ClO_4$ (X = Cl$^-$, Br$^-$, NCS$^-$; NS$_3^{tBu}$ = 2-(*terc*-butylthio)-*N*-(2-(*terc*-butylthio)ethyl)-*N*-((neopentylthio)methyl)ethan-1-amin),[93] ve kterých přítomnost těžšího a měkčího (ve smyslu Pearsonovy teorie) donorového atomu vedla ke zvýšení magnetické anizotropie (více negativní hodnoty parametru *D*) a k pozorování SMM chování i v nulovém externím magnetickém poli.

V případě Co^{II} komplexů s koordinačním číslem 7 s pentagonálně bipyramidální geometrií predikovaly teoretické výpočty, týkající se příspěvků excitovaných magnetických stavů k hodnotě parametru *D*, nejvyšší magnetickou anizotropii takových komplexů, které mají v axiálních polohách koordinované slabé σ-donory a více symetrické ligandové pole v ekvatoriální pentagonální rovině.[77] Úspěch tohoto přístupu (variace axiálních koligandů) byl potvrzen v Co^{II} komplexech [Co(H$_2$**B1a**)(NCS)$_2$] a [Co(**B1a**)(H$_2$O)$_2$],[87] a nejnověji také v [Co(**B4**)(X)$_2$]$^{2+/0}$, kde X = H$_2$O, CN$^-$, NCS$^-$, SPh$^-$,[83] a v sérii komplexů [Co(H$_2$**B1d**)(CH$_3$OH)$_2$], [Co(H$_4$**B1d**)(CH$_3$OH)(NCS)]ClO$_4$, [Co(H$_4$**B1d**)(NCS)$_2$],[94] ačkoli účinek nebyl tak dramatický jako pro pseudotetraedrické komplexy diskutované výše.

Komplexy přechodných kovů (především Mn^{II}, Fe^{II}, Co^{II} a Ni^{II}) s ligandy **15-pydienN$_3$O$_2$**, **15-pydienN$_5$** a dalšími uvedenými na Obr. 7 byly dříve také použity jako anizotropní stavební bloky a byly intenzivně studovány v souvislosti s magnetickými výměnnými interakcemi ve vícejaderných komplexech s různými kyanometaláty ($[M^I(CN)_2]^-$, $[M^{II}(CN)_4]^{2-}$, $[M^{III}(CN)_6]^{3-}$, $[M^{IV}(CN)_8]^{4-}$, M^I = Ag, Au; M^{II} = Ni, Pd, Pt; M^{III} = Fe, Cr; M^{IV} = Nb, Mo, W) nebo jinými můstkujícími skupinami.[73] Velká část z nich se chovala jako SMMs nebo SCMs, např. {[Ni(**B1a**)]$_3$[W(CN)$_8$]$_2$},[78] {[{Fe(**15-pydienN$_3$O$_2$**)(H$_2$O)}$_2${Cr(CN)$_6$}](ClO$_4$)}$_n$,[95] [{(H$_2$O)Fe(**15-pydienN$_5$**)}{Nb(CN)$_8$}{Fe(**15-pydienN$_5$**)}]$_n$,[96] {[Fe(**B1a**)][Ni(CN)$_4$]}$_n$,[79] {[Co(**B4**)(bpe)](BF$_4$)$_2$}$_n$ (bpe = 1,2-bis(4-pyridyl)ethan),[97] {[Co(**B5**)]$_3$[M(CN)$_6$]$_2$}$_n$ (M^{III} = Co, Cr),[84]

7.2. Komplexy lanthanoidů s koordinačním číslem sedm

Navzdory nedávnému pokroku v chemii metalocenů lanthanidů, který poskytl SMMs s rekordními blokovacími teplotami,[31,32,98] zůstávají pentagonálně bipyramidální komplexy

především Dy[III] s koordinačním číslem 7 stále velmi zajímavými kandidáty pro další výzkum jejich vlastností jako SMMs/SIMs.[99] Vykazují velmi vysoké hodnoty energetické bariéry U_{eff} a poskytují, kromě metalocenů, nejlepší blokovací teploty. Ideální symetrie D_5h (ve skutečnosti se blíží lineárnímu uspořádání) okolo Dy[III] poskytuje vhodné krystalové pole způsobující pro Kramersovy dublety silnou axiální anizotropii.[100] Redukce příčné složky anizotropie je odpovědná za minimalizaci QTM, které může způsobit vymizení SMM chování i pro systémy s vysokými energetickými bariérami. Velký zájem o tuto skupinu sloučenin se datuje od roku 2016.[101] Od té doby byly prostudovány různé komplexy Dy[III] s koordinačním číslem 7 obvykle založené na jednoduchých monodentátních ligandech, např. fosfin-oxidu,[102] alkoxidu,[103] pyridinu[103] nebo polydentátních ligandech s otevřeným řetězcem.[101,104] Nicméně komplexům lanthanoidů s makrocyklickými ligandy byla věnována jen velmi malá pozornost, protože doposud bylo studováno jen několik příkladů obsahujících např. **15-pydienN5**,[105] **15-pydienN3O2**,[106] nebo derivát cyklenu (tetra(3,5-dimethyl-2-hydroxybenzyl)-1,4,7,10-tetraazacyklododekan).[107]

8. Ladění magnetické anizotropie I: komplexy s 15-pyN₃O₂

Na začátku výzkumu systémů s makrocyklickým ligandem **15-pyN₃O₂** (Obr. 5 a 8) bylo potřeba zjisti, jaké jsou konkrétní strukturní a magnetické vlastnosti komplexů vybraných 3d přechodných kovů s ligandem **15-pyN₃O₂**, protože do té doby byla známa pouze molekulová struktura dvou pentagonálně bipyramidálních manganatých komplexů [Mn(**15-pyN₃O₂**)(H₂O)Cl](ClO₄) a [Mn(**15-pyN₃O₂**)(Cl)₂][Mn(**15-pyN₃O₂**)(H₂O)Cl]Cl·1.5H₂O,[50] které byly zkoumány pro své využití v MRI, a předpokládala se podobnost s dalšími komplexy Schiffových bází **15-pydienN₃O₂** a **15-pydienN₅** popsanými v předchozí kapitole. Z tohoto důvodu byla nejdříve připravena série komplexů [M[II](**15-pyN₃O₂**)Cl₂], kde M = Mn (**1a**), Co (**1c**), Ni (**1d**), Zn (**1f**), [Fe[III](**15-pyN₃O₂**)Cl₂]Cl (**1b**) a [Cu[II](**15-pyN₃O₂**)Cl]Cl (**1e**)
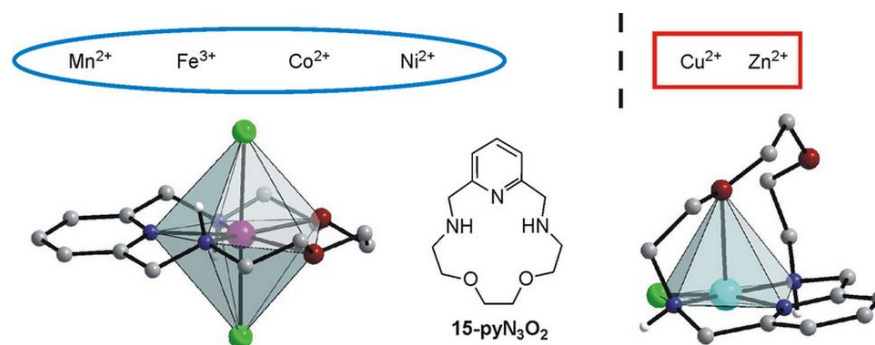

Obrázek 8 Molekulová struktura **1a** (*vlevo*) a [Cu[II](**15-pyN₃O₂**)Cl]⁺ (*vpravo*) společně se znázorněním koordinačního polyedru nalezeného pro komplexy kovů popsaných v horním řádku a se strukturním vzorem použitého ligandu **15-pyN₃O₂** (*uprostřed*).

s jednoduchými chloridovými koligandy (příloha **P1**), u nichž bylo zjištěno koordinační číslo 7 (Mn, Fe, Co), 5+2 (Ni) a dále 4+1 (Cu) a 5 (Zn) (Obr. 8).

Při zmenšování iontového poloměru komplexovaného kovu začala být makrocyklická kavita příliš „veliká" a docházelo ke zkroucení makrocyklického skeletu, k prodlužování vazeb M–O (vedoucí až k úplné dekoordinaci obou kyslíkových atomů v zinečnatém komplexu **1f**) a tomu odpovídajícímu snížení koordinačního čísla ze 7 nebo 5+2 na 5 nebo 4+1, které bylo doprovázeno změnou geometrie z axiálně prodloužené pentagonálně bipyramidální (**1a**, **1b**, **1c**, **1d**) na čtvercově planární (**1e**, **1f**). Kvůli neobvykle dlouhým vzdálenostem M–O byl jejich vazebný charakter prozkoumán pomocí teoretických výpočtů (Mayerův řád vazby, elektronová lokalizační funkce), které potvrdily (i) semikoordinaci dvou atomů kyslíku v případě nikelnatého komplexu **1d** (M–O vzdálenosti 2.506 a 2.663 Å) díky silnému Jahn-Tellerovu efektu, (ii) semikoordinaci jednoho atomu kyslíku v případě měďnatého komplexu **1e** (M–O vzdálenost 2.721 Å), (iii) kompletní dekoordinaci jednoho nebo dvou atomů kyslíku v měďnatém resp. zinečnatém komplexu **1e** resp. **1f**. Aby bylo možné postihnout nejen parametry magnetické anizotropie, ale i také případnou intermolekulární magnetickou výměnu, bylo pro fitování magnetických DC dat využito různých modelů spinového Hamiltoniánu (pro monomerní komplex, dimerní komplex nebo 1D polymerní řetězec, viz kapitola 3.1). Výsledky pro nejlepší fit s posledním z nich ($\hat{H}^{1D}$ popsán rovnicí (3)) jsou uvedeny v Obr. 9. Manganatý a železitý komplex **1a** a **1b** vykazovaly zanedbatelnou magnetickou anizotropii (parametr D nebyl ve fitu uvažován), zatímco pro kobaltnatý a nikelnatý komplex **1c** a **1d** byl parametr D poměrně velký ($D(\text{Co}) \approx 40$ cm^{-1}, $D(\text{Ni}) \approx -6.0$ cm^{-1}). U nikelnatého a měďnatého komplexu **1d** a **1e** byla pozorována slabá antiferomagnetická výměnná interakce ($J_{\text{Ni-Ni}} = -0.48$ cm^{-1}, $J_{\text{Cu-Cu}} = -2.43$ cm^{-1})

	J / cm^{-1}	g	D/ cm^{-1}	E/D	χ_{TIP} / 10^{-9} m^3 mol^{-1}
Mn	−0.051	2.05	–	–	–
Fe	−0.16	2.05	–	–	9.5
Co	−0.018	2.48[a]	40.0	–	10
Ni	−0.48	2.27	−6.02	0.15	–
Cu	−2.43	2.03	–	–	0.5

[a] odpovídá g_{xy}, g_z fixováno na 2.0
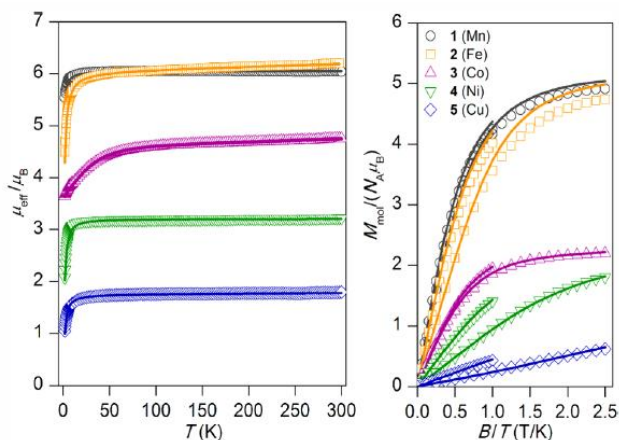
Obrázek 9 Výsledky analýzy magnetických DC dat (*tabulka*). Magnetická data pro studované komplexy: teplotní závislost efektivního magnetického momentu (*uprostřed*) a izotermální molární magnetizace měřené při 2 a 5 K (*vpravo*). Plné čáry odpovídají nejlepšímu fitu podle rovnice (3).

zprostředkovaná vodíkovými vazbami (především NH···Cl nebo CH···Cl). Nakonec byly ještě pomocí cyklické voltametrie nalezeny kvazireverzibilní dvojce Mn$^{(II)/(III)}$ při potenciálu 1.13/0.97 V a téměř reverzibilní dvojce Fe$^{(II)/(III)}$ při 0.51/0.25 V (rozpouštědlo acetonitril).
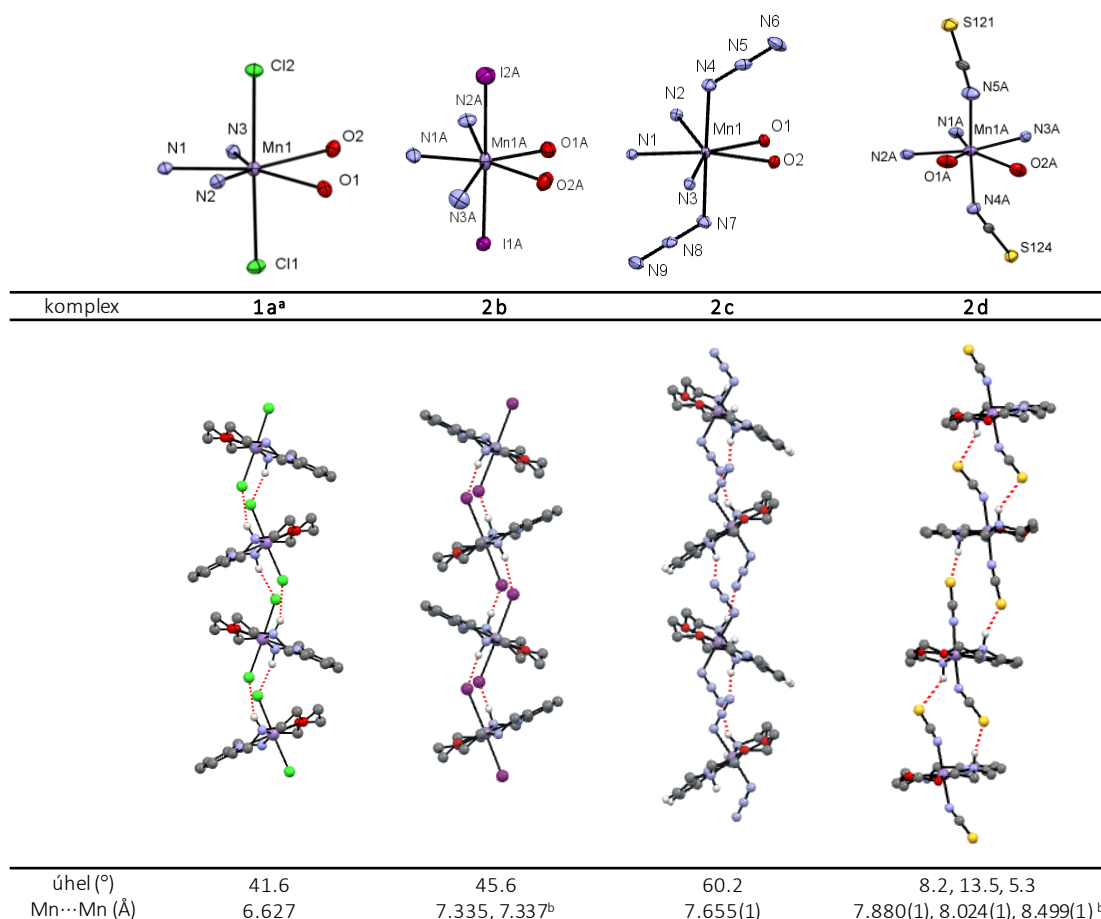
Z této prvotní studie byla získány důležité informace, a to, že (i) **15-pyN₃O₂** vytváří s Mn^{II}, Fe^{III}, Co^{II} a Ni^{II} pentagonálně bipyramidální komplexy, ve který se makrocyklický ligand koordinuje v pentagonální ekvatoriální rovině a axiální polohy jsou obsazeny halogenidovými koligandy, (ii) z hlediska dalšího zkoumání magnetických vlastností budou především vhodné komplexy Co^{II} a Ni^{II}, zatímco komplexy Cu^{II} a Zn^{II} nemají žádnou zajímavost pro výzkum SMMs.

V rámci dalšího studia byla tedy pozornost zaměřena na pentagonálně bipyramidální komplexy s koordinačním číslem 7. Jak bylo uvedeno v kapitole 7, magnetické vlastnosti pentagonálně bipyramidálních komplexů s jinými ligandy byly zkoumány již dříve a bylo zjištěno, že pokud se pentadentátní ligand (acyklický nebo makrocyklický) váže v pentagonální rovině, jednovazné koligandy v axiálních polohách mohou být jednoduše vyměňovány (Obr. 10), čímž může být ovlivňována síla axiálního ligandového pole, a to může mít zásadní vliv na velikost magnetické anizotropie.[77]
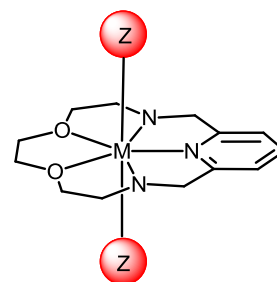
Obrázek 10 Ilustrace použití první strategie ladění magnetické anizotropie na komplexech s **15-pyN₃O₂** a různými monodentátními axiálními koligandy (Z).

V rámci dalšího zkoumání komplexů s **15-pyN₃O₂** byla použita výše zmíněná strategie ladění (zvýšení) magnetické anizotropie, a to výměna koligandů v axiálních pozicích pentagonálně bipyramidálních komplexů (Obr. 10). Nejdříve byla připravena série manganatých komplexů [Mn(**15-pyN₃O₂**)X₂] (X = Br$^-$ (**2a**), I$^-$ (**2b**), N₃$^-$, (**2c**), NCS$^-$ (**2d**)) a polymerní komplex {[Mn(**15-pyN₃O₂**)(μ-CN)](ClO₄)}ₙ (**2e**) (příloha P2), především kvůli dobré syntetické dostupnosti a získání informací a zkušeností s použitým typem substitučních reakcí koligandů, přestože pro vysokospinový systém s elektronovou konfigurací 3d^5 se neočekávala výraznější magnetická anizotropie. Všechny komplexy měly koordinační číslo 7 s geometrií pentagonální bipyramidy a díky vodíkovým vazbám NH···X tvořily supramolekulární 1D řetězce (Obr. 11).

komplex	1aᵃ	2b	2c	2d
úhel (°)	41.6	45.6	60.2	8.2, 13.5, 5.3
Mn⋯Mn (Å)	6.627	7.335, 7.337ᵇ	7.655(1)	7.880(1), 8.024(1), 8.499(1) ᵇ

Obrázek 11 *Nahoře*: Molekulární struktura koordinační sféry Mn^{II} v diskutovaných komplexech. *Dole*: Část krystalové struktury studovaných komplexů znázorňující průběh vodíkových vazeb, díky kterým se tvoří 1D supramolekulární řetězce společně s dalšími parametry (úhlem mezi rovinami proloženými atomy MnN_3O_2 a zjištěnou vzdáleností Mn⋯Mn v rámci 1D řetězce). ᵃ data převzata z P1. ᵇ 2 nebo 3 krystalograficky nezávislé molekuly byly nalezeny v asymetrické jednotce komplexu **2b** nebo **2d**.

Z hlediska magnetických vlastností se Mn^{II} komplexy opravdu ukázaly jako nepříliš zajímavé, protože vykazovaly velice malou magnetickou anizotropii ($|D| < 0.7$ cm^{-1}). Za zmínku stojí jen poslední komplex **2e**, protože průběh izotermálních molárních magnetizací odpovídal jeho předpokládanému polymernímu charakteru a navíc můstkující kyanidový ligand zapříčinil přítomnost slabé antiferomagnetické výměnné interakce $J_{\text{Mn-Mn}} = -1.72$ cm^{-1} potvrzené teoretickým výpočtem (Obr. 12).
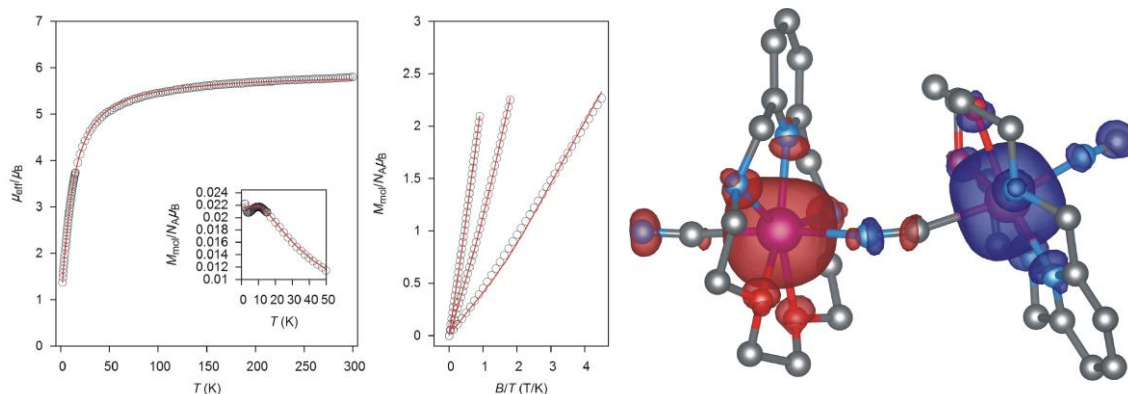
Obrázek 12 Teplotní závislost efektivního magnetického momentu (*vlevo*), teplotní závislost molární magnetizace měřené při $B = 0.1$ T (*inset*) a redukované izotermální mol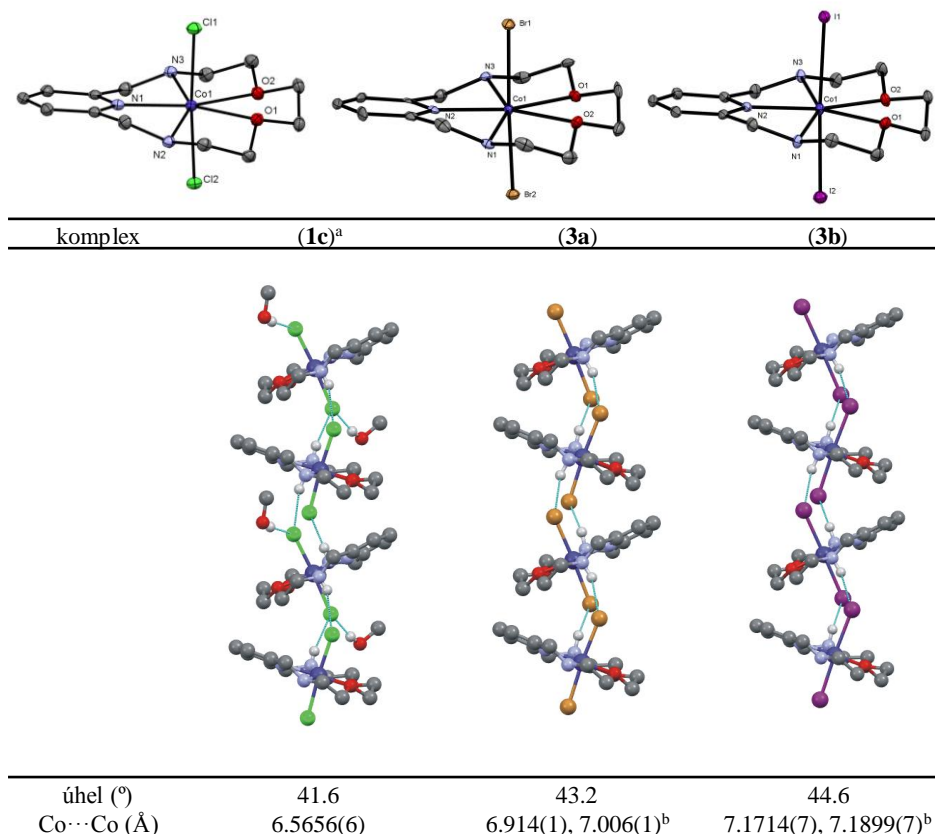ární magnetizace měřené při 2, 5 a 10 K (*uprostřed*). Černé body reprezentují naměřená data a červené křivky nejlepší fit s parametry $J = -1.72(1)$ cm^{-1}, $g = 1.992(2)$, $x_{PI} = 1.3(1)$ %. DFT optimalizovaná geometrie fragmentu [(CN)(**15-pyN$_3$O$_2$**)Mn(μ-CN)Mn(**15-pyN$_3$O$_2$**)(CN)]$^+$ komplexu **2e** a vypočítané plochy kladné (modrou barvou) a záporné (červenou barvou) spinové hustoty (*vpravo*).

Následně byly vyměňovány axiální koligandy u komplexů kobaltnatých, protože v té době bylo zjištěno,[29,30] že se právě kobaltnaté komplexy velmi často chovají jako polem indukované SMMs navzdory kladné hodnotě parametru *D*, pro kterou nebyla relaxace magnetizace vůbec předpokládána. Proto byla připravena série kobaltnatých komplexů [Co(**15-pyN$_3$O$_2$**)X$_2$], s různými halogenidovými koligandy X = Cl$^-$ (**1b**), Br$^-$ (**3a**), I$^-$ (**3b**) (příloha P3). Ve všech třech komplex měl centrální atom kobaltu opět koordinační číslo 7 s geometrií pentagonální bipyramidy (Obr. 13 *nahoře*). Analogicky jako manganaté komplexy diskutované výše (Obr. 11) tvořily kobaltnaté komplexy 1D supramolekulární řetězce pomocí NH···X vodíkových vazeb (Obr. 13 *dole*).

V tomto případě už ale podle očekávání byla zjištěna velká magnetická anizotropie typu lehké roviny, kdy kladný parametr *D* narůstal v pořadí **3b** < **1b** < **3a** tj, 35 cm^{-1} (I$^-$) < 38 cm^{-1} (Cl$^-$) < 41 cm^{-1} (Br$^-$). Tento trend ovšem neodpovídal očekáváním založeným na dříve provedených teoretických výpočtech,[77] a to že s těžším halogenidovým aniontem by se měla snižovat síla axiálního ligandového pole (dle spektrochemické řady) a hodnota parametru *D* by měla narůstat. Na základě výpočtů AOM (z angl. Angular Overlap Model), DFT (z angl. Density Functional Theory), CASSCF/NEVPT2 a CASSCF/CASPT2 (z angl. Complete Active Space Self-Consistent Field/ N-Electron Valence second order Perturbation Theory/ Complete Active Space Perturbation Theory) se ovšem ukázalo, že v případě koordinace těžšího halogenidu začíná narůstat příspěvek kovalence, který způsobuje zvyšování síly vazby. Díky tomu lze vysvětlit největší hodnotu *D* parametru pro komplex **3a** s bromidovými koligandy, protože hodnoty parametru *D* dobře korelují se snižujícím se Mayerovým řádem vazby v pořadí Co−I > Co−Cl > Co−Br.

komplex	(1c)[a]	(3a)	(3b)
úhel (°)	41.6	43.2	44.6
Co···Co (Å)	6.5656(6)	6.914(1), 7.006(1)[b]	7.1714(7), 7.1899(7)[b]

Obrázek 13 *Nahoře*: Molekulární struktura koordinační sféry Co^{II} v diskutovaných komplexech. *Dole*: Část krystalové struktury studovaných komplexů znázorňující průběh vodíkových vazeb, díky kterým se tvoří 1D supramolekulární řetězce společně s dalšími parametry (úhlem mezi rovinami proloženými atomy CoN_3O_2 a zjištěnou vzdáleností Co···Co v rámci 1D řetězce). [a] data převzata z P1. [b] 2 krystalograficky nezávislé molekuly byly nalezeny v asymetrické jednotce komplexu **3a** a **3b**.

Všechny tři komplexy se také chovaly jako polem indukované jednomolekulové magnety (Obr. 14). Debyeův model pro zpracování AC dat mohl být ovšem použit pouze pro komplexy **3a** ($\tau_0 = 1.12 \times 10^{-5}$ s, $U_{eff} = 6.1$ K) a **3b** ($\tau_0 = 1.12 \times 10^{-5}$ s, $U_{eff} = 6.5$ K), protože jen ty obsahovaly dobře definovaná maxima ve frekvenční závislosti imaginární složky molární magnetické susceptibility (Obr. 14, *nahoře uprostřed*). Z tohoto důvodu byly AC data pro všechny tři komplexy také analyzovány pomocí zjednodušeného modelu. Ten je založen na předpokladu, že se v SMMs adiabatická susceptibilita pro dostatečně vysoké teploty blíží nule ($\chi_S \to 0$), a když uvažujeme reálnou a imaginární složku magnetické susceptibility rozepsanou podle rovnic (8) a (9), tak potom poměr těchto složek je dán následovně:

$$\chi_{imag} / \chi_{real} \cong \omega\tau = 2\pi f \tau \tag{12}$$

Pokud se do rovnice (12) dosadí z Arrheniovy rovnice (rovnice (11) pouze se třetím členem), dostane se zjednodušený vztah:

$$\ln(\chi_{imag} / \chi_{real}) = \ln(2\pi f \tau_0) + U / kT \tag{13}$$

Z fitování AC dat podle rovnice (13) se pro čtyři nejvyšší frekvence získaly výrazně vyšší hodnoty U_{eff} (7.9−11.2 K pro **1c**, 13.4−17.6 K pro **3a**, 18.6−30.6 K pro **3b**), které i přesto byly výrazně nižší než předpokládaná teoretická hodnota 2D. Proto byla AC data také analyzována s využitím Ramanova relaxačního procesu, který je pro systém s anizotropií typu lehké roviny více pravděpodobný,[30] což poskytlo srovnatelně dobré výsledky (Obr. 14 *vpravo dole*). Bohužel porovnávání získaných parametrů C a n je složité, protože zatím není znám vztah, jak struktura komplexních sloučenin ovlivňuje hodnoty těchto parametrů.

Obecně lze ale říci, že pozorovaný trend změny hodnot parametru D nekorespondoval s trendem zvyšujících se hodnot relaxačních časů pravděpodobně z toho důvodu, že změny hodnoty parametru D jsou poměrně malé a nikoliv Orbachův, ale právě Ramanův relaxační mechanismu je tím důležitějším procesem relaxace.
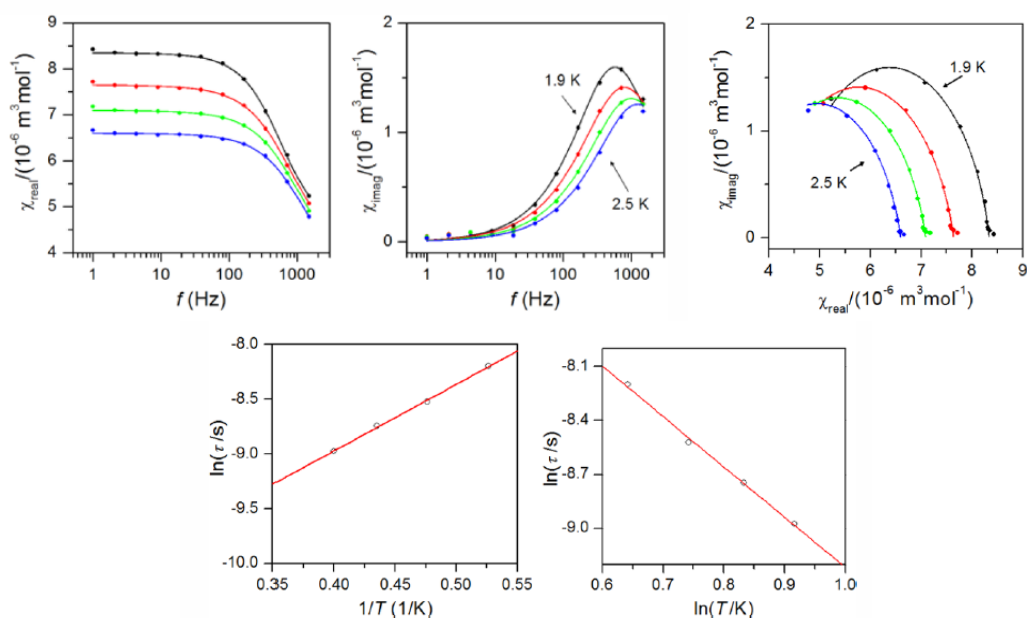
Obrázek 14 *Nahoře zleva*: Frekvenční závislost fázové (reálné, χ_{real}) a mimofázové (imaginární, χ_{imag}) molární susceptibility v externím magnetickém poli 0.1 T, Argandův (Cole-Cole) diagram. Plné čáry představují fit podle Debyeova modelu. *Dole zleva*: Fit výsledných relaxačních časů podle Arrheniovy rovnice uvažující Orbachův relaxační proces (pouze třetí člen rovnice (11)), fit dle rovnice uvažující Ramanův relaxační proces (pouze druhý člen rovnice (11)).

Další provedené AOM výpočty ukázaly, že modifikace ligandového pole v ekvatoriální rovině (snížení jeho síly) by měla mít zásadní vliv na zvýšení hodnoty parametru D, ovšem tento způsob ladění magnetické anizotropie, kdy při zachování stejných axiálních ligandů by byly modifikovány ekvatoriální donor-akceptorové vlastnosti makrocyklického ligandu, nebyl zatím experimentálně zkoumán.

Ve stejném časovém období, kdy byla publikována práce P3, byly studovány i další pentagonálně bipyramidální Co^{II} komplexy a získané hodnoty magnetické anizotropie byly úspěšně laděny v následujících systémech: (i) [Co(**B1a**)(H$_2$O)$_2$] (D = 13.1 cm^{-1})[87] a

[Co(H$_2$**B1a**)(NCS)$_2$] (D = 15.9 cm^{-1}),[87] (ii) [Co(**B4**)(X)$_2$]$^{2+/0}$, kde parametr D narůstal v pořadí X = H$_2$O, CN$^-$, NCS$^-$, SPh$^-$,[83] od 34.5 cm^{-1} do 39.7 cm^{-1}, (iii) [Co(H$_2$**B1d**)(CH$_3$OH)$_2$], [Co(H$_4$**B1d**)(CH$_3$OH)(NCS)]ClO$_4$ a [Co(H$_4$**B1d**)(NCS)$_2$] (D = 43.1, 41.5 a 38.8 cm^{-1}),[94] (iv) série Co^{II} komplexů s H$_2$**B1c** a různými koligandy NCS$^-$, NCSe$^-$, N(CN)$_2$$^-$, C(CN)$_3$$^-$, N$_3$$^-$, H$_2O, Cl^-$,[108] o různém složení s nejvyšší hodnotou D = 40.4 cm^{-1} pro komplex s azidovým koligandem.

U všech výše zmíněných Co^{II} komplexů byla také pozorována pomalá relaxace magnetizace při aplikaci externího DC magnetického pole (všechny komplexy se chovají jako polem indukované SMMs) a byla snaha o to zjistit, jaké jsou dominantní procesy relaxace. Potvrdilo se, že Ramanův relaxační proces je společně s QTM opravdu tím nejdůležitějším mechanismem pomalé relaxace,[83,87,108] a pro některé systémy, např. výše popsaný systém (ii), bylo pozorováno prodloužení relaxačního času se zvyšujícím se parametrem D, tedy má smysl snažit se ladit magnetickou anizotropii.[83] Nicméně aby mohla být nalezena přesnější magneto-strukturní korelace a bylo jednoznačněji zjištěno, jakým způsobem struktura komplexu ovlivňuje mechanismy relaxace magnetizace (což je velice komplexní a komplikovaný problém), bude za potřebí ještě prozkoumat větší množství Co^{II} komplexů.

Ze skupiny železnatých komplexů s **15-pyN$_3$O$_2$** byl doposud připraven a charakterizován pouze jediný a navíc polymerní komplex {[Fe(**15-pyN$_3$O$_2$**)($\mu_{1,3}$-N$_3$)](ClO$_4$)}$_n$ (**4a**) (příloha P4, Obr. 15). Ten ovšem překvapil nejzajímavějšími magnetickými vlastnostmi. Atom železa má v tomto komplexu koordinační číslo 7 s geometrií pentagonální bipyramidy a v axiálních polohách jsou azidové anionty koordinovány můstkujícím způsobem „end-to-end" (Obr. 15B). Komplex tedy vytváří zig-zag 1D polymerní řetězec, protože roviny FeN$_3$O$_2$ resp. vektory N$_{azid}$–Fe–N$_{azid}$ jsou vůči sobě pootočeny a Fe$\cdots$Fe meziatomová vzdálenost v řetězci je 5.847 Å (Obr. 15C). Tyto řetězce jsou mezi sebou spojeny nevazebnými interakcemi aromatických kruhů („π-π stacking") a vytváří tak 2D vrstvy, které jsou mezi sebou izolovány chloristanovými anionty (Obr. 15C a D).

Měření magnetických DC dat (Obr. 15 *vpravo*) ukázalo na (i) přítomnost slabé antiferomagnetické výměnné interakce (J_{Fe-Fe} = −2.14 cm^{-1}) mezi železnatými ionty v rámci 1D řetězce (zprostředkovávají můstkující azidové ligandy) indikované poklesem efektivního magnetického momentu (μ_{eff}) s klesající teplotou do 26 K, (ii) nástup feromagnetického chování s konečným antiferomagnetickým uspořádáním na dlouhou vzdálenost indikovaný prudkým nárůstem μ_{eff} pod 26 K k maximu při 6.2 K následovaný prudkým poklesem.
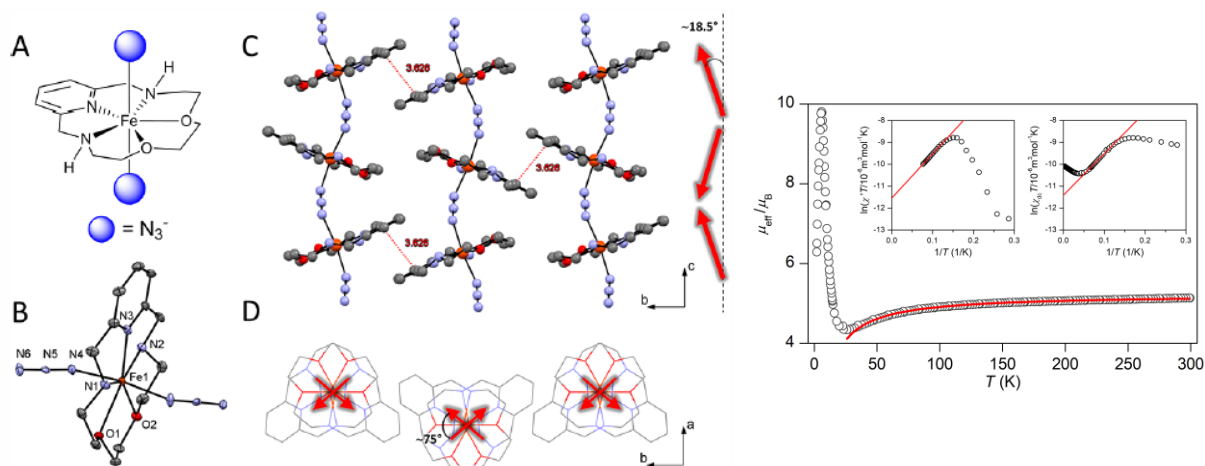
Obrázek 15 *Vlevo*: (A) Schematická ilustrace komplexního kationtu v **4a**, (B) část polymerního 1D řetězce s můstkujícími azidovými ligandy nalezená v krystalové struktuře **4a**, (C) nevazebné interakce aromatických kruhů způsobující tvorbu 2D vrstev, (D) pohled na 1D řetězce ve 2D vrstvě podél krystalografické osy c. *Vpravo*: Teplotní závislost efektivního mag. momentu pro **4a**. Červená plná čára odpovídá fitu podle rovnice (3) s parametry $J = -2.14$ cm^{-1} a g = 2.13. *Inset*: Analýza teplotní závislosti χT s využitím rovnice $\chi'T = C_{eff} \times \exp(\Delta_\xi/kT)$ pro AC data v nulovém DC poli a AC frekvenci $f = 1$ Hz (*vlevo*) a DC data v poli $B_{dc} = 0.1$ T (*vpravo*).

Měření střídavé magnetické susceptibility ukázala, že **4a** se chová jako jednořetězcový magnet (Obr. 16) s hodnotou efektivní bariéry $\Delta_\tau = 87.5$ K ($\tau_0 = 5.27 \times 10^{-10}$), což bylo také potvrzeno změřením hysterezních smyček do teploty 6 K (Obr. 17).
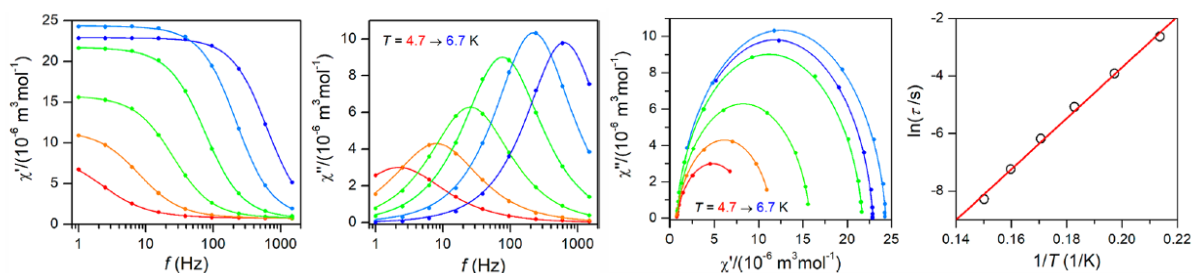
Obrázek 16 *Zleva*: Frekvenční závislost fázové (reálné, χ_{real}) a mimofázové (imaginární, χ_{imag}) molární susceptibility v nulovém externím magnetickém poli, Argandův (Cole-Cole) diagram, fit výsledných relaxačních časů podle Arrheniovy rovnice uvažující Orbachův relaxační proces. Plné čáry představují fit podle Debyeova modelu.

Na základě měření ZFC/FC křivek (z angl. Zero-Field-Cooled / Field-Cooled) se ukázalo, že v látce dochází k antiferomagnetickému uspořádání pod teplotou 6.2 K, které se ovšem v přítomnosti již slabého externího mag. pole (≥0.05 T) mění na feromagnetické, jak je znázorněno na magnetickém fázovém diagramu (Obr. 17), proto lze danou látku považovat za metamagnet.

Velmi neobvyklá kombinace zjištěných magnetických chování (jednořetězcový magnet, metamagnet, antiferomagnetické uspořádání a tzv. „spin canting") byla již dříve pozorována pro analogické komplexy {[Fe(**15-pydienN₅**)(CN)][BF₄]}ₙ a [Fe(**15-pydienN₃O₂**)(CN)](ABSA)}ₙ (ABSA⁻ = 4-aminoazobenzen-4'-sulfonát) s kyanidovým můstkujícím ligandem, kde byla sice silnější antiferomagnetická výměna díky kratší

meziatomové vzdálenosti Fe···Fe, ale energetická bariéra Δ_τ byla mnohem nižší společně s menší mírou magnetické anizotropie systému. Celkově vzato se jedná o první příklad homonukleárního jednořetězcového magnetu založeném na komplexu Fe(II) s pouze azidovými můstkujícími ligandy.
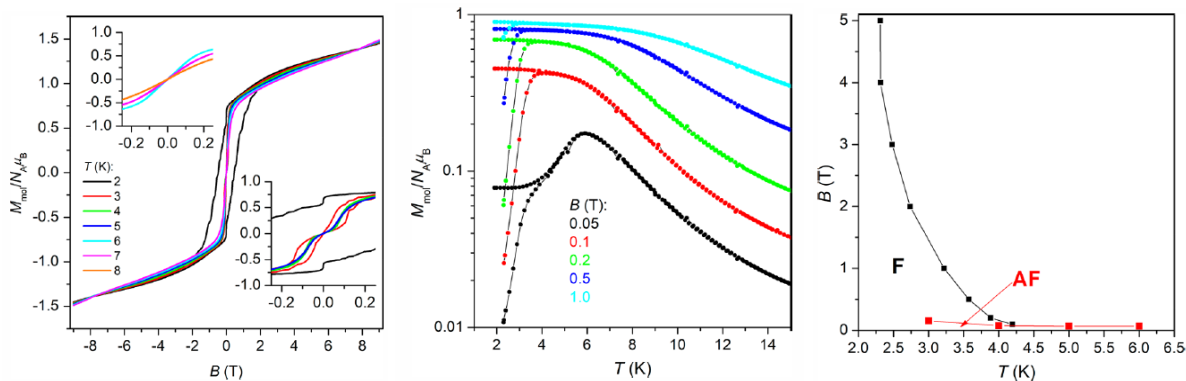
Obrázek 17 *Vlevo*: Hysterezní smyčky při různých teplotách. *Uprostřed*: ZFC/FC křivky pro různá magnetická pole. *Vpravo*: Diagram magnetických fází (černé body získány ze ZFC měření, červené z křivek dM_{mol}/dB. Všechna data pro komplex **4a**.

Problém s přípravou železnatých komplexů je jejich nízká stabilita vůči oxidaci vzdušným kyslíkem, a proto musí být připravovány a krystalizovány pod inertní atmosférou. To je důvod, proč zatím nebyla připravena větší série železnatých komplexů se substituovanými koligandy, přestože lze očekávat zvyšování magnetické anizotropie při použití axiálních koligandů zesilujících ligandové pole.

Dále bylo tímto způsobem vyzkoušeno ladění magnetické anizotropie i na nikelnatých komplexech, kde byla v souladu s teoretickou předpovědí[77] potvrzena zápornější (větší) hodnota D parametru s rostoucí silou axiálních koligandů, ovšem získaná data nebyla doposud publikována. Nicméně tyto výsledky dobře korespondují s prací publikovanou v roce 2019, kde se vůbec poprvé ladila magnetická anizotropie v pentagonálně bipyramidálních Ni^{II} komplexech pomocí axiálních koligandů. Připravený komplex s imidazolovými koligandy [Ni(H$_2$**B1c**))(imidazol)$_2$](NO$_3$)$_2$·2H$_2$O měl mnohem větší D = –28.2 cm^{-1} v porovnání s komplexem s NCS$^-$ koligandy [Ni(H$_2$**B1c**)(SCN)$_2$]·2H$_2$O, který měl D = –11.5 cm^{-1}.[109]

Celkově lze říci, že první způsob ladění mag. anizotropie v pentagonálně bipyramidálních komplexech založený na substituci axiálních koligandů funguje a v závislosti na síle produkovaného ligandového pole (donor/akceptorové vlastnosti koligandů) je možné magnetickou anizotropii zvyšovat. V pochopení toho, jakým způsobem modifikovat ligandové pole, významným způsobem pomohly teoretické CASSCF výpočty. Bohužel pro to, aby se tento efekt projevil v prodloužení relaxačních časů relaxace magnetizace, je potřeba prozkoumat větší počet systémů a lépe vysvětlit, co konkrétně ovlivňuje efektivitu

jednotlivých relaxačních procesů a jaké konkrétní strukturní změny je potřeba udělat pro to, aby byly tyto relaxační procesy co nejvíce eliminovány.

9. Ladění magnetické anizotropie II: komplexy s deriváty 15-pyN₃O₂

Druhým způsobem, jak může být dosaženo zvýšení/ladění magnetické anizotropie, je racionální design ligandu(ů). Jedná se o synteticky náročnější způsob, který pro konkrétní případ pentagonálně bipyramidálních komplexů znamená, že musí být připraven takový ligand, který bude obsazovat všech 7 koordinačních míst a zároveň bude zachována geometrie pentagonální bipyramidy. Zajistit tuto podmínku v praxi není vůbec snadné, naštěstí v tomto směru výrazným způsobem pomáhá použití makrocyklického skeletu. Takže v rámci této druhé strategie ladění magnetické anizotropie bylo přistoupeno ke strukturní modifikaci makrocyklického skeletu **15-pyN₃O₂** pomocí dvou pendantních ramen, která obsahovala různé funkční skupiny (Obr. 18). Předpokladem bylo, že vhodnou volbou těchto funkčních

L1   **L2**   **L3**
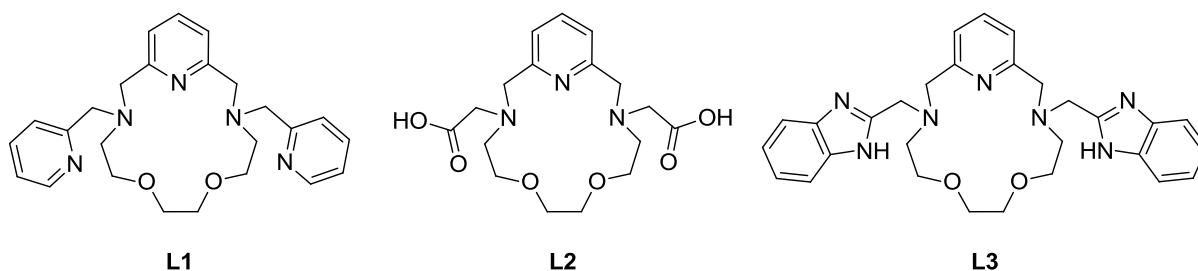
Obrázek 18 Strukturní vzorce připravených ligandů diskutovaných v této kapitole.

skupin v závislosti na jejich donor-akceptorových vlastnostech bude možné ovlivňovat sílu ligandového pole v axiálních polohách (skupiny se budou vázat do axiálních poloh, jak je znázorněno na Obr. 19).

Doposud bylo připraveno již minimálně šest takových ligandů, které by splňovaly výše uvedené podmínky, ovšem publikovány, včetně nezbytné charakterizace jejich komplexů, byly zatím pouze tři z nich uvedené v Obr. 18 – **L1** (příloha P5), **L2** (příloha P6) a **L3** (příloha P7). Vzhledem k tomu, že strukturní i magnetické vlastnosti připravených komplexů jsou si podobné, budou sloučeniny všech tří ligandů diskutovány společně. Ligandy byly připraveny substitučními reakcemi mezi původním cyklem **15-pyN₃O₂** a 2-chlormethylpyridinem (**L1**),
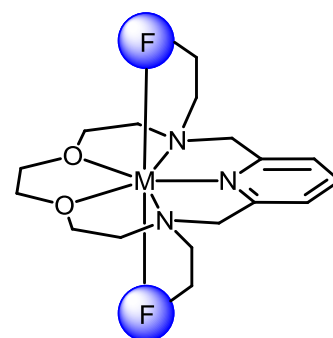
Obrázek 19 Schematické znázornění koordinačního módu připravovaných ligandů (F = koordinující se funkční skupina s různými donor-akceptorovými vlastnostmi).

kyselinou bromoctovou (**L2**) a 2-chloromethylbenzimidazolem (**L3**) a byly přečištěny krystalizací (**L1**), iontovou chromatografií (**L2**) a extrakcí (**L3**). S uvedenými ligandy byly připraveny následující tři série komplexů $[M^{II}(\mathbf{L1})](ClO_4)_2$ (M^{II} = Mn (**5a**), Fe (**5b**), Co (**5c**), Ni (**5d**) a Cu (**5e**)), $[Fe^{III}\mathbf{L2}]ClO_4$ (**6a**), $[M^{II}\mathbf{L2}]\cdot H_2O$ (M^{II} = Fe (**6b**), Co (**6c**), Ni (**6d**)), $[M^{II}(\mathbf{L3})](ClO_4)_2\cdot 1.5CH_3NO_2$ (M^{II} = Mn (**7a**), Fe (**7b**), Co (**7c**) a Ni (**7d**)).

Molekulové struktury potvrdily pentagonálně bipyramidální uspořádání s koordinačním číslem 7 nebo 6+1 u všech uvedených komplexů kromě **5e**, ve kterém měl centrální atom Cu^{II} koordinační číslo 5 s čtvercově pyramidální koordinační geometrií. V případě nikelnatých komplexů, především **5d** a **6d**, docházelo díky Jahn-Tellerovu efektu k prodlužování jedné Ni–O vazby (analogicky se choval i Ni^{II} komplex **1d** popisovaný v předchozí kapitole) a k deformaci pentagonální ekvatoriální roviny koordinovaného makrocyklu (Obr. 20).
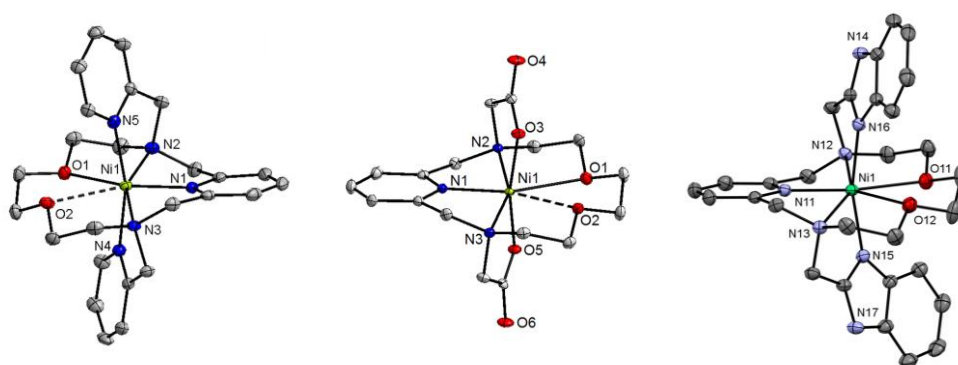
Obrázek 20 Molekulární struktura komplexního kationtu $[Ni\mathbf{L1}]^{2+}$ nalezená v krystalové struktuře **5d** (*vlevo*), komplexu **6d** (*uprostřed*) a komplexního kationtu $[Ni\mathbf{L3}]^{2+}$ nalezená v krystalové struktuře **7d** (*vpravo*). Termální elipsoidy jsou zakresleny s 50% pravděpodobností, vodíkové atomy nejsou zobrazeny z důvodu přehlednosti.

Dále budou porovnávány pouze komplexy Fe^{II}, Co^{II} a Ni^{II}, které mají z hlediska magnetické anizotropie největší význam. Porovnání vazebných délek v jejich komplexech se všemi třemi ligandy **L1**–**L3** je znázorněno na Obr. 21.
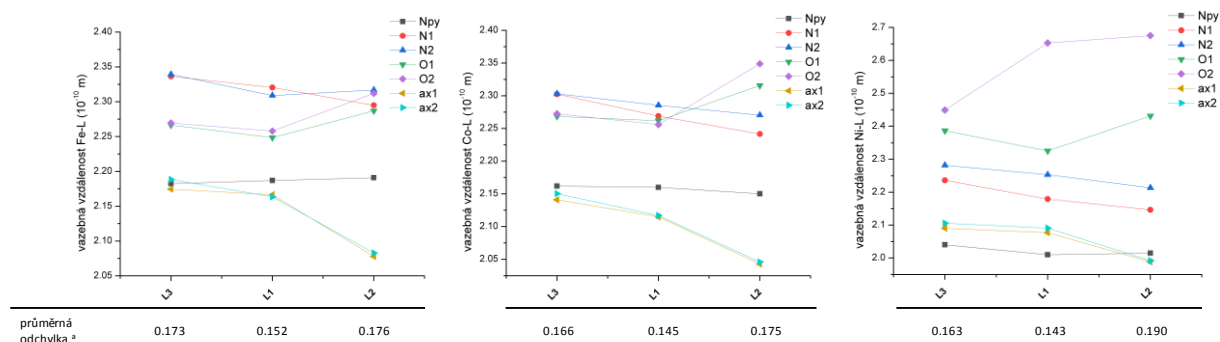
Obrázek 21 Porovnání vazebných délek pro Fe^{II} (*vlevo*), Co^{II} (*uprostřed*) a Ni^{II} (*vpravo*) komplexy studovaných ligandů **L1**, **L2** a **L3**. [a] Průměrná odchylka všech ekvatoriálních donorových atomů ligandu (N_3O_2) od roviny proložené těmito atomy a centrálním atomem (MN_3O_2, její poloha byla spočítána metodou nejmenších čtverců). Data pro dvě krystalograficky nezávislé molekuly nalezené v asymetrické jednotce byly z důvodu přehlednosti zprůměrovány (pro komplexy ligandů **L1** a **L3**).

Vazebná vzdálenosti se v rámci změny ligandu **L3**→**L1**→**L2** (dle strukturní podobnosti funkčních skupin: benzimidazol→pyridin→karboxylát) mění následovně: (i) M–N$_{py}$ se téměř nemění, (ii) vazba k alifatickým dusíkovým atomům M–N$_{1,2}$ se lehce zkracuje, (iii) M–O se lehce zkracuje pro **L3**→**L1** (kromě **5d**), ale výrazně prodlužuje pro **L1**→**L2**, (iv) vazby k axiálním donorovým atomů se zkracují, dochází k axiální kompresy pentagonální bipyramidy, a zkracují se také v pořadí Fe→Co→Ni. Vazebné vzdálenosti M–O jsou v porovnání s M–N$_{1,2}$ kratší v případě Fe^{II} komplexů, srovnatelné v případě Co^{II} komplexů a delší pro komplexy s Ni^{II}. Jak dochází k axiální kompresy v pořadí **L3**→**L1**→**L2**, dochází k symetrizaci ekvatoriální roviny (délky jsou si více podobné) v případě Fe^{II}, ale naopak k deformaci této roviny (délky jsou více odlišné) v případě Co^{II} a především Ni^{II}.

Porovnání těchto strukturních parametrů je velice důležité pro pochopení následující magneto-strukturní korelace zobrazené na Obr. 22.
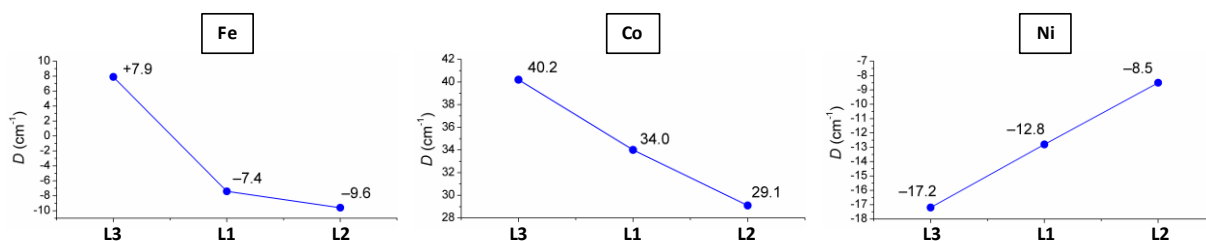
Obrázek 22 Magneto-strukturní korelace pro studované komplexy Fe^{II} (*vlevo*), Co^{II} (*uprostřed*) a Ni^{II} (*vpravo*) s ligandy **L1** , **L2** a **L3** zobrazující změnu axiálního parametru štěpení v nulovém poli D.

V případě železnatých komplexů má jako jediný komplex **7b** neobvyklou kladnou hodnotu parametru D, která ovšem byla potvrzena HF-EPR měřením, protože většina pentagonálně bipyramidálních komplexů, včetně **5b** a **6b** má hodnotu parametru D zápornou. Pro kobaltnaté komplexy magnetická anizotropie vyjádřená parametrem D roste (vyšší kladná hodnota) v pořadí ligandů **L2**→**L1**→**L3** stejně jako roste v případě komplexů nikelnatých (vyšší záporná hodnota parametru D). Takové chování není možné vysvětlit na základě uvažování pouze axiálního ligandového pole, protože jak bylo dříve předpovězeno výpočtem[77] (a potvrzeno celou řadou experimentů, viz předchozí kapitola), s rostoucí silou axiálního ligandového pole má hodnota |D| narůstat v případě pentagonálně bipyramidálních Fe^{II} a Ni^{II} komplexů a klesat v případě komplexů s Co^{II}. Kdyby se tedy uvažoval příspěvek pouze axiálního ligandového pole, musel by být trend u Co^{II} a Ni^{II} komplexů popsaný v Obr. 22 opačný. V tomto případě je proto nutné uvažovat i příspěvek ligandového pole ekvatoriálního, které přispívá ke zvýšení hodnoty D parametru pokud je symetrické a slabé.[77] Jak je zřejmé z Obr. 21, změna funkční skupiny v axiální poloze totiž ovlivňuje i délky vazeb a sílu/symetrii ligandového pole v ekvatoriální rovině. Takže trend pozorovaný na Obr. 22

v pořadí **L2→L1→L3** lze vysvětlit tím, že (i) síla axiálního ligandového pole se spíše snižuje, což koreluje s rostoucí vazebnou vzdáleností axiálních donorů a tomu odpovídá nárůst parametru D pro Co^{II} komplexy, (ii) síla ekvatoriálního pole se snižuje a jeho symetrie se zvyšuje, což má za následek zvětšení $|D|$ pro Ni^{II} komplexy a změnu znaménka pro Fe^{II} komplexy.

V rámci studia všech komplexů byly použity pokročilé CASSCF výpočty k získání parametrů spinového Hamiltoniánu, které ve všech případech velmi dobře korespondovaly s experimentálně zjištěnými hodnotami. Dále také bylo využito teoretických výpočtů k posouzení vlivu síly axiálního a ekvatoriálního ligandového pole na parametry magnetické anizotropie D a E/D (Obr. 23) na příkladu modelového komplexu zobrazeného také na Obr. 23 (měnily se vazebné vzdálenosti jak v ekvatoriální rovině, tak v axiálních polohách). Z uvedeného Obr. 23 vyplývá, že vliv ekvatoriálního ligandového pole má velmi významný vliv na hodnotu D parametru především u Ni^{II} a Fe^{II} komplexů a na hodnotu rombicity E/D u komplexů s Fe^{II}.
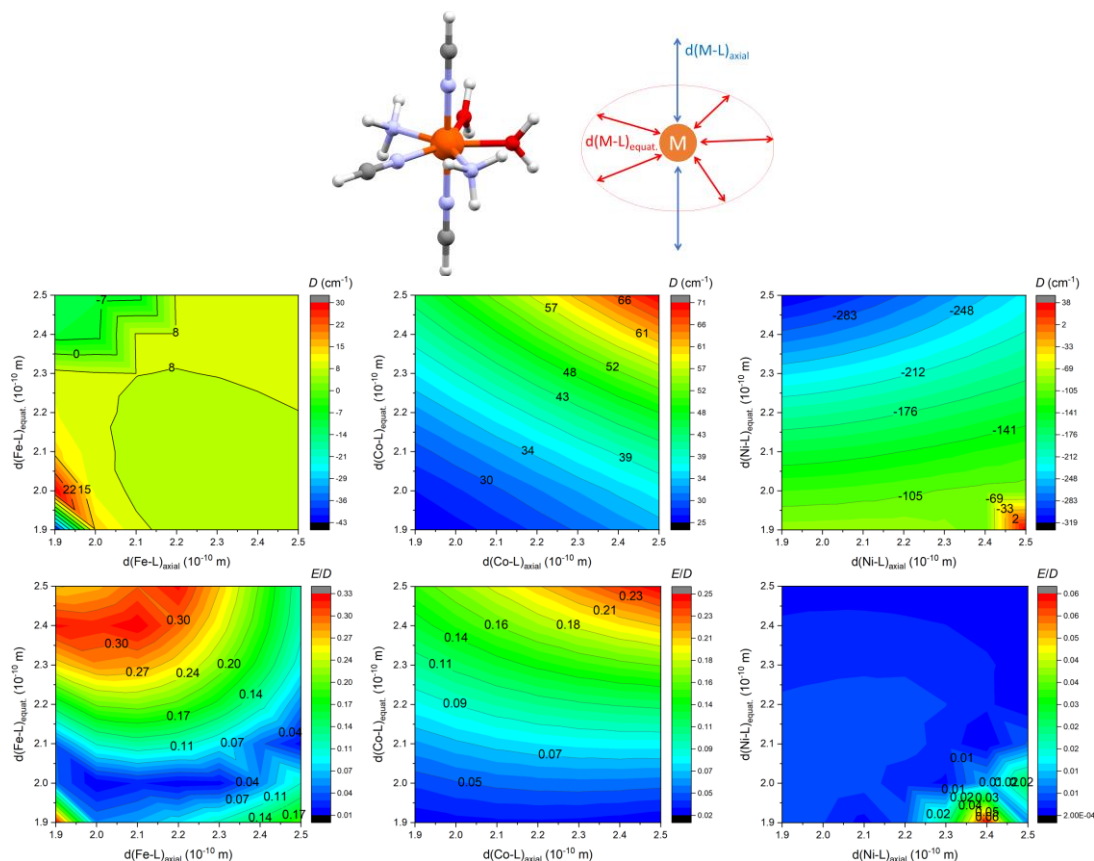
Obrázek 23 *Nahoře*: Obecná molekulová struktura modelového komplexu $[M(NH_3)_2(NCH)_3(H_2O)_2]^{2+}$ (M = Fe^{II}, Co^{II} and Ni^{II}) společně se znázorněním měnících se strukturních parametrů použitých pro výpočty CASSCF/DCD-CAS(2). *Dole*: Konturové diagramy spočítané pomocí CASSCF/DCD-CAS(2) ukazující vliv vazebné délky axiálních a ekvatoriálních ligandů na hodnoty parametrů axiálního a rombického štěpení v nulovém poli D a E/D pro výše uvedenou modelovou sloučeninu.

Všechny kobaltnaté komplexy **5c**, **6c** a **7c** vykazovaly chování polem indukovaných SMMs. Hodnoty efektivní bariéry U_{eff} získané fitováním dat s pomocí Arrheniova vztahu (Orbachův proces) ovšem byly nereálně malé, proto bylo nutné uvažovat i další relaxační mechanismy a data byla analyzována pomocí Ramanova nebo přímého a Ramanova relaxačního mechanismu, což poskytlo mnohem lepší shodu s experimentálními daty (Obr. 24).

U všech sloučenin byly také zkoumány redoxní vlastnosti pomocí cyklické voltametrie, která ukázala, že (i) u komplexů s ligandy **L1** a **L3** byly pozorovány spíše reverzibilní děje a přítomnost π-akceptorových skupin (pyridin a benzimidazol) způsobovala stabilizaci nižších oxidačních stavů, především stavu +II, (ii) u komplexů s ligandem **L2** byly pozorovány děje spíše kvazireverzibilní a docházelo ke stabilizaci vyšších oxidačních stavů (+III) v souladu s π-donorovými vlastnostmi karboxylových skupin.
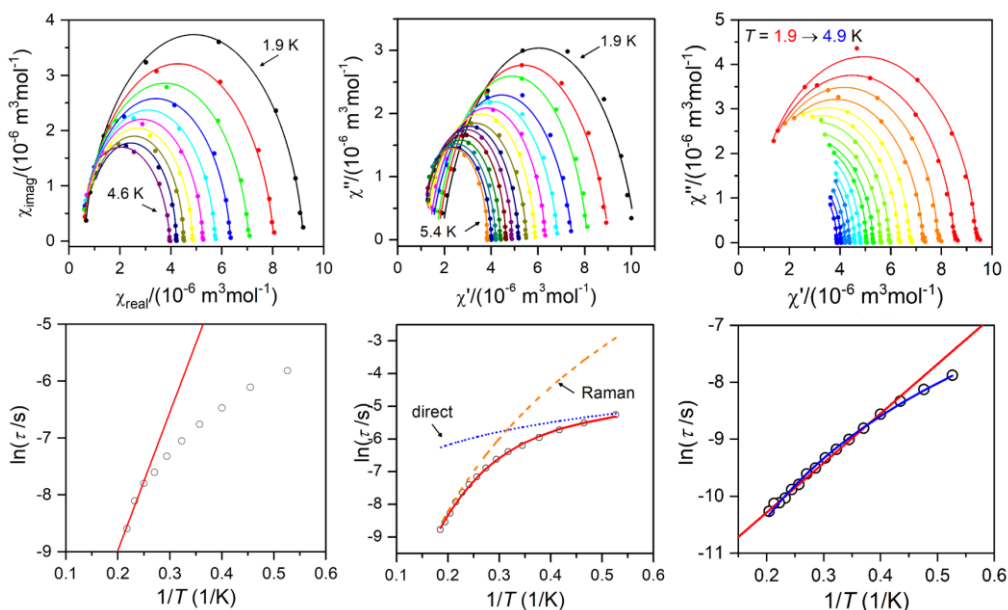
Obrázek 24 *Nahoře*: Argandův diagram (Cole-Cole plot) pro **5c**, **6c** a **7c** (*bráno zleva*), plné čáry představují fit podle Debyeova modelu. *Dole*: fit výsledných relaxačních časů pro **5c**, **6c** a **7c** (*bráno zleva*) podle Arrheniovy rovnice uvažující Orbachův relaxační proces (červená čára pro **5c** a **7c**), uvažující přímý (modrá čárkovaná čára pro **6c**) a Ramanův relaxační proces (oranžová čárkovaná čára pro **6c**, modrá čára pro **7c**).

Protože komplexy lanthanoidů s koordinačním číslem 7 patří mezi jedny z nejefektivnějších jednomolekulových magnetů (kromě nedávno objevených derivátů disprosocenia),[31,32,98] byly připraveny a studovány komplexy [Ln(**L1**)(H$_2$O)(NO$_3$)](NO$_3$)$_2$ (Ln = Tb^{III} (**8a**), Dy^{III} (**8b**), Er^{III} (**8c**)). Na základě molekulových struktur bylo pro všechny tři komplexy zjištěno koordinační číslo 11 s geometrii muffinu (Obr. 25). Lze tedy předpokládat, že makrocyklická kavita je pro koordinaci lanthanoidů příliš malá. Pomalou relaxaci magnetizace vykazovaly všechny tři komplexy avšak až v externím magnetickém poli 0.1 T. Výpočty CASSCF/SINGLE_ANISO umožnili znázornit schéma energetické bariéry pro

změnu orientace magnetizace, které poukazuje na pravděpodobnou relaxaci magnetizace pomocí mechanismu QTM (koresponduje s nulovým signálem mimofázové/imaginární molární susceptibility v nulovém externím poli) a na teplotně aktivovanou relaxaci prostřednictvím prvního excitovaného stavu (Obr. 25). Takže komplexy lanthanoidů s vyššími koordinačními čísly, jako je v tomto případě 11, nejsou z pohledu magnetismu tolik zajímavé, protože v nulovém externím magnetickém poli dochází k tunelování magnetizace, která výrazně urychluje relaxaci magnetizace.
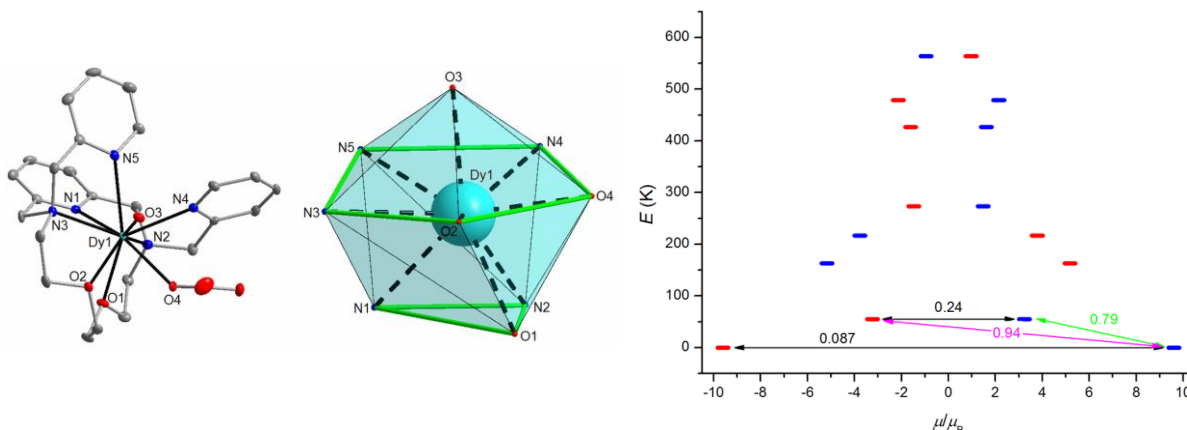
Obrázek 25 *Vlevo*: Molekulární struktura komplexního kationtu $[Dy(\mathbf{L1})(H_2O)(NO_3)]^{2+}$ v komplexu **8b**. Termální elipsoidy jsou zakresleny s 50% pravděpodobností. Vodíkové atomy nejsou zobrazeny kvůli přehlednosti. *Uprostřed*: Koordinační geometrie chromoforu DyN_5O_4 v komplexu **8b**. *Vpravo*: *Ab initio* výpočet energetické bariéry pro změnu orientace magnetizace pro komplex **8b**. Tučné modré/červené čárky indikují Kramersovy dublety jako funkci magnetického momentu. Barevné čáry znázorňují mechanismy návratu magnetizace: přímý (zelená), Orbachův proces (magenta), kvantové tunelování QTM/TA-QTM (černá).

Na závěr lez shrnout, že ladění magnetické anizotropie pomocí strukturní modifikace makrocyklického ligandu, tj. pomocí výše popsané druhé strategie, se jeví jako úspěšné, avšak poměrně náročné, protože strukturní modifikace ligandu ovlivňuje i jeho koordinační schopnosti v ekvatoriální rovině (tj. donorové vlastnosti samotného makrocyklu), což má za následek nesnadno předvídatelné změny v magnetické anizotropii. Díky teoretickým výpočtům již ale existuje představa, jakým směrem se vydat při zvyšování magnetické aniozotropie v pentagonálně bipyramidálních komplexech – tj. je potřeba uvažovat a ladit ligandové pole nejen v axiálních směrech, ale především také v ekvatoriální rovině.

10. SCO komplexy a potenciální multifunkční magnetické materiály

Přehled makrocyklických ligandů, které v komplexech s dvojmocným železem vykazují SCO efekt, byl přehledně shrnut v úvodní kapitole 6. Z pohledu syntetické dostupnosti se jevil systém **Py₂-C** = **A6a** (Obr. 26) jako velmi zajímavý a kvůli dřívějším zkušenostem se

syntézou ligandů odvozených od cyklamu (Obr. 6) bylo přistoupeno k přípravě jeho přemostěného derivátu **Py₂-CB** (Obr. 26) a prozkoumání toho, jestli v případě takové strukturní modifikace bude zachován SCO (Příloha P9). Jak bylo ukázáno na mnoha dříve studovaným systémech (viz kapitola 6), SCO (přítomnost nebo absence, strmost přechodu, teplota přechodu apod.) je velice citlivý k mnoha různým parametrům, a to především (i) síle ligandového pole, tj. počtu a druhu donorových atomů a geometrii koordinační sféry, (ii) druhu protiiontu (aniontu kompenzujícího náboj, „counter" aniontu), (iii) přítomnosti kokrystalizovaných molekul rozpouštědla, (iv) přítomnosti a síle nevazebných interakcí, (v) na celkovém uspořádání atomů v krystalu (tzv. crystal packing).

Py₂-CB byl po několika neúspěšných pokusech založených na syntéze kvarterní dialkylované bis(amoniové) soli **A** (Obr. 26, R = CH₂Py) připraven přímou alkylací **CB** (ten byl připraven z cyklamu podle literatury,[110] Obr. 26) pomocí 2-chlormethylpyridinu. Vzhledem k tomu, že všechny deriváty cross-bridged cyklamu se díky své unikátní konformaci (všechny čtyři volné elektronové páry dusíkových atomů směřují doprostřed makrocyklické kavity) chovají jako tzv. protonové houby (velmi silně váží proton, pK_{a1} je obvykle větší než 12),[111] příprava železnatých komplexů musela být provedena ve striktně bezvodém a inertním prostředí. Syntéza komplexů vycházela z bezvodého $FeCl_2$ a posléze byly halogenidové protiionty vyměněny reakcí s $NaBF_4$ nebo $NaBPh_4$ a tak byla připravena série následujících komplexů [Fe(**Py₂-CB**)][FeCl₄]·H_2O (**9a**·H_2O), [Fe(**Py₂-CB**)]Cl₂·4H_2O (**9b**·4H_2O), [Fe(**Py₂-CB**)](BF₄)₂·0.5CH_3CN (**9c**·0.5CH_3CN) a [Fe(**Py₂-CB**)](BPh₄)₂·CH_3OH (**9d**·CH_3OH).
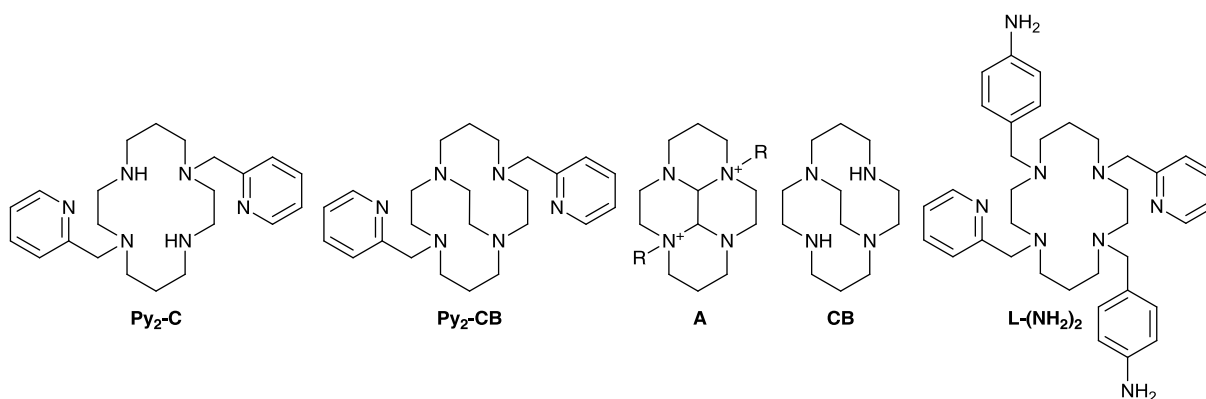
Obrázek 26 Strukturní vzorce sloučenin diskutovaných v textu v rámci této kapitoly.

Ve všech komplexech **9a–9d** měly komplexní kationty [Fe(**Py₂-CB**)]$^{2+}$ *cis*-V uspořádání (Obr. 27, *vlevo*) s *cis* konfigurací pyridinových ramen a deformovanou oktaedrickou geometrií koordinační sféry (Obr. 27, *uprostřed*). Teplotní závislost $\chi_m T$, která je znázorněna na Obr. 28, potvrdila SCO chování všech studovaných komplexů s teplotou přechodu ($T_{1/2}$)

rostoucí v závislosti na aniontu BF_4^- (**9c**) < $[FeCl_4]^{2-}$ (**9a**) < BPh_4^- (**9d**). Nicméně přítomnost SCO pro komplex **9c**·0.5CH$_3$CN byla pozorována až po tom, co došlo díky zvýšení teploty k odstranění kokrystalizovaných molekul acetonitrilu, tj. došlo ke změně krystalografické fáze a vytvoření nového solvatomorfu (bylo potvrzeno i rozdílným práškovým RTG záznamem) a navíc komplex přešel z LS do HS stavu (Obr. 28, *vpravo*), což bylo doprovázeno změnou zbarvení z tmavě hnědo-zelené na světle zelenou. Taková přeměna, nazývaná solvatomorfismus, v rámci jednoho monokrystalu ("single-crystal to single-crystal transformation") doprovázená změnou spinového stavu je pro skupinu Fe^{II} komplexů poměrně vzácná.[112,113]
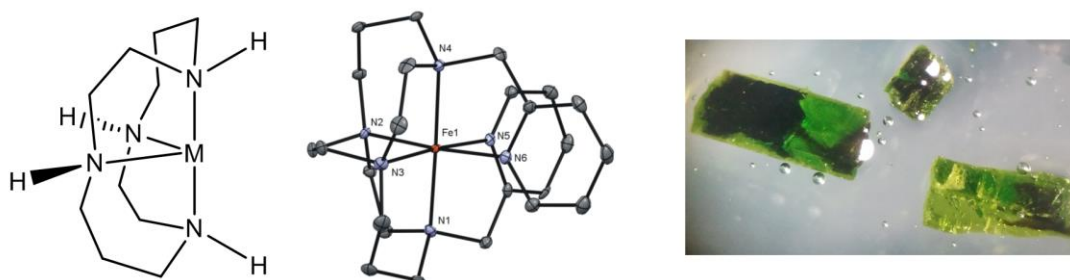
Obrázek 27 *Vlevo*: Ilustrace *cis*-V konfigurace, jedné z šesti možných konfigurací pro komplexy cyklamu. *Uprostřed*: Molekulární struktura komplexního kationtu [Fe(**Py₂-CB**)]$^{2+}$ nalezená v krystalové struktuře **9b**·4H$_2$O (termální elipsoidy jsou nakresleny s 50% pravděpodobností, vodíkové atomy nejsou zobrazeny z důvodu přehlednosti). *Vpravo*: Fotografie krystalů **9c**·0.5CH$_3$CN dokumentující postupnou ztrátu kokrystalizovaného solventu spojenou se změnou spinového stavu (tmavě hnědo-zelená = LS, světle zelená = HS).
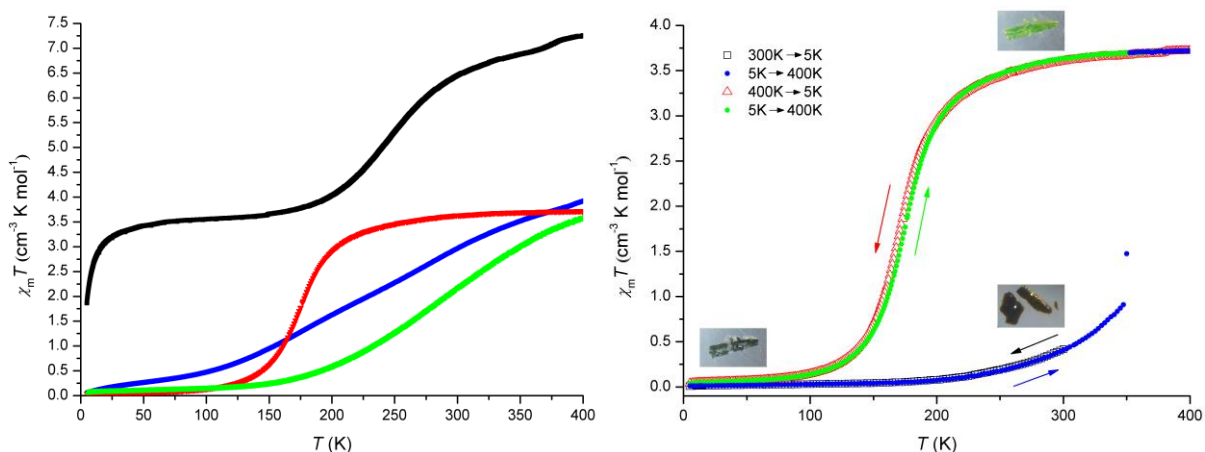
Obrázek 28 *Vlevo*: Teplotní závislost $\chi_m T$ pro **9a**·H$_2$O (*černá*), **9b**·4H$_2$O (*modrá*), **9c** (druhy cyklus 5 K → 400 K, *červená*) a **9d**·CH$_3$OH (první cyklus 5 K → 400 K, *zelená*). *Vpravo*: Teplotní závislost $\chi_m T$ pro **9c**·0.5CH$_3$CN, kdy se teplota mění z 300 K na 5 K (*černá*), z 5 K na 400 K (*modrát*), zpět z 400 K na 5 K (*červená*) a zpět z 5 K na 400 K (*zelená*).

Ztráta kokrystalizovaného acetonitrilu v **9c**·0.5CH$_3$CN probíhala pozvolna už při pokojové teplotě, což bylo prokázáno fotografií velkých krystalů postupně měnících barvu (Obr. 27, vpravo). SCO pro desolvatovaný komplex **9c** byl také doprovázen změnou zbarvení ze světle zelené (HS) na tmavě zelenou (LS), jak je ukázáno na Obr. 28 vpravo. Přítomnost

SCO pro komplex **9c** byla také prokázána rozdílnou hodnotou průměrné vzdálenosti ⟨Fe–N⟩ pozorované v molekulových strukturách **9c** změřených při různých teplotách 120 K (2.086 Å) vs. 293 K (2.197 Å).

Pro moderní aplikace ovšem čisté SCO komplexy již nestačí, protože je snaha kombinovat efekt SCO s dalšími vlastnostmi (např. magnetickou výměnou, kapalnými krystaly, interakcí „host-guest", nelineárními optickými vlastnostmi, elektrickou vodivostí případně luminiscencí),[42] kdy jednou z nejzajímavějších vlastností se jeví právě jednomolekulový magnetismus (SMM), a připravovat tzv. multifunkční magnetické materiály.[39,41] V rámci takového postupu byly použity následující strategie: (i) spojení dvou komplexů, z nichž jeden poskytuje SCO a druhý SMM vlastnosti, pomocí jednoduchého můstkujícího ligandu za tvorby 1D polymerního řetězce,[114] (ii) příprava jednojaderného Fe$^{II/III}$ komplexu, který v sobě kombinuje jak SCO, tak i SMM vlastnosti,[115,116,117] (iii) tzv. kokrystalizace nebo také tzv. ředění iontů kovů (z angl. „metal dilution"), kdy Fe^{II} komplex poskytující SCO efekt je kokrystalizován s Co^{II} komplexem poskytujícím polem indukovaný SMM.[118] V rámci přípravy skupiny potenciálních multifunkčních magnetických materiálů byla věnována pozornost především modifikaci první strategie, která spočívala v přípravě dvoj-/vícejaderného komplexu, ve kterém by byl ale použit speciálně navržený můstkující ligand obsahující dvě specifická vazebná místa umožňující selektivní komplexaci jak železnatých iontů (měly by poskytovat SCO), tak dalších 3d nebo 4f iontů (měly by poskytovat další vlastnost, např. SMM). Takový speciální ligand by tedy měl zajišťovat kovalentní spojení mezi oběma zakomplexovanými kovovými ionty.

Jako první krok v rámci takovém pokusu byl připraven polydentátní bifunkční ligand **10** (Obr. 29)) založený na cyklenovém derivátu DO3A (Příloha P10). Makrocyklická kavita DO3A, která je vhodná pro selektivní komplexaci lanthanoidů, byla propojena s *N*-(2-aminoethyl)propan-1,3-diaminem pomocí rigidního uhlíkatého xylylenového můstku. Lanthanoidový ion zakomplexovaný do makrocyklické kavity by měl fungovat jako SMM a triaminová část sama o sobě, případně po další modifikaci (např. na Schiffovu bázi s využitím o-hydroxynaftaldehydu), by mohla po zakomplexování Fe^{II} nebo jiných iontů přechodných kovů poskytovat SCO efekt. Pětikroková syntéza, znázorněná na Obr. 29, byla založena na reakci *N*-(2-aminoethyl)propan-1,3-diaminu ochráněného ve formě bis(ftalimidu) **10b** s 1,4-bis(brommethyl)benzenem, která vedla ke vzniku brom-derivátu **10c**. Tento brom-derivát byl dále využit v substituční reakci s DO3A ve formě *terc*-butyl esteru vedoucí k tvorbě intermediátu **10d**. V následujících dvou krocích byly odstraněny chránící ftalimidové a *terc*-butylové skupiny, aby mohl být získán výsledný ligand **10** ve formě hydrochloridu. Jednotlivé

meziprodukty stejně jako výsledný ligand byly detailně charakterizovány pomocí elementární analýza, hmotnostní spektrometrie, multinukleární (^{1}H, ^{13}C) a vícedimenzionální NMR spektroskopie. V rámci této publikace byla podrobně popsána pouze tato časově náročná pětikroková syntéza ligandu **10**, avšak prostudování koordinačních vlastností připraveného ligandu by si vyžádalo mnohem více času a může být předmětem dalšího výzkumu.
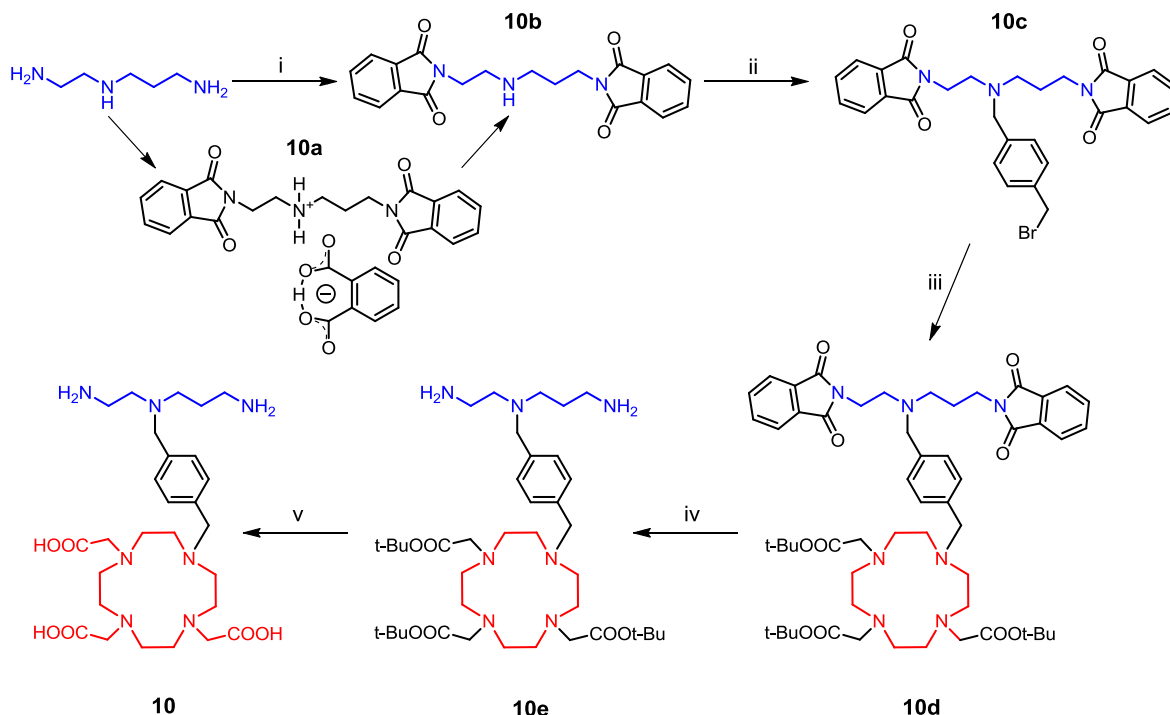
Obrázek 29 Schéma syntézy ligandu **10**. *Reaktanty a podmínky*: (i) ftalanhydid, CH$_3$COOH, reflux 1 h; (ii) 1,4-bis(brommethyl)benzen, K$_2$CO$_3$, MeCN, reflux 0.5 h; (iii) DO3A-tris(*t*-butyl ester), K$_2$CO$_3$, MeCN, reflux 4 h; (iv) hydrazin, EtOH, 25 °C, 12 h; (v) kyselina trifluoroctová, dichlormethan, 25 °C, 12 h.

Na základě zjištění z práce P9, tj. že si Fe^{II} komplexy se strukturně modifikovaným ligandem **Py$_2$-CB** (NH skupiny jsou modifikovány ethylenovým můstkem) SCO zachovávají, byl navržen nový bifunkční ligand **L-NH$_2$** (Obr. 26) odvozený od **Py$_2$-C** a využitelný v první fázi vývoje multifunkčních magnetických materiálů (Příloha P11). Původní makrocyklická část **Py$_2$-C** (měla by selektivně komplexovat Fe^{II} a poskytovat SCO efekt) byla poměrně jednoduše substituována dvěma *p*-aminobenzylovými pendantními rameny (v prvním kroku byly zavedeny dvě *p*-nitrobenzylové skupiny, v druhém kroku byly zredukovány obě nitro skupiny pomocí hydrazinu a Raneyova niklu). Aminová funkční skupina je totiž vhodná pro další transformaci na jiné funkční skupiny, které by mohly komplexovat další přechodné kovy nebo lanthanoidy a poskytovat tak druhou magnetickou zajímavost. Bohužel naměřená magnetická DC data ukázala, že připravený Fe^{II} komplex [Fe(**L-NH$_2$**)]Cl$_2$·2.5H$_2$O (**11**) je vysokospinový. Navíc se ani od komplexu **11** nepodařilo zjistit jeho krystalovou strukturu (mnoho pokusů o krystalizaci komplexu končilo vznikem oleje nebo amorfní sraženiny) a

proto byly provedeny teoretické výpočty s cílem objasnit příčinu absence SCO. Pomocí DFT výpočtů, využívajících hybridní meta-GGA TPSSh funkcionál[119] vhodný pro studium SCO systémů a bázi def2-TZVP, byly optimalizovány molekulové struktury Fe^{II} komplexů s ligandy **Py₂-C**, **Py₂-CB** a **L-NH₂** v jejich *cis/trans* konfiguraci a LS/HS uspořádání a byl vypočítán energetický rozdíl ($\Delta = \varepsilon_{HS} - \varepsilon_{LS}$) mezi LS a HS stavy daného komplexu (Obr. 30).
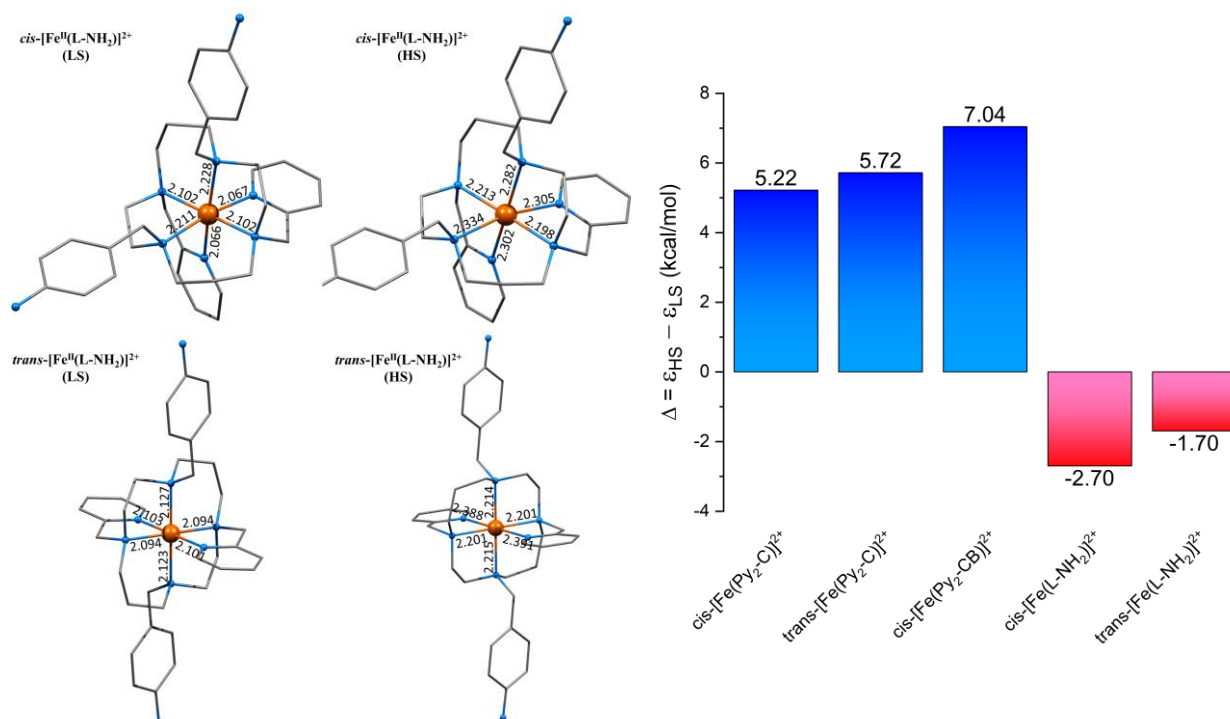
Obrázek 30 *Vlevo*: DFT optimalizované geometrie *cis/trans*-[Fe(**L-NH₂**)]²⁺ pro LS a HS stav. *Vpravo*: Energetický rozdíl HS a LS stavů *cis/trans*-[Fe^{II}(**Py₂-C**)]²⁺, *cis*-[Fe^{II}(**Py₂-CB**)]²⁺ a *cis/trans*-[Fe(**L-NH₂**)]²⁺. Obojí vypočítáno pomocí TPSSh/def2-TZVP.

Kladné hodnoty Δ vypočítané pro *cis/trans*-[Fe^{II}(**Py₂-C**)]²⁺ a *cis*-[Fe^{II}(**Py₂-CB**)]²⁺, tj. komplexy vykazující SCO, indikují preferenci LS stavu, zatímco záporné hodnoty Δ vypočtené pro *cis/trans*-[Fe(**L-NH₂**)]²⁺ ukazují na preferenci HS stavu nezávisle na *cis/trans* konfiguraci, což je v souladu se zjištěným experimentálním výsledkem. Na základě kratších vazebných délek Fe–N$_{benzyl}$ oproti Fe–N$_H$ nebo Fe–N$_{ethylene}$ v optimalizovaných strukturách může vysvětlení HS chování komplexu **11** spočívat v tom, že dvě *p*-aminobenzylová ramena, díky svým elektrony-odčerpávajícím vlastnostem, snižují elektronovou hustotu na dusíkových makrocyklických atomech, na kterých jsou navázány, a tím snižují sílu ligandového pole. Samozřejmě i jiné možné efekty mohou hrát v tomto případě svou roli.

Závěrem lze shrnout, že tento „kovalentní" způsob přípravy multifunkčních magnetických materiálů za pomocí speciálně navrženého můstkujícího ligandu je velice náročný nejen z pohledu jeho zdlouhavé syntézy (nejen ligandu, ale i vícejaderného bimetalického komplexu), ale především z pohledu toho, že míra SCO efektu (přítomnost či dokonce

absence) je závislá na celé řadě parametrů, které jsou diskutovány v úvodu této kapitoly, a které jsou zásadním způsobem ovlivněny strukturní modifikací ligandu. Proto se bohužel zatím nepodařilo nalézt takový ligand nebo takovou strukturní změnu, pro který/kterou by byl SCO u železnatého komplexu s takovým bifunkčním ligandem zachován.

11. Závěr

Cílem této habilitační práce bylo předložit několik možností, jak lze využít komplexy makrocyklických ligandů v oblasti molekulového magnetismu. Vybraný a studovaný makrocyklický ligand **15-pyN$_3$O$_2$** vytvářel Mn^{II}, Fe$^{II/III}$, Co^{II} a Ni^{II} komplexy s méně běžným koordinačním číslem sedm s pentagonálně bipyramidální geometrií koordinační sféry a především komplexy Fe^{II}, Co^{II} a Ni^{II} vykazovaly velkou míru magnetické anizotropie. Její velikost je možné ovlivňovat změnou síly a symetrie ligandového pole, čehož bylo dosaženo především dvěma způsoby: (i) výměnou axiálních koligandů a (ii) modifikací makrocyklického skeletu **15-pyN$_3$O$_2$** pendantními rameny obsahující funkční skupiny s různými donor-akceptorovými vlastnostmi (racionální design ligandu). V rámci prvního postupu bylo připraveno několik Co^{II} komplexů, které se chovaly jako polem indukované SMMs a také byl připraven jeden SCM na bázi polymerního Fe^{II} komplexu s můstkujícím azidovým koligandem. Se změnou axiálních ligandů docházelo ke změně magnetické anizotropie (Co^{II} komplexy), ovšem tento efekt nedosahoval takové efektivity, jak se předpokládalo. Druhým postupem byly zatím připraveny tři deriváty ligandu **15-pyN$_3$O$_2$**, které vytvářely také pentagonálně bipyramidální komplexy (Mn^{II}, Fe$^{II/III}$, Co^{II} a Ni^{II}) s funkčními skupinami pendantních ramen (pyridin, benzimidazol, karboxylát) koordinovanými v axiálních polohách. Změnou funkční skupiny byla ovlivněna/zvýšena magnetická anizotropie výraznějším způsobem. Všechny Co^{II} komplexy se také chovaly jako polem indukované SMMs, ovšem bližší vysvětlení různě zastoupených/intenzivních příspěvků jednotlivých mechanismů relaxace magnetizace (přímý, Ramanův, Orbachův, QTM) bude ještě vyžadovat další studium.

Pro většinu studovaných komplexů byly provedeny teoretické *ab initio* výpočty, které pomohly vysvětlit vztah mezi velikostí ligandového pole v axiálním a ekvatoriálním směru a velikostí magnetické anizotropie vyjádřené parametry D a E. Výsledkem je zjištění, že aby bylo dosaženo větší magnetické anizotropie pro komplexy Fe^{II}, Co^{II} a Ni^{II}, bude zapotřebí především snižovat a symetrizovat sílu ekvatoriálního ligandového pole (konkrétní způsob realizace bude spočívat v racionálním návrhu vhodných/nových ligandů).

Dále bylo prokázáno, že Fe^{II} komplexy s makrocyklickými ligandy, konkrétně s pyridinovým derivátem cross-bridged cyklamu, zachovávají SCO efekt i pro různý typ protiiontu. Také byly připraveny dva bifunkční ligandy (jeden ve formě prekurzoru), které by mohly být vhodné pro komplexaci Fe^{II} a dalšího iontu přechodného kovu nebo lanthanoidu, a tím by byl SCO efekt zkombinován s jinou magnetickou vlastností v tzv. multifunkčním magnetickém materiálu. Bohužel Fe^{II} komplex prvního ligandu byl ve vysokospinovém stavu a SCO efekt nevykazoval, koordinační vlastnosti druhého ligandu nebyly prozatím podrobněji prozkoumány. Výzkum zabývající se přípravou takových multifunkčních materiálů i nadále pokračuje, přestože se tato cesta celkově jeví jako poměrně náročná.

Závěrem lze obecně říci, že se potvrdil úvodní předpoklad, a to že studované makrocyklické ligandy lze chápat jako vhodné univerzální stavební prvky, protože samotné ligandy, jakož i připravené komplexy, lze jednoduše modifikovat a tím ovlivňovat, v tomto konkrétním případě, magnetické vlastnosti připravovaných komplexních sloučenin. Díky tomu může být už tak široké spektrum aplikací makrocyklických ligandů ještě rozšířeno. Navíc jsou výsledky této práce důležité v tom smyslu, že přispívají k pochopení a nalezení vztahu mezi strukturou látky/komplexu a ZFS parametry popisující magnetickou anizotropii, tj. přispívají k nalezení klíče, pomocí kterého by bylo možné racionálně upravovat/ladit tyto parametry, protože zatím (přestože už byly publikovány určité magneto-strukturní korelace) se takový klíč stále hledá.

12.   Reference

Vybrané obrázky nebo jejich části byly převzaty z příslušných příloh: obr. 8, 9 (P1); obr. 11, 12 (P2); obr. 13,14 (P3); obr. 15, 16, 17 (P4); obr. 22,23 (P7); obr. 24 (P5, P6, P7); obr. 25 (P8); obr. 27, 28 (P9); obr. 29 (P10); obr. 30 (P11).

1.   O. Sato, J. Tao, Y. Z. Zhang, *Angew. Chem. Int. Ed.* **2007**, *46*, 2152–2187.
2.   C. Atmani, F. El Hajj, S. Benmansour, M. Marchivie, S. Triki, F. Conan, V. Patinec, H. Handel, G. Dupouy, C. J. Gómez-García, *Coord. Chem. Rev.* **2010**, *254*, 1559–1569.
3.   *Dalton Trans.* **2010**, *39*, Molecular magnets themed issue No. 20, 4653–5040.
4.   *Chem. Soc. Rev.*, **2011**, *40*, Molecule-based magnets themed issue No. 6, 3053–3368.
5.   M. Atanasov, D. Aravena, E. Suturina, E. Bill, D. Maganas, F. Neese, *Coord. Chem. Rev.* **2015**, *289-290*, 177–214.
6.   G. A. Craig, M. Murrie, *Chem. Soc. Rev.* **2015**, *44*, 2135–2147.
7.   S. Gómez-Coca, D. Aravena, R. Morales, E. Ruiz, *Coord. Chem. Rev.* **2015**, *289-290*, 379–392.
8.   A. K. Bar, C. Pichon, J.-P. Sutter, *Coord. Chem. Rev.* **2016**, *308*, 346–380.
9.   J. M. Frost, K. L. M. Harriman, M. Murugesu, *Chem. Sci.* **2016**, *7*, 2470–2491.
10.   J. Ferrando-Soria, J. Vallejo, M. Castellano, J. Martínez-Lillo, E. Pardo, J. Cano, I. Castro, F. Lloret, R. Ruiz-García, M. Julve, *Coord. Chem. Rev.* **2017**, *339*, 17–103.
11.   M. Feng, M. L. Tong, *Chem. Eur. J.* **2018**, *24*, 1–22.
12.   A. Bousseksou, G. Molnar, G. Matouzenko *Eur. J. Inorg. Chem.* **2004**, 4353–4369.
13.   J. A. Real, A. B. Gaspar, M. C. Munoz, *Dalton Trans.* **2005**, 2062–2079.
14.   M. C. Munos, J. A. Real, *Coord. Chem. Rev.* **2011**, *255,* 2068–2093.
15.   D. Gatteshi, R. Sessoli, J. Villain, *Molecular Nanomegnets*, Oxford University Press: New York, **2006**.
16.   *Molecular nanomagnets and related phenomena*; S. Gao, Ed., Strucure and bonding Vol. 164, Springer: Berlin, **2015**.
17.   K. S. Murray, C. J. Kepert, *Top. Curr. Chem.* **2004**, vol. 233–235, Springer.
18.   B. Kim, A. H. Schmieder , A. J. Stacy, T. A. Williams, D. Pan, *J. Am. Chem. Soc.* **2012**, *134*, 10377−1038.
19.   R. Sessoli, D. Gatteschi, A. Caneschi, M. A. Novak, *Nature* **1993**, *365*, 141–143.
20.   H. L. C. Feltham, S. Brooker, *Coord. Chem. Rev.* **2014**, *276*, 1–33.
21.   K. Liu, W. Shi, P. Cheng, *Coord. Chem. Rev.* **2015**, *289-290*, 74–122.
22.   L. Rosado Piquer, E. C. Sanudo, *Dalton transactions* **2015**, *44*, 8771–8780.
23.   D. N. Woodruff, R. E. Winpenny, R. A. Layfield, *Chem. Rev.* **2013**, *113*, 5110–5148.
24.   J. Tang, P. Zhang, *Lanthanide Single Molecule Magnets*, Springer: Berlin, **2015**.
25.   A. K. Bar, P. Kalita, M. K. Singh, G. Rajaraman, V. Chandrasekhar, *Coord. Chem. Rev.* **2018**, *367*, 163–216.
26.   H. Miyasaka, M. Julve, M. Yamashita, R. Clerac, *Inorg. Chem.* **2009**, *48*, 3420–3437.
27.   A. J. Tasiopoulos, A. Vinslava, W. Wernsdorfer, K. A. Abboud, G. Christou, *Angew. Chem. Int. Ed. Engl.* **2004**, *43*, 2117–2121.
28.   F. Neese, D. A. Pantazis, *Faraday Discuss.* **2011**, *148*, 229–238.
29.   R. Herchel, L. Vahovska, I. Potocnak, Z. Travnicek, *Inorg. Chem.* **2014**, *53*, 5896–5898.
30.   S. Gomez-Coca, A. Urtizberea, E. Cremades, P. J. Alonso, A. Camon, E. Ruiz, F. Luis, *Nat. Commun.* **2014**, *5*, 1–8.
31.   C. A. P. Goodwin, F. Ortu, D. Reta, N. F. Chilton, D. P. Mills, *Nature* **2017**, *548*, 439–441.
32.   F.-S. Guo, B. M. Day, Y.-C. Chen, M.-L. Tong, A. Mansikkamäki, R. A. Layfield, *Science* **2018**, *362*, 1400–1403..
33.   P. Zhang, Y.-N. Guo, J. Tang, *Coord. Chem. Rev.* **2013**, *257*, 1728–1763.
34.   A. Yamashita, A. Watanabe, S. Akine, T. Nabeshima, M. Nakano, T. Yamamura, T. Kajiwara, *Angew. Chem. Int. Ed.* **2011**, *50*, 4016–4019.
35.   R. Boča. *Theoretical Foundations of Molecular Magnetism*. Elsevier: Amsterdam, **1999**.

36. J. F. Létard, *J. Mater. Chem.* **2006**, *16*, 2550–2559.
37. M. A. Halcrow, *Chem. Soc. Rev.* **2011**, *40*, 4119–4142.
38. P. Gamez, J. Sanchez Costa, M. Quesada, G. Aromi, *Dalton Trans.* **2009**, 7845–7853.
39. *Spin-crossover materials – properties and applications*, M. A. Halcrow, Ed., John Wiley & Sons: Chichester, UK, **2013**.
40. A. Akou,I. A. Guralskiy, L. Salmon, C. Bartual-Murgui, C. Thibault, C. Vieu, G. Molnar, A. Bousseksou, *J. Mater. Chem.* **2012**, *22*, 3752–3757.
41. P. Gómez-Romero, S. Clément, *Functional hybrid materials*, Wiley-VCH: Wenheim, **2003**.
42. A. B. Gaspar, V. Ksenofontov, M. Seredyuk, P. Gütlich, *Coord. Chem. Rev.* **2005**, 249, 2661–2676.
43. F. Touti, P. Maurin, L. Canaple, O. Beuf, J. Hasserodt, *Inorg. Chem.* **2012**, *51*, 31–35.
44. G. A. Melson, *Coordination chemistry of macrocyclic compounds*. Plenum Press, New York, **1979**.
45. O. Costisor, W. Linert, *Metal mediated template synthesis of ligands*, World Scientific Publishing, Singapore, **2004**.
46. X. Yu, J. Zhang, *Macrocyclic Polyamines: Synthesis and Applications*, Wiley, Weinheim, **2018**.
47. N. V. Gerbeleu, V. B. Arion, J. P. Burgess, *Template Synthesis of Macrocyclic Compounds*, Wiley, Weinheim, **2008**.
48. J. E. Richman, T. J. Atkins, *J. Am. Chem. Soc.*, **1974**, *96 (7)*, 2268–2270
49. V. Alexander, *Chem. Rev.*, **1995**, *95*, 273–275.
50. B. Drahoš, J. Kotek, P. Hermann, I. Lukeš, E. Tóth, *Inorg. Chem.* **2010**, *49*, 3224–3238.
51. T. J. Atkins, J. E. Richman, W. F. Oettle, *Org. Synth.*, **1988**, *6*, 652–663.
52. I. Lázár, *Synth. Commun.*, **1995**, *25 (20)*, 3181–3185.
53. H. J. Kruger, *Coord. Chem. Rev.* **2009**, 253, 2450–2459.
54. J. C. Drabrowiak, P. H. Merrell, D. H. Busch, *Inorg. Chem.* **1972**, *11*, 1979–1988.
55. B. Weber, I. Käpplinger, H. Görls, E. G. Jäger, *Eur. J. Inorg. Chem.* **2005**, 2794–2811.
56. S. Hayami, Z. Gu, Y. Einaga, Y. Kobayashi, Y. Ishikawa, Y. Yamada, A. Fujishima, O. Sato, *Inorg. Chem.* **2001**, *40,* 3240–3242
57. J. S. Costa, C. Balde, C. Carbonera, D. Denux, A. Wattiaux, C. Desplanches, J.-P. Ader, P. Gu1tlich, J.-F. Letard, *Inorg. Chem.* **2007**, *46*, 4114–4119.
58. P. Guionneau, F. Le Gac, A. Kaiba, J. S. Costa, D. Chasseau, J. F. Létard, *Chem. Commun.* **2007**, 3723–3725.
59. D. Aguila, P. Dechambenoit, M. Rouzieres, C. Mathoniere, R. Clerac, *Chem. Commun.* **2017**, *53*, 11588–11591.
60. M. Koikawa, K. B. Jensen, H. Matsushima, T. Tokii, H. Toftlund, *J. Chem. Soc. Dalton Trans.* **1998**, *7*, 1085–1086.
61. A. H. R. Obaidi, J. J. McGarvey, K. P. Taylor, S. E. J. Bell, K. B. Jensen, H. Toftlund, *J. Chem. Soc. Chem. Comm.* **1993**, 536–538.
62. F. El Hajj, G. Sebki,V. Patinec, M. Marchivie, S. Triki, H. Handel, S. Yefsah, R. Tripier, C. J. Gomez-Garcıa, E. Coronado, *Inorg. Chem.* **2009**, *48*, 10416–10423.
63. E. Milin, B. Benaicha, F. El Hajj, V. Patinec, S. Triki, M. Marchivie, C. J. Gómez-García, S. Pillet, *Eur. J. Inorg. Chem.* **2016**, 5305–5314.
64. L. L Martin, K. S. Hagen, A. Hauser, R. L Martin, A. M. Sargeson, *J. Chem. Soc. Chem. Commun.* **1988**, 1313–1315.
65. A. Desideri, J. B. Raynor, *J. Chem. Soc. Dalton Trans.* **1977**, 2051–2054.
66. K. D. Hodges, R. G. Wollmann, S. L. Kessel, D. N. Hendrickson, D. G. Van Derveer, E. K. Barefield, *J. Am. Chem. Soc.* **1979**, 101, 906–917.
67. J. H. Berry, E. Bill, E. Bothe, F. Neese, K. Wieghardt, *J. Am. Chem. Soc.* **2006**, *128*, 13515–13528.
68. T. Beissel, K. S. Buerger, G. Voigt, K. Wieghardt, C. Butzlaff, A. X. Trautwein, *Inorg. Chem.* **1993**, *32*, 124–126.
69. L. Kaustov, M. E. Tal, A. I. Shames, Z. Gross, *Inorg Chem.* **1997**, *36*, 3503–3511.
70. F. Franceschi, J. Hesschenbrouck, E. Solari, C. Floriani, N. Re, C. Rizzoli, A. Chiesi-Villa, *J. Chem. Soc., Dalton Trans.* **2000**, 593–604.

71. S. Brooker, D. J. de Geest, R. J. Kelly, P. G. Plieger, B. Moubaraki, K. S. Murray, G. B. Jameson, *J. Chem. Soc., Dalton Trans.* **2002**, 2080–2087.

72. M. Regueiro-Figueroa, L. M. Lima, V. Blanco, D. Esteban-Gomez, A. de Blas, T. Rodriguez-Blas, R. Delgado, C. Platas-Iglesias, *Inorg. Chem.* **2014**, *53*, 12859–12869.

73. E. L. Gavey, M. Pilkington, *Coord. Chem. Rev.* **2015**, *296*, 125–152.

74. Y. V. Manakin, V. S. Mironov, T. A. Bazhenova, K. A. Lyssenko, I. F. Gilmutdinov, K. S. Bikbaev, A. A. Masitov, E. B. Yagubskii, *Chem. Commun.* **2018**, *54*, 10084–10087.

75. V. S. Mironov, T. A. Bazhenova, Y. V. Manakin, K. A. Lyssenko, A. D. Talantsev, E. B. Yagubskii, *Dalton Trans.* **2017**, *46*, 14083–14087.

76. C. Pichon, B. Elrez, V. Béreau, C. Duhayon, J.-P. Sutter, *Eur. J. Inorg. Chem.* **2018**, 340–348.

77. R. Ruamps, L. J. Batchelor, R. Maurice, N. Gogoi, P. Jiménez-Lozano, N. Guihéry, C. de Graaf, A.-L. Barra, J.-P. Sutter, T. Mallah, *Chem. Eur. J.* **2013**, *19*, 950–956.

78. N. Gogoi, M. Thlijeni, C. Duhayon, J.-P. Sutter, *Inorg. Chem.* **2013**, *52*, 2283–2285.

79. A. K. Bar, C. Pichon, N. Gogoi, C. Duhayon, S. Ramasesha, J.-P. Sutter, *Chem. Commun.* **2015**, *51*, 3616–3619.

80. A. K. Bar, N. Gogoi, C. Pichon, V. M. L. D. P. Goli, M. Thlijeni, C. Duhayon, N. Suaud, N. Guihéry, A.-L. Barra, S. Ramasesha, J.-P. Sutter, *Chem. Eur. J.* **2017**, *23*, 4380–4396.

81. C. Platas-Iglesias, L. Vaiana, D. Esteban-Gómez, F. Avecilla, J. A. Real, A. de Blas, T. Rodríguez-Blas, *Inorg. Chem.* **2005**, *44*, 9704–9713.

82. L. Vaiana, M. Regueiro-Figueroa, M. Mato-Iglesias, C. Platas-Iglesias, D. Esteban-Gómez, A. de Blas, T. Rodríguez-Blas, *Inorg. Chem.* **2007**, *46*, 8271–8282.

83. D. Shao, S. L. Zhang, L. Shi, Y. Q. Zhang, X. Y. Wang, *Inorg. Chem.* **2016**, *55*, 10859–10869.

84. D. Shao, Y. Zhou, Q. Pi, F. X. Shen, S. R. Yang, S. L. Zhang, X. Y. Wang, *Dalton Trans.* **2017**, *46*, 9088–9096.

85. X.-C. Huang, C. Zhou, D. Shao, X.-Y. Wang, *Inorg. Chem.* **2014**, *53*, 12671–12673.

86. F. Habib, I. Korobkov, M. Murugesu, *Dalton Trans.* **2015**, *44*, 6368–6373.

87. M. Dey, S. Dutta, B. Sarma, R. C. Deka, N. Gogoi, *Chem. Commun.* **2016**, *52*, 753–756.

88. Y.-F. Deng, B. Yao, P.-Z. Zhan, D. Gan, Y.-Z. Zhang, K. R. Dunbar, *Dalton Trans.* **2019**, *48*, 3243–3248.

89. Y. Rechkemmer, F. D. Breitgoff, M. van der Meer, M. Atanasov, M. Hakl, M. Orlita, P. Neugebauer, F. Neese, B. Sarkar, J. van Slageren, *Nat. Commun.* **2016**, *7*, 10467.

90. M. R. Saber, K. R. Dunbar, *Chem. Commun.* **2014**, *50*, 12266–12269.

91. J. M. Zadrozny, J. Telser, J. R. Long, *Polyhedron* **2013**, *64*, 209–217.

92. S. Vaidya, et al. *Inorg. Chem.* **2018**, *57*, 3371−3386.

93. F. Shao, B. Cahier, E. Riviere, R. Guillot, N. Guihery, V. E. Campbell, T. Mallah, *Inorg. Chem.* **2017**, *56*, 1104–1111.

94. A. K. Mondal, A. Mondal, B. Dey, S. Konar, *Inorg. Chem.* **2018**, *57*, 9999–10008.

95. Y. Z. Zhang, B. W. Wang, O. Sato, S. Gao, *Chem. Commun.* **2010**, *46*, 6959–6961.

96. T. S. Venkatakrishnan, S. Sahoo, N. Brefuel, C. Duhayon, C. Paulsen, A. L. Barra, S. Ramasesha, J. P. Sutter, *J. Am. Chem. Soc.* **2010**, *132*, 6047–6056.

97. D. Shao, L. Shi, S.-L. Zhang, X.-H. Zhao, D.-Q. Wu, X.-Q. Wei, X.-Y. Wang, *CrystEngComm* **2016**, *18*, 4150–4157.

98. B. M. Day, F. S. Guo, R. A. Layfield, *Acc. Chem. Res.* **2018**, *51*, 1880–1889.

99. Z. Zhu, M. Guo, X.-L. Li, J. Tang, *Coord. Chem. Rev.* **2019**, *378*, 350–364.

100. M. Li, H. Wu, Q. Yang, H. Ke, B. Yin, Q. Shi, W. Wang, Q. Wei, G. Xie, S. Chen, *Chem. Eur. J.* **2017**, *23*, 17775–17787.

101. J. Liu, Y.-C. Chen, J.-L. Liu, V. Vieru, L. Ungur, J.-H. Jia, L. F. Chibotaru, Y. Lan, W. Wernsdorfer, S. Gao, X.-M. Chen, M.-L. Tong, *J. Am. Chem. Soc.* **2016**, *138*, 5441–5450.

102. Y.-C. Chen, J.-L. Liu, L. Ungur, J. Liu, Q.-W. Li, L.-F. Wang, Z.-P. Ni, L. F. Chibotaru, X.-M. Chen, M.-L. Tong, *J. Am. Chem. Soc.* **2016**, *138*, 2829–2837.

103. Y.-S. Ding, N. F. Chilton, R. E. P. Winpenny, Y.-Z. Zheng, *Angew. Chem. Int. Ed.* **2016**, *55*, 16071–16074.

104. A. K. Bar, P. Kalita, J. P. Sutter, V. Chandrasekhar, *Inorg. Chem.* **2018**, *57*, 2398–2401.

105. E. L. Gavey, Y. Beldjoudi, J. M. Rawson, T. C. Stamatatos, M. Pilkington, *Chem. Commun.* **2014**, *50*, 3741–3743.
106. E. L. Gavey, M. Pilkington, *Polyhedron* **2016**, *108*, 122–130.
107. H.-R. Wen, J.-L. Zhang, F.-Y. Liang, K. Yang, S.-J. Liu, C.-M. Liu, *Eur. J. Inorg. Chem.* **2019**, *2019*, 1406–1412.
108. V. A. Kopotkov, D. V. Korchagin, V. D. Sasnovskaya, I. F. Gilmutdinov, E. B. Yagubskii, *Magnetochemistry* **2019**, *5*, 58.
109. M. Dey, P. P. Mudoi, A. Choudhury, B. Sarma, N. Gogoi, *Chem. Commun.* **2019**, *55*, 11547–11550.
110. E. H. Wong, G. R. Weisman, D. C. Hill, D. P. Reed, M. E. Rogers, J. S. Condon, M. A. Fagan, J. C. Calabrese, K.-C. Lam, I. A. Guzei, A. L. Rheingold, *J. Am. Chem. Soc.* **2000**, *122*, 10561–10572.
111. G. R. Weisman, M. E. Rogers, E. H. Wong, J. P. Jasinski, E. S. Paight, *J. Am. Chem. Soc.* **1990**, *112*, 8604–8605.
112. J. Sánchez Costa, S. Rodríguez-Jiménez, G. A. Craig, B. Barth, C. M. Beavers, S. J. Teat, Guillem Aromí, *J. Am. Chem. Soc.*, **2014**, *136*, 3869–3874.
113. C. Bartual-Murgui, C. Codina, O. Roubeau, G. Aromí, *Chem. Eur. J.* **2016**, *22*, 12767–12776.
114. R. Ababei, C. Pichon, O. Roubeau, Y.-G. Li, N. Bréfuel, L. Buisson, P. Guionneau, C. Mathonière, R. Clérac, *J. Am. Chem. Soc.* **2013**, *135*, 14840–14853.
115. S. Mossin, B. L. Tran, D. Adhikari, M. Pink, F. W. Heinemann, J. Sutter, R. K. Szilagyi, K. Meyer, D. J. Mindiola, *J. Am. Chem. Soc.* **2012**, *134*, 13651–13661.
116. X. Feng, C. Mathoniere, R. Jeon Ie, M. Rouzieres, A. Ozarowski, M. L. Aubrey, M. I. Gonzalez, R. Clerac, J. R. Long, *J. Am. Chem. Soc.* **2013**, *135*, 15880–15884.
117. A. Urtizberea, O. Roubeau, *Chem. Sci.* **2017**, *8*, 2290–2295.
118. V. García-López, F. J. Orts-Mula, M. Palacios-Corella, J. M. Clemente-Juan, M. Clemente-León, E. Coronado, *Polyhedron* **2018**, *150*, 54–60.
119. J. Cirera, M. Via-Nadal, E. Ruiz, *Inorg. Chem.* **2018**, *57*, 14097–14105.

13. Seznam příloh

P1)
B. Drahoš, R. Herchel, Z. Trávníček,
Structural, Magnetic, and Redox Diversity of First-Row Transition Metal Complexes of a Pyridine-Based Macrocycle: Well-Marked Trends Supported by Theoretical DFT Calculations. *Inorg. Chem.*, **2015**, *54*, 3352–3369.

P2)
B. Drahoš, R. Herchel, Z. Trávníček,
Structural and magnetic properties of heptacoordinated Mn^{II} complexes containing a 15-membered pyridine-based macrocycle and halido/pseudohalido axial coligands. *RSC Adv.*, **2016**, *6*, 34674–34684.

P3)
B. Drahoš, R. Herchel, Z. Trávníček,
Impact of Halogenido Coligands on Magnetic Anisotropy in Seven-Coordinate Co(II) Complexes. *Inorg. Chem.* **2017**, *56*, 5076−5088.

P4)
B. Drahoš, R. Herchel, Z. Trávníček,
Single-Chain Magnet Based on 1D Polymeric Azido-Bridged Seven-Coordinate Fe(II) Complex with a Pyridine-Based Macrocyclic Ligand. *Inorg. Chem.* **2018**, *57*, 12718–12726.

P5)
P. Antal, B. Drahoš, R. Herchel, Z. Trávníček,
Late First-Row Transition-Metal Complexes Containing a 2‑Pyridylmethyl Pendant-Armed 15-Membered Macrocyclic Ligand. Field-Induced Slow Magnetic Relaxation in a Seven-Coordinate Cobalt(II) Compound. *Inorg. Chem.*, **2016**, *55*, 5957–5972.

P6)
P. Antal, B. Drahoš, R. Herchel, Z. Trávníček,
Structure and Magnetism of Seven-Coordinate Fe^{III}, Fe^{II}, Co^{II} and Ni^{II} Complexes Containing a Heptadentate 15-Membered Pyridine-Based Macrocyclic Ligand. *Eur. J. Inorg. Chem.* **2018**, 4286–4297.

P7)
B. Drahoš, I. Císařová, O. Laguta, V. T. Santana, P. Neugebauer, R. Herchel,
Structural, magnetic, redox and theoretical characterization of seven-coordinate first-row transition metal complexes with macrocyclic ligand containing two benzimidazolyl N-pendant arms. *Dalton Trans.* – přijato k publikování 13. 02. 2020

P8)
P. Antal, B. Drahoš, R. Herchel, Z. Trávníček,
Muffin-like lanthanide complexes with an N5O2-donor macrocyclic ligand showing field-induced single-molecule magnet behaviour. *Dalton Trans.*, **2016**, *45*, 15114–15121.

P9)

B. Drahoš, Z. Trávníček,

Spin crossover Fe(II) complexes of a cross-bridged cyclam derivative. *Dalton Trans.* **2018**, *47*, 6134–6145.

P10)

B. Drahoš, Z. Trávníček,

Synthesis of a Versatile Building Block Combining Cyclen-derivative DO3A with a Polyamine via a Rigid Spacer. *Molecules*, **2013**, *18*, 13940–13956.

P11)

B. Drahoš, I. Šalitroš, R. Herchel,

First step in preparation of multifunctional spin crossover material based on Fe(II) complex of cyclam-based ligand. Magnetism and DFT studies. *Inorg. Chim. Acta* **2019**, *495*, 118921.

Příloha P1

B. Drahoš, R. Herchel, Z. Trávníček,
Structural, Magnetic, and Redox Diversity of First-Row Transition Metal Complexes of a Pyridine-Based Macrocycle: Well-Marked Trends Supported by Theoretical DFT Calculations.
*Inorg. Chem.*, **2015**, *54*, 3352–3369.

Structural, Magnetic, and Redox Diversity of First-Row Transition Metal Complexes of a Pyridine-Based Macrocycle: Well-Marked Trends Supported by Theoretical DFT Calculations

Bohuslav Drahoš, Radovan Herchel, and Zdeněk Trávníček*

Department of Inorganic Chemistry, Regional Centre of Advanced Technologies and Materials, Faculty of Science, Palacký University, 17. listopadu 12, CZ-771 46 Olomouc, Czech Republic

S *Supporting Information*

ABSTRACT: A series of first-row transition metal complexes with 15-membered pyridine-based macrocycle (3,12,18-triaza-6,9-dioxabicyclo[12.3.1]octadeca-1(18),14,16-triene = **L**) was prepared ([$M^{II}(\mathbf{L})Cl_2$], where M = Mn, Co, Ni, Zn (**1**, **3**, **4**, **6**); [$Fe^{III}(\mathbf{L})Cl_2$]Cl (**2**), [$Cu^{II}(\mathbf{L})Cl$]Cl (**5**)) and thoroughly characterized. Depending on the complexated metal atom, the coordination number varies from 7 (Mn, Fe, Co), through 5 + 2 for Ni and 4 + 1 for Cu, to 5 for Zn accompanied by changes in the coordination geometry from the pentagonal bipyramid (**1**−**4**) to the square pyramid (**5** and **6**). Along the series, the metal−oxygen distances were prolonged in such manner that their bonding character was investigated, apart from X-ray structural analysis, also by ab initio calculations (Mayer's bond order, electron localization function), which confirmed that, in **4** and **5**, two and one oxygen donor atoms are semicoordinated, respectively, and one and two oxygen atoms are uncoordinated in **5**, and **6**, respectively. On the basis of the temperature variable magnetic susceptibility measurements, **1** and **2** behave as expected for $3d^5$ high-spin configuration with negligible zero-field splitting (ZFS). On the other hand, a large axial ZFS ($D(Co) \approx 40$ cm^{-1}, $D(Ni) \approx -6.0$ cm^{-1}) was found for **3** and **4**, and rhombic ZFS ($E/D \approx 0.15$) for **4**. Antiferromagnetic exchange coupling was observed for **4** and **5** ($J(Ni) = -0.48$ cm^{-1}, and $J(Cu) = -2.43$ cm^{-1}, respectively). The obtained results correlate well with ab initio calculations of ZFS parameters as well as J-values, which indicate that the antiferromagnetic exchange is mediated by hydrogen bonds. The complexes were also investigated by cyclic voltammetry in water or acetonitrile. A quasi-reversible couple Mn(II)/Mn(III) at 1.13/0.97 V, an almost reversible couple Fe(II)/Fe(III) at 0.51/0.25 V, and a one-step/multistep reduction/oxidation of Cu(II) complex **5** at −0.33 V/0.06−0.61 V were detected.
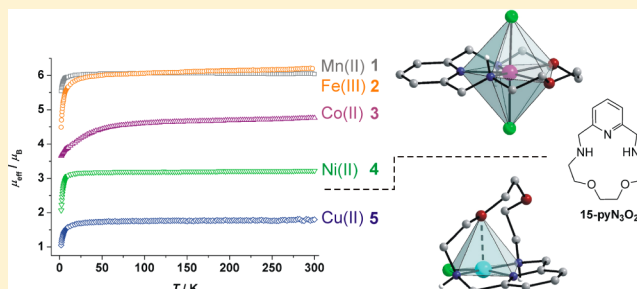
INTRODUCTION

Pyridine-containing macrocycles, in which the pyridine unit represents a part of the macrocyclic scaffold, are widely studied compounds due to their specific coordination abilities. Among such a large number of macrocycles with a different size of the macrocyclic cavity, that is, varying from 12 to 20 ring members and variable donor atoms, our attention has been devoted mainly to the derivatives of 15-membered macrocyclic ligands containing three nitrogen and two oxygen donor atoms in the ligand scaffold. The most common representatives of these ligands are in complexes whose X-ray crystal structures are the most abundant in the Cambridge Structural Database (CSD);[1] they are shown in Figure 1. According to the decreasing number of references regarding each of the compounds, including the metal complexes, they can be ordered as follows: 15-pydienN$_3$O$_2$,[2−18] 3,12,18-triaza-6,9-dioxabicyclo[12.3.1]octadeca-1(18),14,16-triene (15-pyN$_3$O$_2$, **L**),[19−22] 15-pydion-N$_3$O$_2$,[23−26] Me$_2$-15pyN$_3$O$_2$,[27,28] (15-pydienN$_3$O$_2$),[29] **L1**, and **L2**.[30] The above-mentioned ligands were used to complex different d-block transition metals as well as f-block lanthanides, and usually crystal structures and magnetic properties in the

solid state were investigated, but also some experiments in solution regarding their redox properties,[2] their thermodynamic/kinetic stabilities,[28] or their efficiency as magnetic resonance imaging (MRI) contrast agents were performed.[22]

The most variable group of compounds is that of the metal complexes of 15-pydienN$_3$O$_2$. The mononuclear complexes with Mg(II), Fe(II), Mn(II), and Co(II), as well as with Y(III)[6] or few lanthanides,[7] were prepared. Usually the coordination number (CN) of 7 was found in the complexes, and the two axial positions of the pentagonal bipyramidal coordination sphere were occupied by different small monovalent ligands, for example, Cl$^-$, H$_2$O, SCN$^-$, or CN$^-$ (Figure 2). Concerning the mononuclear complexes, the main attention was devoted to [Fe(15-pydienN$_3$O$_2$)(CN)$_2$]·H$_2$O, which shows spin crossover with the spin transition temperature of 159 K[4,8] and light-induced electron spin state trapping effect (LIESST) at $T_{(LIESST)} = 135$ K related to one reversible iron−oxygen bond break.[13] The most recent research has been focused on
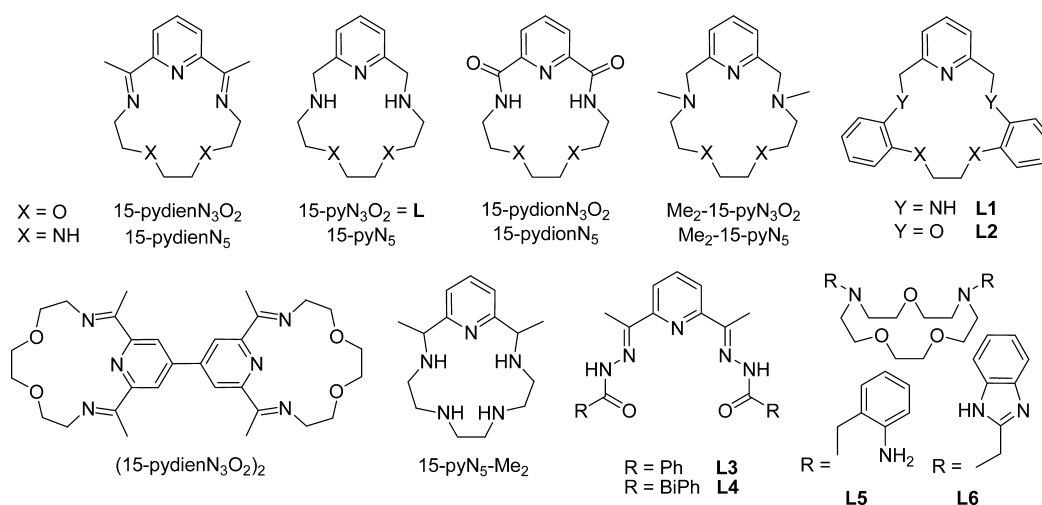
Figure 1. Structural formulas of the most common and discussed 15-membered pyridine-containing ligands with five donor atoms in the ligand scaffold and other selected ligands providing heptacoordination in their metal complexes.
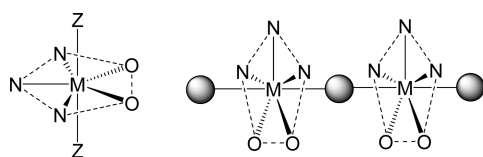
Figure 2. Schematic illustration of coordination modes of discussed ligands previously observed in mononuclear (left) and polynuclear (right) complexes. The dashed lines connecting the donor atoms represent the ligand scaffold. Z = a small monodentate ligand, M = variable metal atom, spheres represent different types of cyanidometallates: $[M^I(CN)_2]$, $[M^{II}(CN)_4]^{2-}$, $[M^{III}(CN)_6]^{3-}$ (M^I = Ag, Au; M^{II} = Ni, Pd, Pt; M^{III} = Fe, Cr, Co).

polynuclear heterometallic one-dimensional (1D) chains or two-dimensional (2D) layers formed upon axial coordination of bidentate bridging units particularly based on cyanidometallates (Figure 2). The cyanido-bridged $[Mn^{II}-M^{II/III}-Mn^{II}]$ heterotrinuclear complexes were prepared by bridging the $[Mn(15\text{-}pydienN_3O_2)]$ building block by $[M(CN)_6]^{4-/3-}$ where M = Fe(II),[9] Fe(III), Cr(III), Co(III).[12] An antiferromagnetic exchange interaction was found between Mn(II) and Cr(III), and a ferromagnetic one was found between Mn(II) and Fe(III). When the same $[Mn(15\text{-}pydienN_3O_2)]$ building block was bridged by $[M(CN)_2]^-$, where M = Au(I) or Ag(I),[16] heterometallic 1D chains were formed, and a very weak antiferromagnetic interaction between neighboring Mn(II) atoms bridged by the diamagnetic NC−M−CN unit was observed. Using $[M(CN)_4]^{2-}$, where M = Ni(II), Pd(II), Pt(II) as a bridging unit, gave rise to a 1D chain without any significant magnetic interaction between Mn(II) atoms.[9]

Besides Mn(II), other metal ions were also complexed by 15-pydienN_3O_2; for example, Fe(II) in a cyanido-bridged Fe^{II}−Mn^{II} 1D chain exhibited spin crossover as well as LIESST effect,[10] and Co(II) in $[Co^{II}(15\text{-}pydienN_3O_2)]_2[Cr^{III}(CN)_6]$ trinuclear complex, which self-assembled into chiral nanotubular structure, which consists of interlocked single and double helices, exhibited ferromagnetic coupling between Co(II) and Cr(III) (J = 1.2 cm^{-1}) and ferromagnetic ordering below 12 K.[17] The trinuclear complex based on two $[Fe^{II}(15\text{-}pydienN_3O_2)(H_2O)]$ units bridged by $[Cr(CN)_6]^{3-}$ was found to be the first Fe(II) cyanido-bridged single-molecule magnet (SMM) with a large anisotropy barrier (U_{eff} = 44.3 K).[18] Except

for cyanidometallates, other bridging units were used to connect the pentagonal $[M(15\text{-}pydienN_3O_2)]$ planes (derivatives of 1,2-bis(pyridine-2-carboxamido)benzenate[14] or $[Fe(salen)(CN)_2]^-$, where H_2salen = N,N'-bis(salicyl)-ethylenediamine).[15]

To the best of our knowledge, there exist only two Mn(II) complexes of **L**.[22] Their structures are similar to those with 15-pydienN_3O_2 with the coordination number of 7 for Mn(II) and two chlorides or one chloride and one water molecule coordinated in the axial positions of the pentagonal bipyramid. Additional characterization of the complexes was performed only in solution (characterization of potential MRI contrast agents), magnetic properties were described by NMR measurements, and quasi-reversible oxidation at high potential 1.2 V (vs standard hydrogen electrode (SHE)) in aqueous solution was found.[22] Only one complex of a bimacrocyclic ligand (15-pydienN_3O_2)_2 with Mn(II) was previously described,[29] with CN of 7 for Mn(II) and one water molecule and one chlorido ligand in axial positions. The investigation of magnetic properties revealed a weak intramolecular antiferromagnetic exchange between the two Mn(II) atoms. In the case of more rigid ligands **L1** and **L2**, their Cu(II), Co(II), and Ni(II) complexes were studied; mainly, the influence of the arrangement of the donor atoms in the ligand on the thermodynamic stability of Cu(II) complexes (complex with **L1** was more stable than that with **L2**) and crystal structures of Cu(II) and Ni(II) complexes of **L2** with CN of 6 for both metals was described.[30]

The 15-pydionN_3O_2 ligand was studied previously only in the case of a Ca(II) complex, in which Ca(II) is situated outside the macrocyclic cavity and coordinated by four amide-oxygen atoms coming from four ligands.[24] Next work was done on structurally similar ligand 15-pydionN_5 having five nitrogen donor atoms in the ligand scaffold whose Fe(II) and Fe(III) complexes with pentagonal bipyramidal geometry were prepared.[31,32] In the Fe(III) complex, a high-spin (HS) state and spin crossover to a long-range antiferromagnetic order at T < 3.2 K occurred. The negatively charged deprotonated amide groups stabilized the oxidation state +III of iron (E(Fe^{III}**L**/Fe^{II}**L**) = −0.57 V vs standard calomel electrode (SCE)).[31] Similarly in the Fe(II) complex, Fe(II) was found in HS state all over the temperature range without any long-range magnetic

ordering at low temperature, and the measured redox potential was identical to that for Fe(III) complex.[32]

Besides the 15-membered pyridine-based macrocycles discussed above, other ligands (Figure 1, **L3**–**L6**), whose complexes have a rather unusual heptacoordinated central transition metal atom, were described previously. It has been found that mononuclear Co(II) and Ni(II) complexes of the pyridine-based Schiff bases **L3** and **L4**[33,34] or derivatives of 1,10-diaza-15-crown-5 **L5** and **L6**[35] show large magnetic anisotropy demonstrated by a large positive and negative value of axial zero-field splitting (ZFS) parameter for Co(II), and Ni(II), respectively.[33,35] On the basis of the negative D-value for Ni(II) complexes of **L3** and **L4**, the building unit $[Ni(\mathbf{L3})]^{2+}$/$[Ni(\mathbf{L4})]^{2+}$ was combined with $[W(CN)_8]^{3-}$ forming a pentanuclear $\{Ni_3W_2\}$ complex that behaved as a single-chain-magnets (SCM).[36]

In this paper, the coordination ability of a rarely utilized 15-membered pyridine-based macrocyclic ligand **L** is investigated on a new series of complexes of selected first-row transition metals (Mn(II), Fe(III), Co(II), Ni(II), Cu(II), and Zn(II)), because no complexes of this ligand, except for two complexes with Mn(II),[22] were described previously. The determined molecular and crystal structures of all the complexes are discussed in detail and correlated with their magnetic properties in the solid state. The experimentally obtained findings are compared with results of ab initio calculations regarding the chemical bonding between metal atoms and the ligands donor atoms, the ZFS tensor parameters, and the intermolecular magnetic interactions. The magnetic data in solid state are compared with those in solution, and the redox behavior of the studied complexes is investigated by cyclic voltammetry. Thorough characterization of this series possesses an observation of several well-marked trends and correlations, which could give better insight into the coordination chemistry and magnetochemistry of complexes with pyridine-based macrocyclic ligands and which would help in the seeking of compounds with desirable magnetic properties and application potential.

■ EXPERIMENTAL SECTION

Materials and Syntheses. The ligand **L** was synthesized according to the literature procedure described elsewhere.[22] All the solvents (Penta, Prague, Czech Republic) and other chemicals were purchased from commercial sources (Across Organics, Geel, Belgium and Sigma Aldrich, St. Louis, MO, USA) and used as received.

[Mn(L)Cl₂] (1). **L** (0.250 g, 1.00 mmol) was dissolved in 25 mL round-bottom flask in 2.5 mL of methanol (MeOH). The solution of MnCl₂·4H₂O (0.195 g, 1.00 mmol) in 2.5 mL of MeOH was added, and the mixture was heated under reflux for 5 min. If any precipitate formed, it was filtered through Millipore syringe filter (0.45 μm). Diethylether (Et₂O) was slowly added dropwise to a stirred solution of the complex until precipitate formed and the color of the solution faded. The precipitate was removed by filtration on a glass frit, washed twice with 10 mL of Et₂O, and stored in vacuum desiccator over KOH for 2 d. The complex was obtained as pale brown powder (0.22 g, yield 55.7%). Mass spectrometry (MS) m/z (+): 341.08 $[Mn(\mathbf{L})Cl]^+$. Anal. Calcd (%) for C₁₃H₂₁Cl₂N₃O₂Mn·H₂O (**1**·H₂O): C, 39.51; H, 5.87; N, 10.63. Found C, 39.65; H, 5.48; N, 10.19.

[Fe(L)Cl₂]Cl (2). All the complexes were prepared similar to the procedure described above for the Mn(II) complex (**1**). The product was obtained as a dark yellow crystalline solid (0.26 g, yield 55.6%). MS m/z (+): 305.02 $[Fe(\mathbf{L}-2H)]^+$, 340.98 $[Fe(\mathbf{L}-H)Cl]^+$, 376.94 $[Fe(\mathbf{L})Cl_2]^+$. Anal. Calcd (%) for C₁₃H₂₁Cl₃N₃O₂Fe·3H₂O·CH₃OH (**2**·3H₂O·CH₃OH): C, 33.66; H, 6.25; N, 8.41. Found: C, 33.40; H, 6.12; N, 8.53.

[Co(L)Cl₂] (3). The product was obtained as a violet powder (0.24 g, 60.1%). MS m/z (+): 345.05 $[Co(\mathbf{L})Cl]^+$. Anal. Calcd (%) for C₁₃H₂₁Cl₂N₃O₂Co·H₂O (**3**·H₂O): C, 39.12; H, 5.81; N, 10.53. Found: C, 39.14; H, 5.46; N, 10.13.

[Ni(L)Cl₂] (4). The product was obtained as a green powder (0.20 g, yield 52.5%). MS m/z (+): 344.02 $[Ni(\mathbf{L})Cl]^+$. Anal. Calcd (%) for C₁₃H₂₁Cl₂N₃O₂Ni (**4**): C, 40.99; H, 5.56; N, 11.03. Found: C, 40.72; H, 5.66; N, 10.62.

[Cu(L)Cl]Cl (5). The product was obtained as a dark blue crystalline solid (0.20 g, yield 51.8%). MS m/z (+): 349.00 $[Cu(\mathbf{L})Cl]^+$, 734.89 $[Cu_2(\mathbf{L})_2Cl_3]^+$. Anal. Calcd (%) for C₁₃H₂₁Cl₂N₃O₂Cu (**5**): C, 40.47; H, 5.49; N, 10.89. Found: C, 40.11; H, 5.80; N, 10.66.

[Zn(L)Cl₂] (6). The product was obtained as a white microcrystalline solid (0.21 g, yield 68.2%). MS m/z (+): 314.24 $[Zn(\mathbf{L}-H)]^+$, 350.27 $[Zn(\mathbf{L})Cl]^+$. Anal. Calcd (%) for C₁₃H₂₁Cl₂N₃O₂Zn (**6**): C, 40.28; H, 5.46; N, 10.84. Found: C, 40.26; H, 5.55; N, 10.27.

Physical Methods. Elemental analysis (C, H, N) was performed on a Flash 2000 CHNO-S Analyzer (Thermo Scientific, Waltham, MA, USA). Infrared (IR) spectra of the complexes were recorded on a Thermo Nicolet NEXUS 670 FT-IR spectrometer (Thermo Nicolet, Waltham, MA, USA) employing the ATR technique on a diamond plate in the range of 400−4000 cm⁻¹. The mass spectra were collected on an LCQ Fleet Ion Mass Trap mass spectrometer (Thermo Scientific, Waltham, MA, USA) equipped with an electrospray ion source and three-dimensional (3D) ion-trap detector in the positive mode. Simultaneous thermogravimetry (TG) and differential thermal analysis (DTA) were carried out using an Exstar TG/DTA 6200 thermal analyzer (Seiko Instruments Inc., Torrance, CA, USA) with a dynamic air atmosphere (100 mL min⁻¹) in the temperature interval of 25−900 °C with the heating rate 5.0 °C min⁻¹. Temperature dependence of the magnetization at B = 0.1 or 1.0 T from 1.9 to 300 K and the isothermal magnetizations at T = 2.0 and 5.0 K up to B = 5 T were measured using MPMS XL-7 SQUID magnetometer (Quantum Design Inc., San Diego, CA, USA). The experimental data were corrected for diamagnetism.[37]

X-ray Diffraction Analysis. Single crystals of complexes **1**·2CH₃OH, **2**·2H₂O, **3**·2CH₃OH, **4**, **5**, and **6** suitable for X-ray analysis were prepared by a vapor diffusion of Et₂O into the MeOH solution of the appropriate complex at 5 °C, except for the complex **6**, which crystallized when its hot aqueous solution cooled to room temperature. X-ray single-crystal diffraction experiments for all the complexes were performed on an Oxford Diffraction Xcalibur2 diffractometer equipped with a Sapphire2 CCD detector using Mo Kα radiation. The CrysAlis software package (Version 1.171.33.52, Oxford Diffraction Ltd.)[38] was used for data collection and reduction. The molecular structures were solved by direct methods and refined by full-matrix least-squares techniques using SHELX97.[39] All non-hydrogen atoms of all the complexes were refined anisotropically. Hydrogen atoms of all the compounds were found in the difference Fourier maps and refined using a riding model, with C−H = 0.95 (CH)$_{ar}$, C−H = 0.99 (CH₂), and C−H = 0.98 (CH₃) Å and with U_{iso}(H) = 1.2U_{eq}(CH, CH₂) and 1.5U_{eq}(CH₃), except for those belonging to N−H groups, which were refined freely in most cases. The Ni, Cl1, and Cl2 atoms in **4** are disordered over two positions with the occupancy factors of 0.876(7) and 0.124(7). The structures of all the studied complexes, depicted in Figures 3, 4, 5, 6 and Supporting Information, Figure S3, were drawn using the Mercury and Diamond software.[40]

Theoretical Methods. The ab initio theoretical calculations were performed using the ORCA 3.0.1 computational package.[41] The relativistic effects were included in all the calculations using the scalar relativistic contracted version of def2-TZVP(-f) basis functions[42] and with zero order regular approximation (ZORA).[43]

The single-point energy calculations based on X-ray geometries were done using the B3LYP functional.[44] The isotropic exchange constants J were calculated by comparing the energies of HS and broken-symmetry (BS) spin states utilizing both Ruiz's approach[45] and Yamaguchi's approach[46] by comparing the energies of HS and BS spin states. In all the cases the calculations were based on the experimental X-ray structures, but the hydrogen atom positions were optimized when these atoms were involved in a magnetic coupling path using the
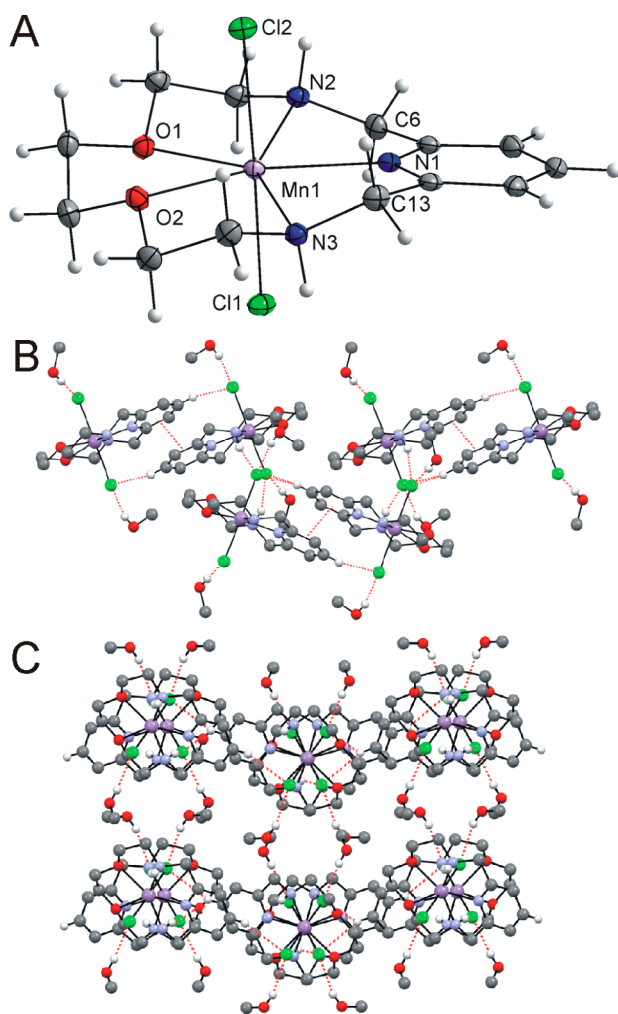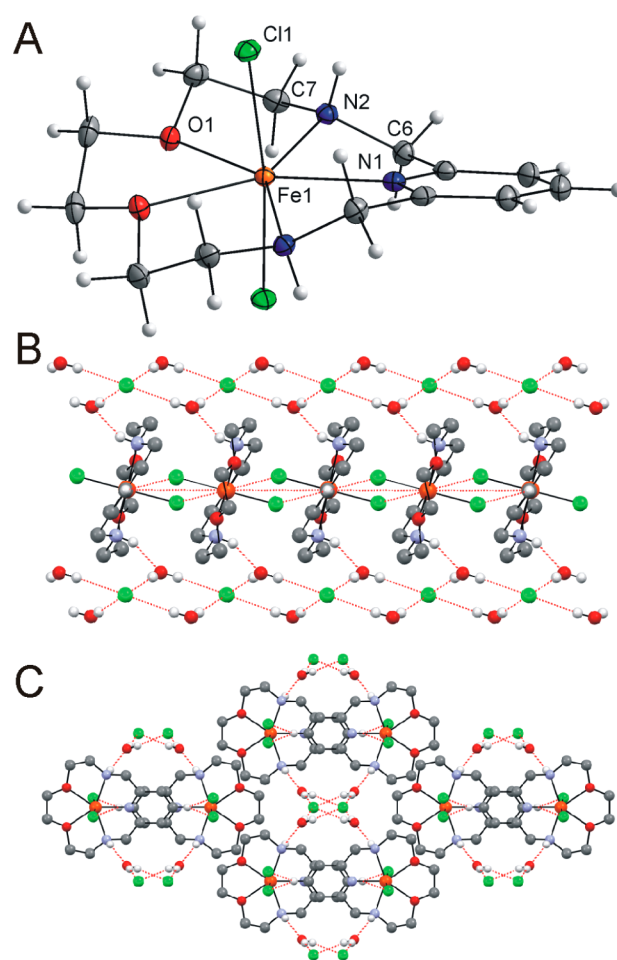
Figure 3. (A) Molecular structure of $[Mn(L)Cl_2]\cdot 2CH_3OH$ (**1**·$2CH_3OH$). The solvent molecules were omitted for clarity. Non-hydrogen atoms are drawn as thermal ellipsoids at the 50% probability level. (B) Part of the crystal structure of **1**·$2CH_3OH$ showing $\pi-\pi$ stacking and N−H···Cl, O−H···Cl, and C−H···Cl noncovalent contacts (red dashed lines, view along c axis). (C) View on the packing of the 2D-sheet structure in **1**·$2CH_3OH$ (red dashed lines represent the above-mentioned contacts). Hydrogen atoms not involved in these contacts were omitted for clarity.

Figure 4. (A) Molecular structure of the $[Fe(L)Cl_2]^+$ complex cation in $[Fe(L)Cl_2]Cl\cdot 2H_2O$ (**2**·$2H_2O$). The crystal water molecules and chloride counterion were omitted for clarity. Non-hydrogen atoms are drawn as thermal ellipsoids at the 50% probability level. (B) Part of the crystal structure of **2**·$2H_2O$ showing $\pi-\pi$ stacking and N−H···O, O−H···Cl, and C−H···Cl noncovalent contacts (red dashed lines, view along b axis). (C) View on the packing of **2**·$2H_2O$ down the c axis (red dashed lines represent the above-mentioned contacts). Hydrogen atoms not involved in these contacts were omitted for clarity.

B3LYP functional and atom-pairwise dispersion correction to the density functional theory (DFT) energy with the Becke−Johnson damping (D3BJ).[47]

The calculations of ZFS parameters were performed using state average complete active space self-consistent field (SA-CASSCF)[48] wave functions complemented by N-electron valence second order perturbation theory (NEVPT2).[49] The active spaces of the CASSCF calculations on metal-based d-orbitals were defined as follows: CAS(5,5) for Mn(II) and Fe(III), CAS(7,5) for Co(II), CAS(8,5) for Ni(II), and CAS(9,5) for Cu(II). In the state-averaged approach all multiplets for given electron configuration were equally weighted. The ZFS parameters, based on dominant spin−orbit coupling contributions from excited states, were calculated through quasi-degenerate perturbation theory (QDPT),[50] in which an approximation to the Breit−Pauli form of the spin−orbit coupling operator (SOMF approximation)[51] and the effective Hamiltonian theory[52] were utilized.

All the above-mentioned calculations utilized the resolution of identity (RI) approximation with the decontracted auxiliary def2-TZV/J or def2-TZV/C Coulomb fitting basis sets and the chain-of-spheres approximation to exact exchange.[53] Increased integration grids

(Grid5 for DFT and Grid4 for CASSCF in ORCA convention) and tight SCF convergence criteria were used in all calculations.

The Multiwfn 3.3.5 (A Multifunctional Wavefunction Analyzer)[54] was used to analyze the results from single-point energy calculations (B3LYP+ZORA/def2-TZVP(-f)) to quantify bond order using Mayer's bond analysis[55] and also by electron localization function (ELF)[56] based on topology analysis technique proposed by Bader.[57]

The spin densities were visualized with the help of program GABEDIT[58] and POV-Ray.[59]

Solution Studies. The bulk magnetic susceptibility (BMS) measurements were performed on a 400 MHz Varian spectrometer at 298 K. Samples in 5 mm NMR tubes contained 5 mM complex and 5% t-butanol by volume in D_2O (or CD_3OD) and an insert NMR tube containing 5% t-butanol by volume in D_2O (or CD_3OD).

The cyclic voltammetry was performed on electrochemical analyzer CHI600C (CH Instrument Inc., Austin, TX, USA). A conventional electrochemical three-electrode-type cell was used with a Ag/AgCl or Ag/Ag+ reference electrode, a platinum wire auxiliary electrode, and a glassy carbon working electrode. The final potential values referred to SHE were obtained using the relation between the two reference electrodes: Ag/AgCl electrode (saturated KCl) versus SHE = +198 mV or using internal ferrocene/ferrocenium standard ($E_{1/2}$ = 0.665 V). The measurements were performed in aqueous solutions in the
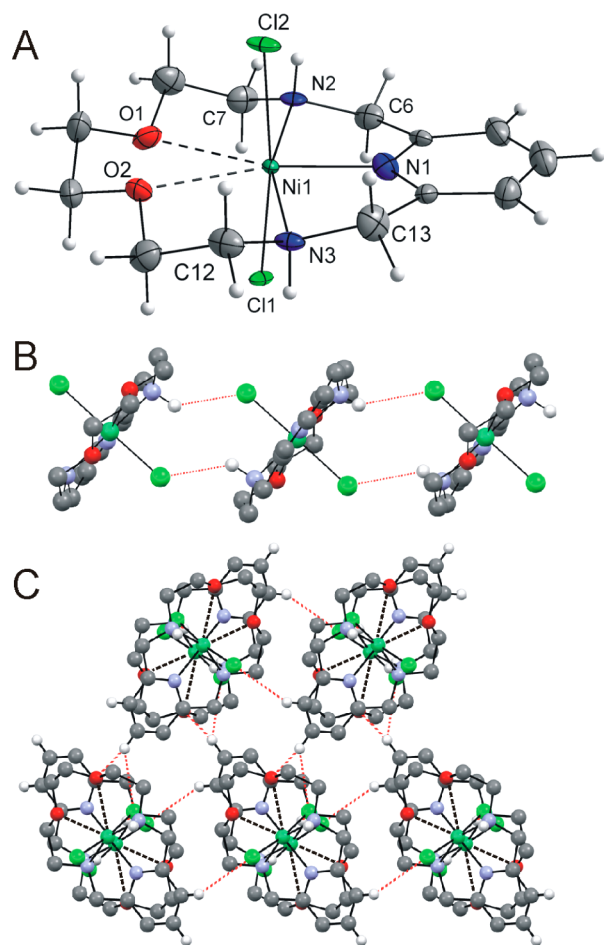
Figure 5. (A) Molecular structure of $[Ni(L)Cl_2]$ (**4**), the second parts of the disordered Ni and Cl atoms are omitted for clarity. The dashed lines between Ni and O atoms represent semicoordination. Non-hydrogen atoms are drawn as thermal ellipsoids at the 50% probability level. (B) Part of the crystal structure of **4** showing N−H⋯Cl hydrogen bonds (red dashed lines). (C) View on the packing of **4** (red dashed lines represent N−H⋯Cl and C−H⋯Cl noncovalent contacts). Hydrogen atoms not involved in these contacts were omitted for clarity.

presence of 0.1 M KCl or in acetonitrile (MeCN) solution in the presence of 0.1 M tetrabutylammonium perchlorate (TBAP) as a supporting electrolyte with scan rate of 100 mV s^{-1} for 5×10^{-3} M concentration of the complexes.

■ RESULTS AND DISCUSSION

Syntheses and General Characterization. The ligand **L** was synthesized according to the previously described literature procedure.[22] All the complexes were prepared by the same procedure based on mixing free **L** and the appropriate metal halide in MeOH in an equimolar ratio and heating to reflux. Solid complexes precipitated from the solution upon addition of excess of Et$_2$O. The solubility of Mn(II), Co(II), Ni(II), and Zn(II) complexes (**1**, **3**, **4**, and **6**) in MeOH was higher than that of Fe(III) and Cu(II) complexes (**2** and **5**), which partially crystallized from MeOH after the solutions cooled to room temperature. Measured IR spectra of the ligand **L** and all the complexes revealed a similar pattern, as it is shown in Supporting Information, Figure S1 (a complete list of peaks for each complex can be found in Supporting Information), showing the presence of **L** within the complexes. They all

contain two medium peaks at ∼1440 and ∼1470 cm^{-1} and a sharp doublet at 1600 and 1580 cm^{-1} corresponding to the wagging vibrations of the pyridine ring. Multiplets at ∼2900 cm^{-1} correspond to the CH$_2$ stretching vibrations, and the medium signal assigned to the stretching mode of the two NH groups is found at ∼3200 cm^{-1} (shifted by ∼100 cm^{-1} to lower wavenumbers upon coordination to the metal). Only in the spectrum of **2**, strong absorption bands between 3300 and 3500 cm^{-1} corresponding to the stretching vibrations of crystal water molecules and broad absorption band at 586 cm^{-1}, which could be assigned to the rocking vibration of water molecule connected to NH group via hydrogen bond,[4] have been observed. The results of simultaneous TG/DTA analyses in a dynamic air atmosphere are shown in Supporting Information, Figure S2 for two representative complexes **1** and **2**. In the temperature range of 25−170 °C, a weight loss corresponding to the elimination of half water molecule, one MeOH molecule, and half water solvate molecule(s) was observed for Mn(II) (**1**), Fe(III) (**2**), and Co(II) (**3**) complexes, respectively (endo effect in DTA curve at 120 °C was found only for **2**). Further thermal decomposition including loss of the rest of water solvate molecules proceeded in two/one step without formation of thermally stable intermediates but with several endo and exo effects. The decomposition was finished above 600 °C, and the final products were not studied in detail. The obtained results also indicated that the fast synthetic method (a precipitation by addition of Et$_2$O) gave complexes with different types and/or numbers of crystal solvent molecules, and thus this discrepancy can be seen looking to results of TG/DTA and X-ray structural data.

Description of Crystal Structures of 1−6. The molecular structures of all the complexes were determined using single-crystal X-ray diffraction analysis, and selected crystallographic data and structural refinement parameters are listed in Table 1.

Mn(II), Fe(III), and Co(II) Complexes (1, 2, and 3). Complexes **1**−**3** revealed similar molecular structures. The molecular structure of **1** is depicted in Figure 3a, while that of **2** is depicted in Figure 4a and that of **3** is in Supporting Information, Figure S3a. Selected structural parameters are listed in Table 2. In all three complexes, the central metal atom adopts pentagonal bipyramidal geometry with the N$_3$O$_2$ donor set forming a planar equatorial plane and two chlorido ligands coordinated in axial positions. The observed CN of 7 is typical for Mn(II) and Fe(III) complexes with the 15-membered pyridine-based macrocycles with five donor atoms (Figures 2, 3a, and 4a), while this CN is rather exceptional for Co(II) complexes. The M−N(pyridine) bond is the shortest from all coordination bonds in **1**−**3** (2.218(2), 2.155(2), and 2.136(2) Å for **1**, **2**, and **3**, respectively) which is a typical feature also for all other studied complexes **4**−**6**. In **1**, the M−N (aliphatic) and M−O bonds have very similar lengths (2.30−2.32 Å), while in **2** and **3** the M−N (aliphatic) distances are a bit shortened (∼0.05−0.1 Å) in comparison with the M−O distances. On the other hand, the pentagonal bipyramid is a little distorted in all the cases, because the axial M−Cl bonds are ∼0.1−0.2 Å longer than the other five coordination bonds to the central metal atom. Additionally, only Fe(III) complex unit has a real twofold rotation axis (C$_2$) lying on the Fe−N(pyridine) coordination bond.

The deformation of the pentagonal bipyramidal coordination environment around the central metal atom in the complex is usually described by the mean deviation value of all ligand donor atoms from the least-squares plane formed by central
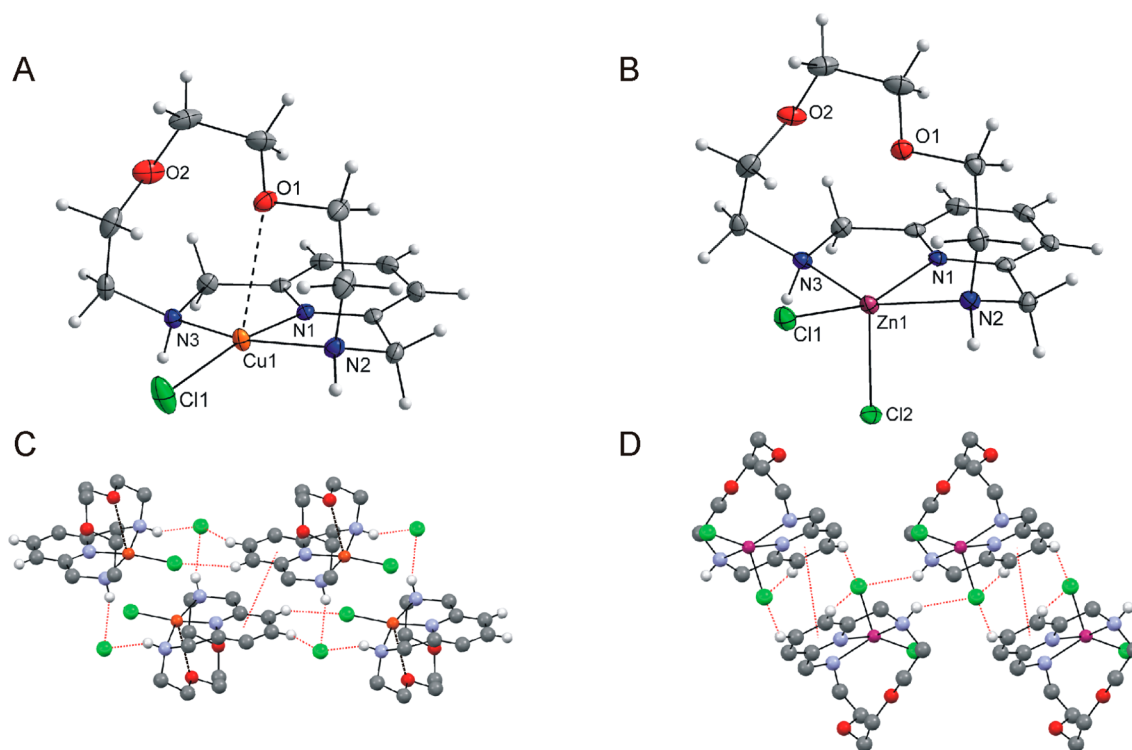
Figure 6. (A) Molecular structure of the [Cu(L)Cl]+ complex cation in [Cu(L)Cl]Cl (**5**). (B) Molecular structure of [Zn(L)Cl$_2$] (**6**). Non-hydrogen atoms are drawn as thermal ellipsoids at the 50% probability level. (C, D) Part of the crystal structure of **5** or **6** showing π−π stacking and N−H···Cl and C−H···Cl noncovalent contacts (red dashed lines). Hydrogen atoms not involved in these contacts were omitted for clarity.

Table 1. Crystallographic Parameters of the Studied Complexes

compound	1·2CH$_3$OH	2·2H$_2$O	3·2CH$_3$OH	4	5	6
formula	C$_{15}$H$_{29}$Cl$_2$N$_3$O$_4$Mn	C$_{13}$H$_{25}$Cl$_3$N$_3$O$_4$Fe	C$_{15}$H$_{29}$Cl$_2$N$_3$O$_4$Co	C$_{13}$H$_{21}$Cl$_2$N$_3$O$_2$Ni	C$_{13}$H$_{21}$Cl$_2$N$_3$O$_2$Cu	C$_{13}$H$_{21}$Cl$_2$N$_3$O$_2$Zn
M_r	441.25	449.56	445.24	380.94	385.77	387.60
color	colorless	yellow plate	violet	green	dark blue	colorless
crystal system	monoclinic	monoclinic	monoclinic	monoclinic	triclinic	triclinic
space group	P2$_1$/n	C2/c	P2$_1$/n	P2$_1$/c	P$\bar{1}$	P$\bar{1}$
a (Å)	10.1808(2)	9.2600(2)	10.0967(5)	13.0687(3)	9.3950(3)	7.6819(4)
b (Å)	16.0983(3)	22.2181(6)	16.0801(5)	7.63859(19)	9.6921(2)	9.1387(4)
c (Å)	12.7156(3)	9.0231(2)	12.6714(6)	16.8592(4)	9.8499(2)	11.5537(4)
α (deg)	90.00	90.00	90.00	90.00	82.7007(19)	91.215(3)
β (deg)	110.430(3)	90.231(2)	110.714(6)	101.070(3)	65.535(3)	92.602(3)
γ (deg)	90.00	90.00	90.00	90.00	77.518(2)	105.474(4)
U, Å^3	1952.92(8)	1856.40(8)	1924.30(14)	1651.69(7)	796.38(4)	780.42(6)
Z	4	4	4	4	2	2
D_{calc}, g cm^{-3}	1.501	1.609	1.537	1.532	1.609	1.649
μ, mm^{-1}	0.974	1.267	1.194	1.504	1.713	1.923
$F(000)$	924	932	932	792	398	400
reflections collected	18 083	8957	17 481	14 842	7573	7293
independent reflections	3435	1640	3378	2893	2805	2736
	[R(int) = 0.0243]	[R(int) = 0.0154]	[R(int) = 0.0206]	[R(int) = 0.0269]	[R(int) = 0.0182]	[R(int) = 0.0151]
data/restraints/parameters	3435/0/228	1640/2/133	3378/0/238	2893/0/220	2805/0/198	2736/0/190
goodness-of-fit on F^2	1.064	1.091	1.060	1.116	1.048	1.083
R_1, wR_2 $(I > 2\sigma(I))^a$	0.0233/0.0633	0.0190/0.0524	0.0221/0.0584	0.0609/0.1689	0.0226 /0.0586	0.0197/0.0528
R_1, wR_2 (all data)^a	0.0282/0.0646	0.0206/0.0531	0.0248/0.0593	0.0677/0.1729	0.0263/0.0594	0.0209/0.0531
largest diff. peak and hole, A^{-3}	0.318 and −0.276	0.298 and −0.168	0.332 and −0.232	2.320 and −0.441	0.337 and −0.212	0.309 and −0.252
CCDC number	1038350	1038349	1038347	1038351	1038348	1038352

$^a R_1 = \sum(|F_o| - |F_c|)/\sum|F_c|$; $wR_2 = [\sum w(F_o{}^2 - F_c{}^2)^2/\Sigma w(F_o{}^2)^2]^{1/2}$.

metal and the donor atoms of the ligand. Its value for **1**, **2**, and **3** is 0.14, 0.05, and 0.13 Å, respectively, which documents that

the best planar location of the plane-forming atoms is for **2** (Fe(III)), while in **1** and **3** (Mn(II) and Co(II)) it is ∼2.5

Table 2. Selected Bond Lengths (Å) and Angles (deg) for All the Studied Complexes

distances	1·2CH₃OH	2·2H₂O	3·2CH₃OH	4	5	6
M−N1	2.2182(13)	2.1553(17)	2.1363(13)	1.987(4)	1.9250(15)	2.0855(13)
M−N2	2.3086(13)	2.2010(12)	2.2183(13)	2.132(3)	2.0258(15)	2.1858(13)
M−N3	2.3081(13)		2.2224(13)	2.118(3)	2.0305(15)	2.2363(13)
M−O1	2.3204(11)	2.2467(10)	2.3382(11)	2.663(3)	2.721(2)	3.113(1)
M−O2	2.2980(11)		2.3119(11)	2.506(3)	3.816(2)	4.030(1)
M−Cl1	2.5347(4)	2.3085(3)	2.4637(4)	2.3804(16)	2.2113(5)	2.2966(4)
M−Cl2	2.5573(4)		2.4721(4)	2.3908(14)		2.3275(4)
angles						
N(1)−M(1)−N(2)	71.86(5)	71.75(3)	73.30(5)	80.05(15)	82.70(6)	77.13(5)
N(1)−M(1)−N(3)	72.43(5)		73.92(5)	80.12(15)	82.27(6)	76.40(5)
N(2)−M(1)−O(1)	73.15(4)	73.28(4)	72.58(4)	69.1(1)	75.20(6)	
O(2)−M(1)−N(3)	73.15(4)		72.60(4)	71.7(1)		
O(2), O(1)ᵃ−M(1)−O(1)	70.96(4)	70.15(5)	68.94(4)	61.3(1)		
N(1)−M(1)−Cl(1)	90.74(3)	93.697(10)	91.33(4)	94.95(11)	169.89(5)	159.71(4)
O(2), O(1)ᵃ−M(1)−Cl(1)	95.53(3)	88.68(3)	93.58(3)	92.61(9)		
N(3), N(2)ᵃ−M(1)−Cl(1)	88.89(4)	89.58(3)	88.97(4)	88.00(10)	98.20(4)	100.48(4)
N(2)−M(1)−Cl(1)	94.10(4)	92.74(3)	94.17(4)	93.19(11)	97.26(5)	99.13(4)
O(1)−M(1)−Cl(1)	84.30(3)	85.27(3)	83.67(3)	79.59(8)	107.12(3)	
N(1)−M(1)−Cl(2)	90.87(3)		92.60(4)	92.00(11)		98.01(4)
O(2)−M(1)−Cl(2)	83.10(3)		83.21(3)	81.56(9)		
N(3)−M(1)−Cl(2)	91.52(3)		92.21(4)	93.76(10)		94.62(4)
N(2)−M(1)−Cl(2)	86.47(3)		86.87(4)	87.44(10)		103.68(4)
O(1)−M(1)−Cl(2)	94.43(3)		93.04(3)	94.17(9)		
Cl(1)−M(1)−Cl(2)	178.388(16)	172.60(2)	176.070(15)	173.02(6)		102.234(16)
dihedral angles—macrocyclic conformation						
N1−C5−C6−N2	25.0(2)	(N1−C3−C6−N2) 32.5(2)	24.8(2)	24.4(5)	−24.4(2)	−21.4(2)
N2−C7−C8−O1	−60.4 (2)	−56.6(2)	−58.6(2)	−63.0(5)	66.2(2)	72.7(2)
O1−C9−C10−O2	59.5(2)	(O1−C9−C9−O1) 55.8(2)	58.1(2)	56.5(5)	−65.8(2)	−66.8(2)
O2−C11−C12−N3	−59.8(2)	(O1−C8−C7−N2) −56.6(2)	−57.8(2)	−59.7(4)	64.8(2)	64.7(2)
N3−C13−C1−N1	32.5(2)	(N2−C6−C3−N1) 27.7(2)	29.8(2)	20.7(5)	−4.7(2)	−3.3(2)

ᵃSymmetry code for **3·2CH₃OH**: $-x + 1, y, -z + 3/2$.

times higher. The difference in the donor atom arrangement around the central metal atom could be explained by higher oxidation state of iron atom, which has smaller ionic radius resulting in shorter and stronger bonds forcing the more rigid and thus more planar arrangement. The better planarity of the ligand-donor atoms is, on the other hand, compensated by larger twisting of the ethylene and benzylene bridges, which is apparent from the deviation of the benzyl carbon atoms (C6 and C13) under and above this plane: 0.55 Å for **1**, 0.74 Å for **2**, 0.56 and 0.55 Å for **3**. The obtained deviation values can be compared only in the case of Mn(II) with the value for complex with the corresponding Schiff base [Mn(15-pydienN₃O₂)Cl₂]·H₂O[16] (0.049 Å), which illustrates much higher flexibility of the macrocyclic scaffold of **L** in comparison with more rigid 15-pydienN₃O₂, but in general, good planar location of these six atoms. The coordination environment of Mn(II) in [Mn(15-pydienN₃O₂)Cl₂]·H₂O[16] is very similar and differs only in shorter Mn−N(imine) distances (~2.25 Å).

The molecular structure of Mn(II) complex is very similar to the previously determined structure of [Mn(L)Cl₂][Mn(L)-(H₂O)Cl]Cl·1.5H₂O[22] in which the same structural unit [Mn(L)Cl₂] was found. The length of Mn−N(pyridine) bond was found to be nearly identical to that determined for **2·2H₂O**, that is, 2.218 Å, and all the other bonds differed only negligibly. Crystal structures of other Mn(II) complexes [Mn(15-pydienN₃O₂)(NCS)₂],[2] [Mn(15-pydienN₃O₂)(H₂O)-Cl]ClO₄·CH₃OH,[14] [Mn(15-pydienN₅)(H₂O)₂]·4H₂O,[60] Mn-(15-pydienN₅)(H₂O)₂]·Cl(ClO₄),[61] and [Mn(15-pydienN₅)-

Cl₂]·H₂O[16] were previously described as well (for the structural formulas of the ligands, see Figure 1).

Complexes of **L** with other transition metals, except for Mn(II), have not been reported yet; thus, there is no crystal structure of structurally similar Fe(III) complex, despite few Fe(III) complexes prepared with 15-pydienN₃O₂ and chlorido coligands.[2] In CSD, there are deposited some X-ray structures of Fe(III) complexes with different ligands, for example, [Fe₂(15-pydienN₅)₂(OH)₂O](ClO₄)₄,[62] [Fe(15-pydienN₅)-(NCS)₂]ClO₄,[62,63] or some Fe(II) complexes, namely, [Fe-(15-pydienN₃O₂)(CN)₂]·H₂O,[8] ([[Fe(15-pydienN₃O₂)-(H₂O))₂Cr(CN)₆](ClO₄)·3H₂O,[18] [Fe(15-pydionN₅)-(CH₃OH)₂]·CH₃OH,[32] or [Fe(15-pydionN₅)(H₂O)₂]·Cl(ClO₄).[64] The total number of previously described Co(II)/(III) complexes of different 15-membered pyridine-based macrocycles is much lower than in the case of Mn(II) or Fe(III)/Fe(II). The crystal structures deposited with the CSD are as follows: [(Co(15-pydienN₃O₂))₂Cr(CN)₆]ClO₄·8H₂O[17] with CN of 7 for Co(II) and [Co(15-pyN₅-Me₂)Cl](ClO₄)₂[65] in which CN of Co(III) is only 6.

Noncovalent contacts, especially hydrogen bonds and π−π stacking, play a crucial role in the final crystal packing of **1−3**. The crystal structures of **1·2CH₃OH** and **3·2CH₃OH** are very similar, and both are stabilized by intermolecular hydrogen bond network. The [M(L)Cl₂] units are connected together through the N−H···Cl hydrogen bonds into a zigzag 1D chain, while two CH₃OH crystal solvent molecules are linked to the [M(L)Cl₂] unit via O−H···Cl hydrogen bonds (Figure 3b,

Table 3. Selected Hydrogen Bond Parameters (Å, deg) for Complexes 1−6

D−H···A[a]	d(D−H)	d(H···A)	d(D···A)	∠(DHA)	D−H···A	d(D−H)	d(H···A)	d(D···A)	∠(DHA)
1·2CH₃OH					**4**				
N(2)−H(2N)···Cl(1)[b]	0.93	2.74	3.5555(14)	146	N(2)−H(2N)···Cl(2)[c]	0.75(5)	2.69(4)	3.305(4)	142
N(3)−H(3N)···Cl(2)[d]	0.93	2.50	3.3415(14)	151	N(3)−H(3N)···Cl(1)[e]	0.92(5)	2.55(5)	3.290(4)	138
O(3)−H(3V)···Cl(1)	0.84	2.31	3.1302(15)	166	C(3)−H(3A)···Cl(1)[f]	0.95	2.8058(16)	3.511(5)	132
O(4)−H(4W)···Cl(2)	0.84	2.34	3.1538(15)	164	C(4)−H(4A)···Cl(2)[g]	0.95	2.8490(23)	3.630(5)	140
C(3)−H(3A)···Cl(1)[h]	0.95	2.8269(4)	3.5276(17)	131	C(3)−H(3A)···O(1)[f]	0.95	2.504(3)	3.289(6)	140
C(3)−H(3A)···Cl(2)[i]	0.95	2.9172(5)	3.6770(18)	138					
2·2H₂O					**5**				
N(2)−H(2N)···O(2)	0.854(18)	2.105(18)	2.8905(17)	153	N(3)−H(3N)···Cl(2)	0.87(2)	2.29(2)	3.1170(17)	158
O(2)−H(2V)···Cl(2)	0.822(18)	2.375(19)	3.1951(12)	176	N(2)−H(2N)···Cl(2)[j]	0.89(2)	2.39(2)	3.2140(17)	155
O(2)−H(2W)···Cl(2)[k]	0.80(2)	2.40(2)	3.1971(13)	174	C(2)−H(2A)···Cl(1)[l]	0.95	2.7499(5)	3.476(2)	134
C(1)−H(1A)···Cl(1)[m]	0.94(3)	2.86(2)	3.4886(15)	125	C(3)−H(3A)···Cl(2)[n]	0.95	2.7966(5)	3.595(2)	142
3·2CH₃OH					**6**				
O(3)−H(3W)···Cl(1)	0.79	2.35	3.1344(15)	172	N(2)−H(2N)···Cl(2)[o]	0.929(1)	2.5474(4)	3.3254(13)	141
O(4)−H(4W)···Cl(2)	0.95	2.21	3.1514(16)	170	C(3)−H(3A)···Cl(2)[p]	0.95	2.7446(4)	3.5024(15)	137
N(2)−H(2N)···Cl(1)[q]	0.871(19)	2.843(19)	3.5929(15)	145	C(4)−H(4A)···Cl(2)[r]	0.95	2.7728(4)	3.7028(18)	166
N(3)−H(3N)···Cl(2)[s]	0.842(19)	2.597(19)	3.3675(15)	153					
C(3)−H(3A)···Cl(1)[t]	0.95	2.8284(4)	3.5376(16)	132					
C(3)−H(3A)···Cl(2)[u]	0.95	2.9289(4)	3.6930(18)	138					

[a]Symmetry transformations used to generate equivalent atoms: [b]$x - 1/2, -y + 3/2, z - 1/2$. [c]$-x, -y + 1, -z + 1$. [d]$x + 1/2, -y + 3/2, z + 1/2$. [e]$-x + 1, -y + 1, -z + 1$. [f]$x, -y + 3/2, z + 1/2$. [g]$x, y + 1, z$. [h]$-x + 3/2, y + 1/2, -z + 3/2$. [i]$-x + 1, -y + 2, -z + 1$. [j]$-x + 1, -y, -z + 1$. [k]$-x, -y, -z + 1$. [l]$x, y + 1, z$. [m]$-x, -y + 1, -z$. [n]$-x + 1, -y + 1, -z + 1$. [o]$-x + 2, -y + 1, -z$. [p]$-x + 1, -y, -z$. [q]$x + 1/2, -y + 1/2, z + 1/2$. [r]$x - 1, y, z$. [s]$x - 1/2, -y + 1/2, z - 1/2$. [t]$-x + 1/2, y + 1/2, -z + 1/2$. [u]$-x + 1, -y + 1, -z + 1$.

Supporting Information, Figure S3b, and Table 3). The two neighboring infinite chains are connected by face-to-face π−π stacking interactions between two pyridine rings of two [M(L)Cl₂] units (the centroid···centroid distance = Cg···Cg = 3.5658(1) Å for **1**, Cg···Cg = 3.5834(2)Å for **3**), and the crystal structure is further stabilized by bifurcated C3−H3A··· Cl1(Cl2) noncovalent contact (with the C···Cl distances of 3.528(2) and 3.677(2) for **1**, 3.538(2) and 3.693(2) for **3**, respectively) resulting in a separated 2D sheet without any noncovalent contacts between each other (Figure 3c and Supporting Information, Figure S3c).

In the case of **2**, one positive charge of the complex [Fe(L)Cl₂]⁺ cation is compensated by one uncoordinated chloride counterion, which is together with the crystal water molecules involved in an extensive system of intermolecular hydrogen bonds (Table 3).

It is clearly shown in Figure 4b that the crystal water molecules and uncoordinated chloride ions form 1D chain mediated by O−H$_{water}$···Cl$_{uncoordinated}$ hydrogen bonds, and the macrocyclic units [Fe(L)Cl₂]⁺ form second 1D chain mediated by weak π−π interactions (Cg···Cg = 4.5205(1) Å) and C−H$_{aromatic}$···Cl contacts. These two chains are connected to each other by a strong N−H···O$_{water}$ hydrogen bond (N···O = 2.891(2) Å), and they alternate in the crystal structure as shown in Figure 4c.

Ni(II) Complex (4). The molecular structure of **4** is shown in Figure 5a, and selected interatomic distances and angles are given in Table 2. The coordination sphere of Ni(II) differs from the above-described complexes, because Ni(II) reveals a markedly distorted pentagonal bipyramidal geometry. Its CN could be classified as 5 + 2, because the Ni−N (1.987(4)− 2.132(3) Å) and Ni−Cl distances (2.380(2) and 2.391(2) Å) are shortened in comparison with the above-described structures of complexes **1−3**, while the Ni−O distances are much more elongated (2.506(3) and 2.663(3) Å) indicating strong decrease in stability of Ni−O coordination bonds, because the mean value of the Ni−O bond distance is only

2.055 Å, and 90% of all the observed Ni−O bonds, as found in CSD, have length in the range of 1.964−2.144 Å. Nevertheless, there are some examples of Ni(II) complexes in which the Ni− O distance is close to or exceeds 2.50 Å.[33]

Additionally, Ni(II) atom and both chloride atoms are disordered between two positions with the occupancy factors of 0.876(7) and 0.124(7). (Note: atoms with higher occupancy factors were taken into account in connection with the above-described interatomic parameter evaluations.) The mean deviation value from the NiN₃O₂ least-squares plane is 0.17 Å illustrating the worst planar location of these atoms in comparison with the all three above-described complexes. The most deviated atoms from this plane are surprisingly aliphatic carbon atoms C7 and C12 (0.39 Å) together with the benzyl carbon atoms C6 and C13 (0.37 and 0.38 Å).

In the crystal structure of **4**, there are N−H···Cl hydrogen bonds, whose presence results in the formation of 1D chainlike structure depicted in Figure 5b.

These chains are connected to each other by additional bifurcated C3−H3A···O1(Cl1) (with C···O and C···Cl distances of 3.289(6) and 3.511(5)) and C−H$_{aromatic}$···Cl noncovalent contacts, and thus, these chains form two alternating layers with parallel arrangement of these chains, which are rotated by 78° in these two layers (Figure 5c, Table 3). Moreover, there is no evidence for any π−π interactions between any pyridine rings in the crystal structure. Surprisingly, there is no Ni(II) complex of 15-membered pyridine-containing macrocycle deposited in the CSD although several Ni(II) complexes of different 15-membered pyridine-based macrocycles have been previously prepared.[66,67]

**Cu(II) and Zn(II) Complexes (5 and 6).** The molecular structures of **5** and **6** are depicted in Figure 6a,b, respectively. In these two cases, drastic change in the coordination environment of the central metal atom occurs, and the macrocyclic ligand is markedly folded. All Cu−N bond lengths are the shortest from all the metal−nitrogen distances within the studied complexes; Cu−N(pyridine) is the shortest one

(1.925(2) Å), while the other two Cu−N(aliphatic) bonds have the length of ∼2.03 Å. All these distances are ∼0.02 Å longer in **6**. The Cu−O distances are much more elongated, one distance is 2.721(2) Å, resulting in a weak semicoordination bond (Jahn−Teller effect), usually found for coordination of water, perchlorato and nitrato ligands or special carboxylates/ sulfonates in Cu(II) complexes (CSD),[1] and the second distance is 3.816(2) Å, which clearly demonstrates that this second oxygen atom is not coordinated to Cu(II). The Zn−O distances are longer than 3 Å (3.113(2) and 4.030(2) Å), which indicates no coordination of these atoms to Zn(II). According to these facts, Cu(II) and Zn(II) adopt distorted square pyramidal geometry with CN 4 + 1 and 5, and the N_3OCl and N_3Cl_2 donor atom set, respectively. The calculated value of Addison's τ parameter helped us to describe the coordination geometry more precisely and to distinguish between the square pyramidal and trigonal bipyramidal arrangement.[68] The values were determined to be 0.09 for **5** and 0.17 for **6**, which suggest the square pyramidal geometry for each complex. In accordance with this fact, Cu(II) or Zn(II) atom is located only 0.06 or 0.30 Å above the MN_3Cl least-squares plane.

Similarly to that of **4**, the structures of **5** and **6** do not contain any solvent molecules; nevertheless, chloride counterions or chlorido ligands play an important role in the formation of hydrogen bonds network (Figure 6c,d and Table 3). Four N− H···Cl(counterion) hydrogen bonds connect two macrocyclic units [Cu(**L**)Cl]$^+$ into a pseudodimer (similarly two N−H··· Cl(coordinated) hydrogen bonds connect two neutral [Zn(**L**)Cl$_2$] units), and these dimers are additionally coupled via $\pi-\pi$ interaction between the pyridine rings (Cg···Cg = 3.8377(1) Å for **5** and Cg···Cg = 3.9266(1) Å for **6**) and via C−H$_{aromatic}$···Cl noncovalent contact(s) into a 1D chainlike structure (Figure 6c,d). The crystal structures of the following Cu(II) complexes with penta-aza macrocyclic ligands have been published to date: [Cu(15-pyN$_5$)](PF$_6$)$_2$[69] and [Cu(15-pyN$_5$-Me$_2$)](PF$_6$)$_2$,[65] in which Cu(II) has CN of 5, while the crystal structures of similar Zn(II) complexes were determined only for [Zn(15-pydienN$_5$)(SCN)$_2$]·C$_2$H$_4$Cl$_2$[70] and [Zn(15-pyN$_5$-Me$_4$)]- (ClO$_4$)$_2$[67] with CN of 7 and 5 for Zn(II), respectively.

Comparison of the Crystal Structures of Complexes 1−6. Several trends can be observed when all the determined crystal structures of the studied complexes are compared. The metal−donor atom distances depend on the complexated metal atom, and their variations are displayed in Figure 7. When the central metal atom is changing from Mn(II) to Cu(II), the metal−nitrogen distances are shortening, while they are a little bit elongated going from Cu(II) to Zn(II). On the other hand, the metal−oxygen distances are elongating within the whole series going from Mn(II) to Zn(II). A consequence of these differences in metal−oxygen and metal-nitrogen distances is the shifting of the metal from the center of the cavity of the macrocyclic ligand closer to its part containing nitrogen atoms. This trend is also illustrated by the value of O−M−O angle (Table 2), which decreases, depending on the metal atom, from Mn(II) to Ni(II) (from complex **1** to **4**). The above-mentioned changes could be related to the changing ionic radius of the complexated metal ion (Table 4),[71] and the observed trend is in good correlation with the Irving−William series. Furthermore, it was published recently that the Jahn−Teller effect operating in Ni(II) complexes with CN of 7 could be another reason for the increase of the metal−oxygen distances.[72] Changing the metal from Mn(II) to Zn(II) (complex **1** to **6**), the macrocyclic cavity becomes too large for smaller cations, which results in a
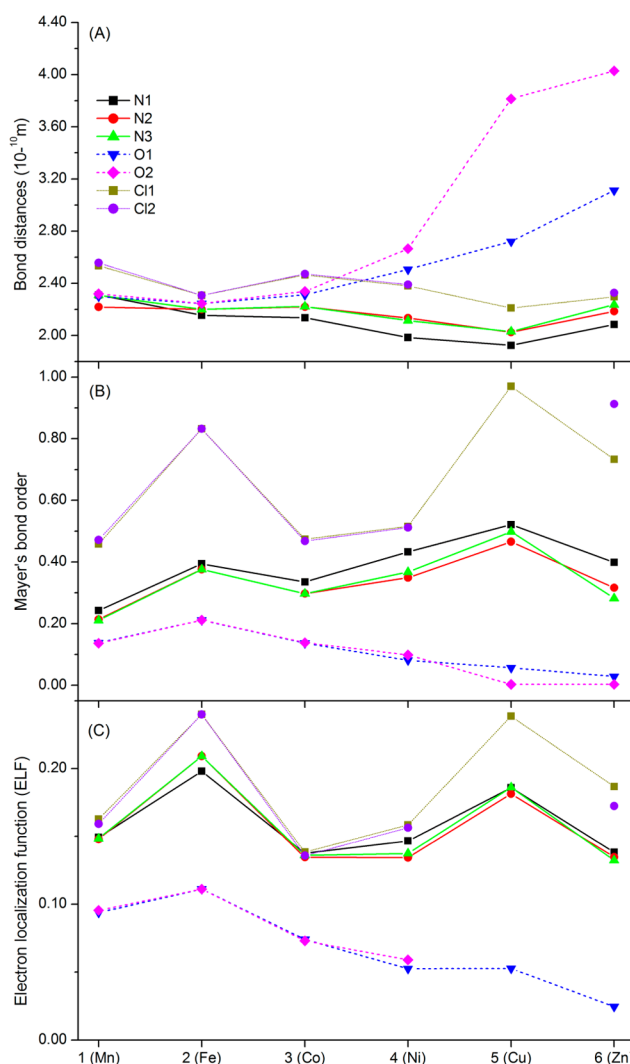
Figure 7. Variation of the metal−donor atom distances (A), Mayer's bond order (B), and electron localization function (C) in the studied complexes depending on the central metal atom.

folding of the macrocycle and reduction of the coordination number from 7 to 5. Mn(II), Fe(III), and Co(II) complexes **1**−**3** reveal CN of 7 with the $N_3O_2Cl_2$ donor atom set; Ni(II) complex **4** is somewhere between this transformation with two semicoordinated oxygen atoms (CN 5 + 2, $N_3O_2Cl_2$ donor atom set) as well as Cu(II) complex **5** with CN 4 + 1 and one semicoordinated oxygen atom (N_3OCl donor atom set). CN of 5 was found in the last-in-row Zn(II) complex **6** with the N_3Cl_2 donor atom set.

To support our conclusions, the molecular structures of complexes **4**−**6** were analyzed by program Shape 2.1 providing continuous shape measures.[73] Any coordination sphere can be described by an ideal polyhedron that has the lowest deviation from the real geometry. Thus, the lowest value of deviation for **4** was found for pentagonal bipyramid (from all possible polyhedra for CN = 5, 6, and 7, Supporting Information, Table S1), square for **5**, and square pyramid for **6** (all possible polyhedra for CN = 4, 5, and 6, Table S1). Except for **5**, the calculated results are in agreement with our previous presumption; nevertheless, low values of deviations were observed also for tetragonal pyramid or octahedron for **5** or **6**, respectively. Therefore, additional ab initio calculations

Table 4. Dihedral Angles between Planes 1–3[a] Together with Donor Atom Deviations and Mean Deviation from the Least-Square Plane Defined by the Ligand Donor Atoms and the Central Metal Atom

complex	1·2CH$_3$OH	2·2H$_2$O	3·2CH$_3$OH	4	5	6
			dihedral angle (deg)			
plane1/plane2[a]	12.86	19.86	12.98	7.02	11.73	10.33
plane1/plane3[a]	77.71	70.53	77.10	82.81	85.89	85.95
plane2/plane3[a]	89.36	89.61	89.59	88.68	77.63	85.47
			deviation from the least-squares plane[b] (Å)			
metal	0.024	0.000	0.012	0.000	0.057	0.302
N1(py)	0.024	0.000	0.031	0.005	0.144	0.073
N2	0.155	0.047	0.146	0.151	0.095	0.068
N3	0.101	0.047[c]	0.088	0.167	0.095	0.067
O1/Cl1[b]	0.215	0.076	0.198	0.251	0.102	0.093
O2	0.209	0.076[c]	0.184	0.262		
mean	0.141	0.049	0.129	0.167	0.109	0.075
	Mn(II)	Fe(III)	Co(II)	Ni(II)	Cu(II)	Zn(II)
r_{ion}, Å[d]	0.83 (6)	0.645 (6)	0.745 (6)	0.69 (6)	0.73 (6)	0.74 (6)
	0.90 (7)			0.63 (5)	0.65 (5)	0.68 (5)

[a]Plane 1 defined by pyridine ring, plane 2 defined by donor atom set (N$_3$O$_2$, N$_3$ for **5** and **6**), plane 3 defined by Cl–M–Cl bond (Cl–Cu–O1 bond for **5**). [b]For **1**–**4** the least-squares plane defined by MN$_3$O$_2$, for **5** and **6** by MN$_3$Cl atoms. [c]In **2** only N2 and O1 are present. [d]r_{ion} = ionic radius for the ions in HS state, the value in parentheses stands for coordination number, ref 71.

concerning the strength of coordination bonds and coordination geometries were performed and are discussed later.

In accordance with this finding is the progress of the values of atom deviations and mean deviation from the least-squares plane MN$_3$O$_2$ listed in Table 4. This deviation is the lowest for Fe(III) (0.049 Å) and increases for Co(II) and Mn(II) (0.129, and 0.141 Å, respectively) to finally reach the largest value for Ni(II) (0.167 Å). The observed trend in the deviations can be related not only to the changes in the ionic radius of the complexated metal ions but also to a different charge of the ions and a different overall symmetry of the coordination spheres. When Fe(III) and Ni(II) complexes **2** and **4** are compared, the ionic radii of the ions are similar (Table 4), but Fe(III) has a larger change than the other ions providing stronger electrostatic attraction between the ion and ligand and thus has the most symmetrical coordination sphere of the series (the difference between the maximal and minimal metal–ligand donor atom distances is only 0.16 Å). On the other hand, Ni(II) complex **4** has lower charge and the most unsymmetrical coordination sphere in the series, related to the expected Jahn–Teller effect (the difference in metal–ligand donor atom distances is even 0.67 Å). The two oxygen atoms in **4** are only semicoordinated and thus have the largest deviation from the least-squares plane MN$_3$O$_2$. It could be also suggested that, for smaller cations, the donor atoms need to be closer to the metal, which could be accomplished by increased folding (rotation) of the macrocyclic scaffold. Other parameters describing the geometric properties of the complex molecules are dihedral angles between three planes 1–3 listed in Table 4 (planes defined by (i) pyridine unit, (ii) nitrogen-oxygen donor atom set, (iii) Cl–M–Cl or Cl–Cu–O1 bonds). The plane2/plane3 dihedral angles are close to 90°, indicating almost perpedicular coordination of both chlorido ligands (no side-deformation of pentagonal bipyramid in axial position), except for **5**, in which the lower value of the angle indicates side-deformation of the apex of the tetragonal pyramid, which is in accordance with the low value of N2–Cu–O1 angle (75.20°). The plane1/plane3 dihedral angles are in the range of 70–85°, which illustrates that the pyridine ring is not perpendicular to Cl–M–Cl or Cl–Cu–O1 vectors but is turned by 15–30°, and the highest value

was found in **2**, while the lowest value was found in **6**. This twisting of pyridine ring to Cl–M–Cl(O1) vectors as well as to nitrogen–oxygen donor atom set is documented by values of plane1/plane2 dihedral angles. The highest torsion was found in **2** (corresponding to the highest deviation of C6 benzyl atoms from the plane formed by central metal and all donor atoms) and the lowest value in **4**. This is in correlation with the mean deviation from the plane defined by all donor atoms and central metal atom, which has an opposite trend. This finding confirmed our presumption that the planar arrangement of the five donor atoms of the macrocycle around the metal center results in a big torsion of all other bonds in terms of higher deviation of the whole macrocycle scaffold from the planarity. This trend can be also illustrated by the values of dihedral angles listed in Table 2.

Concerning the noncovalent contacts, important intermolecular hydrogen bonds network was found in each crystal structure. The most important hydrogen bonds were N–H⋯O, O–H⋯Cl, and N–H⋯Cl with donor⋯acceptor distances ranging from ∼3.1 to ∼3.6 Å indicating their weak bonding character. Only one strong hydrogen bond N–H⋯O$_{water}$ (N⋯O distance 2.89 Å) was found in **2**. The complex units were usually connected together via these hydrogen bonds or weak C–H⋯Cl (C⋯Cl distances from ∼3.5 to ∼3.7 Å) or C–H⋯O (C⋯O distance 3.289(6) Å) hydrogen bonds as well as via π–π interaction between the pyridine rings (not found in **4**) always in slipped (offset) face-to-face alignment (Cg⋯Cg from ∼3.6 to ∼4.5 Å), which significantly contribute to the final 3D crystal packing. Finally the metal⋯metal distances in each complex were investigated, and the value of the shortest distance in each structure increases going from Cu(II) to Fe(III); it later drops for Mn(II) (see later in magnetic measurements section). In context of involved noncovalent contacts, the shortest metal⋯metal distances were found for complex units connected with hydrogen bonds (**1**, **3**, **4**, and **5**) or other noncovalent contacts (**2**). Thus, these noncovalent contacts play an important role in additional investigation of magnetic properties of these compounds (vide infra).

Ab Initio Calculations. Nowadays, there are many properties that can be thoroughly studied by ab initio

Table 5. Comparison of Selected ZFS Parameters and g-Factors Determined for Complexes 1−5 Together with the Results of Magnetic Analysis Using Different Models of the Spin Hamiltonian

compound	1	2	3	4	5
complexed metal	Mn(II)	Fe(III)	Co(II)	Ni(II)	Cu(II)
electron configuration	$3d^5$	$3d^5$	$3d^7$	$3d^8$	$3d^9$
spin state S	5/2	5/2	3/2	1	1/2
ZFS values based on CASSCF/NEVPT2 calculations					
D (cm^{-1})	0.0171	−0.394	45.0	−6.08	
E/D	0.112	0.235	0.0433	0.245	
g_1	2.000	2.000	2.004	2.218	2.068
g_2	2.000	2.000	2.421	2.239	2.071
g_3	2.000	2.000	2.465	2.275	2.349
The largest isotropic exchange J values based on DFT calculations					
J^Y (cm^{-1})	−0.11	−0.11	−0.02	−0.52	−2.49
d(M···M) (Å)	6.6268(4)	7.5084(2)	8.6291(4)	6.528(2)	9.6921(4)
Magnetic analysis with the Curie−Weiss law[a]					
g	2.04	2.10	2.48	2.28	2.07
Θ (K)	−0.05	−3.1	−9.5	−1.6	−3.5
Magnetic analysis with a monomeric model[b,c]					
g	2.05	2.05	g_{xy} = 2.48	2.27	
D (cm^{-1})			40.0	−5.13	
E/D				0.33	
zj (cm^{-1})	−0.11	−0.35	−0.045	−0.84	
χ_{TIM} (1×10^{-9} m^3 mol^{-1})		9.5	10.0		
Magnetic analysis with a dimeric model[b]					
J (cm^{-1})	−0.093	−0.27	−0.028	−0.75	−3.39
g	2.05	2.05	g_{xy} = 2.48	2.27	2.03
D (cm^{-1})			40.2	−6.78	
E/D				0.12	
χ_{TIM} (1×10^{-9} m^3 mol^{-1})		9.5	10.0		0.50
Magnetic analysis with a 1D chain model[b]					
J (cm^{-1})	−0.051	−0.16	−0.018	−0.48	−2.43
g	2.05	2.05	g_{xy} = 2.48	2.27	2.03
D (cm^{-1})			40.0	−6.02	
E/D				0.15	
χ_{TIM} (1×10^{-9} m^3 mol^{-1})		9.5	10.0		0.5

[a]Values for **3** (M = Co) were derived for susceptibility above 50 K. [b]In case of **3** (M = Co) g_z was fixed to 2.0. [c]Model was not applicable to **5** (M = Cu), estimated $zj < −5$ cm^{-1}.

theoretical methods, and in this work we used them with the aim (i) to evaluate the chemical bonding between metal atoms and ligand donor atoms within this series of compounds **1−6**, (ii) to evaluate the ZFS tensor parameters D and E, and (iii) to evaluate the intermolecular magnetic interactions. In all these calculations, the relativistic effects were included with the help of the scalar relativistic contracted version of def2-TZVP(-f) basis functions and with zero order regular approximation (ZORA) using ORCA computational software (see details in Experimental Section).

From the discussion related to X-ray structures of **1−6** follows that the CN varies between 4 + 1 and 7 within the reported series of compounds, and there are some cases in which the assignment based on bond length only is ambiguous. Therefore, the strength of donor−acceptor bonds within all the coordination chromophores in complexes **1−6** was evaluated by DFT calculations using the well-established B3LYP functional. The single-point energy calculations (B3LYP +ZORA/def2-TZVP(-f)) were performed for neutral complex units [M(**L**)Cl$_2$] (**1**, **3**, **4**, **6**) and complex cations of [Fe(**L**)Cl$_2$]$^+$ (in **2**) and [Cu(**L**)Cl]$^+$ (in **5**), and subsequently the geometry-basis-wave function (GBW) file was transformed to MOLDEN format and analyzed using the Multiwfn program.

To quantify donor−acceptor bonds within the complexes, the Mayer's bond analysis was the first choice, and the results are summarized in Figure 7b. According to this bond index, the strongest bonds were calculated between the central metal atoms (M) and chlorido ligands (M−Cl), medium strength bonds were between M and nitrogen atoms of the **L** ligand, and the weakest ones were found for the M−O bonds. In general, the pattern found in this plot copies the trend found for M−Cl/N/O bond lengths very well, which means the shorter bond length correlates with the higher Mayer's bond order. Furthermore, the bond order of the M−O bond type systematically decreases from iron to zinc metal centers, crossing to semicoordination (M−O1 for M = Cu) or lacking any bond at all (M−O1 for M = Zn and M−O2 for M = Cu, Zn).

Moreover, topological analysis was performed using the total molecular electronic density $\rho(r)$ and the Laplacian of $\rho(r)(\nabla^2\rho(r))$ based on atom in molecule (AIM) calculations. The so-called bond critical points of the type (3,−1) were located between M−Cl/N/O bonds, and in these points, the ELF was calculated to quantify these donor−acceptor bonds. The results are plotted in Figure 7c and essentially complement Mayer's bond analysis showing the same trends within the

Table 6. Metal···Metal Distances Found in the Crystal Structures of Complexes 1−5 in Context of Noncovalent Contacts Accompanied by Results of DFT Calculations of Magnetic Exchange^a

complex	1·2CH$_3$OH	2·2H$_2$O	3·2CH$_3$OH	4	5
hydrogen bonds	6.6268(4)		6.5656(6)	6.528(2)	4.2366(3)
Δ (cm^{-1})	[−1.346]		[−0.008]	[−1.046]	[−0.318]
J^R/J^Y (cm^{-1})	−0.09/−0.11		0.00/0.00	−0.35/−0.52	−0.32/−0.64
π−π interactions	8.7238(4)	8.5920(4)	8.6291(4)		
Δ (cm^{-1})	[−0.367]	[−0.499]	[−0.079]		
J^R/J^Y (cm^{-1})	−0.02/−0.03	−0.03/−0.04	−0.01/−0.02		
interchain	7.9151(4)	7.4859(2)	7.9998(4)	7.639(2)	7.3285(4)
Δ (cm^{-1})	[−0.173]	[−0.845]	[0.377]	[−0.627]	[+0.027]
J^R/J^Y (cm^{-1})	−0.01/−0.01	−0.06/−0.07	+0.06/+0.08	−0.21/−0.31	+0.03/+0.05
					9.6921(4)
					[−1.244]
		7.5084(2)			−1.24/−2.49
		[−1.435]			9.8135(4)
		−0.10/−0.11			[−0.072]
					−0.07/−0.14

^{a}M···M distances in angstroms, [Δ] = E_{BS} − E_{HS} in inverse centimeters, the isotropic exchange values J^R/J^Y in inverse centimeters rounded to two decimal places.

series. The M−Cl/N types of bonds are again the strongest ones, but now ELF values of M−Cl and M−N bonds are much closer than in Mayer's bond analysis. Again, ELF of M−O bonds decreases from iron to zinc, but in the case of M = Cu(II), Zn(II), the bond critical points of the type (3,−1) were not found between M and O2 atoms, simply confirming no coordination. Despite the absence of sharp drop in ELF values, we may conclude that the analysis showed that (i) Mn(II), Fe(III), and Co(II) atoms have CN 7 with the N$_3$O$_2$Cl$_2$ donor atom set, (ii) the Ni(II) has 5 + 2 coordination mode with the N$_3$O$_2$Cl$_2$ donor atom set, (iii) the Cu(II) has 4 + 1 coordination mode with the N$_3$OCl donor atom set, and (iv) the Zn(II) has 5 coordination mode with the N$_3$Cl$_2$ donor atom set with both the O atoms situated outside the inner coordination sphere despite the critical point of the type (3,−1) was found for Zn and O1 indicating ∼twofold weaker interaction in comparison with the O1 semicoordination in Ni(II) and Cu(II) complexes 4 and 5.

Such various coordination modes and geometries found in this series have of course substantial impact also on magnetic properties of the ground state for the reported compounds 1−5 (M = Mn, Fe, Co, Ni, Cu). (Note: the Zn(II) complex 6 was excluded form magnetic study owing its diamagnetism.) This is why we employed the ab initio calculations of ZFS parameters based on state-averaged complete-active-space self-consistent field (SA-CASSCF) wave functions accompanied by N-electron valence second-order perturbation theory (NEVPT2). The active space of these CASSCF calculations was composed of the appropriate number of electrons according to metal atom in five metal-based d-orbitals. The dominant spin−orbit coupling contributions from excited states led to ZFS tensors and hence to the determination of axial and rhombic single-ion parameters D and E, respectively (Table 5). The contributions of the excited states to ZFS terms are summarized in Tables S2−S5 (see Supporting Information). The quasi-degenerate perturbation theory was used to extract information about ZFS, but also values calculated by second-order perturbation theory are listed for comparison in Table S6 (see Supporting Information).

The largest D-parameters were found in compound 3 (M = Co), D = 45.0 cm^{-1}, and in compound 4 (M = Ni), D = −6.08 cm^{-1}, while 1 and 2 have |D| less than 1 cm^{-1}. The largest

rhombicity was found for compound 4 (M = Ni), E/D = 0.245. The nature and magnitude of the magnetic anisotropy of Co(II) and Ni(II) complexes 3, and 4, respectively, is completely in accordance with the theoretical and experimental investigations of other heptacoordinated complexes of ligands L3 and L4.[35] The origin of the large positive and negative D-values for Co(II), and Ni(II) complexes, respectively, is related to the different contribution of excited states to the ground state; for Co(II) complex all excited states contribute to a positive D-value, whereas for Ni(II) the contributions are opposite.[35] The axes of ZFS and g-tensors together with molecular structures are visualized in Supporting Information (Figure S4). In all cases, both g-tensor and ZFS-tensor axes coincide; only in the case of compound 1 (M = Mn) there is a little discrepancy, which however can also be related to a very small value of the ZFS tensor parameters, hence, to enhanced numerical noise in extracting ZFS orientation axes. In general, the main axes of ZFS tensors for M = Mn, Fe, Co, Ni are approximately located along the Cl−M−Cl, N2−M−N3, and N1−M bonds (Supporting Information, Figure S4). In the case of M = Cu, the two components of g-tensors lies in the CuN1N2N3Cl1 plane, almost along N2−Cu−N3 and N1−Cu−Cl1 bonds, and the last g-component is perpendicular to this plane. If the main magnetic axis is defined by D-tensor, then the g-axes for compounds 3 and 4 can be assigned as $g_x = g_2 = 2.421$, $g_y = g_3 = 2.465$, $g_z = g_1 = 2.004$ for 3 and $g_x = g_2 = 2.239$, $g_y = g_1 = 2.218$, $g_z = g_3 = 2.275$ for 4 (Figure, S4, see Supporting Information).

The last topic to discuss before focusing on experimental magnetic properties of the reported compounds is the possibility that intermolecular interactions may lead to non-negligible magnetic exchange among mononuclear complexes in solid state. With the aim to estimate such magnetic interactions through noncovalent superexchange pathways (hydrogen bonds, π−π stacking), the isotropic exchange constants J were calculated for various dinuclear moieties using the BS state approach at the B3LYP+ZORA/def2-TZVP(-f) level of theory. Then, the spin Hamiltonian postulated for such dimer

$$\hat{H} = -J(\vec{S}_1 \cdot \vec{S}_2) \tag{1}$$

and the energy difference Δ between the BS spin state and the HS state

$$\Delta = E_{BS} - E_{HS} \qquad (2)$$

were used to calculate J-value either by the Ruiz's approach

$$J^R = 2\Delta/[(S_1 + S_2)(S_1 + S_2 + 1)] \qquad (3)$$

or by a more general Yamaguchi's approach

$$J^Y = 2\Delta/[\langle S^2\rangle_{HS} - \langle S^2\rangle_{BS}] \qquad (4)$$

in which also spin-expectation values of HS and BS states are used.

The outputs of these calculations are summarized in Table 6, in which Δ, J^R, and J^Y are listed for all the relevant dimers according to the X-ray discussion. The relevant molecular fragments are visualized in Figure S5 (Supporting Information). To compare the strength of magnetic exchange for systems with different spins ranging from $S_i = 1/2$ to $S_i = 5/2$, we must note that J-parameter is not the best one, because we would like to compare the overall splitting of S-levels resulting from the isotropic exchange, which means the energy difference between $S_{min} = |S_1 - S_2| = 0$ and $S_{max} = (S_1 + S_2)$ levels, which correlates with above-defined Δ from DFT calculations. The largest Δ values, $|\Delta| > 1$ cm^{-1}, were found (i) in a dinuclear fragment of **1** (d(Mn···Mn) = 6.6268(4)), where the N−H···Cl hydrogen bonds dominates, (ii) in a dinuclear fragment of **2** (d(Fe−Fe) = 7.5084(2)), where weak C−H···O and C−H···Cl noncovalent contacts are present, (iii) in a dinuclear fragment of **4** (d(Ni−Ni) = 6.528(2)), where N−H···Cl hydrogen bond exists, and (iv) in a dinuclear fragment of **5** (d(Cu−Cu) = 9.6921(4)), where C−H···Cl noncovalent contacts are found. The spin densities of the last case are depicted for BS spin state in Figure 8. The important output emerged from these calculations is
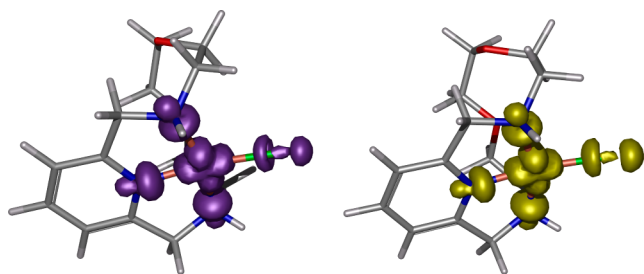
Figure 8. Calculated spin-density distribution using B3LYP+ZORA/ def2-TZVP(-f) for $\{[Cu(\mathbf{L})Cl]_2\}^{2+}$ of **5** (Cu···Cu distance 9.6921(4) Å) for the BS state. Positive and negative spin densities are represented by violet and yellow surfaces, respectively. The isodensity surfaces are plotted with the cutoff values of 0.005 ea$_0^{-3}$.

that the strength of magnetic exchange cannot be solely judged by metal···metal distance and by type of noncovalent contacts. This is nicely demonstrated in the case of Cu(II) complex **5**, in which the strongest antiferromagnetic exchange was found for almost the largest Cu···Cu distance (Table 6). To summarize the J-values, the compounds in presented series can be sorted by increasing expected antiferromagnetic exchange as follows: **3** < **1** < **2** < **4** < **5**, which means minimal magnetic exchange J is estimated for compound **3** (M = Co) and the largest J for compound **5** (M = Cu).

Magnetic Properties. With the aim to extract the spin Hamiltonian parameters describing the magnetic anisotropy and eventually intermolecular magnetic exchange from

experimental magnetization data, several models were applied. First, the mononuclear spin Hamiltonian (H^{mono}) with molecular field correction parameter was postulated

$$\hat{H}^{mono} = D(\hat{S}_z^2 - \hat{S}^2/3) + E(\hat{S}_x^2 - \hat{S}_y^2) + \mu_B Bg\hat{S}_a - zj\langle\hat{S}_a\rangle\hat{S}_a \qquad (4a)$$

where D and E are the single-ion axial and rhombic ZFS parameters, the next part is the Zeeman term, and the last component represented with the zj variable is the common molecular-field correction parameter, which is due to intermolecular interactions. The $\langle S_a\rangle$ is a thermal average of the molecular spin projection in a direction of magnetic field defined as $B_a = B(\sin(\theta)\cos(\varphi), \sin(\theta)\sin(\varphi), \cos(\theta))$ with the help of the polar coordinates. Then, the molar magnetization in a-direction of magnetic field can be numerically calculated as

$$M_a = -N_A \frac{\sum_i \left(\sum_k \sum_l C_{ik}^+(Z_a)_{kl}C_{li}\right)\exp(-\varepsilon_{a,i}/kT)}{\sum_i \exp(-\varepsilon_{a,i}/kT)} \qquad (5)$$

where Z_a is the matrix element of the Zeeman term for the a-direction of the magnetic field, and C are the eigenvectors resulting from the diagonalization of the complete spin Hamiltonian matrix. The inclusion of zj means that iterative procedure must be applied.[37] Then, the averaged molar magnetization of the powder sample was calculated as integral (orientational) average

$$M_{mol} = 1/4\pi \int_0^{2\pi}\int_0^{\pi} M_a\sin\theta\,d\theta\,d\varphi \qquad (6)$$

The second model used to interpret experimental data sets we based on the dinuclear spin Hamiltonian (H^{di})

$$\hat{H}^{di} = -J(\vec{S}_1\cdot\vec{S}_2) + \sum_{i=1}^{2} D_i(\hat{S}_{i,z}^2 - \hat{S}_i^2/3) + E_i(\hat{S}_{i,x}^2 - \hat{S}_{i,y}^2)$$
$$+ \mu_B Bg_i\hat{S}_{i,a} \qquad (7)$$

where the first term describes the isotropic exchange between paramagnetic metal atoms with spin S_i, and the rest of terms were already explained.

The last model tries to mimic 1D uniformly coupled spin chain by finite-sized closed ring with following spin Hamiltonian (H^{1D})

$$\hat{H}^{1D} = -J(\vec{S}_1\cdot\vec{S}_N) - \sum_{i=1}^{K-1} J(\vec{S}_i\cdot\vec{S}_{i+1}) + \sum_{i=1}^{K} D_i(\hat{S}_{i,z}^2 - \hat{S}_i^2/3)$$
$$+ E_i(\hat{S}_{i,x}^2 - \hat{S}_{i,y}^2) + \mu_B Bg_i\hat{S}_{i,a} \qquad (8)$$

In the case of the spin Hamiltonians H^{di} and H^{1D}, the molar magnetization in a-direction of magnetic field was calculated as

$$M_a = N_A kT \frac{d(\ln(Z))}{dB} \qquad (9)$$

where Z is the partition function.

To provide the trustworthy parameters by magnetic analysis, both temperature- and field-dependent magnetization data were fitted simultaneously and are summarized in Table 5 for all the discussed models. In some cases, the temperature-independent magnetism correction χ_{TIM} was applied to describe the effect of either the contribution of excited electronic states, the so-called temperature-independent paramagnetism (χ_{TIP}), or the contribution of traces of magnetic impurities. The magnetic data for all the compounds **1−5** are depicted in Figure 9 for H^{1D}

model, and the results for other two models can be found in Figure S6 (H^{mono}) and Figure S7 (H^{di}) in Supporting Information.
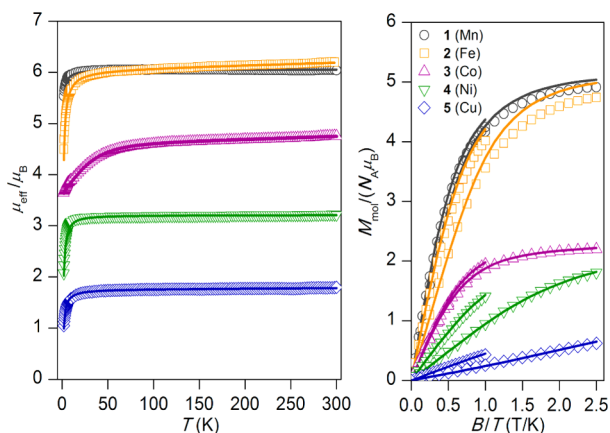
Figure 9. Magnetic data for compounds **1**−**5**. Temperature dependence of the effective magnetic moment (left) and the isothermal molar magnetizations measured at 2 and 5 K (right). The empty circles represent the experimental data points, and the full lines represent the best fits calculated by H^{1D} model (eq (8)) with parameters listed in Table 5. All data are scaled per one paramagnetic ion.

Mn(II) Complex (1). Temperature dependence of the effective magnetic moment for **1** is presented in Figure 9 together with the isothermal molar magnetization data measured at low temperature (2 and 5 K). The value of effective magnetic moment (μ_{eff}/μ_B) is 6.05 at room temperature, and is close to the spin-only value μ_{eff}/μ_B = 5.92 for the system with $S = 5/2$ and $g = 2.0$. A gradual decrease in μ_{eff}/μ_B is observed below 30 K, which can be attributed mainly to the presence of weak intermolecular noncovalent contacts in the solid state. The theoretical calculations predicted that the ZFS on the Mn(II) atom is very small, in a scale undetectable with magnetometry; thus, we simplified the spin Hamiltonian models and fitted experimental data with isotropic models ($D = 0$ and $E = 0$ were fixed). All applied models described experimental data in conformity with experimental data; g-parameter was equal to 2.05, which is expected value for $3d^5$ spin configuration. In case of H^{di}, the fitted J-value −0.093 cm^{-1} is very close to that derived by DFT (J^R/J^Y = −0.09/−0.11 cm^{-1}). However, when 1D chain model (H^{1D}) was applied with $K = 7$,[74] the smaller isotropic exchange was found ($J = -0.051$ cm^{-1}).

Fe(III) Complex (2). The magnetic data for **2** are essentially similar to those for **1** (Figure 9), but the effective magnetic moment is linearly decreasing from the room temperature value of 6.20 μ_B to the value of 5.87 μ_B at 50 K, which suggests the presence of a small amount of unknown magnetic impurity. Subsequent drop of μ_{eff}/μ_B to 4.49 μ_B at $T = 1.9$ K can be attributed to antiferromagnetic intermolecular interactions and eventually also to ZFS as evidenced by CASSCF/NEVPT2 calculations. We already demonstrated that in case of weak-exchange limit also the ZFS parameters of Fe(III) ion can be estimated from magnetic analysis;[75] however, in this case when the experimental data are affected by unknown magnetic impurity, we restricted spin Hamiltonians only to the isotropic case, and the effect of impurity was described by χ_{TIM}. The zj and J-values were found a little higher than those for analogous Mn(II) compound (Table 5) despite DFT J-values that were

found similar for both systems, which possibly suggests that the neglecting of ZFS terms led to overestimation of the isotropic exchange. This is also supported by the fact that the calculated isothermal magnetization data at saturation limit are a bit higher than the experimental ones.

Co(II) Complex (3). The μ_{eff} adopts the value of 4.76 μ_B at room temperature, which is considerably higher than the spin-only value for $S = 3/2$ and $g = 2.0$ (μ_{eff}/μ_B = 3.87) owing to substantial contribution of the orbital angular momentum. When the material cooled, the μ_{eff}/μ_B continuously decreases to value of 3.65 at $T = 1.9$ K, which can be explained by a large ZFS and possibly also by intermolecular interactions. According to theoretical calculations, the large anisotropy of g-tensor is expected; thus, g_z was fixed to value of 2.0 and g_{xy} was left to be varied during the fitting procedure. Also, the theoretical rhombicity of this compound was found negligible, so the constraint $E = 0$ was set. In case of monomeric model H^{mono}, the zj value of −0.045 cm^{-1} is the smallest one within the reported series, and in the case of dimeric model H^{di}, the J-value is equal to −0.028 cm^{-1}, which is pretty close to the theoretical prediction (J^R/J^Y = −0.01/−0.02 cm^{-1}). The g_{xy} = 2.48 is also in good accordance with the calculated average of 2.44 from CASSCF/NEVPT2. The positive $D \approx 40$ cm^{-1} is close to calculated value of $D = 45$ cm^{-1}. The 1D chain model was applied for $K = 5$, which resulted in 1024 magnetic states. Because many matrix diagonalizations are needed in calculating powder average of magnetization, the spin permutational symmetry of the spin Hamiltonian was applied to construct new set of symmetry-adapted spin basis set using D_5 point group.[76] Such procedure split the total interaction matrix into submatrices A1 ($N = 136$), A2 ($N = 72$), E1 ($N = 408$), E2 ($N = 408$), labeled with the irreducible representations.[77] As a result, $J = -0.018$ cm^{-1}, $g_{xy} = 2.48$, and $D = 40.1$ cm^{-1} were found, all parameters close to H^{di} model and also to ab initio calculated parameters. Additionally, little lower positive D-values and values of g_{xy} were observed for other complexes of heptacoordinated Co(II) listed in Table 7.

Table 7. Comparison of Selected ZFS Parameters and g-Factors Determined for Previously Studied Complexes with Heptacoordinated Central Metal Ion

complex	D, cm^{-1}	E/D	g_{iso}	g_{xy}	ref
[Co(**L3**)(H$_2$O)(NO$_3$)](NO$_3$)	31	0	2.22		35
[Co(**L5**)](NO$_3$)$_2$·2CH$_3$CN	25		2.22		33
[Co(**L5**)](ClO$_4$)$_2$	26		2.15		33
[Co(**L6**)](ClO$_4$)$_2$	23.1			2.21	34
[Ni(**L3**)(H$_2$O)$_2$](NO$_3$)$_2$·2H$_2$O	−13.9	0.11	2.26		35
[Ni(**L4**) (NO$_3$)(CH$_3$OH)](NO$_3$)·CH$_3$OH	−12.5	0.10	2.22		36
[Ni(**L5**)](NO$_3$)$_2$·H$_2$O	15			2.27	33

Ni(II) Complex (4). The effective magnetic moment at room temperature, μ_{eff}/μ_B = 3.22, is significantly higher than the spin-only value for the system with $S = 1$ and $g = 2.0$ (μ_{eff}/μ_B = 2.83) for Ni(II) due to orbital momentum contributions. The abrupt decrease of its value at low temperature below 30 K is observed ending with 2.07 μ_B at $T = 1.9$ K in response to ZFS effect and intermolecular interactions. The mononuclear H^{mono} and dinuclear H^{di} confirmed important role of intermolecular interactions, $zj = -0.84$ cm^{-1} and $J = -0.75$ cm^{-1}, respectively, even indicating larger antiferromagnetic exchange than DFT

calculations (J^R/J^Y = −0.35 cm^{-1}/−0.52 cm^{-1}). However, both models provided different values of rhombicity, E/D = 0.33 (D = −5.13 cm^{-1}) for H^{mono} model in contrast with E/D = 0.12 (D = −6.78 cm^{-1}) for H^{di} model. In case of the 1D chain model H^{1D}, the calculations were done for K = 5, and resulted in J = −0.48 cm^{-1}, D = −6.02 cm^{-1}, and E/D = 0.15. In all cases, the axial parameter D of ZFS was found close to value of −6.08 cm^{-1} derived from CASSCF/NEVPT2 procedure. In comparison with other complexes with heptacoordinated Ni(II), the obtained values of discussed parameters are in the same range (Table 7), but only the axial parameter D of ZFS is ∼2 times lower than for Ni(II) complexes of nonmacrocyclic Schiff bases **L3** and **L4**.

Cu(II) Complex (5). The last paramagnetic compound in this series is **5**, which shows magnetic behavior far from Curie-like behavior expected for an isolated mononuclear complex with S = 1/2 (Figure 9). The effective magnetic moment changes from 1.88 μ_B (T = 300 K) to 1.08 μ_B (T = 1.9 K) and also the isothermal magnetizations do not resemble Brillouin function. All these deviations from Curie behavior must be the outcome of intermolecular interactions, which is also supported by DFT calculations, where largest antiferromagnetic exchange was found to be J^R/J^Y = −1.24 cm^{-1}/−2.49 cm^{-1}. Furthermore, the H^{mono} model was not capable of describing this behavior (the iteration procedure failed for $zj < −5$ cm^{-1}). The dinuclear model H^{di} resulted in J = −3.39 cm^{-1}, while the application of H^{1D} model, with K = 19,[78] provided J = −2.43 cm^{-1}, which is close to Yamaguchi's isotropic exchange constant.

Bulk Magnetic Susceptibility Measurements. To compare the magnetic properties of complexes **1**−**5** in solid phase and in solution, the effective magnetic moment of each complex in D$_2$O or CD$_3$OD was calculated from the BMS measurement using Evans method.[79] Obtained results are in good agreement with the data in solid state, and thus no change or decomposition of studied complexes occurred upon dissolution in D$_2$O or CD$_3$OD (Table 8). The small differences

Table 8. Comparison of Effective Magnetic Moments^a Obtained from SQUID Measurement in Solid State and BMS^b Measurements in Solution

| complex	1	2	3	4	5
μ_{eff}/μ_B (solid)	6.05	6.20	4.76	3.22	1.79
μ_{eff}/μ_B (in D$_2$O)	5.63	6.34	4.50	2.90	1.61
μ_{eff}/μ_B (in CD$_3$OD)	5.67	6.07	4.35	3.00	1.66

^{a}Values are expressed in Bohr magnetons at 25 °C. ^{b}BMS = bulk magnetic susceptibility.

between the effective magnetic moments in liquid and solid states could be related to the chlorido ligand substitution by water molecules in aqueous solution.

The stability of the solution samples was checked by measurement after one week, and no change in effective magnetic moment was observed except for **2** in water, for which the reduced μ_{eff} = 3.5 μ_B was found. This difference is in correlation with a drop of pD for solution of **2** from initial pD = 7.4 (same for all complex) to 2.3, which would suggest some complex decomposition resulting in precipitation of some hydroxo- or oxo-bridged species. Small drop of pD to 5.9 was observed for **5**; otherwise, the values of pD were constant for all other complexes.

Redox Properties. The redox properties of the complexes **1**−**6** were probed by cyclic voltammetry measurements. The

cyclic voltammograms of Mn(II), Fe(III), and Cu(II) complexes **1**, **2**, and **5** in aqueous solution are depicted in Figure 10 and in MeCN in Figure 11; other complexes were in
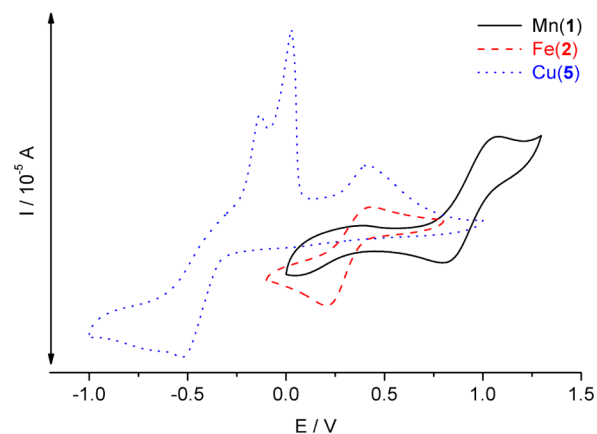
Figure 10. Cyclic voltammograms of 5 mM Mn(II) (**1**, black), Fe(III) (**2**, red), and Cu(II) (**5**, blue) complexes in 0.1 M KCl (glassy carbon working electrode, potential referred to Ag/AgCl reference electrode).
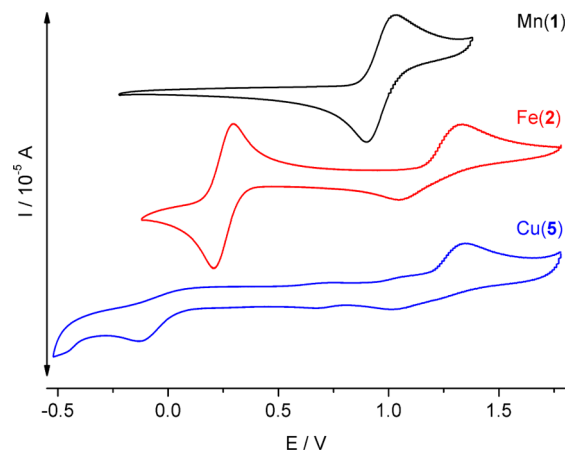
Figure 11. Cyclic voltammograms of 5 mM Mn(II) (**1**, black), Fe(III) (**2**, red), and Cu(II) (**5**, blue) complexes in 0.1 M TBAP in MeCN (glassy carbon working electrode, potential referred to SHE).

the measured range electrochemically silent. The obtained results are listed in Table 9. Quasi-reversible couple Mn(II)/Mn(III) was found at relatively high potential $E_{1/2}$ = 1.13 V with a large ΔE_p = 0.28 V in aqueous solution, which is in agreement with the previously published data for similar complex,[22] and at $E_{1/2}$ = 0.97 V (ΔE_p = 0.13 V) in MeCN. For **2**, a quasi-reversible couple Fe(II)/Fe(III) was found in water

Table 9. Results of Cyclic Voltammetry Measurements

| complex | water | | MeCN | |
	$E_{1/2}$^{a}	ΔE_p^{a}	$E_{1/2}$^{a}	ΔE_p^{a}
1	1133	285	967	129
2	514	221	248	81
5	E_{ox1} = 65	E_{red1} = −333	E_{red1} = −141	
	E_{ox2} = 223			
	E_{ox3} = 609			

^{a}All potential values are given in millivolts for a scan rate of 0.1 V min^{-1}.

($E_{1/2}$ = 0.51 V, ΔE_p = 0.22), whereas in MeCN this reduction wave became reversible ($E_{1/2}$ = 0.25 V, ΔE_p = 81 mV). This value of $E_{1/2}$ in MeCN is the same as that for [Fe(15-pydienN$_3$O$_2$)Cl$_2$]ClO$_4$ ($E_{1/2}$ = 0.25 V, ΔE_p = 110 or 60 mV),[2] which documents the same redox stability of Fe(III) complex of **L** and complex with corresponding Schiff base 15-pydienN$_3$O$_2$. In case of **5** in water, the cyclic voltammogram describes complex system with irreversible behavior providing three oxidation peaks (E_{ox1} = 0.06 V, E_{ox2} = 0.22 V, E_{ox3} = 0.61 V) and one reduction peak (E_{red} = −0.33 V). This peak at negative potential could be ascribed to the reduction of Cu(II) to Cu(I), which is shifted +0.4 V to positive potential in comparison with Cu(II) complex with analogous penta-aza-ligand [Cu(15-pyN$_5$)]$^+$.[69] The oxidation of Cu(I) complex is a multistep process, or probably some chemical reactions proceed on a Cu(I) complex, because the chlorido ligand can be substituted by water molecule (in all the complexes); thus, some hydroxo- or oxo- polynuclear complexes may be formed, and therefore their oxidation potentials differ significantly. There is only one irreversible reduction peak at E_{red} = −0.14 V for **5** in MeCN corresponding to the reduction of Cu(II) to Cu(I). The quality of the voltammogram is low due to the low solubility of **5** in MeCN, and the irreversibility of the Cu(II)/Cu(I) process could be mostly caused by insolubility of the Cu(I) product. Furthermore, the voltammograms of **2** and **5** in MeCN were accompanied by almost irreversible oxidation peak (E_{ox} = 1.33 V) together with low-intense reduction peak (E_{red} = 1.05 V) corresponding to the oxidation of chloride anions/reduction of chlorine, because free chloride counter-ions are presented in these two complexes, and therefore these peaks have much higher intensity than in case of the results for **1**.

In all the cases the peak potentials for observed couples in MeCN have lower values than in aqueous solution, which points to a more facile oxidation of Mn(II) or Fe(II) in MeCN than in water. The separation of the oxidation/reduction peaks was much lower in MeCN than in water. This behavior could be related to the substitution of the chlorido ligands in axial positions by solvent molecules, which is much more efficient in water than in MeCN and which could lead to a formation of differently substituted aqua-/hydroxo-/oxo- species (some chemical reactions can take place) in aqueous solution resulting in quasi-/irreversible behavior of the system.

CONCLUSIONS

In this work, new complexes of a pentadentate macrocyclic ligand **L** with Mn(II), Fe(III), Co(II), Ni(II), Cu(II), and Zn(II) (**1**−**6**) were prepared and thoroughly characterized. In the molecular structures of the first four complexes **1**−**4**, the metal atom is five-coordinated in a relatively planar macrocyclic cavity with two chlorido ligands in apical positions forming distorted pentagonal bipyramidal coordination sphere, while in complexes **5** and **6** the ligand is extensively folded, and the metal, with coordinated one and two chlorido ligands, respectively, adopts distorted square pyramidal geometry. Along the series of the complexes (**1**−**6**), the metal−nitrogen atom distances are reduced from ∼2.2 to ∼2.0 Å, while the metal−oxygen atom distances are elongated, so that both the oxygens are semicoordinated (2.506(3) and 2.663(3) Å) in **4**. On the other hand, one oxygen is semicoordinated (2.721(2) Å), and the second one stays uncoordinated (3.816(2) Å) in **5**, whereas both oxygen atoms are considered as uncoordinated (3.113(2) and 4.030(2) Å) in **6**. Therefore the coordination number is reduced from 7 for **1**−**3** or 5 + 2 for **4** to 4 + 1 for **5**

or 5 for **6**. The findings regarding the bond character were also supported by DFT calculations using the Mayer's bond order and electron localization function. The observed changes in stereochemistry may be related to a variation of the ionic radius of the changing metal ion within the series going from Mn (**1**) to Zn (**6**), because the macrocyclic cavity becomes too large for smaller metal ions, and thus, the ligand is folded with liberation/decoordination of the oxygen donor atom(s). The type of the central metal atom as well as its ionic radius also influences significantly magnetic properties of the complexes from which the parameters describing magnetic anisotropy and intermolecular magnetic exchange were extracted. Complexes **1** and **2** behave as expected for 3d^5 spin configuration. For **3**, a large positive value of $D \approx 40$ cm^{-1} was found, also with a very small negative J-value. For **4**, the best fit of data was obtained for 1D chain model giving a relatively large negative value of D = −6.02 cm^{-1}, non-negligible value of rhombicity (E/D = 0.15), and small antiferromagnetic exchange coupling, with J = −0.48 cm^{-1}. In the case of **5**, the best fit was provided using 1D chain model, which revealed the largest antiferromagnetic exchange, with J = −2.43 cm^{-1}. According to the obtained results, the discussed complexes can be sorted by increasing antiferromagnetic exchange as follows: Co(II) < Mn(II) < Fe(III) < Ni(II) < Cu(II). The obtained ZFS parameters were correlated well with ab initio calculations (SA-CASSCF NEVPT2), and the energy difference Δ between BS and HS states as well as exchange constants J (B3LYP+ZORA/def2-TZVP(-f)) were calculated for all the possible M···M distances to reveal the magnetic interactions through noncovalent superexchange pathways. The strongest magnetic interactions were found for the shortest M···M distances where the two complex units are connected via a network of strong hydrogen bonds (complexes **1**, **2**, and **4**). On the other hand, the largest antiferromagnetic exchange in Cu(II) complex **5** was found for the almost largest Cu···Cu distance, mediated by C−H···Cl hydrogen bond. To conclude, the presented work showed that mutual cooperation between experimental techniques and theoretical methods is essential for better understanding of electronic and magnetic properties of coordination compounds based on 15-membered pyridine-based macrocycle ligand **L**.

ASSOCIATED CONTENT

⑤ Supporting Information

FTIR spectra (**1**−**6**), results of TG/DTA analysis (**1** and **3**), figures and tables referring to the X-ray analysis, magnetic data analysis, and calculated results. This material is available free of charge via the Internet at http://pubs.acs.org.

AUTHOR INFORMATION

Corresponding Author

*Fax: +420 585634954. Phone: +420 585634352. E-mail: zdenek.travnicek@upol.cz.

Notes

The authors declare no competing financial interest.

ACKNOWLEDGMENTS

■ REFERENCES

(1) Allen, F. H. *Acta Crystallogr.* **2002**, *B58*, 380−388.

(2) Drew, M. G. B.; bin Othman, A. H.; McFall, S. G.; Mcllroy, P. D. A.; Nelson, S. M. *J. Chem. Soc., Dalton Trans.* **1977**, *12*, 1173−1180.

(3) Cook, D. H.; Fenton, D. E.; Drew, M. G. B.; McFall, S. G.; Nelson, S. M. *J. Chem. Soc., Dalton Trans.* **1977**, *5*, 446−449.

(4) Nelson, S. M.; Mcllroy, P. D. A.; Stevenson, C. S.; Konig, E.; Ritter, G.; Waigel, J. *J. Chem. Soc., Dalton Trans.* **1986**, *5*, 991−995.

(5) König, E.; Ritter, G.; Dengler, J.; Nelson, S. M. *Inorg. Chem.* **1987**, *26*, 3582−3588.

(6) Radeckaparyzek, W.; Patroniakkrzyminiewska, V. *Polyhedron* **1995**, *14*, 2059−2062.

(7) Patroniak-Krzyminiewska, V.; Radecka-Paryzek, W. *Collect. Czech. Chem. Commun.* **1998**, *63*, 363−370.

(8) Hayami, S.; Gu, Z.; Einaga, Y.; Kobayasi, Y.; Ishikawa, Y.; Yamada, Y.; Fujishima, A.; Sato, O. *Inorg. Chem.* **2001**, *40*, 3240−3242.

(9) Bonadio, F.; Senna, M.-C.; Ensling, J.; Sieber, A.; Neels, A.; Stoeckli-Evans, H.; Decurtins, S. *Inorg. Chem.* **2005**, *44*, 969−978.

(10) Hayami, S.; Juhász, G.; Maeda, Y.; Yokoyama, T.; Sato, O. *Inorg. Chem.* **2005**, *44*, 7289−91.

(11) Bonhommeau, S.; Guillon, T.; Lawson Daku, L. M.; Demont, P.; Sanchez Costa, J.; Létard, J. F.; Molnár, G.; Bousseksou, A. *Angew. Chem., Int. Ed. Engl.* **2006**, *45*, 1625−1629.

(12) Paraschiv, C.; Andruh, M.; Journaux, Y.; Žak, Z.; Kyritsakas, N.; Ricard, L. *J. Mater. Chem.* **2006**, *16*, 2660−2668.

(13) Guionneau, P.; Le Gac, F.; Kaiba, A.; Costa, J. S.; Chasseau, D.; Létard, J. F. *Chem. Commun.* **2007**, *36*, 3723−3725.

(14) Zhang, D.; Wang, H.; Chen, Y.; Ni, Z. H.; Tian, L.; Jiang, J. *Inorg. Chem.* **2009**, *48*, 5488−5496.

(15) Zhang, D.; Wang, H.; Chen, Y.; Zhang, L.; Tian, L.; Ni, Z. H.; Jiang, J. *Dalton Trans.* **2009**, *43*, 9418−9425.

(16) Zhang, D.; Wang, H.; Tian, L.; Jiang, J.; Ni, Z.-H. *Cryst. Eng. Comm.* **2009**, *11*, 2447−2451.

(17) Zhang, Y. Z.; Sato, O. *Inorg. Chem.* **2010**, *49* (4), 1271−1273.

(18) Zhang, Y. Z.; Wang, B. W.; Sato, O.; Gao, S. *Chem. Commun.* **2010**, *46*, 6959−6961.

(19) Lüning, U.; Petersen, S.; Schyja, W.; Hacker, W.; Marquardt, T.; Wagner, K.; Bolte, M. *Eur. J. Org. Chem.* **1998**, 1077−1084.

(20) Storm, O.; Lüning, U. *Chem.—Eur. J.* **2002**, *8*, 793−798.

(21) Wessjohann, L. A.; Rivera, D. G.; León, F. *Org. Lett.* **2007**, *9*, 4733−4736.

(22) Drahoš, B.; Kotek, J.; Hermann, P.; Lukeš, I.; Tóth, E. *Inorg. Chem.* **2010**, *49*, 3224−3238.

(23) Gryko, D. T.; Piatek, P.; Pecak, A.; Palys, M.; Jurczak, J. *Tetrahedron* **1998**, *54*, 7505−7516.

(24) Szumna, A.; Gryko, D. T.; Jurczak, J. *J. Chem. Soc., Perkin Trans. 2* **2000**, 1553−1558.

(25) Gryko, D.; Gryko, D. T.; Sierzputowska-Gracz, H.; Piatek, P.; Jurczak, J. *Helv. Chim. Acta* **2004**, *87*, 156−166.

(26) Latouche, C.; Lanoë, P.-H.; Williams, J. A. G.; Guerchais, V.; Boucekkine, A.; Fillaut, J.-L. *New J. Chem.* **2011**, *35*, 2196−2202.

(27) Oshchepkov, M. S.; Perevalov, V. P.; Kuzmina, L. G.; Anisimov, A. V.; Fedorova, O. A. *Russ. Chem. Bull.* **2011**, *60*, 478−485.

(28) Fedorova, O.; Fedorov, Y.; Oshchepkov, M. *Electroanalysis* **2012**, *24*, 1739−1744.

(29) Wang, J.; Slater, B.; Alberola, A.; Stoeckli-Evans, H.; Razavi, F. S.; Pilkington, M. *Inorg. Chem.* **2007**, *46*, 4763−4765.

(30) Fenton, D. E.; Murphy, B. P.; Leong, A. J.; Lindoy, L. F.; Bashall, A.; Mcpartlin, M. *J. Chem. Soc., Dalton Trans.* **1987**, 2543−2553.

(31) Korendovych, I. V.; Staples, R. J.; Reiff, W. M.; Rybak-Akimova, E. V. *Inorg. Chem.* **2004**, *43*, 3930−3941.

(32) Korendovych, I. V.; Kryatova, O. P.; Reiff, W. M.; Rybak-Akimova, E. V. *Inorg. Chem.* **2007**, *46*, 4197−4211.

(33) Platas-Iglesias, C.; Vaiana, L.; Esteban-Gómez, D.; Avecilla, F.; Real, J. A.; de Blas, A.; Rodríguez-Blas, T. *Inorg. Chem.* **2005**, *44*, 9704−9713.

(34) Vaiana, L.; Regueiro-Figueroa, M.; Mato-Iglesias, M.; Platas-Iglesias, C.; Esteban-Gómez, D.; de Blas, A.; Rodríguez-Blas, T. *Inorg. Chem.* **2007**, *46*, 8271−8282.

(35) Ruamps, R.; Batchelor, L. J.; Maurice, R.; Gogoi, N.; Jiménez-Lozano, P.; Guihéry, N.; de Graaf, C.; Barra, A.-L.; Sutter, J.-P.; Mallah, T. *Chem. Eur. J.* **2013**, *19*, 950−956.

(36) Gogoi, N.; Thlijeni, M.; Duhayon, C.; Sutter, J.-P. *Inorg. Chem.* **2013**, *52*, 2283−2285.

(37) Boča, R. *Theoretical Foundations of Molecular Magnetism*; Elsevier: Amsterdam, 1999.

(38) *CrysAlis CCD and CrysAlis RED*, Version 1.171.33.52; Oxford Diffraction Ltd.: England, 2009.

(39) Sheldrick, G. M. *Acta Crystallogr., Sect. A: Found. Crystallogr.* **2008**, *64*, 112−122.

(40) (a) Macrae, C. F.; Bruno, I. J.; Chisholm, J. A.; Edgington, P. R.; McCabe, P.; Pidcock, E.; Rodriguez-Monge, L.; Taylor, R.; van de Streek, J.; Wood, P. A. *J. Appl. Crystallogr.* **2008**, *41* (2), 466−470. (b) Brandenburg, K. *DIAMOND*, Release 3.2k; Crystal Impact GbR: Bonn, Germany, 2014.

(41) Neese, F. *WIREs Comput. Mol. Sci.* **2012**, *2*, 73−78.

(42) Pantazis, D. A.; Chen, X. Y.; Landis, C. R.; Neese, F. *J. Chem. Theory Comput.* **2008**, *4*, 908−919.

(43) (a) van Lenthe, E.; Baerends, E. J.; Snijders, J. G. *J. Chem. Phys.* **1993**, *99*, 4597−4610. (b) van Wullen, C. *J. Chem. Phys.* **1998**, *109*, 392−399.

(44) (a) Lee, C.; Yang, W.; Parr, R. G. *Phys. Rev. B* **1988**, *37*, 785−789. (b) Becke, A. D. *J. Chem. Phys.* **1993**, *98*, 1372−1377. (c) Becke, A. D. *J. Chem. Phys.* **1993**, *98*, 5648−5652. (d) Stephens, P. J.; Devlin, F. J.; Chabalowski, C. F.; Frisch, M. J. *J. Phys. Chem.* **1994**, *98*, 11623−11627.

(45) (a) Ruiz, E.; Cano, J.; Alvarez, S.; Alemany, P. *J. Comput. Chem.* **1999**, *20*, 1391−1400. (b) Ruiz, E.; Rodríguez-Fortea, A.; Cano, J.; Alvarez, S.; Alemany, P. *J. Comput. Chem.* **2003**, *24*, 982−989.

(46) (a) Yamaguchi, K.; Takahara, Y.; Fueno, T. Ab Initio Molecular Orbital Studies of Structure and Reactivity of Transition Metal-OXO Compounds. In *Applied Quantum Chemistry*; Smith, V. H., Schaefer, H. F., Morokuma, F., Eds.; Reidel: Dordrecht, The Netherlands, 1986; pp 155−184. (b) Soda, T.; Kitagawa, Y.; Onishi, T.; Takano, Y.; Shigeta, Y.; Nagao, H.; Yoshioka, Y.; Yamaguchi, K. *Chem. Phys. Lett.* **2000**, *319*, 223−230.

(47) (a) Grimme, S.; Antony, J.; Ehrlich, S.; Krieg, H. *J. Chem. Phys.* **2010**, *132*, 154104. (b) Grimme, S.; Ehrlich, S.; Goerigk, L. *J. Comput. Chem.* **2011**, *32*, 1456−1465.

(48) Malmqvist, P. A.; Roos, B. O. *Chem. Phys. Lett.* **1989**, *155*, 189−194.

(49) (a) Angeli, C.; Cimiraglia, R.; Evangelisti, S.; Leininger, T.; Malrieu, J. P. *J. Chem. Phys.* **2001**, *114*, 10252−10264. (b) Angeli, C.; Cimiraglia, R.; Malrieu, J. P. *Chem. Phys. Lett.* **2001**, *350*, 297−305. (c) Angeli, C.; Cimiraglia, R.; Malrieu, J. P. *J. Chem. Phys.* **2002**, *117*, 9138−9153. (d) Angeli, C.; Borini, S.; Cestari, M.; Cimiraglia, R. *J. Chem. Phys.* **2004**, *121*, 4043−4049. (e) Angeli, C.; Bories, B.; Cavallini, A.; Cimiraglia, R. *J. Chem. Phys.* **2006**, *124*, 054108.

(50) Ganyushin, D.; Neese, F. *J. Chem. Phys.* **2006**, *125*, 024103.

(51) Neese, F. *J. Chem. Phys.* **2005**, *122*, 034107.

(52) Maurice, R.; Bastardis, R.; Graaf, C.; Suaud, N.; Mallah, T.; Guihéry, N. *J. Chem. Theory Comput.* **2009**, *5*, 2977−2984.

(53) (a) Neese, F.; Wennmohs, F.; Hansen, A.; Becker, U. *Chem. Phys.* **2009**, *356*, 98−109. (b) Izsak, R.; Neese, F. *J. Chem. Phys.* **2011**, *135*, 144105.

(54) Lu, T.; Chen, F. *J. Comput. Chem.* **2012**, *33*, 580−592.

(55) Mayer, I. *Chem. Phys. Lett.* **1983**, *97*, 270−274.

(56) (a) Becke, A. D.; Edgecombe, K. E. *J. Chem. Phys.* **1990**, *92*, 5397. (b) Lu, T.; Chen, F.-W. *Acta Phys.-Chim. Sin.* **2011**, *27*, 2786−2792.

(57) *The Quantum Theory of Atoms in Molecules: From Solid State to DNA and Drug Design*; Matta, C. F., Boyd, R. J., Eds; Wiley-VCH: Weinheim, Germany, 2007.

(58) Allouche, A. R. *J. Comput. Chem.* **2011**, *32*, 174−182.

(59) *POV-Ray 3.6;* Persistence of Vision Raytracer Pty. Ltd.: Williamstown, Victoria, Australia, 2004.

(60) Jimenez-Sandoval, O.; Ramirez-Rosales, D.; Rosales-Hoz, M. D.; Sosa-Torres, M. E.; Zamorano-Ulloa, R. *J. Chem. Soc., Dalton Trans.* **1998**, 1551−1556.

(61) Keypour, H.; Khanmohammadi, H.; wainwright, K. P. *Inorg. Chim. Acta* **2003**, *355*, 286−291.

(62) Fleischer, E.; Hawkinson, S. *Inorg. Chem.* **1967**, *89*, 720−721.

(63) Drew, M. G. B.; Hamid bin Othman, A.; Martin Nelson, S. *J. Chem. Soc., Dalton Trans.* **1976**, 1394−1399.

(64) Venkatakrishnan, T. S.; Sahoo, S.; Brefuel, N.; Duhayon, C.; Paulsen, C.; Barra, A. L.; Ramasesha, S.; Sutter, J. P. *J. Am. Chem. Soc.* **2010**, *132*, 6047−6056.

(65) Drew, M. G. B.; Hollis, S.; Yates, P. C. *J. Chem. Soc., Dalton. Trans.* **1985**, 1829−1834.

(66) Rakowski, M. C.; Rycheck, M.; Busch, D. H. *Inorg. Chem.* **1975**, *14*, 1194−1200.

(67) Alcock, N. W.; Moore, P.; Omar, H. A. A.; Reader, C. J. *J. Chem. Soc., Dalton Trans.* **1987**, 2643−2648.

(68) Addison, A. W.; Rao, T. N.; Reedjik, J.; van Rijn, J.; Verschoor, G. C. *J. Chem. Soc., Dalton Trans.* **1984**, 1349−1356.

(69) Fernandes, A. S.; Cabral, M. F.; Costa, J.; Castro, M.; Delgado, R.; Drew, M. G.; Felix, V. *J. Inorg. Biochem.* **2011**, *105*, 410−419.

(70) XDrew, M. G. B.; Neison, S. H. *Acta Crystallogr., Sect. A: Cryst. Phys., Diffr., Theor. Gen. Crystallogr.* **1975**, *31*, S140−S140.

(71) Shannon, R. D. *Acta Crystallogr.* **1976**, *A32*, 751−767.

(72) Regueiro-Figueroa, M.; Lima, L. M. P.; Blanco, V.; Esteban-Gómez, D.; de Blas, A.; Rodríguez-Blas, T.; Delgado, R.; Platas-Iglesias, C. *Inorg. Chem.* **2014**, *53*, 12859−12869.

(73) (a) Alvarez, S. *Dalton Trans.* **2005**, 2209−2233. (b) Casanova, D.; Alemany, P.; Bofill, J. M.; Alvarez, S. *Chem.—Eur. J.* **2003**, *9*, 1281−1295.

(74) Herchel, R.; Šindelář, Z.; Trávníček, Z.; Zbořil, R.; Vančo, J. *Dalton Trans.* **2009**, 9870−9880.

(75) (a) Herchel, R.; Pavelek, L.; Trávníček, Z. *Dalton Trans.* **2011**, *40*, 11896−11903. (b) Šalitroš, I.; Boča, R.; Herchel, R.; Moncol, J.; Nemec, I.; Ruben, M.; Renz, F. *Inorg. Chem.* **2012**, *51*, 12755−12767.

(76) Waldmann, O. *Phys. Rev. B: Condens. Matter Mater. Phys.* **2000**, *61*, 6138−6144.

(77) Bradley, C. J.; Cracknell, A. P. *The Mathematical Theory of Symmetry in Solids;* Clarendon Press: Oxford, U.K., 1972.

(78) Nemec, I.; Herchel, R.; Šalitroš, I.; Trávníček, Z.; Moncol, J.; Fuess, H.; Ruben, M.; Linert, W. *CrystEngComm* **2012**, *14*, 7015−7024.

(79) (a) Evans, J. F. D. *J. Chem. Soc.* **1959**, 2003. (b) Olatunde, A. O.; Cox, J. M.; Daddario, M. D.; Spernyak, J. A.; Benedict, J. B.; Morrow, J. R. *Inorg. Chem.* **2014**, *53*, 8311−8321.

Příloha P2

B. Drahoš, R. Herchel, Z. Trávníček,

Structural and magnetic properties of heptacoordinated Mn[II] complexes containing a 15-membered pyridine-based macrocycle and halido/pseudohalido axial coligands.

Cite this: *RSC Adv.*, 2016, **6**, 34674

Structural and magnetic properties of heptacoordinated Mn^{II} complexes containing a 15-membered pyridine-based macrocycle and halido/pseudohalido axial coligands†

Bohuslav Drahoš, Radovan Herchel and Zdeněk Trávníček*

A series of heptacoordinated Mn^{II} compounds with a pentadentate 15-membered pyridine-based macrocycle 15-pyN$_3$O$_2$(3,12,18-triaza-6,9-dioxabicyclo[12.3.1]octadeca-1(18),14,16-triene) and two axially coordinated halido/pseudohalido coligands (X), having a monomeric [Mn(15-pyN$_3$O$_2$)X$_2$] (X = Br$^-$ (**1**), I$^-$ (**2**), N$_3^-$ (**3**), NCS$^-$ (**4**)) or polymeric {[Mn(15-pyN$_3$O$_2$)X](ClO$_4$)}$_n$ (X = CN$^-$ (**5**)) composition, was prepared and thoroughly characterized. Single crystal X-ray analysis of **2**, **3** and **4** determined the distorted pentagonal-bipyramidal geometry of the complexes. The analysis of the magnetic data of complexes **1–4** revealed non-zero values of the axial zero-field splitting parameter D ($|D| < 0.7$ cm^{-1}) and weak antiferromagnetic intermolecular interactions (molecular field correction parameter $zj \approx -0.1$ cm^{-1}). As for the 1D polymeric complex **5**, a small antiferromagnetic exchange coupling was found between Mn^{II} centres, with $J = -1.72$ cm^{-1}. The experimentally obtained magnetic parameters (J or zj) were compared with those theoretically calculated at the DFT level in order to reveal the magnetic exchange pathways in **2–4** and to support the polymeric structure of **5** ($J^{EXP} = -2.79$ cm^{-1} *vs.* $J^R/J^Y = -2.54/-3.06$ cm^{-1}, when the dinuclear spin Hamiltonian was used). It has been also found that extensive systems of hydrogen bonds, non-covalent contacts and π–π stacking interactions present in the crystal structures of **2**, **3** and **4** have an impact on the formation of supramolecular 1D chains, and as a consequence of this on the magnetic properties of the complexes. Contrary to non-covalent contacts, the influence of the axial ligands on the magnetic nature of the complexes seems to be negligible.

Introduction

Despite a long history of chemistry of 15-membered pyridine-based macrocycles with five donor atoms, which date from the 1960s and have been recently reviewed,[1,2] these macrocyclic ligands (mainly those with five nitrogen or three nitrogen and two oxygen donor atoms) still attain strong interest of coordination chemists and magnetochemists as well as theoreticians due to their application potential in molecular magnetism, various types of sensors, and spintronics.[3] Among this rather extensive group of compounds, our attention has been mainly focused on the 15-membered macrocycles with a pyridine moiety incorporated into the macrocyclic ligand scaffold and

Department of Inorganic Chemistry & Regional Centre of Advanced Technologies and Materials, Faculty of Science, Palacký University, 17. listopadu 12, CZ-771 46 Olomouc, Czech Republic. E-mail: zdenek.travnicek@upol.cz; Fax: +420 585634954; Tel: +420 585634352

† Electronic supplementary information (ESI) available: Comparison of IR spectra of the complexes **1–5**, TG/DTA results for complex **4**, additional X-ray diffraction analysis data (for complexes **2**, **3** and **4**) and magnetic data for the complexes **1–5**. CCDC 1442331–1442333. For ESI and crystallographic data in CIF or other electronic format see DOI: 10.1039/c6ra03754b

two oxygen and two secondary nitrogen atoms (15-pyN$_3$O$_2$ = **L** in Fig. 1). The synthesis of 15-pyN$_3$O$_2$ is well known[4] and it is based on the cyclization of pyridine-2,6-dicarbaldehyde with 1,8-diamino-3,6-dioxaoctane using Mn^{II} as a template providing a macrocyclic Schiff base followed by reduction with NaBH$_4$.[4] The structural, magnetic and redox properties of the selected transition metal complexes containing 15-pyN$_3$O$_2$ and chlorido coligand(s), *i.e.* [M^{II}**L**Cl$_2$] where M = Mn, Co, Ni, Zn, [Fe^{III}**L**Cl$_2$]Cl and [Cu^{II}**L**Cl]Cl, were described recently.[5] The coordination number of 7 was found in [M**L**Cl$_2$]$^{0/+}$ (M = Mn^{II}, Fe^{III}, Co^{II}) and 5 + 2 in [Ni^{II}**L**Cl$_2$], where the two chlorido ligands occupied two axial positions in the pentagonal bipyramid, whereas the tetragonal-pyramidal coordination environment in [Cu^{II}**L**Cl]Cl and [Zn^{II}**L**Cl$_2$] corresponded to the coordination number of 4 + 1 and 5, respectively.[5] All metals in the above-mentioned complexes were in high-spin (HS) states, with $S = 5/2$ for Mn^{II} and Fe^{III}, $S = 3/2$ for Co^{II}, $S = 1$ for Ni^{II}, and $S = 1/2$ for Cu^{II}. Moreover, a large axial anisotropy was found for Co^{II} and Ni^{II} complexes, with D(Co) ≈ 40 cm^{-1}, and D(Ni) ≈ −6.0 cm^{-1}.[5]

Many Mn^{II} complexes with the structurally similar Schiff base ligand 15-pydienN$_3$O$_2$ (Fig. 1) were studied previously. For example, the [Mn(15-pydienN$_3$O$_2$)(NCS)$_2$][6] complex with two
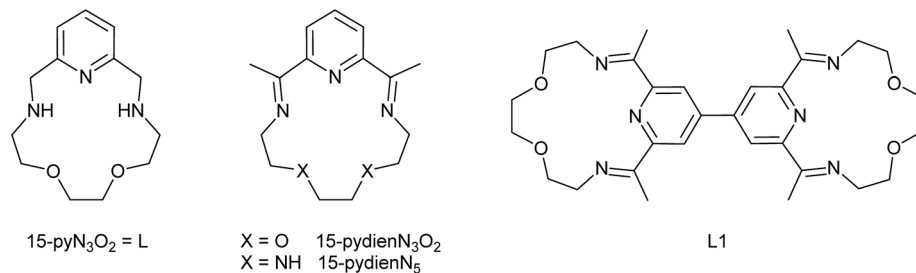
Fig. 1 Structural formulas of the studied ligand (15-pyN$_3$O$_2$ = L) and other ligands discussed in the text.

isothiocyanato ligands coordinated in axial positions of the pentagonal-bipyramid was described. Indeed, the [Mn(15-pydienN$_3$O$_2$)]$^{2+}$ complex unit has been usually coupled into heteronuclear oligomers of polymeric complexes with different cyanidometallates [M^I(CN)$_2$]$^-$,[7] [M^{II}(CN)$_4$]$^{2-}$,[8] or [M^{III}(CN)$_6$]$^{3-}$,[8,9] (M^I = Ag, Au; M^{II} = Ni, Pd, Pt; M^{III} = Fe, Cr, Co), showing antiferromagnetic exchange interactions between Mn^{II} and Cr^{III} [8] or ferromagnetic exchange interactions between Mn^{II} and Fe^{III}.[9] Furthermore, other bridging units like azido[10] or dicyanamido[11] ligands were used to link the Mn^{II} complex of the pentaaza Schiff base analogue 15-pydienN$_5$ (Fig. 1), forming a similar polymeric 1D chain with antiferromagnetic exchange coupling between adjacent Mn^{II} centres ($J = -4.8$ cm^{-1} for azide,[10] $J = -0.49$ cm^{-1} for dicyanamide).[11] Additionally, the Mn^{II} complex of the bimacrocyclic ligand **L1** (Fig. 1) [Mn$_2$(**L1**)Cl$_2$(H$_2$O)$_2$]Cl$_2$ revealed a very weak antiferromagnetic intra-dimer coupling ($J_{ex} = -0.51$ K) between the two Mn^{II} metal centres in the dimeric unit.[12] Nevertheless, the influence of the ligands in axial positions (X) in mononuclear heptacoordinated complexes of the general composition [MLX$_2$] (M = manganese or other transition metals, **L** = a pentadentate pyridine-based macrocyclic ligand) on the magnetic properties of these complexes has not been systematically studied. On the other hand, Mn^{II} complexes showing other interesting magnetic properties, e.g. spin crossover (spin transition induced by external stimuli, usually by changing temperature or upon light irradiation), are very rare. The known examples including Prussian blue analogue Rb^{I}Mn^{II}[Fe^{III}(CN)$_6$], manganocene derivatives (η^5-C$_5$H$_4$R)$_2$Mn (with R = H, Me, Et), or complexes with nitrosyl and dibenzotetramethyltetraaza[14]annulene (tmtaa), [(tmtaa)Mn{NO}]·THF, were already reviewed in the literature.[13]

As has been shown previously for many examples of transition metal complexes with Schiff bases,[14-16] the magnetic properties, especially the spin transition (spin crossover),[13] single molecule magnet (SMM)[17] behaviour, or magnetic anisotropy also for the 3d^5 configuration,[18,19] can be tuned by substitution of the small coligands providing a different ligand field which has an impact on the electronic structure of such systems. Such a strategy has been employed in this work in order to reveal the influence of the axial ligands on the crystal structure, on the system of non-covalent contacts and consequently on the magnetic properties. Therefore a series of Mn^{II} complexes with macrocyclic ligand 15-pyN$_3$O$_2$ and various coligands (i.e. Br$^-$ (**1**), I$^-$ (**2**), N$_3$$^-$ (**3**), SCN$^-$ (**4**) and CN$^-$ (**5**)) is studied. The synthesis and thorough characterization of the prepared compounds by different techniques is described. The X-ray structures of the complexes with two I$^-$ (**2**), N$_3$$^-$ (**3**) and SCN$^-$ (**4**) coligands are described in detail. The variable-temperature and variable-field magnetization measurements, which were performed for all the compounds, are discussed in order to reveal the magnetic properties of the complexes, such as magnetic anisotropy and magnetic exchange interactions. The results following from the magnetic data are supported by DFT calculations which helped us to identify the magnetic exchange pathways. This is the first example of a systematic investigation of pentagonal bipyramidal Mn^{II} complexes where the influence of the axial ligands is studied simultaneously by comparing the molecular structures, temperature/field-dependent magnetic data and DFT calculations.

Experimental

Synthesis

The ligand 15-pyN$_3$O$_2$ = **L** (3,12,18-triaza-6,9-dioxabicyclo[12.3.1]octadeca-1(18),14,16-triene) was synthesized according to the previously described literature procedure.[4] All other chemicals and solvents were purchased from commercial sources (Across Organics, Geel, Belgium and Sigma Aldrich, St. Louis, MO, USA and Penta, Prague, Czech Republic) and used as received.

[MnLBr$_2$] (1). **L** (100 mg, 0.40 mmol) and MnBr$_2$·4H$_2$O (114 mg, 0.40 mmol) were dissolved in 5 mL of methanol (MeOH) at room temperature. The obtained yellow solution was filtered through a Millipore syringe filter (0.45 μm) and the filtrate was left to a vapour diffusion of diethyl ether (Et$_2$O) at 5 °C. After several days, crystals of the desired complex were formed. They were collected by filtration on a glass frit and dried open to air at room temperature. The product was obtained in the form of pale yellow crystals (127 mg, yield 68.6%).

MS m/z (+): 385.21 [MnLBr]$^+$. Anal. calcd (%) for C$_{13}$H$_{21}$N$_3$O$_2$MnBr$_2$: C, 33.50; H, 4.54; N, 9.02. Found: C, 33.54; H, 4.75; N, 8.59.

[MnLI$_2$] (2). **L** (100 mg, 0.40 mmol) and Mn(ClO$_4$)$_2$·6H$_2$O (144 mg, 0.40 mmol) were dissolved in 3 mL of MeOH at room temperature. NH$_4$I (173 mg, 1.20 mmol, 3 eqv.) was dissolved in a 10 mL vial in 2.5 mL of MeOH, and this solution was added to the solution of the Mn^{II} complex prepared in the first step. The

yellow solution obtained was filtered through a Millipore syringe filter (0.45 μm) and the filtrate was left to a vapour diffusion of Et_2O at 5 °C. After several days, well-shaped crystals of the complex were formed. They were collected by filtration on a glass frit and dried open to air at room temperature. The product was obtained as yellow needle-shaped crystals (148 mg, yield 66.4%).

MS m/z (+): 433.17 $[MnLI]^+$. Anal. calcd (%) for $C_{13}H_{21}N_3O_2$-MnI_2: C, 27.88; H, 3.78; N, 7.50. Found: C, 28.21; H, 3.85; N, 7.40.

[MnL(N₃)₂] (3). L (100 mg, 0.40 mmol) and $Mn(OAc)_2 \cdot 6H_2O$ (101 mg, 0.40 mmol) were dissolved in a 25 mL dropping flask in 5 mL of MeOH at room temperature. A suspension of NaN_3 (65 mg, 1.00 mmol, 2.5 eqv.) in 2.5 mL of MeOH was added. The obtained mixture was heated to reflux and a clear yellow solution was formed. The hot solution was filtered through a Millipore syringe filter (0.45 μm) and the filtrate was left to a vapour diffusion of Et_2O at 5 °C. After several days, well-shaped crystals of the complex were formed, collected by filtration on a glass frit and dried open to air at room temperature. The product was obtained in the form of yellow-brown block-shaped crystals (98 mg, yield 63.2%).

MS m/z (+): 347.96 $[MnL(N_3)]^+$. Anal. calcd (%) for $C_{13}H_{21}N_9O_2Mn$: C, 40.00; H, 5.42; N, 32.30. Found: C, 39.60; H, 5.19; N, 32.77.

[MnL(NCS)₂] (4). L (100 mg, 0.40 mmol) and $MnCl_2 \cdot 4H_2O$ (79 mg, 0.40 mmol) were dissolved in 4 mL of MeOH at room temperature. To this yellow solution, NH_4SCN (151 mg, 2.00 mmol, 5 eqv.) dissolved in 2 mL of MeOH was added. After the mixing of both solutions, a white crystalline precipitate was formed and filtrated under reduced pressure on a glass frit, washed twice with 2 mL of MeOH and twice with 4 mL of Et_2O and dried open to air at room temperature. The obtained pale yellow crude product (139 mg) was recrystallized from a hot MeOH/water mixture. The pure product was isolated in the form of yellow block-shaped crystals (96 mg, yield 57.1%).

MS m/z (+): 364.22 $[MnL(SCN)]^+$. Anal. calcd (%) for $C_{15}H_{21}$-$N_5O_2S_2Mn$: C, 42.65; H, 5.01; N, 16.58; S, 15.18. Found: C, 42.78; H, 5.02; N, 16.27; S 15.52.

{[MnL(μ-CN)](ClO₄)}ₙ (5). L (100 mg, 0.40 mmol) and $Mn(ClO_4)_2 \cdot 6H_2O$ (144 mg, 0.40 mmol) were dissolved in 3 mL of MeOH at room temperature. A solution of NaCN (49 mg, 1 mmol, 2.5 eqv.) in 2.5 mL of MeOH was added and a white precipitate immediately formed. A small amount of ascorbic acid (6 mg, 0.04 mmol) was added to prevent the oxidation of Mn^{II} by air. The suspension was heated to reflux and an additional 2 mL of MeOH was added, but the precipitate did not dissolve. After 10 minutes of reflux, the suspension was cooled down to room temperature. The yellow precipitate was filtered under reduced pressure on a glass frit, washed with 2 mL of MeOH and twice with 2 mL of Et_2O and dried open to air at room temperature. The product was obtained as a yellow powder (129 mg, yield 75.0%).

MS m/z (+): 332.06 $[MnL(CN)]^+$, 405.10 $[MnL(ClO_4)]^+$. Anal. calcd (%) for $C_{14}H_{21}N_4O_6ClMn$: C, 38.95; H, 4.90; N, 12.98. Found: C, 38.88; H, 5.01; N, 12.99.

Physical methods

Measurement of elemental analysis (C, H, N) was carried out using a Flash 2000 CHNO-S Analyzer (Thermo Scientific, Waltham, MA, USA). Mass spectrometry (MS) was recorded on a LCQ Fleet Ion Mass Trap mass spectrometer (Thermo Scientific, Waltham, MA, USA) equipped with an electrospray ion source and 3D ion-trap detector in the positive mode. Infrared (IR) spectra of the complexes were collected on a Thermo Nicolet NEXUS 670 FT-IR spectrometer (Thermo Nicolet, Waltham, MA, USA) employing the ATR technique on a diamond plate in the range of 400–4000 cm^{-1}. Simultaneous thermogravimetric (TG) analysis and differential thermal analysis (DTA) were performed on a Exstar TG/DTA 6200 thermal analyzer (Seiko Instruments Inc., Torrance, CA, USA) with a dynamic air atmosphere (100 mL min^{-1}) in the temperature interval of 25–900 °C with a heating rate of 5.0 °C min^{-1}. The magnetic data were measured on powder samples using a SQUID magnetometer MPMS-XL7 (Quantum Design) for **1** and a PPMS Dynacool system (Quantum Design) with the VSM option for **2**–**5**. The experimental data were corrected for the diamagnetism and signal of the sample holder. The X-ray powder diffraction pattern for complex **1** was recorded on a MiniFlex600 (Rigaku) instrument equipped with the Bragg–Brentano geometry and iron-filtered Cu Kα$_{1,2}$ radiation.

X-ray diffraction analysis

Single crystals of complexes **2**, **3** and **4** suitable for X-ray structure analysis were prepared by vapour diffusion of Et_2O into a MeOH solution of the appropriate complex at 5 °C. Moreover, some other recrystallization or diffusion experiments were performed in the case of complexes **1** and **5**, but suitable single crystals were not prepared. X-ray diffraction data of **2** and **4** were collected with a Rigaku HighFlux HomeLab™ universal dual wavelength (Mo Kα and Cu Kα) single crystal diffractometer at 120(2) K, while the Mo Kα radiation ($\lambda = 0.71075$ Å) was used to obtain the diffraction data. The diffractometer was equipped with the Eulerian 3 circle goniometer and the Rigaku Saturn724+ (2×2 bin mode) detector. Data reduction and correction of the absorption effect were performed using the XDS software package.[20] The X-ray diffraction data of **3** were collected on a Bruker D8 QUEST diffractometer equipped with a PHOTON 100 CMOS detector using Mo Kα radiation. The APEX3 software package[21] was used for data collection and reduction of **3**. The molecular structures of **2**–**4** were solved by direct methods and refined by the full-matrix least-squares procedure SHELXL (version 2014/7).[22] Hydrogen atoms of all the structures were found in the difference Fourier maps and refined (except for N-attached H atoms) using a riding model, with C–H = 0.95 (CH)$_{ar}$ and C–H = 0.99 (CH$_2$) Å, and with $U_{iso}(H) = 1.2U_{eq}$ (CH, CH$_2$, NH). The highest peak of 5.82 e Å^{-3} is located 1.61 Å from I1b in **2**, while the peak of 4.01 e Å^{-3} is located 0.82 Å from Mn1b in **4**. The molecular and crystal structures of all the studied complexes, depicted in Fig. 2 and 3, respectively, were drawn using the Mercury software.[23]
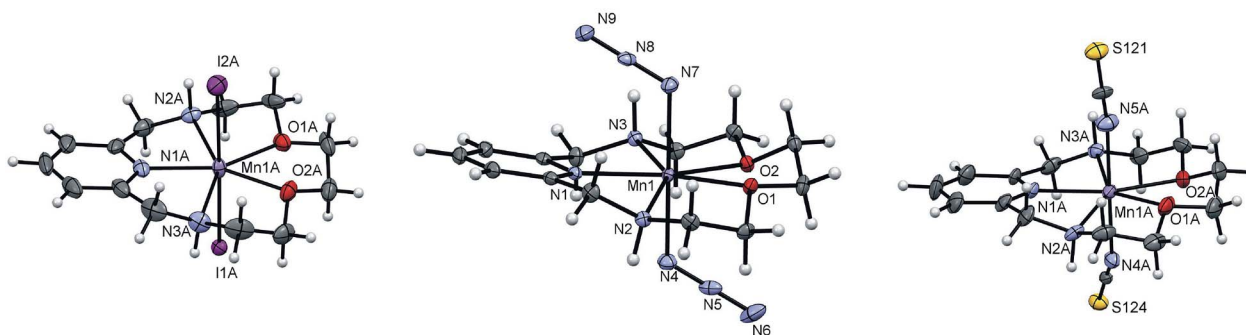
Fig. 2 Molecular structures of [MnLI₂] (**2**) (left), [MnL(N₃)₂] (**3**) (middle), and [MnL(NCS)₂] (**4**) (right). Non-hydrogen atoms are drawn as thermal ellipsoids at the 50% probability level. Only one of two (for **2**) and three (for **4**) crystallographically independent molecules are shown for clarity.

Computational details

The theoretical calculations were carried out with the ORCA 3.0.3 computational package.[24] The calculations of the isotropic exchange parameters J were done by the broken symmetry approach[25] using the hybrid B3LYP functional[26] and polarized triple-ζ quality basis set def2-TZVP(-f) proposed by Ahlrichs and coworkers for all atoms.[27] The calculations utilized the RI approximation with the decontracted auxiliary def2-TZV/J Coulomb fitting basis sets and the chain-of-spheres (RIJCOSX) approximation to exact exchange as implemented in ORCA.[28] Increased integration grids (Grid5 in ORCA convention) and tight SCF convergence criteria were used in all calculations. In all the cases the calculations were based on the experimentally determined X-ray molecular structures, but the all hydrogen atom positions were optimized using the B3LYP functional and atom pairwise dispersion correction to the DFT energy with Becke–Johnson damping (D3BJ).[29] In the case of the molecular fragment [(CN)MnL(μ-CN)MnL(CN)]⁺ of **5**, the whole geometry was optimized using B3LYP/def2-TZVP(-f)+D3BJ. The spin densities were visualized with the program VESTA 3.[30]

Results and discussion

Synthesis

Previously, Mn^{II} complexes with **L** containing coordinated two chlorido coligands[5] or one chlorido coligand and one water molecule[4] were prepared by direct mixing of manganese(II) salt and **L**. This simple procedure was employed in the preparation of complex **1**, for which MnBr₂ was directly complexed by **L**.

complex	[MnLCl₂]^a	[MnLI₂] (**2**)	[MnL(N₃)₂] (**3**)	[MnL(NCS)₂] (**4**)
angle (°)	41.6	45.6	60.2	8.2, 13.5, 5.3
Mn⋯Mn (Å)	6.627(1)	7.337(2), 7.355(2) ^{b}	7.655(1)	7.880(1), 8.024(1), 8.499(1) ^{b}

Fig. 3 Part of the crystal structure of [MnLCl₂],[5] **2**, **3** and **4** showing the N–H⋯Cl, N–H⋯I, N–H⋯N, and N–H⋯S non-covalent contacts (red dashed lines), respectively, forming 1D chain supramolecular structures together with the values of angles between the MnN₃O₂ least-square planes and the Mn⋯Mn distances in the 1D chains. ^{a}Data adopted from ref. 5. ^{b}Two and three crystallographically independent molecules were found in the asymmetric unit of **2** and **4**, respectively.

During the synthesis of compounds **2–5**, various manganese(II) salts, with anions with a low coordination ability (*e.g.* perchlorate or acetate), were complexed by **L** in the first step forming the [MnL]$^{2+}$ complex unit, while an excess of the appropriate coligand in the form of sodium or ammonium salt was added in the second step, during which this anion was coordinated to the manganese(II) centre. These two steps were designed in such a way that the side products were well soluble in MeOH (*i.e.* NH$_4$ClO$_4$, NH$_4$Cl, CH$_3$CO$_2$Na or NaClO$_4$) and did not contaminate the product during its consequent crystallization induced by Et$_2$O vapour diffusion.

X-ray diffraction analysis

The molecular structures of the complexes **2**, **3** and **4** are similar (Tables 1 and 2, Fig. 2, Tables S1 and S2, Fig. S1 and S2†). The crystal structures of **2** and **4** involve two and three, respectively, crystallographically independent molecules in the asymmetric units. However, the data for one of those independent molecules are discussed in the main text and listed in Table 2 (full data sets are available in Table S1,† all independent molecules are shown in Fig. S1 and S2 in the ESI†).

In all the cases, the Mn^{II} central atom adopts pentagonal-bipyramidal geometry with the coordination number of 7 (Fig. 2). The pentadentate macrocycle **L** is coordinated in an equatorial pentagonal plane with the shortest Mn–N$_{py}$ distances

~2.10–2.20 Å in comparison with the Mn–N$_H$ distances, ranging from 2.27 to 2.33 Å, and the Mn–O distance ranging from 2.28 to 2.33 Å (Table 2). The two axial positions are occupied with two iodido ligands in **2**, for which the Mn–I distances are much longer (2.95 and 3.03 Å, Table 2) in comparison with the Mn–N and Mn–O distances providing elongation of the pentagonal-bipyramidal coordination sphere in the axial directions. This is in accordance with the larger ionic radius of the iodide anions. Consequently the Mn–I distances are also longer in comparison with the same complex with coordinated chlorido coligands described previously having Mn–Cl distances of 2.53 and 2.55 Å.[5]

On the other hand, in the case of coordination of two azido or thiocyanato ligands in **3** or **4**, the M–N$_{axial}$ distances are shorter than those to the macrocyclic donor atoms (Table 2) providing axial compression of the pentagonal-bipyramidal coordination sphere. A further interesting feature of complexes **3** (with N$_3^-$) and **4** (with NCS$^-$) is associated with the value of the Mn–N–N(C) angle, which is 119.6/121.2° for **3** indicating a similar coordination fashion of both azido ligands, and 145.7/165.0°, 141.1/142.9° or 165.1/149.1° for **4** (Table 3) pointing to a different coordination mode in each independent molecule found in the asymmetric unit, which shows that the coordination of NCS$^-$ to the Mn^{II} centre is closer to linear in comparison with the N$_3^-$ ligand. For **3**, the observed Mn–N–N angles are very similar to the value 118.8° found in the 1D chain structure of ([Mn(15-pydienN$_5$)(N$_3$)]$^+$)$_n$.[10]

Table 1 Crystal data and structure refinements for the studied complexes

Compound	2	3	4
Formula	C$_{13}$H$_{21}$I$_2$MnN$_3$O$_2$	C$_{13}$H$_{21}$MnN$_9$O$_2$	C$_{15}$H$_{21}$MnN$_5$O$_2$S$_2$
M_r	560.07	390.33	422.43
Colour	Yellow	Orange	Pale brown
Temperature (K)	120(2)	120(2)	120(2)
Wavelength (Å)	0.71073	0.71073	0.71073
Crystal system	Monoclinic	Monoclinic	Triclinic
Space group	$P2_1/n$	$P2_1/n$	$P1^a$
a (Å)	14.6223(10)	9.8283(6)	10.1382(7)
b (Å)	16.5304(12)	12.8416(7)	11.3567(8)
c (Å)	15.2077(11)	13.4703(9)	14.0782(10)
α (°)	90	90	103.348(2)
β (°)	98.7810(10)	100.300(2)	110.850(2)
γ (°)	90	90	101.570(2)
U (Å^3)	3632.8(4)	1672.70(18)	1400.79(17)
Z	8	4	3
D_{calc} (g cm^{-3})	2.048	1.550	1.502
μ (mm^{-1})	4.133	0.819	0.949
F (000)	2136	812	657
θ range for data collection (°)	1.800–24.998	2.375–27.173	1.640–25.000
Refl. collected	27 041	116 071	14 537
Independent refl.	6390	3720	8526
R (int)	0.0311	0.0554	0.0156
Data/restrains/parameters	6390/0/379	3720/0/226	8526/3/677
Completeness to θ (%)	99.8	100.0	98.1
Goodness-of-fit on F^2	1.093	1.088	1.057
$R1$, $wR2$ ($I > 2\sigma(I)$)	0.0641, 0.1746	0.0258, 0.0578	0.0676, 0.1737
$R1$, $wR2$ (all data)	0.0653, 0.1756	0.0330, 0.0608	0.0677, 0.1738
Largest diff. peak and hole (Å^{-3})	5.82 and −2.74	0.24 and −0.28	4.01 and −1.02
CCDC number	1442331	1442332	1442333

^{a} The value of the Flack parameter is 0.54(3).

Table 2 Selected bond distances (Å) and angles (°) for the studied complexes **2–4**[a]

Distances	2	3	4	Angles	2	3	4	Torsion angles	2	3	4
Mn–N1	2.218(7)	2.2020(11)	2.195(6)	N1–Mn–N2	73.0(3)	72.15(4)	72.8(3)	N1–C–C–N2	−29.7	−22.0	−25.7
Mn–N2	2.274(7)	2.3040(11)	2.308(7)	N1–Mn–N3	72.3(3)	73.37(4)	72.3(3)	N2–C–C–O1	57.0	55.8	56.6
Mn–N3	2.292(8)	2.2953(11)	2.334(7)	N2–Mn–O1	72.8(3)	72.87(4)	72.2(3)	O1–C–C–O2	−56.0	−59.1	−54.8
Mn–O1	2.293(6)	2.3019(9)	2.294(6)	O2–Mn–N3	73.8(3)	73.32(4)	73.7(2)	O2–C–C–N3	58.1	59.0	61.4
Mn–O2	2.285(6)	2.3271(10)	2.310(6)	O2–Mn–O1	69.6(2)	70.57(3)	71.3(3)	N3–C–C–N1	−24.1	−33.0	−27.6
Mn–X$_{ax}$1	2.9493(14) I1A	2.2339(12)N4	2.238(7) N4A	X$_{ax}$1–Mn–X$_{ax}$2	178.80(5)	174.68(5)	176.7(3)				
Mn–X$_{ax}$2	3.0329(15) I2A	2.2293(12) N7	2.210(8) N5A								

[a] Entire list of bond distances and angles is available in Table S1 in the ESI.†

For **4**, the observed Mn–N–C angles are little bit higher in comparison with those found in [Mn(15-pydienN$_3$O$_2$)(NCS)$_2$] (126.1° and 130.4°).[6] On the other hand, the X–Mn–X angles (X represents the donor atom of the axial ligand) are close to the ideal linear arrangement (178.8°, 174.7° and 176.7° for **2**, **3** and **4**, respectively, Table 3).

In the crystal structure of all the compounds, an extensive system of N–H⋯X and C–H$_{aromatic}$⋯X hydrogen non-covalent contacts (X = I, N, or S atom of the axial ligand) as well as π–π stacking interactions were found. These non-covalent contacts and interactions strongly influenced the final crystal packing of the complexes (Table S2 in the ESI†) as well as the magnetic properties (see the sections of magnetic properties and DFT calculations). In the crystal structure of **2**, a zig-zag 1D chain is formed by two N–H⋯I hydrogen bonds between the two [MnLI$_2$] units (Fig. 3). Furthermore, these infinite chains are connected to each other by two C–H$_{aromatic}$⋯I non-covalent contacts as well as by face-to-face π–π interactions (centroid⋯centroid distance = Cg⋯Cg = 3.758(1) Å), which all together form almost planar 2D sheets (layers) separated from each other (i.e. no non-covalent contacts observed).

The 1D chain motif can be also found in the crystal structures of **3** and **4**, where again the complex units are connected by N–H⋯N and N–H⋯S hydrogen bonds, respectively. In **3**, similarly as in **2**, this chain can be considered as a zig-zag, while it is almost linear in **4**. This trend can be clearly demonstrated by the values of the dihedral angle between the two MnN$_3$O$_2$ least-square planes in the chain which are 45.6°, 60.2°, and 8.4° for **2**, **3**, and **4**, respectively (Fig. 3). As for **2**, this angle of 45.6° is slightly higher than the 41.6° observed in [MnLCl$_2$].[5] Additionally, in the crystal structure of [Mn(15-pydienN$_3$O$_2$)(NCS)$_2$],[6] there are no NH groups and thus, only C–H$_{aromatic}$⋯S non-covalent contacts and π–π stacking are present, and thus, a completely different arrangement of the complex units was found in comparison with **4**.

On the other hand, the linking of these chains is different in **3** and **4**. In **3**, these 1D chains are linked by C–H$_{aromatic}$⋯N non-covalent contacts and face-to-face π–π interactions (Cg⋯Cg = 3.467(1) Å) forming zig-zag bent 2D sheets which are not connected to each other by any non-covalent contacts, whereas in **4**, these 1D chains are linked by C–H$_{aromatic}$⋯S non-covalent contacts and face-to-face π–π interactions (Cg⋯Cg = 3.698(1)

Table 3 Detailed description of the coordination sphere of Mn^{II} atoms in the molecular structures of complexes **2**, **3** and **4**

Complex	[MnLI$_2$] (2)	[MnL(N$_3$)$_2$] (3)	[MnL(NCS)$_2$] (4)		
Illustration of the coordination sphere of Mn^{II}					
Metal–axial donor atom distance (Å)	I1A 2.9493(14) I2A 3.0329(15)	N4 2.2339(12) N7 2.2293(12)	N4A 2.238(7)[b] N5A 2.210(8)[b]	N4B 2.194(7)[b] N5B 2.202(8)[b]	N4C 2.200(7)[b] N5C 2.233(7)[b]
Angle (°)	—	119.6 121.2	145.7(7)[b] 165.0(8)[b]	141.1(8)[b] 142.9(8)[b]	165.1(8)[b] 149.1(7)[b]
Mn–N–N(S)	—		(Mn1A–N4A–C123)[b] (Mn1A–N5A–C120)[b]	(Mn1B–N4B–C223)[b] (Mn1B–N5B–C220)[b]	(Mn1C–N4C–C323)[b] (Mn1C–N5C–C320)[b]
Angle (°) X–Mn–X[a]	178.80(5), 177.25(5)[b]	174.68(5)	176.7(3)[b]	179.1(3)[b]	174.9(3)[b]

[a] X = axial donor atom. [b] Two and three crystallographically independent molecules in the asymmetric unit of **2** and **4**, respectively, were found.

Å) forming almost planar 2D sheets which are linked to each other by C–H$_{aromatic}\cdots$S non-covalent contacts, thus giving rise to a supramolecular 3D network. Despite many crystallization attempts, single crystals of **1** and **5** suitable for X-ray diffraction analysis were not prepared. But nevertheless, at least a powder diffraction pattern for **1** was recorded (Fig. S3†) and it showed that **1** and **2** are isostructural.

IR spectroscopy

The vibration characteristics for the coordinated ligand **L** were present in the IR spectra of all the complexes (Fig. S4 in the ESI†), *i.e.* a strong broad signal at ~3230 cm^{-1} (stretching vibrations of the two NH groups), strong doublets at ~2900 cm^{-1} (stretching CH$_2$ vibrations), a medium sharp doublet at 1600 and 1575 cm^{-1}, and a medium broad signal(s) at ~1460 cm^{-1} (wagging vibrations of the pyridine ring). Furthermore, characteristic strong absorption bands at 2023, 2059 and 2123 cm^{-1} assigned to the asymmetric stretching vibrations of the N$_3^-$ group in **3**, NCS$^-$ group in **4**, and CN$^-$ group in **5**, respectively, were observed. The position of this band in **4** was almost the same as that observed for [Mn(15-pydienN$_3$O$_2$)(NCS)$_2$] (2058 cm^{-1})[6] or [Mn(cyclam)(NCS)$_2$]$^+$ (2060 cm^{-1}, cyclam = 1,4,8,11-tetraazacyclotetradecane).[31] The position of the broad absorption band of N$_3^-$ in **3** was found at lower wavenumbers than in the case of the end-to-end μ-1,3-bridged azide between two Mn^{II} centres in ([Mn(15-pydienN$_5$)(N$_3$)]$^+$)$_n$ (2049 cm^{-1})[10] as well as in the case of other azido complexes with manganese [Mn(saldien)(N$_3$)] (2067 and 2056 cm^{-1}, saldien = *N*,*N*′-bis(salicylidene)diethylenetriamine)[32] or [N(afa^{Cy})$_3$Mn(N$_3$)] (2067 cm^{-1}, N(afa^{Cy})$_3$ = tris(5-cycloaminoazafulvene-2-methyl)amine).[33] On the other hand, the absorption band of the CN$^-$ group in **5** corresponded to the bridging mode of its coordination, whose position was comparable with the 2113 cm^{-1} observed in [Mn(15-pydienN$_3$O$_2$)(H$_2$O)]$_2$[Mn(CN)$_6$](ClO$_4$)·3H$_2$O[34] and 2110 cm^{-1} observed in [Mn(salen)(CN)]$_n$[35] (H$_2$-salen = bis(salicylidene)-ethylenediamine). These findings together with the broad character of the signal[36] suggested the 1D chain polymeric structure of complex **5**.

TG/DTA analysis

The results of the simultaneous TG/DTA analyses in a dynamic air atmosphere are similar for complexes **1**, **2**, **4** and **5**. The data for the representative complex **4** are shown in the ESI in Fig. S5.† No weight loss was observed until a temperature of ~180 °C, showing the absence of any coordinated/uncoordinated solvent molecules. Above 180 °C (**1** and **5**) or 280 °C (**2** and **4**), the decomposition proceeded in two (**1**, **2** and **4**) or three (**5**) steps without formation of thermally stable intermediates and it was accompanied with a few exo-effects. The decomposition was completed above 600 °C, except for complex **4**, in which an additional weight loss of 5.0% occurred between 613 and 766 °C. The products of thermal decomposition were not studied in detail, but the remaining weight percentage corresponds with the formation of Mn$_2$O$_3$ (% found/calcd: 16.1/16.9, 14.7/14.1, 19.7/18.7 and 18.3/18.3 for **1**, **2**, **4**, and **5**, respectively).

Magnetic properties

For all the prepared Mn^{II} complexes **1–5**, temperature and field dependent magnetic data were acquired and they are depicted in Fig. 4 and S6–S10 (in the ESI†). The room temperature values of the effective magnetic moment (μ_{eff}) span the 5.9–6.1 μ_B interval, which means that they are close to the theoretical spin-only value for $S = 5/2$, equal to 5.9 μ_B ($g = 2.0$). On lowering the temperature, there is a drop of μ_{eff} below 30 K down to 5.3–5.9 μ_B at $T = 1.9$ K
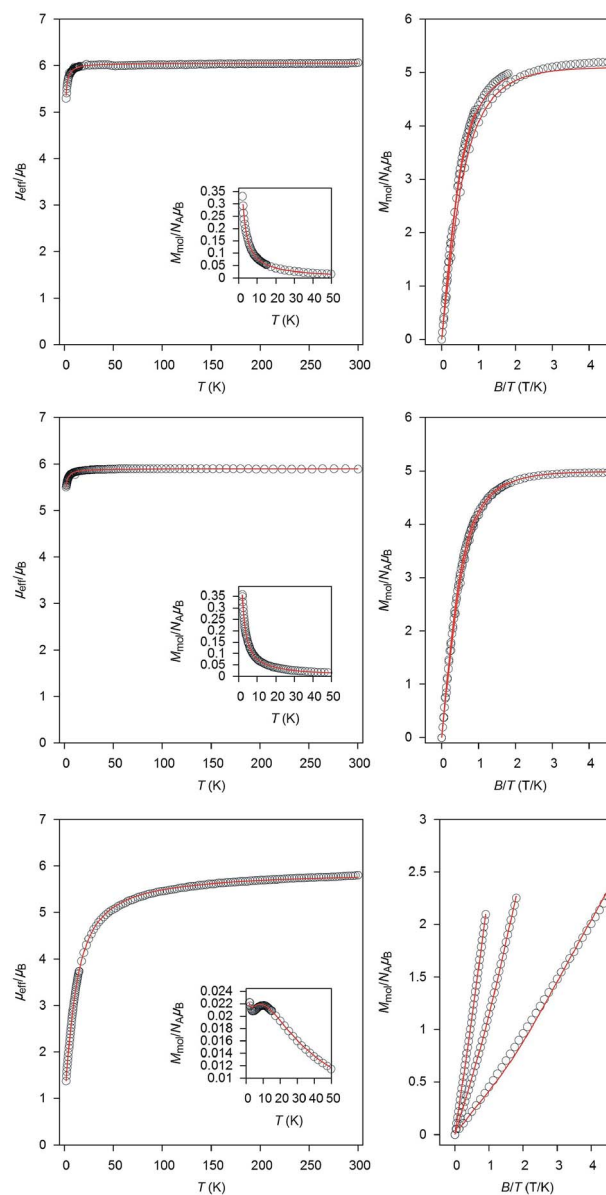

Fig. 4 Magnetic data for compounds **2** (top), **4** (middle) and **5** (bottom). Temperature dependence of the effective magnetic moment and molar magnetization measured at $B = 0.1$ T in the inset (left), and reduced isothermal magnetization measured at $T = 2$, 5 and 10 K (right). The empty circles represent the experimental data points and the full lines represent the best fits calculated with $D = -0.44(3)$ cm^{-1}, $g = 2.046(1)$, and $zj = -0.099(4)$ cm^{-1} for **2**, and $D = 0.12(4)$ cm^{-1}, $g = 1.996(1)$, and $zj = -0.066(1)$ cm^{-1} for **4** using eqn (1), and with $J = -1.72(1)$ cm^{-1}, $g = 1.992(2)$, and $x_{PI} = 1.3(1)$ % for **5** using eqn (6).

for **1–4**, which is most probably the result of weak intermolecular magnetic interactions mediated by non-covalent contacts (hydrogen bonds/π–π stacking) and also by the small magnetic anisotropy of Mn^{II} atoms in the heptacoordinated environment. In the case of **5**, the overall magnetic behaviour is different to **1–4**, the μ_{eff} is continuously decreasing from room temperature down to 1.37 μ_B at $T = 1.9$ K, and there is also a maximum of the M_{mol} vs. T curve at $T = 9.5$ K, which is a fingerprint of antiferromagnetic exchange either in a homo-spin dimer or uniformly coupled 1D chain. Moreover, the isothermal magnetization also significantly deviates from the Brillouin function. We can speculate that this is the result of the isotropic exchange mediated by the cyanido ligands in the bridging mode.

First, the magnetic data of **1–4** were treated with the spin Hamiltonian for a monomeric system

$$\hat{H}^{mono} = D(\hat{S}_z^2 - \hat{S}^2/3) + \mu_B Bg\hat{S}_a - zj\langle\hat{S}_a\rangle\hat{S}_a \quad (1)$$

where the single ion zero-field splitting parameter D, isotropic g-factor and molecular field correction zj parameters are present. $\langle S_a \rangle$ is a thermal average of the molecular spin projection in the a-direction of the magnetic field defined as $B_a = B(\sin\theta\cos\varphi, \sin\theta\sin\varphi, \cos\theta)$ with the help of the polar coordinates. Then, the molar magnetization in the a-direction of the magnetic field can be numerically calculated as:

$$M_a = -N_A \frac{\sum_i \left(\sum_k \sum_l C_{ik}^+ (Z_a)_{kl} C_{li}\right) \exp(-\varepsilon_{a,i}/kT)}{\sum_i \exp(-\varepsilon_{a,i}/kT)} \quad (2)$$

where Z_a is the matrix element of the Zeeman term for the a-direction of the magnetic field and C is the eigenvectors resulting from the diagonalization of the complete spin Hamiltonian matrix. The inclusion of zj means that an iterative procedure was applied.[37] Then, the averaged molar magnetization of the powder sample was calculated as an integral (orientational) average:

$$M_{mol} = 1/4\pi \int_0^{2\pi} \int_0^\pi M_a \sin\theta d\theta d\varphi \quad (3)$$

We also tested both signs of the D parameter during fitting procedures and the results are summarized in Table 4. It is evident that similarly good fits were obtained for both signs of D. The largest magnetic anisotropy, $|D|$, was found in complex **1** ($D = 0.67(7)$ cm^{-1} or $D = -0.55(5)$ cm^{-1}), while a negligible D

parameter was found in **3** ($D = 0$). Moreover, non-negligible magnetic intermolecular interactions seem to be present in compounds **1**, **2** and **3**, where $zj \approx -0.1$ cm^{-1} and slightly weaker interactions were found in **4** ($zj \approx -0.07$ cm^{-1}). Moreover, it must be stressed that we also tried to fit experimental data with simplified models, either by neglecting ZFS (D) or the molecular field correction (zj), but these models were unable to properly describe simultaneously both the temperature and field dependent magnetic data of **1**, **2** and **4**.

In the case of compound **5**, where the exact structural motif is unknown, the two spin Hamiltonian models were tested. First, the experimental data were treated with the dinuclear spin Hamiltonian (H^{dimer}):

$$\hat{H}^{dimer} = -J\left(\vec{S}_1 \cdot \vec{S}_2\right) + \sum_{i=1}^2 D_i\left(\hat{S}_{i,z}^2 - \hat{S}_i^2/3\right) + \mu_B Bg_i\hat{S}_a \quad (4)$$

where the first term describes the isotropic exchange between paramagnetic manganese(II) atoms within the dimer and the rest of the terms were already explained. Now, the molar magnetization in the a-direction of the magnetic field was calculated as:

$$M_a = N_A kT \frac{d\ln Z}{dB} \quad (5)$$

where Z is the partition function and again the integral average was calculated using eqn (3). In this case, the best fit was obtained only for the positive D parameter, which resulted in $J = -2.79(4)$ cm^{-1}, $D = 0.6(3)$ cm^{-1}, $g = 1.978(3)$, and $x_{PI} = 2.2(2)\%$ (Fig. S10†), where also the monomeric paramagnetic impurity (PI) was included in order to describe a low temperature increase of the mean susceptibility. A second model attempts to mimic the 1D uniformly coupled spin chain by a finite-sized closed ring with the following spin Hamiltonian (H^{1D}):

$$\hat{H}^{1D} = -J\left(\vec{S}_1 \cdot \vec{S}_N\right) - J\sum_{i=1}^{N-1}\left(\vec{S}_1 \cdot \vec{S}_{i+1}\right) + \sum_{i=1}^N \mu_B Bg_i\hat{S}_z \quad (6)$$

The number of centres was set to seven ($N = 7$), which resulted in already 279 936 magnetic levels. In order to be able to deal with such a large system, the zero-field term was neglected and then the coupled basis set could be utilized, which significantly simplifies the calculation of the magnetic properties.[39] The advantage of this procedure is that both the temperature and field dependent data can be fitted simultaneously. As a result, these parameters were obtained: $J = -1.72(1)$ cm^{-1}, $g = 1.992(2)$,

Table 4 The spin Hamiltonian parameters (eqn (1)) for **1–4**[a]

Complex	1	2	3	4
$D > 0$	$g = 2.035(2)$	$g = 2.046(1)$		$g = 1.996(1)$
	$D = 0.67(7)$	$D = 0.45(5)$	$g = 2.054(2)$	$D = 0.12(4)$
	$zj = -0.109(7)$	$zj = -0.099(4)$	$D = 0$	$zj = -0.066(1)$
$D < 0$	$g = 2.034(2)$	$g = 2.046(1)$	$zj = -0.099(5)$	$g = 1.996(1)$
	$D = -0.55(5)$	$D = -0.44(3)$		$D = -0.11(4)$
	$zj = -0.104(7)$	$zj = -0.099(4)$		$zj = -0.066(6)$

[a] Values of D and zj parameters are in cm^{-1}.[38]

and $x_{PI} = 1.3(1)\%$ (Fig. 4). As far as we know, Mn^{II}–CN–Mn^{II} systems are very rare, because usually one or both Mn atoms are in the oxidation state +III. One described example is a Mn^{II} complex with 1,4-bis(2-pyridylmethyl)-1,4,7-triazacyclononane (dmptacn) $[\{Mn(dmptacn)\}_2CN](ClO_4)_3$ for which only the negative value of the Weiss constant, $\theta = -0.31$ K,[40] was observed, as well as in some Mn^{II} Prussian blue analogues.[41,42]

DFT calculations

The analysis of the experimental magnetic data revealed weak magnetic interactions among Mn^{II} atoms in the solid state. With the aim to continue in our effort in recognizing/characterizing efficient magnetic exchange pathways mediated by non-covalent contacts,[5,43] we performed theoretical calculations of the isotropic exchange parameter J in selected molecular fragments based on the X-ray structures of **2–4**. Both the interactions within supramolecular 1D chains visualized in Fig. 3 and interchain interactions (shown in the ESI in Table S3†) were calculated using the B3LYP functional together with the def2-TZVP(-f) basis set utilizing the ORCA computational package. The values of J parameters were calculated by two approaches, either using Ruiz's formula:[44]

$$J^{Ruiz} = 2\Delta/[(S_1 + S_2)(S_1 + S_2 + 1)] \tag{7}$$

or Yamaguchi's formula:[45]

$$J^{Yam} = 2\Delta/[\langle S^2 \rangle_{HS} - \langle S^2 \rangle_{BS}] \tag{8}$$

where Δ is the energy difference between the broken symmetry spin state (BS) and high-spin state (HS):

$$\Delta = E_{BS} - E_{HS} \tag{9}$$

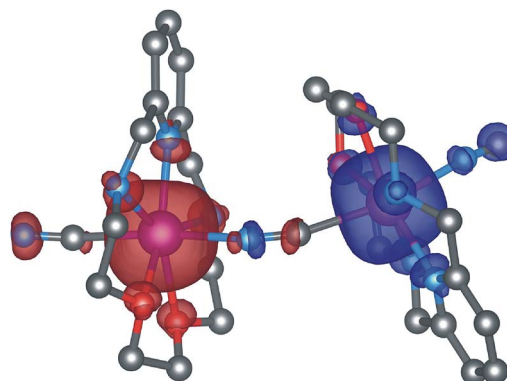using this form of the spin Hamiltonian for the dinuclear system:

$$\hat{H} = -J(\vec{S_1} \cdot \vec{S_2}) \tag{10}$$

The resulting J values are listed in Table 5. It is evident that in the crystal structure of **2**, the strength of the intrachain and

Fig. 5 The DFT optimized geometry of the $[(CN)LMn(\mu\text{-}CN)MnL(CN)]^+$ molecular fragment of **5** and calculated isodensity surfaces of the broken symmetry spin states plotted with the cut-off values of 0.003 ea_0^{-3}. Positive and negative spin densities are represented by dark blue and dark red surfaces, respectively. Selected bond lengths (Å): Mn–N_{py} = 2.228/2.251, Mn–N_H = 2.346/2.337/2.350/2.352, and Mn–O = 2.327/2.469/2.358/2.332. Hydrogen atoms are omitted for clarity.

interchain antiferromagnetic interactions is almost equal. In contrast, in **3**, there is the strongest antiferromagnetic exchange within the supramolecular chain among compounds **2–4**, and negligible interchain interaction. A similar situation is found in **4**, where again intrachain interaction is pronounced. Furthermore, apparently the strength of antiferromagnetic exchange is not a simple function of the metal–metal distance (Table 5), so it is obvious that the utilization of theoretical methods is an inevitable tool for better understanding of magnetic interactions in the solid state.

Furthermore, we also tried to support our presumption that in the case of compound **5**, a polymeric structure of $\{[MnL(\mu\text{-}CN)](ClO_4)\}_n$ is formed, in which cyanide anions act as bridging ligands. Therefore, the dinuclear molecular fragment of $[(CN)LMn(\mu\text{-}CN)MnL(CN)]^+$ was constructed and its geometry optimized at the B3LYP/def2-TZVP(-f) level of theory (Fig. 5). The metal–donor atom distances were found to be similar to those determined in the X-ray structures of **2–4**. Afterwards, the J parameters were calculated for this fragment, which resulted in $J^R/J^Y = -2.54/-3.06$ cm^{-1}. These values are in good agreement with $J = -2.79$ cm^{-1} determined from the experimental magnetic data using the spin Hamiltonian for a dinuclear system. Thus, this finding indirectly supports the formation of a polymeric species, where dominant magnetic exchange is mediated by the cyanido bridging ligands.

Conclusions

A series of heptacoordinated Mn^{II} complexes **1–5** containing a pentadentate 15-membered pyridine-based macrocycle **L** and two axial coligands with different coordination abilities (Br$^-$, I$^-$, N$_3^-$, NCS$^-$ or CN$^-$) was prepared and thoroughly characterized. The pentagonal-bipyramidal coordination sphere of Mn^{II} was axially elongated (in **2**) or compressed (in **3** and **4**) depending on the type of coligand. Based on an analysis of structural and magnetic data for **1–4**, the single ion magnetic anisotropy of

Table 5 The calculated J parameters for selected dinuclear molecular fragments of **2–4** using B3LYP/def2-TZVP(-f)[a]

Complex	2	3	4	4	4
Intrachain					
$d(Mn\cdots Mn)$ (Å)	7.337	7.655	7.880	8.024	8.499
Δ (cm^{-1})	−0.335	−1.476	−0.413	−0.348	−0.653
J^R (cm^{-1})	−0.022	−0.099	−0.028	−0.023	−0.044
J^Y (cm^{-1})	−0.027	−0.12	−0.033	−0.028	−0.052
Interchain					
$d(Mn\cdots Mn)$ (Å)	7.729	6.947	6.918		
Δ (cm^{-1})	−0.348	+0.002	+0.023		
J^R (cm^{-1})	−0.023	0.0	+0.002		
J^Y (cm^{-1})	−0.028	0.0	+0.002		

[a] The respective molecular fragments are shown in the ESI in Table S3.†

Mn^{II} with a 3d^5 configuration in the pentagonal-bipyramidal coordination environment is very small ($|D| < 0.7$ cm^{-1}), which prevented us from drawing a quantitative conclusion about the impact of the axial coligands on D. Therefore no magneto-structural correlation could be carried out reliably in contrast to other studies on complexes with different metal ions or different coordination geometries. On the other hand, the magnetic nature of **1–4** was more markedly influenced by noticeable non-covalent contacts, which are responsible for the 1D chain supramolecular crystal structures of the complexes. Moreover, the performed DFT calculations supported the experimental results and identified that the weak antiferromagnetic exchange in **3** and **4** was exclusively mediated *via* intrachain hydrogen bonds, while it was equally mediated by intrachain as well as interchain hydrogen bonds in **2**. In addition to this, the calculations showed that the Mn···Mn distance cannot be considered as the main criterion for the prediction of the intensity of the magnetic exchange. The polymeric character of **5** was suggested by fitting the magnetic data with a dimeric/polymeric model providing a weak antiferromagnetic exchange coupling, which was subsequently supported by DFT calculations based on the theoretically optimized structure of the dimeric fragment $[(CN)LMn(\mu\text{-}CN)MnL(CN)]^+$ as well. To conclude, this is the first attempt to correlate the structure of Mn^{II} heptacoordinated complexes with their magnetic properties. It is evident that the magnetic anisotropy is little affected by the axial ligands within the pentacoordinate bipyramidal chromophore, but the presented $[MnL]^{2+}$ fragment can be successfully employed as a high-spin ($S = 5/2$) building block for the synthesis of structurally more complex polymeric species with eventually more interesting magnetic properties.

Acknowledgements

Notes and references

1 M. Rezaeivala and H. Keypour, *Coord. Chem. Rev.*, 2014, **280**, 203–253.
2 E. L. Gavey and M. Pilkington, *Coord. Chem. Rev.*, 2015, **296**, 125–152.
3 J. S. Miller and D. Gatteschi, Molecule-based magnets themed issue No. 6, *Chem. Soc. Rev.*, 2011, **40**, 3053–3368.
4 B. Drahoš, J. Kotek, P. Hermann, I. Lukeš and E. Tóth, *Inorg. Chem.*, 2010, **49**, 3224–3238.
5 B. Drahoš, R. Herchel and Z. Trávníček, *Inorg. Chem.*, 2015, **54**, 3352–3369.
6 M. G. B. Drew, A. H. bin Othman, S. G. McFall, P. D. A. Mcllroy and S. M. Nelson, *Dalton Trans.*, 1977, **12**, 1173–1180.
7 D. Zhang, H. Wang, L. Tian, J. Jiang and Z.-H. Ni, *CrystEngComm*, 2009, **11**, 2447–2451.
8 F. Bonadio, M.-C. Senna, J. Ensling, A. Sieber, A. Neels, H. Stoeckli-Evans and S. Decurtins, *Inorg. Chem.*, 2005, **44**, 969–978.
9 C. Paraschiv, M. Andruh, Y. Journaux, Z. Žak, N. Kyritsakas and L. Ricard, *J. Mater. Chem.*, 2006, **16**, 2660–2668.
10 K. A. Sra, J.-P. Sutter, P. Guionneau, D. Chasseau, J. V. Yakhmi and O. Kahn, *Inorg. Chim. Acta*, 2000, **300–302**, 778–782.
11 C. Paraschiv, J.-P. Sutter, M. Schmidtmann, A. Müller and M. Andruh, *Polyhedron*, 2003, **22**, 1611–1615.
12 J. Wang, B. Slater, A. Alberola, H. Stoeckli-Evans, F. S. Razavi and M. Pilkington, *Inorg. Chem.*, 2007, **46**, 4763–4765.
13 K. S. Murray and C. J. Kepert, *Top. Curr. Chem.*, Springer, 2004, vol. 233–235.
14 I. Nemec, R. Herchel, R. Boca, Z. Travnicek, I. Svoboda, H. Fuess and W. Linert, *Dalton Trans.*, 2011, **40**, 10090–10099.
15 C. Krüger, P. Augustín, I. Nemec, Z. Trávníček, H. Oshio, R. Boča and F. Renz, *Eur. J. Inorg. Chem.*, 2013, **2013**, 902–915.
16 P. Masárová, P. Zoufalý, J. Moncoľ, I. Nemec, J. Pavlik, M. Gembický, Z. Trávníček, R. Boča and I. Šalitroš, *New J. Chem.*, 2015, **39**, 508–551.
17 G. A. Craig and M. Murrie, *Chem. Soc. Rev.*, 2015, **44**, 2135–2147.
18 S. E. Stavretis, M. Atanasov, A. A. Podlesnyak, S. C. Hunter, F. Neese and Z.-L. Xue, *Inorg. Chem.*, 2015, **54**, 9790–9801.
19 S. Mossin, B. L. Tran, D. Adhikari, M. Pink, F. W. Heinemann, J. Sutter, R. K. Szilagyi, K. Meyer and D. J. Mindiola, *J. Am. Chem. Soc.*, 2012, **134**, 13651–13661.
20 W. Kabash, XDS, *Acta Crystallogr., Sect. D: Biol. Crystallogr.*, 2010, **66**, 125–132.
21 Bruker, *Apex3*, Bruker AXS Inc., Madison, Wisconsin, USA, 2015.
22 G. M. Sheldrick, *Acta Crystallogr., Sect. C: Struct. Chem.*, 2015, **71**, 3–8.
23 C. F. Macrae, I. J. Bruno, J. A. Chisholm, P. R. Edgington, P. McCabe, E. Pidcock, L. Rodriguez-Monge, R. Taylor, J. van de Streek and P. A. Wood, *J. Appl. Crystallogr.*, 2008, **41**, 466–470.
24 F. Neese, *WIREs Computational Molecular Science*, 2012, **2**, 73–78.
25 F. Neese, *Coord. Chem. Rev.*, 2009, **253**, 526–563.
26 C. Lee, W. Yang and R. G. Parr, *Phys. Rev. B: Condens. Matter Mater. Phys.*, 1988, **37**, 785–789; A. D. Becke, *J. Chem. Phys.*, 1993, **98**, 1372–1377; A. D. Becke, *J. Chem. Phys.*, 1993, **98**, 5648–5652; P. J. Stephens, F. J. Devlin, C. F. Chabalowski and M. J. Frisch, *J. Phys. Chem.*, 1994, **98**, 11623–11627.

27 A. Schafer, H. Horn and R. Ahlrichs, *J. Chem. Phys.*, 1992, **97**, 2571–2577; A. Schafer, C. Huber and R. Ahlrichs, *J. Chem. Phys.*, 1994, **100**, 5829–5835; F. Weigend and R. Ahlrichs, *Phys. Chem. Chem. Phys.*, 2005, **7**, 3297–3305.

28 F. Neese, F. Wennmohs, A. Hansen and U. Becker, *Chem. Phys.*, 2009, **356**, 98–109; R. Izsak and F. Neese, *J. Chem. Phys.*, 2011, **135**, 144105.

29 S. Grimme, J. Antony, S. Ehrlich and H. Krieg, *J. Chem. Phys.*, 2010, **132**, 154104; S. Grimme, S. Ehrlich and L. Goerigk, *J. Comput. Chem.*, 2011, **32**, 1456–1465.

30 K. Momma and F. Izumi, *J. Appl. Crystallogr.*, 2011, **44**, 1272–1276.

31 P.-K. Chan and C.-K. Poon, *J. Chem. Soc., Dalton Trans.*, 1976, 858–862.

32 S. Alavi, H. Hosseini-Monfareda and M. Siczekba, *J. Mol. Catal. A: Chem.*, 2013, **377**, 16–28.

33 E. M. Matson, Y. J. Park, J. A. Bertke and A. R. Fout, *Dalton Trans.*, 2015, **44**, 10377–10384.

34 S. L. Zhang, X. H. Zhao and X. Y. Wang, *Dalton Trans.*, 2015, **44**, 15189–15197.

35 N. Matsumoto, Y. Sunatsuki, H. Miyasaka, Y. Hashimoto, D. Luneau and J.-P. Tuchagues, *Angew. Chem., Int. Ed.*, 1999, **38**, 171–173.

36 Z. Trávníček, R. Zbořil, M. Matiková-Maľarová, B. Drahoš and J. Černák, *Chem. Cent. J.*, 2013, **7**, 28.

37 R. Boča, *Theoretical Foundations of Molecular Magnetism*, Elsevier, Amsterdam, 1999.

38 The standard deviations were calculated as $\sigma_i = (P_{ii}^{-1} S/(N - k))^{-1/2}$, where $P_{ij} = \Sigma(\delta\mu_n/\delta a_i \delta\mu_n/\delta a_j)$ and $S = \Sigma(\mu_n - \mu_n^{\exp})^2$ with $n = 1$ to N; a_i and a_j are fitted parameters, N is the number of experimental points (sum of temperature and field dependent data), and μ_n and $\mu_n^{\exp}$ are the calculated and experimental effective magnetic moments for a given temperature and magnetic field. σ_i was then multiplied by Student's $t_{95\%}$ to provide confidence limits with 95% probabilities listed in the text.

39 R. Herchel, Z. Šindelář, Z. Trávníček, R. Zbořil and J. Vančo, *Dalton Trans.*, 2009, 9870–9880.

40 R. J. Parker, L. Spiccia, B. Moubaraki, K. S. Murray, D. C. R. Hockless, A. D. Rae and A. C. Willis, *Inorg. Chem.*, 2002, **41**, 2489–2495.

41 J.-H. Her, P. W. Stephens, C. M. Kareis, J. G. Moore, K. S. Min, J.-W. Park, G. Bali, B. S. Kennon and J. S. Miller, *Inorg. Chem.*, 2010, **49**, 1524–1534.

42 C. M. Kareis, S. H. Lapidus, J.-H. Her, P. W. Stephens and J. S. Miller, *J. Am. Chem. Soc.*, 2012, **134**, 2246–2254.

43 R. Herchel, I. Nemec, M. Machata and Z. Trávníček, *Inorg. Chem.*, 2015, **54**, 8625–8638; I. Nemec, R. Herchel, T. Šilha and Z. Trávníček, *Dalton Trans.*, 2014, **43**, 15602–15616.

44 E. Ruiz, J. Cano, S. Alvarez and P. Alemany, *J. Comput. Chem.*, 1999, **20**, 1391–1400; E. Ruiz, A. Rodríguez-Fortea, J. Cano, S. Alvarez and P. Alemany, *J. Comput. Chem.*, 2003, **24**, 982–989.

45 K. Yamaguchi, Y. Takahara and T. Fueno, in *Applied Quantum Chemistry*, ed. V. H. Smith, Reidel, Dordrecht, 1986, p. 155; T. Soda, Y. Kitagawa, T. Onishi, Y. Takano, Y. Shigeta, H. Nagao, Y. Yoshioka and K. Yamaguchi, *Chem. Phys. Lett.*, 2000, **319**, 223.

Příloha P3

B. Drahoš, R. Herchel, Z. Trávníček,

Impact of Halogenido Coligands on Magnetic Anisotropy in Seven-Coordinate Co(II) Complexes.

Impact of Halogenido Coligands on Magnetic Anisotropy in Seven-Coordinate Co(II) Complexes

Bohuslav Drahoš, Radovan Herchel,[ID] and Zdeněk Trávníček*[ID]

Department of Inorganic Chemistry, Regional Centre of Advanced Technologies and Materials, Faculty of Science, Palacký University, 17. listopadu 12, CZ-771 46 Olomouc, Czech Republic

S *Supporting Information*

ABSTRACT: The structural and magnetic features of a series of mononuclear seven-coordinate Co^{II} complexes with the general formula $[Co(L)X_2]$, where **L** is a 15-membered pyridine-based macrocyclic ligand (3,12,18-triaza-6,9-dioxabicyclo[12.3.1]octadeca-1(18),14,16-triene) and X = Cl^- (**1**), Br^- (**2**), or I^- (**3**), were investigated experimentally and theoretically in order to reveal how the corresponding halogenido coligands in the apical positions of a distorted pentagonal−bipyramidal coordination polyhedron may affect the magnetic properties of the prepared compounds. The thorough analyses of the magnetic data revealed a large easy-plane type of the magnetic anisotropy ($D > 0$) for all three compounds, with the D-values increasing in the order 35 cm^{-1} for **3** (I^-), 38 cm^{-1} for **1** (Cl^-), and 41 cm^{-1} for **2** (Br^-). Various theoretical methods like the Angular Overlap Model, density functional theory, CASSCF/CASPT2, CASSCF/NEVPT2 were utilized in order to understand the observed trend in magnetic anisotropy. The D-values correlated well with the Mayer bond order (decreasing in order Co−I > Co−Cl > Co−Br), which could be a consequence of two competing factors: (a) the ligand field splitting and (b) the covalence of the Co−X bond. All the complexes also behave as field-induced single-molecule magnets with the spin reversal barrier U_{eff} increasing in order **1** (Cl^-) < **2** (Br^-) < **3** (I^-); however, taking into account the easy-plane type of the magnetic anisotropy, the Raman relaxation process is most likely responsible for slow relaxation of the magnetization. The results of the work revealed that the previously suggested and fully accepted strategy employing heavier halogenido ligands in order to increase the magnetic anisotropy has some limitations in the case of pentagonal−bipyramidal Co^{II} complexes.
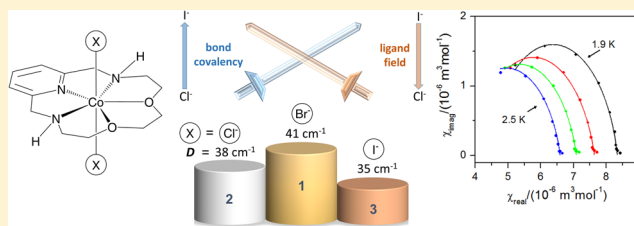
■ INTRODUCTION

Single-molecule magnets (SMMs)[1−3] represent a class of compounds that exhibit a slow relaxation of magnetization based on a pure molecular origin (without any long-range ordering typical for "bulk" magnets) and that have appeared in the center of scientific attention during the last three decades due to their promising application potential in ultradense information storage, quantum computing, and spintronics.[4] The characteristic parameter for SMMs is an energy barrier U for the magnetic moment reversal, which is caused by a large axial magnetic anisotropy (described by the axial zero-field-splitting (ZFS) parameter D within the spin Hamiltonian formalism) splitting the metal ion energy levels in zero magnetic field, and this energy barrier can be defined as $U = |D|S^2$ or $U = |D|(S^2 − 1/4)$ for integer or noninteger ground spin state S.[1,2] In order to understand the behavior of these compounds, extensive studies of polynuclear 3d metal complexes (such as a Mn_{12} complex as the first SMM)[5] were performed in the earlier stages of SMM research. Then investigations of 3d−4f mixed systems[6−8] or mononuclear 4f complexes (usually containing Dy^{III}),[3,9] so-called mononuclear SMMs or single-ion magnets (SIMs), were followed. More recently, mononuclear complexes of 3d metals, also known as 3d-SIMs or mononuclear 3d-SMMs, were studied as well.[10−13]

In order to increase the very low temperature for which the magnetic hysteresis of SMMs occurs, and thus to allow feasible technological applications of SMMs, many efforts have been done to increase the energy barrier U. In the first step, the attention was focused on increasing the total ground spin S of the molecule as possible, usually by synthesis of large polynuclear complexes. However, it turned out that not the total ground spin S but rather the magnetic anisotropy (represented by the D-parameter) has a crucial role in this research.[1,14] Therefore, attention has been devoted to the mononuclear complexes of 3d metals, for which the magnetic anisotropy can be modulated by a rational ligand design. The considerable progress in the group of mononuclear SMMs containing various transition metals in different oxidation states (e.g., Mn^{III}, $Fe^{I/II/III}$, $Co^{I/II/III}$, $Ni^{I/II}$, or Re^{IV}) and coordination geometries (the coordination numbers ranging from 2 to 8) may be clearly documented by an increase in the number of prepared compounds as well as the number of publications.[10−13]

In a large group of mononuclear 3d-SMMs, which usually consist of complexes with lower coordination numbers (ranging
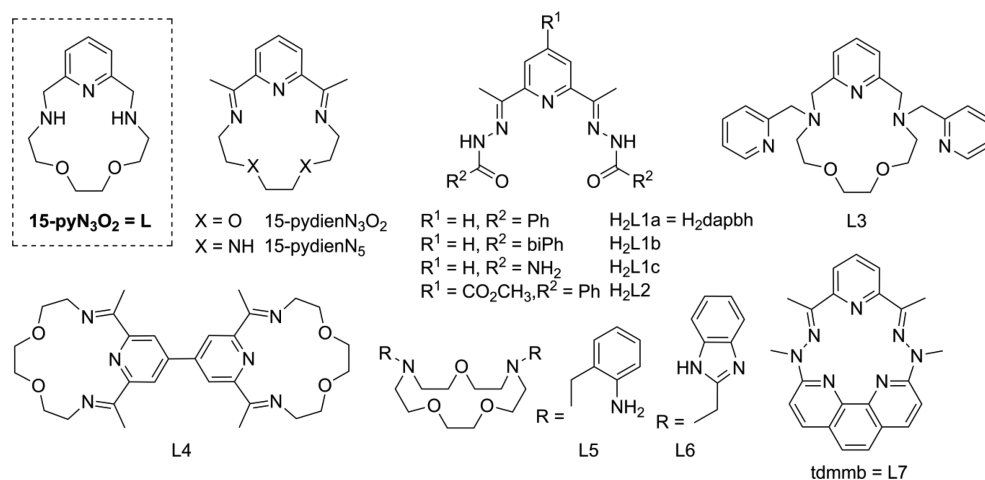
Figure 1. Structural formulas of the used ligand **L** and the ligands discussed in the text.

between 2 and 6), the seven-coordinate complexes[15] represent a relatively small and interesting family of compounds in comparison with a large group of tetra-/pentacoordinate complexes.[12] In most cases, seven-coordinate complexes of Ni^{II}, Fe^{II}, and Co^{II} with pentagonal—bipyramidal geometry involving polyamino/oxo or Schiff base ligands with an open-chain structure, e.g., H_2L1a,[16−18] H_2L1b,[19,20] H_2L1c,[19] and H_2L2,[21] or macrocyclic, e.g., 15-pydienN₃O₂,[22,23] 15-py-dienN₅,[24] 15-pyN₃O₂ = **L**,[25] **L3**,[26] **L4**,[27] **L5**,[28] **L6**,[29] and **L7**[30] (Figure 1) were investigated. Ni^{II} and Fe^{II} complexes revealed usually large easy-axis magnetic anisotropy ($D < 0$) with slow relaxation of magnetization observed in the case of hetero-nuclear complexes $[\{Ni(H_2L1a)\}_3\{W(CN)_8\}_2]$[20] (below the blocking temperature $T_N = 3.6$ K, $\tau_0 = 1.6 \times 10^{-9}$ s, $U_{eff} = 30$ K) and $[Fe(H_2L1a)Ni(CN)_4]_n$ (polymeric one-dimensional (1D) chain with $\tau_0 = 2 \times 10^{-9}$ s and $U_{eff} = 34$ cm^{-1}),[17] and more recently also in the case of mononuclear complexes $[Fe(H_2L1a)Cl_2]$ and $[Fe(H_2L1c)Cl_2]$ ($\tau_0 = 5 \times 10^{-9}$ s and $U_{eff} = 53$ cm^{-1}).[19] On the other hand, Co^{II} complexes represent the largest and the most studied group of seven-coordinate complexes and reveal a large easy-plane magnetic anisotropy ($D > 0$). In spite of the positive value of D-parameter, for which according to the theory should not exist any spin reversal barrier and which should not allow the SMM behavior, many of these Co^{II} complexes show slow relaxation of magnetization, e.g., Co^{II} complexes with 15-pydienN₅,[31] H_2L1a,[31−33] H_2L1b,[19] **L3**,[26] **L7**[30] and also with 4-tert-butylpyridine[34] or isoquinoline[34] (for more details, see Table 3 in the section Static Magnetic Properties). The explanation of the presence of the slow relaxation of magnetization for Kramer's ions with dominant easy-plane magnetic anisotropy, such as Co^{2+}, was given by Ruiz, Luis, and co-workers in 2014,[35] and several mechanisms for the magnetic relaxation dynamics (Orbach, direct, Raman, or quantum tunneling) have been proposed.[36] To distinguish among the above-mentioned mechanisms, which one contributes dominantly to the overall relaxation process is still a matter of debate and a challenge for other sophisticated techniques such as variable-field far-infrared spectroscopy.[37] On the other hand, the slow relaxation of magnetization was observed for some complexes in the presence of a small external magnetic field, which had to be applied in order to suppress the quantum tunneling, and therefore these compounds are called field-induced SMMs.

In order to tune the magnetic anisotropy and to improve the SMM properties, the electronic configuration of the metal center in the complex should be changed. This can be achieved by a variation of the donor atoms in ligands and/or the coordination numbers. Such an approach has been successfully employed in pseudotetrahedral complexes $[Co^{II}(A)I_2]$ (A = quinoline, PPh₃, AsPh₃)[38] or $[Co^{II}(APh)_4]^{2-}$ (A = O, S, Se),[39] where the heavier (in accordance with the proton number) and softer (in accordance with the hard—soft acid base theory) donor atoms enhanced the magnetic anisotropy (more negative D-value was achieved), and led to observation of SMM properties even in zero static magnetic field. More recently, impact of the halogenido coligands has been also studied in trigonal-bipyramidal Co(II) complexes with Me₆tren (tris[2-(dimethylamino)ethyl]amine),[40] NS₃^{tBu} (2-(tert-butylthio)-N-(2-(tert-butylthio)ethyl)-N-((neopentylthio)methyl)ethan-1-amine),[41] and tris(2-pyridylmethyl)amine.[42] In the case of the first two systems, D-values were more negative for the complexes with NS₃^{tBu} ligand containing heavier sulfur donor atoms in comparison with Me₆tren and D-values were increasing (less negative) for the halogenido coligand in the order Cl$^-$ < Br$^-$ < NCS$^-$. On the other hand, for the complexes with the latter ligand, the local symmetry and crystal packing influenced the final magnetic anisotropy and SMM properties more significantly than the coordinated halogenido coligands themselves. In the case of seven-coordinate Co^{II} complexes with the pentagonal—bipyramidal geometry, and according to ab initio calculations,[16] the positive D-value should increase with weaker σ-donors coordinated in the axial positions and with a more symmetrical ligand in the equatorial plane (to be intended in connection with the structure of the ligand). This assumption was already confirmed for Co^{II} complexes $[Co-(H_2L1a)(NCS)_2]$[33] and $[Co(L1a)(H_2O)_2]$,[33] and more recently also for $[Co(L7)(X)_2]^{2+/0}$, where X = H_2O, CN$^-$, NCS$^-$, SPh$^-$,[30] although the effect of the donor atom on the D-value was not as dramatic as for the pseudotetrahedral complexes discussed above. Surprisingly, no systematic study of how the halogenido coligands affect the D-values in seven-coordinate Co^{II} complexes has been performed yet, although the magnetic anisotropy enhancement via the heavy halogenido ligand utilization has been described in the case of pseudotetrahedral Ni^{II},[43] octahedral $Cr^{II/III}$,[44] square-pyramidal Fe^{III},[45] and octahedral[46] or pentagonal—bipyramidal Mn^{II} complexes.[47]

In this paper, a series of seven-coordinate Co^{II} complexes **1**−**3** with a 15-membered pyridine-based macrocycle 15-pyN$_3$O$_2$ (**L**) and two chlorido (**1**), bromido (**2**), or iodido (**3**) coligands in the axial positions of the pentagonal−bipyramidal coordination sphere is studied. The structural aspects of all the herein described complexes are discussed in the context of the results of temperature- and field-dependent DC/AC magnetic measurements, which were performed in order to reveal the impact of the halogenido coligands on the magnetic anisotropy and consequently also on relaxation of the magnetization. Theoretical calculations were performed as well in order to elucidate the trend in a ligand-field strength depending on the type of the halogenido coligand and its impact on the magnetic anisotropy.

■ EXPERIMENTAL SECTION

Synthesis and General Characterization. The ligand **L**[48] and complex [Co(**L**)Cl$_2$]·2CH$_3$OH (**1**)[25] were synthesized according to literature procedures. All the solvents (Penta, Prague, Czech Republic) and other chemicals were purchased from commercial sources (Across Organics, Geel, Belgium and Sigma-Aldrich, St. Louis, MO, USA) and used as received.

Elemental analysis (C, H, N) was performed on a Flash 2000 CHNO-S analyzer (Thermo Scientific, Waltham, MA, USA). Infrared (IR) spectra of the complexes were recorded on a Thermo Nicolet NEXUS 670 FT-IR spectrometer (Thermo Nicolet, Waltham, MA, USA) employing the ATR technique on a diamond plate in the range of 400−4000 cm^{-1}. The mass spectra were collected on an LCQ Fleet ion mass trap mass spectrometer (Thermo Scientific, Waltham, MA, USA) equipped with an electrospray ion source and three-dimensional (3D) ion-trap detector in the positive mode. Temperature dependence of the magnetization at $B = 0.1$ T from 1.9 to 300 K and the isothermal magnetizations at $T = 2$, 5, and 10 K up to $B = 9$ T were measured using PPMS Dynacool using the VSM module (Quantum Design Inc., San Diego, CA, USA). The experimental data were corrected for diamagnetism and signal of the sample holder. Dynamic magnetic properties were studied by measuring AC susceptibility on an MPMS XL7 SQUID magnetometer (Quantum Design Inc., San Diego, CA, USA).

[Co(L)Br$_2$] (2). CoBr$_2$·6H$_2$O (131 mg, 0.40 mmol) and **L** (110 mg, 0.44 mmol) were dissolved in 5 mL of CH$_3$OH to give a red solution, which was filtered. The diffusion of diethyl ether vapors into the red filtrate at 5 °C resulted in formation of dark green crystals after several days, which were filtered off on a glass frit and dried on air at room temperature (146 mg, yield 78.5%). MS m/z (+): 309.12 ([CoL−H]$^+$, calcd. 309.09); 389.01 ([CoLBr]$^+$, calcd. 389.01); elemental analysis for [Co(**L**)Br$_2$], C$_{13}$H$_{21}$CoN$_3$O$_2$Br$_2$, M_r = 470.07, found (calculated): C 33.56 (33.22); H 4.86 (4.50); N 8.56 (8.94). IR mid: ν(N−H)$_{apliphatic}$ = 3214 cm^{-1} (s), ν(C−H)$_{apliphatic}$ = 2913 cm^{-1} (s) and 2893 cm^{-1} (s), ν(C−N)$_{pyridine}$ = 1604 (m), ν(C−C)$_{aromatic}$ = 1579 (m), 1466 (s) and 1444 cm^{-1} (s). Full IR spectra are available in Supporting Information in Figure S1.

[Co(L)I$_2$] (3). Co(ClO$_4$)$_2$·6H$_2$O (73 mg, 0.20 mmol) and **L** (55 mg, 0.22 mmol) were dissolved in 2.5 mL of CH$_3$CN to give a red solution. KI (75 mg, 0.42 mmol, 2.1 equiv) was dissolved in 2.5 mL of CH$_3$OH, and this solution was added to the complex solution prepared in the first step. Immediately a white precipitate of KClO$_4$ (33 mg) formed which was filtered off on a glass frit and washed with 0.5 mL of CH$_3$CN. The diffusion of diethyl ether vapors into the filtrate at 5 °C resulted in formation of cube-shaped green crystals after several days, which were filtered off and dried in air at room temperature (66 mg, yield 58.4%). MS m/z (+): 309.11 ([CoL−H]$^+$, calcd. 309.09); 436.98 ([CoLI]$^+$, calcd. 437.00); elemental analysis for [Co(**L**)I$_2$], C$_{13}$H$_{21}$CoN$_3$O$_2$I$_2$, M_r = 564.07, found (calculated): C 28.10 (27.68); H 3.96 (3.75); N 7.39 (7.45). IR mid: ν(N−H)$_{apliphatic}$ = 3192 cm^{-1} (s), ν(C−H)$_{apliphatic}$ = 2909 cm^{-1} (s) and 2866 cm^{-1} (s), ν(C−N)$_{pyridine}$ = 1604 (m), ν(C−C)$_{aromatic}$ = 1578 (m), 1465 (s) and
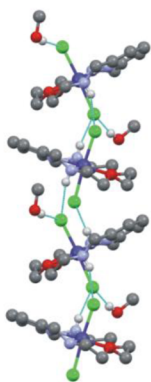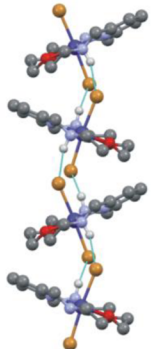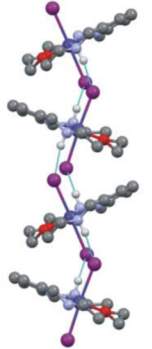
1443 cm^{-1} (s). Full IR spectra are available in Supporting Information in Figure S1.

X-ray Diffraction Analysis. The molecular structure of **1** was published previously.[25] Single crystals of complexes **2** and **3** suitable for X-ray structure analysis were prepared by a vapor diffusion of diethyl ether into the complex solution in CH$_3$OH/CH$_3$NO$_2$ and CH$_3$OH/CH$_3$CN, respectively, at 5 °C. X-ray diffraction data of **2** and **3** were collected with a Bruker D8 QUEST diffractometer equipped with a PHOTON 100 CMOS detector using Mo−Kα radiation. The APEX3 software package[49] was used for data collection and reduction. The molecular structures of **2** and **3** were solved by direct methods and refined by full-matrix least-squares procedure SHELXL (version 2014/7).[50] Hydrogen atoms of all the structures were found in the difference Fourier maps and refined using a riding model with C−H = 0.95 (CH)$_{ar}$, C−H = 0.99 (CH$_2$) Å, and with U_{iso}(H) = 1.2U_{eq}(CH, CH$_2$). The molecular and crystal structures of the studied complexes, depicted in Figures 2 and 3, and S2 and S3, respectively, were drawn using the Mercury software.[51]
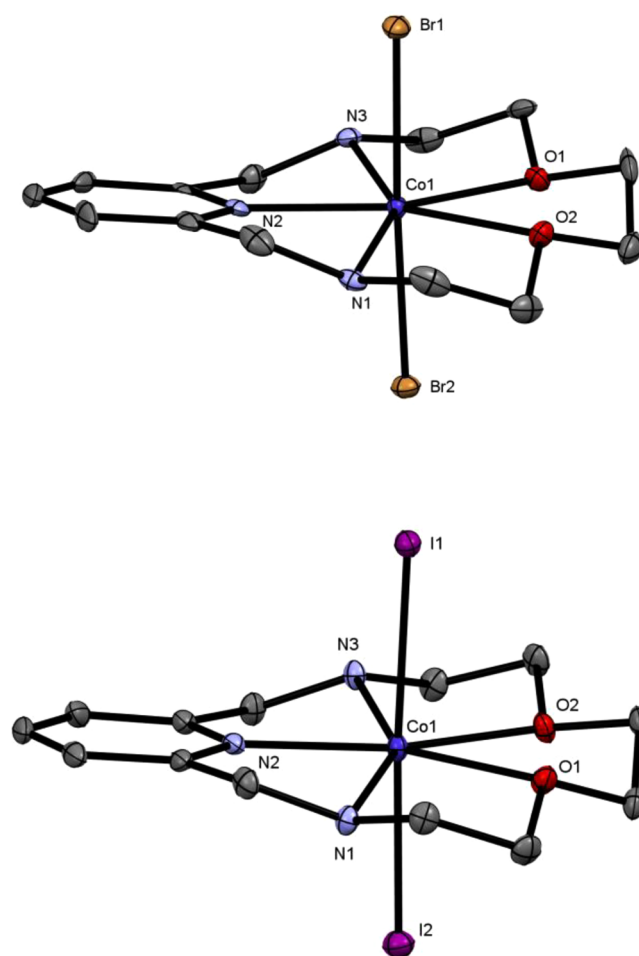
Figure 2. Molecular structure of [Co(**L**)Br$_2$] (**2**, top) and [Co(**L**)I$_2$] (**3**, bottom). Non-hydrogen atoms are drawn as thermal ellipsoids at the 50% probability level. Hydrogen atoms were omitted for clarity. Only one of two crystallographically independent molecules present in the asymmetric unit of **2** and **3** is shown for clarity.

Computational Details. The theoretical calculations regarding the complexes **1**, **2**, and **3** were carried out with the ORCA 3.0.3 computational package[52] accounting for the relativistic effects using the scalar relativistic contracted version of the def2-TZVP(-f) basis functions[53] and zero order regular approximation (ZORA).[54] The calculations of ZFS parameters were done using state average complete active space self-consistent field (SA-CASSCF)[55] wave functions

complex	[CoLCl₂]·2CH₃OH (1)[a]	[CoLBr₂] (2)	[CoLI₂] (3)

	[CoLCl₂]·2CH₃OH (1)[a]	[CoLBr₂] (2)	[CoLI₂] (3)
angle (°)	41.6	43.2	44.6
Co···Co (Å)	6.5656(6)	6.914(1), 7.006(1)[b]	7.1714(7), 7.1899(7)[b]

Figure 3. Part of the crystal structure of 1,[a] 2, and 3 showing the N−H···X (X = Cl, Br, I, respectively) hydrogen bonds (blue dashed lines), forming supramolecular 1D chain structures completed by the values of angles between the pentagonal CoN₃O₂ least-squares planes and Co···Co distances in the 1D chains. [a]Data adopted from ref 25. [b]In the crystal structure of 2 and 3 two crystallographically independent molecules were found in the asymmetric unit (one of them is shown only).

complemented by N-electron valence second order perturbation theory (NEVPT2).[56] The active spaces of the CASSCF calculations on metal-based d-orbitals was defined as CAS(7,5) for Co(II). In the state averaged approach, all multiplets for given electron configuration were equally weighted. The ZFS parameters, based on dominant spin−orbit coupling contributions from excited states, were calculated through the quasi-degenerate perturbation theory (QDPT),[57] in which an approximation to the Breit-Pauli form of the spin−orbit coupling operator (SOMF approximation)[58] and the effective Hamiltonian theory[59] were used. All the above-mentioned calculations utilized the RI approximation with the decontracted auxiliary def2-TZV/C Coulomb fitting basis sets. Increased integration grids (Grid5 in ORCA convention) and tight SCF convergence criteria were used in all calculations. Second, MOLCAS 8.0 was used for analogous calculations.[60] The active space of the CASSCF calculations[61] comprised of seven electrons in 10 d-orbitals to account for the double-shell effect.[62] The RASSCF method was employed in CASSCF calculations with 10 quartets and 40 doublets. The dynamical correlation was included in the next step, by the CASPT2 method,[63] keeping the standard IPEA shift (0.25) and imposing an additional imaginary shift (0.1) to exclude any possible intruder state problems. The spin−orbit coupling based on atomic mean field approximation (AMFI)[64] was taken into account using the RASSI-SO module. The relativistic effects were treated with the Douglas-Kroll Hamiltonian.[65] The following basis sets were employed: Co.ANO-RCC-VTZP, X.ANO-RCC-VDZP (X = Cl, Br, I, N, O), C.ANO-RCC-VDZ, and H.ANO-RCC-VDZ.[66] Cholesky decomposition for two-electron repulsion integrals was used with a threshold of 0.50×10^{-5}. Then, the SINGLE_ANISO module was used to calculate g-tensors and D-tensors.[67] In all the cases the calculations were based on the experimentally determined X-ray molecular structures (the data regarding the structure of 1 were taken from the literature).[25]

The density functional theory (DFT) single-point energy calculations were performed again with ORCA 3.0.3 using the hybrid B3LYP functional,[68] and including the relativistic effects with ZORA together with the scalar relativistic contracted version of the basis functions def2-TZVP(-f) for all atoms. The Multiwfn 3.3.9 (a multifunctional wave function analyzer)[69] software was used to analyze the results from single point DFT energy calculations to quantify the bond order using Mayer's bond analysis.[70] Finally, the program AOMX[71] was used to calculate energies of ligand field terms and multiplets for the idealized geometry of pentagonal−bipyramid (D_{5h} symmetry). The Co^{II} atom was modeled with these Racah's parameters: $B = 989$ cm^{-1}, $C = 4.3 \cdot B$, and with spin−orbit coupling

constant $\xi = 515$ cm^{-1}. The effect of the axial ligands was modeled with ε_σ(equatorial) = 3000 cm^{-1}, ε_π(equatorial) = 0 cm^{-1}, and by varying ε_σ(axial) = 2000−10000 cm^{-1} for pure σ-donors, whereas ε_π(axial) = +0.20·ε_σ(axial) and ε_π(axial) = −0.20·ε_σ(axial) relationships were used to model π-donor and π-acceptor properties, respectively (Figure 9a). The effect of equatorial ligand was modeled with ε_σ(axial) = 3000 cm^{-1}, ε_π(axial) = 0 cm^{-1}, and by varying ε_σ(equatorial) = 2000−10000 cm^{-1} for pure σ-donors, whereas ε_π(equatorial) = +0.20·ε_σ(equatorial) and ε_π(equatorial) = −0.20·ε_σ(equatorial) relationships were used to model π-donor and π-acceptor properties, respectively (Figure 9b). The covalency effect was modeled by varying κ_z = 0.5−1.0, where κ_z is the orbital reduction factor of the spin−orbit interaction (Figure 9c). In these calculations the effect of axial ligands was modeled with ε_σ(equatorial) = 3000 cm^{-1}, ε_π(equatorial) = 0 cm^{-1}, ε_σ(axial) = 3000 cm^{-1} for pure σ-donors, whereas ε_π(axial) = +0.20·ε_σ(axial) and ε_π(axial) = −0.20·ε_σ(axial) relationships were used to model π-donor and π-acceptor properties, respectively.

■ RESULTS AND DISSCUSSION

Synthesis and General Characterization. The ligand L and complex 1 were synthesized according to the literature procedures.[48,25] The complex 2 was prepared by direct mixing of CoBr₂·6H₂O with L in CH₃OH. The complex 3 was synthesized in a different manner. In the first step, Co^{II} complex of the macrocyclic ligand L was prepared by direct mixing of a slight excess of L and Co^{II} perchlorate in CH₃CN, and then the obtained complex was coupled with 2.1 mol equiv of KI in CH₃OH resulting in precipitation of KClO₄ and a solution of the required product. The crystalline forms of the complexes 2 and 3 were prepared by diethyl ether vapor diffusion into their CH₃OH and CH₃OH/CH₃CN solutions, respectively. The IR spectra of obtained complexes 1−3 (Figure S1) have a similar pattern, as was described previously on structurally similar systems,[47,25] confirming the similar coordination mode of L within the complexes.

Structural Features of the Complexes. The molecular structure of complex 1 was described previously,[25] and it is very similar to those determined for the complexes 2 and 3 (Figure 2, Table 1). The asymmetric unit in both crystal structures of 2 and 3 contains two crystallographically independent molecules, and the data for both of them are discussed in the main text and

Table 1. Crystal Data and Structure Refinements for Complexes 2 and 3

compound	2	3
formula	$C_{13}H_{21}Br_2CoN_3O_2$	$C_{13}H_{21}CoI_2N_3O_2$
M_r	470.08	564.06
color	dark green	green
temperature (K)	120(2)	120(2)
wavelength (Å)	0.71073	0.71073
crystal system	monoclinic	monoclinic
space group	$P2_1/n$	$P2_1/n$
a (Å)	13.8834(8)	14.3121(7)
b (Å)	15.9755(9)	16.4346(8)
c (Å)	14.9548(8)	15.0998(7)
α (deg)	90	90
β (deg)	95.121(2)	97.895(2)
γ (deg)	90	90
U, Å^3	3303.6(3)	3518.0(3)
Z	8	8
D_{calc}, g cm^{-3}	1.890	2.130
μ, mm^{-1}	5.884	4.493
$F(000)$	1864	2152
θ range for data collection (deg)	2.303−27.552	2.217−27.175
refln collected	83592	192265
independent refl.	7608	7807
$R(int)$	0.1001	0.0365
data/restraints/parameters	7608/0/379	7807/0/379
completeness to θ (%)	99.9	99.9
goodness-of-fit on F^2	1.156	1.113
R_1, wR_2 ($I > 2\sigma(I)$)	0.0650, 0.0825	0.0244, 0.0587
R_1, wR_2 (all data)	0.0903, 0.0887	0.0296, 0.0622
largest diff peak and hole/A^{-3}	0.575 and −0.816	0.676 and −2.259
CCDC number	1529637	1529636

listed in Table 2 (the two independent molecules are shown in Figure S2 in Supporting Information).

In both cases, the coordination number of the central Co^{II} atom is 7, and it adopts distorted pentagonal−bipyramidal geometry. The pentadentate macrocycle **L** is coordinated in the pentagonal equatorial plane, while the two halogenido ligands occupy the axial (apical) positions. The Co−N$_{py}$ distance, ranging from 2.136(4) to 2.142(4) Å, is the shortest in the equatorial plane in comparison with the Co−N$_H$ distances, ranging from 2.190(4) to 2.214(4) Å, and the Co−O distances,

ranging from 2.274(3) to 2.361(4) Å (Table 2), which is a typical feature for both complexes **2** and **3** as well as for the previously studied complex **1**. When a heavier halogenido ligand X$^-$ is coordinated, the Co−X distance is significantly elongated (∼2.47 Å for **1**,[25] ∼2.64 Å for **2**, ∼2.85 Å for **3**, Table 2), which corresponds to the increasing ionic radius of the corresponding halide ion and which consequently causes axial elongation of the pentagonal−bipyramidal coordination sphere. The X−Co−X angles (X = halogen) are close to the ideal linear arrangement (177.6°/175.7° and 176.7°/179.0° for **2** and **3**, respectively; see Table 2).

The final crystal packing of complexes **2** and **3** is strongly influenced by an extensive system of N−H⋯X hydrogen bonds, C−H$_{aromatic}$⋯X noncovalent contacts (X = Br, I) and also by π−π stacking interactions (Figure 3, S3 and Table S1 in Supporting Information). The crystal structure of **1** was described previously in the literature; see ref 25. In the crystal structure of **2**, zigzag 1D chains are formed by connection two [Co(**L**)Br$_2$] units by two N−H⋯Br hydrogen bonds (Figure 3). Additionally, these infinite 1D zigzag chains are connected to each other by C−H$_{aromatic}$⋯Br noncovalent contacts (one of them is bifurcated for one crystallographically independent unit) as well as by face-to-face π−π stacking interactions (the centroid⋯centroid distance = Cg⋯Cg = 3.585(1) Å, Figure S3 and Table S1 in Supporting Information) all together forming almost planar 2D sheets (layers) separated between each other (i.e., no noncovalent contacts observed). Similar zigzag 1D chains are formed by N−H⋯I hydrogen bonds (Figure 3) and are connected together by C−H$_{aromatic}$⋯I noncovalent contacts as well as by face-to-face π−π stacking interactions (Cg⋯Cg = 3.721(1) Å, Figure S3 and Table S1 in Supporting Information) altogether resulting in similar almost planar and separated 2D sheets (layers). The crystal structure of **1**[25] is similar to those observed for **2** and **3**.

Comparison of the crystal structures of **1**−**3** (Figure 3) nicely illustrates the increasing distance between two Co atoms within chains in the order Cl < Br < I. On the other hand, the angle between the pentagonal CoN$_3$O$_2$ least-squares planes is only slightly affected by the nature of the coordinated halide (slightly increasing in the order 41.6° < 43.2° < 44.6° for **1**, **2**, and **3**, respectively). It has been also revealed that the noncovalent contacts in complexes **2** and **3** have a negligible

Table 2. Selected Bond Distances (Å) and Angles (deg) for Complexes 2 and 3

distances	2^a	3^a	angles	2^a	3^a	torsion angles	2^a	3^a
Co−N1	2.208(4)	2.210(3)	N1−Co−N2	72.9(2)	73.8(1)	N1−C−C−N2	23.3(6)	−22.0(4)
	2.213(4)	2.202(3)		73.6(2)	73.5(1)		22.4(6)	21.8(4)
Co−N2	2.142(4)	2.136(3)	N2−Co−N3	74.0(2)	74.2(1)	N2−C−C−N3	31.2(6)	−26.8(4)
	2.136(4)	2.137(3)		73.8(2)	74.3(1)		29.4(6)	28.2(4)
Co−N3	2.193(4)	2.202(3)	N3−Co−O1	72.7(1)	72.8(1)	N3−C−C−O1	−58.1(5)	54.9(3)
	2.214(4)	2.190(3)		72.9(1)	72.4(1)		−56.4(5)	−56.7(4)
Co−O1	2.306(3)	2.347(2)	O1−Co−O2	68.5(3)	68.2(1)	O1−C−C−O2	57.5(5)	−56.4(3)
	2.274(3)	2.313(2)		68.7(1)	67.8(1)		57.5(5)	55.8(4)
Co−O2	2.327(4)	2.277(2)	O2−Co−N1	72.9(1)	72.2(1)	O2−C−C−N1	−58.7(5)	56.1(3)
	2.361(4)	2.317(2)		72.3(1)	73.1(1)		−58.3(5)	−57.3(3)
Co−X$_{ax}$1	2.6441(9)	2.8985(5)	X$_{ax}$1−Co−X$_{ax}$2	177.62(3)	176.74(2)			
	2.6502(9)	2.8919(5)		175.67(3)	179.01(2)			
Co−X$_{ax}$2	2.6434(9)	2.8155(5)						
	2.6153(9)	2.8493(5)						

^{a}Two values are given for two crystallographically independent molecules found in the asymmetric unit.

effect on the magnetic properties (vide infra). The same was already shown previously for complex **1**.[25]

Static Magnetic Properties. Temperature and field dependent DC magnetic data were acquired for complexes **2** and **3**, and they are depicted in Figure 4 (DC magnetic data for
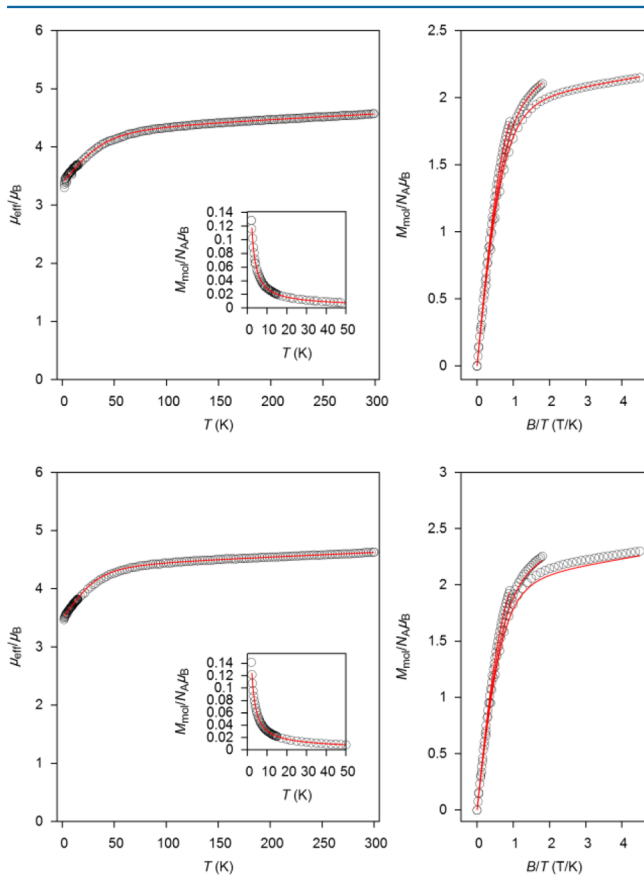
Figure 4. Magnetic data for compounds **2** (top) and **3** (bottom). Temperature dependence of the effective magnetic moment and molar magnetization measured at $B = 0.1$ T in the inset (left) and reduced isothermal magnetizations measured at $T = 2, 5,$ and 10 K (right). The empty circles represent the experimental data points, and the full lines represent the best fits calculated by using eq 1 with parameters listed in Table 3.

complex **1** were described in ref 25 and are also available in Figure S4). The room temperature values of the effective magnetic moment (μ_{eff}) for **1**−**3** span the interval of 4.57−4.76 μ_B, and they are much higher than the theoretical spin only value for high-spin Co^{II} with $g = 2.0$ and $S = 3/2$ ($\mu_{\text{eff}} = 3.87$ μ_B), which can be ascribed to a substantial contribution of the orbital angular momentum. On lowering the temperature, the μ_{eff} continuously decreases to the values 3.30−3.65 μ_B at $T = 1.9$ K, which is attributed to a large ZFS.

In order to evaluate the ZFS parameters describing the magnetic anisotropy from experimental magnetization data, the following spin Hamiltonian was postulated

$$\hat{H} = D(\hat{S}_z^2 - \hat{S}^2/3) + E(\hat{S}_x^2 - \hat{S}_y^2) + \mu_B Bg\hat{S}_a \quad (1)$$

where D and E are the single-ion axial and rhombic ZFS parameters, and the last part is the Zeeman term calculated for the a direction of the magnetic field defined as $\mathbf{B}_a = B \cdot (\sin\theta \cos\varphi, \sin\theta \sin\varphi, \cos\theta)$ with the help of the polar coordinates.

Then, the molar magnetization in the a-direction of magnetic field can be numerically calculated as

$$M_a = N_A kT \frac{\text{d} \ln Z}{\text{d} B_a} \quad (2)$$

where Z is the partition function.[72] Then, the averaged molar magnetization of the powder sample was calculated as integral (orientational) average

$$M_{\text{mol}} = 1/4\pi \int_0^{2\pi} \int_0^{\pi} M_a \sin\theta \, \text{d}\theta \, \text{d}\varphi \quad (3)$$

With the aim to obtain trustworthy parameters, both temperature and field dependent magnetization data were fitted simultaneously. It was found that it is sufficient to take into account only axial ZFS parameter D, which is also supported by our theoretical calculations (see next section). Also, we considered g-anisotropy by fixing g_z to 2.0 and only g_{xy} was varied. The analysis resulted in following parameters: $D = 38(3)$ cm^{-1}, $g_{xy} = 2.47(1)$, $\chi_{\text{TIP}} = 11(1) \times 10^{-9}$ m^3 mol^{-1} for **1** (Figure S4), $D = 41(1)$ cm^{-1}, $g_{xy} = 2.284(5)$, $\chi_{\text{TIP}} = 14(5) \times 10^{-9}$ m^3 mol^{-1} for **2** (Figure 4), $D = 35(1)$ cm^{-1}, $g_{xy} = 2.355(6)$, $\chi_{\text{TIP}} = 12.2(6) \times 10^{-9}$ m^3 mol^{-1} for **3** (Figure 4), where χ_{TIP} is the temperature-independent paramagnetism. Interestingly, compound **2** possesses the largest positive D-parameter for nonpolymeric seven-coordinate Co^{II} complexes (Table 3) reported up to now.

The D-values not only for complexes **1**−**3** can be seen from Table 3. It is evident that the D-values for compounds **1** and **2** are much closer as compared to complex **3**. However, most surprising is the trend of the corresponding D-parameter values ($D(\text{I}^-) < D(\text{Cl}^-) < D(\text{Br}^-)$) in context of the halogenido ligand field strength, which is in contrast to the theoretically predicted trend in seven-coordinate Co^{II} complexes with different axial ligands.[16] It was expected that the decreasing σ-donor ability of the axial coligands should stabilize/decrease the energy of d$_{z^2}$ orbital and thus amplify the positive contributions of the excited doublet/quartet states to D.[16] The ligand strength of the halogenido ligands increases as follows: I$^-$ < Br$^-$ < Cl$^-$, according to the spectrochemical series, and therefore we would expect that the D-parameter should decrease in this order. However, the trend seems to be opposite. First, the influence of the symmetry of the ligand field provided by the donor atoms coordinated in the equatorial plane, which has an impact on the energy levels of orbitals and contributions to D, can be directly excluded because in our case the same macrocyclic ligand **L** is ensuring the same chromophore with the same symmetry (described in the X-ray section). A similar lack of a clear trend between the ligand field strength of the axial ligands and the D-value was recently reported for $[\text{Co}(\mathbf{L7})(\text{A})_2]^{2+/0}$, where A = H$_2O, CN^-$, NCS$^-$, and SPh$^-$.[30] Therefore, the theoretical calculations were performed in order to better understand this behavior, and they are discussed in the section Theoretical Calculations.

Dynamic Magnetic Properties. Due to a large magnetic anisotropy of the compounds **1**−**3**, the dynamic magnetic data were also measured. It was found that upon applying static magnetic field, the nonzero out-of-phase component of AC susceptibility is detected (Figures S5−S7). Therefore, the temperature and frequency dependent AC susceptibility was measured in a small static field and a typical pattern of the slow relaxation of the magnetization in SMMs was observed, Figure 5. Several maxima in χ_{imag} vs T plot were observed in the case of

Table 3. Collection of Mononuclear Seven-Coordinate Co(II) Complexes Together with the Obtained ZFS Parameters and Parameters Describing SMM Properties

complex	D/cm^{-1}	E/D	$\tau_0/10^{-9}$ s	U_{eff}/cm^{-1} (K)	ref
$[Co(H_2L1a)(H_2O)(NO_3)]NO_3$	32.4	0	0.6	56.3 (81.2)	16, 31
$[Co(15\text{-pydienN}_5)(H_2O)_2]Cl_2$	24.6	−0.00057	1200	20.7 (29.8)	31
$[Co(L1a)(im)_2]$	24.8	0.00006	0.087	62.3 (89.6)	31
$[Co(tbp)_3(NO_3)_2]^a$	35.8	0.006	768	17.7 (25.5)	34
$[Co(isq)_3(NO_3)_2]^b$	35.7	0.0006	701	11.0 (15.8)	34
$[Co(L3)](ClO_4)_2$	34	0	99	16.9 (24.3)	26
$[Co(H_2L1a)I(H_2O)]I$	30	0.01			18
$[Co(H_2L1a)Br(H_2O)]Br$	30	0.01			18
$[Co(HL2)(H_2O)(EtOH)]\ BPh_4\cdot3EtOH$	27.65				21
$[Co(L5)](ClO_4)_2$	26				28
$[Co(L5)](NO_3)_2\cdot CH_3CN$	25				28
$[Co(L6)](ClO_4)_2$	23.1				29
$[Co(H_2L1a)(SCN)_2]$	15.9	0			33
$[Co(L1a)(H_2O)_2]$	13.1	0			33
$[Co(H_2L1b)(CH_3OH)(NO_3)]NO_3\cdot CH_3OH$	33.4	0.141			19
$[Co(L7)(H_2O)_2](BF_4)_2$	25.6	−0.039	1100	42.2 (29.3)	30
$[Co(L7)(CN)_2]\cdot2H_2O$	17.4	−0.034	3200	48.9 (34.0)	30
$[Co(L7)(NCS)_2]$	26.3	−0.004	1000	49.2 (34.2)	30
$[Co(L7)(SPh)_2]$	34.5	−0.052	2100	54.7 (38.0)	30
$\mathbf{1} = [Co(L)Cl_2]\cdot2CH_3OH$	38(3)	0			this work
$\mathbf{2} = [Co(L)Br_2]$	41(1)	0	1120	4.2 (6.1)	this work
$\mathbf{3} = [Co(L)I_2]$	35(1)	0	1120	4.5 (6.5)	this work

^{a}tbp = 4-*tert*-butylpyridne. ^{b}isq = isoquinoline.
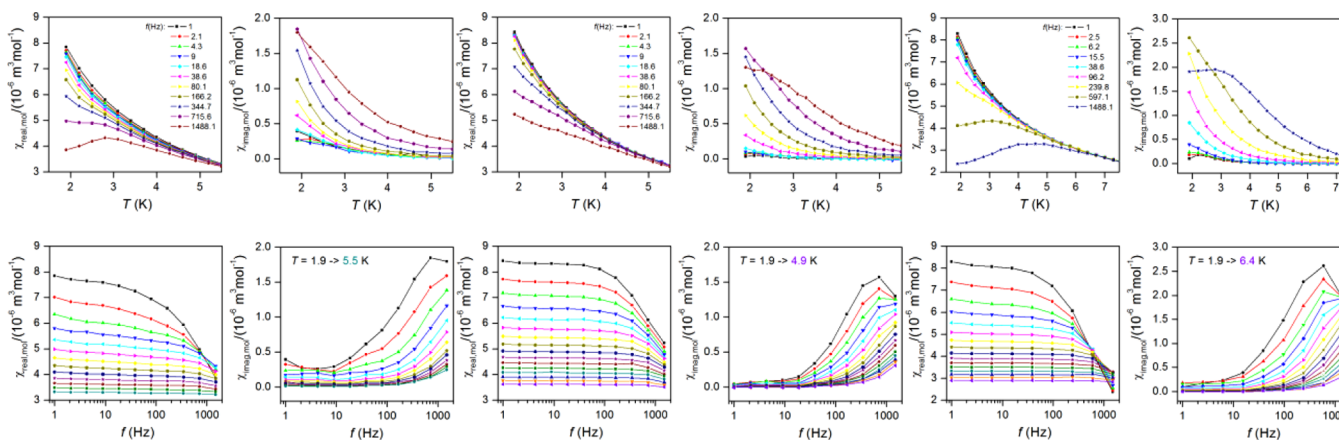
Figure 5. Temperature and frequency dependence of in-phase χ_{real} and out-of-phase χ_{imag} molar susceptibilities in a small applied external magnetic field for complexes **1** (B_{dc} = 0.3 T, left), **2** (B_{dc} = 0.1 T, middle), and **3** (B_{dc} = 0.2 T, right) (full lines are only guides for eyes).

the complexes **2** and **3** and thus, one-component Debye's model was applied based on equation

$$\chi(\omega) = \frac{\chi_T - \chi_S}{1 + (i\omega\tau)^{1-\alpha}} + \chi_S \tag{4}$$

which resulted in isothermal (χ_T) and adiabatic (χ_S) susceptibilities, relaxation times (τ), and distribution parameters (α) (Tables S2−S3). This enabled us to construct the Argand (Cole−Cole) plots (Figure 6 for **2** and Figure S8 in Supporting Information for **3**). Usually, the obtained temperature-dependence of the relaxation times is fitted with the Arrhenius equation

$$\tau = \tau_0 e^{U_{eff}/kT} \tag{5}$$

which resulted in $\tau_0 = 1.12 \times 10^{-5}$ s and the spin reversal barrier $U_{eff} = 6.1$ K (4.2 cm^{-1}) for **2** (Figure 6), and $\tau_0 = 1.12 \times$ 10^{-5} s and the spin reversal barrier $U_{eff} = 6.5$ K (4.5 cm^{-1}) for **3** (Figure S8). However, the values of $\tau_0 \approx 10^{-5}$ s are rather large for SMMs and U_{eff} are very small in comparison with $|D|$ values. Furthermore, in the case of easy plane anisotropy ($D > 0$, E/D = 0), it is hard to justify that the Orbach process is the single process governing the relaxation mechanism, because there is no energy barrier for spin reversal originating from ZFS parameters defined as $U = 2(D^2 + 3E^2)^{1/2}$ for $S = 3/2$ spin system. Therefore, other relaxation processes must be present, namely, direct term induced by the hyperfine interaction dominating at low temperatures and a Raman term dominating at higher temperatures.[10] Consequently, temperature dependence of the relaxation times was fitted with following equation containing the Raman term

$$\tau = CT^{-n} \tag{6}$$

can approximated as

$$\chi''/\chi' \cong \varpi\tau = 2\pi f\tau \tag{9}$$

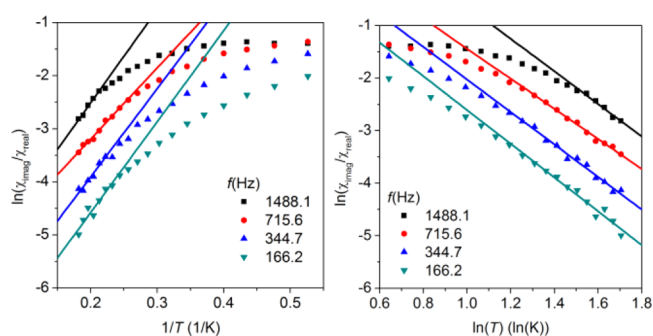This approximation was already used to analyze magnetic data for other SMM compounds[26,73] in order to extract information about Orbach relaxation processes parameters as

$$\ln(\chi''/\chi') = \ln(2\pi f\tau_0) + U/kT \tag{10}$$

Therefore, the experimental data for **1−3** were analyzed with this procedure, Figure 7 and Figure S9 and S10, and as a result,

Figure 7. Simplified analyses of the AC susceptibility data for **2** based on eq 10 (Orbach process, left) and based on eq 11 (Raman process, right).

we obtained a list of parameters summarized in Table 4. The spin reversal barrier parameters were found to be in the range $U_{eff} = 7.9–11.2$ K for **1**, $U_{eff} = 13.4–17.6$ K for **2**, and $U_{eff} = 18.6–30.6$ K for **3**, where only highest four frequencies were taken into account. The variations in the fitted parameters can be also ascribed to the distributions of relaxation processes, which are reflected in eq 4 by parameter α, but are neglected in this simplified model.

Figure 6. Top: frequency dependence of in-phase χ_{real} and out-of-phase χ_{imag} molar susceptibilities of **2** in an external magnetic field 0.1 T; full lines—fitted data using eq 4. Middle: the Argand (Cole–Cole) plot with full lines fitted with eq 4. Bottom: the fit of resulting relaxation times according to the Arrhenius eq 5 under assumption of Orbach relaxation process (left) and fit according to eq 6 under the assumption of Raman relaxation process (right).

Table 4. Parameters Resulting from the Analysis of AC Susceptibility Data for Orbach Relaxation Process Using Equation 10 for Complexes 1−3

		1488.1	715.6	344.7	166.2
1	f (Hz)	1488.1	715.6	344.7	166.2
	τ_0 (10^{-6} s)	2.01	1.89	1.69	1.54
	U_{eff} (K)	7.9	8.8	9.8	11.2
2	f (Hz)	1488.1	715.6	344.7	166.2
	τ_0 (10^{-7} s)	2.57	6.22	3.33	3.18
	U_{eff} (K)	17.6	13.4	16.6	17.2
3	f (Hz)	1488.1	597.1	239.8	96.2
	τ_0 (10^{-7} s)	1.06	2.69	6.02	8.32
	U_{eff} (K)	30.6	24.4	19.6	18.6

and these parameters were found for compound **2**: $C = 1.63 \times 10^{-3}$ and $n = 2.79$ (Figure 6) and for compound **3**: $C = 2.00 \times 10^{-3}$ and $n = 2.82$ (Figure S8). Similar parameters, $C = 2.12 \times 10^{-5}$ and $n = 2.84$, were obtained for previously reported seven-coordinate Co(II) compound comprising analogous macrocyclic ligand $[Co(L3)](ClO_4)_2$[26] and slightly higher Raman coefficients were found in other seven-coordinate Co(II) complexes with easy plane anisotropy ($n = 4.9–8.7$).[30–32]

In contrast to compounds **2** and **3**, compound **1** exhibits only one maximum on the frequency-dependent imaginary part of the molar susceptibility (Figure 5), and therefore similar analysis is unfeasible. However, the simplified model can be utilized to analyze AC susceptibility data, which is derived under the assumption that the adiabatic susceptibility is usually approaching zero in the single-molecule magnets $(\chi_S \rightarrow 0)$,[2] thus the ratio of imaginary and real susceptibilities expressed as in eqs 7−8

$$\chi' = \frac{\chi_T - \chi_S}{1 + \omega^2\tau^2} + \chi_S \tag{7}$$

$$\chi'' = \varpi\tau\frac{\chi_T - \chi_S}{1 + \omega^2\tau^2} \tag{8}$$

Analogously, we used eq 9 to derive also linearized equation suitable for the Raman relaxation process as

$$\ln(\chi''/\chi') = \ln(2\pi fC) - n\cdot\ln T \tag{11}$$

The application of this procedure resulted in parameters listed in Table 5; see also Figure 7, Figures S9 and S10. The Raman parameters were found to be in the range $n = 1.76–2.59$ for **1**, $n = 2.86–3.21$ for **2**, and $n = 2.98–4.50$ for **3**. These factors are close to those extracted with eq 6 for **2** and **3**. To summarize, the AC susceptibility data for **1−3** can be analyzed both by Orbach and Raman processes; however, due to the presence of the easy-plane type of the magnetic anisotropy, the

Table 5. Parameters Resulting from the Analysis of AC Susceptibility Data for Raman Relaxation Process Using Equation 11 for Complexes 1−3

	f (Hz)	1488.1	715.6	344.7	166.2
1	$2\pi f \times C$	1.62	1.76	1.01	0.986
	n	1.76	2.24	2.25	2.59
	f (Hz)	1488.1	715.6	344.7	166.2
2	$2\pi f \times C$	11.8	4.15	2.90	1.83
	n	3.10	2.86	3.09	3.21
	f (Hz)	1488.1	597.1	239.8	96.2
3	$2\pi f \times C$	501	45.6	9.25	2.39
	n	4.50	3.71	3.30	2.98

Raman relaxation processes seems to be a favorable interpretation.

Theoretical Calculations. In order to better understand the impact of the axial coligands on the electronic structure of the seven-coordinate complexes under study, especially on their magnetic anisotropy, the post-Hartree−Fock CASSCF calculations were performed. First, the ORCA 3.0.3 computation package was utilized to perform CASSCF/NEVPT2 calculations for CAS(7,5) using the scalar relativistic contracted version of def2-TZVP(-f) basis functions together with the zero order regular approximation (ZORA). Second, MOLCAS 8.0 computational package was employed for CASSCF/CASPT2 calculations with respective relativistic ANO-RCC basis set and Douglas−Kroll−Hess (DKH) approximation. Now, the double-shell effect was also encountered by enlarging the number of active orbitals (3d + 3d′) as CAS(7,10). In such way, we can compare two traditional theoretical methods in the realm of the SMMs used for calculation of the zero-field splitting and g-tensors. The first approach done with ORCA resulted in a small variation of D-values, D = 43.3−44.8 cm^{-1}, for 1−3, and D is very slightly decreasing toward heavier halogenido ligands. Also, the calculations performed for different complexes of 2 and 3 found in their respective asymmetric units show practically no variation for D (Table 6). On the contrary, there is a much larger variation of D calculated with MOLCAS, D = 45.0−52.1 cm^{-1} for 1−3 with CAS(7,5) and D = 37.0−47.5 cm^{-1} for 1−3 with CAS(7,10), and also this procedure seems to be much more sensitive to small variations of geometry found in two complexes of 2 and 3 in their asymmetric units. The expanding the active space, thus accounting for the double-shell effect, led in all cases to lower D-values with following trend, D(X = Br, 2) < D(X = I, 3) ≈ D(X = Cl, 1). To summarize, all three theoretical methods confirmed large positive D, almost negligible rhombicity, $|E/D|$ < 0.08, thus the easy-plane type of the magnetic anisotropy. Moreover, the both calculation methods, ORCA with CAS(7,5) and MOLCAS with CAS(7,10), resulted in very similar orientations of the axes of respective D-tensors as visualized in Figure S11, and moreover, z-axes coincide with Co-X axial bonds in all cases. Also, there is large anisotropy of g-tensors from which is obvious that g_z = 2.0 and $g_x \approx g_y \approx$ 2.4−2.5. The energy levels and the contributions of the excited spin states to D-tensor are listed in Tables S4 and S5. It is evident that first four excited quartets have a significant contribution to D, and the first two doublets contribute to D as well.

However, there is evidently no obvious trend of the D-values reflecting the analysis of the magnetic data. Therefore, we also performed DFT calculations with B3LYP/ZORA/def2-TZVP(-f) for each complex unit of 1−3 and calculated Mayer bond

Table 6. Comparison of the Spin Hamiltonian Parameters for Complexes 1−3 Derived from the Experimental Magnetic Data and from CASSCF Calculations[a]

compound	1	2	3
CASSCF/NEVPT2/ZORA/def2-TZVP(-f) with CAS(7,5) (ORCA)			
D (cm^{-1})	44.8	44.0/44.0	43.4/43.3
$|E/D|$	0.0444	0.0615/0.0701	0.0665/0.0560
g_x	2.466	2.457/2.469	2.457/2.447
g_y	2.421	2.396/2.398	2.390/2.391
g_z	2.005	1.994/1.999	1.993/1.992
CASSCF/CASPT2/DKH2/ANO-RCC with CAS(7,5) (MOLCAS)			
D (cm^{-1})	50.1	49.8/44.9	45.0/52.1
$|E/D|$	0.0499	0.0724/0.0628	0.0625/0.0789
g_x	2.497	2.506/2.455	2.435/2.541
g_y	2.441	2.421/2.384	2.377/2.442
g_z	2.000	1.992/2.004	1.997/1.986
CASSCF/CASPT2/DKH2/ANO-RCC with CAS(7,10) (MOLCAS)			
D (cm^{-1})	47.5	38.6/37.0	44.3/47.4
$|E/D|$	0.0473	0.0766/0.0617	0.0598/0.0665
g_x	2.488	2.472/2.424	2.447/2.498
g_y	2.435	2.399/2.366	2.388/2.418
g_z	2.002	1.997/2.006	1.996/1.991
Experimentally Determined Magnetic Parameters			
D (cm^{-1})	38(3)	41(1)	35(1)
$|E/D|$ (fixed)	0.0	0.0	0.0
g_{xy}	2.47(1)	2.284(5)	2.355(6)
g_z (fixed)	2.0	2.0	2.0
χ_{TIM} (10^{-9} m^3 mol^{-1})	11(1)	14(5)	12.2(6)

[a]The details of the theoretical calculations are described in the Experimental Section.

orders between cobalt and the corresponding donor atoms. The results are graphically visualized together with the bond distances and the D-values (both experimental and theoretical) in Figure 8.

The DFT calculations revealed that (i) Mayer bond order of the donor−acceptor Co−N/O bonds with the macrocyclic ligand L is almost constant for all the complexes 1−3, thus ensuring that variation of ZFS parameters is solely due to the variation of the axial ligands X; (ii) Mayer bond order of the donor−acceptor Co−X bonds increases in this order: Co−Br < Co−Cl < Co−I, thus these bond orders do not follow the ligand field strength from the general spectrochemical series. Now it is evident that D derived from the analysis of the experimental magnetic data correlates with the axial ligand Mayer bond order (Co−X, X = Cl, Br, I) and not with the ligand field strength which means that the stronger axial donor−acceptor bond is connected with the lower D-value. In order to confirm and generalize this conclusion we used the Angular Overlap Model (AOM) and AOMX program. Here we supposed idealized geometry of the pentagonal bipyramide (D_{5h} symmetry) and modeled effect of the axial and equatorial ligands on the zero-field splitting of the ground spin state S = 3/2. We have also considered all three types of ligands, which means σ-donors with π-donor properties, pure σ-donors, and σ-donors with π-acceptor properties. The calculated energy splitting Δ of the Kramers doublets is equal to 2D in this idealized geometry. The results are depicted in Figure 9a,b, and the conclusions can be summarized as follows: (i) decrease of the ligand field strength both in axial and equatorial positions lead to an increase of the magnetic anisotropy; (ii) increase of D is much pronounced for the equatorial ligands; (iii) the type of the ligand (σ-donor and
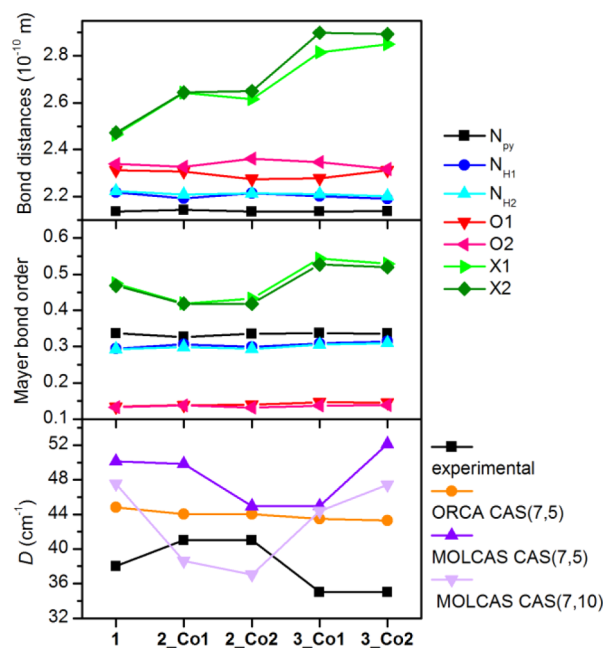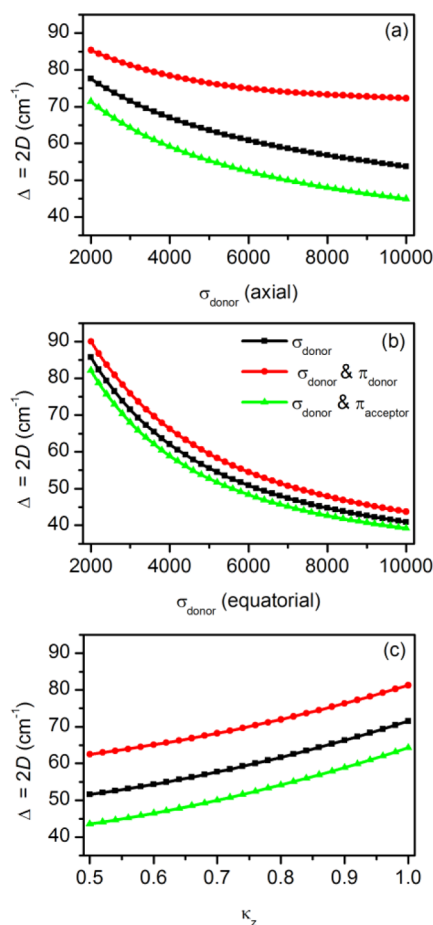
Figure 8. Variation of the cobalt−donor atom distances (top), Mayer's bond order (middle), and ZFS D-parameter (bottom) for **1**−**3**. The solid lines represent just a guideline for the eyes to better follow the trends.

Figure 9. Energy splitting of Kramers doublets for Co(II) seven-coordinate complexes with idealized pentagonal-bipyramidal geometry calculated with the Angular Overlap Model using AOMX program. (a) The effect of the axial ligand strength; (b) the effect of the equatorial ligand strength; (c) the impact of the covalency effect expressed by the orbital reduction factor of the axial ligands (κ_z).

π-donor; σ-donor; σ-donor and π-acceptor) in the axial positions affects the D-parameter much more than that in the equatorial plane. Furthermore, the impact of the covalency effect was also calculated for three types of the axial ligands as depicted in Figure 9c by varying the orbital reduction factor of the spin−orbit interaction in axial positions (κ_z), and we can conclude that D decreases with increasing covalency of the Co−X donor−acceptor bond for all types of the axial ligands.

CONCLUSIONS

In summary, a thorough investigation of the influence of the halogenido coligands occupying the apical positions in seven-coordinate pentagonal-bipyramidal Co^{II} complexes $[Co(\mathbf{L})X_2]$ ($\mathbf{L}$ = pentadentate macrocyclic ligand, X = Cl^- (**1**), Br^- (**2**), or I^- (**3**)) on their magnetic anisotropy is reported. All three compounds possessed a large easy-plane anisotropy with the D-values increasing in the order: 35 cm^{-1} (**3**) < 38 cm^{-1} (**1**) < 41 cm^{-1} (**2**), thus $D(I^-) < D(Cl^-) < D(Br^-)$ in contrast to the expected trend based on the position of the corresponding X ligand in a general spectrochemical series (Δ decreases in the order $Cl^- > Br^- > I^-$ and thus D should increase in the order $D(Cl^-) < D(Br^-) < D(I^-)$).[16] In order to explain this trend, *ab initio* calculations were performed, but they were found to be inefficient to understand the phenomenon. This discrepancy led us to an inspection of the nature of Co−X bonds via DFT calculations, which surprisingly showed that the Mayer bond order decreases in the order: Co−I > Co−Cl > Co−Br most likely as a consequence of interplay between the Co−X bond covalency and the ligand field splitting Δ induced by the X$^-$ ligands. This Mayer bond orders actually nicely correspond with the unexpected trend in the experimental D-values. Furthermore, all the complexes behave as field-induced mononuclear SMMs with the slow relaxation of the magnetization depending on the corresponding halogenido coligand,

which can be characterized most likely with the Raman relaxation process.

Altogether, we can conclude that tuning of magnetic anisotropy is still a very challenging process in which substitution of coligands based simply on their position in spectrochemical series can be misleading and need not give anticipated results, especially when heavier donor atoms (4p and 5p elements) are employed. Moreover, based on additional AOM calculations, further progress in tuning of the magnetic anisotropy in pentagonal−bipyramidal Co(II) complexes would be achieved by structural changes of ligand(s) coordinated in the equatorial plane rather than in the axial positions.

ASSOCIATED CONTENT

Ⓢ Supporting Information

The Supporting Information is available free of charge on the ACS Publications website at DOI: 10.1021/acs.inorgchem.7b00235.

Full IR spectra, additional crystallographic and magnetic data for complexes **1**−**3** (PDF)

■ AUTHOR INFORMATION

Corresponding Author

*Fax: +420 585 634 954. Phone: +420 585 634 352. E-mail:
zdenek.travnicek@upol.cz.

ORCID ⓘ

Radovan Herchel: 0000-0001-8262-4666

Zdeněk Trávníček: 0000-0002-5890-7874

Notes

The authors declare no competing financial interest.

■ REFERENCES

(1) *Single Molecule Magnet and Related Phenomena*; Winpenny, R.,
Ed.; Structure and Bonding, Vol. *122*; Springer: Berlin, 2006.

(2) Gatteshi, D.; Sessoli, R.; Villain, J. *Molecular Nanomegnets*; Oxford
University Press: New York, 2006.

(3) *Molecular Nanomagnets and Related Phenomena*; Gao, S., Ed.;
Structure and Bonding, Vol. *164*; Springer: Berlin, 2015.

(4) Miller, J. S.; Gatteschi, D. Molecule-based magnets themed issue
No. 6. *Chem. Soc. Rev.* **2011**, *40*, 3065.

(5) Sessoli, R.; Gatteschi, D.; Caneschi, A.; Novak, M. A. Magnetic
bistability in a metal-ion cluster. *Nature* **1993**, *365*, 141−143.

(6) Zhang, P.; Guo, Y.-N.; Tang, J. Recent advances in dysprosium-
based single molecule magnets: Structural overview and synthetic
strategies. *Coord. Chem. Rev.* **2013**, *257*, 1728−1763.

(7) Feltham, H. L. C.; Brooker, S. Review of purely 4f and mixed-
metal nd-4f single-molecule magnets containing only one lanthanide
ion. *Coord. Chem. Rev.* **2014**, *276*, 1−33.

(8) Woodruff, D. N.; Winpenny, R. E.; Layfield, R. A. Lanthanide
single-molecule magnets. *Chem. Rev.* **2013**, *113*, 5110−5148.

(9) Tang, J.; Zhang, P. *Lanthanide Single Molecule Magnets*; Springer:
Berlin, 2015.

(10) Gómez-Coca, S.; Aravena, D.; Morales, R.; Ruiz, E. Large
magnetic anisotropy in mononuclear metal complexes. *Coord. Chem.
Rev.* **2015**, *289−290*, 379−392.

(11) Craig, G. A.; Murrie, M. 3d single-ion magnets. *Chem. Soc. Rev.*
2015, *44*, 2135−2147.

(12) Bar, A. K.; Pichon, C.; Sutter, J.-P. Magnetic anisotropy in two-
to eight-coordinated transition−metal complexes: Recent develop-
ments in molecular magnetism. *Coord. Chem. Rev.* **2016**, *308*, 346−
380.

(13) Frost, J. M.; Harriman, K. L. M.; Murugesu, M. The rise of 3-d
single-ion magnets in molecular magnetism: towards materials from
molecules? *Chem. Sci.* **2016**, *7*, 2470−2491.

(14) Neese, F.; Pantazis, D. A. What is not required to make a single
molecule magnet. *Faraday Discuss.* **2011**, *148*, 229−238.

(15) Regueiro-Figueroa, M.; Lima, L. M.; Blanco, V.; Esteban-
Gomez, D.; de Blas, A.; Rodriguez-Blas, T.; Delgado, R.; Platas-
Iglesias, C. Reasons behind the relative abundances of heptacoordinate
complexes along the late first-row transition metal series. *Inorg. Chem.*
2014, *53*, 12859−12869.

(16) Ruamps, R.; Batchelor, L. J.; Maurice, R.; Gogoi, N.; Jiménez-
Lozano, P.; Guihéry, N.; de Graaf, C.; Barra, A.-L.; Sutter, J.-P.; Mallah,
T. Origin of the Magnetic Anisotropy in Heptacoordinate Ni^II and
Co^II Complexes. *Chem. - Eur. J.* **2013**, *19*, 950−956.

(17) Bar, A. K.; Pichon, C.; Gogoi, N.; Duhayon, C.; Ramasesha, S.;
Sutter, J. P. Single-ion magnet behaviour of heptacoordinated Fe(II)
complexes: on the importance of supramolecular organization. *Chem.
Commun.* **2015**, *51*, 3616−3619.

(18) Batchelor, L. J.; Sangalli, M.; Guillot, R.; Guihéry, N.; Maurice,
R.; Tuna, F.; Mallah, T. Pentanuclear Cyanide-Bridged Complexes

Based on Highly Anisotropic Co^II Seven-Coordinate Building Blocks:
Synthesis, Structure, and Magnetic Behavior. *Inorg. Chem.* **2011**, *50*,
12045−12052.

(19) Bar, A. K.; Gogoi, N.; Pichon, C.; Durga Prasat Goli, V. M. L.;
Thlijeni, M.; Duhayon, C.; Suaud, N.; Guihéry, N.; Barra, A.-L.;
Ramasesha, S.; Sutter, J.-P. Pentagonal Bipyramid Fe^II Complexes:
Robust Ising-Spin Units towards Heteropolynuclear Nanomagnets.
Chem. - Eur. J. **2017**, *23*, 4380−4396.

(20) Gogoi, N.; Thlijeni, M.; Duhayon, C.; Sutter, J.-P.
Heptacoordinated Nickel(II) as an Ising-Type Anisotropic Building
Unit: Illustration with a Pentanuclear [(NiL)₃{W(CN)₈}₂] Complex.
Inorg. Chem. **2013**, *52*, 2283−2285.

(21) Schleife, F.; Rodenstein, A.; Kirmse, R.; Kersting, B. Seven-
coordinate Mn(II) and Co(II) complexes of the pentadentate ligand
2,6-diacetyl-4-carboxymethyl-pyridine bis(benzoylhydrazone): Synthe-
sis, crystal structure and magnetic properties. *Inorg. Chim. Acta* **2011**,
374, 521−527.

(22) Zhang, Y. Z.; Sato, O. A cyano-bridged Cr(III)Co(II)
ferromagnet with a chiral nanotubular structure constituted of
interlocked single and double helices. *Inorg. Chem.* **2010**, *49*, 1271−
1273.

(23) Dogaru, A.; Pichon, C.; Ababei, R.; Mitcov, D.; Maxim, C.;
Toupet, L.; Mathonière, C.; Clérac, R.; Andruh, M. New bidimen-
sional honeycomb Co^II−Fe^III and brick wall Fe^II−Co^III cyanido-
bridged coordination polymers: Synthesis, crystal structures and
magnetic properties. *Polyhedron* **2014**, *75*, 146−152.

(24) Venkatakrishnan, T. S.; Sahoo, S.; Brefuel, N.; Duhayon, C.;
Paulsen, C.; Barra, A. L.; Ramasesha, S.; Sutter, J. P. Enhanced Ion
Anisotropy by Nonconventional Coordination Geometry: Single-
Chain Magnet Behavior for a [{Fe^IIL}₂{Nb^IV(CN)₈}] Helical Chain
Compound Designed with Heptacoordinate Fe^II. *J. Am. Chem. Soc.*
2010, *132*, 6047−6056.

(25) Drahoš, B.; Herchel, R.; Trávníček, Z. Structural, Magnetic, and
Redox Diversity of First-Row Transition Metal Complexes of a
Pyridine-Based Macrocycle: Well-Marked Trends Supported by
Theoretical DFT Calculations. *Inorg. Chem.* **2015**, *54*, 3352−3369.

(26) Antal, P.; Drahoš, B.; Herchel, R.; Trávníček, Z. Late First-Row
Transition-Metal Complexes Containing a 2-Pyridylmethyl Pendant-
Armed 15-Membered Macrocyclic Ligand. Field-Induced Slow
Magnetic Relaxation in a Seven-Coordinate Cobalt(II) Compound.
Inorg. Chem. **2016**, *55*, 5957−5972.

(27) Acha, R. T.; Gavey, E. L.; Wang, J.; Rawson, J. M.; Pilkington,
M. The first 1-D cyanide-bridged complex assembled from a covalently
tethered [Co^II(N₃O₂)Cl(OH₂)]^{22+} macrocyclic building block. *Poly-
hedron* **2014**, *76*, 122−127.

(28) Platas-Iglesias, C.; Vaiana, L.; Esteban-Gómez, D.; Avecilla, F.;
Real, J. A.; de Blas, A.; Rodríguez-Blas, T. Electronic Structure Study of
Seven-Coordinate First-Row Transition Metal Complexes Derived
from 1,10-Diaza-15-crown-5: A Successful Marriage of Theory with
Experiment. *Inorg. Chem.* **2005**, *44*, 9704−9713.

(29) Vaiana, L.; Regueiro-Figueroa, M.; Mato-Iglesias, M.; Platas-
Iglesias, C.; Esteban-Gómez, D.; de Blas, A.; Rodríguez-Blas, T. Seven-
Coordination versus Six-Coordination in Divalent First-Row Tran-
sition-Metal Complexes Derived from 1,10-Diaza-15-crown-5. *Inorg.
Chem.* **2007**, *46*, 8271−8282.

(30) Shao, D.; Zhang, S. L.; Shi, L.; Zhang, Y. Q.; Wang, X. Y.
Probing the Effect of Axial Ligands on Easy-Plane Anisotropy of
Pentagonal-Bipyramidal Cobalt(II) Single-Ion Magnets. *Inorg. Chem.*
2016, *55*, 10859−10869.

(31) Huang, X.-C.; Zhou, C.; Shao, D.; Wang, X.-Y. Field-Induced
Slow Magnetic Relaxation in Cobalt(II) Compounds with Pentagonal
Bipyramid Geometry. *Inorg. Chem.* **2014**, *53*, 12671−12673.

(32) Habib, F.; Korobkov, I.; Murugesu, M. Exposing the
intermolecular nature of the second relaxation pathway in a
mononuclear cobalt(II) single-molecule magnet with positive
anisotropy. *Dalton Trans.* **2015**, *44*, 6368−6373.

(33) Dey, M.; Dutta, S.; Sarma, B.; Deka, R. C.; Gogoi, N.
Modulation of the coordination environment: a convenient approach

to tailor magnetic anisotropy in seven coordinate Co(II) complexes. *Chem. Commun.* **2016**, *52*, 753−756.

(34) Chen, L.; Chen, S.-Y.; Sun, Y.-C.; Guo, Y.-M.; Yu, L.; Chen, X.-T.; Wang, Z.; Ouyang, Z. W.; Song, Y.; Xue, Z.- L. Slow magnetic relaxation in mononuclear seven-coordinate cobalt(II) complexes with easy plane anisotropy. *Dalton Trans.* **2015**, *44*, 11482−11490.

(35) Gomez-Coca, S.; Urtizberea, A.; Cremades, E.; Alonso, P. J.; Camon, A.; Ruiz, E.; Luis, F. Origin of slow magnetic relaxation in Kramers ions with non-uniaxial anisotropy. *Nat. Commun.* **2014**, *5*, 1−8.

(36) Atanasov, M.; Aravena, D.; Suturina, E.; Bill, E.; Maganas, D.; Neese, F. First principles approach to the electronic structure, magnetic anisotropy and spin relaxation in mononuclear 3d-transition metal single molecule magnets. *Coord. Chem. Rev.* **2015**, *289−290*, 177−214.

(37) Rechkemmer, Y.; Breitgoff, F. D.; van der Meer, M.; Atanasov, M.; Hakl, M.; Orlita, M.; Neugebauer, P.; Neese, F.; Sarkar, B.; van Slageren, J. A four-coordinate cobalt(II) single-ion magnet with coercivity and a very high energy barrier. *Nat. Commun.* **2016**, *7*, 10467.

(38) Saber, M. R.; Dunbar, K. R. Ligands effects on the magnetic anisotropy of tetrahedral cobalt complexes. *Chem. Commun.* **2014**, *50*, 12266−12269.

(39) Zadrozny, J. M.; Telser, J.; Long, J. R. Slow magnetic relaxation in the tetrahedral cobalt(II) complexes [Co(EPh)$_4$]$^{2-}$ (E = O, S, Se). *Polyhedron* **2013**, *64*, 209−217.

(40) Ruamps, R.; Batchelor, L. J.; Guillot, R.; Zakhia, G.; Barra, A.-L.; Wernsdorfer, W.; Guihéry, N.; Mallah, T. Ising-type magnetic anisotropy and single molecule magnet behaviour in mononuclear trigonal bipyramidal Co(II) complexes. *Chem. Sci.* **2014**, *5*, 3418−3424.

(41) Shao, F.; Cahier, B.; Riviere, E.; Guillot, R.; Guihery, N.; Campbell, V. E.; Mallah, T. Structural Dependence of the Ising-type Magnetic Anisotropy and of the Relaxation Time in Mononuclear Trigonal Bipyramidal Co(II) Single Molecule Magnets. *Inorg. Chem.* **2017**, *56*, 1104−1111.

(42) Woods, T. J.; Ballesteros-Rivas, M. F.; Gomez-Coca, S.; Ruiz, E.; Dunbar, K. R. Relaxation Dynamics of Identical Trigonal Bipyramidal Cobalt Molecules with Different Local Symmetries and Packing Arrangements: Magnetostructural Correlations and ab inito Calculations. *J. Am. Chem. Soc.* **2016**, *138*, 16407−16416.

(43) Desrochers, P. J.; Telser, J.; Zvyagin, S. A.; Ozarowski, A.; Krzystek, J.; Vicic, D. A. Electronic Structure of Four-Coordinate C3v Nickel(II) Scorpionate Complexes: Investigation by High-Frequency and -Field Electron Paramagnetic Resonance and Electronic Absorption Spectroscopies. *Inorg. Chem.* **2006**, *45*, 8930−8941.

(44) Karunadasa, H. I.; Arquero, K. D.; Berben, L. A.; Long, J. R. Enhancing the Magnetic Anisotropy of Cyano-Ligated Chromium(II) and Chromium(III) Complexes via Heavy Halide Ligand Effects. *Inorg. Chem.* **2010**, *49*, 4738−4740.

(45) Stavretis, S. E.; Atanasov, M.; Podlesnyak, A. A.; Hunter, S. C.; Neese, F.; Xue, Z. L. Magnetic Transitions in Iron Porphyrin Halides by Inelastic Neutron Scattering and Ab Initio Studies of Zero-Field Splittings. *Inorg. Chem.* **2015**, *54*, 9790−9801.

(46) Duboc, C.; Phoeung, T.; Zein, S.; Pécaut, J.; Collomb, M.-N.; Neese, F. Origin of the Zero-Field Splitting in Mononuclear Octahedral Dihalide Mn^{II} Complexes: An Investigation by Multifrequency High-Field Electron Paramagnetic Resonance and Density Functional Theory. *Inorg. Chem.* **2007**, *46*, 4905−4916.

(47) Drahoš, B.; Herchel, R.; Trávníček, Z. Structural and magnetic properties of heptacoordinated Mn^{II} complexes containing a 15-membered pyridine-based macrocycle and halido/pseudohalido axial coligands. *RSC Adv.* **2016**, *6*, 34674−34684.

(48) Drahoš, B.; Kotek, J.; Hermann, P.; Lukeš, I.; Tóth, E. Mn^{2+} Complexes with Pyridine-Containing 15-Membered Macrocycles: Thermodynamic, Kinetic, Crystallographic, and ^{1}H/^{17}O Relaxation Studies. *Inorg. Chem.* **2010**, *49*, 3224−3238.

(49) *Apex3*; Bruker AXS Inc: Madison, WI, 2015.

(50) Sheldrick, G. M. Crystal structure refinement with SHELXL. *Acta Crystallogr., Sect. C: Struct. Chem.* **2015**, *71*, 3−8.

(51) Macrae, C. F.; Bruno, I. J.; Chisholm, J. A.; Edgington, P. R.; McCabe, P.; Pidcock, E.; Rodriguez-Monge, L.; Taylor, R.; van de Streek, J.; Wood, P. A. Mercury CSD 2.0 − new features for the visualization and investigation of crystal structures. *J. Appl. Crystallogr.* **2008**, *41*, 466−470.

(52) Neese, F. The ORCA program system. *WIREs Comput. Mol. Sci.* **2012**, *2*, 73−78.

(53) Pantazis, D. A.; Chen, X.-Y.; Landis, C. R.; Neese, F. J. All-electron scalar relativistic basis sets for third-row transition metal atoms. *J. Chem. Theory Comput.* **2008**, *4*, 908−919.

(54) (a) van Lenthe, E.; Baerends, E. J.; Snijders, J. G. Relativistic regular two-component Hamiltonians. *J. Chem. Phys.* **1993**, *99*, 4597−4610. (b) Van Wüllen, C. Molecular density functional calculations in the regular relativistic approximation: Method, application to coinage metal diatomics, hydrides, fluorides and chlorides, and comparison with first-order relativistic calculations. *J. Chem. Phys.* **1998**, *109*, 392−399.

(55) Malmqvist, P. A.; Roos, B. O. The CASSCF state interaction method. *Chem. Phys. Lett.* **1989**, *155*, 189−194.

(56) (a) Angeli, C.; Cimiraglia, R.; Evangelisti, S.; Leininger, T.; Malrieu, J.-P. Introduction of n-electron valence states for multireference perturbation theory. *J. Chem. Phys.* **2001**, *114*, 10252−10264. (b) Angeli, C.; Cimiraglia, R.; Malrieu, J.-P. N-electron valence state perturbation theory: a fast implementation of the strongly contracted variant. *Chem. Phys. Lett.* **2001**, *350*, 297−305. (c) Angeli, C.; Cimiraglia, R.; Malrieu, J.-P. N-electron valence state perturbation theory: A spinless formulation and an efficient implementation of the strongly contracted and of the partially contracted variants. *J. Chem. Phys.* **2002**, *117*, 9138−9153. (d) Angeli, C.; Borini, S.; Cestari, M.; Cimiraglia, R. A quasidegenerate formulation of the second order n-electron valence state perturbation theory approach. *J. Chem. Phys.* **2004**, *121*, 4043−4049. (e) Angeli, C.; Bories, B.; Cavallini, A.; Cimiraglia, R. Third-order multireference perturbation theory: The n-electron valence state perturbation-theory approach. *J. Chem. Phys.* **2006**, *124*, 054108.

(57) Ganyushin, D.; Neese, F. First-principles calculations of zero-field splitting parameters. *J. Chem. Phys.* **2006**, *125*, 024103.

(58) Neese, F. Efficient and accurate approximations to the molecular spin-orbit coupling operator and their use in molecular g-tensor calculations. *J. Chem. Phys.* **2005**, *122*, 034107.

(59) Maurice, R.; Bastardis, R.; De Graaf, C.; Suaud, N.; Mallah, T.; Guihéry, N. Universal theoretical approach to extract anisotropic spin Hamiltonians. *J. Chem. Theory Comput.* **2009**, *5*, 2977−2984.

(60) (a) Aquilante, F.; De Vico, L.; Ferré, N.; Ghigo, G.; Malmqvist, P. A.; Neogrády, P.; Pedersen, T. B.; Pitoňák, M.; Reiher, M.; Roos, B. O.; Serrano-Andrés, L.; Urban, M.; Veryazov, V.; Lindh, R. MOLCAS 7: the next generation. *J. Comput. Chem.* **2010**, *31*, 224−247. (b) Duncan, J. A. MOLCAS 7.2. *J. Am. Chem. Soc.* **2009**, *131*, 2416−2416. (c) Karlström, G.; Lindh, R.; Malmqvist, P. A.; Roos, B. O.; Ryde, U.; Veryazov, V.; Widmark, P.-O.; Cossi, M.; Schimmelpfennig, B.; Neogrády, P.; Seijo, L. MOLCAS: a program package for computational chemistry. *Comput. Mater. Sci.* **2003**, *28*, 222−239. (d) Veryazov, V.; Widmark, P.-O.; Serrano-Andres, L.; Lindh, R.; Roos, B. O. 2MOLCAS as a development platform for quantum chemistry software. *Int. J. Quantum Chem.* **2004**, *100*, 626−635.

(61) Malmqvist, P. A.; Roos, B. O.; Schimmelpfennig, B. The restricted active space (RAS) state interaction approach with spin−orbit coupling. *Chem. Phys. Lett.* **2002**, *357*, 230−240.

(62) (a) Andersson, K.; Roos, B. O. Excitation energies in the nickel atom studied with the complete active space SCF method and second-order perturbation theory. *Chem. Phys. Lett.* **1992**, *191*, 507−514. (b) Roos, B. O.; Andersson, K.; Fulscher, M.; Malmqvist, P.-A.; Serrano-Andrés, L.; Pierloot, K.; Merchan, M. Multiconfigurational perturbation theory: Applications in electronic spectroscopy. *Adv. Chem. Phys.* **1996**, *93*, 219−331.

(63) (a) Andersson, K.; Malmqvist, P.-A.; Roos, B. O.; Sadlej, A. J.; Wolinski, K. Second-Order Perturbation Theory with a CASSCF Reference Function. *J. Phys. Chem.* **1990**, *94*, 5483−5488. (b) Richard Bowen, W.; Hilal, N.; Jain, M.; Lovitt, R. W.; Sharif, A. O.; Wright, C. J.; Finley, J.; Malmqvist, P.-A.; Roos, B. O.; Serrano-Andres, L. The multi-state CASPT2 method. *Chem. Phys. Lett.* **1998**, *288*, 299−306. (c) Andersson, K.; Malmqvist, P.-A; Roos, B. O. Second-order perturbation theory with a complete active space self-consistent field reference function. *J. Chem. Phys.* **1992**, *96*, 1218−1226.

(64) (a) Hess, B. A.; Marian, C. M.; Wahlgren, U.; Gropen, O. A mean-field spin-orbit method applicable to correlated wavefunctions. *Chem. Phys. Lett.* **1996**, *251*, 365−371. (b) Schimmelpfennig, B. AMFI, an atomic mean-field spin-orbit integral program. Stockholm University, 1996.

(65) (a) Douglas, N.; Kroll, N. M. Quantum electrodynamical corrections to the fine structure of helium. *Ann. Phys.* **1974**, *82*, 89−155. (b) Hess, B. A. Relativistic electronic-structure calculations employing a two-component no-pair formalism with external-field projection operators. *Phys. Rev. A: At., Mol., Opt. Phys.* **1986**, *33*, 3742−3748.

(66) (a) Roos, B. O.; Lindh, R.; Malmqvist, P. A.; Veryazov, V.; Widmark, P.-O.; Borin, A. C. New Relativistic Atomic Natural Orbital Basis Sets for Lanthanide Atoms with Applications to the Ce Diatom and LuF_3. *J. Phys. Chem. A* **2008**, *112*, 11431−11435. (b) Roos, B. O.; Lindh, R.; Malmqvist, P. A.; Veryazov, V.; Widmark, P.-O. New relativistic ANO basis sets for actinide atoms. *Chem. Phys. Lett.* **2005**, *409*, 295−299.

(67) (a) Chibotaru, L. F.; Ungur, L.; Soncini, A. The origin of nonmagnetic Kramers doublets in the ground state of dysprosium triangles: evidence for a toroidal magnetic moment. *Angew. Chem., Int. Ed.* **2008**, *47*, 4126−4129. (b) Chibotaru, L. F.; Ungur, L.; Aronica, C.; Elmoll, H.; Pilet, G.; Luneau, D. Structure, magnetism, and theoretical study of a mixed-valence CoII3CoIII4 heptanuclear wheel: lack of smm behavior despite negative magnetic anisotropy. *J. Am. Chem. Soc.* **2008**, *130*, 12445−12455. (c) Chibotaru, L. F.; Ungur, L. Ab initio calculation of anisotropic magnetic properties of complexes. I. Unique definition of pseudospin Hamiltonians and their derivation. *J. Chem. Phys.* **2012**, *137*, 064112. (d) Ungur, L.; Thewissen, M.; Costes, J.-P.; Wernsdorfer, W.; Chibotaru, L. F. Interplay of strongly anisotropic metal ions in magnetic blocking of complexes. *Inorg. Chem.* **2013**, *52*, 6328−6337.

(68) (a) Lee, C.; Yang, W.; Parr, R. G. Development of the Colle-Salvetti correlation-energy formula into a functional of the electron density. *Phys. Rev. B: Condens. Matter Mater. Phys.* **1988**, *37*, 785−789. (b) Becke, A. D. A new mixing of Hartree−Fock and local density-functional theories. *J. Chem. Phys.* **1993**, *98*, 1372−1377. (c) Becke, A. D. Density-functional thermochemistry. III. The role of exact Exchange. *J. Chem. Phys.* **1993**, *98*, 5648−5652. (d) Stephens, P. J.; Devlin, F. J.; Chabalowski, C. F.; Frisch, M. J. Ab Initio Calculation of Vibrational Absorption and Circular Dichroism Spectra Using Density Functional Force Fields. *J. Phys. Chem.* **1994**, *98*, 11623−11627.

(69) Lu, T.; Chen, F. Multiwfn: a multifunctional wavefunction analyzer. *J. Comput. Chem.* **2012**, *33*, 580−592.

(70) Mayer, I. Charge, bond order and valence in the AB initio SCF theory. *Chem. Phys. Lett.* **1983**, *97*, 270−274.

(71) Hoggard, P. E. *Topics in Current Chemistry*; Berlin, Germany: Springer-Verlag, Heinrich Heine Universitat, 1994; Vol. *171*, pp 113−141. The AOMX program is maintained by H. Adamsky, Institut fur Theoretische Chemie, Berlin, Germany, Springer-Verlag, Heinrich Heine Universitat, e-mail adamsky@theochem.uni-duesseldorf.de.

(72) Boča, R. *Theoretical Foundations of Molecular Magnetism*; Elsevier: Amsterdam, 1999.

(73) Němec, I.; Marx, R.; Herchel, R.; Neugebauer, P.; van Slageren, J.; Trávníček, Z. Field-induced slow relaxation of magnetization in a pentacoordinate Co(II) compound $[Co(phen)(DMSO)Cl_2]$. *Dalton Trans.* **2015**, *44*, 15014−15021.

Příloha P4

B. Drahoš, R. Herchel, Z. Trávníček,
Single-Chain Magnet Based on 1D Polymeric Azido-Bridged Seven-Coordinate Fe(II) Complex with a Pyridine-Based Macrocyclic Ligand.
*Inorg. Chem.* **2018**, *57*, 12718–12726.

Single-Chain Magnet Based on 1D Polymeric Azido-Bridged Seven-Coordinate Fe(II) Complex with a Pyridine-Based Macrocyclic Ligand

Bohuslav Drahoš,[ORCID] Radovan Herchel,[ORCID] and Zdeněk Trávníček*[ORCID]

Division of Biologically Active Complexes and Molecular Magnets, Regional Centre of Advanced Technologies and Materials, Faculty of Science, Palacký University, Šlechtitelů 27, CZ-783 71 Olomouc, Czech Republic

S Supporting Information

ABSTRACT: Peculiar magnetic behavior was found for 1D-polymeric seven-coordinate pentagonal bipyramidal Fe(II) complex $\{[Fe(L)(\mu_{1,3}\text{-}N_3)](ClO_4)\}_n$ (**1**) with a pentadentate macrocyclic ligand **L** (3,12,18-triaza-6,9-dioxabicyclo[12.3.1]octadeca-1(18),14,16-triene) coordinated in the pentagonal equatorial plane and with end-to-end bridging azido ligands in axial positions. The static and dynamic magnetic data revealed that spin-canting in the 1D-chain of **1** results in the single-chain magnet (SCM) behavior with high spin-reversal energy barrier U_{eff} (Δ_τ) = 87.5 K, exhibiting magnetic hysteresis below 4 K and coexistence with the metamagnetism altogether resulting in weak 3D-ferromagnetic behavior. This is the first reported example of the exclusively azido-bridged homospin Fe(II)-based SCM.
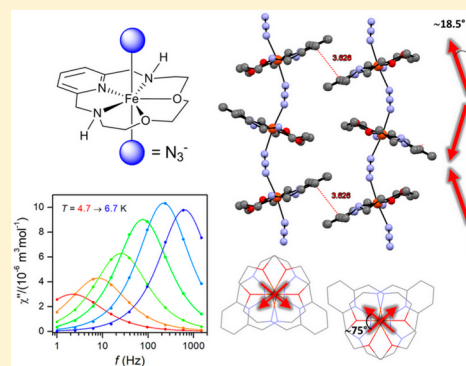
INTRODUCTION

Seven-coordinate complexes of pyridine-based macrocyclic/acyclic ligands (Figure 1) with various transition metals[1,2] as well as lanthanides[3,4] have become a growing group of compounds due to their utilization as versatile building blocks in advanced magnetic materials. Among them, an interesting class of compounds represents single-chain magnets (SCMs) which display slow relaxation of magnetization and magnetic hysteresis of purely molecular origin.[5−7] Strong magnetic anisotropy carries (metal centers preferably with Ising type of anisotropy) as well as strong intrachain magnetic coupling between them are essential requirements for rational design of SCMs.[8,9] Previously it was believed that the interchain magnetic coupling should be minimized in order to prevent 3D magnetic ordering, but with discovery of SCMs in the antiferromagnetic (AF) or ferromagnetic (F) ordered phase, new types of high-temperature SCM have been achieved.[10] However, the design and control of these interchain interactions together with the design of SCMs itself (intrachain interactions) remains a big challenge and therefore the number of SCM-based magnets is rather rarely documented. The majority of SCMs is constructed by using the ferrimagnetic ordering among heterometallic centers, because AF coupling is usually stronger and more common than the F one, with the utilization of different bridges between the spin centers, e.g. phosphonates,[11] carboxylates,[12,13] azides,[14] etc. Moreover, other well-known magnetic coupler cyanide has been employed more recently in the development of multifunctional magnetic materials based on photoswitchable SCMs[15−17] important for the fabrication of the photorecording devices.

As was mentioned above, pentagonal bipyramidal Fe(II), Co(II), and Ni(II) complexes with pentadentate ligands

coordinated in the equatorial plane represent attractive carriers of large magnetic anisotropy.[18] The weakly coordinated axial ligands can be easily substituted by various bridging units, and therefore these complexes could be used as excellent building blocks in preparation of different clusters, chains, or networks.[18] The most studied systems were based on complexes with Schiff bases **L1** and **L2**,[18−20] their reduced analogue **L**,[20−23] and acyclic derivatives **H₂L3-R** (R = phenyl (Ph), biphenyl (biPh), NH_2, etc.)[24−29] as well (Figure 1).

A large group of different magnetically ordered polymeric complexes of $[M(\mathbf{L1})]^{2+}$ or $[M(\mathbf{L2})]^{2+}$ (usually M = Mn^{II}, Fe^{II}, Co^{II}) with various cyanometallates was recently reviewed elsewhere.[18] But there are only a few examples of the previously described 1D-chain complexes containing seven-coordinate Fe(II) and showing slow relaxation of magnetization. This group includes heteronuclear SCMs $[\{(H_2O)Fe(\mathbf{L2})\}\{Nb(CN)_8\}\{Fe(\mathbf{L2})\}]_n$ (U_{eff} = 74 K, τ_0 = 4.6 × 10^{-11} s),[30] $\{[\{Cr(\mathbf{L3\text{-}Ph})(CN)_2\}\{Fe(\mathbf{H_2L3\text{-}NH_2})\}](PF_6)\}_n$ (U_{eff} = 113 K, τ_0 = 1.62 × 10^{-11} s);[29] furthermore, SMMs organized in 1D chains with the help of diamagnetic linkers $[\{Fe(\mathbf{H_2L3\text{-}Ph})\}\{Ni(CN)_4\}]_n$ (U_{eff} = 49 K, τ_0 = 2.0 × 10^{-9} s),[26] and SMM combined with the spin-crossover unit in $[\{Mn(saltmen)\}_2\{Fe(\mathbf{L2})(CN)_2\}](ClO_4)_2\cdot0.5C_4H_{10}O\cdot0.5H_2O$ (U_{eff} = 13.9 K, τ_0 = 1.1 × 10^{-7} s, saltmen = N,N'-(1,1,2,2-tetramethylethylene)bis(salicylideneiminate)).[31] Concerning the homonuclear SCMs, there are only two seven-coordinate Fe^{II} complexes, first $\{[Fe(\mathbf{L2})(CN)][BF_4]\}_n$,[32] for which SCM behavior (U_{eff} = 35.9 K, τ_0 = 5.6 × 10^{-9} s), together with AF ordering below T_N = 5.4 K, "hidden" spin-canting (canting
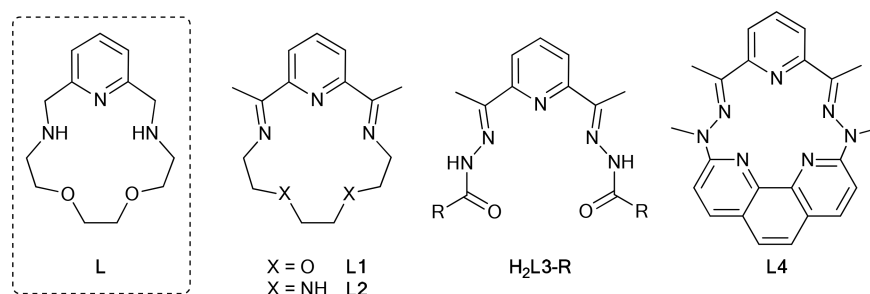
Figure 1. Structural formulas of the ligands discussed in the text.

angle ∼ 7°), and metamagnetism, has been observed. Additional suppressing of the magnetic interactions among the 1D-chains has been achieved by anion exchange in structurally related complex $\{[Fe(L1)(CN)](ABSA)\}_n$ ($U_{eff} = 26.1$ K, $\tau_0 = 8.3 \times 10^{-10}$ s, ABSA⁻ = 4-aminoazobenzene-4'-sulfonate),[33] for which only pure SCM behavior was found. To the best of our knowledge, there are no other examples of SCMs based on homonuclear seven-coordinate transition metals; nevertheless, interesting behavior corresponding to SIM organized in 1-D coordination polymer has also been recently observed for a homonuclear Co(II) complex $\{[Co(L4)-(bpe)][BF_4]\cdot3CH_3CN\}_n$ ($U_{eff} = 19.0$ K, $\tau_0 = 7.5 \times 10^{-6}$ s, bpe = 1,2-di(4-pyridyl)ethane).[34]

Inspired by the above-mentioned SCMs based on seven-coordinate Fe(II) complexes and the fact that azide is well-known as a bridging ligand with a high ability to mediate magnetic interactions,[14,35−38] the polymeric end-to-end azido-bridged Fe(II) complex $\{[Fe(L)(\mu_{1,3}\text{-}N_3)](ClO_4)\}_n$ (**1**) was prepared and its synthesis and structural and magnetic properties are described in detail herein.

■ EXPERIMENTAL SECTION

Synthesis and General Characterization. The ligand **L** (3,12,18-triaza-6,9-dioxabicyclo[12.3.1]octadeca-1(18),14,16-triene)[39,40] was synthesized according to the literature procedures. Oxygen-free CH₃OH and water were prepared by their distillation under argon atmosphere. All other chemicals (Sigma Aldrich, St. Louis, MO, USA) and solvents (VWR International, Fontenay-sous-Blois, France) were purchased from commercial sources and used as received.

$\{[Fe(L)(\mu_{1,3}\text{-}N_3)](ClO_4)\}_n$ (1). All manipulations were done under inert argon atmosphere. **L** (50 mg, 0.199 mmol) and Fe(ClO₄)₂·6H₂O (72 mg, 0.199 mmol) were dissolved in 2.5 mL of oxygen-free CH₃OH to produce a green solution. The solution of NaN₃ (13 mg, 0.199 mmol) in 0.25 mL of oxygen-free water was added to the solution prepared in the previous step. Obtained green-red solution was heated at 60 °C for 5 min and left to cool down to room temperature. A small amount of emerged precipitate was filtered off. The filtrate was allowed to crystallize by diffusion of vapors of diethyl ether at 5 °C. The product was obtained in a form of black crystals (41 mg, yield 46.1%).

MS *m/z* (+): 348.91 ([Fe(**L**)+(N₃)⁻]⁺, calcd. 349.11), 405.95 ([Fe(**L**)+(ClO₄)⁻]⁺, calcd. 406.05).

Anal. Calcd (%) for [Fe(**L**)N₃](ClO₄) (C₁₃H₂₁ClFeN₆O₆). C, 34.43; H, 4.77; N, 19.11. Found C, 34.80; H, 4.72; N, 18.73. IR (ATR, cm⁻¹): 620 (m), 797 (m), 842 (w), 882 (m), 919 (m), 942 (m), 980 (w), 1013 (s), 1070 (s), 1216 (w), 1236 (w), 1278 (w), 1298 (w), 1337 (w), 1352 (w), 1465 (m), 1576 (m), 1600 (m), 2067 (s), 2881 (m), 2925 (m), 3270 (m), 3410 (w).

Caution! Although we have experienced no difficulties, perchlorate salts of metal complexes with organic ligands are potentially explosive and should be handled with great care even in small quantities.

Physical Methods. Elemental analysis (C, H, N) was performed on a Flash 2000 CHNO-S Analyzer (Thermo Scientific, Waltham, MA, USA). The mass spectra were recorded on an LCQ Fleet Ion Mass Trap mass spectrometer (Thermo Scientific, Waltham, MA, USA) equipped with an electrospray ion source and 3D ion-trap detector in the positive mode. Infrared (IR) spectra of the complexes were collected on a Thermo Nicolet NEXUS 670 FT-IR spectrometer (Thermo Nicolet, Waltham, MA, USA) employing the ATR technique on a diamond plate in the range of 400−4000 cm⁻¹. The transmission ⁵⁷Fe Mössbauer spectrum was collected employing a Mössbauer spectrometer operating at a constant acceleration mode and equipped with a 50 mCi ⁵⁷Co(Rh) source. For fitting the Mössbauer spectra, the MossWinn software program was used.[41] The isomer shift values are referred to α-Fe at room temperature. The temperature-dependent and field-dependent magnetization measurements at static magnetic field were performed on PPMS Dynacool with the VSM option. The measurement of the alternating current (AC) susceptibility was done on a MPMS XL-7 SQUID magnetometer. The magnetic data were corrected for the diamagnetism of the constituent atoms and for the diamagnetism of the sample holder. The SI units are employed thorough the work.

X-ray Diffraction Data. Single crystals of complexes **1** suitable for X-ray diffraction analysis were prepared by a vapor diffusion of Et₂O into the solution of the complex at 5 °C. The X-ray diffraction data were collected on a Bruker D8 QUEST diffractometer equipped with a PHOTON 100 CMOS detector using Mo Kα radiation at 120 K. The APEX3 software package[42] was used for data collection and reduction. The molecular structure of **1** was solved by direct methods and refined by the full-matrix least-squares procedure SHELXL (version 2014/7).[43] Hydrogen atoms of the complex were found in the difference Fourier maps and refined using a riding model, with C−H = 0.95 (CH)ₐᵣ and C−H = 0.99 (CH₂) Å, and with U_{iso}(H) = 1.2U_{eq}(CH, CH₂). The molecular and crystal structure of the studied complex depicted in Figure 2 was drawn using the Mercury software.[44]

Theoretical Calculations. The ORCA 4.0 computational package was used for all theoretical calculations.[45] The calculations of ZFS parameters were done using state average complete active space self-consistent field (SA-CASSCF)[46] wave functions complemented by N-electron valence second-order perturbation theory (NEVPT2)[47] using the triple-ζ basis set def2-TZVP(-f)[48] for all atoms. The active space of the CASSCF calculations was composed of six electrons in five metal-based d-orbitals, CAS(6,5), and all 5 quintet and 45 triplet states contributing to ZFS and stemming from 3d⁶ electronic configuration were calculated. The ZFS parameters, based on dominant spin−orbit coupling contributions from excited states, were calculated through quasi-degenerate perturbation theory (QDPT),[49] in which an approximation to the Breit-Pauli form of the spin−orbit coupling operator (SOMF approximation)[50] and the effective Hamiltonian theory[51] were utilized. The calculations utilized the RIJCOSX approximation with the auxiliary coulomb basis def2/JK.[52] Increased integration grids (Grid6 and GridX6 in ORCA convention) and tight SCF convergence criteria were used in all calculations. The *ab initio* ligand field analysis (AILFT) was done as implemented in ORCA to obtain the energies of d-orbitals.[53−55]
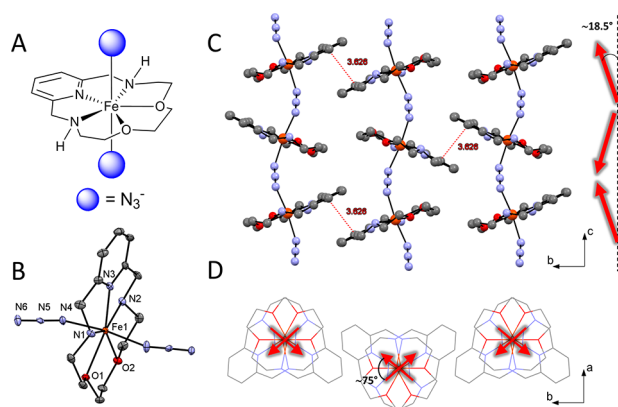
Figure 2. (A) Schematic illustration of the complex cation in **1**, (B) a part of the 1D polymeric azido-bridged structure in **1**, (C) $\pi-\pi$ stacking interactions forming a 2D layered crystal structure, and (D) a view of the 1D chains arrangement in the 2D layers of **1**. Hydrogen atoms were omitted for clarity.

RESULTS AND DISCUSSION

Complex **1** was prepared *via* mixing of $Fe(ClO_4)_2 \cdot 6H_2O$ and L[39,40] in methanol followed by addition of aqueous solution of

Table 1. Crystal Data and Structure Refinements for Complex 1

| Compound	1
Formula	$C_{13}H_{21}ClFeN_6O_6$
M_r	448.66
Temperature (K)	120(2)
Wavelength (Å)	0.71073
Crystal system	Monoclinic
Space group	$P2_1/c$
a (Å)	9.6616(6)
b (Å)	16.8895(10)
c (Å)	11.6736(6)
α (deg)	90
β (deg)	104.850(2)
γ (deg)	90
V, Å^3	1841.27(18)
Z	4
D_{calc}, g cm^{-3}	1.618
μ, mm^{-1}	1.009
$F(000)$	928
Θ range for data collection (deg)	2.412–26.498
Refl. collected	27381
Independent refl.	3820
R(int)	0.0770
Data/restraints/parameters	3820/0/250
Completeness to θ (%)	99.9
Goodness-of-fit on F^2	1.121
$R1$, $wR2$ $(I > 2\sigma(I))^a$	0.0461, 0.0810
$R1$, $wR2$ (all data)^a	0.0657, 0.0882
Largest diff. peak and hole/A^{-3}	0.408 and − 0.464
CCDC number	1852392

$^a R_1 = \sum(|F_o| - |F_c|)/\sum|F_c|$; $wR_2 = [\sum w(F_o^2 - F_c^2)^2/\sum w(F_o^2)^2]^{1/2}$.

NaN$_3$ under inert argon atmosphere (see Experimental Section for details). The presence of Fe(III) species was excluded by measurement of the ^{57}Fe Mössbauer spectrum (Figure S1, Table S1). The X-ray analysis (Table 1, Table 2, and Figure 2) revealed the molecular structure of the complex, which

Table 2. Selected Bond Lengths (Å) and Angles (deg) for Complex 1

| Distances	
Fe(1)−N(1)	2.256(3)
Fe(1)−N(2)	2.238(2)
Fe(1)−N(3)	2.181(2)
Fe(1)−O(1)	2.3181(19)
Fe(1)−O(2)	2.283(2)
Fe(1)−N(4)	2.155(2)
Fe(1)−N(6)$^{\#1}$	2.156(2)
Angles	
N(3)−Fe(1)−N(1)	73.18(9)
N(3)−Fe(1)−N(2)	73.46(9)
N(1)−Fe(1)−O(1)	73.18(8)
N(2)−Fe(1)−O(2)	72.79(8)
O(2)−Fe(1)−O(1)	69.49(7)
N(4)−Fe(1)−N(6)$^{\#1}$	172.60(10)
N(5)−N(6)−Fe(1)$^{\#2}$	128.1(2)
N(5)−N(4)−Fe(1)	127.5(2)
Torsion angles	
N(6)−N(4)−N(6)$^{\#1}$−N(4)	174.8(2)
Fe(1)−N(4)−N(6)$^{\#1}$−Fe(1)$^{\#2}$	124.9(2)

$^{\#1}x, -y + 1/2, z + 1/2.$ $^{\#2}x, -y + 1/2, z - 1/2.$
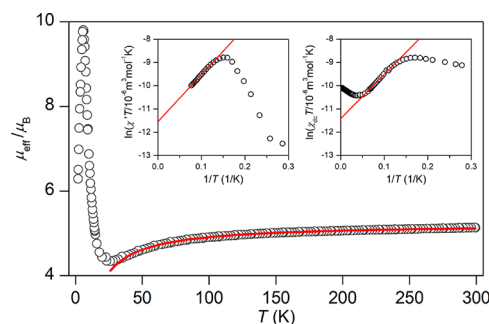
Figure 3. Temperature dependence of the effective magnetic moment for **1**. The red full line corresponds to the fit according to eq 1 with $J = -2.14$ cm^{-1} and g = 2.13. *Inset*: The analysis of χT data with $\chi'T = C_{eff} \times \exp(\Delta_\xi/kT)$ using zero-field ac susceptibility measured at $f = 1$ Hz (*left*) and dc susceptibility measured at $B_{dc} = 0.1$ T (*right*).

contains seven-coordinate Fe(II) atoms having pentagonal bipyramidal geometry with the macrocycle **L** coordinated in the equatorial pentagonal plane with an N$_3$O$_2$ donor set, and the azido ligands coordinated in axial positions (Figure 2A,B). The Fe−N$_{py}$ distance 2.181(2) Å is significantly shorter than other Fe−N distances (2.238(2) and 2.256(3) Å) in the equatorial plane, while the Fe−N$_{azido}$ distances (2.155(2) and 2.156(2) Å) are the shortest of all the Fe−N bond lengths. Concerning also the Fe−O distances (2.3181(19) and 2.283(2) Å), the pentagonal bipyramid is slightly axially compressed. The azido ligands have end-to-end (μ-1,3 or 2.11 in Harris notation)[14] coordination mode and act as bridging ligands between the pentagonal Fe(II) units to provide a 1D zigzag chain (Figure 2C). The metal-azido-metal unit has a large Fe−N(4)−N(6)−Fe torsion angle of − 124.9° with the Fe−N$_{azido}$−N$_{azido}$ angles of 127.5(2)° and 128.1(2)°. The Fe···Fe intrachain distance is 5.847 Å and the dihedral angle between the pentagonal FeN$_3$O$_2$ least-squares planes is 37.0°, and thus, the angle between the c axis and N$_{azido}$−Fe−N$_{azido}$ vector can be reckoned as 18.5° (Figure 2C). Moreover, the angle of ∼ 75° was found between the projections of these
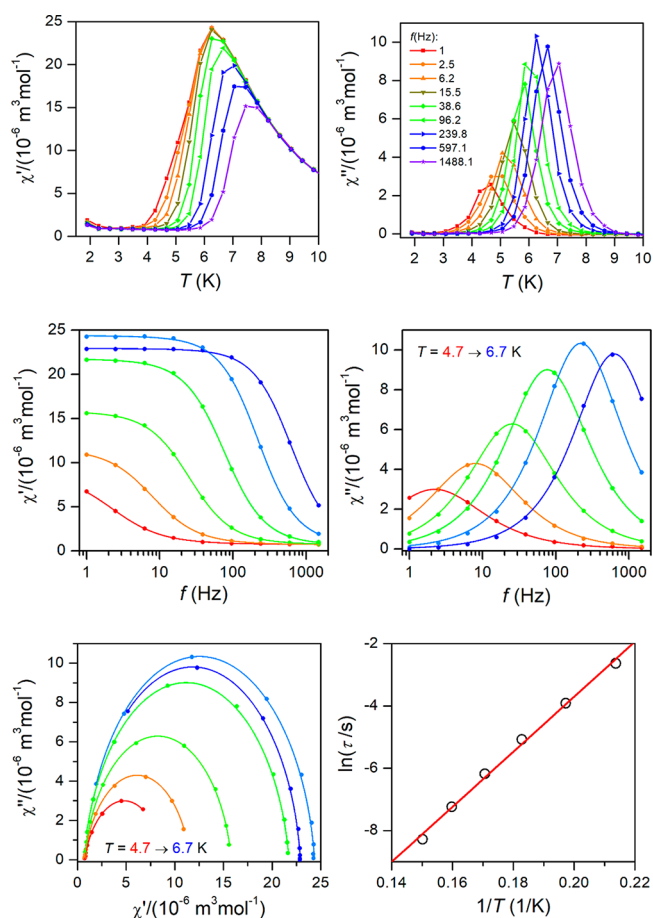
Figure 4. Analysis of ac susceptibility data for **1**. Temperature dependence of in-phase χ' and out-of-phase χ'' molar susceptibilities in zero external magnetic field (*top*). Frequency dependence of in-phase χ' and out-of-phase χ'' molar susceptibilities in zero external magnetic field (*middle*); the Argand (Cole–Cole) plot (*left-down*, full lines—fitted data using Debye's model). Fit of resulting relaxation times according to the Arrhenius equation (*right-down*).

vectors into the ab plane (Figure 2D). These 1D-chains are connected to each other via $\pi-\pi$ stacking interactions ($C_g \cdots C_g$ = 3.626 Å) between the pyridine units (Figure 2C), providing the shortest interchain Fe···Fe distance 8.437 Å and, thus, forming a supramolecular 2D-layered structure. Perchlorate anions are located in between these 2D layers and separate them (Figure S2, Table S2). The crystal structure is stabilized by a network of the N···N, N···O, N-H···O, C-H···O, and C-H···N noncovalent contacts (Table S2).

The results of dc magnetic measurements are displayed in Figure 3 as the temperature dependence (2–300 K) of the effective magnetic moment (μ_{eff}/μ_B). The value of μ_{eff}/μ_B = 5.12 (χT = 3.28 cm^{-3} K mol^{-1}) at room temperature is slightly higher than the theoretical spin only value (μ_{eff}/μ_B = 4.90, χT = 3.00 cm^{-3} K mol^{-1} for S = 2 and g = 2.0) due to a substantial contribution of the orbital angular momentum resulting in high magnetic anisotropy of the Fe^{II} atom in the pentagonal bipyramidal environment. Upon cooling, the μ_{eff}/μ_B value slightly decreased to a minimum of 4.34 at 26.0 K, which is due to weak AF interactions within the chain; then it sharply increased to a maximum of 9.80 at 6.2 K, suggesting onset of the ferromagnetism; and it finally dropped down to 6.29 at 2.0 K indicating saturation of the magnetization.

To estimate the AF exchange interactions within the chain, the temperature-dependent dc data above 25 K were fitted via the spin Hamiltonian for closed finite size ring (N = 7) mimicking 1D infinite chain magnetic behavior

$$\hat{H}^{1D} = -J(\vec{S}_1 \cdot \vec{S}_N) - J \sum_{i=1}^{N-1} (\vec{S}_1 \cdot \vec{S}_{i+1}) + \mu_B B g_i \hat{S}_z \tag{1}$$

which provided J = − 2.14 cm^{-1} and g = 2.13 confirming the AF interaction between the Fe(II) centers mediated by end-to-end azido bridges (Figure 3).

To further explore the nature of the magnetic behavior of **1**, additional ac and dc magnetic measurements were performed. First, the ac susceptibility was measured in zero static magnetic field as shown in Figure 4. Both in-phase (χ') and out-of-phase (χ'') magnetic susceptibility signals below 9 K go through a maximum with a strong frequency dependence reflecting the
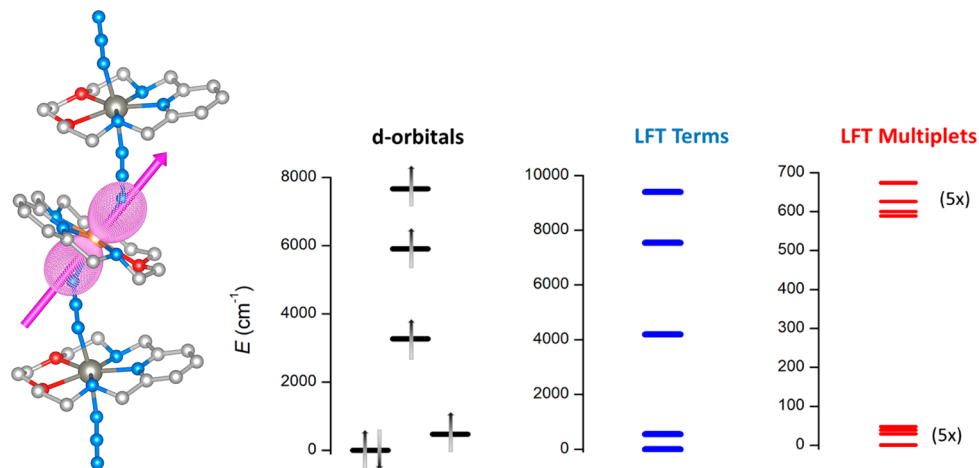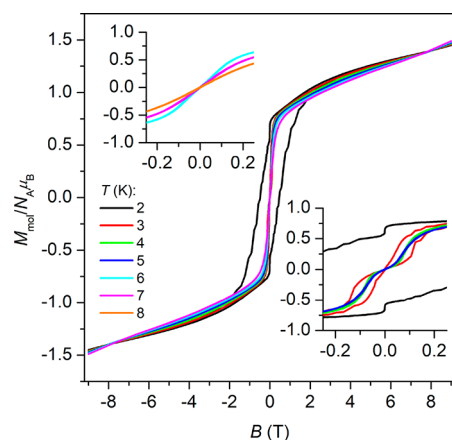

Figure 5. *Left*: the molecular structure of $[N_3(L)Zn(\mu_{1,3}\text{-}N_3)Fe(L)(\mu_{1,3}\text{-}N_3)Zn(L)N_3]$ derived from the experimental X-ray geometry of **1** used for CASSCF/NEVPT2 calculation overlaid with the three-dimensional plot of the calculated molar magnetization at T = 2 K and B = 0.5 T and showing also the easy axis of the D-tensor with the arrow. *Right*: The plots of d-orbitals splitting calculated by *ab initio* ligand field theory (AILFT) using the CASSCF/NEVPT2 method, low-lying ligand-field terms and ligand-field multiplets. *Comment*: the first excited LFT quintet term (548 cm^{-1}) dominantly contributes to the D-parameter (see Table S4–S6).

Table 3. Comparison of Selected Structural and Magnetic Parameters of Studied Complex 1 and Previously Published Complexes 2 and 3
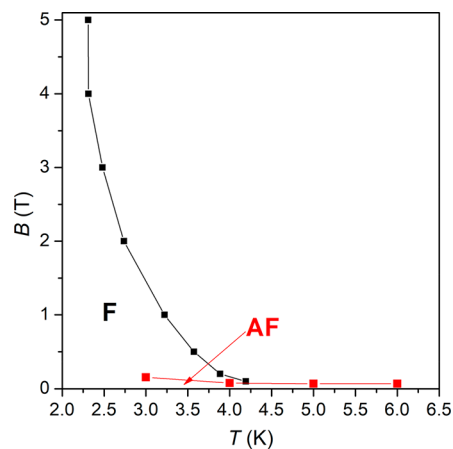
complex	Fe···Fe intrachain distance (Å)	Fe···Fe interchain distance (Å)	canting angle (deg) (X-ray)	canting angle (deg) (dc data)	torsion angle (deg)[a] (X-ray)	C_{eff} (10^{-6} m³ mol⁻¹ K)
1	5.847	8.437	18.5	11	−124.9	9.71 (ac)/11.11(dc)
2[32]	5.387	8.471	7	6.3	−5.4	8.29 (dc)
3[33]	5.296	12.0	6	7.5	+9.8	10.68

complex	J (cm⁻¹)	g	U_{eff} (K)	τ_0 (10^{-10} s)	Δ_ξ (K)	C_{eff} (cm³ mol⁻¹ K)	Δ_{ZFS} (K)
1	−2.14	2.13	87.5	5.27	19.0/20.2	0.77 (ac)/0.88 (dc)	67.3
2[32]	−4.35	2.20	35.9	56	15.8	0.66 (dc)	20.1
3[33]	−4.13	2.13	26.1	8.3	6.0	0.85 (dc)	20.0

[a]Defined as Fe−N(4)−N(6)−Fe in **1** and Fe−N−C−Fe in **2** and **3**.
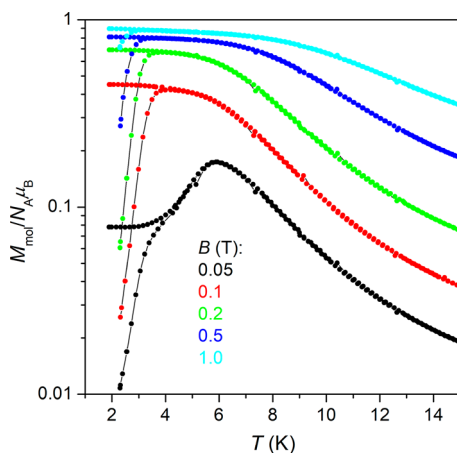
Figure 6. ZFC/FC magnetization curves at various magnetic fields for complex **1**.

Figure 8. Magnetic phase diagram for **1**. The black points were obtained from ZFC magnetization curves and red points from dM_{mol}/dB curves. The lines are a guide for the eyes.

Figure 7. Magnetic hysteresis loops at various temperatures for complex **1**.

slow relaxation of the magnetization typical for SCMs. Several maxima in the χ'' vs T plot were found and using the one-component Debye's model allowed us to calculate isothermal (χ_T) and adiabatic (χ_S) susceptibilities, relaxation times (τ), and distribution parameters (α) (Table S3) and to construct the Argand (Cole−Cole) plot (Figure 4).

The relaxation times were fitted to the Arrhenius law $\tau = \tau_0 \cdot \exp(\Delta_\tau / kT)$, which provided the effective energy barrier $\Delta_\tau = 87.5$ K with the pre-exponential factor $\tau_0 = 5.27 \times 10^{-10}$ s and confirmed that the Orbach process is the single process governing the relaxation mechanism. The SCM behavior of **1** originates in a spin-canting structure within the homospin

chain, and the spin canting angle equal to 11° was estimated from the isothermal magnetization data (Figure S3). This value is slightly lower than that obtained from the X-ray analysis (18.5°) probably because the magnetic axis is slightly tilted away from the N_{azido}−Fe−N_{azido} vector (Figure 5).

To further explore the SCM properties of **1**, the temperature dependence of the correlation length (ξ) was calculated from the magnetic susceptibility data. The analysis was based on the fact that in 1D spin chains (Ising-like or anisotropic Heisenberg chains), the product of $\chi'T$ obeys a thermally activated behavior according to $\chi'T = C_{eff} \times \exp(\Delta_\xi / kT)$, where C_{eff} is the effective Curie constant and Δ_ξ is the energy needed to create a domain wall within the chain.[5,8] The linear regression yielded $C_{eff} = 9.71 \times 10^{-6}$ m³ mol⁻¹ K and $\Delta_\xi = 20.2$ K for ac susceptibility measured at $f = 1$ Hz, and similar values, $C_{eff} = 11.11 \times 10^{-6}$ m³ mol⁻¹ K and $\Delta_\xi = 19.0$ K, were also obtained from dc susceptibility (Figure 3 inset). The values of C_{eff} are similar to those found for two other Fe(II) homospin SCM reported so far − Table 3. Both Δ_ξ and Δ_τ were determined at low temperatures; thus, we can presume that this SCM behaves in the finite-chain size limit for which holds $\Delta_\tau = \Delta_\xi + \Delta_{zfs}$.[5,8] Here, the first term is connected to the isotropic exchange as $\Delta_\xi = 2 |J|S^2$ and using the fitted J-value from eq 1 ($J = −2.14$ cm⁻¹), Δ_ξ is calculated to be 24.6 K (17.1 cm⁻¹), which is close to the values determined from ac and dc susceptibility data, $\Delta_\xi = 19.0$−20.2 K. The second term, Δ_{zfs}, originates from the single-ion anisotropy and it holds $\Delta_{zfs} = |D|S$.[25,8] Then, $\Delta_{zfs} = \Delta_\tau − \Delta_\xi = (87.5 − 20.2)$ K = 67.3 K (46.8 cm⁻¹), so the axial ZFS parameter $|D| = 11.7$ cm⁻¹.

Table 4. Comparison of ZFS Parameters and Parameters Describing SMM/SCM Properties for so Far Studied Seven-Coordinate Fe(II) Complexes

Mononuclear complexes	D/cm^{-1}	E/D	g	$\tau_0/10^{-10}$ s	U_{eff}/K	ref.
[Fe(**L2**)(H$_2$O)$_2$]Cl$_2$	−17.2	0.209	2.12			30
[Fe(H$_2$**L3-Ph**)Cl$_2$]	−13.3	0.001	2.31	a	a	26
[Fe(H$_2$**L3-Ph**)(H$_2$O)(CH$_3$OH)]Cl$_2$	−4.0	0.005	2.28			27
[Fe(H$_2$**L3-biPh**)(CH$_3$OH)Cl]Cl	−6.3	0.025	2.14			27
[Fe(H$_2$**L3-NH$_2$**)Cl$_2$]	−13.0	0.254	2.16	50	53	27
[Fe(**L5**)](ClO$_4$)$_2$[b]	−7.4	0	2.13			40
[Fe(**L6**)][c]	−9.6	0.006	2.11	d	d	54
Homonuclear complexes						
{[Fe(**L2**)(CN)][BF$_4$]}$_n$ (**2**)				56	35.9	32
{[Fe(**L1**)(CN)](ABSA)}$_n$ (**3**)				8.3	26.1	33
Heteronuclear complexes						
[{Fe(H$_2$**L3-Ph**)}{Ni(CN)$_4$}]$_n$	−10.7	0.011	2.22	20	49	26
{[{Cr(**L3-Ph**)(CN)$_2$}{Fe(H$_2$**L3-NH$_2$**)}](PF$_6$)}$_n$				0.162	113	29
[{Fe(**L1**)(H$_2$O)}$_2$Cr(CN)$_6$](ClO$_4$)	−4.7		2.09	14	44.3	55
[{(H$_2$O)Fe(**L2**)}{Nb(CN)$_8$}{Fe(**L2**)}]$_n$	∼ − 16			0.46	74	30
[{Fe(H$_2$**L3-NH$_2$**)}{Ni(CN)$_4$}]$_n$	−8.3	0.217	2.18			27
[{Fe$_3$(H$_2$**L3-biPh**)$_3$(H$_2$O)$_2$}{W(CN)$_8$}$_2$]	−11.0/−4.5[e]		2.07	4.6	35	27

[a]Ac susceptibility data were measured, but no parameters were given. [b]L5 = 3,12-bis(2-methylpyridine)-3,12,18-triaza-6,9-dioxabicyclo[12.3.1]-octadeca-1,14,16-triene. [c]L6 = 3,12-bis(carboxymethyl)-3,12,18-triaza-6,9-dioxabicyclo[12.3.1]octadeca-1,14,16-triene. [d]Very weak out-of phase signal of ac susceptibility was detected upon applying static magnetic field — no parameters obtained. [e]Two chemically nonequivalent Fe(II) units are present.

To endorse this estimate, the post-Hatree-Fock calculations of ZFS parameters were done using the state-averaged complete-active-space self-consistent field (SA-CASSCF) method complemented by N-electron valence second-order perturbation theory (NEVPT2) employing ORCA 4.0 software. The calculations were done for linear trinuclear molecular fragment [N$_3$(**L**)Zn($\mu_{1,3}$-N$_3$)Fe(**L**)($\mu_{1,3}$-N$_3$)Zn(**L**)-N$_3$] derived from the experimental X-ray geometry of **1** (Figure 5), in which two terminal iron(II) atoms were replaced by diamagnetic zinc(II) atoms. As a result, $D = -11.4$ cm^{-1} and $E/D = 0.131$ were calculated. The computed D-value is in a very good agreement with the above calculated value of $|D| = 11.7$ cm^{-1}, indirectly supporting our analysis. Moreover, the CASSCF/NEVPT2 D-value suggests large magnetic anisotropy with the easy axis located perpendicular to the macrocyclic ligand **L** plane and close to the N$_{azido}$-Fe-N$_{azido}$ direction as visualized in Figure 5. The magnetic anisotropy is also visualized by a three-dimensional plot of the molar magnetization, which was calculated using matrices from CASSCF/NEVPT2 calculation of the spin−orbit coupling **H**^{SOC}, the spin momentum operators (**S**$_x$, **S**$_y$, **S**$_z$), and the orbital momentum operators (**L**$_x$, **L**$_y$, **L**$_z$). Then, energy levels for any strength and orientation of the magnetic field are derived by diagonalization of the matrix **H** defined as

$$\mathbf{H} = \mathbf{H}^{SOC} + \mu_B(\mathbf{L} + g_e\mathbf{S})\cdot\mathbf{B} \qquad (2)$$

However, the inspection of calculated energy spectrum also revealed low-lying excited spin states ≈ 600 cm^{-1}, which to some part limits the utilization of the spin Hamiltonian formalism (Figure 5, right). In ideal symmetry of the ligand field corresponding to the pentagonal-bipyramid, D$_{5h}$, the 3d^6 electronic configuration for Fe(II) results in the orbitally degenerate ground state of E-type due to the degeneracy of the lowest d$_{xz}$ and d$_{yz}$ orbitals. In the complex **1**, this degeneracy is only partially quenched as is evident from the energy spectrum of d-orbitals calculated by *ab initio* ligand field theory (AILFT) using the CASSCF/NEVPT2 method (Figure 5, left).

Therefore, there is a close lying LFT term (548 cm^{-1}) above the ground state (Figure 5, middle), which is split upon including the spin−orbit interactions to quintet located close to 600 cm^{-1}. Further inspection also revealed that the first excited quintet dominantly contributes to the D-parameter (Table S4−S6), which emphasizes the role of the orbital angular momentum for ZFS. To summarize, the SCM properties of **1** were established and since $|D/J| > 4/3$, the SCM behaves close to the Ising limit.

The inspection of the isothermal susceptibility χ_T vs T curve from fitted zero-field ac susceptibility data revealed the maximum at $T_N = 6.3$ K (Table S3). This indicates AF ordering, mostly caused by the interchain interactions in the solid state. The coexistence of AF ordering and SCM behavior has already been reported[9] for some heterospin[10] and homospin[11,32] SCM compounds. Therefore, additional zero-field-cooled magnetization (ZFCM) and field-cooled magnetization (FCM) were measured at different static magnetic fields (Figure 6). Both ZFCM/FCM curves measured at B = 0.05 T show a maximum at $T = 5.9$ K, confirming AF ordering, and furthermore these curves diverge at blocking temperature $T_B = 4.3$ K, indicating onset of the ferromagnetism. Analogous ZFCM/FCM curves measured at higher magnetic fields, $B = 0.1, 0.2, 0.5, 1.0$ and up to 5 T, showed no maxima for FCM curves, just a small shift of T_B to lower temperature as depicted in Figure 6. Such behavior is characteristic for the metamagnets; thus, the hysteresis loops were measured at various temperatures (Figure 7), which revealed S-shaped curves for $T = 3-6$ K. On further cooling, the hysteresis loop is opening at $T = 3$ K, showing the butterfly hysteresis loops, and the typical hysteresis loop for the ferromagnets is observed at $T = 2$ K with the coercive field 0.48 T. The critical field was calculated from dM_{mol}/dB virgin magnetization curves and spans the interval $B_c = 0.067-0.106$ T. This data helped us to construct the magnetic phase diagram for **1** shown in Figure 8.

Finally, the results obtained for compound **1** were compared with those for previously studied cyanido-bridged SCMs

$\{[Fe(\textbf{L2})(CN)][BF_4]\}_n$ (**2**) and $\{[Fe(\textbf{L1})(CN)](ABSA)\}_n$ (**3**)—selected structural and magnetic parameters are listed in Table 3.

The isotropic exchange parameter $J = -2.14$ cm^{-3} ($g = 2.13$) in **1** is about one-half of that found in **2** ($J = -4.35$ cm^{-3})[32] or in **3** ($J = -4.13$ cm^{-3}).[33] This is in accordance with the longer Fe···Fe distance found for the azido bridge (5.847 Å) in comparison with the cyanido one (5.387 Å).[32]

The energy needed to create a domain wall within the chain, Δ_ξ, is the highest for **1**, while it is lower for **2** and **3**. Therefore, not only the highest Δ_ξ, but rather the largest $\Delta_{zfs} = 67.3$ K, which is more than three-times larger than in case of **2** and **3**, could account for the highest Δ_τ for **1** in this group, which means that the pentagonal-bipyramidal Fe(II) unit in **1** shows the largest magnetic anisotropy. The obtained value of the axial ZFS parameter $|D| = 11.7$ cm^{-1} for **1** is moderate in comparison with other seven-coordinate mono-/polynuclear Fe(II) complexes (Table 4), for which $|D|$-values were found in the range 4−17 cm^{-1}.[54,55] Compound **1** has the largest canting angle, which is a result of the different coordination fashion of the azido ligand having significantly higher torsion angle in comparison with the cyanido one. Large canting angle is furthermore manifested in magnetic properties as can lead to larger noncompensated magnetization of individual chains, which then results in stronger interchain dipolar interactions. This would explain ferromagnetic hysteresis in **1** measured in static magnetic field in contrast to compound **2** with similar interchain distance, where ZFC/FC curves did not bifurcate down to 2 K and magnetic hysteresis was found only upon sweeping magnetic field with a sweep rate of 500 Oe/s.

CONCLUSIONS

To conclude, the reported Fe(II) 1D chain compound possesses a large axial anisotropy and weak intrachain AF coupling, which result in spin-canted chain magnetic structure acting as homospin SCM with $\Delta_\tau = 87.5$ K. The most likely, the highest Δ_τ among homospin seven-coordinate Fe(II) SCM is related to significant single-ion zero-field splitting of the Fe(II) complex subunit, thus emphasizing the role of rational design for improving magnetic anisotropy properties. Moreover, the SCM feature coexists with metamagnetic behavior characterized with the Neel temperature of 6.3 K and the critical field of 0.07−0.11 T, probably caused by weak interchain interactions. The 3D ferromagnetic ordering manifests itself in magnetic hysteresis at 2 K with large coercive field 0.48 T. To the best of our knowledge, this is the first example of the exclusively azido-bridged homospin Fe(II)-based SCM.

ASSOCIATED CONTENT

S **Supporting Information**

The Supporting Information is available free of charge on the ACS Publications website at DOI: 10.1021/acs.inorgchem.8b01798.

> Additional data concerning X-ray analysis and magnetic measurements for **1** (PDF)

Accession Codes

CCDC 1852392 contains the supplementary crystallographic data for this paper. These data can be obtained free of charge via www.ccdc.cam.ac.uk/data_request/cif, or by emailing data_request@ccdc.cam.ac.uk, or by contacting The Cam-

bridge Crystallographic Data Centre, 12 Union Road, Cambridge CB2 1EZ, UK; fax: +44 1223 336033.

AUTHOR INFORMATION

Corresponding Author

*Fax: +420 585634357, Tel: +420 585634545, e-mail: zdenek.travnicek@upol.cz.

ORCID

Bohuslav Drahoš: 0000-0003-4298-4530
Radovan Herchel: 0000-0001-8262-4666
Zdeněk Trávníček: 0000-0002-5890-7874

Notes

The authors declare no competing financial interest.

REFERENCES

(1) Regueiro-Figueroa, M.; Lima, L. M.; Blanco, V.; Esteban-Gomez, D.; de Blas, A.; Rodriguez-Blas, T.; Delgado, R.; Platas-Iglesias, C. Reasons behind the relative abundances of heptacoordinate complexes along the late first-row transition metal series. *Inorg. Chem.* **2014**, *53*, 12859−12869.

(2) Bar, A. K.; Pichon, C.; Sutter, J.-P. Magnetic anisotropy in two- to eight-coordinated transition−metal complexes: Recent developments in molecular magnetism. *Coord. Chem. Rev.* **2016**, *308*, 346−380.

(3) Liu, J.; Chen, Y.-C.; Liu, J.-L.; Vieru, V.; Ungur, L.; Jia, J.-H.; Chibotaru, L. F.; Lan, Y.; Wernsdorfer, W.; Gao, S.; Chen, X.-M.; Tong, M.-L. A Stable Pentagonal Bipyramidal Dy(III) Single-Ion Magnet with a Record Magnetization Reversal Barrier over 1000 K. *J. Am. Chem. Soc.* **2016**, *138*, 5441−5450.

(4) Bar, A. K.; Kalita, P.; Sutter, J. P.; Chandrasekhar, V. Pentagonal-Bipyramid Ln(III) Complexes Exhibiting Single-Ion-Magnet Behavior: A Rational Synthetic Approach for a Rigid Equatorial Plane. *Inorg. Chem.* **2018**, *57*, 2398−2401.

(5) Coulon, C.; Miyasaka, H.; Clérac, R. In *Single-Molecule Magnets and Related Phenomena*; Winpenny, R., Ed.; Springer Berlin Heidelberg: Berlin, Heidelberg, 2006; pp 163−206.

(6) Gatteschi, D.; Vindigni, A. In *Molecular Magnets: Physics and Applications*; Bartolomé, J., Luis, F., Fernández, J. F., Ed.; Springer Berlin Heidelberg: Berlin, Heidelberg, 2014; pp 191−220.

(7) Coulon, C.; Pianet, V.; Urdampilleta, M.; Clérac, R. In *Molecular Nanomagnets and Related Phenomena*; Gao, S., Ed.; Springer Berlin Heidelberg: Berlin, Heidelberg, 2015; pp 143−184.

(8) Miyasaka, H.; Julve, M.; Yamashita, M.; Clérac, R. Slow Dynamics of the Magnetization in One-Dimensional Coordination Polymers: Single-Chain Magnets. *Inorg. Chem.* **2009**, *48*, 3420−3437.

(9) Sun, H.-L.; Wang, Z.-M.; Gao, S. Strategies towards single-chain magnets. *Coord. Chem. Rev.* **2010**, *254*, 1081−1100.

(10) Miyasaka, H.; Takayama, K.; Saitoh, A.; Furukawa, S.; Yamashita, M.; Clérac, R. Three-Dimensional Antiferromagnetic Order of Single-Chain Magnets: A New Approach to Design Molecule-Based Magnets. *Chem. - Eur. J.* **2010**, *16*, 3656−3662.

(11) Bernot, K.; Luzon, J.; Sessoli, R.; Vindigni, A.; Thion, J.; Richeter, S.; Leclercq, D.; Larionova, J.; van der Lee, A. The Canted Antiferromagnetic Approach to Single-Chain Magnets. *J. Am. Chem. Soc.* **2008**, *130*, 1619−1627.

(12) Wang, Y.-Q.; Yue, Q.; Qi, Y.; Wang, K.; Sun, Q.; Gao, E.-Q. Manganese(II), Iron(II), and Mixed-Metal Metal−Organic Frameworks Based on Chains with Mixed Carboxylate and Azide Bridges: Magnetic Coupling and Slow Relaxation. *Inorg. Chem.* **2013**, *52*, 4259−4268.

(13) Deng, Y.-F.; Han, T.; Xue, W.; Hayashi, N.; Kageyama, H.; Zheng, Y.-Z. An Ising iron(ii) chain exhibits a large finite-size energy barrier and "hard" magnetic behaviour. *Dalton Trans* **2017**, *46*, 1449−1454.

(14) Escuer, A.; Esteban, J.; Perlepes, S. P.; Stamatatos, T. C. The bridging azido ligand as a central "player" in high-nuclearity 3d-metal cluster chemistry. *Coord. Chem. Rev.* **2014**, *275*, 87−129.

(15) Hoshino, N.; Iijima, F.; Newton, G. N.; Yoshida, N.; Shiga, T.; Nojiri, H.; Nakao, A.; Kumai, R.; Murakami, Y.; Oshio, H. Three-way switching in a cyanide-bridged [CoFe] chain. *Nat. Chem.* **2012**, *4*, 921.

(16) Dong, D.-P.; Liu, T.; Kanegawa, S.; Kang, S.; Sato, O.; He, C.; Duan, C.-Y. Photoswitchable Dynamic Magnetic Relaxation in a Well-Isolated {Fe2Co} Double-Zigzag Chain. *Angew. Chem., Int. Ed.* **2012**, *51*, 5119−5123.

(17) Jiang, W.; Jiao, C.; Meng, Y.; Zhao, L.; Liu, Q.; Liu, T. Switching single chain magnet behavior via photoinduced bidirectional metal-to-metal charge transfer. *Chem. Sci.* **2018**, *9*, 617−622.

(18) (a) Gavey, E. L.; Pilkington, M. Coordination complexes of 15-membered pentadentate aza, oxoaza and thiaaza Schiff base macrocycles "Old Complexes Offer New Attractions". *Coord. Chem. Rev.* **2015**, *296*, 125−152. (b) Bar, A. K.; Pichon, C.; Sutter, J.-P. Magnetic anisotropy in two- to eight-coordinated transition−metal complexes: Recent developments in molecular magnetism. *Coord. Chem. Rev.* **2016**, *308*, 346−380.

(19) Rezaeivala, M.; Keypour, H. Schiff base and non-Schiff base macrocyclic ligands and complexes incorporating the pyridine moiety − The first 50 years. *Coord. Chem. Rev.* **2014**, *280*, 203−253.

(20) Haque, A.; Ilmi, R.; Al-Busaidi, I. J.; Khan, M. S. Coordination chemistry and application of mono- and oligopyridine-based macrocycles. *Coord. Chem. Rev.* **2017**, *350*, 320−339.

(21) Drahoš, B.; Herchel, R.; Trávníček, Z. Structural, Magnetic, and Redox Diversity of First-Row Transition Metal Complexes of a Pyridine-Based Macrocycle: Well-Marked Trends Supported by Theoretical DFT Calculations. *Inorg. Chem.* **2015**, *54*, 3352−3369.

(22) Drahoš, B.; Herchel, R.; Trávníček, Z. Structural and magnetic properties of heptacoordinated MnII complexes containing a 15-membered pyridine-based macrocycle and halido/pseudohalido axial coligands. *RSC Adv.* **2016**, *6*, 34674−34684.

(23) Drahoš, B.; Herchel, R.; Trávníček, Z. Impact of Halogenido Coligands on Magnetic Anisotropy in Seven-Coordinate Co(II) Complexes. *Inorg. Chem.* **2017**, *56*, 5076−5088.

(24) Ruamps, R.; Batchelor, L. J.; Maurice, R.; Gogoi, N.; Jiménez-Lozano, P.; Guihéry, N.; de Graaf, C.; Barra, A.-L.; Sutter, J.-P.; Mallah, T. Origin of the Magnetic Anisotropy in Heptacoordinate NiII and CoII Complexes. *Chem. - Eur. J.* **2013**, *19*, 950−956.

(25) Huang, X.-C.; Zhou, C.; Shao, D.; Wang, X.-Y. Field-Induced Slow Magnetic Relaxation in Cobalt(II) Compounds with Pentagonal Bipyramid Geometry. *Inorg. Chem.* **2014**, *53*, 12671−12673.

(26) Bar, A. K.; Pichon, C.; Gogoi, N.; Duhayon, C.; Ramasesha, S.; Sutter, J.-P. Single-ion magnet behaviour of heptacoordinated Fe(ii) complexes: on the importance of supramolecular organization. *Chem. Commun.* **2015**, *51*, 3616−3619.

(27) Bar, A. K.; Gogoi, N.; Pichon, C.; Goli, V. M. L. D. P.; Thlijeni, M.; Duhayon, C.; Suaud, N.; Guihéry, N.; Barra, A.-L.; Ramasesha, S.; Sutter, J.-P. Pentagonal Bipyramid FeII Complexes: Robust Ising-Spin Units towards Heteropolynuclear Nanomagnets. *Chem. - Eur. J.* **2017**, *23*, 4380−4396.

(28) Pichon, C.; Elrez, B.; Béreau, V.; Duhayon, C.; Sutter, J.-P. From Heptacoordinated CrIII Complexes with Cyanide or Isothiocyanate Apical Groups to 1D Heterometallic Assemblages with All-Pentagonal-Bipyramid Coordination Geometries. *Eur. J. Inorg. Chem.* **2018**, *2018*, 340−348.

(29) Pichon, C.; Suaud, N.; Duhayon, C.; Guihery, N.; Sutter, J. P. Cyano-Bridged Fe(II)-Cr(III) Single-Chain Magnet Based on Pentagonal Bipyramid Units: On the Added Value of Aligned Axial Anisotropy. *J. Am. Chem. Soc.* **2018**, *140*, 7698−7704.

(30) Venkatakrishnan, T. S.; Sahoo, S.; Brefuel, N.; Duhayon, C.; Paulsen, C.; Barra, A. L.; Ramasesha, S.; Sutter, J. P. Enhanced Ion Anisotropy by Nonconventional Coordination Geometry: Single-Chain Magnet Behavior for a [{(FeL)-L-II}(2){Nb-IV(CN)(8)}] Helical Chain Compound Designed with Heptacoordinate Fe-II. *J. Am. Chem. Soc.* **2010**, *132*, 6047−6056.

(31) Ababei, R.; Pichon, C.; Roubeau, O.; Li, Y.-G.; Bréfuel, N.; Buisson, L.; Guionneau, P.; Mathonière, C.; Clérac, R. Rational Design of a Photomagnetic Chain: Bridging Single-Molecule Magnets with a Spin-Crossover Complex. *J. Am. Chem. Soc.* **2013**, *135*, 14840−14853.

(32) Shao, D.; Zhang, S. L.; Zhao, X. H.; Wang, X. Y. Spin canting, metamagnetism, and single-chain magnetic behaviour in a cyano-bridged homospin iron(II) compound. *Chem. Commun.* **2015**, *51*, 4360−4363.

(33) Shao, D.; Zhao, X.-H.; Zhang, S.-L.; Wu, D.-Q.; Wei, X.-Q.; Wang, X.-Y. Structural and magnetic tuning from a field-induced single-ion magnet to a single-chain magnet by anions. *Inorg. Chem. Front.* **2015**, *2*, 846−853.

(34) Shao, D.; Shi, L.; Zhang, S.-L.; Zhao, X.-H.; Wu, D.-Q.; Wei, X.-Q.; Wang, X.-Y. Syntheses, structures, and magnetic properties of three new chain compounds based on a pentagonal bipyramidal Co(ii) building block. *CrystEngComm* **2016**, *18*, 4150−4157.

(35) Zhao, X.-H.; Deng, L.-D.; Zhou, Y.; Shao, D.; Wu, D.-Q.; Wei, X.-Q.; Wang, X.-Y. Slow Magnetic Relaxation in One-Dimensional Azido-Bridged CoII Complexes. *Inorg. Chem.* **2017**, *56*, 8058−8067.

(36) Wang, X.-Y.; Wang, Z.-M.; Gao, S. Detailed Magnetic Studies on Co(N3)₂(4-acetylpyridine)₂: a Weak-Ferromagnet with a Very Big Canting Angle. *Inorg. Chem.* **2008**, *47*, 5720−5726.

(37) Liu, X. T.; Wang, X. Y.; Zhang, W. X.; Cui, P.; Gao, S. Weak Ferromagnetism and Dynamic Magnetic Behavior in a Single End-to-End Azide-Bridged Nickel(II) Chain. *Adv. Mater.* **2006**, *18*, 2852−2856.

(38) Hong, C. S.; Son, S.-K.; Lee, Y. S.; Yaung-Soo Kim, Y. D.; Koo, J. Unusual Ferromagnetic Couplings in Single End-to-End Azide-Bridged Cobalt(ii) and Nickel(ii) Chain Systems. *Chem. - Eur. J.* **2001**, *7*, 4243−4252.

(39) Drahoš, B.; Kotek, J.; Hermann, P.; Lukeš, I.; Tóth, E. Mn²⁺ Complexes with Pyridine-Containing 15-Membered Macrocycles: Thermodynamic, Kinetic, Crystallographic, and ¹H/¹⁷O Relaxation Studies. *Inorg. Chem.* **2010**, *49*, 3224−3238.

(40) Antal, P.; Drahoš, B.; Herchel, R.; Trávníček, Z. Late First-Row Transition-Metal Complexes Containing a 2-Pyridylmethyl Pendant-Armed 15-Membered Macrocyclic Ligand. Field-Induced Slow Magnetic Relaxation in a Seven-Coordinate Cobalt(II) Compound. *Inorg. Chem.* **2016**, *55*, 5957−5972.

(41) Klencsar, Z.; Kuzmann, E.; Vertes, A. User-friendly software for Mossbauer spectrum analysis. *J. Radioanal. Nucl. Chem.* **1996**, *210*, 105−118.

(42) Bruker. *Apex3*; Bruker AXS Inc., Madison, Wisconsin, USA, 2015.

(43) Sheldrick, G. M. Crystal structure refinement with SHELXL. *Acta Crystallogr., Sect. C: Struct. Chem.* **2015**, *71*, 3−8.

(44) Macrae, C. F.; Bruno, I. J.; Chisholm, J. A.; Edgington, P. R.; McCabe, P.; Pidcock, E.; Rodriguez-Monge, L.; Taylor, R.; van de Streek, J.; Wood, P. A. New Features for the Visualization and Investigation of Crystal Structures. *J. Appl. Crystallogr.* **2008**, *41*, 466−470.

(45) Neese, F. Software update: the ORCA program system, version 4.0. *WIREs Comput. Mol. Sci.* **2018**, *8*, No. e1327.

(46) Malmqvist, P. A.; Roos, B. O. The CASSCF state interaction method. *Chem. Phys. Lett.* **1989**, *155*, 189−194.

(47) (a) Angeli, C.; Cimiraglia, R.; Malrieu, J.-P. N-electron valence state perturbation theory: a fast implementation of the strongly contracted variant. *Chem. Phys. Lett.* **2001**, *350*, 297−305. (b) Angeli, C.; Cimiraglia, R.; Evangelisti, S.; Leininger, T.; Malrieu, J.-P. Introduction of n-electron valence states for multireference perturbation theory. *J. Chem. Phys.* **2001**, *114*, 10252−10264. (c) Angeli, C.; Cimiraglia, R.; Malrieu, J.-P. N-electron valence state perturbation theory: A spinless formulation and an efficient

implementation of the strongly contracted and of the partially contracted variants. *J. Chem. Phys.* **2002**, *117*, 9138−9153.

(48) Weigend, F.; Ahlrichs, R. Balanced basis sets of split valence, triple zeta valence and quadruple zeta valence quality for H to Rn: Design and assessment of accuracy. *Phys. Chem. Chem. Phys.* **2005**, *7*, 3297−3305.

(49) Ganyushin, D.; Neese, F. First-principles calculations of zero-field splitting parameters. *J. Chem. Phys.* **2006**, *125*, 024103.

(50) Neese, F. Efficient and accurate approximations to the molecular spin-orbit coupling operator and their use in molecular g-tensor calculations. *J. Chem. Phys.* **2005**, *122*, 034107.

(51) Maurice, R.; Bastardis, R.; de Graaf, C.; Suaud, N.; Mallah, T.; Guihéry, N. Universal Theoretical Approach to Extract Anisotropic Spin Hamiltonians. *J. Chem. Theory Comput.* **2009**, *5*, 2977−2984.

(52) Weigend, F. J. Hartree−Fock exchange fitting basis sets for H to Rn. *J. Comput. Chem.* **2008**, *29*, 167−175.

(53) (a) Atanasov, M.; Ganyushin, D.; Sivalingam, K.; Neese, F. In *Molecular Electronic Structures of Transition Metal Complexes II*; Mingos, D. M. P., Day, P., Dahl, J. P., Eds.; Springer Berlin Heidelberg, Berlin, Heidelberg, 2012, pp 149−220. (b) Singh, S. K.; Eng, J.; Atanasov, M.; Neese, F. Covalency and chemical bonding in transition metal complexes: An ab initio based ligand field perspective. *Coord. Chem. Rev.* **2017**, *344*, 2−25.

(54) Antal, P.; Drahoš, B.; Herchel, R.; Trávníček, Z. Structure and Magnetism of Seven-Coordinate Fe(III), Fe(II), Co(II) and Ni(II) Complexes Containing a Heptadentte 15-Membered Pyridine-Based Macrocyclic Ligand. *Eur. J. Inorg. Chem.* **2018** − accepted DOI: 10.1002/ejic.201800769.

(55) Zhang, Y. Z.; Wang, B. W.; Sato, O.; Gao, S. First Fe(II)-based cyano-bridged single molecule magnet [Cr(III)Fe(II)(2)] with a large anisotropy. *Chem. Commun.* **2010**, *46*, 6959−6961.

Příloha P5

P. Antal, B. Drahoš, R. Herchel, Z. Trávníček,

Late First-Row Transition-Metal Complexes Containing a 2‑Pyridylmethyl Pendant-Armed 15-Membered Macrocyclic Ligand. Field-Induced Slow Magnetic Relaxation in a Seven-Coordinate Cobalt(II) Compound.

Late First-Row Transition-Metal Complexes Containing a 2-Pyridylmethyl Pendant-Armed 15-Membered Macrocyclic Ligand. Field-Induced Slow Magnetic Relaxation in a Seven-Coordinate Cobalt(II) Compound

Peter Antal, Bohuslav Drahoš, Radovan Herchel, and Zdeněk Trávníček*

Department of Inorganic Chemistry, Regional Centre of Advanced Technologies and Materials, Faculty of Science, Palacký University, 17. listopadu 12, CZ-771 46 Olomouc, Czech Republic

ⓢ Supporting Information

ABSTRACT: The 2-pyridylmethyl N-pendant-armed hepta-dentate macrocyclic ligand {3,12-bis(2-methylpyridine)-3,12,18-triaza-6,9-dioxabicyclo[12.3.1]octadeca-1,14,16-triene = L} and [M(L)](ClO$_4$)$_2$ complexes, where M = Mn(II) (**1**), Fe(II) (**2**), Co(II) (**3**), Ni(II) (**4**), and Cu(II) (**5**), were prepared and thoroughly characterized, including elucidation of X-ray structures of all the compounds studied. The complexes **1**−**5** crystallize in non-centrosymmetric Sohncke space groups as racemic compounds. The coordination numbers of 7, 6 + 1, and 5 were found in complexes **1**−**3**, **4**, and **5**, respectively, with a distorted pentagonal bipyramidal (**1**−**4**) or square pyramidal (**5**) geometry. On the basis of the magnetic susceptibility experiments, a large axial zero-field splitting (ZFS) was found for **2**, **3**, and **4** (D(Fe) = −7.4(2) cm^{-1}, D(Co) = 34(1) cm^{-1}, and D(Ni) = −12.8(1) cm^{-1}, respectively) together with a rhombic ZFS (E/D = 0.136(3)) for **4**. Despite the easy plane anisotropy ($D > 0$, $E/D = 0$) in **3**, the slow relaxation of the magnetization below 8 K was observed and analyzed either with Orbach relaxation mechanism (the relaxation time τ_0 = 9.90 × 10^{-10} s and spin reversal barrier U_{eff} = 24.3 K (16.9 cm^{-1})) or with Raman relaxation mechanism (C = 2.12 × 10^{-5} and n = 2.84). Therefore, compound **3** enlarges the small family of field-induced single-molecule magnets with pentagonal-bipyramidal chromophore. The cyclic voltammetry in acetonitrile revealed reversible redox processes in **1**−**3** and **5**, except for the Ni(II) complex **4**, where a quasi-reversible process was dominantly observed. Presence of the two 2-pyridylmethyl pendant arms in L with a stronger σ-donor/π-acceptor ability had a great impact on the properties of all the complexes (**1**−**5**), concretely: (i) strong pyridine−metal bonds provided slight axial compression of the coordination sphere, (ii) substantial changes in magnetic anisotropy, and (iii) stabilization of lower oxidation states.
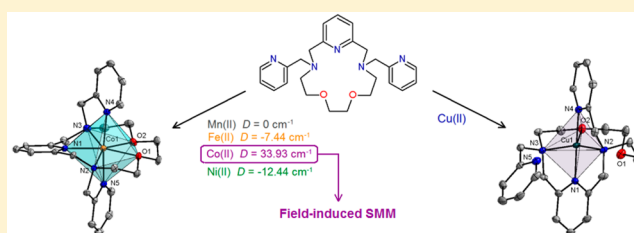
■ INTRODUCTION

Polyaza and polyoxa-aza macrocyclic ligands are very well-known for their specific coordination ability toward transition metals as well as lanthanides resulting in extraordinary properties of their complexes including high thermodynamic and kinetic stability,[1,2] stabilization of unusual oxidation states and coordination geometries,[3] catalytic properties,[4] and many others. Therefore, they have found many applications, for example, imaging agents[5] and therapeutics in medicine,[5,6] various catalysts,[4] and agents for metal recovery.[7] In recent years, more attention has been devoted to their magnetic properties in solid state and not only in context of this, seven-coordinate complexes have become a center of the interest, because they may behave as single-molecule magnets (SMMs),[8] single-chain magnets (SCMs),[9] or show spin-crossover (SCO).[10] Surprisingly, the seven-coordinate first-row transi-tion-metal ions are not common[11,12] in comparison with other coordination geometries, and furthermore their distribution along the series is not uniform. Seven-coordination is more abundant for Mn, Fe, and Co complexes (4.5%, 1.5%, and 0.8%,

respectively, of the total number of structures for given metals found in the Cambridge Structural Database (CSD)), while it is rather rare for Cu and Zn (0.12%, and 0.35%, respectively). And it is the least common in case of Ni complexes (0.08%),[12] because the Jahn−Teller theorem predicts a large distortion and a low stability of regular stereochemistry for seven-coordinate Ni(II) complexes.[13−15]

In the enormous group of polyaza and polyoxo-aza macrocyclic ligands, our attention has been focused on those with 2-pyridylmethyl pendant arm(s) or those providing seven-coordination in their metal complexes (Figure 1). The disubstituted cyclam (tpy$_2$-C, cyclam = 1,4,8,11-tetraazacyclote-tradecane) was studied in six-coordinated complexes with first-row transition metals Fe(II),[16] Ni(II),[17] or Cu(II),[18] and [Fe(tpy$_2$-C)](BF$_4$)$_2$·H$_2$O with a distorted octahedral geometry showed SCO behavior with the spin transition temperature of 150 K.[16] Extended pentaaza macrocycles with two 2-
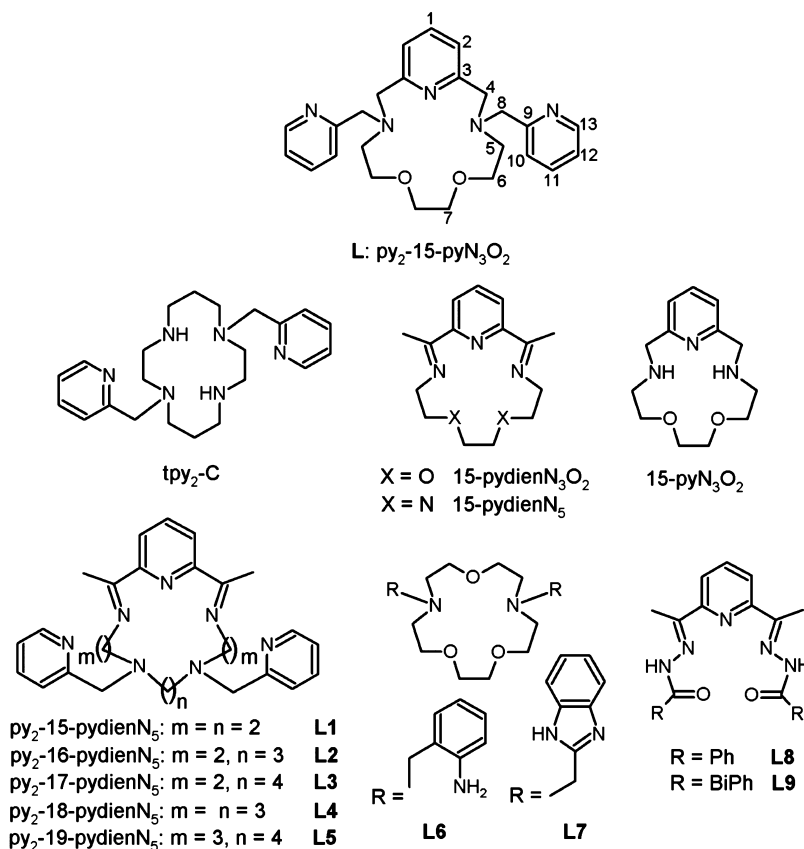
Figure 1. Structural formulas of the prepared ligand **L** with the atom numbering, together with selected 2-pyridylmethyl armed ligands and other ligands mentioned in this work.

pyridylmethyl pendant arms (**L1**−**L5**) were studied only in Mn(II) complexes.[19,20] Seven-coordinate central atoms were confirmed by X-ray analysis in [Mn(**L1**)](ClO$_4$)$_2$·CH$_3$CN,[19] and [Mn(**L4**)](ClO$_4$)$_2$·H$_2$O only,[20] in which the corresponding pentaaza macrocycle was coordinated in an equatorial plane and two nitrogen atoms from pyridine pendant arms in apical positions. Surprisingly, the magnetic properties of latter complexes in solid state were studied only sporadically in contrast to another group of seven-coordinate complexes of structurally related 15-membered macrocycles 15-pydienN$_3$O$_2$ and 15-pydienN$_5$, which have been extensively studied since 1960s[21,22,10a] and recently reviewed.[23,24] On the one hand, SCO with transition temperature of 159 K associated with one Fe−O bond break was observed in [Fe(15-pydienN$_3$O$_2$)-(CN)$_2$]·H$_2$O together with light-induced electron spin state trapping effect (LIESST) at temperature 135 K.[10a,25] On the other hand, structurally similar complex [Fe(15-pydienN$_5$)-(CN)$_2$]·H$_2$O was found only in low-spin state but also with LIESST at temperature 105 K.[26] Transition-metal complexes of these two Schiff-base ligands were previously often coupled into heteronuclear oligomeric of polymeric complexes with different cyanidometallates [M^{I}(CN)$_2$]$^{-}$,[27] [M^{II}(CN)$_4$]$^{2-}$,[9b] [M^{III}(CN)$_6$]$^{3-}$,[9a,b] or [M^{IV}(CN)$_8$]$^{4-}$,[28] (M^{I} = Ag, Au; M^{II} = Ni, Pd, Pt; M^{III} = Fe, Cr, Co; M^{IV} = Nb, Mo, W) providing information about the magnetic exchange (anti-ferromagnetic for Mn^{II}−Cr^{III}[9b] or ferromagnetic for Mn^{II}−Fe^{III}),[9a] showing ferromagnetic ordering below 12 K in [Co(15-pydienN$_3$O$_2$)]$_2$-[Cr(CN)$_6$](ClO$_4$)·8H$_2$O,[29] SCM behavior in three-dimensional (3D) polymeric [Fe(15-pydienN$_3$O$_2$)(H$_2$O)]$_2$[Cr-(CN)$_6$](ClO$_4$)·3H$_2$O[8c] (U_{eff} = 44.3 K) and in one-dimensional

(1D) polymeric {[Fe(15-pydienN$_5$)(H$_2$O)][Nb(CN)$_8$][Fe(15-pydienN$_5$)]}$_n$ with U_{eff} = 74 K,[28] or SCO and LIESST effect in [Fe(15-pydienN$_3$O$_2$)(CN)$_2$][Mn(hfac)$_2$] (where hfac = hexa-fluoroacetylacetone).[30]

This revived interest in the seven-coordinate Fe(II), Co(II), and Ni(II) complexes of 15-pydienN$_3$O$_2$, 15-pydienN$_5$, and ligands **L6**−**L9** (Figure 1) during the past decade can be attributed to their high magnetic anisotropy, which is prerequisite for their SMM behavior. For Co(II) and Ni(II) complexes of **L8** and **L9**, it has been predicted theoretically[31] and consequently also confirmed practically,[32,33] that the value of magnetic anisotropy, usually expressed as axial zero-field splitting (ZFS) parameter D, can be tuned/increased by σ-donor/π-acceptor properties of ligands in axial positions[34] and/or by the symmetry of the equatorial plane (more details are described in Discussion−Static magnetic properties). Recently, the field-induced SMM behavior was also observed/confirmed in various seven-coordinate Co(II) complexes [Co(15-pydienN$_5$)(H$_2$O)$_2$]Cl$_2$·2H$_2$O,[35] [Co(**L8**)(H$_2$O)(NO$_3$)]-(NO$_3$),[35] [Co(**L8**-2H^{+})(imidazole)$_2$)]·H$_2$O,[35] and as well as in Fe(II) complex {[Fe(**L8**)][Ni(CN)$_4$]}$_n$.[8d]

In our previous study, the complexes of a 15-pyN$_3$O$_2$ (Figure 1) with the selected first-row transition metals were investigated in detail.[36] The coordination number of 7 was observed in [M(15-pyN$_3$O$_2$)Cl$_2$]$^{0/+}$, where M = Mn(II), Fe(III), and Co(II), while in [Ni(15-pyN$_3$O$_2$)Cl$_2$] it was found to be 5 + 2. In all the cases, the central atom adopts a distorted pentagonal bipyramidal geometry, with the chlorido coligands in the axial positions. For [Cu(15-pyN$_3$O$_2$)Cl]Cl and [Zn(15-pyN$_3$O$_2$)Cl$_2$], the coordination numbers of 4 + 1 and 5

were observed, respectively, with a distorted square pyramidal geometry (τ = 0.09 and 0.17, respectively). Large axial anisotropy for Co(II) and Ni(II) complexes (D(Co) = 40.0 and D(Ni) = −6.02 cm^{-1}) and anti-ferromagnetic exchange coupling in the case of Ni(II) and Cu(II) complexes (J(Ni) = −0.48 cm^{-1}, and J(Cu) = −2.43 cm^{-1}) were observed.[36] Very recently, a series of seven-coordinate Mn(II) complexes [Mn(15-pyN$_3$O$_2$)X$_2$], where X = Br$^-$, I$^-$, N$_3^-$, NCS$^-$, and {[Mn(15-pyN$_3$O$_2$)(μ-CN)](ClO$_4$)}$_n$ was published,[37] and it was found that the influence of the axial coligands on the magnetic anisotropy was very small ($|D|$ < 0.7 cm^{-1}), and a weak anti-ferromagnetic exchange coupling (J = −1.72 cm^{-1}) was observed in the latter polymeric complex.[37]

To tune the magnetic properties of seven-coordinate first-row transition metal complexes based on macrocyclic ligands, a structurally new derivative of 15-pyN$_3$O$_2$ modified with two 2-pyridylmethyl pendant arms (py$_2$-15-pyN$_3$O$_2$ = **L** = 3,12-bis(2-methylpyridine)-3,12,18-triaza-6,9-dioxabicyclo[12.3.1]-octadeca-1,14,16-triene) was synthesized and characterized, and its Mn(II), Fe(II), Co(II), Ni(II), and Cu(II) complexes were studied in detail to reveal how the modification of 15-pyN$_3$O$_2$ with additional pendant arms with different coordination ability influences the structural, magnetic, and redox properties of the prepared complexes.

■ EXPERIMENTAL SECTION

General Methods. Elemental analysis (C, H, N) was performed on a Flash 2000 CHNO-S Analyzer (Thermo Scientific, Waltham, MA). Infrared spectra (IR) were recorded on a Thermo Nicolet NEXUS 670 FT-IR spectrometer (Thermo Nicolet, Waltham, MA) employing the ATR technique on a diamond plate in the range of 400−4000 cm^{-1}. The mass spectra (MS) were collected on an LCQ Fleet Ion Mass Trap mass spectrometer (Thermo Scientific, Waltham, MA) equipped with an electrospray ion source and three-dimensional ion-trap detector in the positive mode. The ^{1}H and ^{13}C NMR spectra were recorded at 298 K on a Varian 400 MHz (Varian, Palo Alto, CA). The signal assignments in ^{1}H and ^{13}C NMR spectra were based in part on two-dimensional COSY, HMBC, and HMQC experiments. The cyclic voltammetry was performed on an electrochemical analyzer CHI600C (CH Instrument Inc, Austin, TX). A conventional three-electrode type of cell was used with a Ag/Ag$^+$ reference electrode, a platinum wire auxiliary electrode, and a glassy carbon working electrode. The final potential values referred to standard hydrogen electrode (SHE) were obtained by using internal ferrocene/ferrocenium standard (E(Fc/Fc$^+$) = 0.655 V vs SHE).[38] The measurements were performed in argon atmosphere in CH$_3$CN solution in the presence of 0.1 M tetrabutylammonium perchlorate (TBAP) as a supporting electrolyte with scan rate of 100 mV·s^{-1} for 2 mM concentration of the complexes. The temperature-dependent (T = 1.9−300 K, B = 0.1 T) and field-dependent (B = 0−9 T, T = 2, 5, and 10 K) magnetization measurements were performed on PPMS Dynacool (Quantum Design Inc, San Diego, CA). Dynamic magnetic properties were studied by measuring alternating current (AC) susceptibility on an MPMS XL-7 SQUID magnetometer (Quantum Design Inc., San Diego, CA).

X-ray Diffraction Analysis. Single crystals of **L** suitable for X-ray diffraction analysis were prepared by recrystallization of the compound from CH$_3$CN, and single crystals of complexes **1**−**5** were formed upon slow diffusion of diethyl ether vapors into the CH$_3$CN solutions of the appropriate complex at room temperature. X-ray diffraction data of **L** and **1**−**5** were collected on a Bruker D8 QUEST diffractometer equipped with a PHOTON 100 CMOS detector using Mo Kα radiation (λ = 0.710 73 Å) at temperature of 120 K. The APEX3 software package[39] was used for data collection and reduction. The molecular structures were solved by direct methods (SHELXS) and refined by full-matrix least-squares procedure SHELXL (version 2014/7),[40] and with XShell software package.[39] Hydrogen atoms of all the

structures were found in the difference Fourier maps and refined using a rigid model, with C−H = 0.95 (CH)$_{ar}$ and C−H = 0.99 (CH$_2$) Å, and with U_{iso}(H) = 1.2U_{eq}(CH, CH$_2$). The molecular and crystal structures of all the studied compounds, depicted in Figures 3, 4, 5, 6, S2, and S3, were drawn using Diamond software.[41]

Synthesis. 2-(Chloromethyl)pyridine hydrochloride was prepared according to the literature.[42] The starting macrocycle 15-pyN$_3$O$_2$ (3,12,18-triaza-6,9-dioxabicyclo[12.3.1]octadeca-1,14,16-triene) was prepared as described previously,[43] but with some small modifications including increased temperature (60 °C) during the addition of 1,8-diamino-3,6-dioxaoctane to solution of pyridine-2,6-dicarbaldehyde and MnCl$_2$·4H$_2$O, and a different mobile phase (CH$_3$Cl/CH$_3$OH/NH$_3$ (aq), 70:15:3) during product purification via column chromatography. Other chemicals were purchased from commercial sources and used without further purification. ***Caution!*** *Although we have experienced no difficulties, perchlorate salts of metal complexes with organic ligands are potentially explosive and should be handled with care even in small quantities.*

Synthesis of 3,12-Bis(2-methylpyridine)-3,12,18-triaza-6,9-dioxabicyclo[12.3.1]octadeca-1,14,16-triene (L). 15-pyN$_3$O$_2$ (405 mg, 1.61 mmol) was dissolved in CH$_3$CN (20 mL), and potassium carbonate (1.77 g, 12.8 mmol) was added while stirring at room temperature. Then, the suspension was heated to 50 °C and stirred, and 2-(chloromethyl)pyridine hydrochloride (531 mg; 3.24 mmol) was added in small portions; the reaction mixture was heated to reflux with stirring for 14 h. After the filtration of a light brown solid, the orange filtrate was obtained, and solvent was removed by rotary evaporation. The brown oily residue was dissolved in water (20 mL) and extracted with chloroform (3 × 20 mL). The organic layer was evaporated to dryness to give a brownish oily residue. The pure ligand **L** was obtained in the form of colorless crystals after recrystallization from CH$_3$CN (386 mg). Yield: 62%.

^{1}H NMR (DMSO): δ 8.50 (H13, d,2H, $^2J_{HH}$ = 4.8 Hz), 7.77 (H11, t, 2H, $^3J_{HH}$ = 1.7 Hz), 7.67 (H1 + H10, m, 3H) 7.25 (H12, t, 2H, $^3J_{HH}$ = 6.9, 5.5 Hz), 7.22 (H2, d, 2H, $^2J_{HH}$ = 7.6 Hz), 3.99 (H6, s, 4H), 3.72 (H7, s, 4H), 3.35 (H5, t, 4H, $^3J_{HH}$ = 7.1 Hz), 3.31 (H8, s, 4H), 2.70 (H4, s, 4H). ^{13}C{^{1}H} NMR: δ 159.7 (C9), 158.2 (C3), 148.7 (C13), 136.5 (C11), 136.4 (C1), 122.8 (C10), 122.1 (C12), 121.9 (C2), 69.4 (C7), 67.8 (C6), 61.7 (C5), 60.3 (C8), 53.0 (C4). The numbering of atoms in molecule **L** is depicted in Figure 1. MS, m/z (+): 434.28 [L+H]$^+$ (I_{rel} = 33%); 456.27 [L+Na]$^+$ (I_{rel} = 100%). Elemental analysis for C$_{25}$H$_{31}$N$_5$O$_2$ found (calculated): C, 69.26 (69.22); H, 7.21 (7.58); N, 16.15 (16.22)%.

General Procedure for the Preparation of Complexes (M^{II} = Mn, Fe, Co, Ni, and Cu). Equimolar amounts of **L** and M(ClO$_4$)$_2$·6H$_2$O were dissolved in CH$_3$CN (15 mL) and then stirred and heated to 50 °C for 30 min. The obtained solution was evaporated to a half volume and allowed to crystallize by diffusion of diethyl ether vapors at room temperature. The crystals were isolated by filtration, washed with cold diethyl ether (2 × 5 mL), and dried in a vacuum desiccator over NaOH for 2 d.

[MnL](ClO$_4$)$_2$ (1). Colorless crystals were isolated after one week (78 mg, yield 66%). Elemental analysis for C$_{25}$H$_{31}$N$_5$O$_{10}$Cl$_2$Mn$_1$: C, 43.67 (43.68); H, 4.92 (4.55); N, 10.30 (10.19)%. MS m/z (+): 244.30 [MnL]$^{2+}$ (I_{rel} = 2.7%); 587.22 [MnL+(ClO$_4$)]$^+$ (I_{rel} = 100%; Supporting Information, Figure S1).

[FeL](ClO$_4$)$_2$ (2). Greenish-yellow crystals were isolated after 3 d (125 mg, yield 76%). Elemental analysis for C$_{25}$H$_{31}$N$_5$O$_{10}$Cl$_2$Fe$_1$: C, 43.51 (43.63); H, 4.65 (4.54); N, 10.04 (10.17)%. MS m/z (+): 244.73 [FeL]$^{2+}$ (I_{rel} = 3.4%); 588.14 [FeL+(ClO$_4$)]$^+$ (I_{rel} = 100%; Supporting Information, Figure S1).

[CoL](ClO$_4$)$_2$ (3). Brownish-orange crystals were isolated after 2 d (109 mg, yield 81%). Elemental analysis for C$_{25}$H$_{31}$N$_5$O$_{10}$Cl$_2$Co$_1$: C, 43.51 (43.43); H, 4.68 (4.52); N, 10.11 (10.13)%. MS m/z (+): 246.28 [CoL]$^{2+}$ (I_{rel} = 6.3%); 591.19 [CoL+(ClO$_4$)]$^+$ (I_{rel} = 100%; Supporting Information, Figure S1).

[NiL](ClO$_4$)$_2$ (4). Green crystals were isolated after 2 d (93 mg, yield 68%). Elemental analysis for C$_{25}$H$_{31}$N$_5$O$_{10}$Cl$_2$Ni$_1$: C, 43.50 (43.45); H, 4.67 (4.52); N, 10.11 (10.13)%. MS m/z (+): 245.79 [NiL]$^{2+}$ (I_{rel} =

1.3%); 590.19 [NiL+(ClO$_4$)]$^+$ (I_{rel} = 100%; Supporting Information, Figure S1).

[CuL](ClO$_4$)$_2$ (5). Dark blue crystals were isolated after 3 d (80 mg, yield 66%). Elemental analysis for C$_{25}$H$_{31}$N$_5$O$_{10}$Cl$_2$Cu$_1$ found (calculated): C, 43.26 (43.14); H, 4.48 (4.49); N, 9.99 (10.06)%. MS *m/z* (+): 403.19 [CuL−H−CH$_2$py] (I_{rel} = 94.3%); 496.21 [CuL]$^+$ (I_{rel} = 26.5%); 595.06 [CuL+(ClO$_4$)]$^+$ (I_{rel} = 100%; Supporting Information, Figure S1).

Theoretical Methods. The ORCA 3.0.3 computational package was used for all ab initio theoretical calculations.[44] The relativistic effects were included in the calculations using the scalar relativistic contracted version of def2-TZVP(-f) basis functions[45] and with zero order regular approximation (ZORA).[46] The calculations of ZFS parameters were done using state average complete active space self-consistent field (SA-CASSCF)[47] wave functions complemented by *N*-electron valence second-order perturbation theory (NEVPT2).[48] The active spaces of the CASSCF calculations on metal-based d-orbitals were defined as follows: CAS(6,5) for Fe(II), CAS(7,5) for Co(II), and CAS(8,5) for Ni(II). In the state-averaged approach all multiplets for given electron configuration were equally weighted. The ZFS parameters, based on dominant spin−orbit coupling contributions from excited states, were calculated through quasi-degenerate perturbation theory (QDPT),[49] in which an approximations to the Breit−Pauli form of the spin−orbit coupling operator (SOMF approximation)[50] and the effective Hamiltonian theory[51] were utilized. All the above-mentioned calculations utilized the RI approximation with the decontracted auxiliary def2-TZV/C Coulomb fitting basis sets. Increased integration grids (Grid5 in ORCA convention) and tight SCF convergence criteria were used in all calculations. The calculations were done on molecular fragments [M(**L**)]$^{2+}$ of **2−4** extracted from experimental X-ray structures.

■ RESULTS AND DISCUSSION

Syntheses and General Characterization. The ligand **L** was prepared by *N*-alkylation of 15-pyN$_3$O$_2$ using a small excess of 2-chloromethylpyridine, and purified by recrystallization from CH$_3$CN. During the synthesis of 15-membered macrocyclic precursor ligand (15-pyN$_3$O$_2$), two side-products were isolated by column chromatography (see Experimental Section), and their composition and structure were confirmed by NMR and MS spectra (Supporting Information). The **side-product 1** was determined as a 30-membered macrocycle of the formula 3,12,20,29,35,36-hexaaza-6,9,23,26-tetraoxatricyclo-[29.3.1.11^{4,18}]hexatriaconta-1(36),14(35),15,17,31,33-hexaene (Figure 2), while the **side-product 2** was characterized as a noncyclic derivative {6-[({2-[2-(2-aminoethoxy)ethoxy]ethyl}-amino)methyl]pyridine-2-yl}methanol (Figure 2).

All the complexes were prepared by the same synthetic procedure based on mixing of **L** with the corresponding metal perchlorate in CH$_3$CN in an equimolar ratio and heating to 50
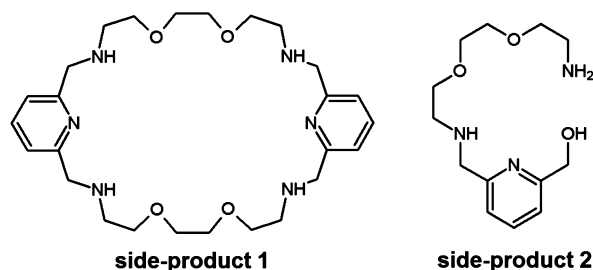
Figure 2. Structural formulas of **side-products 1** and **2** identified during the preparation of the 15-membered macrocyclic precursor ligand 15-pyN$_3$O$_2$.

°C. Compounds in crystalline form were obtained by diffusion of diethyl ether vapors into these solutions.

The infrared spectra of the ligand **L** and complexes **1−5** show similar patterns. The characteristic bands of the coordinated **L** were present in the IR spectra of all the complexes, that is, medium bands at ∼2900 cm^{-1} (stretching CH$_2$ vibrations), a medium doublet at 1600 and 1580 cm^{-1}, and medium bands at ∼1470 cm^{-1} (wagging vibrations of the pyridine ring).[19,52,53] In addition, the spectra of all the complexes exhibit a very strong and broad band at ∼1070 cm^{-1} assignable to the stretching vibrations of the (ClO$_4$)$^-$ anions.

X-ray Structures. Selected crystallographic data and structural refinement parameters for the free ligand **L** and complexes **1−5** are listed in Table 1, while selected interatomic distances and angles for complexes **1−5** can be found in Table 2.

Crystal Structure of L. The 15-membered macrocycle **L** is partially twisted with the pyridine rings in pendant arms pointing to opposite directions, and thus, the molecule has a butterfly-like shape (Figure 3A). The individual molecules of **L** are connected by C−H···N noncovalent interactions formed between pairs of the pyridine rings from macrocycles ($d_{C···N}$ = 3.482(3) Å) and pairs of the pyridine rings from pendant arms of neighboring ligand molecules ($d_{C···N}$ = 3.510(3) and 3.440(3) Å), thus forming 1D chains along the crystallographic axis *a* (Figure 3B, Supporting Information, Table S1). These chains are further interconnected by weak C−H···O non-covalent interactions between aliphatic hydrogen (H10B and H12A) and oxygen (O2) atoms of neighboring 15-membered rings ($d_{C···O}$ = 3.318(3) and 3.261(3) Å; Figure 3C). Surprisingly, no π−π stacking was found in the crystal structure of **L**.

Molecular Structures of Complexes 1−5. Complexes **1−3** have similar molecular structures (Figure 4A and Supporting Information, Figures S2A and S3A). The central atoms are seven-coordinate and adopt pentagonal bipyramidal geometry with the N$_5$O$_2$ donor set. Equatorial positions are occupied by three macrocyclic nitrogen (one from pyridine ring—N$_{py}$ and two from aliphatic chain—N$_{aliph}$) and two oxygen atoms, thus forming a pentagonal pseudoplane. The pentagonal bipyramidal coordination sphere is completed by two nitrogen atoms (N$_{pend}$) from 2-pyridylmethyl pendant arms in axial positions. The M−N$_{aliph}$ bond lengths are longer than those of M−N$_{py}$ or M−N$_{pend}$ (Table 2). The M−N$_{py}$ bond is the shortest in **1** (2.215(7) and 2.238(8) Å), while in **2** (2.166(2) and 2.156(2) Å) and **3** (2.120(3) and 2.110(3) Å) the shortest bonds are M−N$_{pend}$.

The molecular structure of **4** is depicted in Figure 5A. The coordination sphere of Ni(II) in **4** differs from the above-described complexes, because it has a markedly distorted pentagonal bipyramidal geometry. The coordination number could be classified as 6 + 1, because one of the M−O bonds is significantly elongated (Ni−O2, 2.653(2) Å, Table 2), more than other bond lengths of such type. The mean value of the Ni−O bond distance is 2.055 Å, and 90% of all the observed Ni−O bonds, as found in CSD, have lengths in the range of 1.964−2.114 Å.[15] Similar elongation of Ni−O bonds was observed in [Ni(15-pyN$_3$O$_2$)Cl$_2$][36] or [Ni(**L6**)](ClO$_4$)$_2$,[15] with Ni−O bond lengths of 2.506(3), 2.663(3), or 2.554(3) Å, respectively.

The unit cell contains two crystallographically independent entities of **5**. The molecular structure of **5** is depicted in Figure

Table 1. Crystal Data and Structure Refinements for the Ligand L and Complexes 1−5

compound	L	1	2	3	4	5
formula	$C_{25}H_{31}N_5O_2$	$C_{25}H_{31}N_5O_{10}Cl_2Mn_1$	$C_{25}H_{31}N_5O_{10}Cl_2Fe_1$	$C_{25}H_{31}N_5O_{10}Cl_2Co_1$	$C_{25}H_{31}N_5O_{10}Cl_2Ni_1$	$C_{25}H_{31}N_5O_{10}Cl_2Cu_1$
Mr	433.55	687.39	688.30	691.38	691.16	695.99
Color	colorless	colorless	yellow	brownish-orange	green	dark blue
crystal system	triclinic	monoclinic	monoclinic	monoclinic	monoclinic	monoclinic
space group (space group no.)	$P\text{-}1$ (2)	$P2_1$ (4)	$P2_1$ (4)	$P2_1$ (4)	Cc (9)	$P1$ (1)
a (Å)	6.1891(3)	18.4837(11)	18.3758(9)	18.3060(11)	17.425(4)	9.7677(5)
b (Å)	12.1423(9)	9.1361(5)	9.1185(4)	9.1269(5)	10.684(2)	10.6130(6)
c (Å)	15.9337(9)	18.7481(11)	18.8090(8)	18.7659(10)	15.272(3)	15.3827(8)
α (deg)	106.402(2)	90	90	90	90	80.106(2)
β (deg)	97.170(3)	113.011(1)	113.237(1)	113.500(2)	96.54(3)	84.709(2)
γ (deg)	93.392(3)	90	90	90	90	65.812(2)
U (Å³)	1134.40(12)	2914.1(3)	2896.0(2)	2875.3(3)	2824.8(10)	1432.59(13)
Z	2	4	4	4	4	2
λ (Å), Mo Kα	0.710 73	0.710 73	0.710 73	0.710 73	0.710 73	0.710 73
D_{calc} (g·cm⁻³)	1.269	1.567	1.579	1.597	1.625	1.613
μ (mm⁻¹)	0.083	0.701	0.770	0.848	0.942	1.014
F (000)	464	1420	1424	1428	1432	718
reflections collected	34 964	89 125	179 792	73 378	16 418	63 137
independent reflections	4833 [R(int) = 0.1026]	12 897 [R(int) = 0.0731]	13 356 [R(int) = 0.0416]	12 757 [R(int) = 0.0417]	5634 [R(int) = 0.0214]	12 644 [R(int) = 0.0401]
data/restraints/parameters	4833/0/289	12 897/1/746	13 356/1/776	12 757/1/776	5634/2/389	12 644/3/776
goodness-of-fit on F^2	1.067	1.040	1.058	1.047	1.008	1.093
R_1, wR_2 ($I > 2\sigma(I)$)	0.0630/0.1226	0.0656/0.1449	0.0274/0.0664	0.0329/0.0730	0.0257/0.0628	0.0372/0.0835
R_1, wR_2 (all data)	0.1051/0.1370	0.0951/0.1583	0.0310/0.0681	0.0424/0.0777	0.0273/0.0637	0.0459/0.0873
largest diff. peak and hole, A⁻³	0.290/−0.323	1.076/−0.961	0.386/−0.456	0.443/−0.453	0.555/−0.487	0.731/−0.562
CCDC no.	1451957	1451958	1451956	1451954	1451959	1451955

6A. The copper atom is five-coordinated by four nitrogen (N_{py}, two N_{aliph}, N_{pend}) and one oxygen (O2) atoms of **L**, and it adopts a distorted square pyramidal arrangement ($\tau = 0.02$ for Cu1, and 0.08 for Cu2). The M−N_{py} bond in **5** is the shortest (1.933(3) Å (Cu1), 1.909(4) Å (Cu2)) from all M−N coordination bonds within the studied series, while the other two M−N_{aliph} bonds in **5** are longer than 2 Å. On the one hand, one of the M−N_{pend} distances in **5** is the shortest from all M−N_{pend} distances in the studied series, but on the other hand, second M−N_{pend} distance in **5** is longer than 3 Å (3.042(4) Å (Cu1) and 3.160(4) (Cu2)), which clearly demonstrates that this atom is not coordinated to Cu(II) as well as one oxygen atom (one of the M−O distances is 2.750(3) Å for Cu1 and 2.840(3) Å for Cu2).

When all the structures of the prepared complexes are compared between each other, several trends can be observed. The metal−donor atom distances depend on the central metal atom as it is depicted in Figure 7. The M−N_{py}, M−N_{aliph}, as well as M−N_{pend} distances are shortened with decreasing ionic radii of central atoms in order going from Mn(II) (**1**) to Cu(II) (**5**), except for one M−N_{pend} distance (>3 Å) of one uncoordinated pendant arm in **5**. The pyridine−metal atom bonds (M−N_{py} and M−N_{pend}) are the shortest from all coordination bonds in **1**−**5** (Figure 7). On the other hand, the M−O coordination bonds are similar in **1**−**3**, but there are significantly elongated in Ni(II) complex **4** and Cu(II) complex **5**, so that one oxygen atom can be considered as semi-coordinated in **4** (2.653(2) Å) and uncoordinated in **5** (2.8401(3) Å), respectively (Table 2, Figure 7). In accordance with this, the value of the O−M−O angle for **4** and **5** was significantly decreased (Table 2). This observed trend could be

explained by Jahn−Teller effect operating in seven-coordinate Ni(II) and five-coordinated Cu(II) complexes.[12] Indeed, the complexes **1**−**3** revealed coordination number of 7 with the N_5O_2 donor atom set, Ni(II) complex **4** with one semi-coordinated oxygen atom revealed coordination number of 6 + 1 (the N_5O_2 donor atom set), while the molecular structure of Cu(II) complex is completely different (coordination number of 5, the N_4O_1 donor atom set). To support our conclusions, the geometries of coordination polyhedra of **1**−**5** were analyzed by program Shape 2.1 providing continuous shape measurements (deviation of the real geometry from an ideal polyhedron).[54] On the one hand, the lowest value of deviation for complexes **1**−**4** was found for pentagonal bipyramid (from all possible polyhedra for coordination numbers of 6 and 7, Supporting Information, Table S3), which was in complete agreement with suggested coordination numbers. On the other hand, for **5** the lowest deviation was found for trigonal prism and square pyramid (from all possible polyhedra for coordination numbers of 5 and 6, Supporting Information, Table S3). The lowest value of deviation for trigonal prism was unexpected, due to the long Cu−O2 distance (2.8401(3)Å), but it could be caused by a very weak unspecified interaction between Cu(II) and the second macrocyclic O2 atom.

In comparison with the previously published complexes containing unsubstituted macrocycle 15-pyN₃O₂ and two axially coordinated chlorido ligands [M(15-pyN₃O₂)Cl₂]⁰/⁺ (M = Mn(II), Fe(III), Co(II), Ni(II)),[36] the axial coordination bonds to pyridine in the pendant arms of **L** are shorter (~2.1−2.2 Å) than in the case of two axially coordinated Cl⁻ (~2.4−2.5 Å), and thus, the coordination sphere of the studied complexes is more axially compressed. However, if [Cu(15-

**Table 2. Selected Interatomic Distances (Å) and Angles (deg) in Compounds 1−5**

distances	1	2	3	4	5
M−N1	2.215(7)	2.189(2)	2.162(3)	2.010(2)	1.909(4)
	2.238(8)	2.185(2)	2.158(4)		1.933(3)
M−N2	2.371(7)	2.321(2)	2.287(3)	2.179(3)	2.127(4)
	2.334(8)	2.311(2)	2.265(4)		2.122(4)
M−N3	2.361(7)	2.307(2)	2.273(3)	2.253(2)	2.085(4)
	2.347(7)	2.320(2)	2.284(3)		2.083(4)
M−N4	2.220(7)	2.166(2)	2.120(3)	2.077(3)	3.042(4)
	2.219(7)	2.156(2)	2.110(3)		3.160(4)
M−N5	2.235(7)	2.171(2)	2.120(3)	2.091(3)	1.985(4)
	2.242(7)	2.167(2)	2.114(3)		1.979(4)
M−O1	2.240(6)	2.223(2)	2.231(3)	2.325(2)	2.387(3)
	2.267(6)	2.231(2)	2.236(3)		2.480(4)
M−O2	2.286(6)	2.285(2)	2.288(3)	2.653(2)	2.840(3)
	2.279(6)	2.274(2)	2.281(3)		2.750(3)
angles					
N1−M−N2	71.4(3)	71.4(1)	71.8(1)	77.02(9)	81.8(2)
	71.2(3)	71.4(1)	71.8(1)		82.0(2)
N1−M−N3	71.0(3)	71.33(8)	71.7(1)	75.61(9)	83.0(2)
	70.6(3)	71.07(9)	71.5(1)		83.2(2)
N1−M−N4	94.7(3)	94.7(1)	94.0(1)	98.2(1)	70.8(2)
	95.7(3)	95.0(1)	94.5(1)		68.5(1)
N1−M−N5	91.5(3)	91.9(1)	91.9(1)	97.1(1)	160.6(2)
	90.2 (3)	90.8(1)	90.7(1)		153.7(2)
N1−M−O1	143.3(3)	144.10(9)	144.3(1)	151.02(9)	113.5(2)
	144.1(3)	144.68(9)	145.0(1)		118.4(1)
N1−M−O2	144.1(2)	144.60(9)	144.7(1)	144.26(9)	83.3(2)
	144.0(3)	144.40(9)	144.3(1)		93.9(1)
N4−M−N2	75.7(3)	76.9(1)	78.9(1)	80.64(9)	72.4(2)
	76.0(3)	76.68(9)	78.3(1)		69.8(1)
N4−M−N3	107.8(3)	106.43(9)	102.4(1)	103.40(9)	89.8(2)
	107.8(3)	106.09(9)	103.7(1)		89.9(2)
N4−M−N5	173.6(3)	173.2(1)	174.0(1)	164.68(9)	96.4(2)
	173.8(3)	174.0(1)	174.7(1)		89.9(1)
N4−M−O1	88.0(3)	87.10(9)	86.4(1)	84.81(9)	142.4(1)
	87.3(3)	87.09(8)	88.1(1)		142.0(1)
N4−M−O2	89.3(2)	88.92(9)	87.5(1)	83.75(8)	150.4(1)
	89.2(3)	89.51(9)	88.8(1)		154.9(1)
O1−M−O2	72.4(2)	71.17(7)	70.9(1)	64.66(7)	61.5(1)
	71.6(2)	70.72(8)	70.5(1)		61.7(1)

pyN₃O₂)Cl]Cl[36] and **5** are compared, their molecular structures are similar, with square pyramidal geometry and comparable values of τ parameter (0.09 vs 0.02/0.08).

Crystal Structures of Complexes 1−5. The [M(L)]²⁺ complex cations (M = Mn, Fe, Co, Ni, Cu) in the crystal structures of all the complexes **1−5** are chiral (Figure 8). The first source of chirality is related to the presence of two stereogenic centers on two substituted aliphatic nitrogen atoms (N$_{aliph}$). The second one is related with the conformations of the five-membered chelate rings formed upon coordination of ligand in equatorial plane; it can be denoted as left- (λ) or right-handed (δ) depending on the sign of the N(O)−C−C−N(O) torsion angles (λ for negative, and δ for positive). In the crystal structures of **1, 2, 3,** and **4**, equal amounts of [M(R,R)-L]²⁺ complex cations with the ($\delta\lambda\delta\lambda\delta$) conformation and [M(S,S)-L]²⁺ with the ($\lambda\delta\lambda\delta\lambda$) conformation of five-membered chelate rings are present (Figure 4B, Figure 5B, and Supporting Information, Figures S2B and S3B). Nevertheless **1, 2,** and **3** crystallize in the non-centrosymmetric Sohncke space group P2₁ (Table 1). Crystallization of racemic mixture as racemic

compound in non-centrosymmetric space groups is rare.[55] Compound **4** crystallizes in the centrosymmetric space group Cc, and its crystal structure is composed of two types of alternating homochiral layers parallel with (001) (Figure 5B). The perchlorate anions are distributed among the layers. In the case of **5** the crystal structure is different because it contains only [Cu(R,S)-L]²⁺ complex cations but with two types of conformation ($\delta\delta\delta\lambda\lambda$ and $\lambda\delta\delta\lambda\lambda$).

Noncovalent interactions have a crucial role in the final crystal packing of **1−5**. The crystal structures are stabilized by weak C−H···O interactions (Supporting Information, Table S1 and S2), which hold together cations and anions, and create extended 3D supramolecular network (Figure 4C, 5C, and 6B, Supporting Information, Figure S2C and S3C). The C···O separations occur in the range of 3.132(2)−3.411(14) Å for **1**, 3.161(5)−3.438(5) Å for **2**, 3.194(5)−3.463(6) Å for **3**, 3.115(4)−3.451(4) Å for **4**, and 3.135(8)−3.541(7) Å for **5**, the smallest C−H···O angle is 125 (**1**), 124 (**2**), 123 (**3**), 121 (**4**), and 127° (**5**). Anion-π interactions were observed between the pyridine rings of pendant arms and oxygen atoms of
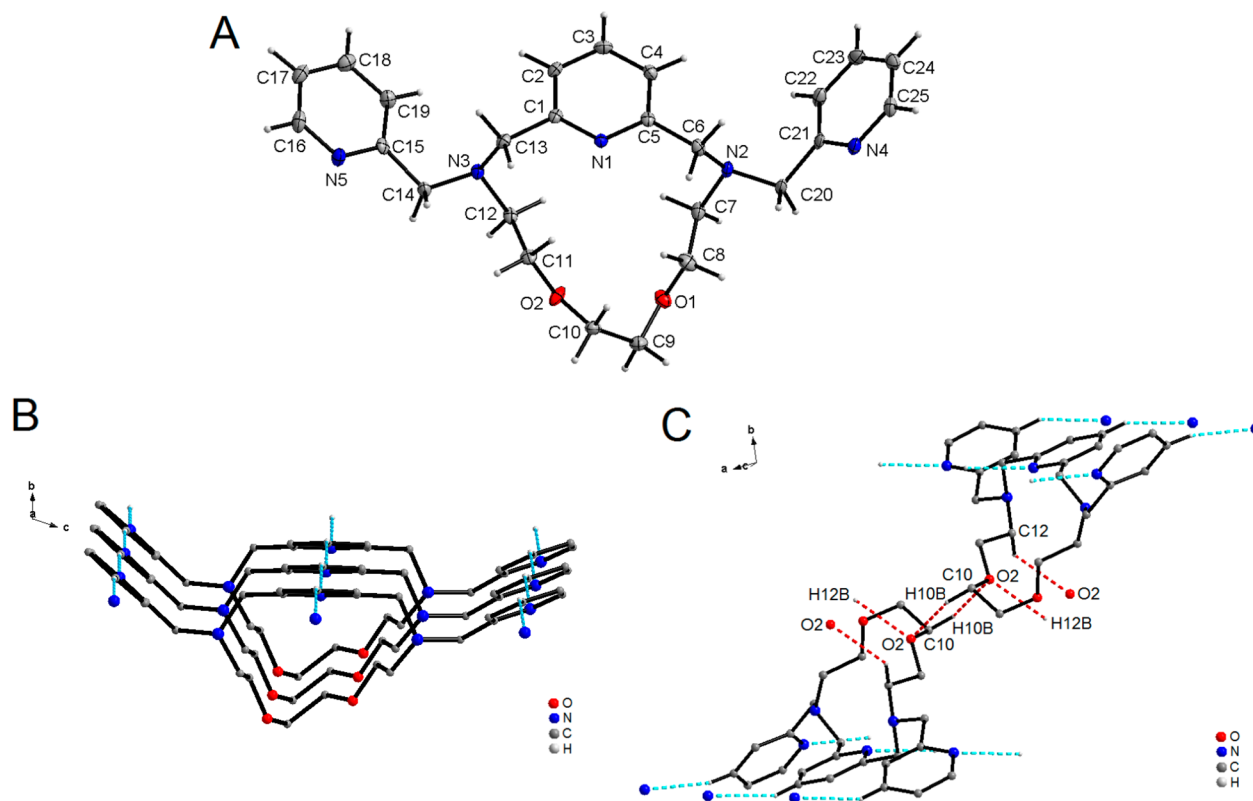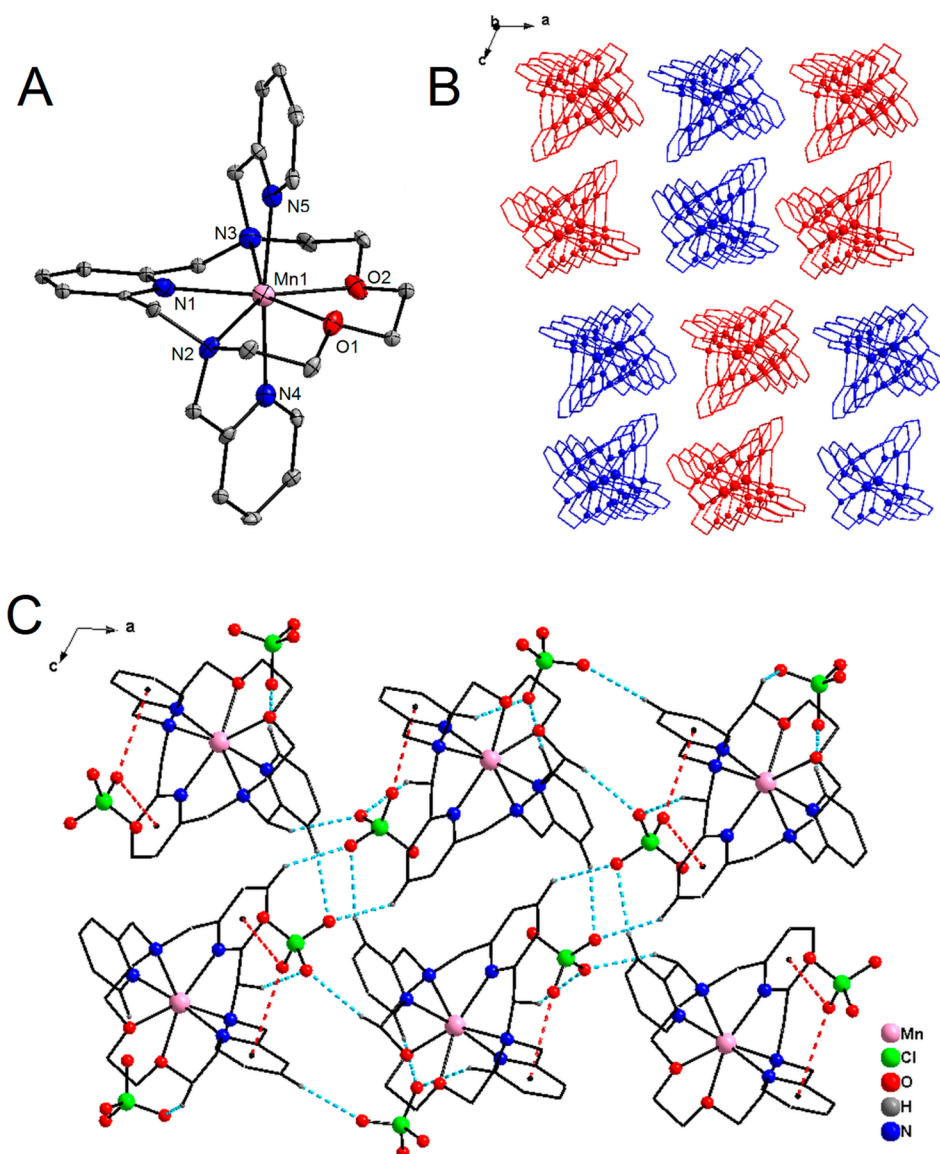
Figure 3. (A) Molecular structure of **L**. The thermal ellipsoids are drawn with the 50% probability level. (B) Part of the crystal structure showing supramolecular 1D chain of individual **L** molecules connected together by C−H⋯N noncovalent interactions (blue dashed lines). (C) These chains are interconnected by C−H⋯O interactions (red dashed lines). Hydrogen atoms not involved in these interactions are omitted for clarity.

perchlorate anions in **1**−**4**, with the oxygen⋯centroid (Cg) distances in the range of 3.0018(3)−3.5155(7) Å, the Cl⋯Cg distances are in the range of 3.9086(9)−4.6792(8) Å, and the Cl−O⋯Cg angles in the range of 119−176° (Supporting Information, Table S2). Despite of presence of many aromatic rings, π−π stacking interactions were observed only in **5**, with the Cg⋯Cg distance 3.5364(2) Å and with angle between the planes of the centroids 22.5°.

Theoretical Calculations. The ab initio calculations are very helpful in molecular magnetism for identifying magnetic exchange mediated by noncovalent interactions[56] or covalent bonds[57] and also for calculation of ZFS D and g tensors.[36,58] Furthermore, the predictive role of such theoretical calculations can be utilized for trustworthy postulation of spin Hamiltonians for analysis of the experimental magnetic data.[59] Herein, we focused on calculations of magnetic anisotropy parameters (D and E) for Fe(II), Co(II), and Ni(II) complexes **2**−**4**, which have higher pre-disposition for the ZFS.[60] We employed the ab initio calculations using ORCA software based on SA-CASSCF wave functions accompanied by NEVPT2. The relativistic effects were also included with the help of the scalar relativistic contracted version of def2-TZVP(-f) basis functions and with ZORA (see more details in Experimental Section). The active space of these CASSCF calculations was composed of the appropriate number of electrons according to metal atom in five metal-based d-orbitals. The dominant spin−orbit coupling contributions from excited states led to ZFS tensors, hence to the determination of axial and rhombic single-ion parameters D and E, respectively (Table 3). The energy levels resulting from CASSCF/NEVPT2 calculations are tabulated in Tables S4−S6 (Supporting Information). Also, the contributions of the

excited states to ZFS terms are summarized in Tables S7−S9 (Supporting Information). The effective Hamiltonian theory was used to extract information about ZFS parameters (Table 3), but also values calculated by second-order perturbation theory are listed for comparison in Table S10 (see Supporting Information). In case of compounds **2** and **3**, all calculations were performed for both molecular fragments present in their asymmetric units. The largest positive D-parameter was found in Co(II) compound **3**, D = 30.69 cm^{-1}, and largest negative D-parameters was found in Ni(II) compound **4**, D = −19.11 cm^{-1}. The largest rhombicity was found for Fe(II) compound **2**, E/D = 0.316. However, in the case of **2**, the extraction of spin Hamiltonian parameters is questionable, because there are close-lying excited states (Supporting Information, Table S4), which means that the spin-Hamiltonian formalism may not be applicable. This is also demonstrated in Table S11 (see Supporting Information), where lowest energy levels resulting from CASSCF/NEVPT2 calculations are calculated with the extracted spin-Hamiltonian parameter. There is perfect match for complexes **3** and **4**, but there is evident discrepancy for complex **2** (Supporting Information, Table S11). Moreover, the axes of D- and g-tensors together with molecular structures are visualized in Figure S4 (Supporting Information). In the cases of **2** and **3**, both g-tensor and ZFS-tensor axes coincide; only in the case of compound **4**, there is a little mismatch. Interestingly, only in Co(II) compound **3**, the z-axis of D-tensor is approximately located along the N−M−N bonds, where these two nitrogen atoms are from pyridine groups in apical positions (Figure S4). In all other cases, the main axes of D- or g-tensors cannot be aligned with specific donor−acceptor bonds. If the main magnetic axis are defined by D-tensor, then

Figure 4. (A) Molecular structure of the $[\text{Mn}(S,S)\text{-}\mathbf{L}]^{2+}$ cation in **1**. Thermal ellipsoids are drawn with the 50% probability level. The second crystallographically independent molecule, perchlorate anions, and hydrogen atoms are omitted for clarity. (B) Representation of arrangement of $[\text{Mn}(\mathbf{L})]^{2+}$ enantiomers in the crystal structure of **1** ($[\text{Mn}(R,R)\text{-}\mathbf{L}]^{2+}$ = red, $[\text{Mn}(S,S)\text{-}\mathbf{L}]^{2+}$ = blue). (C) Representation of 3D packing of **1** with the C−H⋯O noncovalent interactions (blue dashed lines) and anion−π interactions (red dashed line). Hydrogen atoms not involved in these interactions are omitted for clarity.

the g-axes for compounds **2** and **3** can be assigned as $g_x = g_2$, $g_y = g_3$, $g_z = g_1$, while $g_x = g_2$, $g_y = g_1$, $g_z = g_3$ holds for **4** (Table 3, Supporting Information, Figure S4).

Static Magnetic Properties. To extract the spin-Hamiltonian parameters describing the magnetic anisotropy from the experimental magnetic data of **2**−**4**, the mononuclear spin Hamiltonian was postulated

$$\hat{H} = D(\hat{S}_z^{\,2} - \hat{S}^2/3) + E(\hat{S}_x^{\,2} - \hat{S}_y^{\,2}) + \mu_B B g \hat{S}_a \tag{1}$$

where D and E are the single-ion axial and rhombic ZFS parameters and the last component, Zeeman term defined in a direction of magnetic field as $B_a = B(\sin(\theta)\cos(\varphi), \sin(\theta)\sin(\varphi), \cos(\theta))$ with the help of the polar coordinates. Then, the molar magnetization in a-direction of magnetic field can be numerically calculated as

$$M_a = kT \left(\frac{\partial \ln Z}{\partial B_a} \right)_T \tag{2}$$

where Z is the partition function resulting from energy levels. Then, the averaged molar magnetization of the powder sample was calculated as integral (orientational) average.

$$M_{\text{mol}} = \frac{1}{4\pi} \int_0^{2\pi} \int_0^{\pi} M_a \sin\theta \, \mathrm{d}\theta \, \mathrm{d}\phi \tag{3}$$

In case of compounds **1** and **5** with negligible or absent ZFS, the following spin Hamiltonian was used

$$\hat{H} = \mu_B B g \hat{S}_a - zj \langle \hat{S}_z \rangle \hat{S}_z \tag{4}$$

where zj represents the molecular-field correction parameter characterizing possible weak intermolecular interactions. The
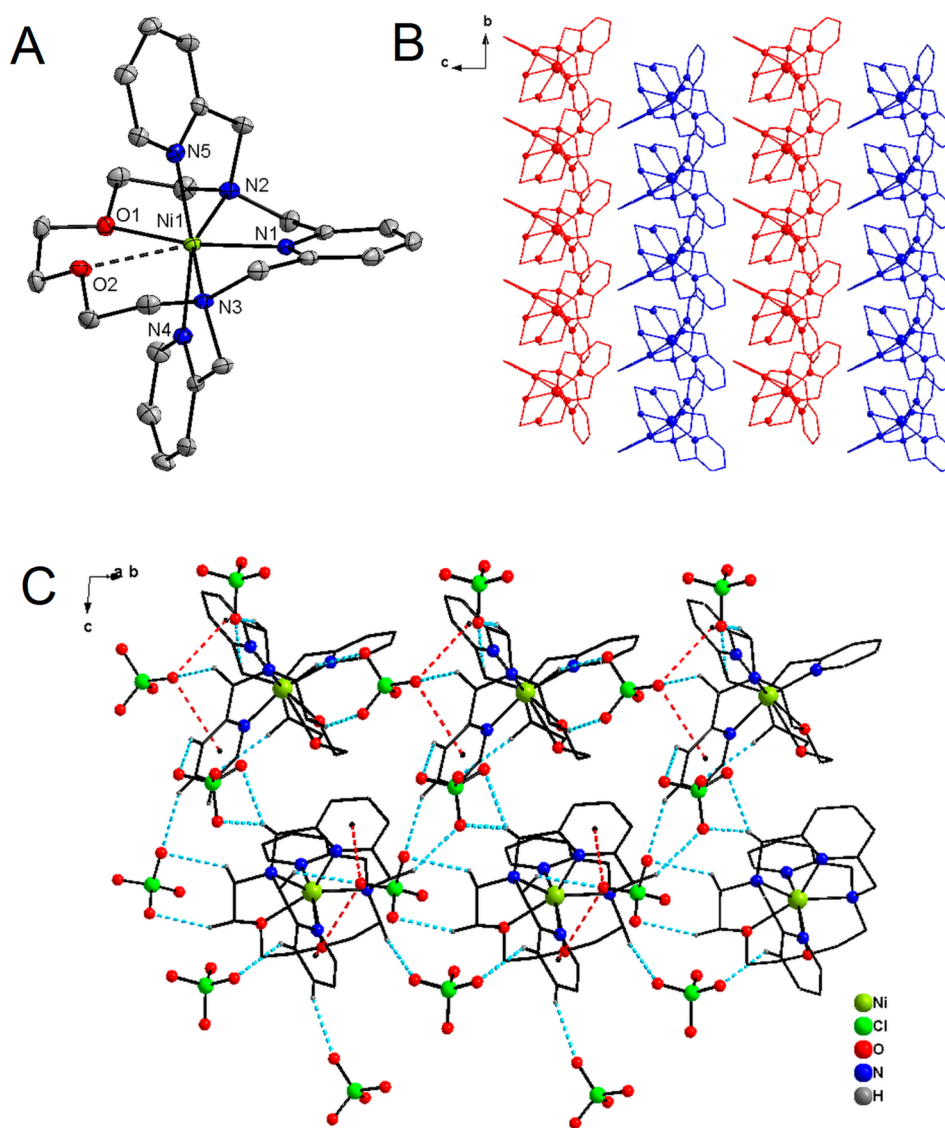
Figure 5. (A) Molecular structure of the $[Ni(R,R)\text{-}L]^{2+}$ cation in **4**. The dashed line between Ni and O atoms represents a semicoordination. Thermal ellipsoids are drawn with the 50% probability level. The second crystallographically independent molecule, hydrogen atoms, and perchlorate anions are omitted for clarity. (B) Arrangement of homochiral layers in the crystal structure of **4** ($[Ni(R,R)\text{-}L]^{2+}$ = red, $[Ni(S,S)\text{-}L]^{2+}$ = blue). Perchlorate anions and hydrogen atoms are omitted for clarity. (C) Representation of 3D packing of **4** with the C−H···O noncovalent interactions (blue dashed lines) and anion-π interactions (red dashed line). Hydrogen atoms not involved in these interactions are omitted for clarity.

$\langle S_z \rangle$ is a thermal average of the molecular spin projection. The molar magnetization is calculated by an iterative procedure as

$$M_{mol} = -N_A \frac{\sum_i \left(\sum_k \sum_l C_{ik}^+ (Z)_{kl} C_{li} \right) \exp(-\varepsilon_i/kT)}{\sum_i \exp(-\varepsilon_i/kT)} \qquad (5)$$

where Z is the matrix element of the Zeeman term, and C are the eigenvectors resulting from the diagonalization of the complete spin-Hamiltonian matrix.[62]

Mn(II) Complex (1). Temperature dependence of the effective magnetic moment (μ_{eff}/μ_B) and the isothermal molar magnetization data measured at low temperatures (2, 5, and 10 K) for **1** are presented in Figure 9. The value of μ_{eff}/μ_B is 5.88 at room temperature, which is close to the spin-only value $\mu_{eff}/\mu_B = 5.92$ for the system with $S = 5/2$ and $g = 2.0$. A very small decrease in μ_{eff}/μ_B observed below 10 K resulted in a final value of 5.82 at 1.9 K, which points to the fact that the intermolecular magnetic interactions in the solid state are negligible as well as possible ZFS. This is also supported by the

fact that isothermal magnetizations are overlapping. Therefore, spin Hamiltonian in eq 4 was used and resulted in $g = 1.995(1)$ and negligible $zj = -0.009(2)$ cm^{-1}. The value of zj was found almost zero, which confirms no presence of any kind of magnetic exchange between $[MnL]^{2+}$ units.

Fe(II) Complex (2). The value of μ_{eff}/μ_B at room temperature is 5.27, which is significantly higher than the theoretical spin-only value ($\mu_{eff}/\mu_B = 4.90$ for $S = 2$ and $g = 2.0$) due to orbital momentum contributions. The abrupt decrease of μ_{eff}/μ_B below 50 K ending with the value 4.16 at $T = 1.9$ K can be attributed mainly to the ZFS effect. The magnetic analysis using spin Hamiltonian in eq 1 resulted in negative value of $D = -7.4(2)$ cm^{-1} with the absence of rhombicity ($E/D = 0.0$).

The negative value of D-parameter is approximately one-half smaller than those for other seven-coordinate Fe(II) complexes (Table 4); however, it contradicts ab initio calculations ($D = 8.12-8.18$ cm^{-1}, $E/D = 0.312-0.316$). Therefore, we calculated magnetic properties of **2** with CASSCF/NEVPT2 energy levels
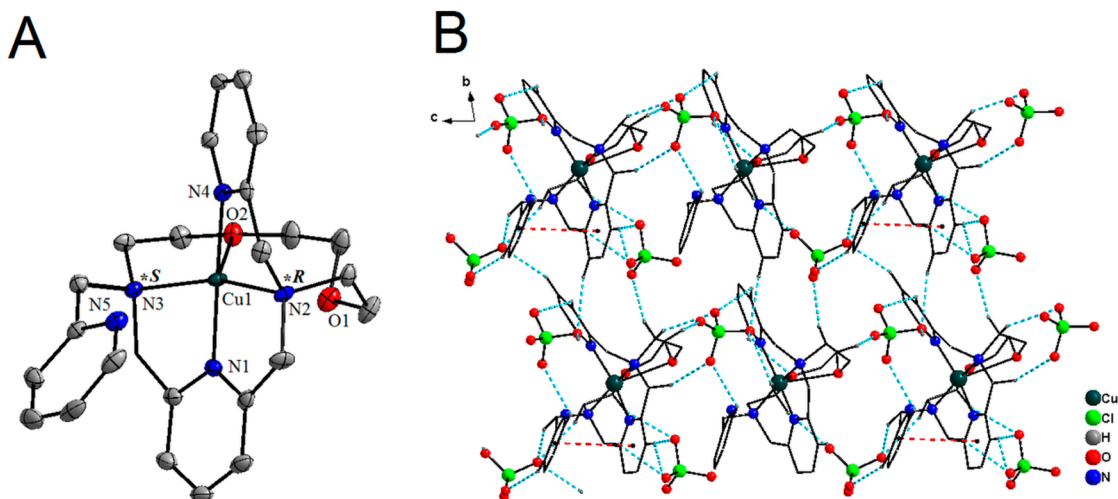
Figure 6. (A) Molecular structure of the $[Cu(R,S)\text{-}L]^{2+}$ cation in **5**. Atoms are drawn as thermal ellipsoids with 50% probability level. The second crystallographically independent molecule, hydrogen atoms, and perchlorate anions are omitted for clarity. (B) Representation of 3D packing of **5** with the C—H···O noncovalent interactions (blue dashed lines) and $\pi-\pi$ stacking interactions (red dashed lines). Hydrogen atoms not involved in these interactions are omitted for clarity.
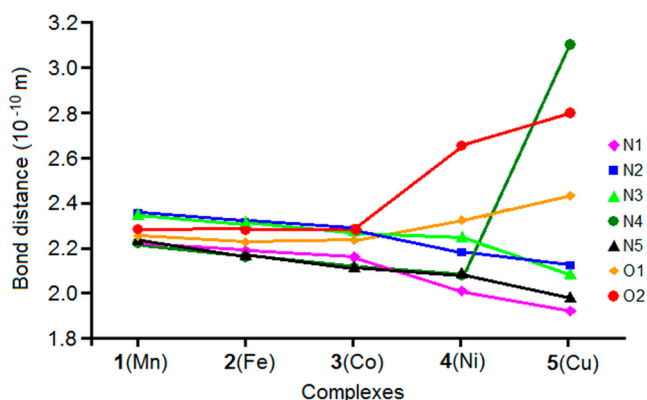
Figure 7. Variation of the metal−donor atom distances in the complexes **1**−**5** depending on the type of the central metal atom.
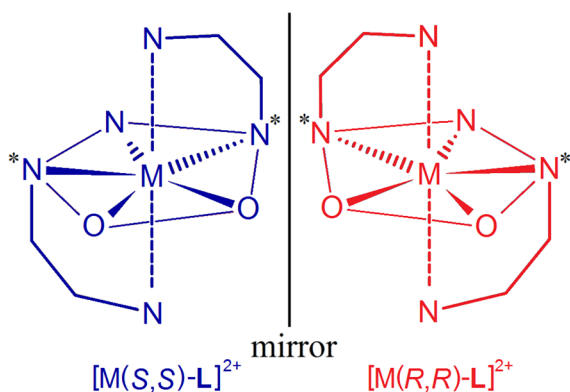
Figure 8. Representations of the enantiomeric forms of $[ML]^{2+}$ complex cation present in crystal structures of **1**−**4**. The $[M(R,R)\text{-}L]^{2+}$ cation with the $(\delta\lambda\delta\lambda\delta)$ conformation of five-membered chelate rings (red), and $[M(S,S)\text{-}L]^{2+}$ with the $(\lambda\delta\lambda\delta\lambda)$ conformation (blue).

and corresponding matrices,[58a] and in such a way calculated magnetic data are both in agreement with the experimental one and also with calculated one with eq 1, and Supporting Information, Figure S5. This means that ab initio calculations correctly predict magnetic properties of **2** and that the

discrepancy of spin-Hamiltonian parameters' values between theory and magnetic analysis lies in the fact that orbital angular momentum is not completely quenched and strongly influence low-lying energy levels. Therefore, more sophisticated model beyond the spin-Hamiltonian approximation is needed for magnetic analysis of this compound. Unfortunately, such theory is not available for Fe(II) high-spin complexes yet.

In comparison with an SCO Schiff-base complex $[\text{Fe}(15\text{-pydienN}_3\text{O}_2)(\text{CN})_2]\cdot\text{H}_2\text{O}$,[25] complex **2** remained in high-spin state through whole temperature range, which could be attributed to the different strengths of Fe−O bonds. By comparing the bond lengths in the pentagonal planes in both complexes, the stronger Fe−N(imine) bonds decrease the strength of Fe−O bond(s) in the case of the Schiff-base complex, and as a consequence of this, one of the Fe−O bonds is broken, which is responsible for the SCO behavior.[25] However, the Fe−N(amine) bonds in **2** were found to be longer (i.e., weaker) as compared to the Fe−N(imine) bond lengths in the SCO complex, and therefore the Fe−O bonds in **2** are stronger (i.e., shorter). The above-mentioned discrepancies in both the coordination spheres may be connected with the absence of SCO in complex **2**.

Co(II) Complex (3). The observed μ_{eff}/μ_B at room temperature, $\mu_{\text{eff}}/\mu_B = 4.34$, is significantly higher than the spin-only value for system with $S = 3/2$ and $g = 2.0$ ($\mu_{\text{eff}}/\mu_B = 3.87$) owing to substantial contribution of the orbital angular momentum. During the cooling, the μ_{eff}/μ_B continuously decreases to value of 3.35 at $T = 1.9$ K, which can be explained by a large ZFS. The effect of ZFS is also demonstrated in the isothermal magnetization data, where saturation limit is well below theoretical value equal to $M_{\text{mol}}/N_A\mu_B = gS$ (Figure 9). The monomeric model in eq 1 was used for the data fitting, and the best fit was obtained for the positive D and negligible rhombicity. The fitted $D = 34(1)$ cm^{-1} for complex **3** is close to the ab initio calculated value of $D \approx 30.60-30.69$ (Table 3). In comparison with structurally similar complex $[\text{Co}(15\text{-pyN}_3\text{O}_2)\text{Cl}_2]$ ($D = 40.0$ cm^{-1}), the value of D for **3** is less positive, as a result of coordination of axial ligand providing stronger ligand field (pyridine groups in **3** vs chlorido ligands in $[\text{Co}(15\text{-pyN}_3\text{O}_2)\text{Cl}_2]$), which was predicted in ref 31. As a consequence

Table 3. Comparison of Ab Initio Calculated and Fitted Spin Hamiltonian Parameters for Complexes 1−5[61]

compound	1	2	3	4	5
the central metal atom	Mn(II)	Fe(II)	Co(II)	Ni(II)	Cu(II)
the electron configuration	$3d^5$	$3d^6$	$3d^7$	$3d^8$	$3d^9$
the spin state S	5/2	2	3/2	1	1/2
ZFS and g values based on CASSCF/NEVPT2 calculations					
D (cm^{-1})		8.12/8.18	30.69/30.60	−19.11	
E/D		0.312/0.316	0.046/0.035	0.152	
g_1		2.007/2.007	2.023/2.022	1.998	
g_2		2.062/2.061	2.270/2.271	2.101	
g_3		2.207/2.208	2.304/2.298	2.189	
magnetic analysis of the experimental data					
g	1.995(1)	2.131(5)	2.208(5)	2.181(2)	2.109(1)
D (cm^{-1})		−7.4(2)	34(1)	−12.8(1)	
E/D		0.0	0.0	0.136(3)	
zj (cm^{-1})	−0.009(2)				−0.12(2)
χ_{TIP} (1×10^{-9} m^3 mol^{-1})		3(1)	1.3(6)	2.2(2)	
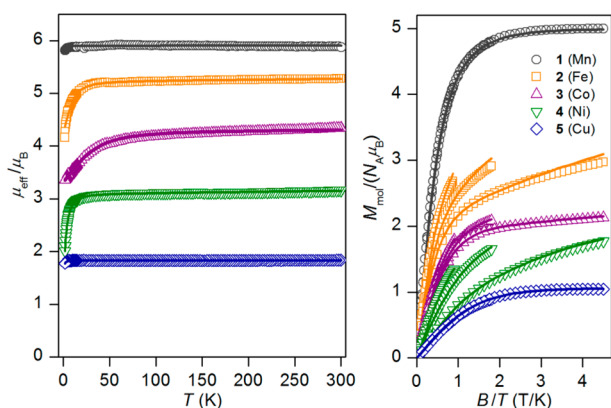
Figure 9. Magnetic data for compounds **1−5**. Temperature dependence of the effective magnetic moment (left) and the isothermal molar magnetizations measured at 2, 5, and 10 K (right). The empty circles represent the experimental data points, and the full lines represent the best fits calculated with spin Hamiltonians in eqs 1 and 4 with parameters listed in Table 3.

of this substitution, destabilization of the d_{z^2} orbital occurred (its energy increased), and the coupling between the magnetic ground state and the higher excited quartet/doublet states, which contribute only positively to the D-value, was reduced. And consequently the D-value was decreased as well. The obtained value of D is comparable with the values found for other seven-coordinate Co(II) complexes in Table 4. For these complexes similar trend can be found only when the complexes containing the same ligand are compared (equatorially five-coordinated ligand affects the D-value as well); otherwise, no evident effect of axial ligands on D-value can be observed.

Ni(II) Complex (4). The effective magnetic moment at room temperature, $\mu_{eff}/\mu_B = 3.16$, is significantly higher than the spin-only value for the system with $S = 1$ and $g = 2.0$ ($\mu_{eff}/\mu_B = 2.83$) due to the orbital momentum contributions to the ground spin state. The abrupt decrease of its value at low temperature below 20 K is observed ending with 2.01 μ_B at $T = 1.9$ K as a result of ZFS effect. A large and negative axial anisotropy, $D = -12.8(1)$ cm^{-1}, was found, and this complex is the only one for which also significant rhombicity, $E/D = 0.136(3)$, was detected. The fitted value is in agreement with the ab initio calculated value of $D = -19.11$ cm^{-1} (Table 3). In comparison with the structurally similar complex $[Ni(15\text{-}pyN_3O_2)Cl_2]$ ($D = -6.02$

cm^{-1}), the value of D is more than 2 times larger. This is again a consequence of the stronger ligand field of the two pyridine groups of **L** coordinated in axial positions. Similarly, as it was explained for Co(II) complex **3** above, destabilization of the d_{z^2} orbital occurred, and the coupling between the magnetic ground state and the excited states resulted in much weaker positive contributions to the D-value than in $[Ni(15\text{-}pyN_3O_2)Cl_2]$; thus, more negative overall D-parameter was found in **4**. This can be understood as a confirmation of the theoretically predicted behavior of D-parameter in pentagonal bipyramidal Ni(II) complexes upon substitution of ligands in axial positions,[31] as was also mentioned in the Introduction.

Cu(II) Complex (5). The effective magnetic moment at room temperature (μ_{eff}/μ_B) is 1.84, which is slightly higher than the spin-only value 1.73 for $S = 1/2$ and $g = 2.0$, and its decrease below 30 K is very small (1.77 at 1.9 K) and it is most probably caused by very weak intermolecular interactions, which was confirmed by successful fitting of the magnetic data with $g = 2.109(1)$ and $zj = -0.12(2)$ cm^{-1}.

Dynamic Magnetic Properties. The coordination compounds with high magnetic anisotropy are interesting candidates for single-molecule magnets, for which the slow relaxation of magnetization is observed. Therefore, the AC susceptibility measurements were performed in zero and nonzero static magnetic field for **2−4**, however, only Co(II) complex **3** showed nonzero out-of-phase signal of AC susceptibility − Figure 10 and Figure S6 (Supporting Information).

The AC susceptibility was measured at $B_{DC} = 0.1$ T and various frequencies of alternating small AC magnetic field. Evidently, there are maxima of out-of-phase susceptibility dependent on applied frequency, which is typical behavior of SMM. These susceptibility data for each temperature were then analyzed with the one-component Debye model

$$\chi(\omega) = \chi_S + (\chi_T - \chi_S)/[1 + (i\omega\tau)^{1-\alpha}] \qquad (6)$$

which resulted in isothermal (χ_T) and adiabatic (χ_S) susceptibilities, relaxation times (τ), and distribution parameters (α)—Supporting Information, Table S12. This enabled us to construct the Argand (Cole−Cole) plot (Figure 10). Applying the Arrhenius equation on the temperature dependence of the relaxation times, the relaxation time $\tau_0 = 9.90 \times 10^{-10}$ s and the spin reversal barrier $U_{eff} = 24.3$ K (16.9 cm^{-1}) was calculated (Figure 10) when only data having maxima in

Table 4. Comparison of Selected Zero-Field Splitting Parameters Determined for 2−4 and Previously Studied Complexes with Seven-Coordinate Central Metal Ions

compound[a]	D [cm^{-1}]	E/D	ref
[Fe(**L**)](ClO$_4$)$_2$	−7.4(2)	0	this work
[Fe(15-pydienN$_5$)(H$_2$O)$_2$]Cl$_2$	−17.2	0.21	32
[Fe(**L8**)Cl$_2$]·0.5CH$_3$OH	−13.3	0	8d
[Co(**L**)](ClO$_4$)$_2$	34(1)	0	this work
[Co(15-pydienN$_5$)(H$_2$O)$_2$]Cl$_2$·4H$_2$O	24.6	0	35
[Co(15-pyN$_3$O$_2$)Cl$_2$]·2CH$_3$OH	40.0	0	36
[Co(**L6**)](NO$_3$)$_2$·CH$_3$CN	25		15
[Co(**L6**)](ClO$_4$)$_2$	26		15
[Co(**L7**)](ClO$_4$)$_2$	23.1		63
[Co(**L8**)(H$_2$O) (NO$_3$)](NO$_3$)	31	0	31
[Co(**L8**)(SCN)$_2$]	15.9	0	34
[Co(**L8**)(H$_2$O)$_2$]	13.1	0	34
[Co(**L8**)I(H$_2$O)]I	30.0	0.3	32
[Co(**L8**)Br(H$_2$O)]Br	30.0	0.3	32
[Co(**L8**-2H$^+$)(imidazole)$_2$]·H$_2$O[a]	24.8	0	35
[Co(**L10**)$_3$(NO$_3$)$_2$][a]	35.8	0.21	8b
[Co(**L11**)$_3$(NO$_3$)$_2$][a]	35.7	0.02	8b
[Ni(**L**)](ClO$_4$)$_2$	−12.8(1)	0.136(3)	this work
[Ni(15-pyN$_3$O$_2$)Cl$_2$]	−6.02	0.15	36
[Ni(**L6**)](NO$_3$)$_2$·H$_2$O	15		15
[Ni(**L8**)(H$_2$O)$_2$](NO$_3$)$_2$·2H$_2$O	−13.9	0.10	31
[Ni(**L9**)(NO$_3$)(CH$_3$OH)](NO$_3$)	−12.5	0.10	33

[a]**L10** = 4-*tert*-butylpyridine, **L11** = isoquinoline. Structural formulas of other ligands mentioned in this table are depicted in Figure 1.

the Argand diagram were used. Here it should be stated that even for the highest temperatures only a few points fulfilled the linear behavior of $\ln(\tau)$ versus $1/T$ and thus, the obtained values of τ_0 and U_{eff} are most probably determined with large errors. The effective value of U_{eff} is 4 times lower than the theoretical prediction based on the parameters derived from magnetic analysis, $U_{\mathrm{mag}} = 2(D^2 + 3E^2)^{1/2} = 67.9$ cm^{-1}, or from the CASSCF/NEVPT2 calculations, $U_{\mathrm{ab\_initio}} = 61.6$ cm^{-1}. However, this kind of discrepancy is observed also in other SMM, because there are also other relaxation processes in play (direct, Raman, and quantum tunneling) except Orbach process.[64] Main source of this discrepancy could be explained by the fact that the analysis based on eq 6 is limited only to AC susceptibility data having maxima in the Argand diagram, which means data measured between $T = 1.9$ and 4.6 K. However, nonzero out-of-phase AC susceptibility is already observed below 8.5 K (Figure 10). As U should reflect only thermally activated Orbach mechanism, it is important to analyze also data above 4.6 K.[58c] Therefore, we used simplified model[65] based on eq 7

$$\ln(\chi''/\chi') = \ln(2\pi f\tau_0) + U/kT \qquad (7)$$

where higher-temperature AC data for higher applied frequencies were included as visualized in Figure 11. As a result, we obtained sets of following parameters: $\tau_0 = 6.13 \times 10^{-12}$ s, $U = 73.6$ cm^{-1} (105.9 K) for $f = 1488.1$ Hz, $\tau_0 = 9.36 \times 10^{-10}$ s, $U = 47.6$ cm^{-1} (68.4 K) for $f = 597.1$ Hz, $\tau_0 = 5.99 \times 10^{-9}$ s, $U = 38.7$ cm^{-1} (55.8 K) for $f = 239.8$ Hz, and $\tau_0 = 4.32 \times 10^{-8}$ s, $U = 29.5$ cm^{-1} (42.4 K) for $f = 96.2$ Hz. Herein, the variation of fitted parameters can be due to omitting the distribution of relaxation processes (parameter α in eq 6). Nonetheless, such derived U parameters are much higher (e.g., $U = 73.6$ cm^{-1} for $f = 1488.1$ Hz) and very close to values predicted by spin-Hamiltonian parameter ($U_{\mathrm{mag}} = 67.9$ cm^{-1}).

However, it was recently pointed out that in case of easy plane anisotropy ($D > 0$, $E/D = 0$), the Orbach process should not be governing relaxation mechanism but direct term induced by the hyperfine interaction dominating at low temperatures and a Raman term dominating at higher temperatures.[66]

That is why we also analyzed relaxation times with eq 8 containing the Raman term

$$\tau = CT^{-n} \qquad (8)$$

for data in temperature range between 2.2 and 4.0 K, which resulted in $C = 2.12 \times 10^{-5}$ and $n = 2.84$ (Figure 12). The fitted n-value is lower than $n = 4.9$ or 8.7 found in other seven-coordinate Co(II) complexes with easy plane anisotropy.[35] To conclude, the analyses of AC susceptibility data and relaxation times showed that both Orbach and Raman processes could be present in **3**.

Electrochemical Properties. The redox properties of **L** and its complexes **1−5** were investigated by cyclic voltammetry in CH$_3$CN solutions only, because of their low solubility in water. The cyclic voltammograms of complexes **1−5** are depicted in Figure 13, and obtained electrochemical data are listed in Table 5.

The cyclic voltammogram of the ligand **L** shows irreversible behavior providing two oxidation peaks at $E_{\mathrm{ox1}} = 1.22$ V and $E_{\mathrm{ox2}} = 1.38$ V (Supporting Information, Figure S7), which may be assigned to the oxidation of both pyridine pendant arms. Reversible couples of Mn(III)/Mn(II), Fe(III)/Fe(II), and Cu(II)/Cu(I) were found at the potentials of $E_{1/2} = 1.75$, 1.26, and 0.17 V in CH$_3$CN solutions of **1**, **2**, and **5**, respectively. These obtained values of $E_{1/2}$ are much higher than those previously found for complexes containing unsubstituted macrocyclic ligands 15-pyN$_3$O$_2$ or 15-pydienN$_3$O$_2$ and axial chlorido coligand(s), that is, [Mn(15-pyN$_3$O$_2$)Cl$_2$] ($E_{1/2} = 0.97$ V, $\Delta E_{\mathrm{p}} = 0.13$ V),[36] [Fe(15-pyN$_3$O$_2$)Cl$_2$]Cl ($E_{1/2} = 0.25$ V, $\Delta E_{\mathrm{p}} = 81$ mV),[36] [Fe(15-pydienN$_3$O$_2$)Cl$_2$]ClO$_4$ ($E_{1/2} = 0.25$ V,
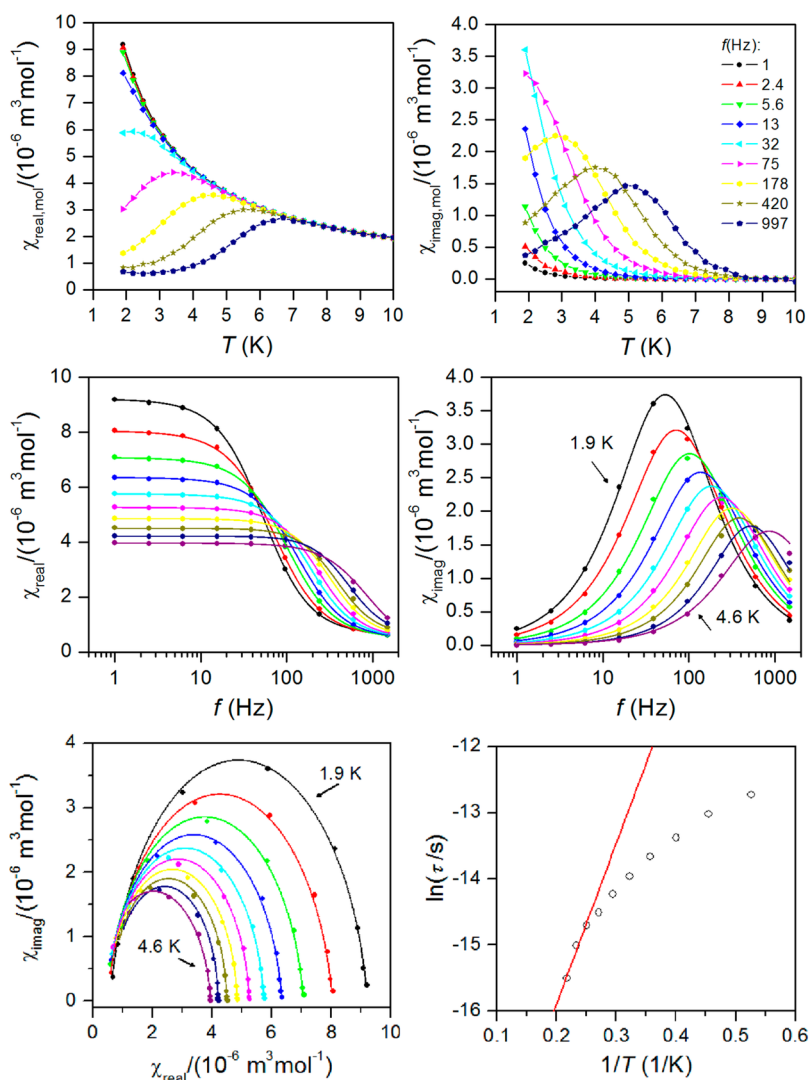
Figure 10. (top) In-phase χ_{real} and out-of-phase χ_{imag} molar susceptibilities for **3** at the applied external field $B_{DC} = 0.1$ T. Lines serve as guides. (middle) Frequency dependence of in-phase χ_{real} and out-of-phase χ_{imag} molar susceptibilities for **3** at $B_{DC} = 0.1$ T. Full points—experimental data, full lines—fitted data using eq 6. (bottom) Argand (Cole–Cole) plot and fit of resulting relaxation times according to Arrhenius law (red line).
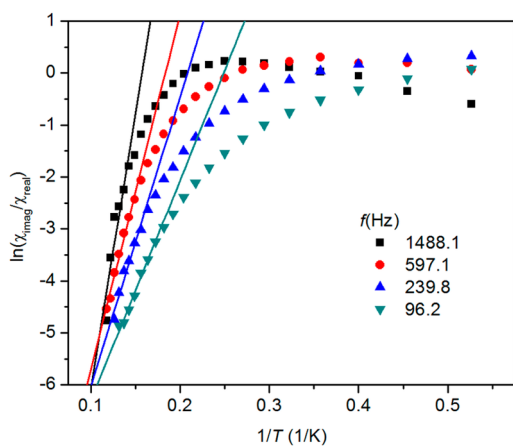

Figure 11. Analysis of in-phase χ_{real} and out-of-phase χ_{imag} molar susceptibilities for **3** measured at the applied external field $B_{DC} = 0.1$ T according to eq 7. Full points—experimental data, full lines—calculated data.
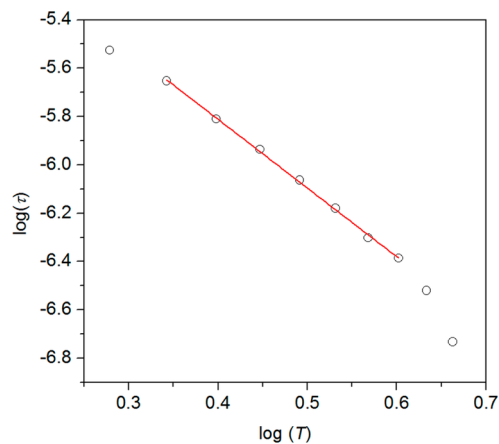
Figure 12. Analysis of relaxation times with Raman term according to eq 8. Full points—experimental data, full line—calculated data.

$\Delta E_p = 110$ or 60 mV),[22] or $[Cu(15\text{-}pyN_3O_2)Cl]Cl$, for which irreversible reduction peak ($E_{red} = -0.14$ V) corresponding to the reduction of Cu(II) to Cu(I) was observed.[36] In the cyclic
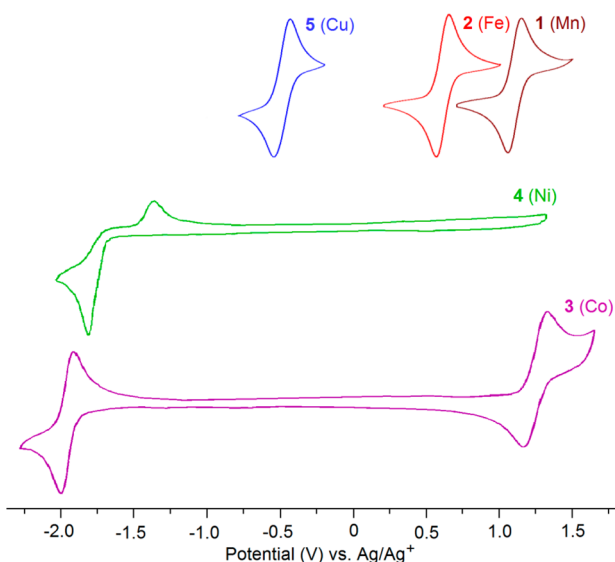
Figure 13. Cyclic voltammograms of complexes **1** (brown), **2** (red), **3** (purple), **4** (green), and **5** (blue) (2 mM) recorded in argon atmosphere with a glassy carbon working electrode in 0.1 M TBAP in CH$_3$CN.

Table 5. Results of Cyclic Voltammetry Measurements

compound	redox process	$E_{1/2}$ [V] vs Ag/Ag$^+$	$E_{1/2}$ [V] vs SHE	ΔE [mV]
L		$E_{ox1} = 0.564$	1.219	
		$E_{ox2} = 0.727$	1.382	
1	Mn^{3+}/Mn^{2+}	1.096	1.751	93
2	Fe^{3+}/Fe^{2+}	0.603	1.258	86
3	Co^{2+}/Co^{1+}	−1.971	−1.316	65
	Co^{3+}/Co^{2+}	1.239	1.894	86
4	Ni^{2+}/Ni^{1+}	$E_{red} = -1.811$	−1.156	
		$E_{ox} = -1.355$	−0.700	
5	Cu^{2+}/Cu$^+$	−0.489	0.166	104

voltammogram of **3**, two reversible couples of Co(III)/Co(II) at 1.89 V and Co(II)/Co(I) at −1.32 V were found. For **4**, a quasi-reversible couple Ni(II)/Ni(I) was found with the reduction peak at −1.16 V and less intense oxidation peak at −0.70 V. The quasi-reversibility of this redox process could be a result of low solubility of the Ni(I) product or its fast consequent decomposition. On the one hand, the much higher redox potentials in comparison with the previously studied similar complexes clearly demonstrate the ability of **L** to stabilize reduced species (lower oxidation states), which is a consequence of the modified structure of **L** containing two tertiary amino groups and two pyridine pendant arms, because it was shown previously on many transition complexes with different linear or macrocyclic polyamines, for example, Ni(II) complexes of cyclen derivatives (Supporting Information, Table S13),[17,18] that when their primary/secondary amino groups were substituted by the tertiary ones[67] and/or the pyridine group with π-acceptor ability were implemented into their structure, the lower oxidation states were stabilized, and the value of $E_{1/2}$ increased. On the other hand, when strong π-donors were coordinated, just as in the case of the chlorido coligands[36] in the above-mentioned complexes of 15-pyN$_3$O$_2$ or pendant arms with anionic or electron rich groups,[17] the oxidized species (higher oxidation states) were stabilized, and the value of $E_{1/2}$ decreased.

CONCLUSIONS

The heptadentate 15-membered macrocyclic ligand modified with two 2-pyridylmethyl pendant arms (**L**) was successfully prepared to stabilize the coordination number of 7, which was subsequently confirmed by X-ray analysis of Mn(II) **1**, Fe(II) **2**, Co(II) **3**, and Ni(II) **4** complexes (one macrocyclic oxygen atom was semicoordinated in **4**), except for Cu(II) complex **5** with the coordination number of 5.

It has been shown that the ligand **L** has a strong impact on the structural, magnetic, as well as redox properties of the studied late first-row transition-metal complexes and that the stronger π-acceptor ability of the axially coordinated pyridine moiety in comparison with the chlorido ligands is reflected in several general aspects, which are as follows: (i) the pyridine–metal bonds are shortened in comparison with all the other coordination bonds; that is, the pentagonal bipyramidal coordination sphere was slightly axially compressed; (ii) substantial changes in values of the axial ZFS parameters (*D*) for Co(II) complex **3** and for Ni(II) complex **4** were observed; and (iii) the high values of determined redox potentials showed significant stabilization of the lower oxidation states (Mn^{II}, Fe^{II}, Co^{I}, Ni^{I}, and Cu^{I}). All these aspects help to improve our understanding of the electronic structure and the magnetic anisotropy in seven-coordinate complexes. Moreover, the Co(II) complex **3** enlarges the small and interesting group of SMMs, in which easy plane anisotropy was observed (*D* = 34(1), *E*/*D* = 0). The detailed analysis of the dynamic magnetic data revealed that both Raman and/or Orbach relaxation mechanisms are involved and are responsible for slow relaxation of the magnetization below ∼8 K. To the best of our knowledge, this is second work, when the slow relaxation of the magnetization in a seven-coordinate Co(II) complex with macrocyclic ligand is reported.

It has been also shown that the targeted structural modification of the macrocyclic scaffold in the organic ligand **L** can serve for tuning of different properties of transition metal complexes, especially those regarding the magnetic anisotropy in seven-coordinate Co(II) and Ni(II) complexes via substitution of the axial coligands with different coordination ability in accordance with the previously formulated theoretical predictions. Nevertheless, for a serious magneto-structural correlation, more ligands with different functional groups in pendant arms would be needed. But anyway, the obtained results could have a beneficial influence on a progress in design of more sophisticated and efficient SMMs and in consequent applications in magnetochemistry or catalysis.

ASSOCIATED CONTENT

Ⓢ Supporting Information

The Supporting Information is available free of charge on the ACS Publications website at DOI: 10.1021/acs.inorgchem.6b00415.

> Side products characterization. Mass spectra of **1**−**5**. Figures referring to X-ray analysis of **2** and **3**. Visualization of principal axes of ZFS tensors for **2**−**4**. Magnetic data for **2** and **3**. Cyclic voltammogram of **L**. Tables characterizing noncovalent interactions. Results of continuous shape measures. Computational data for **2**−**4** and their comparison. Redox potentials for selected Ni(II) complexes of cyclam derivatives. (PDF)
> X-ray crystallographic information. (ZIP)

■ AUTHOR INFORMATION

Corresponding Author
*Fax: +420 585 634 954. Phone: +420 585 634 352. E-mail: zdenek.travnicek@upol.cz.

Notes
The authors declare no competing financial interest.

■ REFERENCES

(1) Melson, G. A. *Coordination Chemistry of Macrocyclic Compounds;* Plenum Press: New York, 1979.

(2) Lindoy, L. F.; Park, K.-M.; Lee, S. S. *Chem. Soc. Rev.* **2013**, *42*, 1713−1727.

(3) (a) Ferreirós-Martinez, R.; Esteban-Gómez, D.; De Blas, A.; Platas-Iglesias, C.; Rodríguez-Blas, T. *Inorg. Chem.* **2009**, *48*, 11821−11831. (b) Fodor, T.; Bányai, I.; Bényei, A.; Platas-Iglesias, C.; Purgel, M.; Horváth, G. L.; Zékány, L.; Tircsó, G.; Tóth, I. *Inorg. Chem.* **2015**, *54*, 5426−5437. (c) Anderson, O. P.; Reibenspies, J. H. *Acta Crystallogr., Sect. C: Cryst. Struct. Commun.* **1996**, *52*, 792−795. (d) Meurant, G. *Stereochemical and stereophysical behaviour of macrocycles;* Elsevier Science: Amsterdam, 1987.

(4) (a) Yu, L.; Li, F.-Z.; Wu, J.-Q.; Xie, J.-Q.; Li, S. *J. Inorg. Biochem.* **2016**, *154*, 89−102. (b) Warner, G. R.; Mills, M. R.; Enslin, C.; Pattanayak, S.; Panda, C.; Panda, T. K.; Gupta, S. S.; Ryabov, A. D.; Collins, T. *Chem. - Eur. J.* **2015**, *21*, 6226−6233. (c) Suh, Y.; Seo, M. S.; Kim, K. M.; Kim, S. Y.; Jang, H. G.; Tosha, T.; Kitagawa, T.; Kim, J.; Nam, W. *J. Inorg. Biochem.* **2006**, *100*, 627−633.

(5) (a) Tóth, É.; Merbach, A. E. *The Chemistry of Contrast Agents in Medical Magnetic Resonance Imaging;* John Wiley & Sons: Chichester, U.K., 2001. (b) Wadas, J. T.; Wong, E. H.; Weisman, G. R.; Anderson, C. J. *Chem. Rev.* **2010**, *110*, 2858−2902. (c) Mewis, R. E.; Archibald, S. J. *Coord. Chem. Rev.* **2010**, *254*, 1686−1712. (d) Rodríguez-Rodríguez, A.; Garda, Z.; Ruscsák, E.; Esteban-Gómez, D.; De Blas, A.; Rodríguez-Blas, T.; Lima, L. M. P.; Beyler, M.; Tripier, R.; Tircsó, G.; Platas-Iglesias, C. *Dalton Trans.* **2015**, *44*, 5017−5031.

(6) Donnelly, P. S. *Dalton Trans.* **2011**, *40*, 999−1010.

(7) (a) Paúrová, M.; Havlíčková, J.; Pospíšilová, J.; Vetrík, M.; Císařová, I.; Stephan, H.; Pietzsch, H.-J.; Hrubý, M.; Hermann, P.; Kotek, J. *Chem. - Eur. J.* **2015**, *21*, 4671−4687. (b) Shen, J.; Ma, W.; Yu, L.; Li, J.-B.; Tao, H.-C.; Zhang, K.; Zeng, H. *Chem. Commun.* **2014**, *50*, 12730−12733. (c) Adhikari, B. B.; Gurung, M.; Chetry, A. B.; Kawakita, H.; Ohto, K. *RSC Adv.* **2013**, *3*, 25950−25959. (d) Jensen, M. P.; Chiarizia, R.; Ulicki, J. S.; Spindler, B. D.; Murphy, D. J.; Hossain, M. M.; Roca-Sabio, A.; De Blas, A.; Rodríguez-Blas, T. *Solvent Extr. Ion Exch.* **2015**, *33*, 329−345.

(8) (a) Habib, F.; Korobkov, I.; Murugesu, M. *Dalton Trans.* **2015**, *44*, 6368−6373. (b) Chen, L.; Chen, S.-Y.; Sun, Y.-C.; Guo, Y.-M.; Yu, L.; Chen, X.-T.; Wang, Z.; Ouyang, Z. W.; Song, Y.; Xue, Z.-L. *Dalton Trans.* **2015**, *44*, 11482−11490. (c) Zhang, Y.-Z.; Wang, B.-W.; Sato, O.; Gao, S. *Chem. Commun.* **2010**, *46*, 6959−6961. (d) Bar, A. K.; Pichon, C.; Gogoi, N.; Duhayon, C.; Ramasesha, S.; Sutter, J.-P. *Chem. Commun.* **2015**, *51*, 3616−3619. (e) Bar, A. K.; Pichon, C.; Sutter, J. P. *Coord. Chem. Rev.* **2016**, *308*, 346−380.

(9) (a) Paraschiv, C.; Andruh, M.; Journaux, Y.; Žák, Z.; Kyritsakas, N.; Ricard, L. *J. Mater. Chem.* **2006**, *16*, 2660−2668. (b) Bonadio, F.; Senna, M.-C.; Ensling, J.; Sieber, A.; Neels, A.; Stoeckli-Evans, H.; Decurtins, S. *Inorg. Chem.* **2005**, *44*, 969−978. (c) Dhers, S.; Feltham, H. L. C.; Brooker, S. *Coord. Chem. Rev.* **2015**, *296*, 24−44. (d) Shao, D.; Zhao, X.-H.; Zhang, S.-L.; Wu, D.-Q.; Wei, X.-Q.; Wang, X.-Y. *Inorg. Chem. Front.* **2015**, *2*, 846−853.

(10) (a) Nelson, S. M.; McIlroy, P. D. A.; Stevenson, C. S. *J. Chem. Soc., Dalton Trans.* **1986**, 991−995. (b) Hayami, S.; Gu, Z.-Z.; Einaga, Y.; Kobayasi, Y.; Ishikawa, Y.; Yamada, Y.; Fujishima, A.; Sato, O. *Inorg. Chem.* **2001**, *40*, 3240−3242. (c) Wang, Q.; Venneri, S.; Zarrabi, N.; Wang, H.; Desplanches, C.; Létard, J.-F.; Seda, T.; Pilkington, M. *Dalton Trans.* **2015**, *44*, 6711−6714. (d) Halcrow, M. A. *Chem. Soc. Rev.* **2011**, *40*, 4119−4142. (e) Wang, H.; Grosjean, A.; Sinito, Ch.; Kaiba, A.; Baldé, Ch.; Desplanches, C.; Létard, J.-F.; Guionneau, P. *CrystEngComm* **2015**, *17*, 4075−4079.

(11) Casanova, D.; Alemany, P.; Bofill, J. M.; Alvarez, S. *Chem. - Eur. J.* **2003**, *9*, 1281−1295.

(12) Regueiro-Figueroa, M.; Lima, L. M. P.; Blanco, V.; Esteban-Gómez, D.; De Blas, A.; Rodríguez-Blas, T.; Delgado, R.; Platas-Iglesias, C. *Inorg. Chem.* **2014**, *53*, 12859−12869.

(13) Giordano, T. J.; Palenik, G. J.; Palenik, R. C.; Sullivan, D. A. *Inorg. Chem.* **1979**, *18*, 2445−2450.

(14) Jahn, H. A.; Teller, E. *Proc. R. Soc. London, Ser. A* **1937**, *161*, 220−235.

(15) Platas-Iglesias, C.; Vaiana, L.; Esteban-Gómez, D.; Avecilla, F.; Real, J. A.; De Blas, A.; Rodríguez-Blas, T. *Inorg. Chem.* **2005**, *44*, 9704−9713.

(16) El Hajj, F.; Sebki, G.; Patinec, V.; Marchivie, M.; Triki, S.; Handel, H.; Yefsah, S.; Tripier, R.; Gómez-García, C. J.; Coronado, E. *Inorg. Chem.* **2009**, *48*, 10416−10423.

(17) Batsanov, A. S.; Goeta, A. E.; Howard, J. A. K.; Maffeo, D.; Puschmann, H.; Williams, J. A. G. *Polyhedron* **2001**, *20*, 981−986.

(18) Goeta, A. E.; Howard, J. K. A.; Maffeo, D.; Puschmann, H.; Williams, J. A. G.; Yufit, D. S. *J. Chem. Soc., Dalton Trans.* **2000**, 1873−1880.

(19) Keypour, H.; Dehghani-Firouzabadi, A. A.; Khavasi, H. R. *Transition Met. Chem.* **2011**, *36*, 307−311.

(20) Keypour, H.; Zebarjadian, H. M.; Rezaeivala, M.; Chehreghani, A.; Amiri-Rudbari, H.; Bruno, G. *J. Iran. Chem. Soc.* **2014**, *11*, 101−109.

(21) (a) Nelson, S. M.; Busch, D. H. *Inorg. Chem.* **1969**, *8*, 1859−1863. (b) Drew, M. G. B.; Grimshaw, J.; McIlroy, P. D. A.; Nelson, S. M. *J. Chem. Soc., Dalton Trans.* **1976**, 1388−1394. (c) Drew, M. G. B.; bin Othman, A. H.; McFall, S. G.; McIlroy, P. D. A.; Nelson, S. M. *J. Chem. Soc., Dalton Trans.* **1977**, *5*, 438−446.

(22) Drew, M. G. B.; bin Othman, A. H.; McFall, S. G.; McIlroy, P. D. A.; Nelson, S. M. *J. Chem. Soc., Dalton Trans.* **1977**, *12*, 1173−1180.

(23) Rezaeivala, M.; Keypour, H. *Coord. Chem. Rev.* **2014**, *280*, 203−253.

(24) Gavey, E. L.; Pilkington, M. *Coord. Chem. Rev.* **2015**, *296*, 125−152.

(25) Guionneau, P.; Le Gac, F.; Kaiba, A.; Sánchez Costa, J.; Chasseau, D.; Létard, J.-F. *Chem. Commun.* **2007**, 3723−3725.

(26) Costa, J. S.; Balde, C.; Carbonera, C.; Denux, D.; Wattiaux, A.; Desplanches, C.; Ader, J.-P.; Gütlich, P.; Létard, J.-F. *Inorg. Chem.* **2007**, *46*, 4114−4119.

(27) Zhang, D.; Wang, H.; Tian, L.; Jiang, J.; Ni, Z.-H. *CrystEngComm* **2009**, *11*, 2447−2451.

(28) Venkatakrishnan, T. S.; Sahoo, S.; Bréfuel, N.; Duhayon, C.; Paulsen, C.; Barra, A.-L.; Ramasesha, S.; Sutter, J.-P. *J. Am. Chem. Soc.* **2010**, *132*, 6047−6056.

(29) Zhang, Y. Z.; Sato, O. *Inorg. Chem.* **2010**, *49*, 1271−1273.

(30) Hayami, S.; Juhász, G.; Maeda, Y.; Yokoyama, T.; Sato, O. *Inorg. Chem.* **2005**, *44*, 7289−7291.

(31) Ruamps, R.; Batchelor, L. J.; Maurice, R.; Gogoi, N.; Jiménez-Lozano, P.; Guihéry, N.; de Graaf, C.; Barra, A.-L.; Sutter, J.-P.; Mallah, T. *Chem. - Eur. J.* **2013**, *19*, 950−956.

(32) Batchelor, L. J.; Sangalli, M.; Guillot, R.; Guihéry, N.; Maurice, R.; Tuna, F.; Mallah, T. *Inorg. Chem.* **2011**, *50*, 12045−12052.

(33) Gogoi, N.; Thlijeni, M.; Duhayon, C.; Sutter, J.-P. *Inorg. Chem.* **2013**, *52*, 2283−2285.

(34) Dey, M.; Dutta, S.; Sarma, B.; Deka, Ch.R.; Gogoi, N. *Chem. Commun.* **2016**, *52*, 753−756.

(35) Huang, X.-C.; Zhou, C.; Shao, D.; Wang, X.-Y. *Inorg. Chem.* **2014**, *53*, 12671−12673.

(36) Drahoš, B.; Herchel, R.; Trávníček, Z. *Inorg. Chem.* **2015**, *54*, 3352−3369.

(37) Drahoš, B.; Herchel, R.; Trávníček, Z. *RSC Adv.* **2016**, *6*, 34674−34684.

(38) Bard, A. J.; Faulkner, L. R. *Electrochemical Methods: Fundamentals and Applications*; John Wiley & Sons, Inc: New York, 1980.

(39) Bruker. *Apex3*; Bruker AXS Inc: Madison, WI, 2015.

(40) Sheldrick, G. M. *Acta Crystallogr., Sect. C: Struct. Chem.* **2015**, *71*, 3−8.

(41) Brandenburg, K. *DIAMOND*, Release 3.2k; Crystal Impact GbR: Bonn, Germany, 2004.

(42) Zhang, J.; Cui, H.; Hojo, M.; Shuang, S.; Dong, C. *Bioorg. Med. Chem. Lett.* **2012**, *22*, 343−346.

(43) Drahoš, B.; Kotek, J.; Hermann, P.; Lukeš, I.; Tóth, É. *Inorg. Chem.* **2010**, *49*, 3224−3238.

(44) Neese, F. *WIREs Comput. Mol. Sci.* **2012**, *2*, 73−78.

(45) Pantazis, D. A.; Chen, X.-Y.; Landis, C. R.; Neese, F. *J. Chem. Theory Comput.* **2008**, *4*, 908−919.

(46) (a) Van Lenthe, E.; Baerends, E. J.; Snijders, J. G. *J. Chem. Phys.* **1993**, *99*, 4597−4610. (b) Van Wüllen, C. *J. Chem. Phys.* **1998**, *109*, 392−399.

(47) Malmqvist, P. Å.; Roos, B. O. *Chem. Phys. Lett.* **1989**, *155*, 189−194.

(48) (a) Angeli, C.; Cimiraglia, R.; Evangelisti, S.; Leininger, T.; Malrieu, J.-P. *J. Chem. Phys.* **2001**, *114*, 10252−10264. (b) Angeli, C.; Cimiraglia, R.; Malrieu, J.-P. *Chem. Phys. Lett.* **2001**, *350*, 297−305. (c) Angeli, C.; Cimiraglia, R.; Malrieu, J.-P. *J. Chem. Phys.* **2002**, *117*, 9138−9153. (d) Angeli, C.; Borini, S.; Cestari, M.; Cimiraglia, R. *J. Chem. Phys.* **2004**, *121*, 4043−4049. (e) Angeli, C.; Bories, B.; Cavallini, A.; Cimiraglia, R. *J. Chem. Phys.* **2006**, *124*, 054108.

(49) Ganyushin, D.; Neese, F. *J. Chem. Phys.* **2006**, *125*, 024103.

(50) Neese, F. *J. Chem. Phys.* **2005**, *122*, 034107.

(51) Maurice, R.; Bastardis, R.; De Graaf, C.; Suaud, N.; Mallah, T.; Guihéry, N. *J. Chem. Theory Comput.* **2009**, *5*, 2977−2984.

(52) Nakamoto, K. *Infrared and Raman Spectra of Inorganic and Coordination Compounds, Part B: Applications in Coordination, Organometallic and Bioinorganic Chemistry*; Wiley: NJ, 2009.

(53) Duncan, J. F.; Mok, K. F. *Aust. J. Chem.* **1966**, *19*, 701−703.

(54) (a) Alvarez, S. *Dalton Trans.* **2005**, 2209−2233. (b) Casanova, D.; Alemany, P.; Bofill, J. M.; Alvarez, S. *Chem. - Eur. J.* **2003**, *9*, 1281−1295.

(55) Amouri, H.; Gruselle, M. *Chirality in Transition Metal Chemistry: Molecules, Supramolecular Assemblies and Materials*; Wiley: Chichester, U.K., 2008.

(56) See, for example, (a) Nemec, I.; Šilha, T.; Herchel, R.; Trávníček, Z. *Eur. J. Inorg. Chem.* **2013**, *2013*, 5781−5789. (b) Šilha, T.; Nemec, I.; Herchel, R.; Trávníček, Z. *CrystEngComm* **2013**, *15*, 5351−5358. (c) Nemec, I.; Herchel, R.; Šilha, T.; Trávníček, Z. *Dalton Trans.* **2014**, *43*, 15602−15616.

(57) See, for example, (a) Leng, J.-D.; Xing, S.-K.; Herchel, R.; Liu, J.-L.; Tong, M.-L. *Inorg. Chem.* **2014**, *53*, 5458−5466. (b) Massoud, S. S.; Spell, M.; Ledet, C. C.; Junk, T.; Herchel, R.; Fischer, R. C.; Trávníček, Z.; Mautner, F. A. *Dalton Trans.* **2015**, *44*, 2110−2121. (c) Mathivathanan, L.; Al-Ameed, K.; Lazarou, K.; Trávníček, Z.; Sanakis, Y.; Herchel, R.; McGrady, J. E.; Raptis, R. G. *Dalton Trans.* **2015**, *44*, 20685−20691.

(58) See, for example, (a) Herchel, R.; Váhovská, L.; Potočňák, I.; Trávníček, Z. *Inorg. Chem.* **2014**, *53*, 5896−5898. (b) Nemec, I.; Herchel, R.; Svoboda, I.; Boča, R.; Trávníček, Z. *Dalton Trans.* **2015**, *44*, 9551−9560. (c) Nemec, I.; Marx, R.; Herchel, R.; Neugebauer, P.; Van Slageren, J.; Trávníček, Z. *Dalton Trans.* **2015**, *44*, 15014−15021.

(59) Herchel, R.; Nemec, I.; Machata, M.; Trávníček, Z. *Inorg. Chem.* **2015**, *54*, 8625−8638.

(60) Boča, R. *Coord. Chem. Rev.* **2004**, *248*, 757−815.

(61) The standard deviations were calculated as $\sigma_i = (P_{ii}^{-1} \cdot S/(N-k))^{-1/2}$, where $P_{ij} = \sum(\delta\mu_n/\delta a_i \cdot \delta\mu_n/\delta a_j)$ and $S = \sum(\mu_n - \mu_n^{exp})^2$ with $n = 1$ to N; a_i and a_j are fitted parameters, N is number of experimental points (sum of temperature and field dependent data), μ_n and μ_n^{exp} are the calculated and experimental effective magnetic moments for given temperature and magnetic field. The σ_i was then multiplied by Student's $t_{95\%}$ to provide confidence limits with 95% probabilities listed in text.

(62) Boča, R. *Theoretical Foundations of Molecular Magnetism*; Elsevier: Amsterdam, 1999.

(63) Vaiana, L.; Regueiro-Figueroa, M.; Mato-Iglesias, M.; Platas-Iglesias, C.; Esteban-Gómez, D.; De Blas, A.; Rodríguez-Blas, T. *Inorg. Chem.* **2007**, *46*, 8271−8282.

(64) Rechkemmer, Y.; Fischer, J. E.; Marx, R.; Dörfel, M.; Neugebauer, P.; Horvath, S.; Gysler, M.; Brock-Nannestad, T.; Frey, W.; Reid, M. F.; Van Slageren, J. *J. Am. Chem. Soc.* **2015**, *137*, 13114−13120.

(65) (a) Bartolomé, J.; Filoti, G.; Kuncser, V.; Schinteie, G.; Mereacre, V.; Anson, C. E.; Powell, A. K.; Prodius, D.; Turta, C. *Phys. Rev. B: Condens. Matter Mater. Phys.* **2009**, *80*, 014430. (b) Ishikawa, R.; Miyamoto, R.; Nojiri, H.; Breedlove, B. K.; Yamashita, M. *Inorg. Chem.* **2013**, *52*, 8300−8302.

(66) Gómez-Coca, S.; Aravena, D.; Morales, R.; Ruiz, E. *Coord. Chem. Rev.* **2015**, *289−290*, 379−392.

(67) (a) Meyerstein, D. *Coord. Chem. Rev.* **1999**, *185−186*, 141−147. (b) Kent Barefield, E. *Coord. Chem. Rev.* **2010**, *254*, 1607−1627. (c) Dong, Y.; Lawrance, G. A.; Lindoy, L. F.; Turner, P. *Dalton Trans.* **2003**, 1567−1576.

Příloha P6

P. Antal, B. Drahoš, R. Herchel, Z. Trávníček,

Structure and Magnetism of Seven-Coordinate Fe^{III}, Fe^{II}, Co^{II} and Ni^{II} Complexes Containing a Heptadentate 15-Membered Pyridine-Based Macrocyclic Ligand.

Molecular Magnetism

Structure and Magnetism of Seven-Coordinate Fe^{III}, Fe^{II}, Co^{II} and Ni^{II} Complexes Containing a Heptadentate 15-Membered Pyridine-Based Macrocyclic Ligand

Peter Antal,[a] Bohuslav Drahoš,[a] Radovan Herchel,[a] and Zdeněk Trávníček*[a]

Abstract: A heptadentate macrocyclic ligand, **H₂L** (3,12,18-triaza-6,9-dioxabicyclo[12.3.1]octadeca-1,14,16-triene-3,12-diacetic acid) with two acetate pendant arms, and its complexes [Fe^{III}**L**]ClO₄ (**1**), [Fe^{II}**L**]·H₂O (**2**), [Co^{II}**L**]·H₂O (**3**), and [Ni^{II}**L**]·H₂O (**4**) were synthesized. The complexes possess an axially compressed pentagonal bipyramidal geometry with the coordination numbers of 7 for **2** and **3**, and 6 + 1 for **4**. The magnetic susceptibility measurements revealed magnetic anisotropy for compounds **1**–**4** expressed by axial zero-field splitting (ZFS) parameters (D = –1.3 cm^{-1} for **1**, –9.6 cm^{-1} for **2**, 29.1 cm^{-1} for **3**, and –8.5 cm^{-1} for **4**), with a rhombic ZFS (E/D = 0, 0.006, 0, and 0.193, respectively). Field-induced slow relaxation of magnetization was observed for the Co^{II} complex **3** only. The structural and magnetic features of **1**–**4** were compared with those of similar complexes containing ligand with two 2-pyridylmethyl pendant arms. Magnetic features of the complexes were also evaluated using theoretical calculations (DFT, CASSCF/NEVPT2).

Introduction

Design and synthesis of new macrocyclic ligands of different sizes, structures, donor atoms sets and properties represent a very topical area of research due to their applications in many fields of chemistry,[1] biology[2] and medicine.[3] Macrocyclic ligands can serve as suitable ligands for coordination to a variety of metal ions depending on the cavity size, ring structure and type of metal ion. Due to the high thermodynamic stability and kinetic inertness of their transition metal complexes, macrocycles can be utilized for metal separation,[4] as radiopharmaceuticals in radiotherapy,[5] as contrast-enhancing agents in magnetic resonance imaging (MRI),[6] or as models to study the magnetic phenomena, such as spin-crossover (SCO) or molecular magnetism.[7]

In the last decade, more attention has been devoted to the study the complexes with interesting magnetic properties such as SCO or molecular magnetism [single-molecule magnets (SMMs) and single-chain magnets (SCMs)] due to their potential applications in high-density data storage devices[8] and quantum computing.[9] The SMMs are compounds showing slow relaxation of magnetization and magnetic hysteresis below the critical temperature. There are several mechanisms for the dynamics of the relaxation of the magnetization (Orbach, direct, Raman, or quantum tunnelling) and elucidation which mechanism contributes dominantly to the overall relaxation process is still very challenging. Previously, the Orbach mechanism was usually considered as the most important one and therefore SMMs were often characterized by the parameter called energy barrier U for the magnetic moment reversal, which appears as a consequence of a large axial magnetic anisotropy [described by the axial zero-field splitting (ZFS) parameter D within the spin Hamiltonian formalism], which splits the metal ion energy spin levels in zero magnetic field, and this energy barrier can be defined as $U = |D|S^2$ or $U = |D|(S^2 - 1/4)$ for integer or non-integer ground spin state S.

In order to significantly increase the magnetic anisotropy in transition metal complexes,[10] which is the crucial tuneable parameter for SMMs improvement, the modification of the coordination environment, provided by higher coordination numbers (seven or eight), and/or axial symmetry were employed.[11] The coordination number of seven is not common for first-row transition metals and its abundance along the series is irregular.[12,13] It is most abundant for Mn, Fe, and Co complexes, while in the case of Ni complexes is very rare due to the Jahn–Teller effect, which cause strong deformation of coordination sphere and low stability of these type of. geometry.[14,15] Nevertheless, several examples of linear (H₂dabph)[16] or macrocyclic ligands (15-pydienN₃O₂,[17] 15-pydienN₅,[18] 15-pyN₃O₂,[19] tdmmb,[20] or more recent TODA)[21] (Figure S1) provided seven-coordinate pentagonal bipyramidal complexes with a pentadentate ligand in the equatorial plane, which show a large easy-axis magnetic anisotropy ($D < 0$) in the case of Fe^{II} and Ni^{II} complexes, and on the other side, a large easy-plane magnetic anisotropy ($D > 0$) in the case of Co^{II} complexes. Slow relaxation of magnetization was observed for [Fe(H₂dabph)Cl₂] and [Fe(H₂dabph-NH₂)Cl₂] ($\tau_0 = 5 \times 10^{-9}$ s and $U_{eff} = 53$ cm^{-1}),[16] for

[a] *Division of Biologically Active Complexes and Molecular Magnets,*
Regional Centre of Advanced Technologies and Materials,
Faculty of Science, Palacký University,
Šlechtitelů 27, 78371 Olomouc, Czech Republic
Fax: +420 585 634 954
E-mail: zdenek.travnicek@upol.cz
https://www.rcptm.com/research-divisions/biologically-active-complexes-and-molecular-magnets-2/http://agch.upol.cz/en/

Supporting information and ORCID(s) from the author(s) for this article are available on the WWW under https://doi.org/10.1002/ejic.201800769.

★ ChemPubSoc
Europe

EurJIC
European Journal
of Inorganic Chemistry

Full Paper

[{Ni(H$_2$dabph)}$_3${W(CN)$_8$}$_2$] (below the blocking temperature T_N = 3.6 K, τ_0 = 1.6 × 10^{-9} s, U_{eff} = 30 K),[22] and for many different Co^{II} complexes.[10,18,23,24] Furthermore, the magnetic anisotropy has been tuned by playing with donor/acceptor properties of two axial coligands, as was shown on series of Co^{II} complexes, e.g. [Co(tdmmb)(X)$_2$]$^{2+/0}$,[20] where X = H$_2$O, CN$^-$, NCS$^-$, SPh$^-$, with the more pronounced anisotropy for the complex with SPh$^-$ (D = 39.7 cm^{-1}), or [Co(15-pyN$_3$O$_2$)X$_2$],[23] where X = Cl$^-$, Br$^-$ and I$^-$ with the highest D = 41 cm^{-1} for the dibromido complex, and also on Mn^{II} complexes [Mn(15-pyN$_3$O$_2$)X],[25] where X = Br$^-$, I$^-$, N$_3^-$, NCS$^-$, with a small influence of axial coligands on the magnetic anisotropy ($|D|$ < 0.7 cm^{-1}).

The recent results suggest that also seven-coordinate lanthanide complexes with pentagonal bipyramidal geometry show remarkable properties,[26] concretely a very high magnetization reversal barrier was found for [Dy(OPCy$_3$)(H$_2$O)$_5$]$^{3+}$,[27] [Dy(tBuPO(NHiPr)$_2$)$_2$(H$_2$O)$_5$]$^{3+}$,[28] [Dy(bbpen)Cl], and [Dy-(bbpen)Br][29] with U_{eff} = 543, 735, 708, and 1025 K, respectively.

A different approach how to tune desired structural and magnetic properties of complexes can be associated with modification of the original pentadentate macrocycle, e.g. 15-pyN$_3$O$_2$, with two pendant arms containing different functional groups providing heptadentate ligand and seven-coordinate complexes. Variations in the functional groups of the pendant arms can provide fine tuning of the ligand field for the complexed metal ions. Such approach was successfully employed in our previous study concerning the seven-coordinate Mn^{II}, Fe^{II}, Co^{II}, and Ni^{II} complexes of py$_2$-15-pyN$_3$O$_2$ (Figure 1) with two 2-pyridylmethyl pendant arms.[30] Magnetic measurements revealed noticeable values of magnetic anisotropy for [Fe(py$_2$-15-pyN$_3$O$_2$)](ClO$_4$)$_2$ (D = −7.4 cm^{-1}), [Co(py$_2$-15-pyN$_3$O$_2$)](ClO$_4$)$_2$ (D = 34 cm^{-1}), and [Ni(py$_2$-15-pyN$_3$O$_2$)](ClO$_4$)$_2$ (D = −12.8 cm^{-1}, E/D = 0.136). Moreover, the slow relaxation of the magnetization was observed [τ_0 = 9.90 × 10^{-10} s, U_{eff} = 24.3 K (16.9 cm^{-1})] for [Co(py$_2$-15-pyN$_3$O$_2$)](ClO$_4$)$_2$.[30]
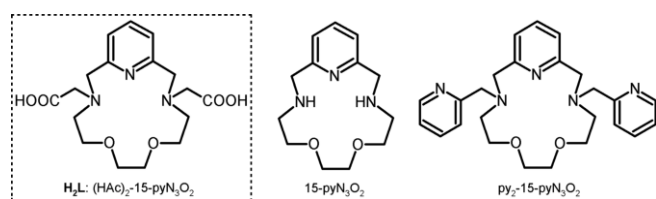
Figure 1. Structural formula of the 15-pyN$_3$O$_2$ ligand and its derivatives (HAc)$_2$-15pyN$_3$O$_2$ (H$_2$L) and py$_2$-15-pyN$_3$O$_2$.

In order to tune of the magnetic anisotropy via different axial coligands and to investigate the effect of axial coligands also on the structural and redox properties of the selected first-row transition metals, the original unsubstituted 15-pyN$_3$O$_2$ was modified with two acetate pendant arms, which have a different π-donor/acceptor ability in comparison with the previously studied pyridine functional groups. The motif of linear or macrocyclic acetate N-pendant-armed ligands is well known from the literature and even several seven-coordinate complexes of di- and trivalent first-row transition metal were previously prepared, e.g. [{Mn(Hedta)(H$_2$O)}$_2${μ-Mn(H$_2$O)$_4$}]·4H$_2$O,[31] [Co-

(Hedta)(H$_2$O)]·2H$_2$O,[32] [Mn(1,4-DO2A)]$_2$·2CH$_3$OH,[33] [Fe$_2$(1,4-DO2A)$_2$]I$_{1.5}$,[34] [Fe(DO3A)]·3H$_2$O,[35] Na[Fe(DOTA)]·5H$_2$O,[35] [Cu((HAc)$_2$-15-N$_2$O$_3$)]·2H$_2$O.[36] Surprisingly, their magnetic properties were studied only sporadically or even not at all.

In this work we describe the synthesis and characterization of pentagonal bipyramidal Fe^{III}, Fe^{II}, Co^{II}, and Ni^{II} complexes with a macrocyclic ligand containing two acetate pendant arms [H$_2$L = 3,12-bis(carboxymethyl)-6,9-dioxa-3,12,18-triazabicyclo-[12.3.1]octadeca-1(18),14,16-triene] and we discuss the impact of the axial ligands on the structural, magnetic and redox properties. Moreover, we compare these newly obtained data with those for the previously reported complexes with py$_2$-15-pyN$_3$O$_2$ and 15-pyN$_3$O$_2$. Moreover, we also performed various theoretical calculations with the aim to better understand the effect of modification of pendant arms on physical properties of the complexes.

Results and Discussion

Syntheses and General Characterizations

The ligand H$_2$L was prepared by N-alkylation of 15-pyN$_3$O$_2$ using a small excess of bromoacetic acid,[37] and purified by ion-exchange chromatography. The complexes were prepared by direct mixing of H$_2$L with the corresponding metal perchlorate or chloride in acetonitrile/methanol (1) or water/methanol mixture (2–4) in an equimolar ratio and heating to 60 °C. The compounds in their crystalline forms were obtained by slow diffusion of diethyl ether (1) or acetone vapors (2–4) into these solutions.

The diffuse-reflectance spectra were measured for all the studied complexes and are shown in Figure S2. Moreover, they are compared to the electronic absorption spectra of the selected complexes 2 and 3 measured in 5 mM aqueous and methanolic solutions (Figure S3). Each of the diffuse-reflectance spectrum contains one or more intense bands at various positions, but all spectra correspond well to those of the previously studied seven-coordinate complexes of Fe^{III},[38,39] Fe^{II},[40] Co^{II}[41] or Ni^{II}.[42,43] Furthermore, the solution spectra of 2 and 3 in both solvents well correspond to the diffuse-reflectance spectra, which demonstrate that the coordination sphere of both complexes in solution is similar to that in solid-state. Based on the values of molar absorption coefficients for the most intense bands [e.g. ε(534 nm) = 8.4 M^{-1} cm^{-1} for 3 in H$_2$O, ε(400 nm) = 88 M^{-1} cm^{-1} for 2 in H$_2$O], the observed bands could be assigned to d–d transitions.

Crystal Structure Analysis

X-ray diffraction data for compounds 2–4 indicate that the Fe^{II}, Co^{II} and Ni^{II} complexes are isostructural, and crystallize in the monoclinic space group $P2_{1/c}$ (Table 1). The compounds crystallize as racemic compounds with both enantiomeric forms of the [M(L)] complexes in the unit cell (Figure S4).

Molecular Structures of Complexes 2, 3 and 4

The complexes 2 and 3 have similar molecular structures (Figure 2 and Figure S5). The central atoms of Fe^{II} in 2 and Co^{II} in

★ ChemPubSoc
Europe

EurJIC
European Journal
of Inorganic Chemistry

Full Paper

Table 1. Crystal data and structure refinements for the compounds **2**–**4**.

Compound	2	3	4
Formula	$C_{17}H_{25}N_3O_7Fe_1$	$C_{17}H_{25}N_3O_7Co_1$	$C_{17}H_{25}N_3O_7Ni_1$
Mr	439.24	442.33	442.11
Colour	Orange	Dark purple	Green
Crystal system	Monoclinic	Monoclinic	Monoclinic
Space group (space group no.)	$P2_1/c$ (14)	$P2_1/c$ (14)	$P2_1/c$ (14)
a [Å]	11.535(10)	11.490(3)	11.465(3)
b [Å]	12.107(11)	12.037(4)	12.017(3)
c [Å]	13.935(12)	13.929(4)	14.047(4)
α [°]	90	90	90
β [°]	107.25(3)	107.149(11)	108.255(8)
γ [°]	90	90	90
U [Å³]	1859(3)	1840.7(10)	1837.9(8)
Z	4	4	4
λ [Å], Mo-K_α	0.71073	0.71073	0.71073
D_{calc} [g cm⁻³]	1.570	1.596	1.598
μ [mm⁻¹]	0.858	0.979	1.103
F (000)	920	924	928
Reflections collected	29566	55323	52902
Independent reflections	4268 [R(int) = 0.0817]	5690 [R(int) = 0.0832]	4771 [R(int) = 0.0508]
Data/restraints/parameters	4268/3/259	5690/3/259	4771/3/259
Goodness-of-fit on F^2	1.024	1.033	1.017
R_1, wR_1 [$I > 2\sigma(I)$]	0.0363/0.0713	0.0362/0.0659	0.0262/0.0630
R_2, wR_2 (all data)	0.0618/0.0796	0.0683/0.0747	0.0369/0.0679
Largest diff. peak and hole [Å⁻³]	0.288/–0.523	0.417/–0.469	0.332/–0.520
CCDC no.	1811164	1811163	1811165

3 are seven-coordinate and for that reason just X-ray structure of complex **2** is shown in the main text, while the molecular structure of complex **3** is depicted in Figure S5. The coordination environment can be described as pentagonal bipyramidal, with the equatorial pentagonal plane defined by three nitrogen atoms (one from the pyridine ring – N_{py} and two from the aliphatic chains – N_{aliph}) and two oxygen atoms (O_{aliph}) from the macrocyclic ring of the ligand. The axial positions are occupied by two oxygen atoms (O_{pend}) from the carboxylate groups of the pendant arms. The M–O_{pend} bonds are the shortest coordination bonds in **2** and **3** (Table 2), and at the same time the Co–O_{pend} bonds are the shortest axial coordination bonds in series of [Co(15-pyN$_3$O$_2$)Cl$_2$][19] and [Co(py$_2$-15-pyN$_3$O$_2$)](ClO$_4$)$_2$[30] (Table 3).

Table 2. Selected interatomic distances (Å) and angles (°) in compounds **2**, **3**, and **4**.

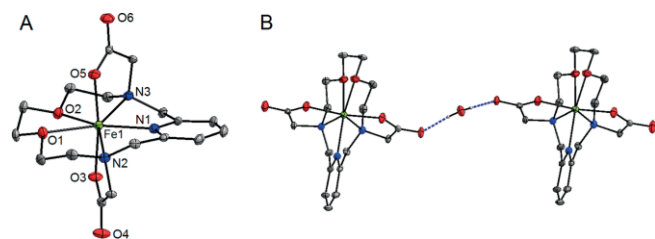| Distances	2	3	4
M–N1	2.191(2)	2.1503(15)	2.0150(12)
M–N2	2.295(2)	2.2416(14)	2.1463(12)
M–N3	2.317(2)	2.2705(14)	2.2132(12)
M–O1	2.287(2)	2.3156(13)	2.4313(11)
M–O2	2.312(2)	2.3489(13)	2.6754(11)
M–O3	2.078(2)	2.0429(13)	1.9886(11)
M–O5	2.083(2)	2.0460(13)	1.9918(11)
Angles			
N1–M–N2	72.54(8)	73.64(5)	78.37(5)
N1–M–N3	71.67(9)	72.49(5)	76.51(5)
N1–M–O1	145.61(7)	146.34(5)	151.72(5)
N1–M–O2	144.23(7)	146.34(5)	145.12(4)
N1–M–O3	92.92(7)	92.84(5)	95.33(4)
N1–M–O5	94.53(7)	94.48(5)	96.59(4)
N2–M–O1	74.31(6)	74.00(5)	74.55(4)
N3–M–O2	73.93(8)	73.50(5)	63.16(4)
O1–M–O2	70.16(7)	68.98(4)	70.15(4)
O3–M–O5	172.40(6)	172.45(5)	167.80(4)

Figure 2. (A) Molecular structure of **2**. Thermal ellipsoids are drawn with the 50 % probability level. The water molecules of crystallization and hydrogen atoms are omitted for clarity. (B) Representation of 1D chain in the crystal structure of **2**. The individual [Fe**L**] molecules are connected by the O–H•••O hydrogen bonds (dark blue dashed lines) going through the crystal water molecules. Hydrogen atoms not involved in these interactions are omitted for clarity.

The central atom of Ni^{II} in **4** is coordinated by the N$_3$O$_4$ donor set of the ligand (Figure 3A). The coordination number could be classified as 6+1, because one of the Ni–O_{aliph} bond is significantly elongated [Ni–O2, 2.6754(11) Å, Table 2]. It is more elongated than the other bond lengths of such type, because the mean value of the Ni–O bond length is 2.055 Å, and 90 % of all the observed Ni–O bonds have lengths in the range of 1.964–2.114 Å. Similar elongation of the Ni–O bonds was observed in other Ni^{II} complexes with macrocyclic ligands (Figure 1 and S1), [Ni(Ac$_2$-15N$_2$O$_3$)](ClO$_4$)$_2$,[15] [Ni(15-pyN$_3$O$_2$)Cl$_2$][19] or [Ni(py$_2$-15-pyN$_3$O$_2$)](ClO$_4$)$_2$,[30] with the Ni–O bond lengths of 2.554(3), 2.506(3) and 2.663(3), and 2.653(2) Å, respectively.

ChemPubSoc
Europe

EurJIC
European Journal
of Inorganic Chemistry

Full Paper

Table 3. Comparison of the selected interatomic parameters in complexes Fe^{II} (**2**), Co^{II} (**3**), and Ni^{II} (**4**) with **H₂L**, and their analogues containing 15-pyN_3O_2 and py$_2$-15-pyN_3O_2.

	[M(15-pyN_3O_2)Cl_2][a]	[M(py$_2$-15-pyN_3O_2)]$^{2+}$[b]	[M(**L**)][c]
central atom–axial donor atom distances (Å)			
Fe		2.165(6)	2.081(3)
Co	2.468(4)	2.116(4)	2.044(2)
Ni	2.386(6)	2.084(7)	1.991(3)
deviation of central atom from the least-square plane (Å)[d]			
Fe		0.026[e]	0.000
Co	0.012	0.019[e]	0.001
Ni	0.000	0.007	0.008
mean deviation of equatorial donor atoms from least-square plane (Å)[f]			
Fe		0.104[e]	0.111
Co	0.088	0.098[e]	0.111
Ni	0.105	0.092	0.123

[a] Ref.[19]. [b] Ref.[30]. [c] This work. [d] The least-squares planes are defined by the MN_3O_2 atoms. [e] Mean deviation for both enantiomeric forms. [f] The equatorial donor atoms are N_{py}, N_{aliph}, and O_{aliph}.
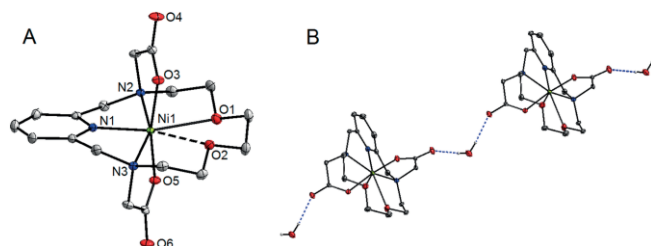
Figure 3. (A) Molecular structure of **4**. Thermal ellipsoids are drawn with the 50 % probability level. The water molecules of crystallization and hydrogen atoms are omitted for clarity. (B) Representation of 1D chain in the crystal structure of **4** formed by the individual [Ni**L**] molecules connected by the O–H•••O hydrogen bonds (dark blue dashed lines) going through the crystal water molecules. Hydrogen atoms not involved in these interactions are omitted for clarity.

When the molecular structures of complexes **2**, **3**, and **4** are compared among each other, similar trends can be observed as well as in the series of previously studied complexes of Fe^{II}, Co^{II}, and Ni^{II} with 15-pyN_3O_2[19] and py$_2$-15-pyN_3O_2.[30] The metal–nitrogen atom distances are shortening, while metal–oxygen atom distances are elongating with decreasing ionic radii of central atoms in order from Fe^{II} (**2**) to Ni^{II} (**4**) (Table 3).

In the case of Ni^{II}, one of the Ni–O_{aliph} bonds is significantly elongated. It could be explained by Jahn–Teller effect operating in seven-coordinate Ni^{II} complexes.[13] The M–O_{pend} bonds are the shortest coordination bonds in complexes **2**, **3**, and **4** (Table 2), and at the same time the shortest axial coordination bonds in series of [M(15-pyN_3O_2)Cl_2][19] and [M(py$_2$-15-pyN_3O_2)](ClO_4)$_2$[30] complexes (Table 3). The significant shortening of M–O_{pend} bonds lead to axial compression of coordination sphere. The deformation of coordination sphere around the central atom can be described as mean deviation value of all the donor atoms from the least-square plane defined by central atom and donor atoms in the equatorial positions (the MN_3O_2 set). Its value is the highest for complexes of **L**$^{2-}$ (Table 3), which also documents the stronger deformation of coordination sphere in comparison with other discussed compounds.

The geometry of coordination polyhedra of complexes **2**, **3**, and **4** were analysed by the Shape 2.1 software.[44] The lowest value of the deviation between the real geometry and the ideal coordination polyhedron (all the possible polyhedra for the co-ordination numbers of 6 and 7, in the case of complex **4** also for coordination number of 5) for complexes **2**, **3**, and **4** was found for pentagonal bipyramid (Table S1).

Crystal Structures of Complexes 2, 3 and 4

The crystal structures of compounds **2**, **3**, and **4** are stabilized by O–H•••O hydrogen bonds between the uncoordinated oxygen atoms of the carboxylate group and water molecules (Table S2), which hold together [M(**L**)] molecules and create 1D chains along the crystallographic axis *b* (Figure 2B and Figure 3B). In addition, the 1D chains are mutually connected by weak C–H•••C and C–H•••O interactions (Table S2).

Magnetic Properties

Static Magnetic Measurements

The temperature- and field-dependent experimental magnetic data for **2**–**4** are depicted in Figure 4. Firstly, the magnetic properties of M^{II} compounds **2**–**4** will be discussed.

The effective magnetic moments at room temperature (μ_{eff}/μ_B = 5.2 for **2**, μ_{eff}/μ_B = 4.4 for **3** and μ_{eff}/μ_B = 3.2 for **4**) is slightly higher than the spin-only values (μ_{eff}/μ_B = 4.9 for S = 2, μ_{eff}/μ_B = 3.9 for S = 3/2 and μ_{eff}/μ_B = 2.8 for S = 1) calculated with g = 2.0, which indicates non-negligible contribution of spin-orbit coupling to the ground state and g > 2.0. The drop of the effective magnetic moment is observed for all the compounds **2**–**4** at low temperature, which indicates significant zero-field splitting. Further evidence of ZFS is visible from the isothermal magnetization data (Figure 4) were $M_{mol}/N_A\mu_B$ at T = 2 K and B = 9 T reached values much lower than theoretical limit value of $M_{mol}/N_A\mu_B \rightarrow g \cdot S$.

ChemPubSoc
Europe

EurJIC
European Journal
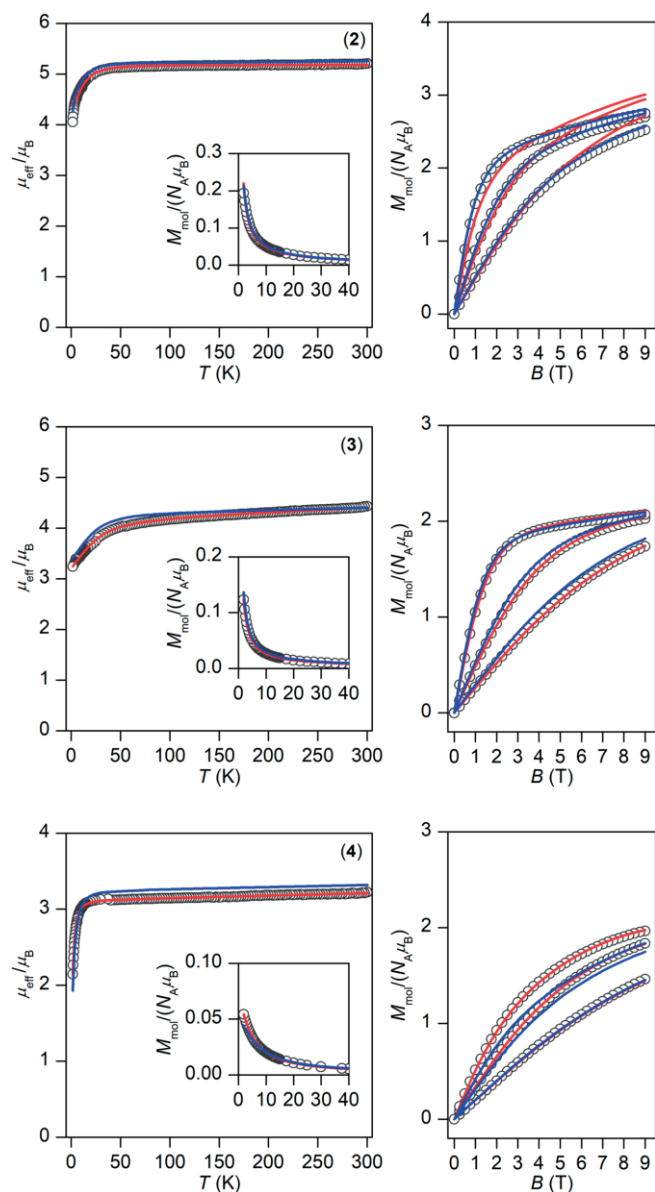of Inorganic Chemistry

Full Paper

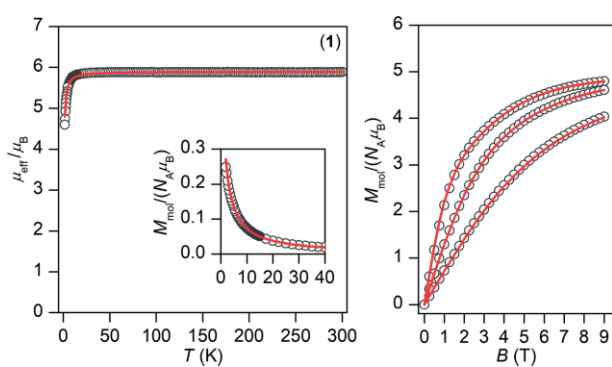Figure 4. Magnetic data for **2** (*top*), **3** (*middle*), and **4** (*bottom*). *Left*: temperature dependence of the effective magnetic moment and molar magnetization measured at $B = 0.1$ T. *Right*: isothermal magnetizations measured at $T = 2$, 5, and 10 K. The empty circles represent the experimental data, red full lines represent the fitted data using Equation 1 with parameters listed in Table 4. The blue full lines represent the calculated data using the CASSCF/NEVPT2 energy levels from CAS(n, 10) calculations.

Therefore, the spin Hamiltonian describing the magnetic anisotropy was postulated to extract ZFS parameters from the experimental magnetic data as

$$\hat{H} = D(\hat{S}_z^2 - \hat{S}^2/3) + E(\hat{S}_x^2 - \hat{S}_y^2) + \mu_B B g \hat{S}_a \qquad (1)$$

where D and E are the single-ion axial, and rhombic ZFS parameters, respectively, and the last component represents the Zeeman term defined in a direction of magnetic field as $B_a = B[\sin(\theta)\cos(\varphi), \sin(\theta)\sin(\varphi), \cos(\theta)]$ with the help of the polar

coordinates.[45] Then, the molar magnetization in *a*-direction of magnetic field can be numerically calculated as in Equation (2).

$$M_a = kT \left(\frac{\partial \ln Z}{\partial B_a} \right)_T \qquad (2)$$

where Z is the partition function resulting from energy levels. Afterwards, the averaged molar magnetization of the powder sample was calculated as integral (orientation) average [Equation (3)].

$$M_{mol} = \frac{1}{4\pi} \int_0^{2\pi} \int_0^{\pi} M_a \sin\theta d\theta d\phi \qquad (3)$$

It must be stressed that both temperature and field-dependent magnetic experimental data were fitted simultaneously in order to get most trustworthy parameters. The fitted parameters are summarized in Table 4. The negative *d*-values, $D = -9.6$ cm^{-1} and $D = -8.5$ cm^{-1}, were found for compounds **2**, and **4**, respectively, with considerable rhombicity in case of **4** ($E/D = 0.19$).

Table 4. Comparison of *Ab initio* calculated and fitted spin Hamiltonian parameters for complexes **1**–**4**.

Compound	1	2[a]	3	4
central metal atom	Fe^{III}	Fe^{II}	Co^{II}	Ni^{II}
electron configuration	3d^5	3d^6	3d^7	3d^8
spin state S	5/2	2	3/2	1
ZFS and g values based on CASSCF/NEVPT2 calculations with CAS(n,5)				
D (cm^{-1})		−15.1	+25.7	−11.5
E/D		0.194	0.070	0.192
g_x		2.070	2.378	2.243
g_y		1.999	2.429	2.211
g_z		2.331	2.193	2.308
ZFS and g values based on CASSCF/NEVPT2 calculations with CAS(n,10)				
D (cm^{-1})		−12.8	+28.5	−13.3
E/D		0.221	0.048	0.183
g_x		2.069	2.407	2.274
g_y		2.001	2.446	2.239
g_z		2.307	2.190	2.351
Magnetic analysis of the experimental data				
g	1.99	2.11	2.13	2.20
D (cm^{-1})	−1.3	−9.6	+29.1	−8.5
E/D	0	0.006	0	0.19
χ_{TIP} (1 × 10^{-9} m^3 mol^{-1})	0	0	12.7	3.2

[a] The first excited state is relative close to the ground state.

On contrary, Co^{II} complex **3** provided positive and large axial ZFS parameter, $D = +29.1$ cm^{-1}. In comparison with previously studied similar complexes with 2-pyridylmethyl pendant arm [M(py$_2$-15-pyN$_3$O$_2$)](ClO$_4$)$_2$ (Table 5), we observe that utilization of the acetate *N*-pendant arm resulted in larger magnetic anisotropy for Fe^{II} (*d*-value shifted from −7.4 cm^{-1} to −9.6 cm^{-1}), whereas smaller magnetic anisotropy was found for Co^{II} (*d*-value shifted from +34.0 cm^{-1} to +29.1 cm^{-1}) and Ni^{II} (*d*-value shifted from −12.8 cm^{-1} to −8.5 cm^{-1}) analogues.

ChemPubSoc
Europe

EurJIC
European Journal
of Inorganic Chemistry

Full Paper

Table 5. Comparison of *Ab initio* calculated and fitted spin Hamiltonian parameters for [M(py$_2$-15-pyN$_3$O$_2$)](ClO$_4$)$_2$ complexes **2^{py}–4^{py}**.

Compound	2$^{py[a]}$	3^{py}	4^{py}
central metal atom	Fe^{II}	Co^{II}	Ni^{II}
electron configuration	3d^6	3d^7	3d^8
spin state S	2	3/2	1
ZFS and g values based on CASSCF/NEVPT2 calculations with CAS(n,5)			
D (cm^{-1})	+8.70	+32.9	–14.7
E/D	0.321	0.051	0.132
g$_x$	2.068	2.288	2.227
g$_y$	2.219	2.327	2.203
g$_z$	2.008	2.026	2.314
B	990.3	1035.9	1260.2
C	3672.1	3998.0	4675.4
SOC constant zeta	412.3	523.9	654.9
ZFS and g values based on CASSCF/NEVPT2 calculations with CAS(n,10)			
D (cm^{-1})	+7.85	+33.9	–17.8
E/D	0.278	0.050	0.120
g$_x$	2.067	2.302	2.258
g$_y$	2.204	2.343	2.231
g$_z$	2.009	2.024	2.365
Magnetic analysis of the experimental data[b]			
g	2.13	2.21	2.18
D (cm^{-1})	–7.4	+34.0	–12.8
E/D	0.0	0.0	0.14
χ_{TIP} (1 × 10^{-9} m^3 mol^{-1})	3	1.3	2.2

[a] The first excited state is relative close to the ground state. [b] The value adopted from ref. 30.

In the case of Fe^{III} complex **1** the experimental data shown in Figure 5 could not be satisfactorily fitted with the spin Hamiltonian in Equation (1). Thus, the modified spin Hamiltonian in Equation (4).

$$\hat{H} = D(\hat{S}_z^2 - \hat{S}^2/3) + \mu_B Bg\hat{S}_a - zJ\langle\hat{S}_a\rangle\hat{S}_a \quad (4)$$

Figure 5. Magnetic data for **1**. *Left*: temperature dependence of the effective magnetic moment and molar magnetization measured at *B* = 0.1 T. *Right*: isothermal magnetizations measured at *T* = 2, 5, and 10 K. The empty circles represent the experimental data, and the red full lines represent the fitted data using Equation 4 with *g* = 1.99, *D* = –1.3 cm^{-1} and *zJ* = –0.11 cm^{-1}.

where, except for the single-ion zero-field splitting parameter *D*, the molecular field correction *zJ* parameter is present. The $\langle S_a \rangle$ is a thermal average of the molecular spin projection in *a*-direction of magnetic field. Then, the molar magnetization is calculated as in Equation (5).

$$M_a = -N_A \frac{\sum_i \left(\sum_k \sum_l C_{ik}^+ (Z_a)_{kl} C_{li} \right) \exp(-\varepsilon_{a,i}/kT)}{\sum_i \exp(-\varepsilon_{a,i}/kT)} \quad (5)$$

where Z_a is the matrix element of the Zeeman term for the *a*-direction of the magnetic field and *C* are the eigenvectors resulting from the diagonalization of the complete spin Hamiltonian matrix. The inclusion of *zj* means that iterative procedure was applied. The averaged molar magnetization of the powder sample was calculated as integral (orientational) average defined in Equation (3). The best-fit was found for *g* = 1.99, *D* = –1.3 cm^{-1} and *zJ* = –0.11 cm^{-1} (Figure 5) suggesting weak antiferromagnetic intermolecular interactions in solid state.

Dynamic Magnetic Measurements

The temperature- and frequency-dependent alternating current (AC) susceptibly measurement was performed for **2**–**4**. We did not find out-of-phase signals in a zero static magnetic field, but upon turning on the magnetic field, the imaginary susceptibility became non-zero for compounds **2** and **3**, while there were no non-zero out-of-phase signal for compound **4** (Figures S6–S8).
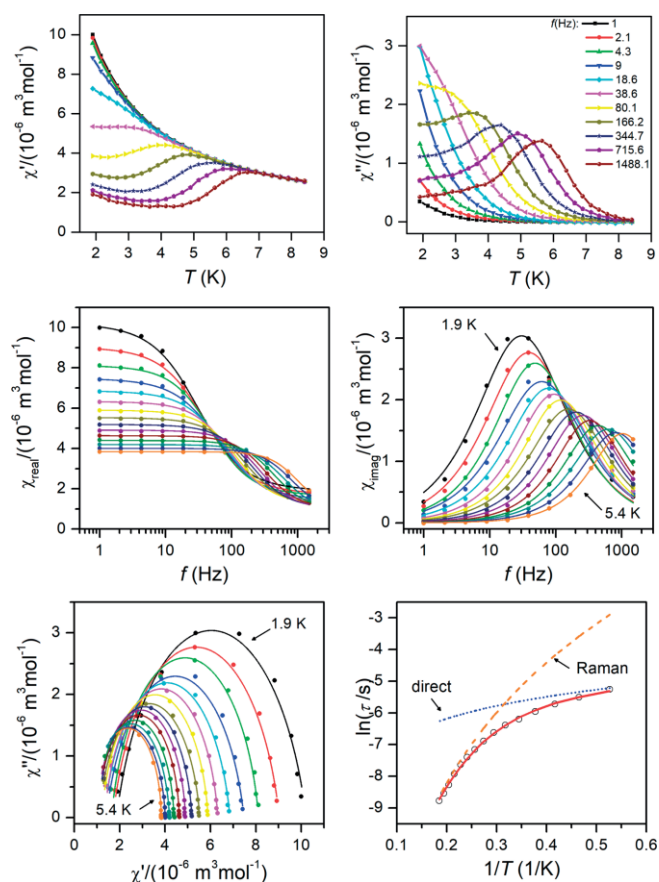

Figure 6. *Top*: in-phase χ′ and out-of-phase χ″ molar susceptibilities for 3 at the applied external magnetic field *B*$_{DC}$ = 0.1 T (full lines are only guides for eyes). *Middle*: frequency dependence of in-phase χ′ and out-of-phase χ″ molar susceptibilities for 3 at the applied external magnetic field *B*$_{DC}$ = 0.1 T. The full lines represent the fitted data using Equation 6. *Bottom*: the Argand (Cole–Cole) plot with full lines fitted with Equation 6 and the fit of resulting, relaxation times τ with direct and Raman spin-lattice relaxation processes according to Equation 7.

★ChemPubSoc
Europe

EurJIC
European Journal
of Inorganic Chemistry

Full Paper

In the case of compound **2**, a weak out-of-phase signal of AC susceptibility was detected at stronger static magnetic field, thus temperature and frequency ac susceptibility data were acquired at B_{DC} = 0.4 T as showed in Figure S9. Finally, clearly defined maxima of out-of-phase signal of AC susceptibility depended on applied frequency were found for compound **3** already at a weak static field B_{DC} = 0.1 T, which is the typical behaviour of SMMs (Figure 6), and thus one-component Debye's model was applied based on Equation (6).

$$\chi(\omega) = \frac{\chi_T - \chi_S}{1 + (i\omega\tau)^{1-\alpha}} + \chi_S$$
(6)

which resulted in isothermal (χ_T) and adiabatic (χ_S) susceptibilities, relaxation times (τ) and distribution parameters (α) (Table S3). This enabled us to construct the Argand (Cole–Cole) plot (Figure 6).

In general, there are several processes in solid state responsible for the observation of the slow relaxation of the magnetization: one-phonon direct process, two-phonon Raman and Orbach processes and quantum tunnelling. Recently, we have shown that temperature-dependence of the relaxation times for seven-coordinate Co^{II} complexes can be fitted either with the Orbach or Raman relaxation process.[23,30] In case of **3**, large and positive D together with negligible E/D ratio means that the easy-plane type of the magnetic anisotropy is present, and therefore the existence of the spin reversal barrier $U_{eff} = |D| \times (S^2 - 1/4)$ is hard to imagine.

However, τ vs. T can be well fitted by considering direct and Raman spin-lattice relaxation processes using Equation (7).

$$\frac{1}{\tau} = AT + CT^n$$
(7)

where the former is operative at lower temperature and the latter is active at higher temperatures (Figure 6). The fitting procedure resulted in A = 96.9 K^{-1} s^{-1}, C = 0.535 K^{-1} s^{-n} and n = 5.49. In general, the Raman coefficient n is expected to be between 5 and 9 for Kramers ions depending on energy separation of the doublets.[46]

Electrochemical Properties

The redox properties of **H₂L** and its complexes **1**, **3** and **4** were investigated by cyclic voltammetry in acetonitrile solutions. The experiments could not be performed for complex **2** owing its low solubility. However, it can be expected for complex **2** that it should provide nearly identical qualitative data as complex **1** (the same Fe$^{II/III}$ couple is present). The cyclic voltammograms of **H₂L** and complexes **1**, **3**, and **4** are depicted in Figure 7, and the obtained electrochemical data are listed in Table 6. The cyclic voltammogram of the ligand **H₂L** solution in acetonitrile (Figure 7) shows irreversible behaviour providing two oxidation peaks at very high potentials (E_{ox1} = 1.06 V and E_{ox2} = 1.61 V) and two reduction peaks at very low potentials (E_{red1} = −1.46 V and E_{red2} = −1.76 V), which may be assigned to the oxidation/ reduction of both carboxylate pendant arms. One reversible couple Fe^{III}/Fe^{II} was found at the potentials of $E_{1/2}$ = 0.23 V in acetonitrile solution of **1** together with the irreversible reduc-

tion peak at E_{red} = −1.94 V corresponding probably to the reduction of Fe^{II} to Fe^{I} and consequent reaction/decomposition of the complex.
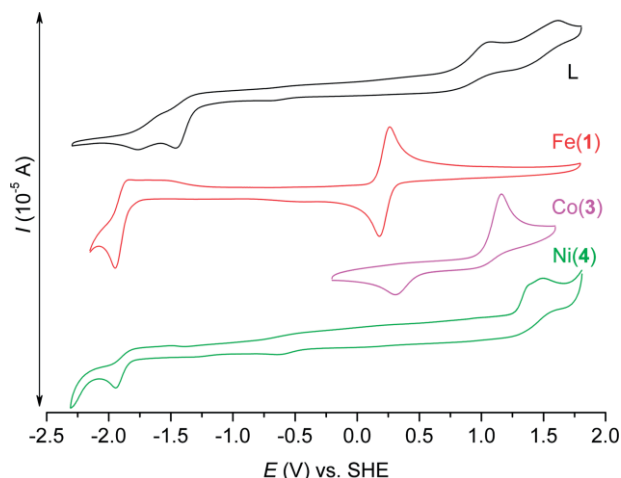

Figure 7. Cyclic voltammograms of the ligand **H₂L** (black) and complexes **1** (red), **3** (purple), and **4** (green) (ca. 1 mM) recorded in argon atmosphere with a glassy carbon working electrode in 0.1 M TBAP in acetonitrile.

Table 6. Results of cyclic voltammetry experiments.

Compound	Redox process	$E_{1/2}$ [V] vs. SHE
H₂L		E_{ox1} = 1.063
		E_{ox2} = 1.609
		E_{red1} = −1.463
		E_{red2} = −1.761
1	Fe^{3+}/Fe^{2+}	0.226
		(ΔE_p = 85 mV)
	Fe^{2+}/Fe^{+}	E_{red} = −1.943
3	Co^{3+}/Co^{2+}	E_{ox} = 1.167
		E_{red} = 0.318
4	Ni^{3+}/Ni^2	E_{ox} = 1.485
	Ni^{2+}/Ni^{+}	E_{red} = −1.932

In the case of **3**, a quasi-reversible couple Co^{III}/Co^{II} with the oxidation peak at E_{ox} = 1.17 V and reduction peak at E_{red} = 0.32 V and a very large peak separation ΔE_p = 849 mV were observed. In the cyclic voltammogram of **4**, an irreversible oxidation peak corresponding to the oxidation of Ni^{II} to Ni^{III} was found at E_{ox} = 1.48 V together with the irreversible reduction peak corresponding to the reduction of Ni^{II} to Ni^{I} at E_{red} = −1.93 V. The obtained values of $E_{1/2}$, E_{ox} or E_{red} are much lower (cca. 0.7–1.0 V) than those previously found for complexes with structurally similar ligand py₂-15-pyN₃O₂ containing two 2-methylpyridine pendant arms; [M(py₂-15-pyN₃O₂)](ClO₄)₂, M = Fe^{II}, Co^{II} and Ni^{II}; E(Fe^{3+}/Fe^{2+})$_{1/2}$ = 1.26 V, ΔE_p = 86 mV; $E_{1/2}$(Co^{3+}/ Co^{2+}) = 1.89 V, ΔE_p = 86 mV, $E_{1/2}$(Co^{2+}/Co^{+}) = −1.32 V, ΔE_p = 65 mV; E_{red}(Ni^{2+}/Ni^{+}) = −1.16 V.[30] Thus, in comparison with the complexes containing pyridine as axial ligands, the lower $E_{1/2}$, E_{ox} or E_{red} values in the case of complexes **1**, **3** and **4** clearly indicate that **L^{2-}** stabilizes higher oxidation states in its complexes, because the carboxylate group has rather weak π-donor ability in comparison with the pyridine functional groups in py₂-15-pyN₃O₂ with π-acceptor ability. Additional important factor is the negative charge of the carboxylate group, because it was shown previously that negatively charged ligands stabi-

ChemPubSoc
Europe

EurJIC
European Journal
of Inorganic Chemistry

Full Paper

lizes higher oxidation states.[47] In accordance with this is observation that $E_{1/2}$ for Fe^{III}/Fe^{II} couple is similar to that found for complexes with unsubstituted macrocyclic ligand 15-pyN$_3$O$_2$ and two axial chlorido coligands, [Fe(15-pyN$_3$O$_2$)Cl$_2$]Cl [$E_{1/2}$(Fe^{3+}/Fe^{2+}) = 0.25 V, ΔE_p = 81 mV].[19]

Another observed aspect based on irreversibility of many processes is fact that the ligand **L**$^{2-}$ cannot stabilize complexes in very high or low oxidation states (Ni^{III}, Ni^I, Fe^I), because its carboxylate group(s) are more electrochemically active in comparison with the coordinated pyridine group(s) in [M(py$_2$-15-pyN$_3$O$_2$)](ClO$_4$)$_2$ and cannot provide electrochemically stable coordination sphere (reduction or oxidation of the carboxylate group may occur) or the complexes are subject to consequent decomposition.

Theoretical Calculations

With the aim to elucidate the effect of alternation of the pyridine *N*-pendant arm with the acetate *N*-pendant one on electronic properties of the seven-coordinate complexes, the DFT and post-Hartree–Fock CASSCF calculations were performed with the ORCA 4.0.0 computation package. Firstly, the DFT was employed to assess bonding properties in both series of M^{II} complexes using B3LYP functional and def2-TZVP(-f) basis set (Figure 8). Interestingly, the bond lengths M–N$_{py}$ are very similar in both series, but the bond order is much enhanced for the series with the pyridine *N*-pendant arm (**2^{py}–4^{py}**), e.g. d(Ni–N$_{py}$) = 2.015 Å in **4** and d(Ni–N$_{py}$) = 2.010 Å in **4^{py}**, but the bond orders are 0.47 and 0.58, respectively. On the contrary, the bond lengths M–O$_{aliph}$ seem to be slightly longer for **2–4** than for **2^{py}–4^{py}**, which is also reflected in slightly weaker bond orders (Figure 8). The bond lengths M–O$_{pend}$ in **2–4** are shorter than M–N$_{pend}$ in **2^{py}–4^{py}**, but the bond orders are almost similar, e.g. d(Co–O$_{pend}$) = 2.043/2.046 Å in **3** and d(Co–N$_{pend}$) = 2.120 Å in **3^{py}** result in bond orders 0.43/0.41 in **3**, and 0.42/0.45 in **3^{py}**, respectively. To conclude, the change of the *N*-pendant arm from pyridine to acetate resulted also in changes of bond lengths and donor properties of the core macrocyclic part (15-pyN$_3$O$_2$), and thus both axial and equatorial donor atoms influence the changes in electronic structures, and hence magnetic properties observed between two series of M^{II} complexes with (HAc)$_2$-15-pyN$_3$O$_2$ and py$_2$-15-pyN$_3$O$_2$ ligands. Next, CASSCF/NEVPT2 calculations were performed with the same basis set def2-TZVP(-f) for all the atoms. Firstly, the active space of each complex with a metal ion of the 3d^n configuration was defined by *n*-electrons in five d-orbitals - CAS(*n*,5). Secondly, the double-shell effect was also encountered by enlarging the number of active orbitals (3d + 4d) as CAS(*n*,10). For both type of the calculations, the number of multiplets were as follows: 5 quintets and 45 triplets for Fe^{II}, 10 quartets and 40 doublets for Co^{II}, and 10 triplets and 15 singlets for Ni^{II}. The energies of lowest terms and multiplets for both series derived from CAS(*n*,10) calculations are depicted in Figure 9. In general holds for Fe^{II} and Ni^{II} complexes that a perfect ligand field symmetry of a pentagonal bipyramid (D_{5h}) would result into orbitally degenerate ground state. However, the orbital degeneracy is lifted by a lower symmetry ligand field induced by (HAc)$_2$-15-pyN$_3$O$_2$

and py$_2$-15-pyN$_3$O$_2$ ligands in real complexes **2**, **4**, **2^{py}**, and **4^{py}**. The declination from ideal symmetry is more pronounced in Ni^{II} complexes **4** and **4^{py}**, which results into well separated ground state term with the first excited terms energies larger than 6000 cm^{-1} (Figure 9). Thus, the subsequent splitting of the ground term into (2S + 1) multiplet can be adequately described by the spin Hamiltonian formalism. The situation is different in Fe^{II} complexes of **2** and **2^{py}**, where first excited terms are very close to the ground state (948 cm^{-1} for **2** and 1086 cm^{-1} for **2^{py}**), which means that spin Hamiltonian model is not adequate anymore, and fitted or calculated ZFS parameters must be considered with great care. The variation of the molecular geometries and the ligand field in studied series is reflected also in splitting of d-orbitals, which energies calculated by ab initio ligand field theory (AILFT)[48] from CAS(*n*,5) multireference computations are plotted in Figure S10.
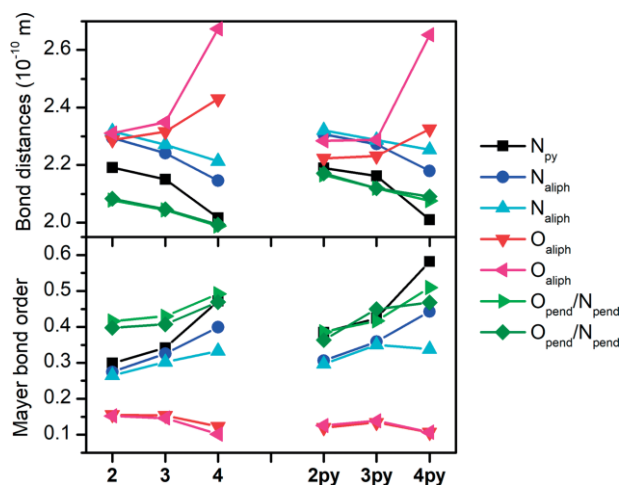

Figure 8. Variations of the metal–donor atom distances (*top*) and Mayer's bond orders (*bottom*) calculated with B3LYP/de2-TZVP(-f) in the studied compounds 2–4 and their analogues 2^{py}–4^{py}.
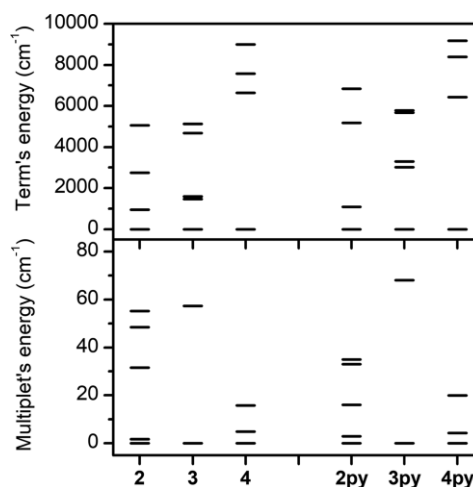

Figure 9. The lowest energy levels based on the CASSCF/NEVPT2 calculations with CAS(*n*,10) active space for 2–4 and 2^{py}–4^{py} complexes – ligand field terms (*top*) and ligand field multiplets (*bottom*).

The analysis of CASSCF/NEVPT2 calculated multiplets with effective Hamiltonian theory resulted in ZFS parameters *D* and

ChemPubSoc
Europe

EurJIC
European Journal
of Inorganic Chemistry

Full Paper

E, and g-tensors listed in Table 4 and Table 5. In general, the enlarging the active space from CAS(n,5) to CAS(n,10) resulted in smaller $|D|$ values for Fe^{II} complexes, while for Co^{II} and Ni^{II} complexes the double shell effect resulted in larger $|D|$ values. Furthermore, the calculations supported trend of d-values induced by the alternation of the pendant arms as found from the analysis of the experimental magnetic data: $|D|$ of **2** > $|D|$ of **2^{py}**, $|D|$ of **3** < $|D|$ of **3^{py}**, and $|D|$ of **4** < $|D|$ of **4^{py}**. Moreover, the axes of d-tensors together with molecular structures are visualized in Figure S11. Interestingly, the z-axis of d-tensor is approximately located along the O$_{pend}$–M–O$_{pend}$ and N$_{pend}$–M–N$_{pend}$ axial bonds, except for compound **2^{py}**. Other axes are roughly located within the plane of the macrocyclic ligand with one axis directed to the M–N$_{py}$ bond (Figure S11). Finally, the calculated CAS(n,10)-CASSCF/NEVPT2 matrices of the spin-orbit coupling $\mathbf{H}^{SOC}$, the spin momentum operators ($\mathbf{S}_x$, $\mathbf{S}_y$, $\mathbf{S}_z$) and the orbital momentum operators ($\mathbf{L}_x$, $\mathbf{L}_y$, $\mathbf{L}_z$) were used to calculate energy levels for any strength and orientation of the magnetic field by diagonalization of the matrix $\mathbf{H}$ defined as in Equation (8).

$$\mathbf{H} = \mathbf{H}^{SOC} + \mu_B(\mathbf{L} + g_e\mathbf{S}) \cdot \mathbf{B} \qquad (8)$$

which enabled us to calculate the partition function Z and finally the integral average of the molar magnetization M_{mol} for **2–4**. The great advantage of this procedure is the fact that no restriction of spin Hamiltonian formalism is applied, thus no ZFS or g-tensors parameters are used. The calculated data are displayed in Figure 4. There is almost perfect agreement with the experimental data for compound **2** for which fitting with ZFS parameters using Equation (1) show deviation in the isothermal magnetization (Figure 4). This particularly demonstrates the strength of this approach for the coordination compounds with unquenched orbital angular momentum. The similarly good agreement was obtained for compound **3** as shown in Figure 4.

Only for the compound **4**, the deviation of the calculated magnetic data from the experimental ones is noticeable, which is expected as the calculated d-value is much more negative than the fitted one (Table 4).

In order to better understand the effect of the axial ligands, herein different pendant arms, the model complexes of the general formula [M(NH$_3$)$_3$(H$_2$O)$_2$(OH)$_2$] (M = Fe^{II}, Co^{II} and Ni^{II}) were treated with CASSCF/NEVPT2 using CAS(n,5) active space. The amino and aqua ligands were placed into fixed positions within the equatorial plane, whereas the distance between the central atom and the hydroxido ligands in axial positions was varied to modulate the ligand field strength of potential pendant arms. The dependence of D and E/D on d(M–OH) is depicted in Figure 10. The d-parameters are large and positive for a Co^{II} model complex within whole range of d(Co–OH) values, the D is increasing with decreasing ligand field in the axial positions, which agrees with our previous AOM prediction.[23] The rhombicity is very small down to d(Co–OH) = 2.1 Å, and then starts to increase up to almost E/D = 1/3, which suggest that for very strong axial ligand field, the D could be negative.

In the case of a Ni^{II} model complex, the D is negative and very large (–76 cm^{-1} < D < –52.3 cm^{-1}), whereas the rhombicity
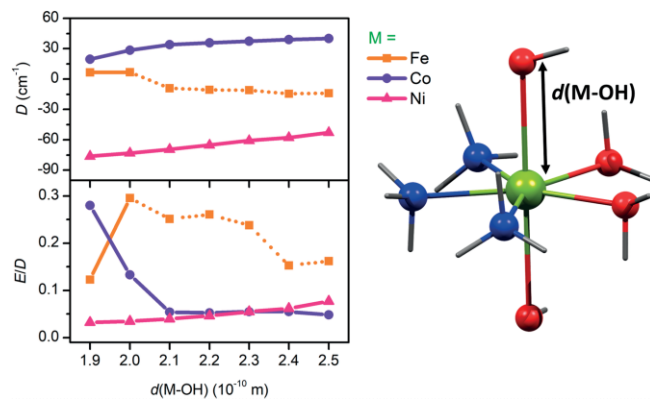

Figure 10. The calculated variations of the ZFS parameters using CASSCF/NEVPT2 with CAS(n,5) (left) for model compounds [M(NH$_3$)$_3$(H$_2$O)$_2$(OH)$_2$], where M = Fe, Co or Ni (right). The dotted line for M = Fe means that there are close lying excited states and the spin Hamiltonian model with ZFS may not be adequate.

is very small (E/D < 0.1), which means that such complexes could be ideal candidates for study of SMM behaviour.[67–70] The Fe^{II} model complex exhibit small and positive D for strong axial ligand field, which is switched to negative values for d(Fe–OH) > 2 Å. However, for larger distance of axial hydroxide ligands, the ground state is not sufficiently separated from the excited states, so the spin Hamiltonian formalism, hence ZFS parameters, must be taken with great care.

Conclusions

In summary, we report on the investigation of tuning of the magnetic anisotropy in pentagonal bipyramidal Fe^{III}, Fe^{II}, Co^{II}, and Ni^{II} complexes **1–4** with a heptadentate pyridine-based macrocyclic ligand (H$_2$L) containing two N-pendant arms with the acetate functional groups. The obtained structural, magnetic and redox features of complexes **2–4** were compared with those of structurally similar and recently published complexes **2^{py}–4^{py}** containing an analogous 2-pyridylmethyl N-pendant-armed ligand (py$_2$-15-pyN$_3$O$_2$). Larger axial compression of the pentagonal bipyramidal coordination environment was observed in the complexes **2–4** as compared to **2^{py}–4^{py}**, probably due to the negative charge of the carboxylate group providing an extra "charge assisted" component to the coordination bonds. Surprisingly, this bond shortening was not reflected in the Mayer bond orders, which were similar or slightly higher for **2^{py}–4^{py}**. The largest magnetic anisotropy within the series of **2–4** and **2^{py}–4^{py}** was found for the Co^{II} complexes, where the d-value value changed from +34.0 cm^{-1} (**3^{py}**) to +29.1 cm^{-1} (**3**). As for the Fe^{II} and Ni^{II} complexes, their d-values changed from –7.4 cm^{-1} (**2^{py}**) to –9.6 cm^{-1} (**2**), and from –12.8 cm^{-1} (**4^{py}**) to –8.5 cm^{-1} (**4**), respectively. In order to better understand such an ambiguous trend, the CASSCF/NEVPT2 calculations were performed and they showed that an increase of the magnetic anisotropy could be achieved by stronger axial ligand field for Ni^{II} complexes, whereas by weaker axial ligand field in the case of Fe^{II} and Co^{II} complexes. Considering these findings during comparison of the magnetic anisotropy of **2–4** and **2^{py}–4^{py}**, the

increase in |*D*|-value for Fe^{II} complexes (**2^{py}→2**) and decrease for Ni^{II} complexes (**4^{py}→4**) is in good agreement with the expected weaker ligand field provided by two axially coordinated carboxylate pendant arms of **L^{2-}** in comparison with the pyridine ones of py$_2$-15-pyN$_3$O$_2$. On the other hand, the |*D*|-value for Co^{II} complex **3** should be higher than that of **3^{py}**, but it is not. Anyway, field-induced slow relaxation of magnetization was observed for Co^{II} complex **3** only, which can be characterized most likely using direct and Raman relaxation mechanisms without considering Orbach relaxation mechanisms due to the easy-plane type of the magnetic anisotropy. Very weak out-of-phase signal of AC susceptibility was detected upon applying static magnetic field for compound **2**.

Altogether we can conclude that the substitution of the pyridine by carboxylate group coordinated in axial positions of pentagonal bipyramidal first-row transition metal complexes resulted in changes in bond lengths, donor/acceptor properties, electrochemical properties and also in rather complicated changes in magnetic anisotropy. These changes in magnetic anisotropy could be explained by the fact that the modification of the functional group in the ligand pendant arm influences also the donor properties of the equatorial macrocyclic part and thus, both axial and equatorial donor atoms contribute to the final electronic structure of the complexes (the axial effect cannot be exclusively distinguished from the equatorial one), which is responsible for their magnetic behaviour. Therefore, only part of the obtained data correlates with the expected trends observed previously or calculated theoretically.

Experimental Section

Materials and Methods: The starting macrocycle (15-pyN$_3$O$_2$ = 3,12,18-triaza-6,9-dioxabicyclo[12.3.1]octadeca-1,14,16-triene) was prepared as described in the literature.[30,49] All the solvents, chemicals and ion-exchange resins (DOWEX 50, DOWEX 1 × 8) were purchased from commercial sources (Lachner, Neratovice, Czech Republic; Penta, Prague, Czech Republic; Across Organics, Geel, Belgium, and Sigma Aldrich, St. Louis, MO, USA) and used without further purification.

Elemental analysis (C, H, N) was performed on a Flash 2000 CHNO-S Analyzer (Thermo Scientific, Waltham, MA, USA). Infrared spectra (IR) were recorded on a Thermo Nicolet NEXUS 670 FT-IR spectrometer (Thermo Nicolet, Waltham, MA, USA) by using the ATR technique on a diamond plate in the range 400–4000 cm^{-1}. The mass spectra (MS) were collected on an LCQ Fleet Ion Mass Trap mass spectrometer (Thermo Scientific, Waltham, MA, USA) equipped with an electrospray ion source and three-dimensional ion-trap detector in the positive mode. The ^{1}H and ^{13}C NMR spectra were registered at 298 K on a JEOL JNM-ECA 600II (JEOL, Tokyo, Japan) operating at 600.00 MHz (^{1}H) and 150.86 MHz (^{13}C). The signal assignments in ^{1}H and ^{13}C NMR spectra were based in part on two-dimensional COSY, HMBC and HMQC experiments. The temperature-dependent (*T* = 1.9–300 K, *B* = 0.1 T) and field-dependent (*B* = 0–9 T, *T* = 2, 5, 10 K) magnetization measurements were performed on PPMS Dynacool (Quantum design Inc., San Diego, CA, USA). Dynamic magnetic properties were studied by measuring alternating current (AC) susceptibility on an MPMS XL-7 SQUID magnetometer (Quantum design Inc., San Diego, CA, USA). The cyclic voltammetry was performed on electrochemical analyser CHI600C (CH Instrument

Inc., Austin, TX, USA). A conventional electrochemical three-electrode-type cell was used with Ag/Ag$^+$ reference electrode (0.01 M AgNO$_3$ in 0.1 M TBAP), a platinum wire auxiliary electrode, and a glassy carbon working electrode. The final potential values referred to SHE were obtained using internal ferrocene/ferrocenium standard (*E*$_{1/2}$ = 0.220 V vs. our Ag/Ag$^+$ electrode, *E*$_{1/2}$ = 0.624 V vs. SHE).[50] The measurements were performed in acetonitrile solution in the presence of 0.1 M tetrabutylammonium perchlorate (TBAP) as a supporting electrolyte with the scan rate of 100 mV s^{-1} for 1 × 10^{-3} M concentration of the complexes. The diffuse-reflectance spectra (400–1000 nm, Nujol mull technique) and electronic absorption spectra (350–1000 nm, 5 mM complex solutions in water or methanol) were recorded on a Lambda-40 spectrophotometer (Perkin–Elmer, Waltham, MA, USA) at room temperature.

Crystal Data: Single crystals of complexes **2**, **3**, and **4** suitable for X-ray diffraction analysis were formed upon a slow diffusion of acetone vapors into the solutions of the appropriate complex at room temperature. X-ray diffraction data were collected on a Bruker D8 QUEST diffractometer equipped with a PHOTON 100 CMOS detector using Mo-*K*$_\alpha$ radiation (*λ* = 0.71073 Å) at temperature of 120 K. The APEX3 software package[51] was used for data collection and reduction. The molecular structures were solved by direct methods (SHELXS) and refined using the SHELXTL software package.[52] All the hydrogen atoms were found in the difference Fourier maps and refined using a rigid model, with C–H = 0.95 (CH)$_{ar}$ and C–H = 0.99 (CH$_2$) Å, and with *U*$_{iso}$(H) = 1.2*U*$_{eq}$(CH, CH$_2$). The crystallographic data and structure refinement parameters for complexes **2**–**4** are listed in Table 1, while selected interatomic distances and angles can be found in Table 2. The molecular and crystal structures of all the studied compounds, depicted in Figure 2 (complex **2**), 3 (complex **4**), S4 and S5 (complex **3**), were drawn using Diamond software.[53] The attempts to prepare crystals of complex **1**, suitable for a single X-ray analysis, were unsuccessful.

CCDC 1811164 (for **2**) and 1811163 (for **3**) and 1811165 (for **4**) contain the supplementary crystallographic data for this paper. These data can be obtained free of charge from The Cambridge Crystallographic Data Centre.

Synthesis of the H$_2$L ligand

The **H$_2$L** ligand was synthesized according to the modified literature procedure.[37] 3,12,18-triaza-6,9-dioxabicyclo[12.3.1]octadeca-1,14,16-triene (2.20 g, 8.75 mmol) was dissolved in water (10 mL) and then solid bromoacetic acid (4.87 g, 35.0 mmol) was added. The solution of sodium hydroxide (1.50 g, 37.5 mmol) in water (20 mL) was added dropwise, and the pH value of the obtained solution was corrected to pH = 10 with an aqueous solution of sodium hydroxide (1 mol/L). The reaction mixture was refluxed 4 hours and then hydrochloric acid (6 mL, final pH = 3) and methanol (10 mL) was added. White precipitate of sodium bromide and chloride was filtered off and the obtained brownish yellow filtrate was evaporated under reduced pressure to give a yellow oil. The crude product was purified by cation-exchange chromatography (DOWEX 50, H$^+$ form, eluted by 5 % aq. NH$_3$) for removal of bromide, chloride, and bromoacetate anions, followed by anion-exchange chromatography (DOWEX 1 × 8, OH$^-$ form, eluted by 5 % aq. HCl) for removal of sodium cations, and finally cation-exchange chromatography (DOWEX 50, H$^+$ form, eluted by 5 % aq. NH$_3$) was used for obtaining of the zwitterionic form of ligand (**H$_2$L**). The eluate containing the desired product was evaporated to dryness in vacuo. The obtained colourless oil crystallized in the form of hygroscopic colourless crystals at 5 °C (refrigerator) after 48 hours. Yield: 1.67 g (52 %). ^{1}H NMR (DMSO): *δ* = 7.76 (t, $^3J_{HH}$ = 7.6 Hz, 1 H, C*H* arom.), 7.32 (d, $^2J_{HH}$ = 7.6 Hz, 2 H, C*H* arom.), 3.93 (s, 4 H, pyC*H$_2$*N), 3.50 (s,

★ ChemPubSoc
Europe

EurJIC
European Journal
of Inorganic Chemistry

Full Paper

4 H, OCH_2CH_2O), 3.29 (t, 4 H, OCH_2CH$_2$N), 3.24 (s, 4 H, NCH_2COOH), 2.85 (m, 4 H, OCH$_2$CH_2N) ppm. ^{13}C{^{1}H} NMR: δ = 172.7 (2 C, *C*OOH), 158.4 (2 C, *C*CH$_2$), 137.6 (1 C, *C*H arom.), 121.9 (2 C, *C*H arom.), 69.8 (2 C, O*C*H$_2$CH$_2$N), 68.4 (2 C, O*C*H$_2$CH$_2$O), 60.3 (2 C, N*C*H$_2$py), 58.0 (2 C, N*C*H$_2$COOH), 54.4 (2 C, N*C*H$_2$CH$_2$O) ppm. MS, *m/z* (+) found (calculated, relative intensity): 368.21 [H$_2$**L**+H]$^+$ (368.18, I_{rel} = 100 %); 390.20 [H$_2$**L**+Na]$^+$ (390.16, I_{rel} = 53 %). MS, *m/z* (–): 366.31 [H**L**]$^-$ (366.17, I_{rel} = 100 %). Elemental analysis for H$_2$**L**·5H$_2$O (C$_{17}$H$_{35}$N$_3$O$_{11}$) found (calculated): C, 44.29 (44.63); H, 7.89 (7.71); N, 9.56 (9.19). IR (ATR): $\tilde{v}$ = 861 (w), 910 (w), 1104 (m), 1118 (m), 1150 (m), 1320 (sh), 1335 (s), 1361 (m), 1387 (m), 1493 (w), 1577 (m), 1601 (s), 1626 (s), 1643 (s) cm^{-1}.

Synthesis of complexes 1–4

[FeL](ClO$_4$) (1): Solid Fe(ClO$_4$)$_3$·6H$_2$O (0.171 g, 0.37 mmol) was added to a solution of **H$_2$L** (136 mg, 0.37 mmol) in a mixture of acetonitrile/methanol (20 mL; *V/V* = 1:1). The obtained solution was stirred and heated at 60 °C for 1 hour, and resulting yellow solution was left to crystallize by slow diffusion of diethyl ether vapors into the acetonitrile/methanol mixture at room temperature. The yellow crystals were isolated after 24 hours (166 mg, 86 %). C$_{17}$H$_{23}$N$_3$O$_{10}$Cl$_1$Fe$_1$ found (calculated): C, 39.13 (39.21); H, 4.46 (4.45); N, 7.90 (8.07) %. MS: *m/z* = (+) found (calculated, relative intensity): 421.04 [Fe**L**]$^+$ (421.09, I_{rel} = 100 %).

[FeL]·H$_2$O (2): Solid FeCl$_2$ (0.033 g, 0.26 mmol) and **H$_2$L** (0.095 g, 0.26 mmol) were dissolved in a mixture of methanol (2 mL) and water (0.5 mL) under inert argon atmosphere. Bu$_3$N (150 mg, 0.81 mmol) was added to this solution and the mixture was stirred and heated at 60 °C for 10 minutes. The obtained yellow solution was filtered via 45 μm teflon syringe filter and allowed to crystallize by slow diffusion of acetone vapors at room temperature. The orange crystals were isolated after 48 hours (91 mg, 80 %). C$_{17}$H$_{25}$N$_3$O$_7$Fe$_1$ found (calculated): C, 46.44 (46.49); H, 6.00 (5.74); N, 9.50 (9.57) %. MS: *m/z* (+) found (calculated, relative intensity): 422.15 [Fe(**L**+H)]$^+$ (422.10, I_{rel} = 100 %); 843.06 [Fe$_2$**L**$_2$+H]$^+$ (843.19, I_{rel} = 29 %); 865.07 [Fe$_2$L$_2$+Na]$^+$ (865.18, I_{rel} = 70 %).

[CoL]·H$_2$O (3): Solid CoCl$_2$·6H$_2$O (119 mg, 0.50 mmol) was added to a solution of **H$_2$L** (0.184 g, 0.50 mmol) in 15 mL of a water/methanol mixture (*V/V* = 1:1). The obtained solution was stirred and heated at 60 °C for 1 hour, and then was evaporated to dryness. The solid residue was dissolved in minimal volume of water/methanol mixture (*V/V* = 1:1) and allowed to crystallize by a slow diffusion of acetone vapors at room temperature. The dark purple crystals were isolated after 48 hours (155 mg, 70 %). C$_{17}$H$_{25}$N$_3$O$_7$Co$_1$ found (calculated): C, 46.06 (46.16); H, 5.47 (5.70); N, 9.44 (9.50) %. MS: *m/z* (+) found (calculated, relative intensity): 425.09 [Co(**L**+H)]$^+$ (425.10, I_{rel} = 94 %); 848.94 [Co$_2$**L**$_2$+H]$^+$ (849.19, I_{rel} = 100 %).

[NiL]·H$_2$O (4): The compound was prepared by the same procedure as described above for **2**, but using NiCl$_2$·6H$_2$O (120 mg, 0.50 mmol) instead of CoCl$_2$·6H$_2$O. The green crystals were isolated after 48 hours (201 mg, 91 %). C$_{17}$H$_{25}$N$_3$O$_7$Ni$_1$ found (calculated): C, 46.16 (46.19); H, 5.74 (5.70); N, 9.41 (9.50) %. MS: *m/z* (+) found (calculated, relative intensity): 424.15 [Ni**L**+H]$^+$ (424.10, I_{rel} = 100 %); 846.95 [Ni$_2$**L**$_2$+H]$^+$ (847.20, I_{rel} = 80 %).

Theoretical Methods: The ORCA 4.0.0 computational package was used for all the theoretical calculations.[54] The Mayer's bond orders were calculated with the B3LYP functional[55] and triple-ζ basis set def2-TZVP(-f).[56] The auxiliary def/J basis set was also utilized[57] together with the chain-of-spheres (RIJCOSX) approximation to exact exchange[58] as implemented in ORCA. The calculations of ZFS parameters were done using state average complete active space self-consistent field (SA-CASSCF)[59] wave functions complemented

by *N*-electron valence second-order perturbation theory (NEVPT2).[60] In the state-averaged approach all multiplets for given electron configuration were equally weighted. The ZFS parameters, based on dominant spin-orbit coupling contributions from excited states, were calculated through quasi-degenerate perturbation theory (QDPT),[61] in which an approximations to the Breit-Pauli form of the spin-orbit coupling operator (SOMF approximation)[62] and the effective Hamiltonian theory[63] were utilized. The calculations utilized the RIJCOSX approximation with the auxiliary coulomb basis def2/JK.[64] Increased integration grids (Grid6 in ORCA convention) and tight SCF convergence criteria were used in all calculations. The calculations were done on molecular fragments [M(**L**)] of **2**–**4** and [M(py$_2$-15-pyN$_3$O$_2$)]$^{2+}$ of **2^{py}**–**4^{py}** extracted from experimental X-ray structures. The model compounds [M(NH$_3$)$_3$-(H$_2$O)$_2$(OH)] (M = Fe^{II}, Co^{II} and Ni^{II}) were constructed in such a way that *d*(M–N) and *d*(M–O) of amino and aqua ligands were fixed to 2.1 Å, and *d*(M-O) of axial hydroxide ligand was varied between 1.9 and 2.5 Å. Only the positions of hydrogen atoms were optimized using the BP86 functional[55a,65] and def2-TZVP(-f) basis set together with Grimme's atom-pairwise dispersion correction and Becke–Johnson damping (D3BJ).[66]

Acknowledgments

[1] B. P. Burke, S. J. Archibald, *Annu. Rep. Prog. Chem. Sect. A* **2013**, *104*, 232–253.

[2] a) T. J. Collins, K. L. Kostka, E. S. Uffelman, T. L. Weinberger, *Inorg. Chem.* **1991**, *30*, 4204–4210; b) D. P. Riley, *Chem. Rev.* **1999**, *99*, 2573–2587.

[3] a) T. Storr, *Ligand Design in Medicinal Inorganic Chemistry*, John Wiley & Sons, U. K. **2014**; b) B. Drahoš, I. Lukeš, É. Tóth, *Eur. J. Inorg. Chem.* **2012**, *12*, 1975–1986.

[4] V. Gasperov, S. G. Galbraith, L. F. Lindoy, B. R. Rumbel, B. W. Skelton, P. A. Tasker, A. H. White, *Dalton Trans.* **2005**, 139–145.

[5] a) G. Hao, W. Liu, G. Hassan, K. O. Öz, Z. Kovacs, X. Sun, *Bioorg. Med. Chem. Lett.* **2015**, *25*, 571–574; b) A. Amoroso, I. A. Fallis, S. J. A. Pope, *Coord. Chem. Rev.* **2017**, *340*, 198–219; c) R. Bergmann, M. Meckel, V. Kubíček, J. Pietzsch, J. Steinbach, P. Hermann, F. Rösch, *EJNMMI Res.* **2016**, *6*, 1–12.

[6] a) A. S. Merbach, L. Helm, É. Tóth, *The Chemistry of Contrast Agents in Medical Magnetic Resonance*, John Wiley & Sons, U. K. **2013**; b) R. E. Mewis, S. J. Archibald, *Coord. Chem. Rev.* **2010**, *254*, 1686–1712.

[7] a) F. Touti, P. Maurin, L. Canaple, O. Beuf, J. Hasserodt, *Inorg. Chem.* **2012**, *51*, 31–33; b) J. Wen, Z. Geng, Y. Yin, Z. Wang, *Inorg. Chem. Commun.* **2012**, *21*, 16–20; c) S.-Y. Lin, Y.-N. Guo, Y. Guo, L. Zhao, P. Zhang, H. Ke, J. Tang, *Chem. Commun.* **2012**, *48*, 6924–6926; d) S.-Y. Lin, C. Wang, L. Zhao, J. Tang, *Chem. Asian J.* **2014**, *9*, 3558–3564.

[8] S.-Y. Lin, C. Wang, L. Zhao, J. Wu, J. Tang, *Dalton Trans.* **2015**, *44*, 223–229.

[9] A. Dei, D. Gatteschi, *Angew. Chem. Int. Ed.* **2011**, *50*, 11852–11858; *Angew. Chem.* **2011**, *123*, 12054.

[10] A. K. Bar, C. Pichon, J.-P. Sutter, *Coord. Chem. Rev.* **2016**, *308*, 346–380.

[11] a) J. M. Zadrozny, D. J. Xiao, M. Atanasov, G. J. Long, F. Grandjean, F. Neese, J. R. Long, *Nat. Chem.* **2013**, *5*, 577–881; b) X.-N. Yao, J.-Z. Du, Y.-Q. Zhang, X.-B. Leng, M.-W. Yang, S.-D. Jiang, Z.-X. Wang, Z.-W. Ouyang, L. Deng, B.-W. Wang, S. Gao, *J. Am. Chem. Soc.* **2017**, *139*, 373–380; c) R. Ruamps, L. J. Batchelor, R. Maurice, N. Gogoi, P. Jiménez-Lozano, N. Gui-

héry, C. de Graaf, A.-L. Barra, J.-P. Sutter, T. Mallah, *Chem. Eur. J.* **2013**, *19*, 950–956.

[12] D. Casanova, P. Alemany, J. M. Bofill, S. Alvarez, *Chem. Eur. J.* **2003**, *9*, 1281–1295.

[13] M. Regueiro-Figueroa, P. M. L. Lima, V. Blanco, D. Esteban-Gómez, A. de Blas, T. Rodríguez-Blas, R. Delgado, C. Platas-Iglesias, *Inorg. Chem.* **2014**, *53*, 12859–12869.

[14] T. J. Giordano, G. J. Palenik, R. C. Palenik, D. A. Sullivan, *Inorg. Chem.* **1979**, *18*, 2445–2450.

[15] C. Platas-Iglesias, L. Vaiana, D. Esteban-Gómez, F. Avecilla, J. A. Real, A. De Blas, T. Rodríguez-Blas, *Inorg. Chem.* **2005**, *44*, 9704–9713.

[16] A. K. Bar, N. Gogoi, C. Pichon, V. M. L. Durga Prasad Goli, M. Thlijeni, C. Duhayon, N. Suaud, N. Guihéry, A.-L. Barra, S. Ramasesha, J.-P. Sutter, *Chem. Eur. J.* **2017**, *23*, 4380–4396.

[17] Y.-Z. Zhang, O. Sato, *Inorg. Chem.* **2010**, *49*, 1271–1273.

[18] X.-C. Huang, C. Zhou, D. Shao, X.-Y. Wang, *Inorg. Chem.* **2014**, *53*, 12671–12673.

[19] B. Drahoš, R. Herchel, Z. Trávníček, *Inorg. Chem.* **2015**, *54*, 3352–3369.

[20] D. Shao, S. L. Zhang, L. Shi, Y. Q. Zhang, X. Y. Wang, *Inorg. Chem.* **2016**, *55*, 10859–10869.

[21] D. Shao, Y. Zhou, Q. Pi, F.-X. Shen, S.-R. Yang, S.-L. Zhang, X.-Y. Wang, *Dalton Trans.* **2017**, *46*, 9088–9096.

[22] N. Gogoi, M. Thlijeni, C. Duhayon, J.-P. Sutter, *Inorg. Chem.* **2013**, *52*, 2283–2285.

[23] B. Drahoš, R. Herchel, Z. Trávníček, *Inorg. Chem.* **2017**, *56*, 5076–5088.

[24] a) L. Chen, S.-Y. Chen, Y.-C. Sun, Y.-M. Gou, L. Yu, X.-T. Chen, Z. Wang, Z. W. Ouyang, Y. Song, Z.-L. Xue, *Dalton Trans.* **2015**, *44*, 11482–11490; b) L. Chen, J. Wang, J. M. Wei, W. Wernsdorfer, X. T. Chen, Y. Q. Zhang, Y. Song, Z. L. Xue, *J. Am. Chem. Soc.* **2014**, *136*, 12213–12216.

[25] B. Drahoš, R. Herchel, Z. Trávníček, *RSC Adv.* **2016**, *6*, 34674–34684.

[26] a) Y.-S. Ding, N. F. Chilton, R. E. P. Winpenny, Y.-Z. Zheng, *Angew. Chem. Int. Ed.* **2016**, *55*, 16071–16074; b) T. Pugh, N. F. Chilton, R. A. Layfield, *Angew. Chem. Int. Ed.* **2016**, *128*, 10082–10085.

[27] Y.-C. Chen, J.-L. Liu, L. Ungur, J. Liu, Q.-W. Li, L.-F. Wang, Z.-P. Ni, L. F. Chibotaru, X.-M. Chen, M.-L. Tong, *J. Am. Chem. Soc.* **2016**, *138*, 2829–2837.

[28] S. K. Gupta, T. Rajeshkumar, G. Rajaraman, R. Murugavel, *Chem. Sci.* **2016**, *7*, 5181–5191.

[29] J. Liu, Y.-C. Chen, J.-L. Liu, V. Vieru, L. Ungur, J.-H. Jia, L. F. Chibotaru, Y. Lan, W. Wernsdorfer, S. Gao, X.-M. Chen, M.-L. Tong, *J. Am. Chem. Soc.* **2016**, *138*, 5441–5450.

[30] P. Antal, B. Drahoš, R. Herchel, Z. Trávníček, *Inorg. Chem.* **2016**, *55*, 5957–5972.

[31] S. Richards, B. Pedersen, J. V. Silverton, J. L. Hoard, *Inorg. Chem.* **1964**, *3*, 27–33.

[32] J. D. Zubkowski, D. L. Perry, E. J. Valente, S. Lott, *Inorg. Chem.* **1995**, *34*, 6409–6411.

[33] A. Bianchi, L. Calabi, C. Giorgi, P. Losi, P. Mariani, D. Palano, P. Paoli, P. Rossi, B. Valtancoli, *J. Chem. Soc., Dalton Trans.* **2001**, 917–922.

[34] A.-A. H. Abu-Nawwas, C. A. Muryn, M. A. Malik, *Inorg. Chem. Commun.* **2009**, *12*, 125–127.

[35] C. A. Chang, L. C. Francesconi, M. F. Malley, K. Kumar, J. Z. Gougoutas, M. F. Tweedle, *Inorg. Chem.* **1993**, *32*, 3501–3508.

[36] Z. Urbańczyk-Lipkowska, P. Gluziński, J. W. Krajewsky, R. A. Koliński, A. Kemme, A. Mishnyov, *J. Cryst. Spectrosc.* **1989**, *19*, 387–397.

[37] H. Stetter, W. Frank, R. Mertens, *Tetrahedron* **1981**, *37*, 767–772.

[38] M. Nelson, D. H. Busch, *Inorg. Chem.* **1969**, *8*, 1859–1863.

[39] M. G. B. Drew, A. H. bin Othman, P. D. A. McIlroy, S. M. Nelson, *J. Chem. Soc., Dalton Trans.* **1975**, 2507–2516.

[40] H. S. Soo, M. T. Sougrati, F. Grandjean, G. J. Long, C. J. Chang, *Inorg. Chim. Acta* **2011**, *369*, 82–91.

[41] M. Gerloch, I. Morgenstern-Badarau, J.-P. Audiere, *Inorg. Chem.* **1979**, *18*, 3220–3225.

[42] M. Gerloch, I. Morgenstern-Badarau, *Inorg. Chem.* **1979**, *18*, 3225–3229.

[43] C. Cairns, S. G. McFall, S. M. Nelson, M. G. B. Drew, *J. Chem. Soc., Dalton Trans.* **1979**, *3*, 446–453.

[44] a) S. Alvarez, *Dalton Trans.* **2005**, 2209–2233; b) D. Casanova, P. Alemany, J. M. Bofill, S. Alvarez, *Chem. Eur. J.* **2003**, *9*, 1218–1295.

[45] R. Boča, *Theoretical Foundations of Molecular Magnetism*, Elsevier, Amsterdam, **1999**.

[46] R. L. Carlin, *Magnetochemistry*, Springer, Berlin, **1986**.

[47] A. S. Batsanov, A. E. Goeta, J. A. K. Howard, D. Maffeo, H. Puschmann, J. A. G. Williams, *Polyhedron* **2001**, *20*, 981–986.

[48] a) M. Atanasov, D. Ganyushin, K. Sivalingam, F. Neese, *A Modern First-Principles View on Ligand Field Theory Through the Eyes of Correlated Multireference Wavefunctions*, In: D. M. P. Mingos, P. Day, J. P. Dahl (Eds.), *Molecular Electronic Structures of Transition Metal Complexes II. Structure and Bonding*, 143, Springer, Berlin, Heidelberg, **2012**; b) S. K. Singh, J. Eng, M. Atanasov, F. Neese, *Coord. Chem. Rev.* **2017**, *344*, 2–25.

[49] B. Drahoš, J. Kotek, P. Hermann, I. Lukeš, É. Tóth, *Inorg. Chem.* **2010**, *49*, 3224–3238.

[50] V. V. Pavlishchuk, A. W. Addison, *Inorg. Chim. Acta* **2000**, *298*, 97–102.

[51] Bruker. *Apex*3; Bruker AXS Inc., Madison, WI, **2015**.

[52] G. M. Sheldrick, *Acta Crystallogr., Sect. A Acta Crystallogr., Sect. C: Struct. Chem.* **2015**, *71*, 3–8.

[53] K. Brandenburg, *DIAMOND*, Release 4.0.3; Crystal Impact GbR, Bonn, Germany, **2015**.

[54] F. Neese, *WIREs Comput. Mol. Sci.* **2012**, *2*, 73–78.

[55] a) A. D. Becke, *Phys. Rev. A* **1988**, *38*, 3098–3100; b) C. Lee, W. Yang, R. G. Parr, *Phys. Rev. B* **1988**, *37*, 785–789; c) P. J. Stephens, F. J. Devlin, C. F. Chabalowski, M. J. Frisch, *J. Phys. Chem.* **1994**, *98*, 11623–11627.

[56] F. Weigend, R. Ahlrichs, *Phys. Chem. Chem. Phys.* **2005**, *7*, 3297–3305.

[57] F. Weigend, *Phys. Chem. Chem. Phys.* **2005**, *8*, 1057–1065.

[58] a) F. Neese, F. Wennmohs, A. Hansen, U. Becker, *Chem. Phys.* **2009**, *356*, 98–109; b) R. Izsak, F. Neese, *J. Chem. Phys.* **2011**, *135*, 144105.

[59] P. Å. Malmqvist, B. O. Roos, *Chem. Phys. Lett.* **1989**, *155*, 189–194.

[60] a) C. Angeli, R. Cimiraglia, J.-P. Malrieu, *Chem. Phys. Lett.* **2001**, *350*, 297–305; b) C. Angeli, R. Cimiraglia, S. Evangelisti, T. Leininger, J.-P. Malrieu, *J. Chem. Phys.* **2001**, *114*, 10252–10264; c) C. Angeli, R. Cimiraglia, J.-P. Malrieu, *J. Chem. Phys.* **2002**, *117*, 9138–9153.

[61] D. Ganyushin, F. Neese, *J. Chem. Phys.* **2006**, *125*, 024103.

[62] F. Neese, *J. Chem. Phys.* **2005**, *122*, 034107.

[63] R. Maurice, R. Bastardis, C. De Graaf, N. Suaud, T. Mallah, N. Guihéry, *J. Chem. Theory Comput.* **2009**, *5*, 2977–2984.

[64] F. Weigend, *J. Comput. Chem.* **2008**, *29*, 167–175.

[65] J. P. Perdew, *Phys. Rev. B* **1986**, *33*, 8822–8824.

[66] a) S. Grimme, J. Antony, S. Ehrlich, H. Krieg, *J. Chem. Phys.* **2010**, *132*, 154104; b) S. Grimme, S. Ehrlich, L. Goerigk, *J. Comput. Chem.* **2011**, *32*, 1456–1465.

[67] K. E. R. Marriott, L. Bhaskaran, C. Wilson, M. Medarde, S. T. Ochsenbein, S. Hill, M. Murrie, *Chem. Sci.* **2015**, *6*, 6823–6828.

[68] J. Miklovič, D. Valigura, R. Boča, J. Titiš, *Dalton Trans.* **2015**, *44*, 12484–12487.

[69] D. Lomjanský, J. Moncol, C. Rajnák, J. Titiš, R. Boča, *Chem. Commun.* **2017**, *53*, 6930–6932.

[70] J. Titiš, C. Rajnák, D. Valigura, R. Boča, *Dalton Trans.* **2018**, *47*, 7879–7882.

Příloha P7

B. Drahoš, I. Císařová, O. Laguta, V. T. Santana, P. Neugebauer, R. Herchel,
Structural, magnetic, redox and theoretical characterization of seven-coordinate first-row transition metal complexes with macrocyclic ligand containing two benzimidazolyl *N*-pendant arms.

Structural, magnetic, redox and theoretical characterization of seven-coordinate first-row transition metal complexes with macrocyclic ligand containing two benzimidazolyl *N*-pendant arms

Bohuslav Drahoš,[a]* Ivana Císařová,[b] Oleksii Laguta,[c] Vinicius T. Santana,[c] Petr Neugebauer[c] and Radovan Herchel[a]

Structurally new heptadentate derivative of 15-membered pyridine-based macrocycle containing two benzimidazol-2-yl-methyl *N*-pendant arms (**L** = 3,12-bis((1*H*-benzimidazol-2-yl)methyl)-6,9-dioxa-3,12,18-triazabicyclo[12.3.1]octadeca-1(18),14,16-triene) was synthesized and its complexes with general formula $[M(L)](ClO_4)_2 \cdot 1.5CH_3NO_2$ (M = Mn^{II} (**1**), Fe^{II} (**2**), Co^{II} (**3**) and Ni^{II} (**4**)) were thoroughly investigated. X-ray crystal structures confirmed that all complexes are seven-coordinate with axially compressed pentagonal bipyramidal geometry having the largest distortion for Ni^{II} complex **4**. Fe^{II}, Co^{II} and Ni^{II} complexes **2**, **3** and **4** show rather large magnetic anisotropy manifested by moderate to high obtained values of axial zero-field splitting parameter *D* (7.9, 40.3, −17.2 cm^{-1}, respectively). Magneto-structural correlation for Fe^{II}, Co^{II} and Ni^{II} complexes with **L** and with previously studied structurally similar ligands revealed significant impact of the functional group in pendant arms on the magnetic anisotropy especially of Co^{II} and Ni^{II} complexes and some recommendations concerning the ligand-field design important for anisotropy tuning in future. Furthermore, complex **3** showed field-induced single-molecule magnet behavior described with Raman (*C* = 507 K^{-n}s^{-1} for *n* = 2.58) relaxation process. Magnetic properties of studied complexes were supported by theoretical calculations, which very well correspond with the experimental data for magnetic anisotropy. Electrochemical measurements revealed high positive redox potentials for $M^{3+/2+}$ couples and high negative potentials for $M^{2+/+}$ couples, which indicate stabilization of oxidation state +II expected for σ-donor/π-acceptor ability of benzimidazol functional groups.

Introduction

In the last decade, a growing attention has been devoted to the seven-coordinate pentagonal bipyramidal complexes of transition metals[1] as well as lanthanides[2,3,4,5,6] due to their interesting magnetic properties, which was demonstrated on an increasing number of published papers and reviews concerning this topic.[7,8,9] These seven-coordinate pentagonal bipyramidal complexes especially of Fe^{II},[10,11,12,13,14,15,16] Co^{II},[12,17,18,19,20,21,22] Ni^{II},[12,17,23] and more recently also 4d/5d metals like $Mo^{IV/III}$ [24,25] possess a large magnetic anisotropy, which is commonly expressed in terms of axial and rhombic zero-field splitting (ZFS) parameters *D* and *E* for transition metal complexes.[26] Due to their large axial magnetic anisotropy, they have been successfully employed in construction of Single-Molecule Magnets (SMMs).[27,28] SMMs are compounds showing slow relaxation of magnetization based on pure molecular origin (no long range ordering typical for bulk magnets) and therefore they behave as "nanomagnets" which could find many applications in different field of interest, *e.g.* in high-density storage media, in spintronics or quantum computing etc.[29] Unfortunately, SMMs operate at very low temperatures. The biggest progress has been obtained for dysprosium metallocenes with the blocking temperature of 60 K,[30] and the current record breaking the liquid nitrogen temperature is 80 K.[31] In order to increase this temperature, it is necessary to (i) increase the energy for magnetic moment reversal (U_{eff}), which is defined for transition metal complexes as $U_{eff} = |D|S^2$ or $U_{eff} = |D|(S^2 - \frac{1}{4})$ for integer or non-integer ground spin state *S*, respectively,[27,28] while for lanthanides with inner shell 4f electrons, large unquenched orbital moments and strong spin-orbit coupling (total momentum *J* is used) it is based on strong single-ion anisotropy and can not be described in terms of ZFS spin Hamiltonian parameters, and to (ii) slow down the relaxation of magnetization by understanding of all potential relaxation mechanisms including Orbach, direct and Raman mechanisms or quantum tunneling, and by their consequent elimination. Nevertheless, because the relaxation processes are rather complex, the approach (ii) is quite complicated and despite some first attempts,[32] still many questions remain unclear in this field. On the other hand, it was found out that for high U_{eff}, not the total spin (*S*) of the magnetic ground state, but the axial magnetic anisotropy (*D*) is in fact the key parameter, which has to be tuned and enlarged in order to construct more efficient SMMs.

Such tuning can be provided by modification of the coordination environment of the metal centre, i.e. rational ligand design. In case of pentagonal bipyramidal complexes, two strategies have been successfully employed previously. In the first one, the pentadentate acyclic (**L4**,[11,22,33] **L5**)[19] or macrocyclic ligand (**L1**, Fig. 1)[21,34] is coordinated in the equatorial plane (these ligands differ in donor atoms, rigidity, electron distribution, cavity size) while the two apical monodentate co-ligands (varying in σ-donor/π-acceptor properties) are exchanged. The second strategy is based on

structural modification of the pentadentate macrocyclic ligand (e.g. **L1** or 1,10-diaza-15-crown-5)[35,36] with two pendant arms containing various functional groups with different coordination ability (2-pyridylmethyl in **L2**,[12,37] acetate in **L3**,[38] 2-aminobenzyl in **L6**[35] and 2-benzimidazolylmethyl in **L7**, Fig. 1).[36] Significant influence on the magnetic anisotropy of Fe[II/III], Co[II] and Ni[II] complexes with **L2**[12] and **L3**[38] has been observed (Fig. 1), but unfortunately, no clear trend could be elucidated because of very complex description of bond character in the complexes and various contradictory structural parameters.

In order to further investigate the effect of different functional group in pendant arms and to obtain any reasonable magneto-structural correlation,[39] the macrocyclic ligand **L1** has been modified with two 2-benzimidazolylmethyl pendant arms to give structurally new ligand **L** (Fig. 1). In fact, benzimidazolyl group can act as a better σ-donor in comparison with pyridine moiety[40,41] and thus, it could provide stronger axial ligand field, which according to the theoretical predictions[17] could beneficially influence the magnetic anisotropy especially in case of pentagonal bipyramidal Fe[II] and Ni[II] complexes.[17] Moreover, this ligand is a new member of a relatively small family of rarely documented macrocycles modified with benzimidazolyl pendant arms (Fig. 1, **L7**,[36] differently-substituted triazacyclononanes **L8**,[42,43] tetraazacyclododecanes (cyclenes) **L9**,[44,45] its dioxa-derivative **L10**,[46] tetraazacyclotetradecanes (cyclames) **L11**[47] and DO3A derivative **L12**).[48]

Thus, in this paper, structurally new ligand **L** has been synthesized and its Mn[II], Fe[II], Co[II] and Ni[II] complexes have been prepared and studied in details. Their structural, magnetic as well as redox properties were thoroughly investigated and compared with previously studied systems containing ligands **L2** and **L3**. Obtained results were supported by extensive theoretical calculations.
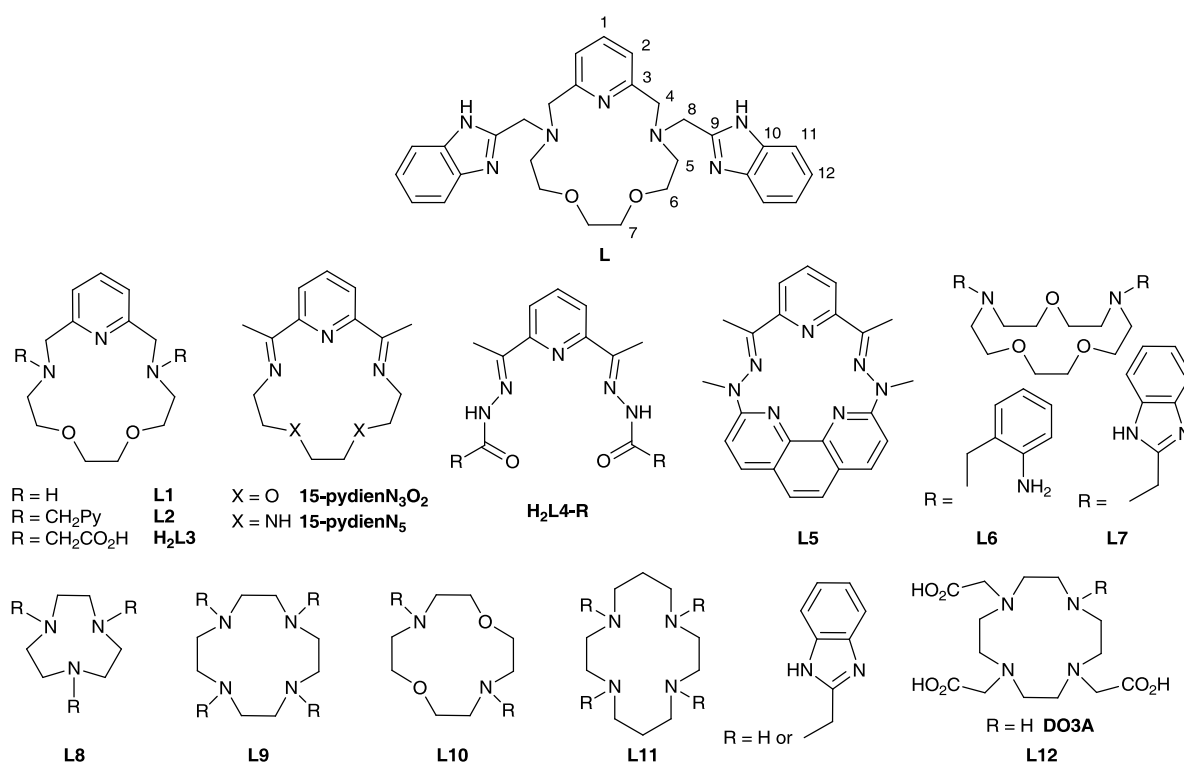
Fig. 1 Structural formulas of studied ligand **L** together with its atom numbering (applied for assignment of NMR signals) and ligands discussed in the text.

Experimental section

Materials and methods

The ligand **L1**[49,12] and 2-chloromethylbenzimidazole[50] were synthesized according to the literature procedures. All the solvents (VWR International, Fontenay-sous-Blois, France) and other chemicals were purchased from commercial sources (Across Organics, Geel, Belgium and Sigma-Aldrich, St. Louis, MO, USA) and used as received.

Elemental analysis (C, H, N) was performed on a Flash 2000 CHNO-S analyzer (Thermo Scientific, Waltham, MA, USA). The mass spectra (Fig. S1) were collected on an LCQ Fleet mass spectrometer (Thermo Scientific, Waltham, MA, USA) equipped with an electro spray ion source and three-dimensional (3D) ion-trap detector in the positive/negative mode. Infrared (IR) spectra of the ligand and studied complexes (Fig. S2) were recorded on a Thermo Nicolet NEXUS 670 FT-IR spectrometer (Thermo Nicolet, Waltham, MA, USA) or Jasco FT/IR-4700 spectrometer (Jasco, Easton, MD, USA) using the ATR technique on a diamond plate in the range of $400-4000$ cm^{-1}. ^{1}H and ^{13}C NMR spectra were recorded on a 400-MR NMR spectrometer (Varian, Palo Alto, CA, USA) at 25 °C: ^{1}H 399.95 MHz, chloroform-d (CDCl$_3$, tetramethylsilane) $\delta = 0.00$ ppm, ^{13}C 100.60 MHz, (CDCl$_3$, residual solvent peak) $\delta = 77.0$ ppm. Multiplicity of the

signals is indicated as follows: s – singlet, d – doublet, t – triplet, m – multiplet, bs – broad singlet. Deuterated solvent CDCl₃ containing 0.03 % of TMS purchased from Sigma Aldrich was used as received. The atom numbering scheme used for NMR data interpretation is shown in Fig. 1. The carbon as well as hydrogen atoms were assigned according to the spectra obtained from two-dimensional correlation experiments ^1H–^1H gs-COSY, ^1H–^{13}C gs-HMQC and ^1H–^{13}C gs-HMBS (see Fig. S3 and S4). Temperature dependence of the magnetization at $B = 0.1$ T from 1.9 to 300 K and the isothermal magnetizations at $T = 2, 5$, and 10 K up to $B = 9$ T were measured using PPMS Dynacool with the VSM module (Quantum Design Inc., San Diego, CA, USA). The experimental data were corrected for diamagnetism and signal of the sample holder. Dynamic magnetic properties were studied by measuring AC susceptibility on an MPMS XL7 SQUID magnetometer (Quantum Design Inc., San Diego, CA, USA). High frequency/field electron paramagnetic resonance spectroscopy (HFEPR) was performed at CEITEC (Brno, CZ) in a home-built spectrometer equipped with a cryogen-free 16 T superconducting magnet (Cryogenics Ltd., London, UK), microwave source for measurements from 90 GHz to 500 GHz (Virginia Diodes Inc., Charlottesville, VA, USA), and quasi-optics components for the same range (Thomas Keating Ltd., Billingshurst, UK). The samples were milled with a 20% eicosane and made into a ∅5 mm pellet to be placed insed the sample holder for induction mode HFEPR with modulation frequency of 10 kHz and amplitude of 0.4 mT. Spectra were obtained at 4 K and 15 K. Simulations were performed using EasySpin[51] in MATLAB.[52] The cyclic voltammetry was measured on electrochemical analyzer CHI600C (CH Instrument Inc., Austin, TX, USA). A conventional electrochemical three-electrode-type cell with Ag/Ag⁺ reference electrode (0.01M AgNO₃ in 0.1M TBAP), a platinum wire auxiliary electrode and a glassy carbon working electrode was used during the measurements with the scan rate of 100 mV s⁻¹. The internal ferrocene/ferrocenium standard ($E_{1/2} = 0.452/0.478$ V vs. our Ag/Ag⁺ electrode, $E_{1/2} = 0.624$ V vs. SHE)[53] was employed in order to obtain final potential values referred to SHE. The measurements were performed under inert argon atmosphere in acetonitrile solution containing tetrabutylammonium perchlorate (TBAP) as a supporting electrolyte (0.1 M) and appropriate complex (2×10^{-3} M).

Crystal data

Single crystals of studied complexes **1–4** suitable for X-ray structure analysis were prepared as described in the experimental section. X-ray diffraction data were collected on Nonius Kappa CCD diffractometer equipped with Bruker APEX-II CCD detector by monochromatized MoKα radiation ($\lambda = 0.71073$ Å) at the temperature of 150(2) K. The molecular structures of studied complexes were solved by direct methods and refined by full matrix least squares based on F^2 (SHELXL 2014/07).[54] The hydrogen atoms on carbon atoms were fixed into idealized positions (riding model) and assigned temperature factors either $H_{iso}(H) = 1.2\ U_{eq}$(pivot atom) or $H_{iso}(H) = 1.5\ U_{eq}$ (pivot atom) for methyl moiety.

The hydrogen of H–N moieties were found on difference electron density map and refined as riding on corresponding pivot atom. All four crystals were isostructural, differing mostly in their quality with regard of degree of disorder of perchlorate anions as well as solvating nitromethane molecules. One of the nitromethane is situated near inversion center of the P-1 space group and is disordered over four positions at least. To improved precision of important part of the structures, PLATON[55] / SQUEEZE procedures were applied to correct the diffraction data for its contribution in all structures. The molecular and crystal structures of the studied complexes, depicted in Figures 2 and 4 were drawn using the Mercury software.[56]

Syntheses

3,12-bis((1*H*-benzimidazol-2-yl)methyl)-6,9-dioxa-3,12,18-triazabicyclo[12.3.1]octadeca-1(18),14,16-triene (**L**)

Ligand **L1** (0.50 g, 1.99 mmol), 2-chloromethylbenzimidazole (0.70 g, 4.20 mmol, 2.1 eqv.), K₂CO₃ (2.74 g, 19.9 mmol, 10 eqv.) and NaI (0.30 g, 1.99 mmol) were suspended in 60 mL of CH₃CN and refluxed for 12h. The hot suspension was filtered on a glass frit and the filtrate was evaporated under reduced pressure to give 1.16 g of yellow solid foam. This solid was redissolved in 50 mL CHCl₃, obtained solution was extracted three times with 50 mL of deionized water, dried with anhydrous Na₂SO₄, filtered on a grass frit and evaporated under reduced pressure. The product was obtained in form of pale yellow foam (0.84 g, 82.3 %).

MS *m/z* (+): 512.24 ([**L**+H⁺]⁺, calcd. 512.28), 534.29 ([**L**+Na⁺]⁺, calcd. 534.26), 550.22 ([**L**+K⁺]⁺, calcd. 550.23).

^1H NMR(CDCl₃): δ 3.19 (H5, t, $^3J_{HH} = 4.9$ Hz, 4H), 3.41 (H7, s, 4H), 3.50 (H6, t, $^3J_{HH} = 4.9$ Hz, 4H), 3.94 (H4, s, 4H), 4.04 (H8, s, 4H), 6.93 (H2, d, $^3J_{HH} = 7.8$ Hz, 2H), 7.14 (H12, m, 4H), 7.39 (H1, t, $^3J_{HH} = 7.8$ Hz, 1H), 7.48 (H11, m, 2H), 7.60 (H11, m, 2H), 11.55 (NH, bs, 2H)

$^{13}C\{^1H\}$ NMR (CDCl₃): δ 53.75 (C8), 57.76 (C5), 62.85 (C4), 68.41 (C6), 69.79 (C7), 111.26 (C11), 118.66 (C11), 121.39 (C12), 121.82 (C2), 121.90 (C12), 133.77 (C10), 136.92 (C1), 143.96 (C10), 155.34 (C9), 158.50 (C3).

General procedure for the preparation of complexes 1–4.

Ligand **L** (100 mg, 0.195 mmol) and appropriate amount of M(ClO₄)₂·6H₂O (0.186 mmol, 67 mg of Mn(ClO₄)₂·6H₂O and Fe(ClO₄)₂·6H₂O or 68 mg of Co(ClO₄)₂·6H₂O and Ni(ClO₄)₂·6H₂O) were dissolved in 4 mL of CH₃OH and left to diethyl ether vapor diffusion at 5 ℃. After several days, the well-shaped crystals of complex were formed, isolated by filtration and re-dissolved in 1 mL of CH₃NO₂. Obtained solution was filtered via Millipore syringe filter (0.45 μm). The diffusion of diethyl ether vapors into the filtrate at 5 °C resulted in formation of well-shaped crystals, which were filtered off and dried in air at room temperature. These crystals were also suitable for X-ray diffraction analysis. **Caution!** *Although we have experienced no difficulties, perchlorate salts of metal complexes with organic ligands are potentially explosive and should be handled with great care even in small quantities.*

[MnL](ClO₄)₂·1.5CH₃NO₂ (1)

Product was isolated in form of light yellow crystals (84 mg, 52.7 %).

MS *m/z* (+): 565.11 ([Mn(**L**–H⁺)]⁺, calcd. 565.20), 664.89 (MnL+(ClO₄)⁻]⁺, calcd. 665.16).

MS *m/z* (−): 864.24 ([MnL+3×(ClO₄)⁻]⁻, calcd. 863.05), 1628.86 ([2×(MnL)+5×(ClO₄)⁻]⁻, calcd. 1629.15).

Anal. Calcd (%) for [MnL](ClO₄)₂·1.5CH₃NO₂ ($C_{30.5}H_{37.5}Cl_2MnN_{8.5}O_{13}$, M_r = 857.02): C, 42.74; H, 4.41; N, 13.89. Found C, 43.12; H, 4.58; N, 13.80.

[FeL](ClO₄)₂·1.5CH₃NO₂ (2)

Product was isolated in form of green-brown crystals (61 mg, yield 38.2 %).

MS *m/z* (+): 566.09 ([Fe(**L**–H⁺)]⁺, calcd. 566.20), 665.84 ([FeL+(ClO₄)⁻]⁺, calcd. 666.15).

MS *m/z* (−): 865.02 ([FeL+3×(ClO₄)⁻]⁻, calcd. 864.05), 1631.01 ([2×(FeL)+5×(ClO₄)⁻]⁻, calcd. 1631.15).

Anal. Calcd (%) for [FeL](ClO₄)₂·1.5CH₃NO₂ ($C_{30.5}H_{37.5}Cl_2FeN_{8.5}O_{13}$, M_r = 857.92): C, 42.70; H, 4.41; N, 13.88. Found C, 42.22; H, 4.25; N, 13.40.

[CoL](ClO₄)₂·1.5CH₃NO₂ (3)

Product was isolated in form of pink crystals (98 mg, yield 61.2 %).

MS *m/z* (+): 569.12 ([Co(**L**–H⁺)]⁺, calcd. 569.19), 668.83 ([CoL+(ClO₄)⁻]⁺, calcd. 669.15).

MS *m/z* (−): 869.27 ([CoL+3×(ClO₄)⁻]⁻, calcd. 869.05), 1637.11 ([2×(CoL)+5×(ClO₄)⁻]⁻, calcd. 1637.15).

Anal. Calcd (%) for [CoL](ClO₄)₂·1.5CH₃NO₂ ($C_{30.5}H_{37.5}Cl_2CoN_{8.5}O_{13}$, M_r = 861.01): C, 42.55; H, 4.39; N, 13.83. Found C, 42.65; H, 4.32; N, 13.52.

[NiL](ClO₄)₂·1.5CH₃NO₂ (4)

Product was isolated in form of green crystals (65 mg, yield 40.6 %).

MS *m/z* (+): 568.17 ([Ni(**L**–H⁺)]⁺, calcd. 568.20), 667.78 ([NiL+(ClO₄)⁻]⁺, calcd. 668.15)

MS *m/z* (−): 868.62 ([NiL+3×(ClO₄)⁻]⁻, calcd. 868.05), 1637.42 ([2×(NiL)+5×(ClO₄)⁻]⁻, calcd. 1635.15).

Anal. Calcd (%) for [NiL](ClO₄)₂·1.5CH₃NO₂ ($C_{30.5}H_{37.5}Cl_2N_{8.5}NiO_{13}$, M_r = 860.77): C, 42.56; H, 4.39; N, 13.83. Found C, 42.30; H, 4.52; N, 13.72.

Theoretical methods

The ORCA 4.1 computational package was used for quantum chemical calculations.[57,58] The calculations of ZFS parameters were done using state average complete active space self-consistent field (SA-CASSCF)[59] wave functions complemented by *N*-electron valence second-order perturbation theory (NEVPT2)[60,61,62] using triple-ζ basis set def2-TZVP[63] for all atoms. In the state-averaged approach all

multiplets for given electron configuration were equally weighted. The ZFS parameters, based on dominant spin-orbit coupling contributions from excited states, were calculated through quasi-degenerate perturbation theory (QDPT),[64] in which an approximation to the Breit-Pauli form of the spin-orbit coupling operator (SOMF approximation)[65] and the effective Hamiltonian theory[66] were utilized. The calculations utilized the RIJCOSX approximation with the auxiliary basis sets def2/J[67] and def2-TZVP/C.[68] Increased integration grids (Grid5 and GridX5 in ORCA convention) and tight SCF convergence criteria were used in all calculations. Moreover, recently introduced dynamic correlation dressed CAS with the second-order treatment (DCD-CAS(2)) were also utilized to calculate ZFS parameters, where the spin-orbit and the spin-spin interactions were included.[69] VESTA 3 program was used to visualize results of the calculations.[70]

Results and Discussions

Syntheses and general characterizations

The ligand **L** was prepared by a common S_N2 substitution reaction of parent macrocycle **L1** and 2-chloromethylbenzimidazole in CH₃CN with K₂CO₃ as a base. Synthesis of all studied complexes was simply based on mixing of **L** with perchlorate of appropriate metal ion in CH₃OH. Products in crystalline form obtained after diethyl ether vapors diffusion at 5° C were sensitive to loose co-crystallized CH₃OH solvent molecule(s) and therefore they were re-crystallized from CH₃NO₂. Obtained complexes with co-crystallized CH₃NO₂ molecules were stable on air and were thoughtfully characterized by elemental analysis, mass spectrometry (Fig. S1) and IR spectroscopy. Measured IR spectra of studied complexes **1–4** are displayed in Fig. S2 and they are identical, which is in accordance with their similar composition and isostructurality (see later). The spectral pattern of all studied complexes **1–4** contains vibrations of perchlorate anion at 1070 cm⁻¹, stretching C=C and C=N aromatic vibrations at ~1450 cm⁻¹, vibration of MeNO₂ at 1550 cm⁻¹, aliphatic CH stretching vibrations at 2880, 2920 and 3090 cm⁻¹, and NH stretching vibrations at 3560 cm⁻¹.

Crystal structure analysis

Molecular structures of complex cations of all studied complexes **1–4** are shown in Fig. 2 and crystal data and structure refinements for studied complexes **1–4** can be found in ESI in Table S1. All the complexes **1–4** are isostructural, they all crystallized in triclinic P−1 space group and their molecular structures have a similar structural pattern. The macrocyclic part of the ligand is coordinated in the pentagonal equatorial plane, while the two benzimidazolyl pendant arms are coordinated in apical positions. Thus, all the central atoms are seven-coordinate with pentagonal bipyramidal geometry and N₅O₂ donor atom set.
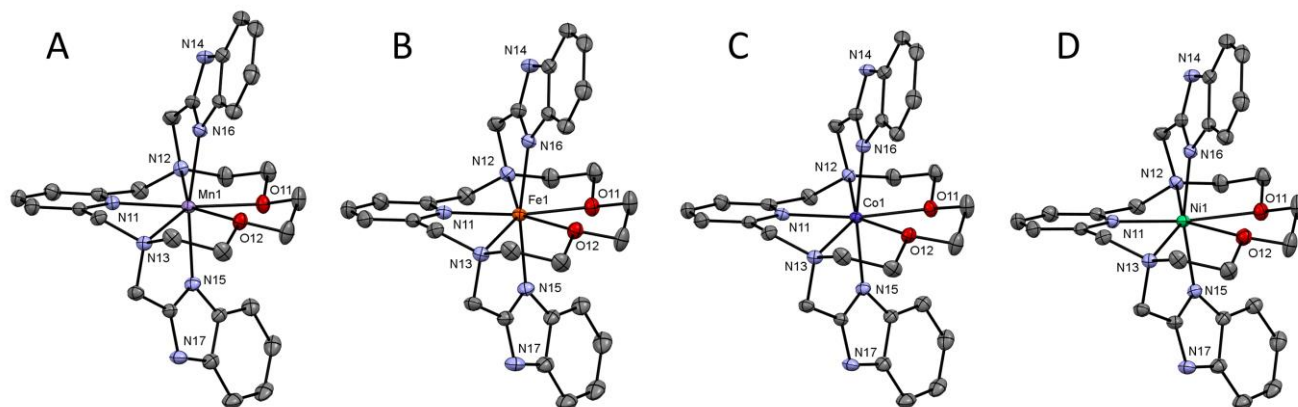
Fig. 2 The molecular structures of the cation [ML]²⁺ cation in complex **1** (M = Mn^II, **A**), complex **2** (M = Fe^II, **B**), **3** (M = Co^II, **C**) and **4** (M = Ni^II, **D**). Non-hydrogen atoms are drawn as thermal ellipsoids at the 50% probability level. Hydrogen atoms and anions were omitted for clarity. Only one of two crystallographically independent molecules present in the asymmetric unit of each complex is shown for clarity

The comparison of M–donor atom distances is shown in Fig. 3, listed in Table 1 and indicates several trends. M–N$_{(benzimidazole)}$ distances are comparable to those of M–N$_{py}$ and are much shorter than other bonds in equatorial pentagonal plane, and thus, the pentagonal bipyramid can be considered as slightly axially compressed. Furthermore, in the order going from Mn^II to Ni^II complex **1**→**4** all M–N distances decrease, which is in agreement with decreasing ionic radius of complexed metal ions. On the other hand, M–O distances remain the same for **1–3** and significantly increase in case of Ni^II complex **4** due to the Jahn-Teller effect,[71] which is typical for structurally similar seven-coordinate pentagonal bipyramidal Ni^II complexes [NiL1Cl₂],[72] [NiL2](ClO₄)₂,[12] [NiL3],[38] [NiL6](ClO₄)₂[35] for which Ni–O distances often exceed 2.5 Å. And thus, the pentagonal bipyramidal geometry of Ni^II centre in **4** is the most distorted (Ni–O is 2.413(2) and 2.416(2) Å) and this distortion for the second crystallographically independent molecules present in the asymmetric unit is even more pronounced (Ni–O is 2.357(2) and 2.486(2) Å, see Table 1 and Fig. 3 – empty symbols). This observation was confirmed by the analysis of the geometry of coordination polyhedra of all complexes **1–4** based on comparison of continuous shape measures obtained by program Shape 2.1 (deviation between the real and ideal geometry of the polyhedron, Table S2),[73,74] because the lowest deviation values were obtained for pentagonal bipyramidal arrangement.
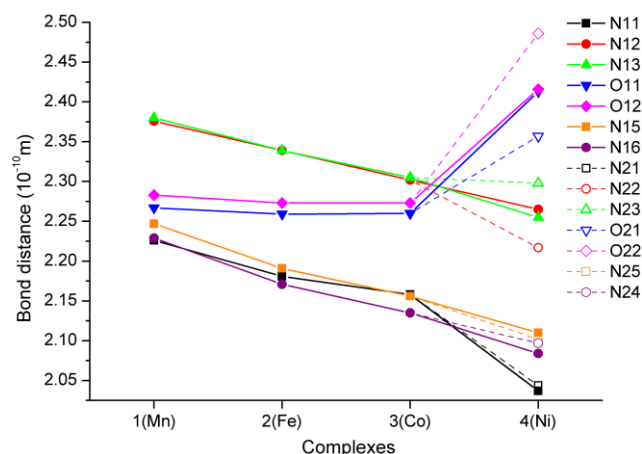
Fig. 3 Comparison of the metal−donor atom distances in the complexes **1−4** depending on the type of the central metal atom. The empty symbols and dashed lines correspond to the values for the second crystallographically independent molecule present in the asymmetric unit in **4**. Lines serve as guides.

The final crystal packing of all studied complexes **1–4** is influenced by π–π stacking interactions between the benzimidazol units in the pendant arms (centroid···centroid distance C_g···C_g = 3.664/3.665/4.016/4.563 Å (**1**), 3.672/3.673/4.035/4.549 Å (**2**), 3.679/3.680/4.060/4.605 Å (**3**), 3.668/3.678/4.057/4.620 Å (**4**)), which are responsible for formation of supramolecular linear 1D chains along c-axis (Fig. 4). Each supramolecular 1D chain contains only one enantiomeric form of the complex cation and these 1D chains regularly alternate in the final crystal packing as shown in Fig. 4. Furthermore, these 1D chains are connected to each other by large number of hydrogen bonds (N–H···O–Cl, C–H$_{aromatic}$···O–Cl, C–H$_{aromatic}$···O–N) among the perchlorate counter-ions, complex cations and nitromethane solvent molecules.

**Table 1** Selected interatomic distances [Å] and angles [°] in compounds **1–4**.

distances	**1**	**2**	**3**	**4**
M–N11/21	2.230(3)/ 2.226(3)	2.184(3)/ 2.181(3)	2.166(2)/ 2.158(3)	2.044(2)/ 2.037(2)
M–N12/22	2.381(3)/ 2.376(3)	2.334(3)/ 2.339(3)	2.300(2)/ 2.302(2)	2.217(2)/ 2.265(2)
M–N13/23	2.378(3)/ 2.380(3)	2.340(3)/ 2.339(3)	2.304(2)/ 2.305(2)	2.298(2)/ 2.255(2)
M–O11/21	2.278(2)/ 2.267(2)	2.260(2)/ 2.259(2)	2.264(2)/ 2.260(2)	2.357(2)/ 2.413(2)
M–O12/22	2.281(2)/ 2.283(2)	2.280(2)/ 2.273(2)	2.281(2)/ 2.273(2)	2.486(2)/ 2.416(2)
M–N16/24	2.241(3)/ 2.247(3)	2.178(3)/ 2.191(3)	2.147(2)/ 2.156(2)	2.097(2)/ 2.110(2)
M–N15/25	2.251(3)/ 2.229(3)	2.186(3)/ 2.171(3)	2.145(2)/ 2.135(2)	2.102(2)/ 2.084(2)
angles[a]				
N11–M–N12	71.54(9)	71.95(9)	72.09(9)	76.10(8)
N12–M–O11	74.89(8)	74.89(9)	74.54(8)	75.04(7)
O11–M–O12	72.00(8)	70.69(8)	70.74(7)	66.44(6)
N13–M–O12	73.63(8)	73.47(9)	73.20(8)	70.45(7)
N11–M–N13	70.99(9)	71.54(9)	71.75(9)	74.08(8)
N11–M–N15	92.62(9)	93.60(10)	93.11(9)	95.63(8)
N12–M–N15	104.57(9)	104.88(9)	103.06(9)	103.57(8)
N13–M–N15	76.39(9)	77.27(9)	78.89(9)	79.54(8)
O11–M–N15	84.43(9)	84.78(9)	84.66(9)	82.46(8)
O12–M–N15	87.54(9)	86.51(9)	87.65(8)	85.22(7)
N11–M–N16	97.83(9)	97.76(9)	97.07(9)	99.13(8)
N12–M–N16	75.60(9)	76.61(9)	78.11(9)	79.99(8)
N13–M–N16	110.42(9)	108.59(9)	106.42(9)	104.64(8)
O11–M–N16	84.98(9)	84.53(9)	85.71(9)	84.71(8)
O12–M–N16	86.19(9)	85.69(9)	85.42(8)	82.98(7)
N15–M–N16	168.95(10)	168.39(10)	169.58(9)	165.24(8)

[a] Values for one of two crystallographically independent molecules present in the asymmetric unit of each complex are present.

Comparison of obtained molecular structures with those of previously studied complexes containing L2 and L3

The molecular structure of metal complexes is crucial for understanding of their magnetic anisotropy (see next section Magnetic analysis) and therefore it is important to compare obtained molecular structures of Fe^{II}, Co^{II} and Ni^{II} complexes containing **L** with those of previously studied complexes containing structurally similar ligands **L2** and **L3** (Fig. 5) in order to reveal any trends which could explain observed magnetic properties.
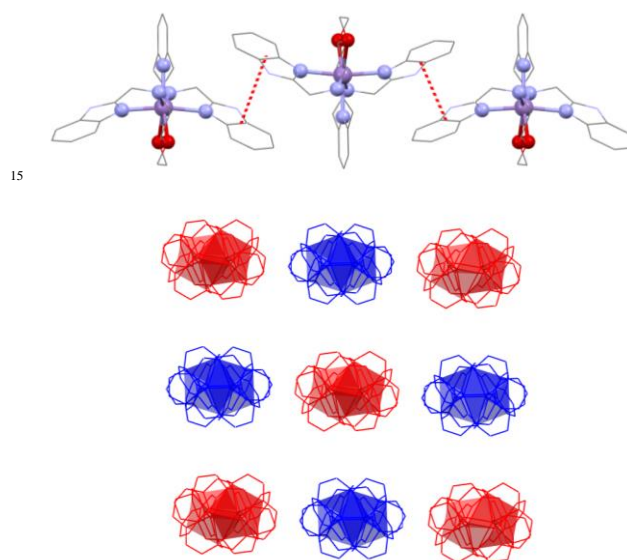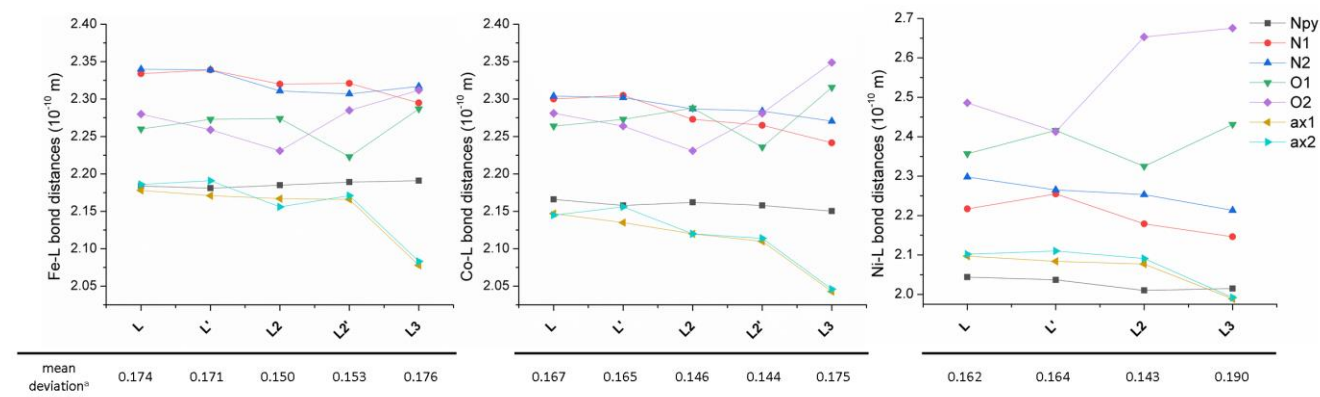
Fig. 4 (*top*) Part of the crystal structure of **1** showing supramolecular 1D chain of individual [ML]$^{2+}$ complex cations connected together by π–π stacking interactions (red dashed lines). (*bottom*) View along *c* axis on the arrangement of supramolecular 1D chains of [ML]$^{2+}$ complex cations in **1** with indication of their enantiomeric forms (*red* for [Mn(S,S)-**L**)]$^{2+}$, *blue* for [Mn(R,R)-**L**)]$^{2+}$).

The N$_{py}$–M distance is not much changing going from **L** to **L3** for all three metals, but its value decreases from Fe^{II} to Ni^{II} according to decreasing ionic radius. The N(1,2-aliphatic)–M distances almost always decrease for **L**→**L3** (only N2–M distance slightly increases in case of Fe^{II} complex when going from **L2** to **L3**). On the other hand, the effect on O–M distances is opposite. When going from **L** to **L2**, one distance decreases while the other increases for all metals (but the mean values for both crystallographically independent molecules slightly decrease), but both values increase when going from **L2** to **L3**. The most significant increase is observed for Ni^{II} complex due to the operating Jahn-Teller effect. The distances between metal and axial donor atoms decrease when going from **L** to **L3** for all three metals. This indicates, in comparison with **L**, stronger axial binding in case of pyridine analogue **L2** (both **L** and **L2** are neutral) and significant electrostatic contribution in case of negatively charged carboxylate analogue **L3**.

Thus when going from **L** to **L3** in all Fe^{II}, Co^{II} and Ni^{II} complexes, the metal in equatorial plane is shifted towards the N-donor containing part and moving away from the O-donor part of the macrocycle, and the axial donor atoms are getting closer to the metal atom. One has to also pursue the variation of the distances in the equatorial plane, because observed axial compression of pentagonal bipyramid (**L→L3**) resulted either in more symmetric equatorial plane in case of Fe^{II} complex of **L3** (N–M and O–M distances are close to each other) or more asymmetric equatorial plane in case of Co^{II} and especially Ni^{II} complex of **L3** (N–M and O–M distances are very different). From Fig. 5 is also evident, that M–O distances in comparison with M–N(aliphatic) are shorter in case of Fe^{II} complexes, are comparable in case of Co^{II} complexes and longer in case of Ni^{II} complexes, which is in accordance with the oxophilic character of Fe^{II} and *N*-donors preference of Ni^{II}.

Moreover, additional interesting parameter is the planarity of the equatorial plane, which can be described by the mean deviation of equatorial donor atoms (N$_3$O$_2$) from the least-squares plane defined by the central metal atom and all equatorial donor atoms (MN$_3$O$_2$). Complexes with the most planar equatorial plane form pyridine ligand **L2** followed by benzimidazol ligand **L** and carboxylate ligand **L3** (Fig. 5). In the series of complexes with **L** and **L2**, planarity increases from Fe^{II} to Ni^{II} (mean deviation decreases), while in the case of complexes with **L3**, the lowest planarity (highest mean deviation) is observed for Ni^{II} complex. But in general, it can be concluded, that the equatorial planarity for all complexes (similar structural type) is comparable.

Magnetic analysis

Static magnetic measurements

The temperature- and field-dependent experimental magnetic data for **1**–**4** are depicted in Fig. 6. The room temperature values of the effective magnetic moment (μ_{eff}/μ_B) are close to the theoretical values for the high-spin divalent metal complexes (μ_{eff}/μ_B = 5.92 for S = 2.5 (Mn^{II}), μ_{eff}/μ_B = 4.90 for S = 2 (Fe^{II}), μ_{eff}/μ_B = 3.87 for S = 3/2 (Co^{II}) and μ_{eff}/μ_B = 2.83 for S = 1 (Ni^{II})). On lowering the temperature, there is a significant drop of the effective magnetic moment observed for compounds **2**–**4** indicating significant magnetic anisotropy, hence the zero-field splitting (ZFS). This is also supported by lower values of the isothermal magnetizations at highest applied magnetic field in comparison with theoretically expected values derived by Brillouin function as $M_{mol}/N_A\mu_B = g\cdot S$, where S = 2 for **2**, S = 3/2 for **3** and S = 1 for **4**. On contrary, the situation for **1** is much different, the μ_{eff} is almost constant in the whole temperature range and also the isothermal magnetization is close to the Brillouin function, which indicates minute ZFS in **1** as expected for 3d^5 electronic configuration.
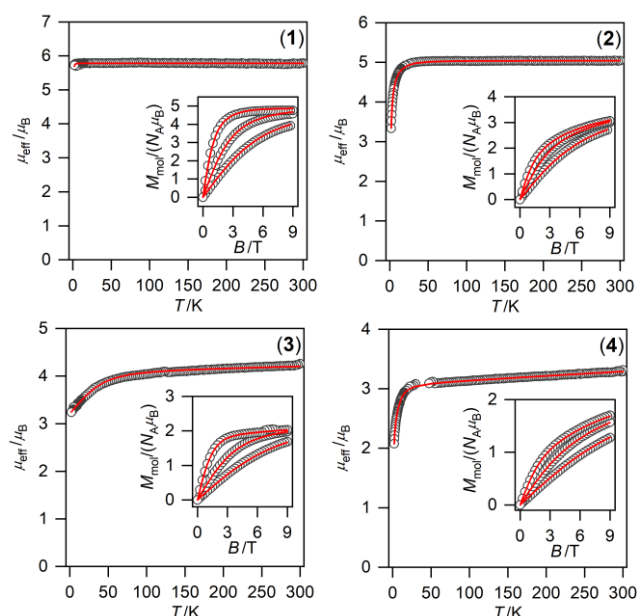
Fig. 6 Magnetic data for compounds **1**–**4**. Temperature dependence of the effective magnetic moment and the isothermal magnetizations measured at T = 2, 5, and 10 K. The empty circles represent the experimental data points, and the full lines represent the best fits calculated by using eq. 1 with parameters listed in Table 2.

Thus, the experimental magnetic data were treated with the spin Hamiltonian comprising the ZFS terms describing the magnetic anisotropy and Zeeman term postulated as

$$\hat{H} = D(\hat{S}_z^{\,2} - \hat{S}^2/3) + E(\hat{S}_x^{\,2} - \hat{S}_y^{\,2}) + \mu_B B g \hat{S}_a \qquad (1)$$

where D and E are the single-ion axial, and rhombic ZFS parameters, respectively, and the last component represents the Zeeman term defined in a direction of magnetic field as B_a = $B(\sin(\theta)\cos(\varphi),\ \sin(\theta)\sin(\varphi),\ \cos(\theta))$ with the help of the polar coordinates.[75] Then, the averaged molar magnetization corresponding to the powder samples was calculated.

To obtain reliable parameters, both temperature and field-dependent magnetic experimental data were fitted concurrently. The best-fitted parameters are listed in Table 2.[76] The large and negative D-value was found for Ni^{II} compound **4** (–17.2 cm^{-1}) whereas the large and positive D-values were found for Co^{II} and Fe^{II} compounds **3** (40.3 cm^{-1}) and **2** (7.9 cm^{-1}), respectively. This is in accordance with the different low temperature values of μ_{eff}/μ_B observed for **2**–**4** (Fig. 6).

When the obtained D-values are compared with those for previously studied complexes with **L2** and **L3** (Table 2),[12,38] they are very similar for Mn^{II} and Fe^{II} complexes **1** and **2**, but they are much higher for Co^{II} and Ni^{II} complexes **3** and **4** revealing their larger magnetic anisotropy. The sign of D-value for **2** is positive and thus, different from previously studied Fe^{II} complexes of **L2** and **L3** (Table 2), but it is in accordance with CASSCF/NEVPT2 calculations for **2** (Table 2) and also with previously performed calculations (see Fig.

10 in ref. 38). These calculations showed, that strong axial ligand field in seven-coordinate Fe^{II} complex can provide small positive D-values while when this ligand field is reduced, D becomes larger and negative. Moreover, HF-EPR
5 measurements (Fig. S5) confirmed the positive sign of D. The data for 180 GHz, 321 GHz and 415 GHz at 4 K were successfully simulated for a spin $S = 2$ with $D = +8.2$ cm^{-1} and $E/D = 0.29$ and the g values from Table 2. The EPR signal vanishes at 15 K in agreement with simulated data, which
10 predicts a significant decrease of the absorption intensity with increasing temperature. Both complexes 3 and 4 show among the highest magnetic anisotropies reported for pentagonal bipyramidal Co^{II} (Table 3) or Ni^{II} complexes (Table 2). If the calculations previously reported by Sutter and Mallah are
15 considered,[17] the stronger axial ligand field should provide larger magnetic anisotropy in case of Ni^{II} complexes while an opposite effect on magnetic anisotropy is expected for Co^{II} complexes. Similar trend as for Ni^{II} complexes was recently observed for Fe^{II} complexes,[11] but the description/explanation
20 was more complex concerning contribution(s) to the D value from different excited states and also differential π-interactions Fe^{II}–axial ligands between the x and y directions. Thus, according to the large magnetic anisotropy of Co^{II} complex 3, the axial field should be weaker, but on the other
25 hand according to the large magnetic anisotropy of Ni^{II} complex 4 and the positive sign of D for Fe^{II} complex 3, the axial field should be stronger. So, not only the axial, but also the equatorial effect (more symmetric field provides larger anisotropy) should be taken into account, which makes the
30 elucidation of any trend for complexes of N-pendant armed macrocycles not as straightforward as expected. We tried to establish such a magneto-structural correlation as shown in Fig. 7, where the average equatorial and the axial metal to donor atom distances together with values of D-parameter are
35 displayed for each metal ion as a function of coordinated ligand (L, L2 and L3). The D is becoming more positive both for Fe^{II} and Co^{II} complexes, while D is becoming more negative for Ni^{II} complexes considering the change of ligands L3→L (Fig. 7).
40 If we consider that the increasing average distance of axial donor atoms (L3→L) can be interpreted in term of weaker axial ligand field (although benzimidazole is stronger σ-donor than pyridine, it is also a weaker π-acceptor),[40] the increasing magnetic anisotropy of Co^{II} complexes is in agreement with
45 theoretically predicted trend. This is in contrast to the behavior of Ni^{II} complexes, where the magnetic anisotropy twice increased (L3→L), which can be rather explained by the more symmetric equatorial ligand field (Fig. 5 right) and this can be quantified by deviations from PBPY-7 ideal
50 symmetry obtained by the program SHAPE (1.112 and 1.201 for L, Table S2, 1.237 for L2,[12] 2.988 for L3)[38]. As the

change in equatorial ligand field has more dramatic impact on value of D than the variation of the axial ligand field in Ni^{II} complexes (see Fig. 12 later in the section Theoretical
55 calculations), the increase of negative D for Ni^{II} complexes (L3→L), is more likely governed by the decreasing the deviation from ideal D$_{5h}$ symmetry. The absolute values of D, $|D|$, for Fe^{II} complexes is almost the same, which is in agreement with our theoretical simulations (*vide infra*)
60 showing small impact of the ligand field change on the size of the magnetic anisotropy. Moreover, the variation of ZFS parameters for Fe^{II} complexes must be taken with great care, because usually the low lying excited states reduce validation of the spin Hamiltonian approach.
65 In conclusion, both axial as well as equatorial ligand fields have to be considered when analyzing the magnetic anisotropy, because change in each field has differently strong and sometimes opposite impact on the resulting anisotropy. Moreover these effects have different extent for different
70 central metal ions and thus, general analysis for more metals appears to be intricate.

Table 2 Comparison of *ab initio* calculated and fitted spin Hamiltonian parameters for complexes 1–4[a] and for complexes with L2 and L3.

compound	1	2	3	4
central metal atom	Mn(II)	Fe(II)	Co(II)	Ni(II)
electron configuration	3d^5	3d^6	3d^7	3d^8
spin state S	5/2	2	3/2	1
ZFS and g values based on CASSCF/NEVPT2 calculations				
D (cm^{-1})	−0.071/−0.076	7.41/7.55	34.4/34.0	−23.8/−25.6
E/D	0.101/0.087	0.200/0.183	0.082/0.085	0.067/0.043
g_x	2.000/2.000	2.079/2.081	2.320/2.312	2.251/2.245
g_y	2.000/2.000	2.172/2.175	2.383/2.378	2.233/2.234
g_z	2.000/2.000	2.017/2.016	2.042/2.041	2.404/2.414
ZFS values based on CASSCF/DCD-CAS(2) calculations				
D (cm^{-1})	−0.114/−0.122	7.67/7.80	38.4/37.9	−23.6/−25.5
E/D	0.069/0.070	0.145/0.122	0.067/0.074	0.062/0.040
magnetic analysis of the experimental data[b]				
D (cm^{-1})	−0.30(3)	7.90(6)	40.3(1.5)	−17.2(2)
E/D	0.0	0.220(4)	0.10(3)	0.076(1)
g	1.9538(9)	2.057(1)	g_{xy} = 2.156(6) g_z = 2.00	2.165(3)
χ_{TIP} (10^{-9} m^3 mol^{-1})	0.0	0.0	5.3(5)	7.5(2)
Data for complexes with L2[12]				
D (cm^{-1})	0	−7.4	34.0	−12.8
E/D		0.0	0.0	0.136
Data for complexes with L3[38]				
D (cm^{-1})	–	−9.6	29.1	−8.5
E/D		0.006	0	0.19

[a] the theoretical calculations were done for both crystallographically independent molecules present in the asymmetric unit. [b] detailed procedure of calculation of standard deviations is described ref. 76.
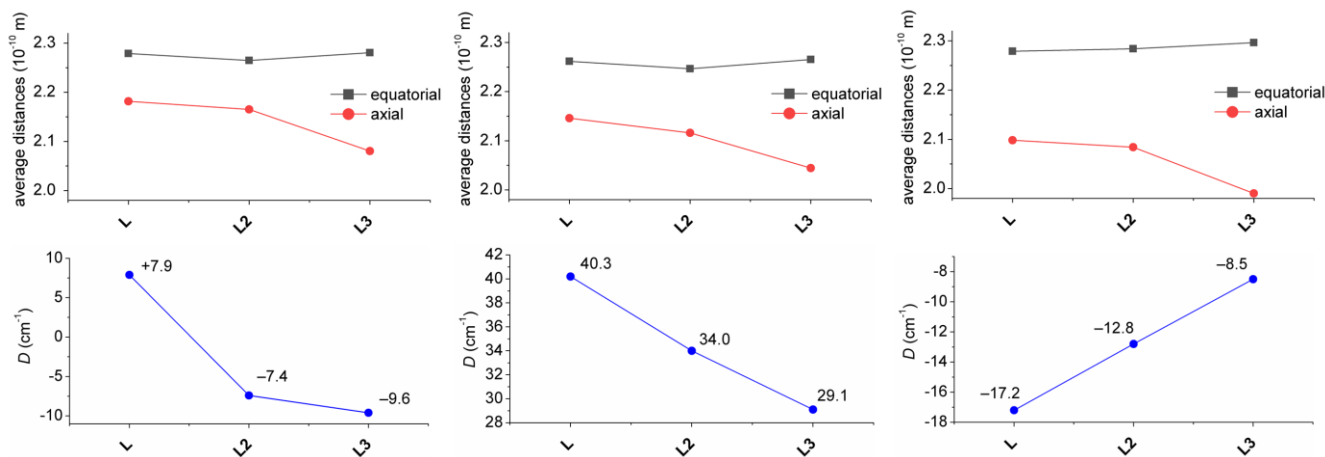
Fig. 7 Magneto-structural correlation for Fe^{II} (*left*), Co^{II} (*middle*) and Ni^{II} (*right*) complexes of studied ligand **L** and previously studied structurally similar ligands **L2** and **L3**. Variation of the average bond distance in equatorial plane and in axial positions (*top*) and variation of the axial zero-field-splitting parameter D (*bottom*). Lines serve as guides. In case of two crystallographically independent molecules were found in the asymmetric unit, average values are given.

Dynamic magnetic measurements

The alternating current (AC) susceptibly measurement was performed for **2**–**4**, however, the non-zero out-of-phase signal was found only for Co^{II} compound **3** upon applying weak static magnetic field (Fig. S6). Therefore, temperature and frequency AC susceptibility data were acquired at B_{DC} = 0.1 T (Fig. 8) and clearly defined maxima of out-of-phase signal of AC susceptibility depended on applied frequency were found for compound **3**, which is the characteristic behavior of SMMs. Next, the one-component Debye's model was applied based on the equation

$$\chi(\omega) = \frac{\chi_T - \chi_S}{1 + (i\omega\tau)^{1-\alpha}} + \chi_S$$
(2)

which resulted in isothermal (χ_T) and adiabatic (χ_S) susceptibilities, relaxation times (τ) and distribution parameters (α) (Table S3). Afterwards, the Argand (Cole-Cole) plot was constructed as showed in Fig. 8. The application of Arrhenius law to the temperature dependence of the relaxation times revealed τ_0 = 6.04×10^{-6} s and U_{eff} = 6.0 cm^{-1} (8.7 K). Such physically unreasonable value of U_{eff} can be ascribed to the fact that D-parameter is positive and E/D very small, hence, the easy-plane type of magnetic anisotropy is operational, which means that there is no energy barrier U defined by $|D|(S^2-¼)$. Origin of the slow relaxation of magnetization in Kramers ions (such as Co^{II}) with dominant easy-plane magnetic anisotropy was investigated in detail by E. Ruiz, F. Luis et al.,[77] and such spin-lattice relaxation was rather described by one-phonon direct processes and two-phonon Raman processes. Therefore, the temperature dependence of the relaxation times was successfully fitted considering Raman relaxation mechanism described by following equation

$$\frac{1}{\tau} = CT^n$$
(3)

with C = 507 K^{-n}s^{-1} and n = 2.58 (Fig. 8). Similar values of n were also reported for other seven-coordinate Co^{II} complexes (Table 3).[12,21] Here we also note that inclusion of the direct term in eq. 3 did not lead to better fit.
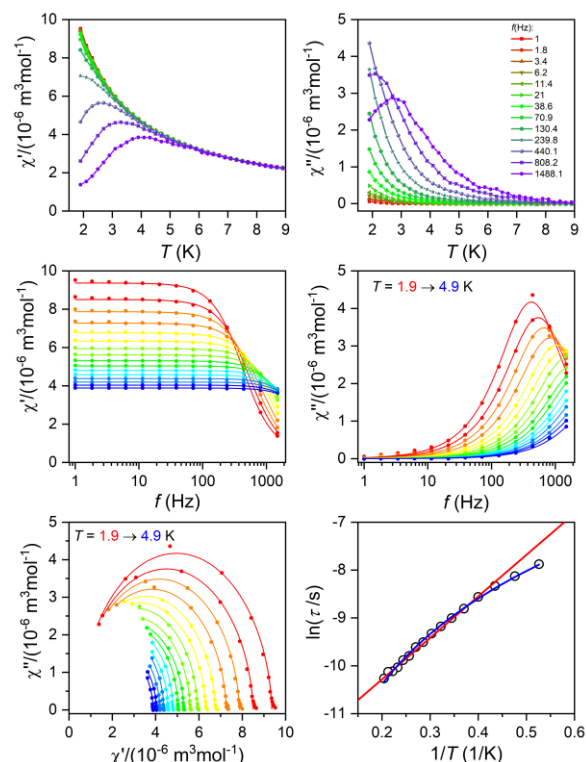
Fig. 8 AC susceptibility data of **3**. *Top*: in-phase χ' and out-of-phase χ'' molar susceptibilities at the applied external magnetic field B_{DC} = 0.1 T (full lines are only guides for eyes). *Middle*: frequency dependence of in-phase χ' and out-of-phase χ'' molar susceptibilities. The full lines represent the fitted data using eq. 2. *Bottom*: the Argand (Cole-Cole) plot with full line fitted with eq. 2 and the fit of resulting relaxation times τ with Arrhenius law (red line) and Raman relaxation process (blue line).

Table 3 List of mononuclear seven-coordinate Co[II] SMMs together with the obtained ZFS parameters and parameters describing the relaxation of magnetization.

| complex	ZFS			Orbach	Direct	Raman		ref.
	D/cm^{-1}	E/D	$\tau_0/10^{-9}$ s	$U_{\text{eff}}/\text{cm}^{-1}$ (K)	$A/\text{K}^{-1}\text{s}^{-1}$	$C/\text{K}^{-n}\text{s}^{-1}$	n	ref.
[Co(H$_2$**L4-Ph**)(H$_2$O)(NO$_3$)]NO$_3$	32.4	0	0.6	56.3 (81.2)				17,18
[Co(15-pydienN$_5$)(H$_2$O)$_2$]Cl$_2$	24.6	−0.014	1200	20.7 (29.8)				18
[Co(**L4-Ph**)(im)$_2$] [a]	24.8	0.0016	0.087	62.3 (89.6)				18
[Co(**tbp**)$_3$(NO$_3$)$_2$] [a]	35.8	0.006	768	17.7 (25.5)				78
[Co(**isq**)$_3$(NO$_3$)$_2$] [a]	35.7	0.0006	701	11.0 (15.8)				78
[Co(**L5**)(H$_2$O)$_2$](BF$_4$)$_2$	25.6	−0.039	1100	42.2 (29.3)				19
[Co(**L5**)(CN)$_2$]·2H$_2$O	17.4	−0.034	3200	48.9 (34.0)				19
[Co(**L5**)(NCS)$_2$]	26.3	−0.004	1000	49.2 (34.2)				19
[Co(**L5**)(SPh)$_2$]	34.5	−0.052	2100	54.7 (38.0)				19
[Co(**L1**)Cl$_2$]·2CH$_3$OH	38(3)	0	–[b]	5.5–7.8 (7.9–11.2) [b]		0.99–1.62[b]	1.76–2.59[b]	21
[Co(**L1**)Br$_2$]	41(1)	0	1120	4.2 (6.1)		613	2.79	21
[Co(**L1**)I$_2$]	35(1)	0	1120	4.5 (6.5)		500	2.82	21
[Co(**L2**)](ClO$_4$)$_2$	34	0	990	16.9 (24.3)		47.3	2.84	12
[Co(**L3**)]·H$_2$O	29.0	0	–	–	96.9	0.535	5.49	38
[Co(15-pydienN$_3$O$_2$)(CH$_3$CN)$_2$](BPh$_4$)$_2$	36.9	0.005	0.034(2)	62 (89)		131(9)	2.1(1)	79
[Co(**L4-PhOH**)(CH$_3$OH)$_2$]	43.1	0.077	7400	23.3 (33.5)			4.7	22
[Co(H$_2$**L4-PhOH**)(NCS)(CH$_3$OH)]ClO$_4$·CH$_3$OH	41.5	0.036	5600	19.7 (28.4)			4.2	22
[Co(H$_2$**L4-PhOH**)(NCS)$_2$]·2CH$_3$OH	38.8	0.54	4800	16.4 (23.6)			3.7	22
[Co(H$_2$**L4-NH$_2$**)(NCS)$_2$]·0.5C$_2$H$_5$OH	35.6	0.17	–	–	1.03×10^{-3} [c]	0.00106	9 [d]	33
[Co(H$_2$**L4-NH$_2$**)(NCSe)$_2$]·0.5C$_2$H$_5$OH	38.2	0	–	–	4.10×10^{-4} [c]	0.02	7.4	33
[Co(H$_2$**L4-NH$_2$**){N(CN)$_2$}$_2$]·2H$_2$O	35.3	0.101	–	–	1.29×10^{-4} [c]	0.017	7.3	33
[Co(H$_2$**L4-NH$_2$**)(H$_2$O){C(CN)$_3$}]NO$_3$·1.16H$_2$O	33.6	0.149	–	–	7.7×10^{-5} [c]	0.4	5.6	33
{[Co(H$_2$**L4-NH$_2$**)(H$_2$O)(N$_3$)][Co(H$_2$**L4-NH$_2$**)(N$_3$)$_2$]}N$_3$·4H$_2$O	40.4	0	–	–	2.9×10^{-4} [c]	0.26	5.8	33
[Co(**L**)](ClO$_4$)$_2$·1.5CH$_3$NO$_2$	40.3	0.1	6040	6.0 (8.7)		507	2.58	this work

[a] im = imidazole, tbp = 4-*tert*-butylpyridne, isq = isoquinoline; [b] calculated by simplified model described in corresponding literature; [c] in the unit Oe^{-2}K^{-1}s^{-1}; [d] fixed during the fitting procedure

Obtained values of τ_0 and U_{eff} for Orbach relaxation process or C and n for Raman relaxation process are compared with previously studied pentagonal bipyramidal Co[II] SMMs in Table 3. U_{eff} values are comparable with those for Co[II] complexes of structurally similar ligands **L1**, **L2**, **L3**, but are smaller in comparison with other ligands having more rigid macrocyclic part (**15-pydienN$_3$O$_2$**, **L4-Ph**, **L5**). This "equatorial rigidity" effect appears to have a more significant influence on the relaxation times than the magnetic anisotropy represented by D-value. Thus, there is no clear relationship between the magnetic anisotropy (D) and the values of relaxation times, which can be attributed to the fact that Orbach relaxation mechanism is not active for such easy-plane systems and the direct and Raman relaxation processes should stand at the centre of our focus. Therefore, in order to increase the relaxation time, the C and n parameters of Raman relaxation process should be decreased. However, the lack of these parameters from literature means that further investigation of Co[II] complexes has to be done to better understand the relationship between the molecular structure and relaxation properties.

Electrochemistry

In order to investigate the electrochemical properties of prepared complexes **1**–**4**, the measurement of cyclic voltammetry was performed in acetonitrile solution. Obtained cyclic voltammograms are depicted in Fig. 9 and the redox potentials are listed in Table 4. All $E_{1/2}$ potentials for Mn$^{3+/2+}$, Fe$^{3+/2+}$ and Co$^{3+/2+}$ couples are very high (1.596, 1.043 and 1.853V, respectively), which indicate that the lower oxidation states (Mn^{2+}/Fe^{2+}/Co^{2+}) are stabilized due to the π-acceptor ability of axially coordinated two benzimidazolyl pendant arms. Moreover, Ni$^{3+/2+}$ redox couple is even not visible in the range of available potentials during the measurement. Thus, the oxidation state +III for Ni[II] complexes is not accessible, which is in accordance with the π-acceptor properties of benzimidazole functional groups. On the other hand, lower oxidation states Mn$^+$/Fe$^+$/Co$^+$/Ni$^+$ are accessible in quasi-reversible/quasi-reversible/reversible/quasi-reversible processes at relatively high negative potentials (see Table 4). Furthermore, irreversible reduction peaks at ca −1.25 and −1.40 V were detected and correspond to the reduction of CH$_3$NO$_2$ co-crystallized solvent molecule as was confirmed by measurement of MeCN solution with extra addition of CH$_3$NO$_2$ (Fig. S7).
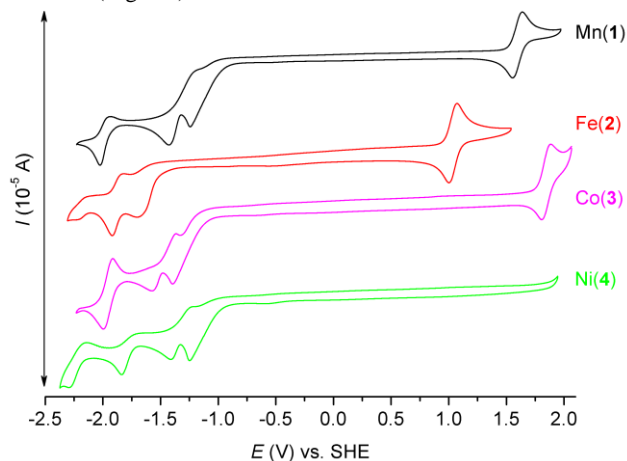
Fig. 9 Cyclic voltammograms of complexes **1** (black), **2** (red), **3** (purple), and **4** (green) (~2 mM) recorded under argon atmosphere in 0.1 M TBAP in acetonitrile with a glassy carbon working electrode. Complex **2** was the

only one used for the measurement in its form prior to recrystallization from CH_3NO_2.

The cyclic voltammogram of the ligand **L** was measured as well and it shows one irreversible oxidation peak at $E_{ox} = 1.450$ V (Fig. S8), which may be assigned to the oxidation of both benzimidazolyl pendant arms, and one irreversible reduction peak at $E_{red} = -2.063$ V.

When obtained results are compared with those for complexes containing structurally similar pyridine analogue **L2**, several aspects can be found. $E_{1/2}$ potentials for $Mn^{3+/2+}$ and $Fe^{3+/2+}$ couples are slightly lower than those found for complexes with **L2** ($E_{1/2(Mn)} = 1.624$V, $E_{1/2(Fe)} = 1.132$V vs. SHE, see Fig. S9 and S10), but $E_{1/2}$ potential for $Co^{3+/2+}$ couple is slightly higher than that for complex of **L2** ($E_{1/2(Co)} = 1.744$ V vs. SHE, see Fig. S11).[80] Therefore the oxidation states Mn^{2+} and Fe^{2+} are more stabilized in complexes with **L2**, while the oxidation state Co^{2+} is more stabilized in complex with **L**. On the other hand, lower oxidation states $Mn^+/Fe^+/Co^+$ are easily accessible in complexes with **L2** because complexes **2–4** with **L** have more negative reduction potentials (see Figs. S9–S11). This is in accordance with weaker π-acceptor ability of benzimidazol moiety in comparison with pyridine one. In conclusion the electrochemical behavior of complexes with **L** and **L2** is rather similar, but in case of complexes with **L** the lower oxidation states are less accessible and thus, the oxidation state +II is more stabilized.

Table 4 Results of cyclic voltammetry experiments.

| Compound	Redox process	$E_{1/2}$ [V] vs. Fc/Fc$^+$	$E_{1/2}$ [V] vs. SHE	ΔE [mV]
1	Mn^{3+}/Mn^{2+}	0.972	1.596	84
	Mn^{2+}/Mn^+	−2.604	−1.980	91
2	Fe^{3+}/Fe^{2+}	0.419	1.043	70
	Fe^{2+}/Fe^+	−2.496	−1.872	93
3	Co^{3+}/Co^{2+}	1.229	1.853	76
	Co^{2+}/Co^+	−2.584	−1.960	80
4	Ni^{2+}/Ni^+	−2.375	−1.751	140

Theoretical calculations

The electronic structure of reported complexes was also studied by theoretical methods using computational package ORCA 4.1. First, the post-Hartree-Fock multireference calculations based on the state-averaged complete active space self-consistent field method (SA-CASSCF) were employed together with def2-TZVP basis set to reveal the impact of the spin-orbit coupling and ligand field on the spin Hamiltonian parameters, especially on the zero-field splitting parameters D and E. The active space was defined by n-electrons in five d-orbitals, CAS(n,5) and we have used two methods to cover dynamic electron correlation effect, well-known N-electron valence state perturbation theory (NEVPT) and also recently introduced dynamic correlation dressed CAS with the second-order treatment (DCD-CAS(2)). The *ab initio* ligand field theory (AILFT)[81,82] was used to calculate the energy of the d-orbitals as depicted in Fig. 10. The ideal D$_{5h}$ ligand field symmetry leads to splitting of the d-orbitals into three sets, e_1'' (d$_{xz}$, d$_{yz}$), e_2' (d$_{xy}$, d$_{x2-y2}$) and a_1' (d$_{z2}$), and such pattern is

visible in case of **1**, but even in this complex, the degeneracy of d-orbitals is removed due to non-homogenous ligand field. Evidently, the pattern of the splitting of the d-orbitals is continuously changing from **1** to **4** and is interconnected with weakening of M-O donor-acceptor bonds.
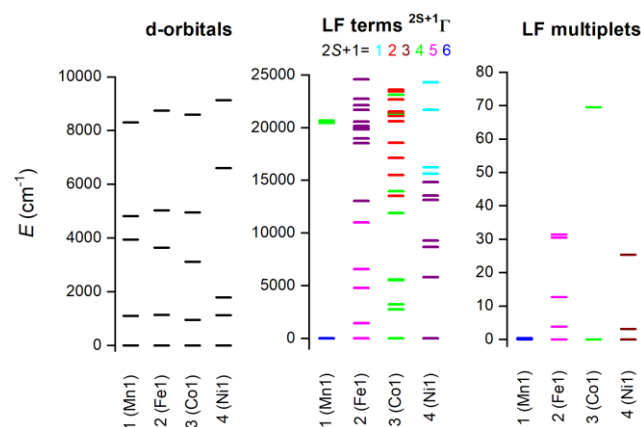

Fig. 10 Graphical output of the CASSCF/NEVPT2 calculations for the mononuclear molecular fragments [ML]$^{2+}$ of **1–4**. Plot of the d-orbitals splitting calculated by *ab initio* ligand field theory (AILFT) (*left*), low-lying ligand-field terms with various multiplicities (*middle*), and ligand-field multiplets (*right*).

Subsequently, the ligand-field terms are showed in Fig. 10 and it is evident that except for **1**, there are close lying terms with the same or lower multiplicities which do contribute to the zero-field splitting of the ground spin state multiplet (Fig. 10, right). The calculated ZFS and g-tensor parameters are summarized in Table 2, where calculations for both metal complexes within asymmetric units were done. The reported values are in very good agreement with the fitted ones, especially for compounds **2** and **3**, e.g. $D = 38.4/37.9$ cm^{-1} for **3** derived by DCD-CAS(2) and the fitted value of D is 40.2 cm^{-1}. The main axes of calculated D-tensors for complexes with large magnetic anisotropy, **2–4**, are showed in Fig. 11 together with three-dimensional plot of the calculated molar magnetization. Evidently, the easy-plane type of the magnetic anisotropy is present in Co^{II} complex and coincides with the equatorial pentagonal plane, while easy-axis type is found both in Fe^{II} and Ni^{II} complexes. In case of Ni^{II}, this behavior is natural due to negative value of D-parameter, however, in case of Fe^{II}, D-parameter is positive but due to large rhombicity, the easy-axis type of the magnetic anisotropy is operational.
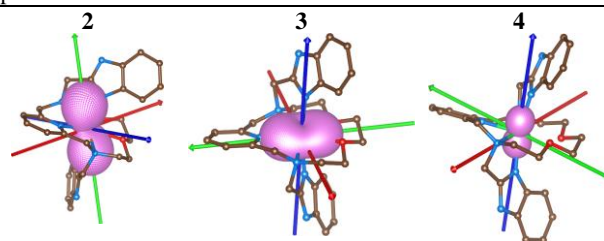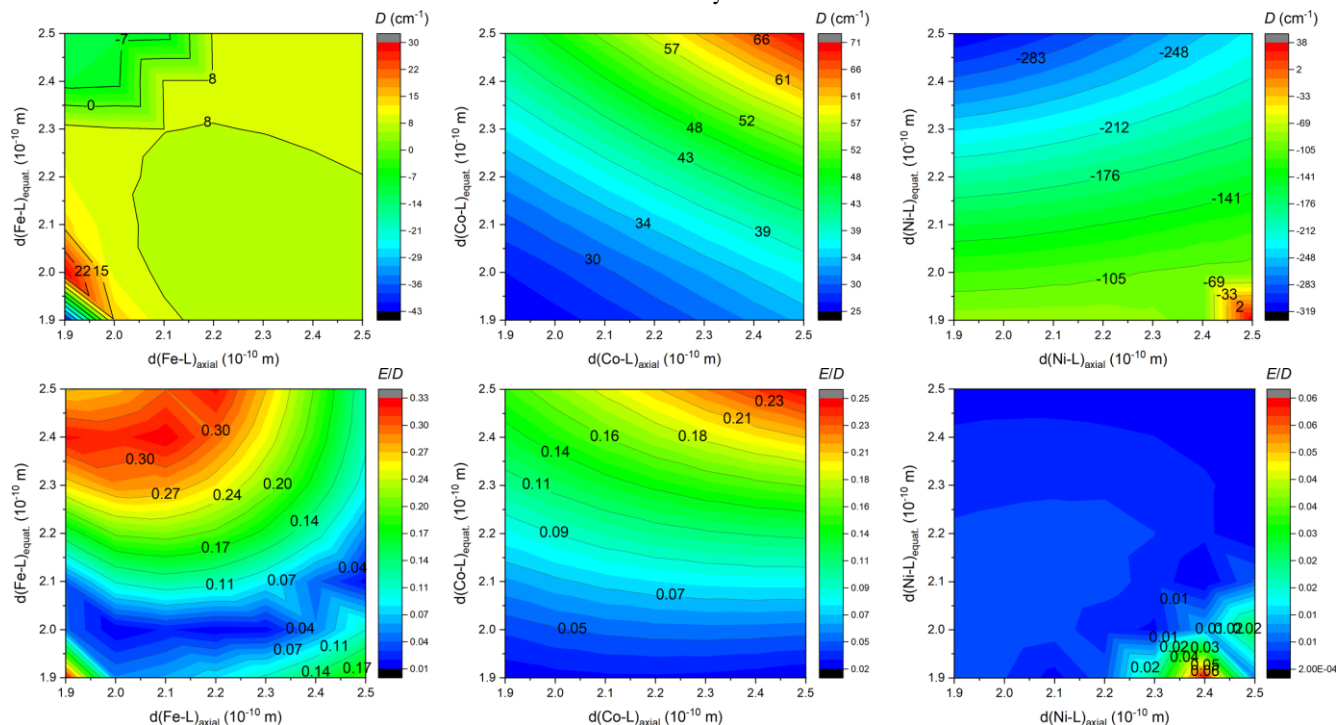

Fig. 11 The molecular structures of **2–4** derived from the experimental X-ray geometries used for CASSCF/NEVPT2 calculation overlaid with three-dimensional plot of the calculated molar magnetization at $T = 2$ K and $B = 1$ T and showing also principal axes of D-tensors (x/y/z-axes colored as red/green/blue arrows). The hydrogen atoms are not shown.

With the aim to get more insight into the role of the equatorial and the axial ligand field strength on the zero-field splitting in such pentagonal bipyramidal complexes of late transition metal complexes, we performed the CASSCF/DCD-CAS(2) calculation for model complexes $[M(NH_3)_2(NCH)_3(H_2O)_2]^{2+}$ (M = Fe^{II}, Co^{II} and Ni^{II}) – Fig. 12. Both the in-plane and the axial metal-donor interatomic distances were varied in the range 1.9 to 2.5 Å, which enabled creation of the contour plots of the axial and rhombic ZFS parameters – Fig. 13.
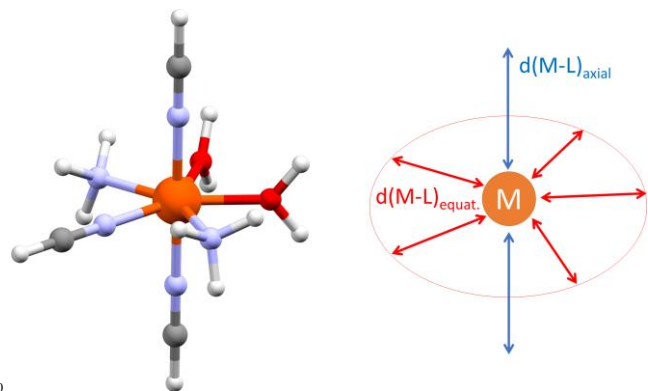
Fig. 12 The general molecular structure of the model complexes $[M(NH_3)_2(NCH)_3(H_2O)_2]^{2+}$ (M = Fe^{II}, Co^{II} and Ni^{II}) together with depiction of the varied structural parameters used for the CASSCF/DCD-CAS(2) calculations.

Evidently, there is small impact on ZFS parameters in Fe^{II} complexes, relatively small and positive D prevail, but the axial type of the magnetic anisotropy in the model complex can be achieved by increasing the rhombicity ($E/D \rightarrow 1/3$) by weakening the ligand field in the equatorial plane and strengthening the ligand field in the axial positions. In case of Co^{II} complexes, the D is definitively positive and large, its value can be increased by weakening the ligand field in both axial and equatorial directions, which also leads to escalation of E. The model of Ni^{II} complex provided very large and negative D almost in the whole simulation range, which in general makes such complexes good candidates for observing the axial type of the magnetic anisotropy taking into the account also very small rhombicity. The equatorial ligands have indisputably the larger impact on the value of D, thus weakening of the equatorial ligand field would increase $|D|$ substantially. To summarize, the careful and rational design of the macrocyclic ligands and the axial pendant arms is crucial to prepare magnetically interesting complex compounds, however, the design of the rigid ligands may be necessary to suppress the deformation of the ideal D$_{5h}$ symmetry induced by the Jahn-Teller effect.

Fig. 13 The contour plot showing the impact of variation of the ligand field of the axial and the equatorial ligands on the axial and rhombic ZFS parameters D and E/D for model compounds $[M(NH_3)_2(NCH)_3(H_2O)_2]^{2+}$ (M = Fe^{II}, Co^{II} and Ni^{II}) calculated at CASSCF/DCD-CAS(2) level of theory.

Conclusions

Structurally new macrocyclic ligand with two 2-benzimizazolyl pendant arms (**L**) has been synthesized and it provided axially compressed pentagonal bipyramidal Mn^{II}, Fe^{II}, Co^{II} and Ni^{II} complexes with the largest distortion observed for Ni^{II} complex **4** due to the Jahn-Teller effect. The large magnetic anisotropy was confirmed for Fe^{II}, Co^{II} and Ni^{II} complexes **2–4** and Co^{II} complex **3** behaved as a field-induced SMM with preferential Raman mechanism of relaxation of magnetization. Obtained results were supported by theoretical CASSCF calculations, which very well correspond to the obtained values of magnetic anisotropy. The CASSCF/CAS-DCD(2) based theoretical simulations provided detailed information about the effect of equatorial

and axial ligand field on the magnetic anisotropy in this class of the seven-coordinate Fe^{II}, Co^{II} and Ni^{II} complexes. Furthermore, they provide important information on how to tune/increase the magnetic anisotropy in future: (i) for Co^{II} complexes the equatorial as well as axial ligand field should be decreased and the effect of changing each of them is rather equal, (ii) for Ni^{II} complexes the equatorial field should be decreased while the axial field increased, but the effect of the equatorial one is much more pronounced, (iii) for Fe^{II} complexes the changes in both ligand fields alter $|D|$ to lesser extent, but large variation of the rhombicity E/D is observed. With this respect, more rigid macrocycle containing rather five nitrogen donor atoms could be a reasonable way how to fulfill above-mentioned requirements for magnetic anisotropy enhancement. Furthermore, deprotonization of **L** is even possible, so this could be another way how to additionally increase the axial ligand field and enhance the magnetic anisotropy at least for Ni^{II} complexes, and how to utilize these complexes as building blocks for the synthesis of more complex polymeric coordination compounds.

According to the electrochemical measurements, ligand **L** stabilizes the oxidation state +II in contrast to +I or +III due to its weaker π-acceptor ability in comparison with its pyridine-analogue **L2**. The trend in redox potentials for $M^{3+/2+}$ couples (M = Mn, Fe, Co and Ni) in complexes of **L** and **L2** was found as $E_{1/2}([ML2]^{3+/2+}) > E_{1/2}([ML]^{3+/2+}$ for M = Mn and Fe, while it is opposite for $E_{1/2}([CoL2]^{3+/2+}) < E_{1/2}([CoL]^{3+/2+}$ and could be related to the different stabilization of high spin Mn^{III}/Fe^{III} and low spin Co^{III} complexes as well as stronger σ-donor/weaker π-acceptor ability of benzimidazole group.

In conclusion, modification of the macrocycle with the two benzimidazolyl moieties has a beneficial effect on the magnetic anisotropy of especially Co^{II} and Ni^{II} complexes and also modifies the redox properties of the prepared complexes. But altogether can be concluded that the tuning of magnetic anisotropy in seven-coordinate pentagonal bipyramidal late-first-row transition metal complexes with macrocyclic ligands modified by pendant arms is a rather complex problem. More factors including not only strength of the axial ligand field, but mainly strength and symmetry of the equatorial ligand field have to be considered with great care during rational design of new suitable ligands.

Acknowledgements

Associated contents

^{a} Department of Inorganic Chemistry, Faculty of Science, Palacký University, 17. listopadu 12, 771 46 Olomouc, Czech Republic, Fax: +420 585 634 954. Tel: +420 585 634 429. E-mail: bohuslav.drahos@upol.cz
^{b} Department of Inorganic Chemistry, Faculty of Science, Charles University, Hlavova 2030, 128 00 Prague, Czech Republic
^{c} Central European Institute of Technology, CEITEC BUT, Purkyňova 656/123, 61200 Brno, Czech Republic

† Electronic Supplementary Information (ESI) available: [IR and MS spectra of the ligand and studied complexes, 2D NMR spectra of the ligand **L**, HFEPR data, additional magnetic data and cyclic voltammograms, crystal data and structure refinements, results of continuous shape measures, parameters of one-component Debye model].

Notes

The authors declare no competing financial interest.

References

1 E. L. Gavey and M. Pilkington, *Coord. Chem. Rev.* **2015**, *296*, 125-152.

2 J. Liu, Y.-C. Chen, J.-L. Liu, V. Vieru, L. Ungur, J.-H. Jia, L. F. Chibotaru, Y. Lan, W. Wernsdorfer, S. Gao, X.-M. Chen and M.-L. Tong, *J. Am. Chem. Soc.* **2016**, *138*, 5441-5450.

3 Y.-S. Ding, N. F. Chilton, R. E. P. Winpenny and Y.-Z. Zheng, *Angew. Chem. Int. Ed.* **2016**, *55*, 16071-16074.

4 Y.-C. Chen, J.-L. Liu, L. Ungur, J. Liu, Q.-W. Li, L.-F. Wang, Z.-P. Ni, L. F. Chibotaru, X.-M. Chen and M.-L. Tong, *J. Am. Chem. Soc.* **2016**, *138*, 2829-2837.

5 Z. Zhu, M. Guo, X.-L. Li and J. Tang, *Coord. Chem. Rev.* **2019**, *378*, 350-364.

6 A. K. Bar, P. Kalita, J. P. Sutter and V. Chandrasekhar, *Inorg. Chem.* **2018**, *57*, 2398–2401.

7 A. K. Bar, C. Pichon and J.-P. Sutter, *Coord. Chem. Rev.* **2016**, *308*, 346–380.

8 J. Ferrando-Soria, J. Vallejo, M. Castellano, J. Martínez-Lillo, E. Pardo, J. Cano, I. Castro, F. Lloret, R. Ruiz-García and M. Julve, *Coord. Chem. Rev.* **2017**, *339*, 17-103.

9 M. Feng and M. L. Tong, *Chemistry – A European Journal* **2018**, *24*, 1-22.

10 A. K. Bar, C. Pichon, N. Gogoi, C. Duhayon, S. Ramasesha and J.-P. Sutter, *Chem. Commun.* **2015**, *51*, 3616–3619.

11 A. K. Bar, N. Gogoi, C. Pichon, V. M. L. D. P. Goli, M. Thlijeni, C. Duhayon, N. Suaud, N. Guihéry, A.-L. Barra, S. Ramasesha and J.-P. Sutter, *Chem. Eur. J.* **2017**, *23*, 4380–4396.

12 P. Antal, B. Drahoš, R. Herchel and Z. Trávníček, *Inorg. Chem.* **2016**, *55*, 5957-5972.

13 D. Shao, S. L. Zhang, X. H. Zhao and X. Y. Wang, *Chem. Commun.* **2015**, *51*, 4360–4363.

14 D. Shao, X.-H. Zhao, S.-L. Zhang, D.-Q. Wu, X.-Q. Wei and X.-Y. Wang, *Inorg. Chem. Front.* **2015**, *2*, 846–853.

15 B. Drahoš, R. Herchel and Z. Trávníček, *Inorg. Chem.* **2018**, *57*, 12718–12726.

16 C. Pichon, N. Suaud, C. Duhayon, N. Guihery and J. P. Sutter, *J. Am. Chem. Soc.* **2018**, *140*, 7698–7704.

17 R. Ruamps, L. J. Batchelor, R. Maurice, N. Gogoi, P. Jiménez-Lozano, N. Guihéry, C. de Graaf, A.-L. Barra, J.-P. Sutter and T. Mallah, *Chem. Eur. J.* **2013**, *19*, 950–956.

18 X.-C. Huang, C. Zhou, D. Shao and X.-Y. Wang, *Inorg. Chem.* **2014**, *53*, 12671–12673.

19 D. Shao, S. L. Zhang, L. Shi, Y. Q. Zhang and X. Y. Wang, *Inorg. Chem.* **2016**, *55*, 10859–10869.

20 D. Shao, L. Shi, S.-L. Zhang, X.-H. Zhao, D.-Q. Wu, X.-Q. Wei and X.-Y. Wang, *CrystEngComm* **2016**, *18*, 4150-4157.

21 B. Drahoš, R. Herchel and Z. Trávníček, *Inorg. Chem.* **2017**, *56*, 5076–5088.

22 A. K. Mondal, A. Mondal, B. Dey and S. Konar, *Inorg. Chem.* **2018**, *57*, 9999-10008.

23 N. Gogoi, M. Thlijeni, C. Duhayon and J.-P. Sutter, *Inorg. Chem.* **2013**, *52*, 2283–2285.

24 V. S. Mironov, T. A. Bazhenova, Y. V. Manakin, K. A. Lyssenko, A. D. Talantsev and E. B. Yagubskii, *Dalton Trans.* **2017**, *46*, 14083–14087.

25 Y. V. Manakin, V. S. Mironov, T. A. Bazhenova, K. A. Lyssenko, I. F. Gilmutdinov, K. S. Bikbaev, A. A. Masitov and E. B. Yagubskii, *Chem. Commun.* **2018**, *54*, 10084-10087.

26 R. Boča, Zero-field splitting in metal complexes. *Coord. Chem. Rev.* **2004**, *248*, 757–815.

27 D. Gatteshi, R. Sessoli, J. Villain, *Molecular Nanomegnets*; Oxford University Press: New York, 2006.

28 *Molecular Nanomagnets and Related Phenomena*; S. Gao, Ed.; Structure and Bonding, Vol. 164; Springer: Berlin, 2015.

29 J. S. Miller, D. Gatteschi, Molecule-based magnets themed issue No. 6. *Chem. Soc. Rev.* **2011**, *40*, 3065–3365.

30 C. A. P. Goodwin, F. Ortu, D. Reta, N. F. Chilton and D. P. Mills, *Nature* **2017**, *548*, 439–441.

31 F.-S. Guo, B. M. Day, Y.-C. Chen, M.-L. Tong, A. Mansikkamäki and R. A. Layfield, *Science* **2018**, *362*, 1400–1403.

32 M. Atanasov, D. Aravena, E. Suturina, E. Bill, D. Maganas and F. Neese, *Coord. Chem. Rev.* **2015**, *289-290*, 177–214.

33 V. A. Kopotkov, D. V. Korchagin, V. D. Sasnovskaya, I. F. Gilmutdinov and E. B. Yagubskii, *Magnetochemistry* **2019**, *5*, 58.

34 B. Drahoš, R. Herchel and Z. Trávníček, *RSC Adv.* **2016**, *6*, 34674–34684.

35 C. Platas-Iglesias, L. Vaiana, D. Esteban-Gómez, F. Avecilla, J. A. Real, A. de Blas and T. Rodríguez-Blas, *Inorg. Chem.* **2005**, *44*, 9704–9713.

36 L. Vaiana, M. Regueiro-Figueroa, M. Mato-Iglesias, C. Platas-Iglesias, D. Esteban-Gómez, A. de Blas and T. Rodríguez-Blas, *Inorg. Chem.* **2007**, *46*, 8271–8282.

37 P. Antal, B. Drahoš, R. Herchel and Z. Trávníček, *Dalton Trans.* **2016**, *45*, 15114–15121.

38 P. Antal, B. Drahoš, R. Herchel and Z. Trávníček, *Eur. J. Inorg. Chem.* **2018**, *2018*, 4286–4297.

39 I. Nemec, R. Herchel, I. Svoboda, R. Boca and Z. Travnicek, *Dalton Trans.* **2015**, *44*, 9551–9560.

40 X. Xiaoming, M.-a. Haga, T. Matsumura-Inoue, Y. Ru, A. W. Addison and K. Kano, *J. Chem. Soc., Dalton Trans.* **1993**, 16, 2477–2484.

41 M. Boča, R. F. Jameson and W. Linert, *Coord. Chem. Rev.* **2011**, *255*, 290-317.

42 Q.-X. Li, Q.-H. Luo, Y.-Z. Li, C.-Y. Duan and Q.-Y. Tu, *Inorg. Chim. Acta* **2005**, *358*, 504–512.

43 A. Rodríguez-Rodríguez, I. Carreira-Barral, D. Esteban-Gómez, C. Platas-Iglesias, A. de Blas and T. Rodríguez-Blas, *Inorg. Chim. Acta* **2014**, *417*, 155–162.

44 A. El Majzoub, C. Cadiou, I. Déchamps-Olivier, F. Chuburu and M. Aplincourt, *Eur. J. Inorg. Chem.* **2007**, 32, 5087–5097.

45 A. E. Majzoub, C. Cadiou, I. Déchamps-Olivier, F. Chuburu, M. Aplincourt and B. Tinant, *Inorg. Chim. Acta* **2009**, *362*, 1169–1178.

46 M. Regueiro-Figueroa, D. Esteban-Gómez, C. Platas-Iglesias, A. de Blas and T. Rodríguez-Blas, *Eur. J. Inorg. Chem.* **2007**, 15, 2198–2207.

47 A. El Majzoub, C. Cadiou, I. Dechamps-Olivier, B. Tinant and F. Chuburu, *Inorg. Chem.* **2011**, *50*, 4029–4038.

48 C. M. Fisher, E. Fuller, B. P. Burke, V. Mogilireddy, S. J. Pope, A. E. Sparke, I. Dechamps-Olivier, C. Cadiou, F. Chuburu, S. Faulkner and S. J. Archibald, *Dalton Trans.* **2014**, *43*, 9567–9578.

49 B. Drahoš, J. Kotek, P. Hermann, I. Lukeš and E. Tóth, *Inorg. Chem.* **2010**, *49*, 3224–3238.

50 J. Prousek, *Collect. Chem. Czech. Commun.* **1991**, *56*, 1358–1360.

51 S. Stoll and A. Schweiger, *J. Magn. Reson.*, **2006**, *178*, 42–55.

52 Matlab, The Mathworks Inc.: Natick, MA, USA

53 V. V. Pavlishchuk and A. W. Addison, *Inorg. Chim. Acta* **2000**, *298*, 97–102.

54 G. M. Sheldrick, *Acta Cryst. C.* **2015**, *71*, 3–8.

55 A. L. Spek, *Acta Cryst. D.* **2009**, *65*, 148–155.

56 C. F. Macrae, I. J. Bruno, J. A. Chisholm, P. R. Edgington, P. McCabe, E. Pidcock, L. Rodriguez-Monge, R. Taylor, J. van de Streek and P. A. Wood, *J. Appl. Crystallogr.* **2008**, *41*, 466–470.

57 F. Neese, *Wiley Interdiscip. Rev.: Comput. Mol. Sci.* **2012**, *2*, 73–78.

58 F. Neese, *WIREs Comput. Mol. Sci.*, **2018**, *8*, e1327.

59 P. A. Malmqvist and B. O. Roos, *Chem. Phys. Lett.* **1989**, *155*, 189–194.

60 C. Angeli, R. Cimiraglia and J.-P. Malrieu, *Chem. Phys. Lett.* **2001**, *350*, 297–305.

61 C. Angeli, R. Cimiraglia, S. Evangelisti, T. Leininger and J.-P. Malrieu, *J. Chem. Phys.* **2001**, *114*, 10252–10264.

62 C. Angeli, R. Cimiraglia and J.-P. Malrieu, *J. Chem. Phys.* **2002**, *117*, 9138–9153.

63 F. Weigend and R. Ahlrichs, *Phys. Chem. Chem. Phys.* **2005**, *7*, 3297–3305.

64 D. Ganyushin and F. Neese, *J. Chem. Phys.* **2006**, *125*, 024103.

65 F. Neese, *J. Chem. Phys.* **2005**, *122*, 034107.

66 R. Maurice, R. Bastardis, C. de Graaf, N. Suaud, T. Mallah and N. Guihéry, *J. Chem. Theory Comput.* **2009**, *5*, 2977–2984.

67 F. Weigend, *Phys. Chem. Chem. Phys.* **2006**, *8*, 1057–1065.

68 A. Hellweg, C. Hättig, S. Höfener and W. Klopper, *Theor. Chem. Acc.* **2007**, *117*, 587–597.

69 S. Pathak, L. Lang and F. Neese, *J. Chem. Phys.* **2017**, *147*, 234109.

70 K. Momma and F. Izumi, *J. Appl. Crystallogr.* **2011**, *44*, 1272–1276.

71 M. Regueiro-Figueroa, L. M. Lima, V. Blanco, D. Esteban-Gomez, A. de Blas, T. Rodriguez-Blas, R. Delgado and C. Platas-Iglesias, *Inorg. Chem.* **2014**, *53*, 12859–12869.

72 B. Drahoš, R. Herchel and Z. Trávníček, *Inorg. Chem.* **2015**, *54*, 3352–3369.

73 S. Alvarez, *Dalton Trans.* **2005**, 13, 2209–2233.

74 D. Casanova, P. Alemany, J. M. Bofill and S. Alvarez, *Chem. Eur. J.* **2003**, *9*, 1281–1295.

75 R. Boča, *Theoretical Foundations of Molecular Magnetism*; Elsevier: Amsterdam, 1999.

76 The standard deviations were calculated as $\sigma_i = (P_{ii}^{-1} \cdot S/(N-k))^{-1/2}$, where $P_{ij} = \Sigma(\delta\mu_n/\delta a_i \cdot \delta\mu_n/\delta a_j)$ and $S = \Sigma(\mu_n - \mu_n^{exp})^2$ with $n = 1$ to N; a_i and a_j are fitted parameters, N is number of experimental points (sum of temperature and field dependent data), μ_n and μ_n^{exp} are the calculated and experimental effective magnetic moments for given temperature and magnetic field. The σ_i was then multiplied by Student's $t_{95\%}$ to provide confidence limits with 95% probabilities listed in text.

77 S. Gomez-Coca, A. Urtizberea, E. Cremades, P. J. Alonso, A. Camon, E. Ruiz and F. Luis, *Nat. Commun.* **2014**, *5*, 1–8.

78 L. Chen, S.-Y. Chen, Y.-C. Sun, Y.-M. Guo, L. Yu, X.-T. Chen, Z. Wang, Z.-W. Ouyang, Y. Song and Z.-L. Xue, *Dalton Trans.* **2015**, *44*, 11482–11490.

79 Y.-F. Deng, B. Yao, P.-Z. Zhan, D. Gan, Y.-Z. Zhang and K. R. Dunbar, *Dalton Trans.* **2019**, *48*, 3243–3248.

80 Mn^{II}, Fe^{II} and Co^{II} complexes of **L2** were resynthesized according to ref. 12 and the $E_{1/2}$ values were remeasured. Obtained data are in very good agreement with previously published data in ref. 12 if these data were recalculated using the new value $E_{1/2} = 0.624$ V vs. SHE for ferrocene/ferrocenium standard and its potential $E_{1/2} = 0.075$ V vs. Ag/Ag$^+$ during the measurement.

81 M. Atanasov, D. Ganyushin, K. Sivalingam and F. Neese, In *Molecular Electronic Structures of Transition Metal Complexes II*, D. M. P. Mingos, P. Day, J. P. Dahl, Eds.; Springer: Berlin Heidelberg, Berlin, Heidelberg, **2012**, pp. 149–220.

82 S. K. Singh, J. Eng, M. Atanasov and F. Neese, *Coord. Chem. Rev.* **2017**, *344*, 2–25.

Příloha P8

P. Antal, B. Drahoš, R. Herchel, Z. Trávníček,

Muffin-like lanthanide complexes with an N5O2-donor macrocyclic ligand showing field-induced single-molecule magnet behaviour.

PAPER

CrossMark
← click for updates

Muffin-like lanthanide complexes with an N_5O_2-donor macrocyclic ligand showing field-induced single-molecule magnet behaviour†

Peter Antal, Bohuslav Drahoš, Radovan Herchel and Zdeněk Trávníček*

Three mononuclear lanthanide complexes of a 2-pyridylmethyl pendant-armed 15-membered ligand {(3,12-bis(2-pyridylmethyl)-3,12,18-triaza-6,9-dioxabicyclo-[12.3.1]octadeca-1,14,16-triene); **L**} with general formula $[Ln(\mathbf{L})(H_2O)(NO_3)](NO_3)_2$ (Ln = Tb (**1**), Dy (**2**), and Er (**3**)) are reported. Based on X-ray diffraction analysis of **1** and **2**, the central lanthanide atoms are nine-coordinated with the N_5O_4 donor set originating from the ligand **L** and one coordinated water molecule and one monodentate-bonded nitrato ligand. The coordination geometry of the $[LnN_5O_4]$ cores can be described as a muffin-like shape. Magnetic measurements revealed that all three compounds show field-induced single-molecule magnet behaviour, with estimated energy barriers $U \approx 44\text{–}82$ K. The experimental study was complemented by CASSCF calculations showing a trend of an increasing first excited energy gap (Tb → Dy → Er) within the muffin-like geometry with the lowest magnetization tunnelling probability for the Dy^{III} complex **2**.

Introduction

Lanthanide ions reveal many unique physical and photophysical properties, such as large magnetic moments and magnetic anisotropy as well as long-life luminescence with sharp emission lines.[1] Therefore, their complexes have found many applications in luminescent sensors,[2] MRI contrast agents,[3] radionuclide therapy,[4,5] and magnetically active liquid crystals.[6] In the past few decades, more attention has been devoted to the magnetic properties of lanthanide complexes, because they were found as ideal candidates for single molecular magnets (SMMs)[7,8] or single ion magnets (SIMs)[9–11] due to their large magnetic moments and high magnetic anisotropy, and because of their potential applications in quantum computing,[12] high-density memory storage devices and molecule spintronics[13] and single molecule transistors.[14]

Many complexes of lanthanides with pthalocyanines,[15] Schiff bases,[16] β-diketones,[17] and polyoxometalates[18] show a high effective spin-reversal energy barrier (U_{eff}) and blocking temperature (T_B), *i.e.* parameters usually characterizing the SMM/SIM properties.[7–11] An attractive alternative to the above-mentioned ligands may be macrocycles with a variable cavity size and donor atom set favouring the desired types/sizes of metal ions.

In the past, only a few complexes of lanthanides with 2-pyridylmethyl pendant armed polyaza- or polyoxa-aza macrocyclic ligands were prepared and studied (Scheme 1). The tetrakis(2-pyridylmethyl) derivative of cyclen **L1** was studied in complexes with select lanthanides (La, Pr, Nd, Eu, Gd, Tb, Er, and Yb),[19,20] which were nine-coordinated with approximately monocapped square-antiprismatic geometry (twisted for Pr, Nd and Eu). The complex cations were chiral and they crystallized as racemic compounds.[19,20] An extended 18-membered hexaaza macrocyclic ligand with four 2-pyridylmethyl pendant arms (**L2**) and its complexes with general formula $Ln[Ln(\mathbf{L2})](NO_3)_6 \cdot nH_2O$, where $n = 2\text{–}4$, Ln = La, Ce, Pr, Gd, Tb, Er and Tm, were studied.[21] Lanthanide atoms in $[Ln(\mathbf{L2})]^{3+}$ were ten-coordinated and showed a distorted bicapped square antiprismatic geometry. The 18-membered tetraoxa-diaza macrocyclic ligand **L3** was studied only in its La^{3+} complex and only in solution.[22] Surprisingly, no magnetic or luminescence properties of the above-mentioned complexes have been investigated in detail to date. On the other hand, our attention was more devoted to rather unusual seven-coordinate lanthanide complexes, because they may represent a very promising geometry for optimal/effective preparation of lanthanide-based SMMs/SIMs. As it was published recently, the highest magnetization reversal barrier, even higher than 1000 K ($U_{eff} = 708$ or 1025 K), was observed in seven-coordinate Dy^{III} complexes $[Dy(\mathbf{L4})X]$,[23] where $X = Cl^-$ or Br^-, with a pentagonal bipyramidal coordination sphere confirmed by X-ray analysis. Among these seven-

Department of Inorganic Chemistry, Regional Centre of Advanced Technologies and Materials, Faculty of Science, Palacký University, 17. listopadu 12, CZ-771 46 Olomouc, Czech Republic. E-mail: zdenek.travnicek@upol.cz; Fax: +420 585 634 954
†Electronic supplementary information (ESI) available. CCDC 1487175 and 1487176. For ESI and crystallographic data in CIF or other electronic format see DOI: 10.1039/c6dt02537d
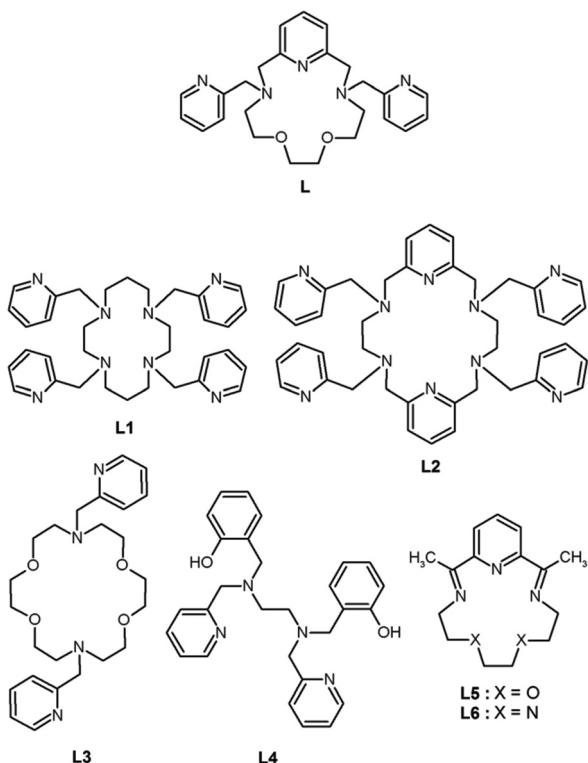
Scheme 1 The structural formulae of the ligand **L** (this work) and other ligands **L1**–**L6** mentioned within the text.

coordinate complexes, to the best of our knowledge, there are only three studies dealing with lanthanide complexes of 15-membered macrocyclic ligands (**L5**,[24] and **L6**)[25,26] and lanthanides (Dy[III],[24–26] Er[III], Tm[III], Lu[III]),[24] in which the central atom should adopt the pentagonal bipyramidal geometry, which unfortunately have not been confirmed by X-ray analysis yet. Nevertheless, the Dy[III] complexes [Dy(**L5**)Cl₂]Cl·6H₂O,[25,26] and [Dy(**L6**)Cl₂]Cl·4H₂O[25] revealed large magnetic anisotropy which was reflected in their SMM/SIM behavior (U_{eff} = 7.75 and 23.7 K; τ_0 = 7.52 × 10⁻⁷ and 6.4 × 10⁻⁶ s, respectively).[26] In this perspective, herein, we report the syntheses, X-ray crystal structures and magnetic properties of three mononuclear lanthanide complexes (Tb[III], Dy[III], and Er[III]) with the 2-pyridylmethyl pendant-armed 15-membered macrocyclic ligand (**L**), which was recently synthesized and proved to provide seven-coordinate late first-row transition metal complexes, and even a Co(II) mononuclear SMM.[27] In this work, we tested the coordination mode of **L** in lanthanide complexes and their magnetic properties.

Experimental section

Materials and methods

3,12-Bis(2-pyridylmethyl)-3,12,18-triaza-6,9-dioxabicyclo-[12.3.1] octadeca-1,14,16-triene (**L**) was prepared according to the literature.[27] Other chemicals were purchased from commercial sources and used without further purification. Elemental analysis (C, H, N) was performed on a Flash 2000 CHNO-S

Analyzer (Thermo Scientific, Waltham, MA, USA). Infrared spectra (IR) were recorded on a Thermo Nicolet NEXUS 670 FT-IR spectrometer (Thermo Nicolet, Waltham, MA, USA) employing the ATR technique on a diamond plate in the range of 200–4000 cm⁻¹. The mass spectra (MS) were collected on a LCQ Fleet Ion Mass Trap mass spectrometer (Thermo Scientific, Waltham, MA, USA) equipped with an electrospray ion source and a three-dimensional ion-trap detector in the positive mode. The temperature dependent (T = 1.9–300 K, B = 0.1 T) and field dependent (B = 0–9 T, T = 2, 5, and 10 K) magnetization measurements were performed on a PPMS Dynacool (Quantum Design Inc., San Diego, CA, USA). Dynamic magnetic properties were studied by measuring ac susceptibility on a MPMS XL-7 SQUID magnetometer (Quantum Design Inc., San Diego, CA, USA). Powder XRD patterns were recorded with a MiniFlex600 (Rigaku) using Cu Kα radiation (λ = 1.5418 Å). Emission spectra were recorded in an acetonitrile/methanol mixture (V/V = 1 : 1) at room temperature using an AvaSpec-HS1024×122TE spectrometer. The excitation source was a deuterium arc lamp.

Synthesis of [Tb(L)(NO₃)(H₂O)](NO₃)₂ (1)

To a stirred solution of **L** (71.0 mg, 0.16 mmol) in 10 mL of acetonitrile, Tb(NO₃)₃·5H₂O (71.2 mg, 0.16 mmol) was added. The resulting solution was refluxed under stirring for 2 h. The obtained clear colourless solution was allowed to crystallize by diffusion of diethyl ether vapour at room temperature. After 3 days, colourless crystals (66 mg, yield 52%) were isolated by filtration on a glass frit, washed with cold diethyl ether (2 × 1 mL) and dried under vacuum over NaOH for the next 2 days. Anal. Calcd for C₂₅H₃₃N₈O₁₂Tb₁: C, 37.70; H, 4.18; N, 14.07%. Found: C, 37.81; H, 4.22; N, 13.88%. MS, m/z (+): 434.28 [L + H]⁺ (I_{rel} = 100%); 456.29 [L + Na]⁺ (I_{rel} = 61%); 653.08 [(TbL (NO₃)₂)−4O + H]⁺ (I_{rel} = 53%); 685.06 [(TbL(NO₃)₂)−2O + H]⁺ (I_{rel} = 32%); 716.08 [TbL(NO₃)₂]⁺ (I_{rel} = 39%). IR (ATR, cm⁻¹): 831 (m), 950 (m), 1011 (m), 1033 (s), 1057 (m), 1082 (m), 1283 (s), 1296 (s), 1322 (s), 1370 (s), 1445 (m), 1605 (m), 2893 (s), 2909 (s), 2952 (s).

Synthesis of [Dy(L)(NO₃)(H₂O)](NO₃)₂ (2)

The synthesis follows the same procedure as described for **1** except that Dy(NO₃)₃·6H₂O was used as the starting material instead of Tb(NO₃)₃·5H₂O. Colourless crystals were isolated after 1 day (121 mg, yield 84%). Anal. Calcd for C₂₅H₃₃N₈O₁₂Dy₁: C, 37.53; H, 4.15; N, 14.01%. Found: C, 37.64; H, 4.19; N, 13.89%. MS, m/z (+): 434.28 [L + H]⁺ (I_{rel} = 100%); 456.28 [L + Na]⁺ (I_{rel} = 67%); 658.08 [(DyL(NO₃)₂)−4O + H]⁺ (I_{rel} = 16%); 690.07 [(DyL(NO₃)₂)−2O + H]⁺ (I_{rel} = 11%); 721.08 [DyL (NO₃)₂]⁺ (I_{rel} = 12%). IR (ATR, cm⁻¹): 832 (m), 950 (m), 1011 (m), 1032 (s), 1057 (m), 1082 (m), 1281 (s), 1296 (s), 1323 (s), 1370 (s), 1446 (m), 1605 (m), 2894 (s), 2909 (s), 2954 (s).

Synthesis of [Er(L)(NO₃)(H₂O)](NO₃)₂ (3)

The synthesis follows the same procedure as described for **1** except that Er(NO₃)₃·5H₂O was used as the starting material instead of Tb(NO₃)₃·5H₂O. Light pink crystals were isolated

after 3 days (92 mg, yield 67%). Anal. Calcd for $C_{25}H_{33}N_8O_{12}Er_1$: C, 37.31; H, 4.13; N, 13.92%. Found: C, 37.29; H, 4.27; N, 13.78%. MS, m/z (+): 434.27 $[L + H]^+$ (I_{rel} = 100%); 456.28 $[L + Na]^+$ (I_{rel} = 77%); 662.07 $[(ErL(NO_3)_2)-4O + H]^+$(I_{rel} = 15%); 694.04 $[(ErL(NO_3)_2)-2O + H]^+$ (I_{rel} = 10%); 725.06 $[ErL(NO_3)_2]^+$ (I_{rel} = 10%). IR (ATR, cm^{-1}): 833 (m), 951 (m), 1012 (m), 1033 (s), 1058 (m), 1082 (m), 1282 (s), 1296 (s), 1324 (s), 1369 (s), 1446 (m), 1606 (m), 2869 (s), 2910 (s), 2956 (s).

X-ray structure analysis

Single crystals of **1** and **2** suitable for X-ray diffraction analysis were prepared by slow diffusion of diethyl ether vapour into the acetonitrile solutions of the appropriate complex at room temperature. Crystallographic data were collected at 120 K on a Bruker D8 QUEST diffractometer equipped with a PHOTON 100 CMOS detector using Mo-Kα radiation (λ = 0.71073 Å). The APEX3 software package[28] was used for data collection and reduction. The molecular structures were solved by direct methods (SHELXS) and refined by full-matrix least-squares procedure SHELXL (version 2014/7),[29] and using XShell software package.[28] Hydrogen atoms of both structures were found in the difference Fourier maps and refined using a rigid model, except for O-attached hydrogens whose positions were refined freely, with C–H = 0.95 (CH)$_{ar}$ and C–H = 0.99 Å (CH$_2$), and with U_{iso}(H) = 1.2U_{eq}(OH, CH, CH$_2$). The molecular and crystal structures of the studied compounds, depicted in Fig. 1 and Fig. S2,† were drawn using Diamond software.[30]

Theoretical calculations

The post-Hartree–Fock calculations performed on the $[Ln(L)(NO_3)(H_2O)](NO_3)_2$ complexes **1–3** using the geometries experimentally determined by X-ray analysis were done with the MOLCAS 8.0 program package.[31] The active space of the CASSCF calculations[32] comprised of eight, nine and eleven electrons in seven metal-based f-orbitals for **1**, **2**, and **3**, respectively. The Restricted Active Space Self-Consistent Field (RASSCF) method was employed in CASSCF calculations with the following numbers of multiplets: 7 septets, 140 quintets, 306 triplets and 245 singlets for Tb^{III}, 21 sextets, 224 quartets and 490 doublets for Dy^{III}, 35 quartets and 112 doublets for Er^{III}. The spin–orbit coupling based on atomic mean field

approximation (AMFI)[33] was taken into account using RASSI-SO with the following numbers of multiplets: 7 septets, 110 quintets, 180 triplets and 180 singlets for Tb^{III}, 21 sextets, 128 quartets and 130 doublets for Dy^{III}, 35 quartets and 112 doublets for Er^{III}. The relativistic effects were treated with the Douglas–Kroll Hamiltonian.[34] The following basis sets were employed: Ln·ANO-RCC-VQZP (Ln = Tb, Dy and Er for **1–3**), O·ANO-RCC-VDZP, N·ANO-RCC-VDZP, C·ANO-RCC-VDZ and H·ANO-RCC-VDZ.[35] Then, the SINGLE_ANISO module[36] was used to calculate all relevant information and magnetic data.

Results and discussion

Description of crystal structures

Single-crystal X-ray diffraction analysis (for **1** and **2**) and powder diffraction analysis (for **3**) revealed that all the three compounds are isostructural (Fig. S1†), and crystallize in the tetragonal non-centrosymmetric $P4_1$ space group. The crystallographic data and structure refinements for complexes **1** and **2** are given in Table 1, and the selected bond lengths and angles are listed in Table 2. The asymmetric units of **1** and **2** contain one $[Ln(L)(H_2O)(NO_3)]^{2+}$ complex cation and two nitrate anions. The central Ln^{III} atom is coordinated by the heptadentate ligand (**L**) with the N_5O_2 donor set, which is twisted due to its high flexibility and because the large size of the Ln^{3+} ion does not fit into the small macrocyclic cavity, and by one oxygen atom from the water molecule (O3), and one oxygen atom from the nitrato ligand (O4) (Fig. 1A and S2A†).

Table 1 Crystal data and structure refinements for the complexes **1** and **2**

Compound	**1**	**2**
Formula	$C_{25}H_{33}N_8O_{12}Tb_1$	$C_{25}H_{33}N_8O_{12}Dy_1$
M_r	796.50	800.08
Color	Colorless	Colorless
Crystal system	Tetragonal	Tetragonal
Space group (no.)	$P4_1$ (76)	$P4_1$ (76)
a (Å)	11.4208(4)	11.4177(4)
b (Å)	11.4208(4)	11.4177(4)
c (Å)	22.4435(11)	22.4321(11)
α (°)	90	90
β (°)	90	90
γ (°)	90	90
U (Å^3)	2927.4(3)	2924.3(3)
Z	4	4
λ (Å), Mo Kα	0.71073	0.71073
T (K)	120	120
D_{calc} (g cm^{-3})	1.807	1.817
μ (mm^{-1})	2.494	2.634
F (000)	1600	1604
Reflections collected	125 618	98 029
Independent reflections	6717 [R(int) = 0.0351]	6670 [R(int) = 0.0285]
Data/restraints/parameters	6717, 3, 421	6670, 3, 421
Goodness-of-fit on F^2	1.110	1.126
R_1, wR_2 ($I > 2\sigma(I)$)	0.0127, 0.0311	0.0151, 0.0361
R_1, wR_2 (all data)	0.0138, 0.0315	0.0161, 0.0365
Largest diff. peak and hole, A^{-3}	0.184, −0.632	0.581, −0.768
CCDC number	1487176	1487175
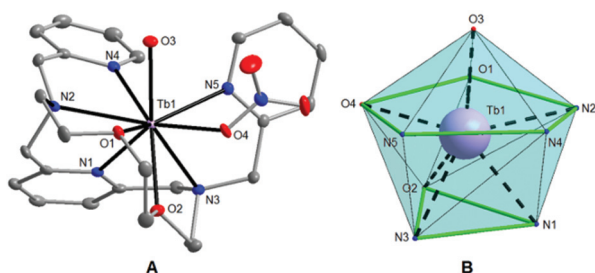
Fig. 1 (A) Molecular structure of the $[Tb(L)(H_2O)(NO_3)]^{2+}$ complex cation in **1**. The thermal ellipsoids are drawn with the 50% probability level. The hydrogen atoms are omitted for clarity. (B) The muffin-like coordination geometry of the $[TbN_5O_4]$ core in **1**.

Table 2 Selected interatomic distances (Å) and angles (°) in complexes **1** and **2**

Distances	1	2
Ln–N1	2.510(2)	2.500(3)
Ln–N2	2.599(2)	2.567(2)
Ln–N3	2.579(2)	2.591(3)
Ln–N4	2.671(2)	2.522(3)
Ln–N5	2.528(2)	2.659(3)
Ln–O1	2.4847(18)	2.489(2)
Ln–O2	2.4961(18)	2.479(2)
Ln–O3	2.3468(19)	2.331(2)
Ln–O4	2.3611(19)	2.348(2)
Angles		
O3–Ln–N1	135.01(7)	135.08(9)
O3–Ln–N2	77.87(7)	146.84(9)
O3–Ln–N3	146.96(8)	77.74(9)
O3–Ln–N4	75.74(7)	81.08(9)
O3–Ln–N5	81.35(7)	75.89(8)
O3–Ln–O1	73.90(6)	132.74(8)
O3–Ln–O2	132.85(6)	73.68(8)
O3–Ln–O4	81.97(7)	81.82(8)

Thus, the coordination number of the Ln^{III} atom in both complexes is nine. The geometries of the coordination polyhedra of lanthanide ions in **1** and **2** were analysed by the program Shape 2.1.[37] The lowest value of deviation was found for a muffin shape (Table S1†), with the basal trigonal plane formed by O2, N1, and N3 atoms in **1** (O1, N1, and N2 in **2**), the equatorial pentagonal plane (O1, O4, N2, N4, and N5 in **1**; O2, O4, N3, N4, and N5 in **2**), and an O3 atom at the vertex of the muffin (Fig. 1B and S2B†).

The Tb–N bond lengths are in the range of 2.510(2) to 2.671(2) Å and Tb–O bonds vary from 2.347(2) to 2.496(2) Å in **1**. The Dy–N bond lengths are in the range of 2.500(3) to 2.659(3) Å, while the Dy–O bonds vary from 2.331(2) to 2.489(2) Å.

Crystal structures of **1** and **2** are stabilized by networks of strong O–H⋯O hydrogen bonds and weak non-covalent C–H⋯O and C–H⋯N interactions. The O–H⋯O hydrogen bonds connect the coordinated water molecules and non-coordinated nitrate anions, with the O⋯O separations of 2.746(3) and 2.660(3) Å for **1**. Selected non-covalent contacts are summarized in Table S2 (ESI†).

Photoluminescence properties

While many lanthanide complexes show interesting luminescence properties, the luminescence spectra of all the complexes **1–3** were measured. In accordance with the literature[38] a reasonable signal was obtained only in the case of complex **1**. Its photoluminescence spectrum in the acetonitrile/methanol mixture ($c = 1 \times 10^{-3}$ mol dm^{-3}) recorded at room temperature exhibited a broad minor peak at 306 nm assignable to the $\pi \rightarrow \pi^*$ transition and intensive peaks with the maxima at 492, 547, 587 and 622 nm, attributable to the $^5D_4 \rightarrow {}^7F_6$, $^5D_4 \rightarrow {}^7F_5$, $^5D_4 \rightarrow {}^7F_4$, and $^5D_4 \rightarrow {}^7F_3$ transitions, which are typically observed in spectra of Tb^{III} complexes.[38] In order to investigate an "antenna effect" of the 2-pyridylmethyl pendant arms in **L**, a comparison of **1** with the Tb^{III} complex with a parent macrocycle 15-pyN$_3$O$_2$[39] without pendant arms was performed. As is

shown in Fig. S3,† complex **1** exhibits a strong characteristic emission in the visible region. This observation is in accordance with the fact that the pyridine moiety is well known for sensing of lanthanide emission.[38,40]

Magnetic properties

Static magnetic properties. The temperature and field dependent static magnetic data were acquired on polycrystalline samples of **1–3** as shown in Fig. 2. The value of μ_{eff}/μ_B at room temperature is 9.68 for **1**, 10.39 for **2**, and 9.16 for **3**, and is close to the expected paramagnetic value of 9.72 (Tb^{III}, $^7F_6$), 10.65 (Dy^{III}, $^6H_{15/2}$), and 9.58 (Er^{III}, $^4I_{13/2}$). There is a gradual decrease of μ_{eff}/μ_B upon cooling the samples to 1.9 K for all compounds **1–3**, which is due to depopulation of ligand field multiplets arising from ground atomic terms effected by spin–orbit coupling and a ligand field of the chromophores. There
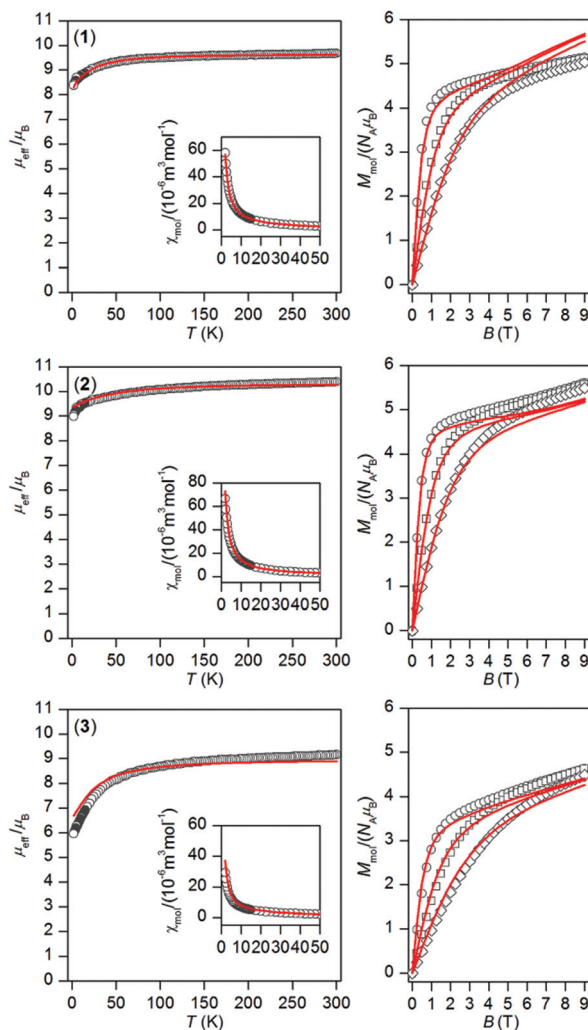
Fig. 2 Magnetic data of complexes **1–3**. Temperature dependence of the effective magnetic moment (left) and the isothermal molar magnetizations measured at 2 (○), 5 (□) and 10 (◇) K (right). The full lines correspond to *ab initio* CASSCF calculations done with MOLCAS/SINGLE_ANISO, and were scaled by the factors: $f = 0.990$ for **1**, $f = 0.947$ for **2** and $f = 0.877$ for **3**.

are no maxima on susceptibility, which excludes the existence of significant intermolecular contacts of the antiferromagnetic nature. The reciprocal susceptibilities were analysed using the Curie–Weiss law in the temperature range of 25–300 K (Fig. S4†), which resulted in $C = 1.49 \times 10^{-4}$ m^3 mol^{-1} K, $\Theta = -4.9$ K and $g = 1.50$ for **1**, $C = 1.73 \times 10^{-4}$ m^3 mol^{-1} K, $\Theta = -7.9$ K and $g = 1.31$ for **2**, $C = 1.38 \times 10^{-4}$ m^3 mol^{-1} K, $\Theta = -16.3$ K and $g = 1.17$ for **3**. All the Weiss constants are of negative values and g-factors are close to theoretical Landé g-factors, i.e. 1.50, 1.33, and 1.20 for Tb^{III}, Dy^{III}, and Er^{III}, respectively. The isothermal magnetization data, $M_{mol}/N_A\mu_B$, measured at $T = 2$ K saturate to 5.1 for **1**, 5.6 for **2** and 4.6 for **3** and these values are well below theoretically predicted values based on J and Landé g-factors, which are 9.0 for Tb^{III}, 10.0 for Dy^{III} and 9.0 for Er^{III}. This points out to large magnetic anisotropy of these complexes.

Dynamic magnetic properties

In order to examine the possible SMM properties of the herein studied coordination compounds **1–3**, the ac susceptibility measurements were performed first in zero and nonzero static magnetic fields as depicted in Fig. S5.† None of the compounds showed a nonzero out-of-phase signal of ac susceptibility at zero static magnetic field, but evidently, a small magnetic field must be applied to observe slow relaxation of magnetization and suppression of the tunneling effect. Therefore, the temperature dependence of ac susceptibility was measured at $B_{DC} = 0.1$ T for frequencies of 1–1500 Hz as shown in Fig. 3. Only in the case of the Dy^{III} compound **2**, we observed clearly maxima of out-of-phase susceptibility dependent of the applied frequency and these data were then analysed with the one-component Debye model

$$\chi(\varpi) = \chi_S + (\chi_T - \chi_S)/|1 + (i\varpi\tau)^{1-\alpha}| \tag{1}$$

which resulted in isothermal (χ_T) and adiabatic (χ_S) susceptibilities, relaxation times (τ) and distribution parameters (α) (Table S3†) and construction of the Argand (Cole–Cole) plot (Fig. S6†). Then, the Arrhenius equation was applied to the temperature dependence of the relaxation times, which resulted in the relaxation time $\tau_0 = 2.63 \times 10^{-8}$ s and the effective magnetization reversal barrier $U = 24.4$ K (16.9 cm^{-1}) – Fig. S6.† The ac susceptibility data for **1** and **3** cannot be analysed with eqn (1) due to the absence of maxima on imaginary susceptibility. Therefore, we used a simplified model[41] according to eqn. (2)

$$\ln(\chi''/\chi') = \ln(2\pi f \tau_0) + U/kT \tag{2}$$

where higher temperature ac data for higher applied frequencies were included as shown in Fig. S7.† The linear regression analysis resulted in sets of parameters listed in Table 3. The variations in the fitted parameters refer to the distributions of relaxation processes, which are reflected in eqn (1) by parameter α. Maximal U were found as $U = 43.5$ K for **1**, $U = 64.1$ K for **2** and $U = 82.2$ K for **3**. In the case of **2**, $U = 64.1$ K is 2.7 times larger than $U = 24.4$ K derived from eqn (1), which can
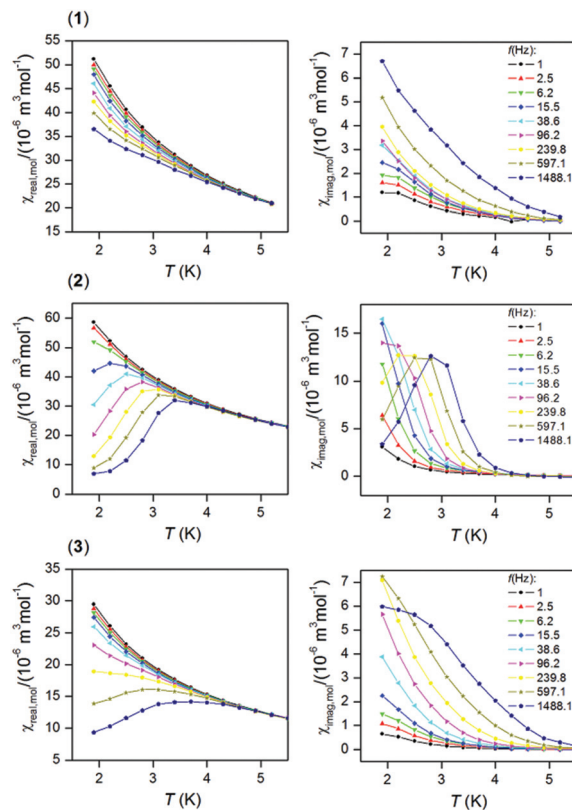

Fig. 3 In-phase χ_{real} (left) and out-of-phase χ_{imag} (right) molar susceptibilities for **1–3** at the applied external field $B_{DC} = 0.1$ T. Lines serve as guides.

Table 3 The parameters resulting from the analysis of ac susceptibility data using eqn (2) for complexes **1–3**

	f (Hz)	1488.1	597.1	239.8	96.2
1 (Tb)	τ_0 (10^{-10} s)	2.33	2.68	20.1	38.6
	U (cm^{-1})	30.2	29.2	23.9	24.0
	U (K)	43.5	42.0	34.4	34.6
2 (Dy)	τ_0 (10^{-10} s)	0.00368	0.0204	17.9	434
	U (cm^{-1})	44.6	39.4	22.0	16.3
	U (K)	64.1	56.7	31.6	23.5
3 (Er)	τ_0 (10^{-10} s)	0.00288	0.340	4.45	58.1
	U (cm^{-1})	57.1	39.3	31.3	23.6
	U (K)	82.2	56.5	45.0	34.0

be explained by the fact that the analysis based on eqn (1) is limited only to ac susceptibility data having maxima in the Argand diagram, which means data measured between $T = 1.9$ and 2.8 K. However, a non-zero out-of-phase ac susceptibility is already observed below 4 K (Fig. 3) and especially high temperature data should correspond to the Orbach relaxation mechanism, thus eqn (2) could lead to a better estimate of the relaxation barrier.

Theoretical calculations

In order to better understand the magnetic properties of these compounds, the CASSCF calculations were performed using

MOLCAS 8.0 together with the SINGLE_ANISO program on complexes [Ln(L)(NO$_3$)(H$_2$O)](NO$_3$)$_2$ **1–3** using geometries following from experimental X-ray data. The resulting wave functions and the energies of the molecular multiplets were used for the calculation of the magnetic properties, g tensors of the lowest Kramers doublet states (Tables S4–S6,† Fig. S8†). In the case of Tb^{III} compound **1**, *a priori* there are no Kramers doublets arising from atomic multiplet $^7F_6$, however, the two lowest energy states are almost degenerate, and treating them as Kramers doublets with $S_{eff} = 1/2$ resulted in $g_z = 16.7$ and $g_x = g_y \approx 0.00$ (Table S4†), which means that there is large axial magnetic anisotropy. In the case of Kramers doublet ions, Dy^{III} and Er^{III}, we were able to construct a scheme of the magnetization blocking barrier as shown in Fig. 4. The values displayed on each arrow are the mean absolute values for the corresponding matrix elements of the transition magnetic moment and for values larger than 0.1 an efficient relaxation mechanism is expected.[9] Evidently, the tunnelling mechanism is probable in both compounds **2** and **3**, and also thermal relaxation through the first excited state. The coefficients are slightly lower in the case of **2**, which probably explains slower relax-

ation of the magnetization in the case of the Dy^{III} compound in spite of the larger U in the Er^{III} compound. The maximal U values extracted from ac susceptibility data with eqn (2), $U = 43.5$ K for **1**, $U = 64.1$ K for **2** and $U = 82.2$ K for **3**, follow the trend from the calculated energies of the first excited state within this series by CASSCF, 33.3 K for **1**, 55.0 K for **2** and 69.0 K for **3** (Tables S4–S6†). Also, the magnetic properties were calculated with the SINGLE_ANISO module, and are compared to the experimental ones in Fig. 2.

Conclusions

In summary, we have successfully prepared three mononuclear lanthanide complexes (Tb^{III} **1**, Dy^{III} **2**, and Er^{III} **3**) with a macrocyclic ligand {(3,12-bis(2-pyridylmethyl)-3,12,18-triaza-6,9-dioxabicyclo-[12.3.1]octadeca-1,14,16-triene; **L**} containing two 2-pyridylmethyl pendant arms, and these complexes were characterized structurally and magnetically. In all the cases, a central lanthanide(III) atom was coordinated by a N$_5$O$_2$-donor set of **L**, but due to the high ligand flexibility, the coordination sphere was completed by one water molecule and one nitrato ligand. Thus, the lanthanide(III) atom revealed a coordination number of nine with the N$_5$O$_4$-donor set, with a muffin-like geometry. The ac susceptibility measurements showed that all three compounds behave as field-induced single-molecule magnets with the estimated energy barriers $U \approx 44$–82 K. The CASSCF calculations analysed with the SINGLE_ANISO module were helpful in understanding this behaviour, and the reasons for that are as follows: (i) the same increasing trend (Tb → Dy → Er) for the first excited state energy gap was found as resulted from the analysis of ac susceptibility; (ii) the lowest transition probabilities for the relaxation of the magnetization were found for **2**, for which several maxima out-of-phase ac susceptibilities were already observed; (iii) a relatively small energy splitting and large non-colinearity of the easy axes explain why this series of SMMs shows fast relaxation of magnetization. To summarize, the herein reported compounds **1–3** are the first lanthanide-based SMMs comprising a 2-pyridyl-methyl pendant-armed macrocyclic ligand. Nevertheless, the herein reported 15-membered macrocyclic ligand **L** was proved to be prospective for the synthesis of magnetically interesting coordination compounds, and the investigation of alternative arm-groups is underway.
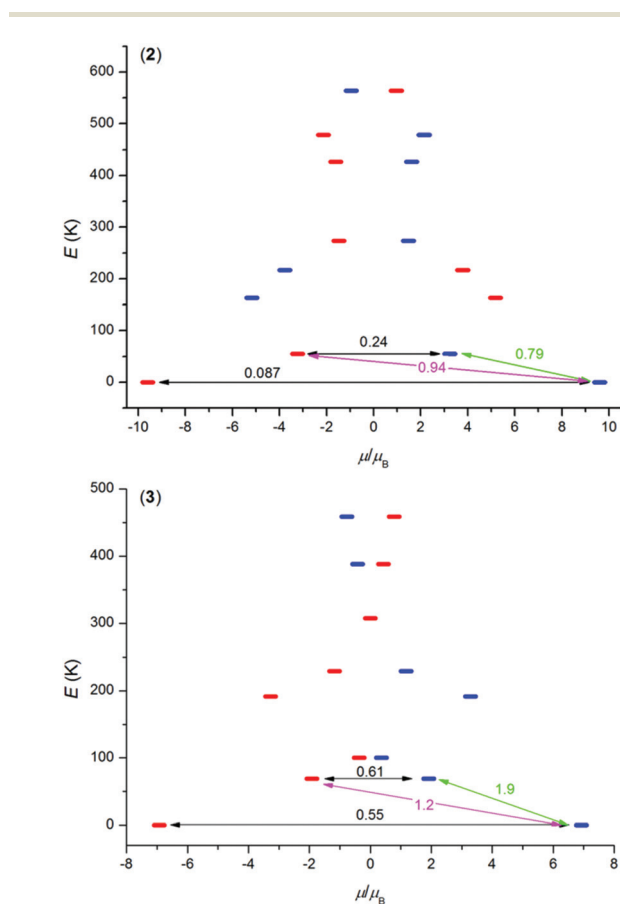
Acknowledgements

Fig. 4 The *ab initio* computed magnetization blocking barrier for complexes **2** and **3**. The thick blue/red bars indicate the Kramer's doublets (KDs) as a function of magnetic moment. Green lines indicate the magnetization reversal mechanism. The magenta lines show the possible pathway of the Orbach process. The black lines represent the presence of QTM/TA-QTM between the connecting pairs.

Notes and references

1 S. Cotton, *Lanthanide and Actinide Chemistry*, Wiley, Chippenham, 2006.

2 (a) A. De Bettencourt-Dias, *Luminescence of Lanthanide Ions in Coordination Compounds and Nanomaterials*, John Wiley & Sons, Chichester, United Kingdom, 2014; (b) P. Vaněk, P. Lubal, P. Hermann and P. Anzenbacher Jr., *J. Fluoresc.*, 2013, **23**, 57–69.

3 (a) A. Merbach, L. Helm and É. Tóth, *The Chemistry of Contrast Agents in Medicinal Magnetic Resonance Imaging*, John Wiley & Sons, Chichester, United Kingdom, 2013; (b) A. J. Amoroso and S. J. A. Pope, *Chem. Soc. Rev.*, 2015, **44**, 4723–4742.

4 (a) R. D. Teo, J. Termini and H. B. Gray, *J. Med. Chem.*, 2016, **59**, 6012–6024; (b) A. Majkowska and A. Bilewicz, *J. Inorg. Biochem.*, 2011, **105**, 313–320.

5 T. W. Speer, *Targeted Radionuclide Therapy*, Lippincott Williams & Wilkins, Philadelphia, USA, 2010.

6 (a) K. Binnemans, Y. G. Galyametdinov, R. Van Deun, D. W. Bruce, S. R. Collinson, A. P. Polishchuk, I. Bikchantaev, W. Haase, A. V. Prosvirin, L. Tinchurina, I. Litvinov, A. Gubajdullin, A. Rakhmatullin, K. Uytterhoeven and L. Van Meervelt, *J. Am. Chem. Soc.*, 2000, **122**, 4335–4344; (b) Ch. Lu, S. Das, N. Siraj, P. K. S. Magut, M. Li and I. Warner, *J. Phys. Chem. A*, 2015, **119**, 4780–4786.

7 (a) H. L. C. Feltham and S. Brooker, *Coord. Chem. Rev.*, 2014, **276**, 1–33.

8 (a) J. Tang and P. Zhang, *Lanthanide Single Molecule Magnets*, Springer, Berlin, Germany, 2015; (b) C. Benelli and D. Gatteschi, *Introduction to Molecular Magnetism*, Wiley-VCH, Weinheim, Germany, 2015; (c) R. A. Layfield and M. Murugesu, *Lanthanides and Actinides in Molecular Magnetism*, Wiley-VCH, Weinheim, Germany, 2015.

9 S. Gómez-Coca, D. Aravena, R. Morales and E. Ruiz, *Coord. Chem. Rev.*, 2015, **289**, 379–392.

10 A. K. Bar, C. Pichon and J.-P. Sutter, *Coord. Chem. Rev.*, 2016, **308**, 346–380.

11 J. M. Frost, K. L. M. Harriman and M. Murugesu, *Chem. Sci.*, 2016, **7**, 2470–2491.

12 A. Dei and D. Gatteschi, *Angew. Chem., Int. Ed.*, 2011, **50**, 11852–11858.

13 S.-Y. Lin, C. Wang, L. Zhao, J. Wu and J. Tang, *Dalton Trans.*, 2015, **44**, 223–229.

14 R. Vincent, S. Klyatskaya, M. Ruben, W. Wernsdorfer and F. Balestro, *Nature*, 2012, **488**, 357–360.

15 (a) S. Takamatsu and N. Ishikawa, *Polyhedron*, 2007, **26**, 1859–1862; (b) H. Wang, B.-W. Wang, Y. Bian, S. Gao and J. Jiang, *Coord. Chem. Rev.*, 2016, **306**, 195–216.

16 (a) M.-X. Yao, Z. Qi, F. Gao, Y.-Z. Li, Y. Song and J.-L. Zuo, *Dalton Trans.*, 2012, **41**, 13682–13690; (b) H. L. C. Feltham, F. Klöwer, S. A. Cameron, D. S. Larsen, Y. Lan, M. Tropiano, S. Faulkner, A. K. Powell and S. Brooker, *Dalton Trans.*, 2011, **40**, 11425–11432.

17 (a) N. F. Chilton, S. K. Langley, B. Moubaraki, A. Soncini, S. R. Batten and K. S. Murray, *Chem. Sci.*, 2013, **4**, 1719–1730; (b) G.-J. Chen, Y.-N. Guo, J.-L. Tian, J. Tang, W. Gu, X. Liu, S.-P. Yan, P. Cheng and D.-Z. Liao, *Chem. – Eur. J.*, 2012, **18**, 2484–2487.

18 (a) M. A. AlDamen, J. M. Clemente-Juan, E. Coronado, C. Martí-Gastaldo and A. Gaita-Ariño, *J. Am. Chem. Soc.*, 2008, **130**, 8874–8875; (b) M. A. AlDamen, S. Cardona-Serra, J. M. Clemente-Juan, E. Coronado, A. Gaita- Ariño, C. Martí-Gastaldo, F. Luis and O. Montero, *Inorg. Chem.*, 2009, **48**, 3467–3479.

19 L. S. Natrajan, N. M. Khoabane, B. L. Dadds, C. A. Muryn, R. G. Pritchard, S. L. Heath, A. M. Kenwright, I. Kuprov and S. Faulkner, *Inorg. Chem.*, 2010, **49**, 7700–7709.

20 J. J. Wilson, E. R. Birnbaum, E. R. Batista, R. L. Martin and K. D. John, *Inorg. Chem.*, 2015, **54**, 97–109.

21 M. del, C. Fernández-Fernández, R. Bastida, A. Macías, P. Pérez-Lourido, C. Platas-Iglesias and L. Valencia, *Inorg. Chem.*, 2006, **45**, 4484–4496.

22 K. V. Damu, M. S. Shaikjee, J. P. Michael, A. S. Howard and R. D. Hancock, *Inorg. Chem.*, 1986, **25**, 3879–3883.

23 J. Liu, Y.-C. Chen, J.-L. Liu, V. Vieru, L. Ungur, J.-H. Jia, L. F. Chibotaru, Y. Lan, W. Wernsdorfer, S. Gao, X.-M. Chen and M.-L. Tong, *J. Am. Chem. Soc.*, 2016, **138**, 5441–5450.

24 V. Patroniak-Krzyminiewska and W. Radecka-Paryzek, *Collect. Czech. Chem. Commun.*, 1998, **63**, 363–370.

25 E. L. Gravey, Y. Beldjoudi, J. M. Rawson, T. C. Stamatatos and M. Pilkington, *Chem. Commun.*, 2014, **50**, 3741–3743.

26 E. L. Gravey and M. Pilkington, *Polyhedron*, 2016, **108**, 122–130.

27 P. Antal, B. Drahoš, R. Herchel and Z. Trávníček, *Inorg. Chem.*, 2016, **55**, 5957–5972.

28 *Bruker. APEX3*, Bruker AXS Inc., Madison, Wisconsin, USA, 2015.

29 G. M. Sheldrick, *Acta Crystallogr., Sect. C: Cryst. Struct. Commun.*, 2015, **71**, 3–8.

30 K. Brandenburg, *DIAMOND, Release 3.2k*, Crystal Impact GbR, Bonn, Germany, 2004.

31 (a) F. Aquilante, L. De Vico, N. Ferré, G. Ghigo, P. Å. Malmqvist, P. Neogrády, T. B. Pedersen, M. Pitoňák, M. Reiher, B. O. Roos, L. Serrano-Andrés, M. Urban, V. Veryazov and R. Lindh, *J. Comput. Chem.*, 2010, **31**, 224–247; (b) J. A. Duncan, *J. Am. Chem. Soc.*, 2009, **131**, 2416; (c) G. Karlström, R. Lindh, P. Å. Malmqvist, B. O. Roos, U. Ryde, V. Veryazov, P.-O. Widmark, M. Cossi, B. Schimmelpfennig, P. Neogrády and L. Seijo, *Comput. Mater. Sci.*, 2003, **28**, 222–239; (d) V. Veryazov, P.-O. Widmark, L. Serrano-Andres, R. Lindh and B. O. Roos, *Int. J. Quantum Chem.*, 2004, **100**, 626–635.

32 P. Å. Malmqvist, B. O. Roos and B. Schimmelpfennig, *Chem. Phys. Lett.*, 2002, **357**, 230–240.

33 (a) B. A. Hess, C. M. Marian, U. Wahlgren and O. Gropen, *Chem. Phys. Lett.*, 1996, **251**, 365–371; (b) B. Schimmelpfennig, *AMFI, an atomic mean-field spin-orbit integral program*, Stockholm University, 1996.

34 (a) N. Douglas and N. M. Kroll, *Ann. Phys.*, 1974, **82**, 89–155; (b) B. A. Hess, *Phys. Rev. A*, 1986, **33**, 3742–3748.

35 (a) B. O. Roos, R. Lindh, P. Å. Malmqvist, V. Veryazov and P.-O. Widmark, *J. Phys. Chem. A*, 2008, **112**, 11431–11435;

(*b*) B. O. Roos, R. Lindh, P. Å. Malmqvist, V. Veryazov and P.-O. Widmark, *Chem. Phys. Lett.*, 2005, **409**, 295–299.

36 (*a*) L. F. Chibotaru, L. Ungur and A. Soncini, *Angew. Chem., Int. Ed.*, 2008, **47**, 4126–4129; (*b*) L. F. Chibotaru, L. Ungur, C. Aronica, H. Elmoll, G. Pillet and D. Luneau, *J. Am. Chem. Soc.*, 2008, **130**, 12445–12455; (*c*) L. F. Chibotaru and L. Ungur, *J. Chem. Phys.*, 2012, **137**, 064112; (*d*) L. Ungur, M. Thewissen, J.-P. Costes, W. Wernsdorfer and L. F. Chibotaru, *Inorg. Chem.*, 2013, **52**, 6328–6337.

37 (*a*) M. Llunell, D. Casanova, J. Cicera, P. Alemany and S. Alvarez, *SHAPE, Version 2.1*, Barcelona, Spain, 2013; (*b*) S. Alvarez, *Dalton Trans.*, 2005, 2209–2233; (*c*) D. Casanova, P. Alemany, J. M. Bofill and S. Alvarez, *Chem. – Eur. J.*, 2003, **9**, 1281–1295; (*d*) A. Ruiz-Martínez, D. Casanova and S. Alvarez, *Chem. – Eur. J.*, 2008, **14**, 1291–1303; (*e*) A. Ruiz-Martínez, D. Casanova and S. Alvarez, *Dalton Trans.*, 2008, 2583–2591.

38 (*a*) M. Sobieray, J. Gode, C. Seidel, M. Poß, C. Feldmann and U. Ruschewitz, *Dalton Trans.*, 2015, **44**, 6249–6259; (*b*) T. Güden-Silber, K. Klein and M. Seitz, *Dalton Trans.*,

2013, **42**, 13882–13888; (*c*) S. V. Eliseeva, D. N. Pleshkov, K. A. Lyssenko, L. S. Lepnev, J.-C. G. Bünzli and N. Kuzmina, *Inorg. Chem.*, 2011, **50**, 5137–5144; (*d*) S. Pandya, J. Yu and D. Parker, *Dalton Trans.*, 2006, 2757–2766; (*e*) A. de Bettencourt-Dias, P. S. Barber and S. Viswanthan, *Coord. Chem. Rev.*, 2014, **273–274**, 165–200.

39 B. Drahoš, J. Kotek, P. Hermann, I. Lukeš and É. Tóth, *Inorg. Chem.*, 2010, **49**, 3224–3238.

40 (*a*) L. Pellegatti, J. Zhang, B. Drahoš, S. Villette, F. Suzenet, G. Guillaumet, S. Petoud and É. Tóth, *Chem. Commun.*, 2008, 6591–6593; (*b*) C. S. Bonnet, F. Buron, F. Caillé, C. M. Shade, B. Drahoš, L. Pellegatti, J. Zhang, S. Villette, L. Helm, C. Pichon, F. Suzenet, S. Petoud and É. Tóth, *Chem. – Eur. J.*, 2012, **18**, 1419–1431.

41 (*a*) J. Bartolomé, G. Filoti, V. Kuncser, G. Schinteie, V. Mereacre, C. E. Anson, A. K. Powell, D. Prodius and C. Turta, *Phys. Rev. B: Condens. Matter*, 2009, **80**, 014430; (*b*) R. Ishikawa, R. Miyamoto, H. Nojiri, B. K. Breedlove and M. Yamashita, *Inorg. Chem.*, 2013, **52**, 8300–8302.

Příloha P9

B. Drahoš, Z. Trávníček,
Spin crossover Fe(II) complexes of a cross-bridged cyclam derivative.
Dalton Trans. **2018**, *47*, 6134–6145.

PAPER

Spin crossover Fe(ɪɪ) complexes of a cross-bridged cyclam derivative†

Bohuslav Drahoš ⓘD and Zdeněk Trávníček ⓘD *

A cross-bridged cyclam derivative containing two 2-pyridylmethyl pendant arms (**L** = 4,11-bis((pyridin-2-yl)methyl)-1,4,8,11-tetraaza-bicyclo[6.6.2]hexadecane) was synthesized by dialkylation of the cross-bridged cyclam with 2-chloromethylpyridine. A series of Fe(ɪɪ) complexes with **L** and different counter-anions of the formulas $[Fe(L)][FeCl_4] \cdot H_2O$ (**1**·H_2O), $[Fe(L)]Cl_2 \cdot 4H_2O$ (**2**·$4H_2O$), $[Fe(L)](BF_4)_2 \cdot 0.5CH_3CN$ (**3**·$0.5CH_3CN$) and $[Fe(L)](BPh_4)_2 \cdot CH_3OH$ (**4**·CH_3OH) was prepared and thoroughly characterized. In all the cases, the $[Fe(L)]^{2+}$ cation adopts a *cis*-V configuration with a distorted octahedral geometry, and with the FeN_6 donor set. The magnetic measurements within the temperature interval of 5–400 K revealed the spin crossover (SCO) behaviour of all the complexes with the transition temperature $T_{1/2}$ increasing with the counter anion in the order BF_4^- (**3**) < $[FeCl_4]^{2-}$ (**1**) < BPh_4^- (**4**). However, the SCO process was complete in the case of compound **3** only, with $T_{1/2}$ = 177 K, which proceeded after removal of co-crystallized CH_3CN molecules accompanied by a change of the crystallographic phase. The SCO behaviour of **3** was also confirmed by a single crystal X-ray analysis providing the average ⟨Fe–N⟩ distances of 2.086 Å at 120 K and 2.197 Å at 293 K typical of low-spin, and high-spin Fe^{II} complexes, respectively. The obtained results clearly showed that the nature of the counter anion and the presence/absence of co-crystallized solvent molecule(s) significantly affected the temperature as well as the abruptness of the spin transition. This is the first report of SCO behaviour observed for iron complexes containing a cross-bridged cyclam derivative.

Department of Inorganic Chemistry, Regional Centre of Advanced Technologies and Materials, Faculty of Science, Palacký University, 17. listopadu 12, CZ-771 46 Olomouc, Czech Republic. E-mail: zdenek.travnicek@upol.cz; Fax: +420 585 634 954 ; Tel: +420 585 634 352

Introduction

The structural motif of 12- and 14-membered tetraazamacrocycles called cyclen (1,4,7,10-tetrazacyclododecane) and cyclam (1,4,8,11-tetraazacyclotetradecane), respectively, is very well-known and transition metals as well as lanthanide complexes containing the derivatives of the above-mentioned ligands have found many different applications.[1–4] On the other hand, the reinforced modifications of cyclen and cyclam with ethylene-bridged adjacent (side-bridged) and opposite (cross-bridged) nitrogen atoms known since 1980s and 1990s,[5] respectively, are not so common in comparison with the parent macrocycles.[6] Many of these derivatives and their complexes have been investigated since that time.[4,7,8] Nevertheless,

due to their various properties and application potential as oxidation catalysts,[9,10] rapid $^{64}Cu/^{67}Cu$ chelators important for positron emission tomography (PET) imaging/radiotherapy,[11–14] contrast agents for magnetic resonance imaging (MRI),[15–17] or biologically active species,[18,19] are still in focus. Among these classes of compounds, our attention is mainly focused on the ethylene cross-bridged cyclam (EBC) and ethylene cross-bridged cyclen (EBCN, Fig. 1) derivatives with pendant arm(s) containing pyridine moiety(s). These derivatives are shown in Fig. 1 (py_2-EBCN,[20] Me,Py-EBC,[21] pic-EBC,[14] pic_2-EBC,[22] and also unbridged Py_2–CN^{20} and Py_2–$C^{23,24}$). Surprisingly, the disubstituted Py_2-EBC derivative has not been prepared and studied yet.

Two synthetic strategies were employed for the preparation of the above-mentioned pyridine-derivatives of EBC or EBCN. The first approach is based on alkylation of the protected macrocycle in the form of bis-aminal **A** (Fig. 2)[5,25,26] providing the *exo*-monoalkylated quaternary ammonium salt **B**[27] in non-polar solvents (*e.g.* toluene). In polar solvents (*e.g.* acetonitrile), a highly regioselective second alkylation[28] provides the dialkylated bis(ammonium) salt **C**. The consequent synthetic step is a double-ring expansion using reduction with $NaBH_4$ in ethanol in order to obtain the cross-bridged macrocycles[12] or
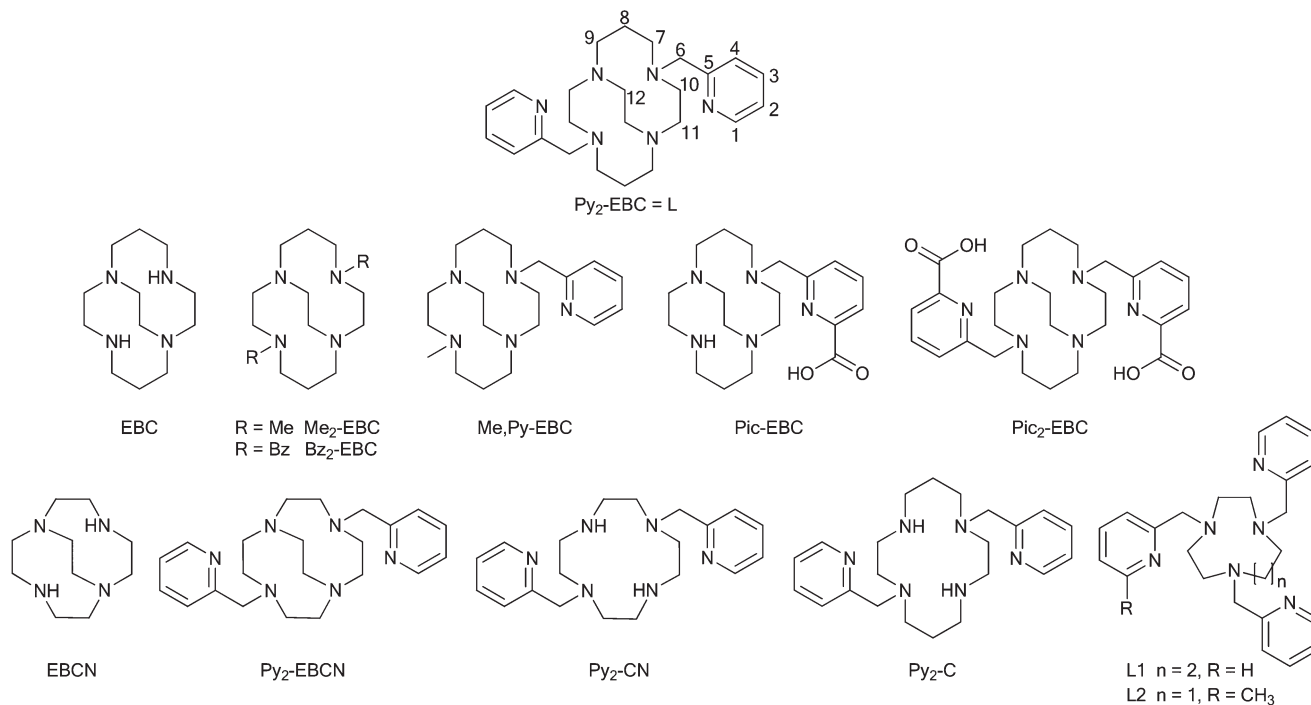
Fig. 1 Structural formulas of the prepared ligand **L** with the atom numbering together with structurally similar ligands studied previously and discussed in the text.
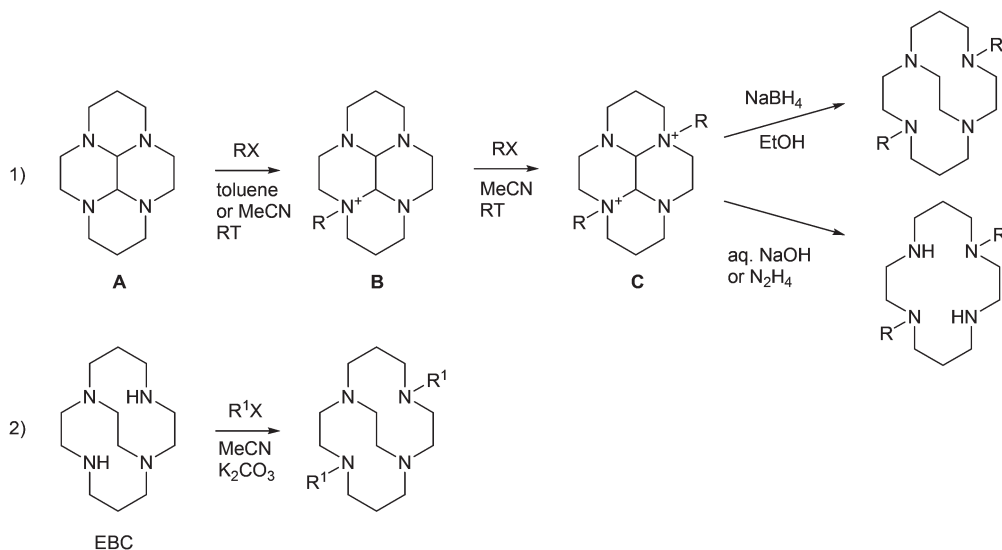
Fig. 2 The two most common synthetic strategies for the preparation of EBC derivatives (particular experimental conditions can be varied depending on the substituent R). RX can be MeI, BzBr or PyCH$_2$Cl. R^{1}X can be BrCH$_2$COOEt, ClCH$_2$CONH$_2$, ClCH$_2$PyCOOMe, etc.[20,28]

complete deprotection using aqueous NaOH solution,[28] hydrazine hydrate,[27] hydroxylamine or ethylenediamine[29] to produce unbridged macrocycles.

The second synthetic approach is based on a direct substitution of the secondary amino groups in EBC usually using 2 equivalents of alkylating agent and excess of a base in acetonitrile.[12,14] This approach is suitable for the modification of EBC with pendant arms containing various functional groups

in those cases when either the formation of **C** is slow and accompanied by undesirable side reactions or NaBH$_4$ reduction could change/modify the functional group in the pendant arm.[12,14,22] Particularly, for the preparation of the above-mentioned pyridine or picolinate derivatives, synthetically more available alkyl chlorides (e.g. 2-chloromethyl-pyridine/2-picolyl chloride[30] or methyl(6-chloromethyl-pyridine)-2-carboxylate/methyl 6-(chloromethyl)picolinate)[31]

were employed and in this case, KI or NaI was added in order to increase the low reactivity of alkyl chlorides toward S_N2 substitution.[21,24]

Both categories of EBC and EBCN derivatives have a very strong ability to bind one proton or small cations (such as Li^+), which is a result of the ligand conformation with all four nitrogen lone electron pairs convergent on a cavity for the complexation of metal ions. Due to this fact, very high values of pK_1, usually higher than 12, are observed.[5] Therefore, these ligands are often called "proton sponges" and only some metals (Co^{II}, Ni^{II}, Cu^{II} or Zn^{II}) are capable of forming the complexes with these ligands in their protonated forms (i.e. they are able to substitute the proton from the macrocyclic cavity), whereas the complexes of other metals ($Mn^{II/III}$, $Fe^{II/III}$) have to be prepared by using deprotonated ligands under strictly dry/inert conditions.

In the beginning, it was Weisman and co-workers who started to investigate EBC and its derivatives Me_2-EBC[5] and Bz_2-EBC[25] (Fig. 1). Hubin et al. continued the systematic study of these ligands and revealed the cis-V configuration (in the Bosnich–Tobe nomenclature, Fig. 3)[32] for their complexes with $Mn^{II/III/IV}$ and $Fe^{II/III}$ (with two chlorido,[33–36] aqua or hydroxido co-ligands),[37] and that the complexed metals (Mn^{II} and Fe^{II})[34] remained in the high-spin (HS) state throughout the temperature range. On the other hand, the coordination number of 5 was found for Cu^{II} complexes.[25]

Some attention was also devoted to Py_2-EBCN whose coordination ability towards Co^{II}, Cu^{II} and Zn^{II} was studied and compared with the unbridged analogue Py_2–CN.[20] Tripier et al. systematically studied different macrocycles with picolinate pendant arm(s) including Pic-EBC[14] and Pic_2-EBC[22] in complexes with Cu^{II}[14] and lanthanides(III),[22] respectively.

The newest ligand prepared is Me,Py-EBC. The redox behaviour together with the testing of catalytic oxidation properties of its Mn^{II}, Fe^{II}, Co^{II}, Ni^{II} and Cu^{II} complexes was studied recently.[21] The coordination number of 6 with the cis-V configuration (Fig. 3) was observed for all the complexes; one coordination position was occupied by the chlorido ligand.[21] For the Cu^{II} complex, the coordination number of 5 was found.[21]

On the other hand, unbridged Py_2–C represents an interesting pyridine-based derivative, mentioned mainly because of comparison with its bridged analogue. Surprisingly, its Fe^{II}

Fig. 3 Illustration of cis-V configuration, one of the six possible configurations for metal complexes with cyclam.

complex $[Fe(Py_2–C)](BF_4)_2 \cdot H_2O$ showed the spin transition between the low-spin state (LS, $S = 0$) and the high-spin state (HS, $S = 2$), so called spin crossover (SCO) which can be induced by different external constraints (in general e.g. by temperature, pressure or light), with the critical temperature of the spin transition ($T_{1/2}$ defined as the temperature when the fraction of the complex in the HS state is equal to that in the LS state) around 150 K (ref. 24) in this case, whereas the analogous Fe^{II} complex of Py_2–CN remained in the HS state over the whole temperature range.[24] More recently, $[Fe(Py_2–C)]$ $(C(CN)_3)_2 \cdot 2H_2O$ with $T_{1/2}\downarrow/T_{1/2}\uparrow = 136/145$ K and $[Fe(Py_2–C)][Ni(CN)_4]\cdot H_2O$ with $T_{1/2}\downarrow\uparrow = 85$ K have been described together with the modulation of $T_{1/2}$ by the presence/absence of crystal water molecules.[38] On the other hand, there are only few examples of SCO Fe(II) complexes with other macrocyclic N6 ligands. The Fe(II) complex of L1 (Fig. 1) showed SCO with $T_{1/2}$ of 282 K in propionitrile solution while $[Fe(L2)](ClO_4)_2$ (Fig. 1) showed SCO in the solid state with $T_{1/2}$ of 380 K.[39]

The critical temperature $T_{1/2}$ as well as the abruptness of the spin transition are strongly dependent on many parameters (e.g. counter ions, crystal solvent molecules, types of non-covalent contacts between the molecules and the crystal packing in general) and finding the relation how these parameters influence SCO in order to rationally design/tune new advanced SCO materials is still in a strong interest of many chemists and magnetochemists. Recently, it has been demonstrated on several Fe(II) systems that the spin transition and even its occurrence can be significantly influenced by transformation between the polymorphs[40] or can be induced by loss of crystal solvent molecule(s), i.e. transformation between the solvatomorphs.[41–44]

In this paper, the synthesis of Py_2-EBC (**L**), the last in the series of pyridine-based EBC derivatives, is described and the two above-mentioned common synthetic approaches, which have been used for its preparation, are compared and discussed in detail. The synthesis of its Fe^{II} complexes with different anions is reported together with their thorough characterization including description of their molecular and crystal structures determined using a single crystal X-ray analysis. The magnetic properties, namely the SCO behaviour of the complexes with respect to the particular counter anion and the solvatomorphism, are also discussed. Moreover, a comparison with the Fe^{II} complex of an analogous unbridged ligand Py_2–C is given in order to elucidate the effect of the cross-bridge on the SCO behaviour.
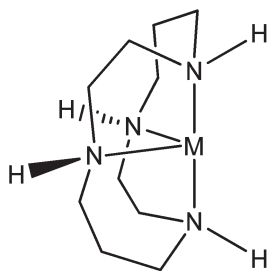
Experimental

2-Chloromethylpyridine hydrochloride[30] and EBC[27,28] were prepared according to the literature procedures. Dry CH_3CN was prepared by distillation using P_2O_5 under argon, whilst dry DMF was prepared by distillation using BaO under argon.[45] All other chemicals (Across Organics, Geel, Belgium and Sigma Aldrich, St. Louis, MO, USA) and solvents (Penta, Prague, Czech Republic) were purchased from commercial

sources and used as received. The stability of the anhydrous $FeCl_2$ towards oxidation was provided by a negative test on Prussian blue formation.

4,11-Bis((pyridin-2-yl)methyl)-1,4,8,11-tetraaza-bicyclo[6.6.2] hexadecane (Py$_2$-EBC = L)

2-Chloromethylpyridine hydrochloride (1.44 g, 8.8 mmol, 2 equiv.) and anhydrous K_2CO_3 (3.50 g, 25.4 mmol, 6 equiv.) were suspended in 50 ml of CH_3CN and heated to 70 °C for 10 minutes. EBC (1.00 g, 4.4 mmol, 1 equiv.) was dissolved in 20 ml of hot CH_3CN and it was added to the hot suspension prepared in the previous step. The red colour of the mixture changed to yellow in several minutes and the reaction mixture was refluxed overnight. The progress of the reaction was monitored by mass spectrometry (MS); an additional amount of 2-chloromethylpyridine hydrochloride (0.14 g, 0.8 mmol, 0.1 equiv.) was added until no peak of unsubstituted as well as monosubstituted EBC was detected in the mass spectrum. The obtained mixture was filtered on a glass frit, washed with 10 ml of CH_3CN and the volume of the filtrate was reduced to 1/3 under reduced pressure. The product was obtained upon cooling of this hot solution in the form of colourless crystals, which were filtered on a glass frit, washed with a small amount of cold CH_3CN, diethyl ether (Et_2O) and dried in air. The product was isolated in a form of colourless crystals (1.28 g, yield 70.7%).

MS m/z (+): 409.36 $[L + H]^+$.

Anal. calcd (%) for $C_{24}H_{36}N_6$: C, 70.55; H, 8.88; N, 20.57. Found C, 70.42; H, 8.70; N, 20.95.

^1H NMR ($CDCl_3$): δ 1.32–1.42 (H8, m, 2H), 1.49–1.58 (H8, m, 2H), 2.27–2.38 (H9 + H11, m, 4H), 2.42–2.50 (H7 + H10 + H11 + H12, m, 10H), 2.79 (H9, ddd, 2H, J_{HH} = 13.0, 10.7, 4.1 Hz), 3.11–3.20 (H12, m, 2H), 3.44 and 3.84 (H6, AX, 4H, $^2J_{HH}$ = 14.5 Hz), 3.97 (H7, ddd, 2H, J_{HH} = 12.4, 10.5, 4.5 Hz), 7.10 (H2, m, 1H), 7.46 (H4, d, 1H, $^3J_{HH}$ = 7.6 Hz), 7.62 (H3, td, 1H, $^3J_{HH}$ = 7.6, 2.0 Hz), 8.47 (H1, m, 1H).

$^{13}C\{^1H\}$ NMR ($CDCl_3$): δ 27.8 (C8), 52.1 (C9), 54.0 (C7), 56.5 (C12), 57.4 (C10), 57.6 (C11), 61.8 (C6), 121.6 (C2), 123.0(C4), 136.1 (C3), 148.8 (C1), 161.1 (C5).

[Fe(L)][FeCl$_4$]·H$_2$O (1·H$_2$O)

L (100 mg, 0.24 mmol) and anhydrous $FeCl_2$ (62 mg, 0.49 mmol, 2 equiv.) were suspended in 5 ml of dry CH_3CN under an argon atmosphere. The obtained suspension was stirred at room temperature overnight and a yellow fine precipitate formed. The solid was filtered on a glass frit, washed with 2 ml of CH_3CN, 5 ml of Et_2O and dried in air. The product was obtained in the form of yellow powder (140 mg, yield 83.9%).

MS m/z (+): 232.33 $[Fe(L)]^{2+}$, 499.27 $[Fe(L) + Cl^-]^+$.

Anal. calcd (%) for [Fe(L)][FeCl$_4$]·H$_2$O ($C_{24}H_{38}Cl_4Fe_2N_6O$): C, 42.38; H, 5.63; N, 12.36. Found C, 42.72; H, 5.53; N, 12.57.

[Fe(L)]Cl$_2$·4H$_2$O (2·4H$_2$O)

L (100 mg, 0.24 mmol) and anhydrous $FeCl_2$ (38 mg, 0.30 mmol, 1.2 equiv.) were suspended in 2.5 ml of dry DMF

under an argon atmosphere. The obtained suspension was stirred at 150 °C for 1 h while the colour changed to yellow and most of the solid dissolved. In order to redissolve the remaining solid, 2.5 ml of CH_3CN and 2.5 ml of CH_3OH were added. The obtained mixture was left to cool down to room temperature and the small amount of yellow precipitate was filtered off. 40 ml of Et_2O was added to the filtrate and a brown oily solid formed. The solution was poured out and then the brown product was triturated with additional 10 ml of Et_2O. The solid was filtered on a glass frit and left in a vacuum desiccator overnight. The product was obtained in a form of brown–green powder (58 mg, yield 38.9%).

MS m/z (+): 499.27 $[Fe(L) + Cl^-]^+$.

Anal. calcd (%) for [Fe(L)]Cl$_2$·4H$_2$O ($C_{24}H_{44}Cl_2FeN_6O_4$): C, 47.46; H, 7.30; N, 13.84. Found C, 46.97; H, 7.31; N, 13.61.

[Fe(L)](BF$_4$)$_2$·0.5CH$_3$CN (3·0.5CH$_3$CN)

L (50 mg, 0.12 mmol), anhydrous $FeCl_2$ (20 mg, 0.16 mmol, 1.3 equiv.) and $NaBF_4$ (34 mg, 0.31 mmol, 2.5 equiv.) were suspended in 5 ml of dry CH_3CN under an argon atmosphere. The obtained suspension was heated to 60 °C for 10 minutes and then stirred overnight at room temperature. The yellow/dark green precipitate was filtered off on a glass frit and the filtrate was allowed to crystallize by diffusion of Et_2O vapours at 5 °C. The product was obtained in the form of dark green block shaped crystals (38 mg, yield 48.7%).

MS m/z (+): 232.29 $[Fe(L)]^{2+}$, 551.33 $[Fe(L) + BF_4^-]^+$.

Anal. calcd (%) for [Fe(L)](BF$_4$)$_2$·0.5CH$_3$CN ($C_{25}H_{37.5}B_2F_8FeN_{6.5}$): C, 45.59; H, 5.74; N, 13.82. Found C, 45.67; H, 6.21; N, 13.66.

[Fe(L)](BPh$_4$)$_2$·CH$_3$OH (4·CH$_3$OH)

L (50 mg, 0.12 mmol) and anhydrous $FeCl_2$ (20 mg, 0.16 mmol, 1.3 equiv.) were suspended in 10 ml of dry CH_3CN under an argon atmosphere and stirred overnight at room temperature. The small amount of orange precipitate was filtered through a Millipore syringe filter (0.45 μm) and a suspension of $NaBPh_4$ (84 mg, 0.25 mmol, 2 equiv.) in the mixture of 2.5 ml CH_3CN and 1 ml of CH_3OH was added to the filtrate. The suspension was stirred at room temperature overnight. The precipitate was filtered through a Millipore syringe filter (0.45 μm) and the filtrate was allowed to crystallize by diffusion of Et_2O vapours at 5 °C. The product was obtained in a form of dark green block shaped crystals (26 mg, yield 18.7%).

MS m/z (+): 783.37 $[Fe(L) + BPh_4^-]^+$.

Anal. calcd (%) for [Fe(L)](BPh$_4$)$_2$·CH$_3$OH ($C_{73}H_{80}B_2FeN_6O$): C, 77.25; H, 7.11; N, 7.40. Found C, 77.70; H, 7.60; N, 7.57.

Physical methods

^1H and ^{13}C NMR spectra were recorded on a 400 MHz NMR spectrometer (Varian, Palo Alto, CA, USA) at 25 °C: ^1H 399.95 MHz, chloroform-d ($CDCl_3$, residual solvent peak) δ = 7.26 ppm, ^{13}C 100.60 MHz, ($CDCl_3$, residual solvent peak) δ = 77.2 ppm. The multiplicity of the signals is indicated as follows: s – singlet, d – doublet, t – triplet, m – multiplet. The deuterated solvent $CDCl_3$ from Sigma Aldrich was used as
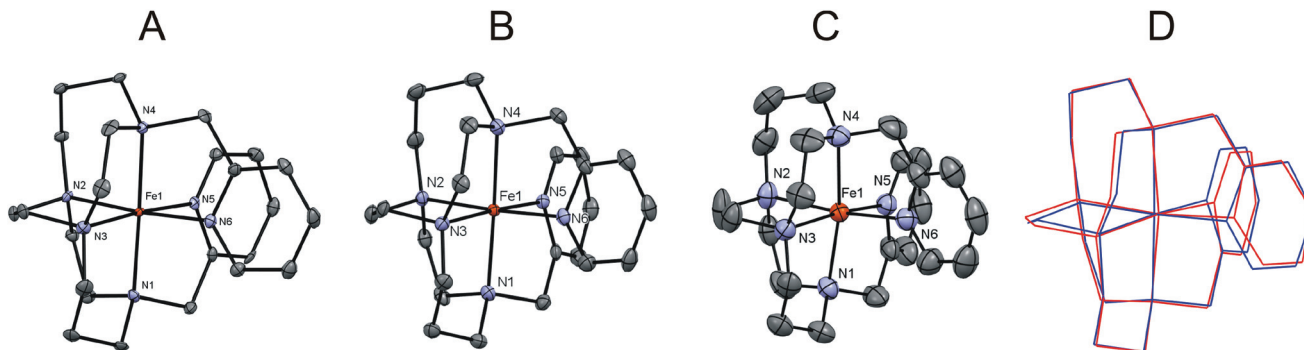
Fig. 4 The molecular structures of the complex cation $[Fe(L)]^{2+}$ in the crystal structure of **2**·1.5H$_2$O (A) and **3** at 120 K (B) and **3** at 293 K (C) together with the overlay of the structures of **3** (D, blue – **3** at 120 K, red – **3** at 293 K, Root Mean Square Deviation (RMSD) was 0.1706 for the overlay). Non-hydrogen atoms are drawn as thermal ellipsoids at the 50% probability level. Hydrogen atoms were omitted for clarity. Only one of the two crystallographically independent molecules found in the asymmetric unit of **2** is shown for clarity.

received. The atom numbering scheme used for NMR data interpretation is shown in Fig. 1. The carbon as well as hydrogen atoms were assigned according to the spectra obtained from two-dimensional correlation experiments ^{1}H–^{1}H gs-COSY, ^{1}H–^{13}C gs-HMQC and ^{1}H–^{13}C gs-HMBS (see Fig. S1–S3 in the ESI†). Elemental analysis (C, H, and N) was performed on a Flash 2000 CHNO-S Analyzer (Thermo Scientific, Waltham, MA, USA). The mass spectra were recorded on an LCQ Fleet ion trap mass spectrometer (Thermo Scientific, Waltham, MA, USA) equipped with an electrospray ion source and a 3D ion-trap detector in the positive mode. Infrared (IR) spectra of the complexes were collected on a Thermo Nicolet NEXUS 670 FT-IR spectrometer (Thermo Nicolet, Waltham, MA, USA) employing the ATR technique on a diamond plate in the range of 400–4000 cm^{-1}. Simultaneous thermogravimetry (TG) and differential scanning calorimetry (DSC) were performed on a TG/DSC analyser STA449 F1 (Netzsch GmbH & Co. KG, Selb, Germany) under a dynamic air atmosphere (100 mL min^{-1}) in the temperature interval of 25–900 °C with the heating rate of 5.0 °C min^{-1}. The magnetic data were measured on powder samples using a PPMS Dynacool system (Quantum Design, San Diego, CA, USA) with the VSM option. The experimental data were corrected for the diamagnetism and signal of the sample holder. The heating/cooling rate was 1 K min^{-1}. The X-ray powder diffraction patterns were recorded with a MiniFlex600 (Rigaku) using Cu Kα radiation (λ = 1.5418 Å).

X-ray diffraction analysis

Single crystals of complexes **2**·1.5H$_2$O and **3**·0.5CH$_3$CN suitable for X-ray diffraction analysis were prepared by a vapour diffusion of Et$_2$O into the MeCN solution of the appropriate complex at 5 °C. Single crystals of **3** were obtained by allowing **3**·0.5CH$_3$CN to stand at room temperature in air. During the recrystallization of **1**·1H$_2$O from CH$_3$CN/CH$_3$OH solution, oxidation of the $[FeCl_4]^{2-}$ anion occurred and single crystals of the complex $[Fe(L)][FeCl_4]_2$ (**1a**) were obtained. The X-ray diffraction data were collected on a Bruker D8 QUEST diffracto-

meter equipped with a PHOTON 100 CMOS detector using Mo–Kα radiation. X-ray diffraction experiments at 120 and 293 K were performed on the same single crystal of complex **3**. The APEX3 software package[46] was used for data collection and reduction. The molecular structures of **1a**, **2**·1.5H$_2$O and **3** were solved by direct methods and refined by the full-matrix least-squares procedure of SHELXL (version 2014/7).[47] Hydrogen atoms of the complexes were found in the difference Fourier maps and refined using a riding model, with C–H = 0.95 (CH)$_{ar}$ and C–H = 0.99 (CH$_2$) Å, and with U_{iso}(H) = 1.2U_{eq}(CH, CH$_2$). The molecular and crystal structures of the studied complexes and the molecular overlay (calculated by using the smallest difference between two sets of atom positions in two molecules characterized by Root Mean Square Deviation (RMSD)) are depicted in Fig. 4, and S8–S12,† respectively, and were drawn using the Mercury software.[48] We also tried to prepare single crystals of **4**·CH$_3$OH suitable for X-ray analysis. Unfortunately, we were able to prepare crystals of only poor quality and although we measured a few of them on the diffractometer, the refinement of the molecular structure was possible only with parameters unacceptable for publication. Therefore, the best structural model obtained is shown in the ESI as Fig. S9† only, from which the composition and the molecular structure of **4** are clearly seen.

Results and discussion

Synthesis and general characterization

Many different types of ethylene-cross-bridged cyclam (EBC) derivatives were synthesized previously,[7,8] but a derivative containing two 2-pyridylmethyl pendant arms (Py$_2$-EBC = **L**) has not been prepared yet, although several structurally similar compounds also containing a pyridine moiety are known, *e.g.* Me, Py-EBC, Pic-EBC, and Pic$_2$-EBC (see Fig. 1). Both synthetic strategies described in Fig. 2 were used during the synthesis of **L**. The first one based on the dialkylated bis(ammonium) salt **C** (Fig. 2, R = CH$_2$Py) was the first choice. 2-Chloromethylpyridine was used as an alkylating agent and

various iodides (NaI, KI, and NBu$_4$I) were added in order to increase the reactivity of 2-chloromethylpyridine toward S$_N$2 substitution. Although the reaction was performed in many types of solvents with different polarities (*i.e.* toluene, CHCl$_3$, CCl$_4$, tetrahydrofurane, acetone, and propylene carbonate) at room or increased temperature, only the monoalkylated product **B** (Fig. 2, R = CH$_2$Py) or an unidentifiable mixture of red-coloured by-products was obtained without any indication of the formation of the desired product **C**. Thus, it can be concluded that the self-alkylation reaction of 2-chloromethyl-pyridine under employed experimental conditions is much faster than the alkylation of the second macrocyclic nitrogen atom and that only the monoalkylated product **B** can be prepared *via* this approach (recently it was successfully used in the synthesis of Me,Py-EBC).[21] Therefore, the second synthetic approach based on the direct alkylation of EBC was used. EBC was prepared according to the previously described literature procedure[12] based on the synthesis of Bz$_2$–EBC according to the approach 1 as shown in Fig. 2 and its consequent debenzylation using N$_2$H$_4$/Pd–C.[49] In this case, the desired product **L** was formed according to the expectation with a good yield of 71% and furthermore, it crystallized from the CH$_3$CN reaction solution, which helped to obtain the ligand in very good purity. The obtained 2D NMR spectra (^{1}H–^{1}H gs-COSY, ^{1}H–^{13}C gs-HMQC and ^{1}H–^{13}C gs-HMBC), which were used for the final signal–atom assignment (Fig. 1), can be found in the ESI in Fig. S1–S3.†

The syntheses of Fe^{II} complexes **1·H$_2$O**, **2·4H$_2$O**, **3·0.5CH$_3$CN** and **4·CH$_3$OH** were done according to the modified literature procedures used for the syntheses of [Fe(Me$_2$-EBC)Cl$_2$],[34] [Fe(Bz$_2$-EBC)Cl$_2$][36] or [Fe(Bz$_2$-EBCN)Cl$_2$][36] under dry conditions and an inert argon atmosphere. Anhydrous FeCl$_2$ was used as a starting material in all the cases and the complete complex formation was checked using mass spectra. When FeCl$_2$ and **L** were directly mixed and reacted in dry CH$_3$CN, the complexation of Fe^{2+} by **L** caused the release of the chlorido ligands, which consequently reacted with free FeCl$_2$ to form the [FeCl$_4$]$^{2-}$ anions, which induced the precipitation of [Fe(**L**)]$^{2+}$ in the form of [Fe(**L**)][FeCl$_4$] (**1**) from the solution. In the case when equimolar amounts of FeCl$_2$ and **L** were used, a free **L** always remained in the reaction mixture because of the above-mentioned Fe^{II}-consuming reaction. Thus, a slight excess of FeCl$_2$ was used together with prolonged heating in a different solvent (DMF) for the preparation of the complex **2·4H$_2$O** with the chloride counter ions, which was capable to better dissolve FeCl$_2$. The chloride counter ions were replaced by BF$_4^-$ and BPh$_4^-$ during the preparation of complexes **3·0.5CH$_3$CN**, and **4·CH$_3$OH**, respectively, by the addition of 2.5 and 2 equivalents of NaBF$_4$ and NaBPh$_4$, respectively, to the FeCl$_2$ and **L** reaction mixture. Direct synthesis of **3** from Fe(BF$_4$)$_2$·6H$_2$O and **L** was unsuccessful even after prolonged reflux in CH$_3$CN.

In order to reveal the thermal stability of the studied complexes, simultaneous TG/DSC measurements were performed under a dynamic air atmosphere and the obtained results are shown in Fig. S4 (ESI†). For each of the compounds, the fol-lowing weight losses, demonstrating solvent molecule elimination, were found: 2.7% (**1·H$_2$O**, 2.6% calcd), 11.6% (**2·4H$_2$O**, 11.9% calcd), 3.1% (**3·0.5CH$_3$CN**, 3.1% calcd) and 2.5% (**4·CH$_3$OH**, 2.8% calcd) occurred in the temperature range of 25–200 °C, which well corresponded to the elimination of the appropriate number of solvent molecules of crystallization. Further thermal decomposition proceeded in several steps without the formation of thermally stable intermediates accompanied by several *exo* effects. The decomposition was finished above 550–600 °C.

The measured IR spectra of the ligand **L** are compared with those of the studied Fe^{II} complexes (see Fig. S5 in the ESI†) and their similar patterns confirm the presence of **L** within the complexes. Broad multiplets at ~2800 and ~2900 cm^{-1} correspond to the CH$_2$ stretching vibrations of **L**, which are shifted to ~2850 and ~2950 cm^{-1} upon the ligand coordination to Fe^{II} in the spectra of all the complexes. The spectra also contain medium bands at ~1430, ~1450, and ~1480 cm^{-1} and a strong sharp peak(s) at 1600 and 1580 cm^{-1} which can be assigned to stretching vibrations of the aromatic C=C and C=N bonds together with CH$_2$ bending vibrations and wagging vibrations of the pyridine ring. Characteristic absorption bands due to the presence of free counter ions were found in the spectra of **3** (a strong broad band at 1035 cm^{-1} and a weak band at 520 cm^{-1} corresponding to BF$_4^-$)[50] and **4·CH$_3$OH** (strong bands at 703, 733 and 749 cm^{-1} corresponding to BPh$_4^-$ and strong bands at ~3000 cm^{-1} of aromatic CH stretching vibrations).[50] A strong broad signal at ~3300 cm^{-1} corresponding to the stretching vibration of the water molecules was observed only for **2·4H$_2$O**, while a weak broad signal was visible in the spectrum of **1·H$_2$O**, which well corresponded to the presence of water of crystallization in these compounds.

Powder X-ray diffraction patterns of all the studied complexes (Fig. S6 and S7 in the ESI†) confirmed good crystallinity for complexes **1·H$_2$O**, **3·CH$_3$CN** and **3** and lower crystallinity for complexes **2·4H$_2$O** and **4·CH$_3$OH**. This fact may affect, among others, the SCO behaviour of the complexes (see later in the section of Magnetic properties).

X-ray analysis

The molecular structures of compounds **2·1.5H$_2$O**, **3** (at 120 K and 293 K) and **1a** (a product of the oxidation of **1·H$_2$O**, *vide infra*) were determined by single crystal X-ray analysis (Fig. 4, Fig. S8–S12 in the ESI†) and the crystal data and structure refinements are listed in Table 1 and Table S1 in the ESI.† The single crystals of **3·0.5CH$_3$CN** were prepared as well, but the solvent molecules were bound very weakly within the crystal structure because their loss occurred slowly also at room temperature and not only above *ca.* 350 K as indicated by the TG curve (see Fig. S4 in the ESI†) and magnetic measurements (see later in the section of Magnetic properties). This process of solvent loss was accompanied by a colour change from dark brown-green to light green, which is shown in Fig. 5 containing the picture of the crystals of **3·0.5CH$_3$CN** during their gradual single-crystal-to-single-crystal (SCSC) transformation (can be followed by naked eye on big crystals).

Table 1 Crystal data and structure refinements for complexes **2**·1.5H$_2$O and **3**

Compound	**2**·1.5H$_2$O	**3**	**3**
Formula	C$_{48}$H$_{78}$Cl$_4$Fe$_2$N$_{12}$O$_3$	C$_{24}$H$_{36}$B$_2$F$_8$FeN$_6$	C$_{24}$H$_{36}$B$_2$F$_8$FeN$_6$
M_r	1124.72	638.06	638.06
Temperature (K)	120(2)	120(2)	293(2)
Wavelength (Å)	0.71073	0.71073	0.71073
Crystal system	Monoclinic	Monoclinic	Monoclinic
Space group	$P2_1/c$	$P2_1/n$	$P21/n$
a (Å)	23.5964(15)	11.072(5)	11.0789(10)
b (Å)	13.0895(9)	11.983(6)	12.0262(11)
c (Å)	17.5179(12)	21.198(11)	21.201(2)
α (°)	90	90	90
β (°)	111.314(2)	102.346(17)	102.212(3)
γ (°)	90	90	90
V, Å^3	5040.6(6)	2747(2)	2760.8(4)
Z	4	4	4
D_{calc}, g cm^{-3}	1.482	1.543	1.535
μ, mm^{-1}	0.843	0.631	0.628
$F(000)$	2376	1320	1320
θ range for data collection (°)	2.325–24.999	2.303–24.217	2.531–24.999
Refl. collected	78 326	33 934	35 819
Independent refl.	8866	4268	4608
R(int)	0.1303	0.0966	0.1771
Data/restrains/parameters	8866/0/650	4268/0/407	4608/0/407
Completeness to θ (%)	99.9	96.6	94.8
Goodness-of-fit on F^2	1.022	1.035	1.040
R_1, wR_2 ($I > 2\sigma(I)$)^a	0.0451, 0.0911	0.0372, 0.0734	0.0569, 0.1310
R_1, wR_2 (all data)^a	0.0747, 0.0986	0.0567, 0.0797	0.1303, 0.1489
Largest diff. peak and hole/A^{-3}	1.341 and −0.658	0.346 and −0.277	0.562 and −0.470
CCDC number	1820712	1820713	1820714

^{a} $R_1 = \sum(|F_o| - |F_c|)/\sum|F_c|$; w$R_2 = [\sum w(F_o^2 - F_c^2)^2/\sum w(F_o^2)^2]^{1/2}$.
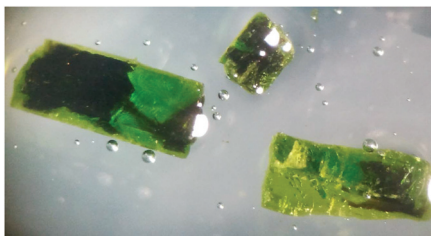

Fig. 5 Photograph of crystals of **3**·0.5CH$_3$CN (dark brown-green = solvatomorph I, in the LS state) during their transformation to **3** (light green = solvatomorph II, in the HS state) induced by the loss of crystal solvent molecules.

Furthermore, this solvent loss was accompanied by a change of the crystallographic phase, which was confirmed by a different X-ray powder diffraction pattern of freshly prepared **3**·0.5CH$_3$CN (solvatomorph I) and a desolvated form of **3** (solvatomorph II) depicted in Fig. S7 in the ESI,† and it was associated with a transition of the complex from the LS to the HS state (see the section of Magnetic properties) as well. Despite many attempts to determine the molecular structures of several different single crystals of **3**·0.5CH$_3$CN (solvatomorph I), they could not be elucidated due to a very low quality of the obtained diffraction data, which can be related to the occurring loss of the crystal solvents in the crystals. Furthermore, the recrystallization of complex **3** from CH$_3$CN resulted in the formation of light yellow [Fe(**L**)]F$_3$ (confirmed by MS m/z (+):

502.21 [Fe(**L**) + 2F]$^+$ as a product of complex oxidation and decomposition.

Such solvatomorphism has been previously observed for other Fe(II) SCO systems, *e.g.* [Fe(bpp)(H$_2$L)](ClO$_4$)$_2$·1.5C$_3$H$_6$O (bpp = 2,6-bis(pyrazol-3-yl)pyridine, H$_2$L = 2,6-bis(5-(2-methoxyphenyl)pyrazol-3-yl)pyridine) with a kinetically slow extrusion of 0.5 acetone molecule above 375 K (SCSC transformation from the LS to the HS state),[42] which was reversible and allowed determination of different ordered phases in one crystal.[44]

The recrystallization of **1**·1H$_2$O from CH$_3$CN/CH$_3$OH solution by the diffusion of Et$_2$O vapours was accompanied by the oxidation of the [FeCl$_4$]$^{2-}$ anion to the [FeCl$_4$]$^-$ one, which led to the formation of [Fe(**L**)][FeCl$_4$]$_2$ (**1a**). Its molecular structure was determined and is shown in Fig. S8 in the ESI.† The complex cation [Fe(**L**)]$^{2+}$ reveals symmetric (C_2 axis) and slightly distorted octahedral *cis*-V geometry with an average ⟨Fe–N⟩ distance value of 2.060 Å (Fig. S8 and Table S2 in the ESI†) corresponding to the LS state of the Fe(II) atom. Apart from the [Fe(**L**)]$^{2+}$ cation, the molecular structure consists of two tetrahedral [FeCl$_4$]$^-$ anions. The crystal structure is further stabilized by the C–H···Cl non-covalent contacts (Table S3†) connecting individual molecule ions into a 3D supramolecular structure.

The molecular structures of compounds **2**·1.5H$_2$O (120 K), **3** (solvatomorph II at 120 K) and **3** (solvatomorph II at 293 K) are very similar (Fig. 4). The complex cation [Fe(**L**)]$^{2+}$ reveals distorted octahedral geometry with a *cis*-V ligand coordination mode (Fig. 4). The largest bite angle is provided by the coordi-

nation of two macrocyclic nitrogen atoms connected by a pro-pylene bridge (~92–97°, N(1)–Fe–N(3) and N(2)–Fe–N(4), Table 2), while it decreases for the nitrogen atoms connected by an ethylene bridge (~81–88°, N(1)–Fe–N(2), N(3)–Fe–N(4), and N(2)–Fe–N(3), Table 2) and it is the smallest for the co-ordinated pendant pyridines (~79–81°, N(1)–Fe–N(5) and N(4)–Fe–N(6), Table 2).

In the case of the molecular structures of **2**·1.5H$_2$O and **3** (120 K), the Fe–N$_{alif}$ bonds range from 2.022(3) Å to 2.126(3) Å, while the significantly shorter Fe–N$_{py}$ bond ranges from 2.004(3) to 2.078(3) Å (Table 2). On the other hand, this difference in the Fe–N$_{alif}$ and Fe–N$_{py}$ bond lengths is not observed in the molecular structure of **3** at 293 K. The average ⟨Fe–N⟩ distance value is 2.051 and 2.086 Å (Table 2) for **2** and **3** (120 K), respectively, which clearly indicates that both complexes were in the LS state at 120 K. It is because the typical Fe–N distances for octahedral Fe(II) complexes in the HS state are *ca.* 0.15 Å longer, *i.e.* ~2.2 Å.[39] Such a value of the average ⟨Fe–N⟩ distance, concretely 2.197 Å (Table 2), was found for **3** at 293 K which confirmed the HS state of the complex **3** at room temperature. The obtained values are very close to the ⟨Fe–N⟩ bond distances of 2.077 Å (the LS state at 90 K) and 2.197 Å (the HS state at 293 K) observed in [Fe(Py$_2$–C)](BF$_4$)$_2$,[24] the SCO complex of a structurally similar unbridged ligand Py$_2$–C. The overlay of the molecular structures of **3** in the LS (120 K) and HS (293 K) state is depicted in Fig. 4D, which clearly shows the shorter Fe–N distances at 120 K (especially for pyridine N5 and N6 atoms) and a small

shift of the metal atom outside the cross-bridged cyclam macrocyclic cavity.

The spin transition of **3** from the LS to the HS state was accompanied by additional structural changes. Firstly, the cell volume was increased from 2747(2) Å^3 to 2760.8(4) Å^3 (Tables 1 and 3). Secondly, the degree of the deformation of the coordination polyhedron expressed in the case of the octahedron by the structural parameter Σ,[39,51] which is equal to zero for an ideal octahedral geometry and increases with the deformation, was increased for about 20° (Table 3), which is slightly lower than the typical value (30% of Σ for the HS state) observed for the spin transition in other Fe(II) SCO complexes.[39]

Unfortunately, the single crystals of **4** were of very poor quality, and therefore the molecular structure of **4** is only reported in the ESI in Fig. S9.† Nevertheless, it clearly confirms a similar distorted octahedral geometry of [Fe(**L**)]$^{2+}$ as observed in **2**·1.5H$_2$O or **3** and the presence of the appropriate counter ions as well. Moreover, the Fe–N bond lengths of **4** are within the interval of 2.030–2.072 Å, thus supporting the presence of the Fe(II) atom in the LS state at 120 K.

In the crystal structure of **2**·1.5H$_2$O, two crystallographically independent [Fe(**L**)]$^{2+}$ cations were found in the asymmetric unit (Fig. S10 in ESI†) together with four chloride counter ions as well as three water molecules. The chloride anions as well as water molecules participate in an extensive system of the O–H···Cl hydrogen bonds and C–H$_{aromatic}$···Cl/O non-covalent contacts (Fig. S11, Table S4 in the ESI†) altogether helping to form a 3D supramolecular structure. The difference in the number of co-crystallized solvent molecules in complex **2** determined using X-ray analysis (**2**·1.5H$_2$O), and by elemental analysis and thermogravimetric analysis (**2**·4H$_2$O) is most likely caused by a slightly different synthetic procedure used for the preparation of the polycrystalline solid sample (product precipitation induced by direct Et$_2$O addition) and single crystals (recrystallization using a slow diffusion of Et$_2$O vapours into CH$_3$CN solution) suitable for X-ray analysis.

In the crystal structure of **3** determined at 120 K as well as at 293 K, the [Fe(**L**)]$^{2+}$ cations were accompanied by two BF$_4^-$ counter anions and the F5, F6, F7 and F8 atoms were disordered over two positions with the occupancy factors as follows: 0.55/0.45 (120 K) and 0.38/0.62 (293 K) for F5a, F6a, F7a, F8a/F5b, F6b, F7b, and F8b. The crystal structure of **3** is

Table 2 Selected bond lengths (Å) and angles (°) for the studied complexes

Distances	**2**^{a}	**3**^{b}	**3**^{c}
Fe–N(1)	2.092(3)/2.108(3)	2.126(2)	2.200(3)
Fe–N(2)	2.036(3)/2.022(3)	2.072(2)	2.195(3)
Fe–N(3)	2.041(3)/2.032(3)	2.048(2)	2.188(3)
Fe–N(4)	2.099(3)/2.111(3)	2.125(2)	2.213(4)
Fe–N(5)	2.034(2)/2.004(3)	2.067(2)	2.205(3)
Fe–N(6)	2.017(3)/2.015(3)	2.078(2)	2.183(4)
⟨Fe–N⟩	2.051	2.086	2.197

Angles	**2**^{a}	**3**^{b}	**3**^{c}
N(3)–Fe–N(1)	95.22(10)/94.62(10)	95.99(9)	92.60(13)
N(2)–Fe–N(4)	94.65(10)/94.80(10)	96.51(9)	91.64(14)
N(2)–Fe–N(1)	84.21(10)/84.18(10)	82.43(9)	81.99(13)
N(3)–Fe–N(4)	84.01(10)/84.31(10)	82.85(10)	81.04(13)
N(2)–Fe–N(3)	86.51(10)/87.65(11)	87.50(9)	80.99(13)
N(5)–Fe–N(1)	80.46(10)/81.30(10)	79.86(9)	78.74(13)
N(6)–Fe–N(4)	81.05(10)/81.06(10)	79.50(9)	79.28(13)
N(6)–Fe–N(5)	86.54(10)/85.25(10)	92.76(9)	93.08(13)
N(6)–Fe–N(2)	175.66(10)/175.49(10)	175.52(9)	170.13(14)
N(5)–Fe–N(2)	93.78(10)/93.73(11)	90.01(9)	93.39(13)
N(6)–Fe–N(1)	93.51(10)/93.70(11)	89.97(9)	93.56(13)
N(5)–Fe–N(3)	175.61(10)/175.53(10)	175.42(9)	170.32(13)
N(6)–Fe–N(1)	100.11(10)/99.99(10)	101.52(9)	106.61(13)
N(5)–Fe–N(4)	100.33(10)/99.79(10)	101.26(9)	107.14(12)
N(1)–Fe–N(4)	178.66(10)/178.56(11)	178.47(9)	171.70(13)

^{a} Two values are given for two crystallographically independent molecules found in the asymmetric unit. ^{b} For 120 K. ^{c} For 293 K.

Table 3 Structural, shades of colour and spin changes for complex **3**

Complex	**3**·0.5 CH$_3$CN	**3**	**3**
Solvatomorph	I	II	II
Space group	—	$P2_1/n$	$P2_1/n$
Spin state	LS	HS	LS
Temperature (K)	120/293	293	120
Cell volume (Å^3)	—	2760.(4)	2747(2)
⟨Fe–N⟩	—	2.197	2.086
Σ^{51}	—	96.0	75.9

stabilized by a variety of the $C–H_{aromatic}\cdots F$ non-covalent contacts (Fig. S12 in the ESI†).

Magnetic properties

The magnetic measurements for **1·H$_2$O**, **2·4H$_2$O**, **3·0.5CH$_3$CN** and **4·CH$_3$OH** in the temperature range of 5–400 K were performed and the obtained results are expressed as the temperature dependence of $\chi_m T$ in Fig. 6. The values of $\chi_m T$ as well as values of effective magnetic moment (μ_{eff}/μ_B) for the studied compounds at selected temperatures are listed in Table 4. There are two types of Fe^{II} centres present in **1·H$_2$O**, *i.e.* the complex cation [Fe(**L**)]$^{2+}$ and complex anion [FeCl$_4$]$^{2−}$. The initial $\chi_m T$ value of 7.24 cm$^{−3}$ K mol$^{−1}$ at 400 K is almost the same as the theoretical value of 7.26 cm$^{−3}$ K mol$^{−1}$ for two Fe^{II} centres with $S = 2$ and $g = 2.2$ (higher values of g-factor close to 2.2 are usually found for HS Fe^{II} complexes due to a substantial contribution of the orbital angular momentum from excited states).[52–54] The $\chi_m T$ value gradually decreases between 400 and 300 K, while below 300 K, it decreases abruptly to

reach a plateau between 150 and 50 K at the $\chi_m T$ value of 3.66–3.42 cm$^{−3}$ K mol$^{−1}$, which is in accordance with the spin-only value of 3.63 cm$^{−3}$ K mol$^{−1}$ for one Fe^{II} with $S = 2$ and $g = 2.2$. An additional decrease of $\chi_m T$ below 50 K can be attributed mainly to the zero field splitting and/or any intermolecular non-covalent interactions. Observed magnetic behaviour can be explained by considering the [Fe(**L**)]$^{2+}$ unit responsible for the spin transition with $T_{1/2} \sim 245$ K, estimated from the first derivative of $\chi_m T$ (Fig. S13 in the ESI†), and the [FeCl$_4$]$^{2−}$ unit remaining in the HS state in the whole temperature range (a weak tetrahedral ligand field). Surprisingly, complex **1·H$_2$O** is a very rare example of a SCO Fe(II) complex containing the [FeX$_4$]$^{−/2−}$ anion. To the best of our knowledge, there are only two examples of such a system based on [Fe(Metz)$_6$][FeBr$_4$]$_2$ (Metz = 1-methyltetrazole), for which $T_{1/2}$ is around 165 K and [FeBr$_4$]$^−$ anions are magnetically ordered at low temperature,[55,56] and [Fe(AIBN)$_3$][FeCl$_4$]$_2$ (AIBN = 2,2′-azobisisobutyronitrile) displaying a 'half' spin transition ($T_{1/2} = 170$ K).[57] Due to a very low amount of obtained complex **1a**, its magnetic properties were not possible to study in detail.

In the case of complex **2·4H$_2$O**, a gradual decrease in the $\chi_m T$ value, from 3.94 cm$^{−3}$ K mol$^{−1}$ at 400 K (slightly higher than 3.63 for one Fe^{II} with $S = 2$ and $g = 2.2$) to 0.06 cm$^{−3}$ K mol$^{−1}$ at 5 K, was observed. Based on the powder XRD pattern of **2·4H$_2$O** (Fig. S6 in the ESI†), the poor crystallinity of the bulk sample could contribute to the low cooperativity in the sample, thus affecting the SCO behaviour.

For all the studied compounds, the temperature cycles of 300 K → 5 K → 400 K → 5 K → 400 K were measured. The obtained magnetic curves were almost similar for all studied compounds, except for **3·0.5CH$_3$CN** containing the BF$_4^−$ counter anions. This indicates that the loss of co-crystallized solvent molecules at a high temperature has a significant effect on SCO only in the case of compound **3·0.5CH$_3$CN**. In this case (Fig. 7), the initial $\chi_m T$ value of 0.42 cm$^{−3}$ K mol$^{−1}$ at
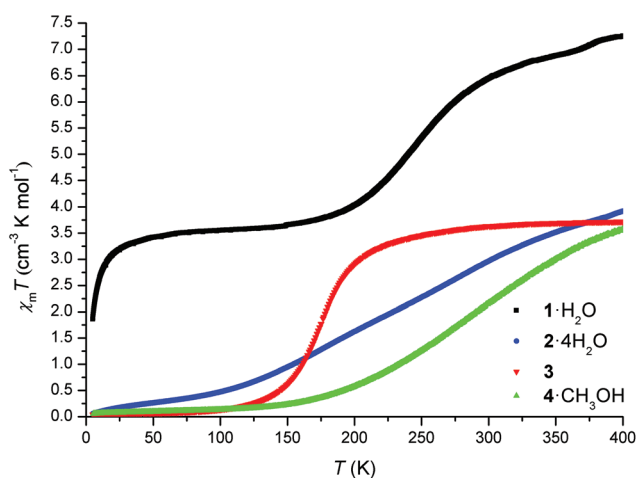

Fig. 6 Temperature dependence of $\chi_m T$ for compounds **1·H$_2$O**, **2·4H$_2$O**, **4·CH$_3$OH** (1st cycle 5 K → 400 K) and **3** (2nd cycle 5 K → 400 K).

Table 4 The values of $\chi_m T$ and effective magnetic moments at the selected temperatures

Compound	T [K]	$\chi_m T$ [cm^3 K mol$^{−1}$]	μ_{eff} [μ_B][a]
1	400	7.24	7.61
1·H$_2$O	100	3.55	5.33
1·H$_2$O	5	1.86	3.86
2	400	3.94	5.61
2·4H$_2$O	5	0.06	0.68
3·0.5CH$_3$CN	300	0.42[b]	1.82[b]
3	400	3.72	5.45
3	5	0.04	0.56
4	400	3.57	5.35
4·CH$_3$OH	5	0.06	0.67

[a] μ_B is the Bohr magneton. The formula of $\mu_{eff} = (8\chi_m T)^{1/2}$ was used for the recalculation. [b] The initial values obtained before heating to 400 K.
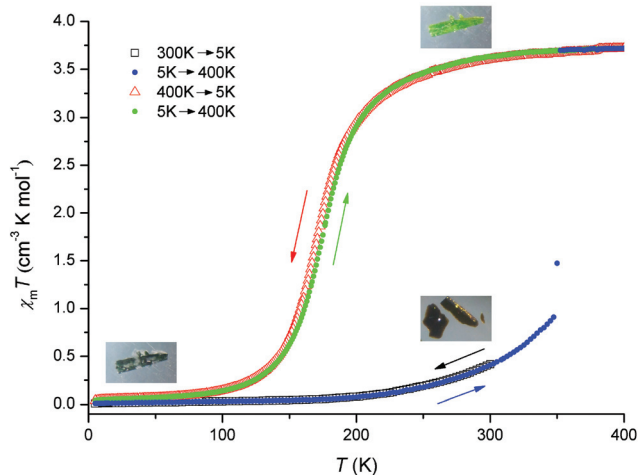

Fig. 7 Temperature dependences of $\chi_m T$ of compound **3·0.5CH$_3$CN** with the temperatures changing from 300 K to 5 K (black), from 5 K to 400 K (blue), from 400 K to 5 K (red) and from 5 K to 400 K (green).

300 K indicated that the majority of the complex (~89%) was in the LS state at the beginning of the measurement. When the sample was cooled down (Fig. 7), the $\chi_m T$ value gradually decreased to 0.009 cm^{-3} K mol^{-1} at 5 K, which confirmed the LS state of the complex. The curve for heating up to 300 K was identical to that for cooling. Upon further heating of the sample, a very sharp increase of $\chi_m T$ from 0.91 to 3.70 cm^{-3} K mol^{-1} (spin-only value of 3.63 for one Fe^{II} with S = 2 and g = 2.2) at 350 K was observed and followed by almost constant progress of $\chi_m T$ up to 400 K (Fig. 7). By cooling the sample down, the SCO occurred with $T_{1/2}$ = 177 K (ref. 58) and $\chi_m T$ decreased from the value of 3.72 cm^{-3} K mol^{-1} at 400 K to 0.04 cm^{-3} K mol^{-1} at 5 K (Fig. 6 and 7), with an almost identical curve for sample heating back to 400 K. As mentioned before, the LS state of [Fe(**L**)]$^{2+}$ cations at 120 K was also confirmed by X-ray analysis. The observed sharp transition to the HS state at 350 K is most likely related to the loss of co-crystallized solvent molecules of CH$_3$CN (3.1% of the mass loss in TG well corresponds to the 0.5 molecule of CH$_3$CN, see Fig. S4 in the ESI†). As was already described in the section X-ray analysis, this first spin transition at 350 K (**3**·0.5CH$_3$CN – solvatomorph I, LS → **3** – solvatomorph II, HS) was accompanied by the crystallographic phase change and by the colour change from dark brown-green to light green (Table 3, Fig. 7), while the spin transition at 177 K (**3** – solvatomorph II, HS ↔ **3** – solvatomorph II, LS) only by colour change from light green to dark green and back.

A similar spin transition upon co-crystallized solvent desorption was previously observed for [Fe(bpp)(H$_2$L)](ClO$_4$)$_2$·1.5C$_3$H$_6$O (bpp = 2,6-bis(pyrazol-3-yl)pyridine, H$_2$L = 2,6-bis(5-(2-methoxyphenyl)pyrazol-3-yl)pyridine), for which a kinetically slow extrusion of 0.5 acetone molecule above 375 K was accompanied by SCSC transformation from the LS to the HS state and it was reversible.[42] The acetone molecules were able to be reversibly replaced by water and methanol molecules, which induced reverse transition from the HS to the LS state. The desolvated phase showed SCO with 5 K hysteresis ($T_{1/2}\downarrow/T_{1/2}\uparrow$ = 235/240 K).[42] Another similarly behaving complex was [Fe(1,3-bpp)$_2$](ClO$_4$)$_2$·nH$_2$O (n = 0, 1, 2; 1,3-bpp = 2-(pyrazol-1-yl)-6-(pyrazol-3-yl)pyridine) for which two dehydrated polymorphs with different $T_{1/2}$ (278 and 315 K) were found together with SCO behaviour for the monohydrated solvatomorph as well.[43]

The last compound **4**·CH$_3$OH contained BPh$_4^-$ anions, and this anion exchange led to SCO with $T_{1/2}$ ~ 290 K having similar high- and low-temperature $\chi_m T$ values (3.57 and 0.06 cm^{-3} K mol^{-1}) as observed for **2**·4H$_2$O and **3**.

The value of $\chi_m T$ for the octahedral LS Fe^{II} complexes should be zero due to their diamagnetism, and in our case, the observed close-to-zero $\chi_m T$ values at low-temperature for complexes **2**·4H$_2$O, **3** and **4**·CH$_3$OH indicate the complete transition to the LS state without any occurrence of the residual HS fraction (less than 1.6%). In the case of **1**·H$_2$O, the complete transition to the LS state occurred only for the [Fe(**L**)]$^{2+}$ cation and the $\chi_m T$ values below 150 K correspond to the presence of [Fe^{II}Cl$_4$]$^{2-}$ in the HS state. On the other hand, at high tempera-

ture, the transition to the HS state can be considered as complete only for **3**.

The comparison of the obtained magnetic data well documents that the transition temperature is significantly affected by the counter anions; it increases in the order BF$_4^-$ < [FeCl$_4$]$^{2-}$ < BPh$_4^-$, as well as by the presence/absence of co-crystallized solvent molecule(s). Such behaviour and modulation of SCO is well known for various previously described Fe^{II}-based[38,40,41,59–62] or even Fe^{III}-based SCO systems.[63,64]

In order to elucidate the effect of the cross-bridge in **L** on SCO, the magnetic data for **3** were compared to those for [Fe(**Py$_2$–C**)](BF$_4$)$_2$·H$_2$O[24] containing the unbridged Py$_2$–C ligand. The SCO occurs with $T_{1/2}$ = 177 K in **3** while in [Fe(**Py$_2$–C**)](BF$_4$)$_2$·H$_2$O it occurs with $T_{1/2}$ ~ 150 K. Because both complexes have the same anions and the cations have the same *cis*-V configuration, one could consider that the presence of the cross-bridge might be responsible for this increase of transition temperature. This is not surprising especially when properties of both ligands are compared in detail. The replacement of the secondary amino groups in **Py$_2$–C** with the tertiary ones in **L** causes an increase of the donor-properties of these nitrogen atoms as a result of the well-known electron-donating effect of the alkyl groups, which was observed in structurally similar cylen[20] or cyclam systems with different degrees of alkylation (*e.g.* 1–4 × Me)[65] and it is also documented by the shortening of the Fe–N distances by ~0.01 Å in **3** in comparison with the Fe–NH ones. As a consequence of this, a slightly stronger ligand field is applied to the Fe^{II} centre in **3**, which could be responsible for the increase of $T_{1/2}$. A further aspect, which could play a role, is the higher rigidity of **L**. On the other hand, both compounds differ in their space group and their crystal packing is significantly different as well. Even more, they differ in the co-crystallized solvent molecule (0.5CH$_3$CN *vs.* H$_2$O). All these factors significantly affect the SCO behaviour ($T_{1/2}$ or the abruptness of transition)[66] or even the presence of SCO itself.[67] Thus, in this case, it is not possible to reveal undoubtedly the effect of the cross-bridge on the SCO behaviour in comparison with the similar Fe^{II} complex with unbridged ligand.

Conclusions

A new cross-bridged cyclam derivative containing two 2-pyridylmethyl pendant arms (**L**), the last in a series of pyridine-based cross-bridged cyclams, was synthesized and its Fe^{II} complexes containing different counter anions ([FeCl$_4$]$^{2-}$ (**1**·H$_2$O), Cl$^-$ (**2**·4H$_2$O), BF$_4^-$ (**3**·0.5CH$_3$CN) and BPh$_4^-$ (**4**·CH$_3$OH)) were prepared and thoroughly characterized. The complexes revealed the *cis*-V configuration for the [Fe(**L**)]$^{2+}$ cation and showed SCO behaviour with the transition temperature $T_{1/2}$ depending on the counter ion(s). The lowest $T_{1/2}$ = 177 K was found for **3** (BF$_4^-$), while higher $T_{1/2}$ values were observed for **1**·H$_2$O ([FeCl$_4$]$^{2-}$) and **4**·CH$_3$OH (BPh$_4^-$) (~245 K, and ~290 K, respectively), and gradual and incomplete transition for **2**·4H$_2$O (Cl$^-$). The complex **3** showed the most abrupt and com-

plete SCO, which proceeded after the elimination of the co-crystallized 0.5 CH_3CN solvent molecule and this solvent loss induced the formation of a different crystallographic phase. The presence or absence of co-crystallized solvent molecule(s) has a significant effect on SCO behaviour only in the case of complex **3·0.5CH₃CN**. $T_{1/2}$ for **3** is slightly higher (177 K) in comparison with the previously studied Fe^{II} complex containing a structurally similar unbridged ligand [Fe(**Py₂–C**)] $(BF_4)_2 \cdot H_2O$ with $T_{1/2} \sim 150$ K.[24]

In conclusion, this is the first example of SCO complexes with a cross-bridged cyclam-based ligand. By varying the anion, one can change dramatically the temperature as well as the abruptness of the spin transition. The observed SCO behaviour is similar to that of the complexes with the unbridged cyclam-based ligand; however the impact of the cross-bridge on the SCO behaviour cannot be unambiguously elucidated, because other factors like counter ions, crystal solvent molecules and crystal packing play a more important role.

Conflicts of interest

There are no conflicts to declare.

Acknowledgements

Notes and references

1 X. Liang and P. J. Sadler, *Chem. Soc. Rev.*, 2004, **33**, 246–266.

2 T. Joshi, B. Graham and L. Spiccia, *Acc. Chem. Res.*, 2015, **48**, 2366–2379.

3 F. Davis and S. Higson, *Macrocycles: Construction, Chemistry and Nanotechnology Applications*, John Wiley & Sons, Chichester, United Kingdom, 2011.

4 A. Merbach, L. Helm and É. Tóth, *The Chemistry of Contrast Agents in Medicinal Magnetic Resonance Imaging*, John Wiley & Sons, Chichester, United Kingdom, 2013.

5 G. R. Weisman, M. E. Rogers, E. H. Wong, J. P. Jasinski and E. S. Paight, *J. Am. Chem. Soc.*, 1990, **112**, 8604–8605.

6 The SciFinder search for keywords "cyclen", "cyclam", "cross-bridged cyclen", and "cross-bridged cyclam" provided 2204, 2888, 23, and 93 records, respectively (23.01.2018).

7 T. Hubin, *Coord. Chem. Rev.*, 2003, **241**, 27–46.

8 J. C. Timmons and T. J. Hubin, *Coord. Chem. Rev.*, 2010, **254**, 1661–1685.

9 D. H. Busch, S. R. Collinson and T. J. Hubin, Catalysts and Methods for Catalytic Oxidation, *U.S. Patent* 2011/0143925Al, 2011.

10 G. Yin, A. M. Danby, D. Kitko, J. D. Carter, W. M. Scheper and D. H. Busch, *Inorg. Chem.*, 2007, **46**, 2173–2180.

11 C. S. Cutler, H. M. Hennkens, N. Sisay, S. Huclier-Markai and S. S. Jurisson, *Chem. Rev.*, 2013, **113**, 858–883.

12 E. H. Wong, G. R. Weisman, D. C. Hill, D. P. Reed, M. E. Rogers, J. S. Condon, M. A. Fagan, J. C. Calabrese, K.-C. Lam, I. A. Guzei and A. L. Rheingold, *J. Am. Chem. Soc.*, 2000, **122**, 10561–10572.

13 R. Ferdani, D. J. Stigers, A. L. Fiamengo, L. Wei, B. T. Li, J. A. Golen, A. L. Rheingold, G. R. Weisman, E. H. Wong and C. J. Anderson, *Dalton Trans.*, 2012, **41**, 1938–1950.

14 L. M. Lima, Z. Halime, R. Marion, N. Camus, R. Delgado, C. Platas-Iglesias and R. Tripier, *Inorg. Chem.*, 2014, **53**, 5269–5279.

15 *The Chemistry of Contrast Agents in Medicinal Magnetic Resonance Imaging*, ed. A. Merbach, L. Helm and E. Tóth, Wiley, 2013.

16 T. J. Wadas, E. H. Wong, G. R. Weisman and C. J. Anderson, *Chem. Rev.*, 2010, **110**, 2858–2902.

17 C. M. Perkins and D. J. Kitko, *International patent WO* 02/26267Al, 2002.

18 R. Smith, D. Huskens, D. Daelemans, R. E. Mewis, C. D. Garcia, A. N. Cain, T. N. Freeman, C. Pannecouque, E. De Clercq, D. Schols, T. J. Hubin and S. J. Archibald, *Dalton Trans.*, 2012, **41**, 11369–11377.

19 T. J. Hubin, P. N. A. Amoyaw, K. D. Roewe, N. C. Simpson, R. D. Maples, T. N. Carder Freeman, A. N. Cain, J. G. Le, S. J. Archibald, S. I. Khan, B. L. Tekwani and M. O. F. Khan, *Bioorg. Med. Chem.*, 2014, **22**, 3239–3244.

20 N. Bernier, J. Costa, R. Delgado, V. Felix, G. Royal and R. Tripier, *Dalton Trans.*, 2011, **40**, 4514–4526.

21 D. G. Jones, K. R. Wilson, D. J. Cannon-Smith, A. D. Shircliff, Z. Zhang, Z. Chen, T. J. Prior, G. Yin and T. J. Hubin, *Inorg. Chem.*, 2015, **54**, 2221–2234.

22 A. Rodriguez-Rodriguez, D. Esteban-Gomez, R. Tripier, G. Tircso, Z. Garda, I. Toth, A. de Blas, T. Rodriguez-Blas and C. Platas-Iglesias, *J. Am. Chem. Soc.*, 2014, **136**, 17954–17957.

23 G. Royal, V. Dahaoui-Gindrey, S. Dahaoui, A. Tabard, R. Guilard, P. Pullumbi and C. Lecomte, *Eur. J. Org. Chem.*, 1998, 1971–1975.

24 F. El Hajj, G. Sebki, V. Patinec, M. Marchivie, S. Triki, H. Handel, S. Yefsah, R. Tripier, C. J. Gomez-Garcia and E. Coronado, *Inorg. Chem.*, 2009, **48**, 10416–10423.

25 G. R. Weisman, E. H. Wong, D. C. Hill, M. E. Rogers, D. P. Reed and J. C. Calabrese, *Chem. Commun.*, 1996, 947–948, DOI: 10.1039/CC9960000947.

26 S. Rojas-Lima, N. Farfán, R. Santillan, D. Castillo, M. E. Sosa-Torres and H. Höpfl, *Tetrahedron*, 2000, **56**, 6427–6433.

27 M. Le Baccon, F. Chuburu, L. Toupet, H. Handel, M. Soibinet, I. De'champs-Olivier, J.-P. Barbier and M. Aplincourt, *New J. Chem.*, 2001, **25**, 1168–1174.

28 J. Kotek, P. Hermann, P. Vojtíšek, J. Rohovec and I. Lukeš, *Collect. Czech. Chem. Commun.*, 2000, **65**, 243–266.

29 F. Oukhatar, M. Beyler and R. Tripier, *Tetrahedron*, 2015, **71**, 3857–3862.

30 J. Zhang, H. Cui, M. Hojo, S. Shuang and Ch. Dong, *Bioorg. Med. Chem. Lett.*, 2012, **12**(1), 343–346.

31 M. Mato-Iglesias, A. Roca-Sabio, Z. Pálinkás, D. Esteban-Gómez, C. Platas-Iglesias, É. Tóth, A. de Blas and T. Rodríguez-Blas, *Inorg. Chem.*, 2008, **47**, 7840–7851.

32 B. Bosnich, C. K. Poon and M. L. Tobe, *Inorg. Chem.*, 1965, **4**, 1102–1108.

33 T. J. Hubin, J. M. McCormick, S. R. Collinson, D. H. Busch and N. W. Alcock, *Chem. Commun.*, 1998, 1675–1676.

34 T. J. Hubin, J. M. McCormick, S. R. Collinson, M. Buchalova, C. M. Perkins, N. W. Alcock, P. K. Kahol, A. Raghunathan and D. H. Busch, *J. Am. Chem. Soc.*, 2000, **122**, 2512–2522.

35 T. J. Hubin, J. M. McCormick, N. W. Alcock and D. H. Busch, *Inorg. Chem.*, 2001, **40**, 435–444.

36 T. J. Hubin, J. M. McCormick, S. R. Collinson, N. W. Alcock, H. J. Clase and D. H. Busch, *Inorg. Chim. Acta*, 2003, **346**, 76–86.

37 G. Yin, J. M. McCormick, M. Buchalova, A. M. Danby, K. Rodgers, V. W. Day, K. Smith, C. M. Perkins, D. Kitko, J. D. Carter, W. M. Scheper and D. H. Busch, *Inorg. Chem.*, 2006, **45**, 8052–8061.

38 E. Milin, B. Benaicha, F. El Hajj, V. Patinec, S. Triki, M. Marchivie, C. J. Gómez-García and S. Pillet, *Eur. J. Inorg. Chem.*, 2016, 5305–5314.

39 P. Gutlich and H. A. Goodwin, *Top. Curr. Chem.*, 2004, 233–235.

40 I. Šalitroš, O. Fuhr, A. Eichhöfer, R. Kruk, J. Pavlik, L. Dlháň, R. Boča and M. Ruben, *Dalton Trans.*, 2012, **54**, 5163–5171.

41 I. Šalitroš, O. Fuhr and M. Ruben, *Materials*, 2016, **9**, 585.

42 J. Sánchez Costa, S. Rodríguez-Jiménez, G. A. Craig, B. Barth, C. M. Beavers, S. J. Teat and G. Aromí, *J. Am. Chem. Soc.*, 2014, **136**, 3869–3874.

43 C. Bartual-Murgui, C. Codina, O. Roubeau and G. Aromí, *Chem. – Eur. J.*, 2016, **22**, 12767–12776.

44 G. Aromí, C. M. Beavers, J. Sánchez Costa, G. A. Craig, G. Mínguez Espallargas, A. Orerad and O. Roubeau, *Chem. Sci.*, 2016, **7**, 2907–2915.

45 *Purification of Laboratory Chemicals*, ed. D. D. Perrin, Pergamon Press, Oxford, U. K., 1988.

46 Bruker, *Apex3*, Bruker AXS Inc., Madison, Wisconsin, USA, 2015.

47 G. M. Sheldrick, *Acta Crystallogr., Sect. C: Struct. Chem.*, 2015, **71**, 3–8.

48 C. F. Macrae, I. J. Bruno, J. A. Chisholm, P. R. Edgington, P. McCabe, E. Pidcock, L. Rodriguez-Monge, R. Taylor, J. van de Streek and P. A. Wood, *J. Appl. Crystallogr.*, 2008, **41**, 466–470.

49 S. Sonda, T. Kawahara, K. Katayama, N. Sato and K. Asano, *Bioorg. Med. Chem.*, 2005, **13**, 3295–3308.

50 K. Nakamoto, *Infrared and Raman spectra of Inorganic and Coordination Compounds*, Wiley, New Jersey, USA, 2009.

51 $\sum = \sum_{i=1}^{12} (|\phi_i - 90°|)$; where φ_i is the value of the N–Fe–N octahedron angle. Adapted from the reference: P. Guionneau, M. Marchivie, G. Bravic, J. F. Létard and D. Chasseau, *Top. Curr. Chem.*, 2004, **234**, 97–128.

52 R. Boča, *Coord. Chem. Rev.*, 2004, **248**, 757–815.

53 A. K. Bar, C. Pichon and J.-P. Sutter, *Coord. Chem. Rev.*, 2016, **308**, 346–380.

54 P. Antal, B. Drahoš, R. Herchel and Z. Trávníček, *Inorg. Chem.*, 2016, **55**, 5957–5972.

55 O. Roubeau, M. Evangelistia and E. Natividad, *Chem. Commun.*, 2012, **48**, 7604–7606.

56 J. A. Rodríguez-Velamazán, O. Fabelo, C. M. Beavers, E. Natividad, M. Evangelisti and O. Roubeau, *Chem. – Eur. J.*, 2014, **20**, 7956–7961.

57 K. Chainok, S. M. Neville, B. Moubaraki, S. R. Batten, K. S. Murray, C. M. Forsyth and J. D. Cashion, *Dalton Trans.*, 2010, **39**, 10900–10909.

58 $T_{1/2}$ was determined by using the equation of $\chi(T)T = \gamma_{HS}\chi_{HS}T + (1 - \gamma_{HS})\chi_{LS}T$,[39] where $\chi_{HS}T$ and $\chi_{LS}T$ are χT values for the pure HS and LS states, respectively, obtained from the measurement (3.72, and 0.04 cm^{-3} K mol^{-1}, respectively) and γ_{HS} is the mole fraction of the HS state equal to 0.5.

59 R. Herchel, Z. Trávníček and R. Zbořil, *Inorg. Chem.*, 2011, **50**, 12390–12392.

60 G. Lemercier, N. Brefuel, S. Shova, J. A. Wolny, F. Dahan, M. Verelst, H. Paulsen, A. X. Trautwein and J.-P. Tuchagues, *Chem. – Eur. J.*, 2006, **12**, 7421–7432.

61 B. A. Leita, S. M. Neville, G. J. Halder, B. Moubaraki, C. J. Kepert, J.-F. Letard and K. S. Murray, *Inorg. Chem.*, 2007, **46**, 8784–8795.

62 J. A. Kitchen, N. G. White, G. N. L. Jameson, J. L. Tallon and S. Brooker, *Inorg. Chem.*, 2011, **50**, 4586–4597.

63 I. Nemec, R. Herchel, I. Šalitroš, Z. Trávníček, J. Moncol, H. Fuess, M. Ruben and W. Linert, *CrystEngComm*, 2012, **14**, 7015–7024.

64 I. Nemec, R. Herchel, R. Boča, Z. Trávníček, I. Svoboda, H. Fuess and W. Linert, *Dalton Trans.*, 2011, **40**, 10090–10099.

65 E. K. Barefield, *Coord. Chem. Rev.*, 2010, **254**, 1607–1627.

66 J. Tao, R.-J. Wei, R.-B. Huang and L.-S. Zheng, *Chem. Soc. Rev.*, 2012, **41**, 703–737.

67 C. Krüger, P. Augustín, L. Dlhán, J. Pavlik, J. Moncol', I. Nemec, R. Boča and F. Renz, *Polyhedron*, 2015, **87**, 194–201.

Příloha P10

Article

Synthesis of a Versatile Building Block Combining Cyclen-derivative DO3A with a Polyamine via a Rigid Spacer

Bohuslav Drahoš and Zdeněk Trávníček *

Department of Inorganic Chemistry & Regional Centre of Advanced Technologies and Materials, Faculty of Science, Palacký University, 17. listopadu 12, Olomouc CZ-77146, Czech Republic; E-Mail: bohuslav.drahos@upol.cz

* Author to whom correspondence should be addressed; E-Mail: zdenek.travnicek@upol.cz; Tel.: +420-585-634-352; Fax: +420-585-634-954.
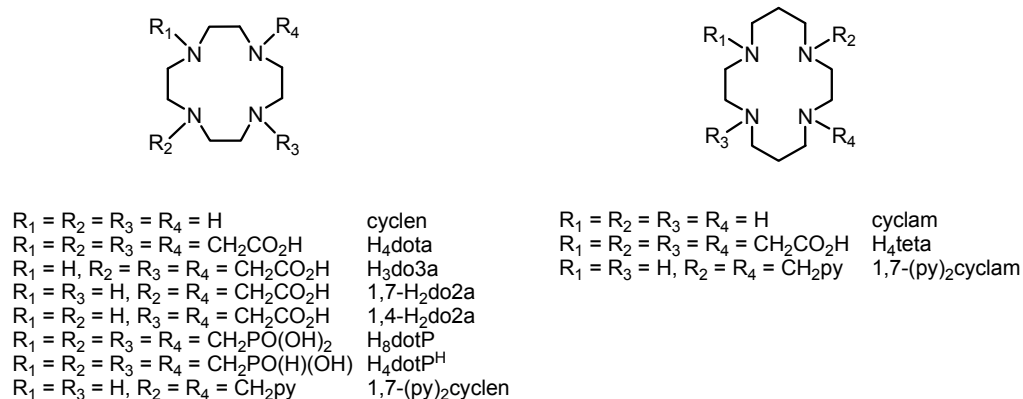
Abstract: The five-step synthesis of a polydentate building block combining a cyclen-based macrocycle (DO3A) with *N*-(2-aminoethyl)propane-1,3-diamine, which are linked through the xylylen moiety as a rigid C-spacer is described. These two molecular parts were coupled by subsequent bromine atom substitution in 1,4-bis(bromomethyl)benzene. First, *N*-(2-aminoethyl)propane-1,3-diamine was protected by phthaloyl moieties and then it was reacted with 1,4-bis(bromomethyl)benzene to form (2-phthalimidoethyl)(3-phthalimido-prop-1-yl)(4-bromomethylbenzyl)amine (**2**). This compound underwent a substitution reaction with DO3A in the form of its *tert*-butyl esters leading to the intermediate 1-{4-[(2-phthalimidoethyl)(3-phthalimidoprop-1-yl)aminomethyl]phenylmethyl}-4,7,10-tris(*t*-butoxy-carbonylmethyl)-1,4,7,10-tetraazacyclododecane (**3**). The phthaloyl as well as the *t*-butyl protecting groups were removed in the next two reaction steps to form the final product 1-{4-[(2-aminoethyl)(3-aminoprop-1-yl)aminomethyl]phenylmethyl}-4,7,10-tris(carboxy-methyl)-1,4,7,10-tetraazacyclododecane (**5**). The intermediates **1**–**4** as well as the final product **5** were characterized by elemental analysis, mass spectrometry, and multinuclear (¹H and ¹³C) and two-dimensional NMR spectroscopy. The final product **5** could serve as a potential building block in subsequent syntheses of binuclear complexes of lanthanides and/or transition metals.

Keywords: synthesis; DO3A macrocycle; building block; NMR spectroscopy; mass spectrometry

1. Introduction

Polyazamacrocycles have become a large and variable group of important organic substances because they represent irreplaceable ligands in complexes with transition metals, lanthanides, actinides or they are chemical and structural bases of different anion receptors. One group of the most common examples involves tetraazamacrocycles, namely cyclen (1,4,7,10-tetraazacyclododecane) and cyclam (1,5,8,11-tetraazacyclotetradecane), which have found many applications as contrast agents for Magnetic Resonance Imaging (MRI) [1], in optical imaging [2], Positron Emission Tomography (PET) [3], Single-Photon Emission Computed Tomography (SPECT) [3] and as radiotherapeutics [4] as well. Many structurally modified analogues have been prepared (representative examples are shown in Figure 1), such as the well-known *N*-substituted derivatives with a different number of pendant arms containing carboxylic acids (H$_4$dota 1,4,7,10-tetraazacyclododecane-1,4,7,10-tetraacetic acid, H$_3$do3a 1,4,7,10-tetraazacyclododecane-1,4,7-triacetic acid, H$_2$do2a 1,4,7,10-tetraazacyclododecane-1,4- or -1,7-dicarboxylic acid, H$_4$teta 1,4,8,11-tetraazacyclotetradecane-1,4,8,11-tetraacetic acid, and many others), phosphonic acid (H$_8$dotP 1,4,7,10-tetraazacyclododecane-1,4,7,10-tetrakis(methylphosphonic acid) *etc.*) or phosphinic acid (H$_4$dotP^H 1,4,7,10-tetraazacyclododecane-1,4,7,10-tetra-kis(methylphosphinic acid)) [1]. Gd(III) complexes with these compounds have found a unique application as contrast agents for MRI, ([Gd(dota)H$_2$O]$^-$ is one of the most stable and inert gadolinium complexes known under the trade name DOTAREM$^®$), and complexes of other lanthanides are employed in luminescence imaging and assay, or their complexes with $^{64/67}$Cu serve as PET agents.

Figure 1. Structural representations and abbreviations of selected macrocycles derived from cyclen (*left*) and cyclam (*right*).

R$_1$ = R$_2$ = R$_3$ = R$_4$ = H   cyclen
R$_1$ = R$_2$ = R$_3$ = R$_4$ = CH$_2$CO$_2$H   H$_4$dota
R$_1$ = H, R$_2$ = R$_3$ = R$_4$ = CH$_2$CO$_2$H   H$_3$do3a
R$_1$ = R$_3$ = H, R$_2$ = R$_4$ = CH$_2$CO$_2$H   1,7-H$_2$do2a
R$_1$ = R$_2$ = H, R$_3$ = R$_4$ = CH$_2$CO$_2$H   1,4-H$_2$do2a
R$_1$ = R$_2$ = R$_3$ = R$_4$ = CH$_2$PO(OH)$_2$ H$_8$dotP
R$_1$ = R$_2$ = R$_3$ = R$_4$ = CH$_2$PO(H)(OH)   H$_4$dotP^H
R$_1$ = R$_3$ = H, R$_2$ = R$_4$ = CH$_2$py   1,7-(py)$_2$cyclen

R$_1$ = R$_2$ = R$_3$ = R$_4$ = H   cyclam
R$_1$ = R$_2$ = R$_3$ = R$_4$ = CH$_2$CO$_2$H   H$_4$teta
R$_1$ = R$_3$ = H, R$_2$ = R$_4$ = CH$_2$py   1,7-(py)$_2$cyclam

Surprisingly, not much attention has been devoted to the characterization of the magnetic properties of solid metal complexes with this type of macrocyclic ligands, except for a series of Fe(II) complexes with cyclen/cyclam modified on nitrogen atoms with different alkyls or pyridine-containing pendant arms (1,7-(py)$_2$cyclen or 1,7-(py)$_2$cyclam), e.g., [Fe(1,7-(py)$_2$cyclam)](BF$_4$)$_2$·H$_2$O showed spin-crossover behavior [5]. Additional progress in cyclen/cyclam-based chemistry was achieved by connecting the macrocycles, usually by a rigid linker, to produce receptors for different anions (e.g., phosphates recognized by a Zn(II) complex of cyclen anchored onto a polymer, Figure 2a) [6], cations (Cu(II) or Zn(II) receptors having cyclen attached to a chromophore—dansyl (5-(dimethyl-amino)naphthalene-1-sulfonyl), or anthryl group, Figure 2b) or neutral molecules (riboflavin, creatinine or thymine) [7].

Figure 2. Examples of structures combining macrocycles with each other or with other molecules of interest. (**a**) Zn(II)-cyclen part connected to a polymer (represented as a sphere). (**b**) Cyclen modified with anthrylmethylamino group. (**c**) DO3A moiety connected by the amide bridge to G0–G5 poly(amidoamine) (PAMAM) dendrimers (represented as a sphere). (**d**) Thiourea bridge between the macrocycle and G2 PAMAM dendrimer (represented as a sphere). (**e**) Example of two macrocycles connected via "click chemistry" reaction (copper catalyzed [3+2] cycloaddition between alkyne and organic azide) and the mode of lanthanide coordination.
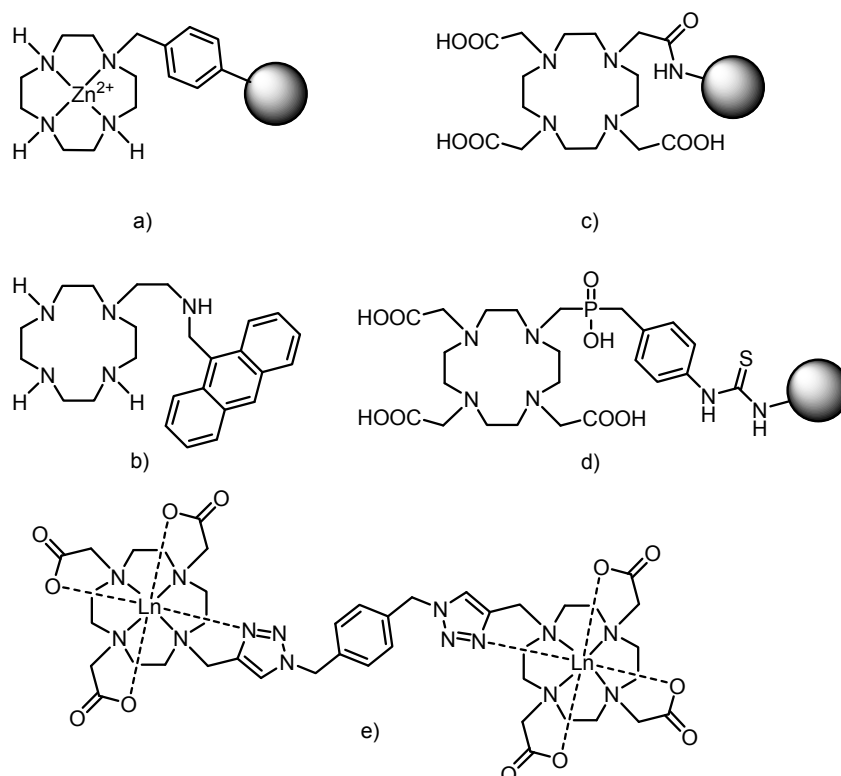
Further improvement, especially in the field of MRI contrast agents and radiotherapeutics, was achieved by linking the macrocycles with another molecule of interest. Gd(III) complexes of macrocycles linked to the macromolecules (dendrimers, cyclodextrins, proteins, nanotubes, *etc.*) showed improved efficiency as MRI contrast agents (slowing down molecular rotation and tumbling) [1]. The second group of molecules, which were linked to the macrocycle, could be considered as biological targets and provided specific delivery or metabolic pathway of the molecule in living organisms [8]. The third group is comprised of molecules which showed a specific function and/or property, and when they were combined with the macrocycle, new classes of multimodal/multifunctional compounds were obtained (MRI and near-infrared (NIR) contrast agents, MRI and PET agents, "theranostic" agents combining contrast agent and therapeutics into one molecule, *etc.*) [9].

The DO3A moiety has been widely used for the above-mentioned linking because it contains only one site for possible substitution. Many different spacers between the macrocycle and the other molecule of interest have been used and they are mostly based on the amide bond (Figure 2c) [10], thiourea bridge (Figure 2d) [11] and different types of "click chemistry" bonding (e.g., particularly copper catalyzed [3+2] cycloaddition reactions between alkynes and organic azides, Figure 2e) [12].

Here it should be stated that only representative examples of each group of compounds are mentioned because their complete lists are well beyond the scope of this Introduction and they can be found in many monographs and reviews [1,13].

The rigid xylylen (1,4-dimethylbenzene-1,4-diyl) bridge has already been employed as a linker between the macrocyle and polyamine, but not exactly in the way described in this work. Two cyclen or cyclam molecules were linked by the xylylen bridge in the synthesis of selective anti-HIV-1 agents (as Zn(II) complexes or free amines, Figure 3a,b) [7] and previously discussed anion receptors [6]. Two DO3A macrocycles were already connected into one molecule by the xylylen bridge (Figure 3c) [14] and its lanthanide complexes showed enhanced luminescence due to the presence of the benzene ring (xylylen) which acted as a sensitizing chromophore and caused efficient energy transfer (an antenna effect) [14].

Figure 3. Schematic representations of compounds in which cyclen/cyclam (or its derivatives) were connected to polyamine via the xylylen bridge. For (d) R_1 = H or Me, R_2 = 2-, 3- or 4-pyridine or 2-aminophenyl, 4-aminophenyl, 5-methylpiperazine.
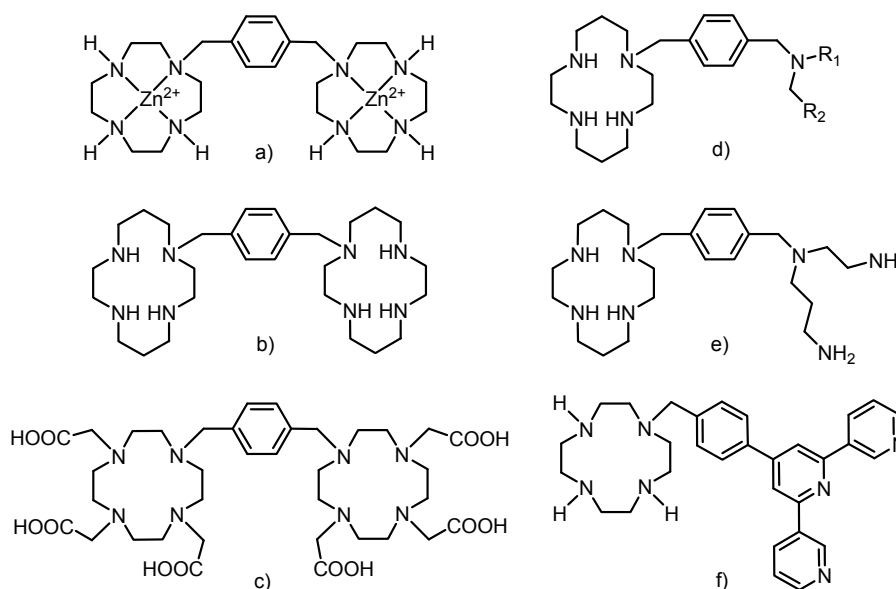
Structurally similar compounds to that studied in this paper were prepared by connection of cyclen or cyclam with linear polyamines. The anti-HIV-1 activity was described for monosubstituted cyclam containing different monoamines modified by pyridine or aminophenyl groups (Figure 3d) [15] as well as cyclam substituted with *N*-(2-aminoethyl)propane-1,3-diamine (Figure 3e) [16,17]. The synthesis of the latter used phthaoyl protecting groups, but in comparison with our work, the further modification of the macrocycle with acetate pendant arms was not persued.

The synthetic approach used for the preparation of the above-mentioned ligands was based on the reaction of protected cyclen/cyclams with 1,4-bis(bromomethyl)benzene (one bromine atom is substituted) and the obtained monobrominated intermediate reacted with differently protected molecules (other cyclen/cyclam, linear polyamines, *etc.*). The terpyridine moiety was connected to DO3A via a structurally similar rigid phenylmethyl bridge (Figure 3f) to obtain a self-assembly heterotrinuclear gadolinium(III)–iron(II) complex which belongs to a new class of MRI contrast agents called metallostars [18,19].

In this paper, the synthesis of a polydentate polyamino-polyacetate 1-{4-[(2-aminoethyl)(3-aminoprop-1-yl)aminomethyl]phenylmethyl}-4,7,10-tris(carboxymethyl)-1,4,7,10-tetraazacyclododecane (**5**) combining DO3A with *N*-(2-aminoethyl)propane-1,3-diamine connected with the rigid xylylen bridge is described. All synthetic steps are described in detail and compared with similar previously published procedures. This type of molecule has been chosen because it provides a good starting point for the synthesis of more sophisticated ligands belonging to the above-mentioned group of multimodal/multifunctional compounds. The synthetically readily available DO3A cavity is a selective chelator of lanthanides (providing e.g., luminescence) and the polyamine part can complex different transition metals (providing e.g., spin-crossover behavior). Additionally, the polyamine part of the molecule is simply modifiable in a way necessary for required complexation properties. The xylylen linker has been chosen because it is relatively rigid and short enough, and moreover, it involves a delocalized electron density, which all together may be a good condition for the preparation of complexes showing interesting magnetic properties in the case of incorporation of two suitable transition metals into the structure of **5**. Moreover, despite a large number of structurally similar compounds, to the best of our knowledge, no such motif of the rigid C-bonded (xylylen) bridge between DO3A and a linear polyamine can be found in the literature so far.

2. Results and Discussion

The synthesis of the desired polydentate molecule **5** was done in five steps which are outlined in Scheme 1 and the corresponding electrospray ionization (ESI) mass spectra are depicted in Figure 4. The well-known phthalimide protection was employed in the first step of the synthesis. The intermediate **1** was prepared in a good yield of 69% according to the procedure described in [20,21] with a little modification. Glacial acetic acid was used as a solvent and in this case, the product, which precipitated from the ethanolic (EtOH) solution, was slightly contaminated with diphthalimidodiethylammonium hydrogen phthalate (**1a**, see Experimental section) [21]. The deprotonation of **1a**, leading to **1**, and additional removal of the hydrogen phthalate anion were done by treatment with 10% aqueous solution of Na_2CO_3. This step was necessary for the removal of the prevailing traces of acetic acid as well. The similar reaction using acetonitrile (MeCN) as a solvent, described in [22] was unsuccessful, probably due to the low solubility of phthalic acid anhydride in MeCN. In the second step, the (4-bromomethyl)benzyl group was incorporated into the molecule of **1** to produce the intermediate **2**. The treatment of **1** with an excess of 1,4-bis(bromomethyl)benzene in refluxing MeCN with K_2CO_3 gave **2** in a moderate yield of 51%. The reaction was monitored by thin layer chromatography (TLC) and was completed in 30 min after dropwise addition of **1** to the refluxing mixture of 1,4-bis(bromomethyl)benzene and K_2CO_3. The main intermediate **2** was separated from the unreacted 1,4-bis(bromomethyl)benzene and unwanted by-product **2a** (Figure 5) by means of silica gel column chromatography (dichloromethane (DCHM): diethylether from 10:0 to 10:1). To eliminate the formation of the by-product **2a**, the reactants, *i.e.*, **1** and 1,4-bis(bromomethyl)benzene, should be mixed in the molar ratio of 1:2. Additionally, the mass spectra analysis revealed the presence of polymeric substances **2b** and **2c** depicted in Figure 5, which could be related to the utilization of non-dried solvents.

**Scheme 1.** The synthetic pathway leading to the final product **5**.
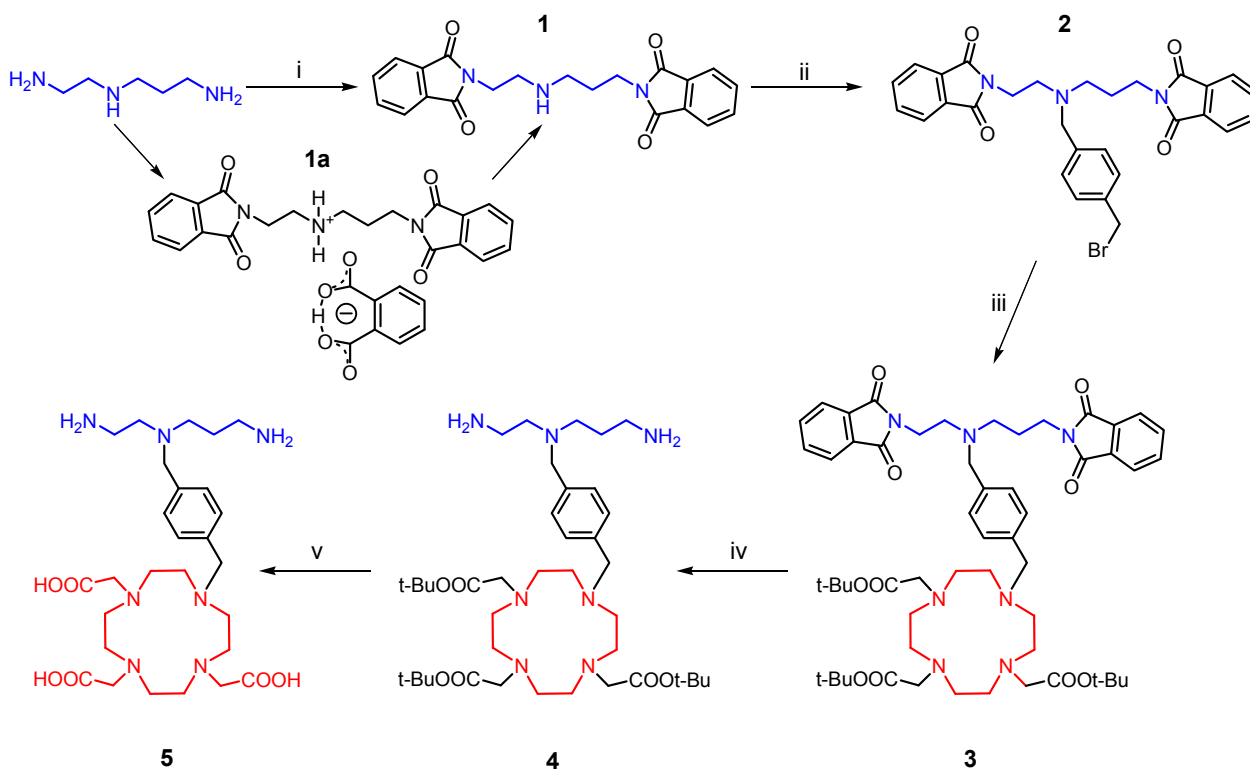
Reagents and Conditions: (i) phthalic acid anhydride, CH₃COOH, reflux 1 h; (ii) 1,4-bis(bromomethyl)benzene, K₂CO₃, MeCN, reflux 0.5 h; (iii) DO3A-tris(*t*-butyl ester), K₂CO₃, MeCN, reflux 4 h; (iv) hydrazine, EtOH, 25 °C, 12 h; (v) trifluoroacetic acid, dichloromethane, 25 °C, 12 h.

In the next step, the intermediate **2** was coupled with DO3A in the protected form of *t*-butyl esters. The reaction conditions were similar as for the synthesis of **2**, but the reactants were mixed almost immediately. The bromine atom substitution was completed after four hours of reflux resulting in the desired product **3** (see Scheme 1). The crude product was purified by silica gel column chromatography (CHCl₃–MeOH ≈ 25:1).

Further reaction steps involved the deprotection of the amino and carboxylate groups. Firstly, the elimination of the phthaloyl protection group was performed by the reaction with an excess of hydrazine in EtOH according to the literature procedure [23]. After stirring of this solution at room temperature for 12 h, precipitated phthalhydrazide was filtered off and the intermediate **4** was obtained after the evaporation of the solvent *in vacuo*. The rest of the phthalhydrazide present was removed by precipitation and filtration from the CHCl₃ solution of the residue.

To deprotect the carboxylic groups on the macrocycle, a familiar reaction with trifluoroacetic acid (TFA) in DCHM was used [24]. Overnight stirring at room temperature was satisfactory, because no signal of *t*-butyl groups was observed in the ¹H-NMR spectrum of the product obtained after the evaporation of all solvents. In the end, the free amino-carboxylate was purified by cation-exchange and then anion-exchange chromatography. The presence of the carboxylic groups was confirmed by the fragmentation pattern of the molecular ion *m/z* 566.50 in the MS² spectrum (Figure 4) which consists of peaks with the *m/z* = 18 difference which corresponds to the elimination of one, two or three water molecules from one, two or three carboxylates, respectively, in the molecule.

Figure 4. ESI mass spectra of intermediates **1**–**4** and the final product **5** showing the molecular peaks (adducts with H$^+$, Na$^+$ or K$^+$) together with MS^2 pattern of the molecular ion *m/z* 566.50 (**A**).
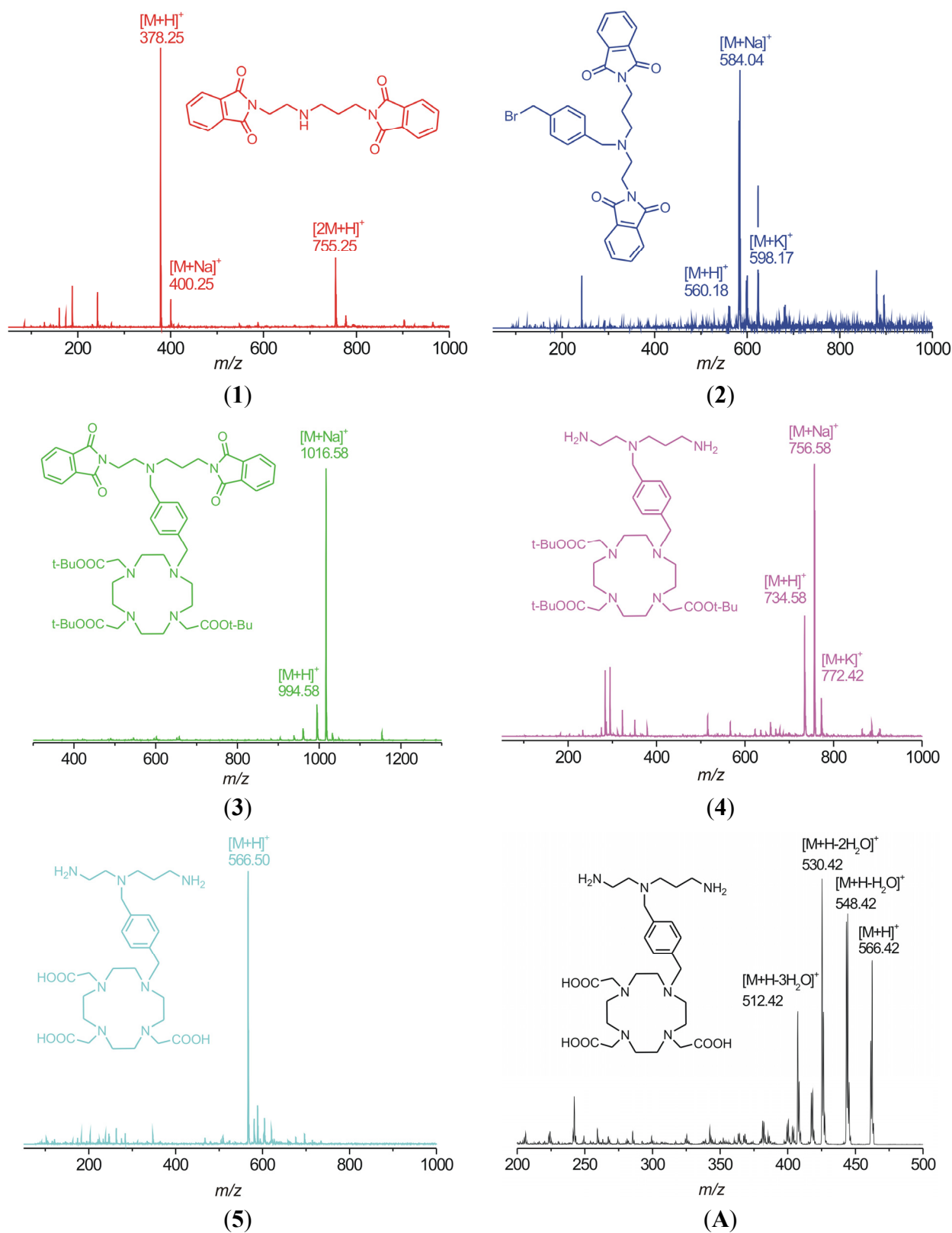
Figure 5. Suggested structures of species identified in the mass spectrum of the reaction mixture during the preparation of **2**. *m/z* values for **2a**: 856.25 [M+H]+, **2b**: 681.17 [M+H]+ and **2c**: 977.17 [M+H]+.


       2a   **2b**   **2c**
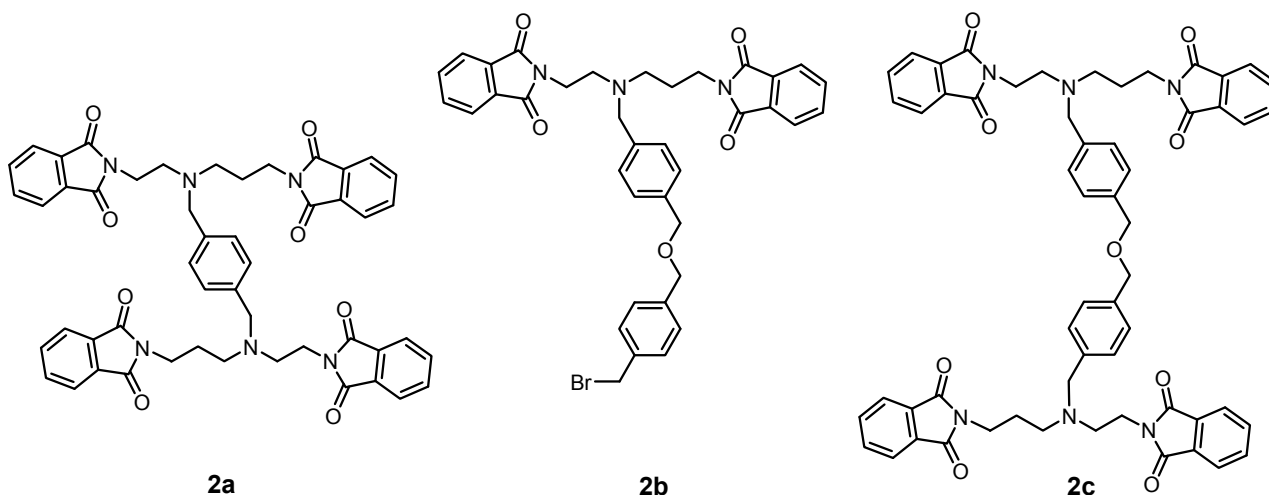
    With the aim to ambiguously characterize the composition and structure of the final product **5**, many attempts to prepare single-crystals suitable for single-crystal X-ray analysis were done, however, all without success. That is why we decided to optimize the geometry of **5** by means of theoretical calculations. Thus, the geometry of **5** was optimized at the density functional level of theory (DFT), using the B3LYB functional with the 6-311G * basis set. The optimized structure of **5** is depicted in Figure 6. The macrocyclic part of **5** has a cage-like structure with four nitrogen atoms, N1–N4, forming the basal plane (in blue colour in Figure 6) and three oxygen atoms forming the capping plane (in red colour in Figure 6). These two planes are nearly coplanar, forming a dihedral angle of 4.7°. The xylylen spacer with the polyamine part (N5–N7) is situated along the three acetic acid pendant arms and the dihedral angle between the plane formed by its benzene ring (in yellow colour in Figure 6) and basal, and capping plane is 57.7°, and 69.2°, respectively. As for the optimized geometry structure of **5**, the bond lengths and angles of the main individual parts are in good agreement with those determined for DOTA by single-crystal X-ray analysis [25], but only the macrocyclic cavity is slightly expanded (interatomic distances for N1–N3 and N2–N4 are 5.092 Å, and 4.634 Å, respectively). However, we are aware of the fact that the calculations were performed in vacuum and thus, the influence of non-covalent contacts on the molecular structure, playing also a significant role within the real crystal structure, were not taken into account. Nevertheless, the calculated geometry is typical for DOTA-like compounds, which is highly suitable for a lanthanide complexation [1].

    To better illustrate the progress of the whole synthetic pathway, a comparison of ^{13}C-NMR spectra of the precursor *N*-(2-aminoethyl)propane-1,3-diamine and all the described compounds **1**–**5** is shown in Figure 7. Based on the analysis of two-dimensional NMR spectra (selected spectra can be found in the Supplementary Materials Figures S1–S7), all signals in ^{13}C-NMR spectra were assigned to the corresponding atoms, whose numbering is displayed in each spectrum in Figure 7, except for the macrocyclic carbon atoms (in the spectra labeled as do3a), which were not sufficiently resolved even at higher temperature. But such signal broadening is typical for this type of cyclen-based compounds and it usually complicates especially ^{1}H-NMR spectra interpretation. Nevertheless, this ^{13}C-NMR

spectra comparison sufficiently documents each synthetic step because the presence of new signals corresponding to the new-bounded molecular parts (compounds **1–3**, synthetic steps i–iii in Scheme 1) and the absence of signals of the removed protecting groups (compounds **4** and **5**, synthetic steps iv and v in Scheme 1) are evident.

Figure 6. Geometry of **5** optimized at the B3LYB/6-311G * level of theory (*left*, **a**), showing selected least-square planes (*right*, **b**) going through the macrocyclic nitrogen atoms N1–N4 (blue), the carboxylic oxygen atoms O1–O3 (red) and the benzene ring (yellow). Hydrogen atoms are omitted for clarity (b).

(**a**)   (**b**)
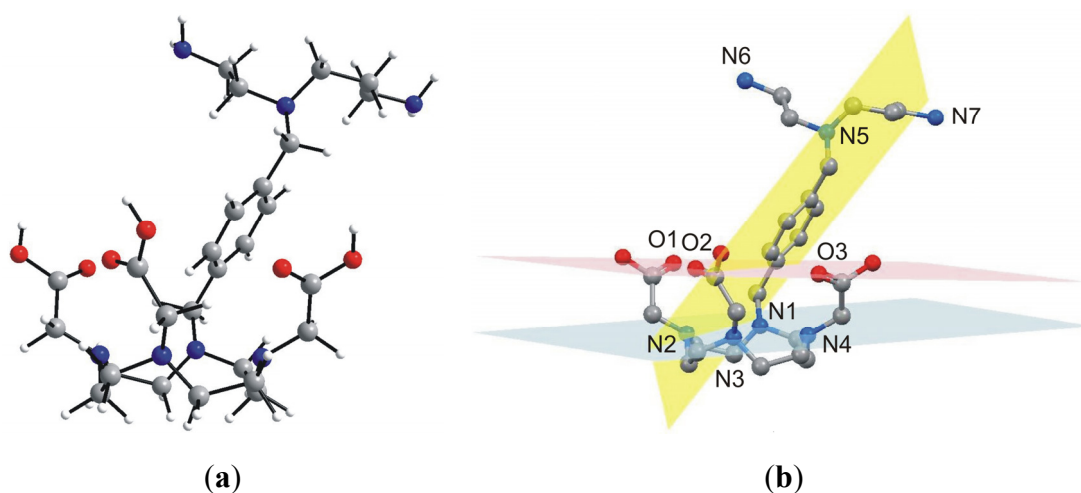
The described synthetic approach is relatively rapid, facile and provides pure products in good to moderate yields. The traces of acetic acid after the phthaloyl protection have to be removed otherwise undesired side-products are formed during the synthesis of **1**. Unfortunately, this operation significantly reduces the reaction yield. Especially, the yield of the synthesis of the intermediate **2** could be improved by increasing the excess of 1,4-bis(bromomethyl)benzene. Both phthaloyl and *t*-butyl protecting groups are easily and almost quantitatively removed providing the desired compounds, *i.e.*, **4**, and **5**, respectively. The prepared compound **5** itself may serve as a polydentate ligand involving the DO3A cavity suitable for complexation of lanthanide ions and a linear non-symmetrical triamine part for complexation of transition metal ions. Such a binuclear bimetallic system promises an interesting study of influence of the two metals and could provide combinations of different properties coming from different metals incorporated into a concrete complex (e.g., magnetic properties, spin-transition and luminescence). The xylylen spacer is not so common for linking DO3A with other molecules and it was proven that the xylylen substituent on the DO3A macrocycle has a positive effect on the lanthanide luminescence in the complex [14]. Moreover, the prepared compound scaffold is a versatile platform suitable for further structural modifications on the secondary amino groups. These secondary nitrogen atoms can be substituted with different pendant arms (acetate, methylphosphonate or methylenepyridine). This triamine part is also available for cyclization to produce a second macrocycle (possible different substituents) or a preparation of different types of Schiff bases can be taken into account as well. The described synthetic procedure is also applicable to *N*-(2-aminoethyl)ethane-1,3-diamine or *N*-(2-aminopropyl)propane-1,3-diamine instead of *N*-(2-aminoethyl)propane-1,3-diamine which would lead to more symmetrical species.

Figure 7. Comparison of ^{13}C-NMR spectra of the precursor *N*-(2-aminoethyl)propane-1,3-diamine (**A**), intermediates **1–4** and the final product **5**, together with signals assignment (do3a represents unnumbered carbon atoms of the macrocycle).
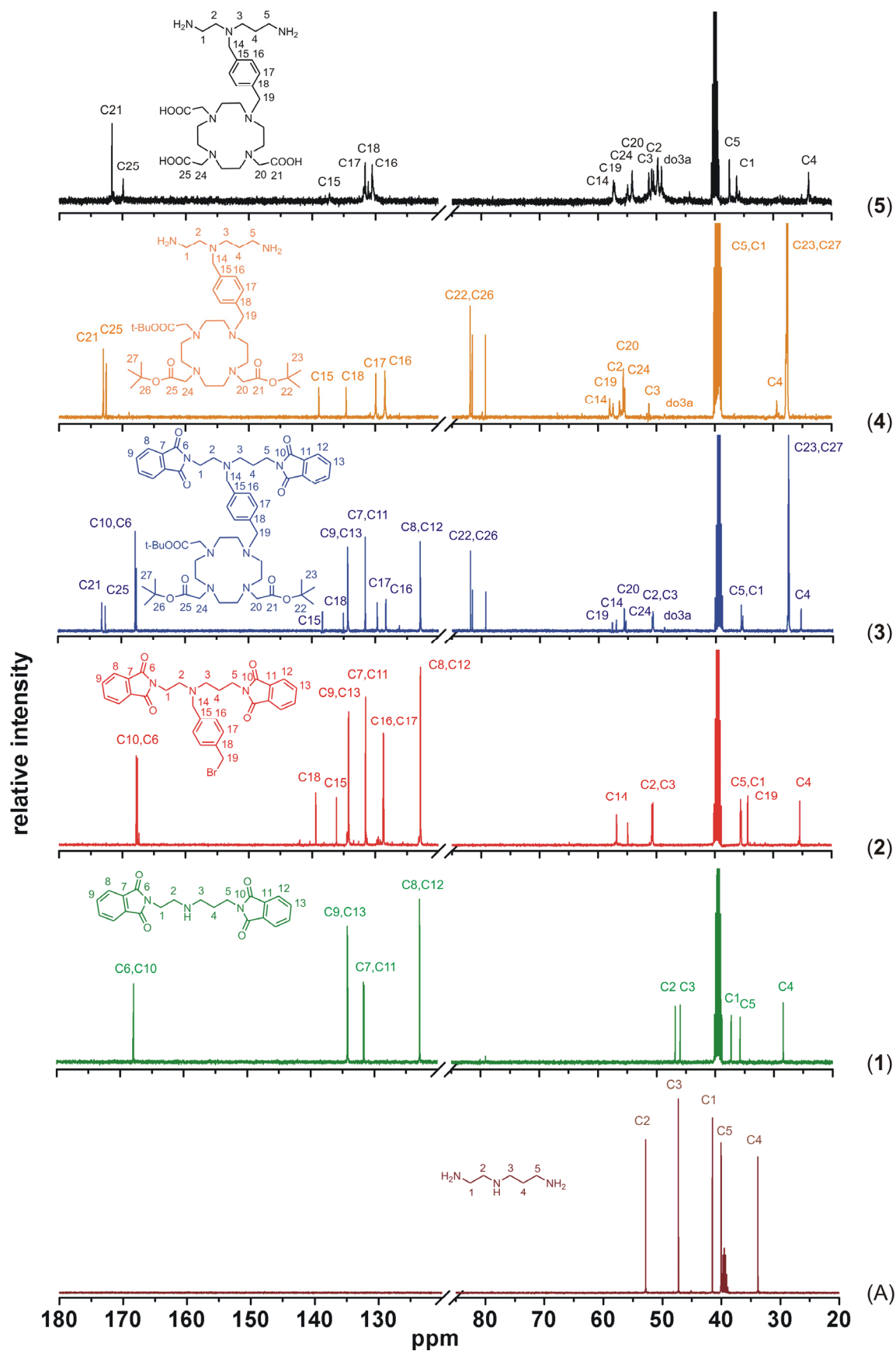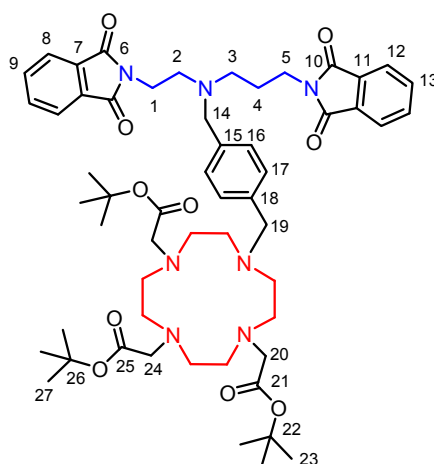
3. Experimental

3.1. General

Phthalic acid anhydride, *N*-(2-aminoethyl)propane-1,3-diamine, 1,4-bis(bromomethyl)benzene, hydrazine monohydrate, trifloroacetic acid and all solvents were purchased from commercial sources (Sigma–Aldrich, St. Louis, MO, USA; Penta, Prague, Czech Republic) and they were used as received. DO3A-tris(*tert*-butyl ester) hydrobromide was a gift from Dr. V. Kubíček from Charles University in Prague.

^{1}H- and ^{13}C-NMR spectra were recorded on a 400 MHz NMR Varian spectrometer (Varian, Santa Clara, CA, USA) at 25 °C and 85 °C (^{1}H-NMR spectra of compound **3**–**5**): [1]H 399.95 MHz, dimethyl sulfoxide-d_6 (DMSO, residual solvent peak) δ = 2.50 ppm, [13]C 100.60 MHz, DMSO (residual solvent peak) δ = 39.51 ppm. Multiplicity of the signals is indicated as follows: s—singlet, d—doublet, t—triplet, qr—quartet, q—quintet, m—multiplet, br—broad. The deuterated solvent DMSO-d_6 from Sigma Aldrich was used as received. The atom numbering scheme used for NMR data interpretation of all described compounds is shown in Figure 8.

Figure 8. Schematic representation of the intermediate **3**, together with the atom numbering used for the interpretation of NMR spectra of all intermediates as well as the final product **5**.

The carbon as well as hydrogen atoms were assigned according to the spectra obtained from two-dimensional correlation experiments ^{1}H–^{1}H gs-COSY, [1]H–[13]C gs-HMQC and [1]H–[13]C gs-HMBS (gs = gradient selected, COSY = correlation spectroscopy, HMQC = heteronuclear multiple quantum coherence and HMBC = heteronuclear multiple bond coherence). Examples of two-dimensional NMR spectra can be found in Supplementary Materials (Figures S1–S7). Mass spectra were measured on an LCQ Fleet Ion Mass Trap mass spectrometer (Thermo Scientific, Waltham, MA, USA) equipped with an electrospray ion source and 3D ion-trap detector in the positive mode. Elemental analyses (C, H, N) were performed on a Flash 2000 CHNS-O Elemental Analyzer (Thermo Scientific). Elemental analysis for compounds **4** and **5** was not done due to its hydroscopic character. Merck (Darmstadt, Germany) aluminum foils with silica gel 60 F254 impregnated with a fluorescent dye were used for thin layer chromatography.

Theoretical calculations at the DFT level were used to optimize the geometry of the final product **5**. The calculations were performed with a Gaussian 03 program [26] based on the B3LYP functional with the 6-311G * basis set.

3.2. (2-Phthalimidoethyl)(3-phthalimidoprop-1-yl)amine (**1**)

Compound **1** was synthesized according to a slightly modified literature procedure [20,21]. The solid obtained after crystallization from EtOH (22.6 g) was dissolved in CHCl$_3$ (200 mL) and extracted twice with 10% aqueous solution of Na$_2$CO$_3$, once with water and dried over anhydrous Na$_2$SO$_4$. The desired product was obtained after the evaporation of the solvent in a form of a pale yellow crystalline solid (15.1 g; 69% yield based on 7.04 g of *N*-(2-aminoethyl)propane-1,3-diamine). The compound **1a** was obtained after the evaporation of EtOH mother liquor and crystallization from MeOH (1.20 g).

(**1a**): NMR (DMSO): ^{1}H δ 1.91 (H4, 2H, m); 2.99 (H3, 2H, m); 3.19 (H2, 2H, t, $^3J_{HH}$ = 5.7 Hz); 3.63 (H5, 2H, t, $^3J_{HH}$ = 6.7 Hz); 3.85 (H1, 2H, t, $^3J_{HH}$ = 5.7 Hz); 7.49 (CH phthalate, 2H, m); 7.81–7.87 (H8, H9, H12, H13, 8H, m); 8.12 (CH phthalate, 2H, m); ^{13}C{^{1}H} δ 25.12 (C4, 1C, s); 34.44 (C5, 1C, s); 34.83 (C1, 1C, s); 44.74 (C3, 1C, s); 45.28 (C2, 1C, s); 123.03 (C12, 2C, s); 123.10 (C8, 2C, s); 130.30 (CH phthalate, 2C, s); 131.71 (C11, 2C, s); 131.85 (C6, 2C, s); 132.38 (C phthalate, 2C, s); 134.39 (C13, 2C, s); 134.43 (C9, 2C, s); 134.82 (CH phthalate, 2C, s); 167.93 (C10, 2C, s); 168.00 (C6, 2C, s); 168.15 (CO phthalate, 2C, s).

(**1**): NMR (DMSO): ^{1}H δ 1.65 (H4, 2H, t, $^3J_{HH}$ = 7.0 Hz); 1.86 (NH, 1H, bs); 2.52 (H3, 2H, t, $^3J_{HH}$ = 7.0 Hz); 2.71 (H2, 2H, t, $^3J_{HH}$ = 6.5 Hz); 3.57 (H5, 2H, t, $^3J_{HH}$ = 7.0 Hz); 3.61 (H1, 2H, t, $^3J_{HH}$ = 6.5 Hz); 7.80–7.85 (H8, H9, H12, H13, 8H, m); ^{13}C{^{1}H} δ 28.43 (C4, 1C, s); 35.78 (C5, 1C, s); 37.30 (C1, 1C, s); 46.00 (C3, 1C, s); 46.84 (C2, 1C, s); 122.85 (C12, 2C, s); 122.90 (C8, 2C, s); 131.62 (C11, 2C, s); 131.73 (C7, 2C, s); 134.19 (C13, 2C, s); 134.26 (C9, 2C, s); 167.90 (C10, 2C, s); 167.96 (C6, 2C, s); MS(+): *m/z* 378.25 [M+H]$^+$, 400.25 [M+Na]$^+$, 755.25 [2M+H]$^+$; elemental analysis for C$_{21}$H$_{19}$N$_3$O$_4$, M_r = 377.39, found (calculated): C 66.93 (66.83); H 5.12 (5.07); N 11.09 (11.13).

3.3. (2-Phthalimidoethyl)(3-phthalimidoprop-1-yl)(4-bromomethylbenzyl)amine (**2**)

1,4-bis(Bromomethyl)benzene (4.5 g, 17.0 mmol, 2.2 eqv.) and anhydrous K$_2$CO$_3$ (6.10 g, 44.2 mmol, 5.6 eqv.) were placed in the two-neck 250 mL round bottom flask and MeCN (100 mL) was added. One neck was equipped with a spiral condenser and the second neck with a dropping funnel containing the solution of **1** (3.0 g, 7.9 mmol) in CHCl$_3$ (20 mL). The mixture in the flask was heated to reflux under stirring and the solution was added dropwise during 30 min. The reaction was monitored by TLC (SiO$_2$, ethyl acetate-heptane 1:1, R_f = 0.5). For completion of the reaction, the mixture was refluxed for additional 30 min and then it was cooled down to room temperature. The solution was filtered through an S4 glass frit and the solvents were removed under reduced pressure. The crude product was purified by silica gel chromatography (DCHM–diethylether from 10:0 to 10:1). The desired compound was obtained after the evaporation of all solvents as a colorless solid (2.28 g, 51% yield). NMR (DMSO): ^{1}H δ 1.72 (H4, 2H, q, $^3J_{HH}$ = 7.0 Hz); 2.49 (H3, 2H, m); 2.58 (H2, 2H, t, $^3J_{HH}$ = 5.7 Hz); 3.49 (H14, 2H, s); 3.55 (H5, 2H, t, $^3J_{HH}$ = 7.0 Hz); 3.62 (H1, 2H, t, $^3J_{HH}$ = 5.9 Hz);

4.53 (H19, 2H, s); 7.05 (H16–H17, 4H, AA'BB'); 7.82 (H8,H9,H12,H13, 8H, m); ^{13}C{^{1}H} δ 25.45 (C4, 1C, s); 34.36 (C19, 1C, s); 35.47 (C1, 1C, s); 35.60 (C5, 1C, s); 50.60 (C3, 1C, s); 50.77 (C2, 1C, s); 56.81 (C14, 1C, s); 122.89 (C8, C12, 4C, s); 128.68 (C17, 2C, s); 128.77 (C16, 2C, s); 131.57 (C7, C11, 4C, m); 134.25 (C9, C13, 4C, m); 136.16 (C15, 1C, s); 139.41 (C18, 1C, s); 167.65 (C6, 2C, s); 167.82 (C10, 2C, s); MS (+): *m/z* 560.18 [M+H]$^{+}$, 584.08 [M+Na]$^{+}$, 598.17 [M+K]$^{+}$; elemental analysis for $C_{29}H_{26}BrN_3O_4$, M_r = 560.44, found (calculated): C 61.63 (62.15); H 4.72 (4.68); N 7.15 (7.50), Br 15.20 (14.26).

3.4. 1-{4-[(2-Phthalimidoethyl)(3-phthalimidoprop-1-yl)aminomethyl]phenylmethyl}-4,7,10-tris(t-butoxycarbonylmethyl)-1,4,7,10-tetraazacyclododecane (**3**)

Compound **3** was synthesized according to the modified literature procedure [27]. DO3A-tris(*t*-butyl ester) hydrobromide (1.59 g, 2.67 mmol) and anhydrous K_2CO_3 (1.94 g, 14.05 mmol, 5 eqv.) were placed into a 250 mL round bottom flask and MeCN (150 mL) was added. The mixture was heated to reflux under stirring. The solution of **2** (1.57 g, 2.81 mmol, 1.05 eqv.) in MeCN (20 mL) in a syringe was added dropwise in 5 min. The reaction mixture was refluxed for other 4 h and then it was cooled down to room temperature. The inorganic salts were filtered off on an S4 glass frit and the filtrate was evaporated under reduced pressure. The crude product was purified by silica gel column chromatography (CHCl$_3$–MeOH = 25:1). The desired compound was obtained after the evaporation of the solvents as a light yellow solid foam (2.55 g, 96% yield). NMR (DMSO): ^{1}H δ 1.42 (H23, 18H, s); 1.43 (H27, 9H, s); 1.74 (H4, 2H, q, $^{3}J_{HH}$ = 7.2 Hz); 2.45 (CH$_2$-do3a, 12H, bs); 2.52 (H3, 2H, t, $^{3}J_{HH}$ = 7.2 Hz); 2.62 (H2, 2H, t, $^{3}J_{HH}$ = 6.3 Hz); 3.01 (CH$_2$-do3a, 4H, bs); 3.08 (H20, H24, 6H, m); 3.51 (H14, H19, 4H, bs); 3.55 (H5, 2H, t,$^{3}J_{HH}$ = 7.2 Hz); 3.63 (H1, 2H, t, $^{3}J_{HH}$ = 6.3 Hz); 7.07 (H16, H17, 4H, bs); 7.73–7.82 (H8, H9, H12, H13, 8H, m); ^{13}C{^{1}H} δ 25.47 (C4, 1C, s); 27.53 (C27, 3C, s); 27.63 (C23, 6C, s); 35.43 (C1, 1C, s); 35.67 (C5, 1C, s); 48.76 (CH$_2$-do3a, 8C, bs); 50.73 (C3, 1C, s); 50.86 (C2, 1C, s); 55.36 (C24, 1C, s); 55.64 (C20, 2C, s); 56.98 (C14, 1C, s); 57.67 (C19, 1C, s); 81.55 (C26, 1C, s); 81.86 (C22, 2C, s); 122.88 (C12, 2C, s); 122.95 (C8, 2C, s); 128.35 (C16, 2C, s); 129.71 (C17, 2C, s); 132.57 (C11, 2C, s); 131.67 (C7, 2C, s); 134.34 (C13, 2C, s); 134.36 (C9, 2C, s); 135.04 (C18, 1C, s); 138.34 (C15, 1C, s); 167.66 (C6, 2C, s); 167.86 (C10, 2C, s); 172.55 (C25, 1C, s); 173.14 (C21, 2C, s); MS(+): *m/z* 994.58 [M+H]$^{+}$, 1016.58 [M+Na]$^{+}$; elemental analysis for $C_{55}H_{75}N_7O_{10}$·1.6CHCl$_3$, M_r = 1173.29, found (calculated): C 57.25(57.36); H 6.68 (6.51); N 8.30 (8.27).

3.5. 1-{4-[(2-Aminoethyl)(3-aminoprop-1-yl)aminomethyl]phenylmethyl}-4,7,10-tris(t-butoxycarbonyl-methyl)-1,4,7,10-tetraazacyclododecane (**4**)

The synthesis of **4** was done according to the literature procedure [23] with minor modifications. Absolute EtOH was not used. The rest of phthalhydrazide present in the residue was removed by filtration of the CHCl$_3$ solution (the residue dissolved in 20 mL of CHCl$_3$) through an S4 glass frit. The desired product was obtained as yellow oil (0.70 g, 95% yield based on 1.00 g of **3**). NMR (DMSO): ^{1}H δ 1.46 (H23, H27, 27H, m); 1.55 (H4, 2H, q, $^{3}J_{HH}$ = 6.8 Hz); 2.46 (H2, H3, 4H, m); 2.55 (CH$_2$-do3a, 12H, bm); 2.60 (H1, H5, 4H, m); 3.08 (CH$_2$-do3a, 4H, bs); 3.13 (H20, H24, 6H, bs); 3.53 (H14, 2H, s), 3.62 (H19, 2H, s); 7.27 (H16–17, 4H, AA'BB'); ^{13}C{^{1}H} δ 27.53 (C27, 3C, s); 27.64 (C23, 6C, s); 29.39 (C4, 1C, s); 39.26 (C1, 1C, s); 39.84 (C5, 1C, s); 48.58 (CH$_2$-do3a, 4C, bs); 51.26

(C3, 1C, s); 51.60 (CH$_2$-do3a, 4C, bs); 55.41 (C24, 1C, s); 55.65 (C20, 2C, s); 56.32 (C2, 1C, s); 57.43 (C19, 1C, s); 58.00 (C14, 1C, s); 81.52 (C26, 1C, s); 81.87 (C22, 2C, s); 128.50 (C16, 2C, s); 129.93 (C17, 2C, s); 134.63 (C18, 1C, s); 138.93 (C15, 1C, s); 172.56 (C25, 1C, s); 173.01 (C21, 2C, s); MS (+): *m/z* 734.58 [M+H]$^+$, 756.58 [M+Na]$^+$, 772.42 [M+K]$^+$.

3.6. 1-{4-[(2-Aminoethyl)(3-aminoprop-1-yl)aminomethyl]phenylmethyl}-4,7,10-tris(carboxymethyl)-1,4,7,10-tetraazacyclododecane (**5**)

The deprotection of the *t*-butyl ester groups was done according to the literature procedure using TFA in DCHM [24]. The reactant **4** (0.70 g, 0.95 mmol) was dissolved in DCHM (5 mL) in a 50 mL round bottom flask and TFA (5 mL) was added dropwise under cooling to 0 °C in a water/ice bath. A slightly yellow solution was formed and additionally stirred at room temperature for 12 h. The solvents were removed *in vacuo*. The residue was purified on a cation-exchange column (Dowex 50, H$^+$-form, 50 mL, elution with water and 15% aq. HCl) and an anion-exchange column (Dowex 1 × 8, OH$^-$-form, 100 mL, elution with water and 15% aq. HCl). The solvent was removed under reduced pressure, and the residue was dissolved in MeOH. The desired compound was obtained after the evaporation of the MeOH solution as a yellow solid in the form of the corresponding hydrochloride (0.644 g, 90% yield). NMR (DMSO): ^{1}H δ 1.90 (H4, 2H, q, $^3J_{HH}$ = 7.2 Hz); 2.76 (H3, 2H, t, $^3J_{HH}$ = 7.2 Hz); 2.87 (H5, 2H, t, $^3J_{HH}$ = 7.2 Hz); 2.93 (H2, 2H, t, $^3J_{HH}$ = 6.8 Hz); 3.05 (H1, 2H, t, $^3J_{HH}$ = 6.8 Hz); 3.10 (CH$_2$-do3a, 4H, bs); 3.20 (CH$_2$-do3a, 8H, m); 3.28 (CH$_2$-do3a, 4H, bs); 3.44 (H20, 4H, bs); 3.87 (H14,H24, 4H, bs); 4.34 (H19, 2H, s); 7.38–7.56 (H16–17, 4H, AA'BB'); ^{13}C{^{1}H} δ 23.51 (C4, 1C, s); 35.82 (C1, 1C, s); 37.08 (C5, 1C, s); 48.70 (CH$_2$-do3a, 2C, bs); 49.30 (CH$_2$-do3a, 4C, bs); 50.08 (C2, 1C, s); 50.35 (C3, 1C, s); 50.87 (CH$_2$-do3a, 2C, bs); 53.72 (C20, 2C, s); 54.47 (C24, 1C, s); 56.71 (C19, 1C, s); 56.93 (C14, 1C, s); 130.08 (C16, 2C, s); 130.70 (C18, 2C, s); 131.19 (C17, 2C, s); 136.83 (C15, 1C, s); 169.44 (C25, 1C, s); 171.22 (C21, 2C, s); MS (+): *m/z* 566.50 [M+H]$^+$; MS^2 (+): *m/z* 548.22 [M+H–H$_2$O]$^+$, 530.42 [M+H–2H$_2$O]$^+$, 512.42 [M+H–3H$_2$O]$^+$.

4. Conclusions

The compound 1-{4-[(2-aminoethyl)(3-aminoprop-1-yl)aminomethyl]phenylmethyl}-4,7,10-tris-(carboxymethyl)-1,4,7,10-tetraazacyclododecane (**5**) was prepared and characterized with the aim to design a molecule which could be usable as a versatile polydentate ligand in the field of coordination chemistry. The molecule combines a macrocyclic part which could be suitable for the complexation of lanthanides and linear amine part usable for the complexation of other (transition) metal ions. All the intermediates as well as final product were thoroughly characterized. The reaction conditions for the preparation of the intermediate **2** were investigated and optimized, while the other synthetic steps proceeded according to the slightly modified previously described literature procedures. The xylylen linker was chosen for the connection of the polyamino and DO3A parts due to its rigidity and short length providing a possible interaction between the two metal centers in a bimetallic complex, good synthetic availability. Surprisingly, such a motif is not so common in the literature. Altogether, the prepared compound **5** represents a versatile ligand with at least two sites of possible coordination of a lanthanide and transition metal. Further structural modifications on secondary amino groups are straightforward and could provide an additional possibility of the system transformation/tuning.

Supplementary Materials

Supplementary materials, containing 2D NMR spectra of **1–5** (Figures S1–S7), can be accessed at: http://www.mdpi.com/1420-3049/18/11/13940/s1.

Acknowledgments

Conflicts of Interest

The authors declare no conflict of interest.

References

1. *The Chemistry of Contrast Agents in Medicinal Magnetic Resonance Imaging*; Merbach, A., Helm, L., Tóth, É., Eds.; John Wiley & Sons: Chichester, UK, 2013.
2. Montgomery, G.P.; Murray, B.S.; New, E.J.; Pal, R.; Parker, D. Cell-penetrating metal complex optical probes: Targeted and responsive systems based on lanthanide luminescence. *Acc. Chem. Res.* **2009**, *42*, 925–937.
3. *Contrast Agents III, Radiopharmaceuticals—From Diagnosticts to Therapeutics*; Krause, W., Ed.; Springer: Heidelberg, Germany, 2005.
4. Tweedle, M.F. Peptide-targeted diagnostics and radiotherapeutics. *Acc. Chem. Res.* **2009**, *42*, 958–968.
5. Atmani, C.; El Hajj, F.; Benmansour, S.; Marchivie, M.; Triki, S.; Conan, F.; Patinec, V.; Handel, H.; Dupouy, G.; Gómez-García, C.J. Guidelines to design new spin crossover materials. *Coord. Chem. Rev.* **2010**, *254*, 1559–1569.
6. Develay, S.; Tripier, R.; Bernier, N.; Le Baccon, M.; Patinec, V.; Serratrice, G.; Handel, H. Cyclen based bis-macrocyclic ligands as phosphates receptors. A potentiometric and NMR study. *Dalton Trans.* **2005**, doi:10.1039/B507819A.
7. König, B.; Svoboda, J. Azamacrocyclic systems with different supramolecular function. In *Macrocyclic Chemistry: Current Trends and Future Perspectives*; Gloe, K., Ed.; Springer: Dordrecht, The Netherlands, 2005; pp. 87–103.
8. Caravan, P. Protein-targeted gadolinium-based Magnetic Resonance Imaging (MRI) contrast agents: Design and mechanism of action. *Acc. Chem. Res.* **2009**, *42*, 851–862.
9. Bonnet, C.S.; Buron, F.; Caillé, F.; Shade, Ch.M.; Drahoš, B.; Pellegatti, L.; Zhang, J.; Villette, S.; Helm, L.; Pichon, Ch.; *et al.* Pyridine-based lanthanide complexes combining MRI and NIR luminescence activities. *Chem. Eur. J.* **2012**, *18*, 1419–1431.
10. Wängler, C.; Wängler, B.; Eisenhut, M.; Haberkorn, U.; Mier, W. Improved syntheses and applicability of different DOTA building blocks for multiply derivatized scaffolds. *Bioorg. Med. Chem.* **2008**, *16*, 2606–2616.

11. Rudovsky, J.; Botta, M.; Hermann, P.; Hardcastle, K.I.; Lukeš, I.; Aime, S. PAMAM dendrimeric conjugates with a Gd-DOTA phosphinate derivative and their adducts with polyaminoacids: The Interplay of global motion, internal rotation, and fast water exchange. *Bioconjug. Chem.* **2006**, *17*, 975–987.

12. Jauregui, M.; Perry, W.S.; Allain, C.; Vidler, L.R.; Willis, M.C.; Kenwright, A.M.; Snaith, J.S.; Stasiuk, G.J.; Lowe, M.P.; Faulkner, S. Changing the local coordination environment in mono- and bi-nuclear lanthanide complexes through "click" chemistry. *Dalton Trans.* **2009**, doi:10.1039/B911588A.

13. Botta, M.; Tei, L. Relaxivity enhancement in macromolecular and nanosized Gd^{III}-based MRI contrast agents. *Eur. J. Inorg. Chem.* **2012**, *12*, 1945–1960.

14. Pope, S.J.A.; Kenwright, A.M.; Boote, V.A.; Faulkner, S. Synthesis and luminescence properties of dinuclear lanthanide complexes derived from covalently linked macrocyclic ligands. *Dalton Trans.* **2003**, doi:10.1039/B309115E.

15. Bridger, G.J.; Skerlj, R.T.; Hernandez-Abad, P.E.; Bogucki, D.E.; Wang, Z.; Zhou, Y.; Nan, S.; Boehringer, E.M.; Wilson, T.; Crawford, J.; *et al.* Synthesis and structure-activity relationships of Azamacrocyclic C-X-C chemokine receptor 4 antagonists: Analogues containing a single azamacrocyclic ring are potent inhibitors of T-Cell tropic (X4) HIV-1 replication. *J. Med. Chem.* **2010**, *53*, 1250–1260.

16. Gupta, S.K. Method for inducing chemotaxis in endothelial cells by administering stromal cell derived factor-1alpha. U.S. Patent 2002/0107195 A1, 8 August 2002.

17. Luengo, J.I.; Price, A.T.; Shaw, A.; Wiggall, K. CXCR-4 receptor antagonists and thrombopoietin mimetics. WIPO Patent WO/2000/066112, 9 November 2000.

18. Livramento, J.B.; Sour, A.; Borel, A.; Merbach, A.E.; Tóth, É. A starburst-shaped heterometallic compound incorporating six densely packed Gd^{3+} ions. *Chem. Eur. J.* **2006**, *12*, 989–1003.

19. Li, W.S.; Luo, J.; Chen, Z.N. A self-assembly heterotrinuclear gadolinium(III)–iron(II) complex as a MRI contrast agent. *Inorg. Chem. Commun.* **2011**, *14*, 1898–1900.

20. Ng, C.Y.; Motekaitis, R.J.; Martell, A.E. New multidentate ligands. 18. Synthesis of 1,4-Bis(bis(2-aminoethyl)aminomethyl)benzene: Binuclear chelating tendencies and mixed-ligand binuclear chelate formation. *Inorg. Chem.* **1979**, *18*, 2982–2986.

21. Barrett, D.M.Y.; Kahwa, I.A.; Mague, J.T.; McPherson, G.L. Preparations, crystal structures, and unusual proton NMR characteristics of some phthalimides. *J. Org. Chem.* **1995**, *60*, 5946–5953.

22. Kang, S.O.; Powell, D.; Day, V.W.; Bowman-James, K. Trapped Bifluoride. *Angew. Chem. Int. Ed.* **2006**, *45*, 1921–1925.

23. Gali, H.; Prabhu, K.R.; Karra, S.R.; Katti, K.V. Facile Ring-opening reactions of Phthalimides as a new strategy to synthesize amide-functionalized phosphonates, primary phosphines, and bisphosphines. *J. Org. Chem.* **2000**, *65*, 676–680.

24. Drahoš, B.; Kotek, J.; Císařová, I.; Hermann, P.; Helm, L.; Lukeš, I.; Tóth, É. Mn^{2+} complexes with 12-membered pyridine based macrocycles bearing carboxylate or phosphonate pendant arm: Crystallographic, thermodynamic, kinetic, redox, and ^{1}H/^{17}O relaxation studies. *Inorg. Chem.* **2011**, *50*, 12785–12801.

25. Aime, S.; Barge, A.; Bruce, J.I.; Botta, M.; Howard, J.A.K.; Moloney, J.M.; Parker, D.; de Sousa, A.S.; Woods, M. NMR, relaxometric, and structural studies of the hydration and exchange dynamics of cationic lanthanide complexes of macrocyclic tetraamide ligands. *J. Am. Chem. Soc.* **1999**, *121*, 5762–5771.

26. Frisch, M.J.; Trucks, G.W.; Schlegel, H.B.; Scuseria, G.E.; Robb, M.A.; Cheeseman, J.R.; Montgomery, J.A., Jr.; Vreven, T.; Kudin, K.N.; Burant, J.C.; *et al. Gaussian 03, Revision C.02*; Gaussian, Inc.: Wallingford, CT, USA, 2004.

27. Aime, S.; Gianolio, E.; Terreno, E.; Giovenzana, G.B.; Pagliarin, R.; Sisti, M.; Palmisano, G.; Botta, M.; Lowe, M.P.; Parker, D. Ternary Gd(III)L-HSA adducts: Evidence for the replacement of inner-sphere water molecules by coordinating groups of the protein. Implications for the design of contrast agents for MRI. *J. Biol. Inorg. Chem.* **2000**, *5*, 488–497.

Sample Availability: Samples of the compounds **1**–**5** are available from the authors.

Příloha P11

B. Drahoš, I. Šalitroš, R. Herchel,
First step in preparation of multifunctional spin crossover material based on Fe(II) complex of cyclam-based ligand. Magnetism and DFT studies.
Inorg. Chim. Acta **2019**, *495*, 118921.
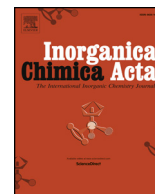
Research paper

First step in preparation of multifunctional spin crossover material based on Fe(II) complex of cyclam-based ligand. Magnetism and DFT studies

Bohuslav Drahoš[a,*], Ivan Šalitroš[a,b], Radovan Herchel[a]

[a] *Department of Inorganic Chemistry, Faculty of Science, Palacký University, 17. listopadu 12, CZ-771 46 Olomouc, Czech Republic*
[b] *Department of Inorganic Chemistry, Faculty of Chemical and Food Technology, Slovak University of Technology in Bratislava, Bratislava SK-81237, Slovakia*

A B S T R A C T

With the aim to make the first step in preparation of magnetic multifunctional material combining spin crossover (SCO) together with single-molecule magnet (SMM) properties in one molecule (polynuclear complex), a specially designed ligand **L-NH₂** (1,8-bis(4-aminobenzyl)-4,11-bis(pyridin-2-ylmethyl)-1,4,8,11-tetra-azacyclotetradecane) was synthesized. It contains (i) macrocyclic cyclam core substituted with two 2-pyridylmethyl pendant arms suitable for complexation of Fe(II), because such system was previously proven to provide SCO, and (ii) two *p*-aminobenzyl pendant arms introducing NH₂ groups suitable for consequent attachment of SMM molecule (e.g. transformation to functional groups for selective complexation of other metals). Furthermore, Fe(II) complex [Fe(**L-NH₂**)]Cl₂·2.5H₂O was prepared and characterized. Unfortunately, according to the magnetic measurements, SCO behavior was not observed and the complex remained in high-spin state with relatively high magnetic anisotropy ($D = -17.7$ cm^{-1}, $E/D = 0.31$). This magnetic behavior was rationalized by the DFT computational study, which identified high-spin state as preferential for prepared complex in contrast to other structurally similar SCO systems with low-spin state preference. The most probable reason behind this difference appeared to be the electron-withdrawing effect of benzyl groups providing weaker ligand field of macrocyclic nitrogen donor atoms.

1. Introduction

In the field of molecular magnetism, spin crossover phenomenon (SCO) represent a very fascinating and strongly developing subject of interest. SCO compounds, usually octahedral complexes containing a central metal ion of 3d⁴–3d⁷ electronic valence shell configuration, show the spin transition between the low-spin state (LS, for Fe^{II} $S = 0$) and high-spin state (HS, for Fe^{II} $S = 2$) induced by different chemical or physical external constraints (in general *e.g.* by ligand and solvent effects or by temperature, pressure, magnetic field or light irradiation) [1]. When the constrain is temperature, the material is usually characterized by the critical temperature of the spin transition ($T_{1/2}$ defined as the temperature when the fraction of the complex in HS state is equal to that in LS state) and its abruptness depending of the cooperative effect. The SCO compounds can be utilized in many remarkable applications including the miniaturization of components used in the construction of electronic devices such as high capacity memories (at the molecular level), molecular switches or low-energy demanding displays [2].

The more recent research has been extended to development of magnetic multifunctional materials which could combine two or more functionalities of interest. Here concretely SCO can be combined with e.g. magnetic coupling, liquid crystalline properties, host-quest interactions, non-linear optics, electric conductivity or luminescence [3].

Probably one of the most interesting magnetic property of interest represents Single-Molecule Magnets (SMMs) [4,5], which are compounds showing slow relaxation of magnetization based on pure molecular origin (no long range ordering typical for bulk magnets) and thus, they behave as "nanomagnets". Furthermore, these compounds could find many spectacular applications in different field of interest, e.g. in high-density storage media, in spintronics or quantum computing etc. [6]

Surprisingly, there is very little known about compounds combining both above-mentioned properties – i.e. SMM together with SCO. Such a combination of properties opens many questions - how the spin transition will influence the SMM properties, the relaxation mechanisms etc. So far, only a few examples of systems combining SMM and SCO have been described previously. Single-chain magnet (SCM) based on {Mn^{III}(**saltmen**)}₂ unit was combined with spin-crossover unit [Fe^{II}(**L1**)(CN)₂] in [{Mn(**saltmen**)}₂{Fe(**L1**)(CN)₂}](ClO₄)₂·0.5C₄H₁₀O·0.5H₂O ($U_{eff} = 13.9$ K, $\tau_0 = 1.1 \times 10^{-7}$ s, saltmen = *N,N'*-(1,1,2,2-tetra-methylethylene)bis(salicylideneiminate), Fig. 1) [7]. SMM Fe^{III} complex [Fe(**PNP**)Cl₂] (Fig. 1) displayed an unexpected $S = 5/2$ to $S = 3/2$ transition below 80 K with $U_{eff} = 47$–52 K, $\tau_0 = 2 \times 10^{-8}$–$6 \times 10^{-9}$ s [8], SMM properties can be switched on and off by light irradiation for [Fe(**1-propyltetrazole**)₆](BF₄) (505 and 850 nm, respectively, $U_{eff} = 22$ K, $\tau_0 = 4.2 \times 10^{-8}$ s) [9] and [Fe(**1-methyltetrazole**)₆](CF₃SO₃)₂ (green ligth 500–650 nm and red light 650–900 nm, respectively, $U_{eff} = 55$ K, $T_{1/2\downarrow} = 161$ K, $T_{1/2\uparrow} = 178$ K) [10], and SMM can
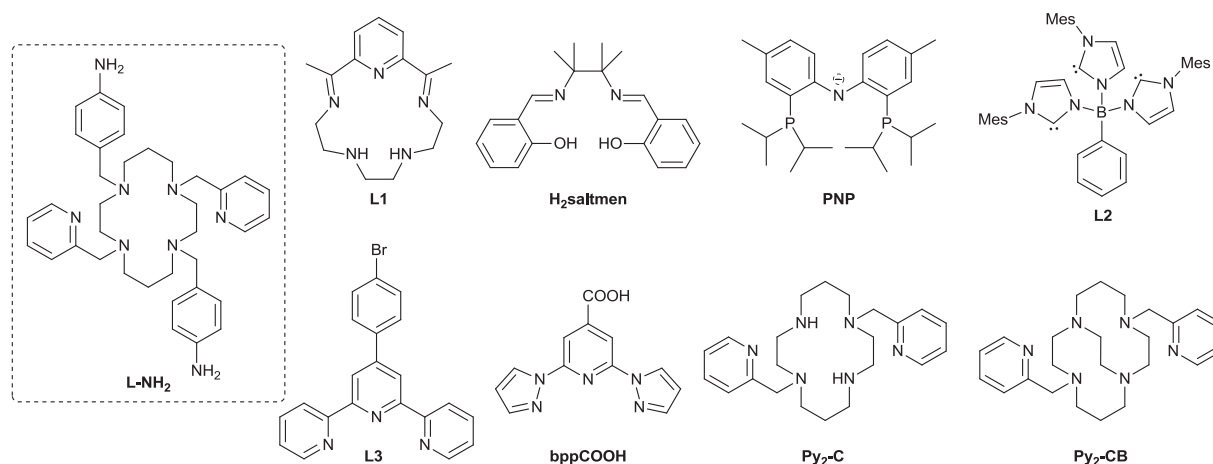

Fig. 1. Structural formulas of studied ligand **L-NH₂** and ligands discussed in the text.

be also switched on by light irradiation (white light) of carbene SCO complex [(**L2**)₃}Fe(N = PPh₃)] (Fig. 1, $T_{1/2} = 81$ K, $U_{eff} = 22$ K, $\tau_0 = 8.7 \times 10^{-7}$ s) [11].

Combination of field-induced SMM properties and SCO between $S = 3/2$ and $S = 1/2$ has been recently observed for tetragonal–pyramidal [Co(**3,4-lutidine**)₄Br]Br [12], and [Co(**L3**)₂] (DPAS)₂·DMF·2H₂O (Fig. 1) exhibited reversible on–off switching between SCO and SMM during crystal-to-crystal transformation (dehydration–rehydration process, DPAS⁻ = 4-(phenylamino)benzenesulfonate) [13]. The only one system containing combination of Fe(II) (SCO) and Co(II) (field-induced SMM) centers in one compound is [Fe₀.₉₂Co₀.₀₈(**bppCOOH**)₂](ClO₄)₂ (Fig. 1) [14].

One strategy how to obtain such a multifunctional compound is to combine required properties, here SCO with SMM, in one molecule or more exactly in one polynuclear complex. This requires preparation of specially designed ligands with two or more specific coordination sites suitable for complexation of either different transition metals or transition metals and lanthanides. However, such approach is quite challenging and often requires a careful molecular design and advanced organic syntheses.

In this work, a structurally new ligand **L-NH₂** (Fig. 1) was synthesized. It was based on cyclam part containing two pyridine pendant arms (**Py₂-C**, Fig. 1), because Fe(II) complexes of **Py₂-C** showed SCO, e.g. [Fe(**Py₂-C**)](BF₄)₂·H₂O ($T_{1/2} \sim 150$ K) [15], [Fe(**Py₂-C**)] (C(CN)₃)₂·2H₂O with $T_{1/2}\downarrow / T_{1/2}\uparrow = 136 / 145$ K and [Fe(**Py₂-C**)][Ni (CN)₄]·H₂O with $T_{1/2}\downarrow\uparrow = 85$ K [16], as well as Fe(II) complexes of the cross-bridged **Py₂-CB** [17] analogue (Fig. 1). This **Py₂-C** macrocyclic part was structurally modified with two *p*-aminobenzyl pendant arms in order to introduce NH₂ group, which could be consequently easily

transformed to various different functional groups allowing introduction of molecule with SMM properties. Furthermore Fe(II) complex of **L-NH₂** was prepared as well and its magnetic properties were investigated and discussed. Obtained results were supported by theoretical DFT calculations.

2. Experimental section

2.1. Materials and methods

The ligand **Py₂-C** [18] and 2-chloromethylpyridine [19] were synthesized according to the literature procedures. All the solvents (VWR International, Fontenay-sous-Blois, France) and other chemicals were purchased from commercial sources (Across Organics, Geel, Belgium and Sigma-Aldrich, St. Louis, MO, USA) and used as received.

Elemental analysis (C, H, N) was performed on a Flash 2000 CHNO-S analyzer (Thermo Scientific, Waltham, MA, USA). ¹H and ¹³C NMR spectra were recorded on a 400-MR NMR spectrometer (Varian, Palo Alto, CA, USA) at 25 °C: ¹H 399.95 MHz, chloroform-*d* (CDCl₃, tetramethylsilane) $\delta = 0.00$ ppm, ¹³C 100.60 MHz, (CDCl₃, residual solvent peak) $\delta = 77.0$ ppm. Multiplicity of the signals is indicated as follows: s – singlet, d – doublet, t – triplet, quin – quintet, m – multiplet. Deuterated solvent CDCl₃, containing 0.03% of TMS, from Sigma Aldrich was used as received. The atom numbering scheme used for NMR data interpretation is shown in Fig. 2. The carbon as well as hydrogen atoms were assigned according to the spectra obtained from two-dimensional correlation experiments ¹H–¹H gs-COSY, ¹H–¹³C gs-HMQC and ¹H–¹³C gs-HMBS (see Figs. S1–S4). The mass spectra were collected on an LCQ Fleet mass spectrometer (Thermo Scientific,
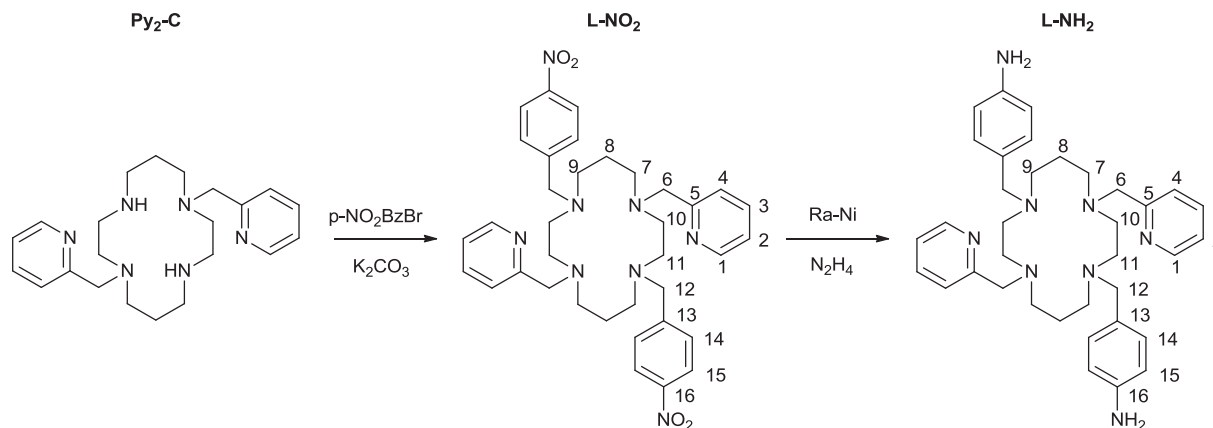

Fig. 2. Synthetic scheme of preparation of ligand **L-NH₂** together with atom numbering of both **L-NO₂** and **L-NH₂** used in ¹H/¹³C NMR data interpretation.

Waltham, MA, USA) equipped with an electrospray ion source and three-dimensional (3D) ion-trap detector in the positive mode. IR spectra were collected on Jasco FT/IR-4700 spectrometer (Jasco, Easton, MD, USA). Temperature and field dependence of the magnetization was measured using MPMS SQUID magnetometer (Quantum Design Inc., San Diego, CA, USA). The experimental data were corrected for diamagnetism and signal of the sample holder.

2.2. Syntheses

2.2.1. 1,8-bis(4-nitrobenzyl)-4,11-bis(pyridin-2-ylmethyl)-1,4,8,11-tetraazacyclotetradecane (L-NO₂)

Macrocycle **Py₂-C** (1.00 g, 2.61 mmol), *p*-nitrobenzylbromide (1.15 g, 5.32 mmol, 2.04 eqv.) and K_2CO_3 (1.80 g, 13.07 mmol, 5 eqv.) were suspended in 70 mL of CH_3CN and refluxed for 1 h. The progress of the reaction was monitored by mass spectrometry and therefore additional amount of *p*-nitrobenzylbromide (0.22 g, 1.02 mmol, 0.39 eqv.) and K_2CO_3 (1.80 g, 13.07 mmol, 5 eqv.) was added to the reaction mixture in 2 portions followed by 2x30 min reflux till only signal of disubstituted product was observed in the mass spectrum. The hot suspension was filtered on a glass frit and the filtrate was evaporated under reduced pressure. The residue was dissolved in 50 mL of $CHCl_3$, obtained solution was extracted three times with 50 mL of deionized water, organic phase was dried with anhydrous Na_2SO_4, filtered on a glass frit and evaporated under reduced pressure. Obtained red-brown oil was redissolved in 50 mL of hot CH_3CN and leave to slowly cool down to room temperature. Well-shaped crystals of the product were formed and separated by filtration on a glass frit (1.41 g, yield 82.5 %).

MS *m/z* (+): 653.46 ([**L** + H]$^+$, calcd. 653.36), 675.36 ([**L** + Na]$^+$, calcd. 675.34).

^{1}H NMR (CDCl₃): δ 1.78 (4H, quin, $^3J_{HH}$ = 6.9 Hz, H-8), 2.51 (4H, t, $^3J_{HH}$ = 6.9 Hz, H-9), 2.60 (4H, t, $^3J_{HH}$ = 6.9 Hz, H-7), 2.66 (8H, m, H-10 + H-11), 3.50 (4H, s, H-12), 3.62 (4H, s, H-6), 7.11 (2H, m, H-2), 7.39 (2H, d, $^3J_{HH}$ = 7.8 Hz, H-4), 7.46 (4H, m, AA′BB′, H-14), 7.53 (2H, m, H-3), 8.11 (4H, m, AA′BB′, H-15), 8.48 (2H, m, H-1).

^{13}C{^{1}H} NMR (CDCl₃): δ 23.83 (2C, C-8), 50.46 (2C, C-11), 50.97 (2C, C-10), 51.26 (2C, C-7), 51.77 (2C, C-9), 58.57 (2C, C-12), 61.18 (2C, C-6), 121.84 (2C, C-2), 122.81 (2C, C-4), 123.31 (4C, C-15), 129.20 (4C, C-14), 136.09 (2C, C-3), 146.89 (2C, C-16), 148.12 (2C, C-13), 148.89 (2C, C-1), 160.06 (2C, C-5).

2.2.2. 1,8-bis(4-aminobenzyl)-4,11-bis(pyridin-2-ylmethyl)-1,4,8,11-tetraazacyclotetradecane (L-NH₂)

Synthesis of **L-NH₂** was done according to modified literature procedure [20]. **L-NO₂** (1.41 g, 2.16 mmol) and hydrazine monohydrate (2.20 g, 43.20 mmol) were dissolved in 75 mL of hot CH_3OH. Raney-Ni (Ra-Ni) was added (ca 100 mg in form of wet solid) in one portion and the suspension was vigorously stirred and reflux for 10 min. The reaction progress was controlled by mass spectrometry. Further 2–3 additions of the same amount of Ra-Ni were necessary in order to observed only the signals of the product in the mass spectrum. The reaction mixture was filtered off and the filtrate was evaporated under reduced pressure. Remaining oily solid was redisolved in 50 mL of $CHCl_3$, organic phase was extracted with 25 mL of deionized water, dried with anhydrous Na_2SO_4, filtered on a glass frit and evaporated to dryness under reduced pressure. The product was obtained as light-yellow powder (1.21 g, yield 94.5 %).

MS *m/z* (+): 593.35 ([**L** + H]$^+$, calcd. 593.41), 615.41 ([**L** + Na]$^+$, calcd. 615.39).

^{1}H NMR (CDCl₃): δ 1.73 (4H, quin, $^3J_{HH}$ = 6.9 Hz, H-8), 2.51 (4H, t, $^3J_{HH}$ = 6.9 Hz, H-9), 2.58 (8H, m, H-10 + H-7), 2.66 (4H, m, H-11), 3.34 (4H, s, H-12), 3.57 (4H, s, NH₂), 3.62 (4H, s, H-6), 6.57 (4H, m, AA′BB′, H-15), 7.03 (4H, m, AA′BB′, H-14), 7.11 (2H, m, H-2), 7.48 (2H, d, $^3J_{HH}$ = 7.8 Hz, H-4), 7.58 (2H, m, H-3), 8.48 (2H, m, H-1).

^{13}C{^{1}H} NMR (CDCl₃): δ 23.45 (2C, C-8), 50.10 (2C, C-11), 50.75 (2C, C-10), 51.01 (2C, C-9), 51.69 (2C, C-7), 58.86 (2C, C-12), 61.31

(2C, C-6), 114.83 (4C, C-15), 121.66 (2C, C-2), 122.98 (2C, C-4), 129.59 (2C, C-13), 129.89 (4C, C-14), 136.19 (2C, C-3), 144.98 (2C, C-16), 148.70 (2C, C-1), 160.69 (2C, C-5).

2.3. [Fe(L-NH₂)]Cl₂·2.5H₂O

Ligand **L-NH₂** (100 mg, 0.169 mmol) was dissolved in 5 mL of hot CH_3OH and solid anhydrous $FeCl_2$ (22 mg, 0.169 mmol) was dissolved in 1 mL of dimethylformamide, both done under inert argon atmosphere. Both solutions were mixed together under stirring and the reaction mixture was heated to reflux for 1 min. Then the solution was cooled down, small amount of dark brown precipitate was filtered off via 0.45 μm teflon syringe filter and excess of diethyl ether (ca 50 mL) was added to the filtrate slowly under stirring. Obtained precipitate was decanted with diethyl ether and dried under flow of argon. Product was isolated in form of yellow powder (89 mg, yield 69.0 %).

MS *m/z* (+): 683.19 ([Fe(**L-NH₂**) + Cl]$^+$, calcd. 683.30).

Anal. Calcd. (%) for [Fe(**L-NH₂**)]Cl₂·2.5H₂O ($C_{36}H_{53}Cl_2FeN_8O_{2.5}$, M_r = 764.61): C, 56.55; H, 6.99; N, 14.66. Found: C, 56.44; H, 6.80; N, 14.78.

2.4. Theoretical calculations

The theoretical calculations were carried out with the ORCA 4.1 computational package [21]. TPSSh DFT functional [22] together with polarized triple-ζ quality basis set def2-TZVP proposed by Ahlrichs and co-workers [23] was used for geometry optimization setting tightopt optimization criteria in ORCA. The calculations utilized the RI approximation with the decontracted auxiliary def2/J Coulomb fitting basis set [24] and the chain-of-spheres (RIJCOSX) approximation to exact exchange [25] as implemented in ORCA. Increased integration grids (Grid5 and Gridx5 in ORCA convention) and tight SCF convergence criteria were used in all calculations.

3. Results and discussions

3.1. Syntheses and general characterizations

The ligand **L-NH₂** was synthesized in two steps which are shown in Fig. 2. In the first one, the parent macrocycle **Py₂-C** reacted with *p*-nitrobenzylbromide in common S_N2 substitution reaction to produce **L-NO₂** derivative. The progress of the reaction was monitored by mass spectrometry and because the signals of monosubstituted product as well as unreacted **Py₂-C** were identified (Fig. 3A), additional amount (0.4 equivalent) of *p*-nitrobenzylbromide had to be added till only the signal of disubstituted product was observed in the mass spectrum (see Fig. 3B). Obtained product was purified by recrystallization from acetonitrile.

In the next step, aromatic nitro groups were reduced to amino groups. In the literature, there are many procedures for such reduction – e.g. Zn or Sn/HCl [26], hydrogen gas with Pd/C [27], $NaBH_4$ with Ra-Ni [28], or hydrazine hydrate with Pd/C [29]. But we chose very fast previously described method using cheaper catalyst Ra-Ni and hydrazine hydrate as a source of hydrogen [20]. The progress of the reaction was monitored by mass spectrometry. In the mass spectra, it was possible to determine the signals of hydroxylamines - intermediates of the reduction reaction (Fig. 3C). Therefore, 2–3 more portions of the same amount of Ra-Ni as in the beginning had to be added to the reaction mixture in order to complete the reduction of all intermediates to **L-NH₂** (Fig. 3D). The *p*-aminobenzyl groups appeared to have a high ability to decompose during the measurement of mass spectra (electrospray ionization) and therefore the signals of unsubstituted **Py₂-C** and monosubstituted NH₂-product were also identified in the mass spectrum of **L-NH₂** (Fig. 3D) as a result of fragmentation of the molecular ion.

Fe(II) complex [Fe(**L-NH₂**)]Cl₂·2.5H₂O was prepared by direct
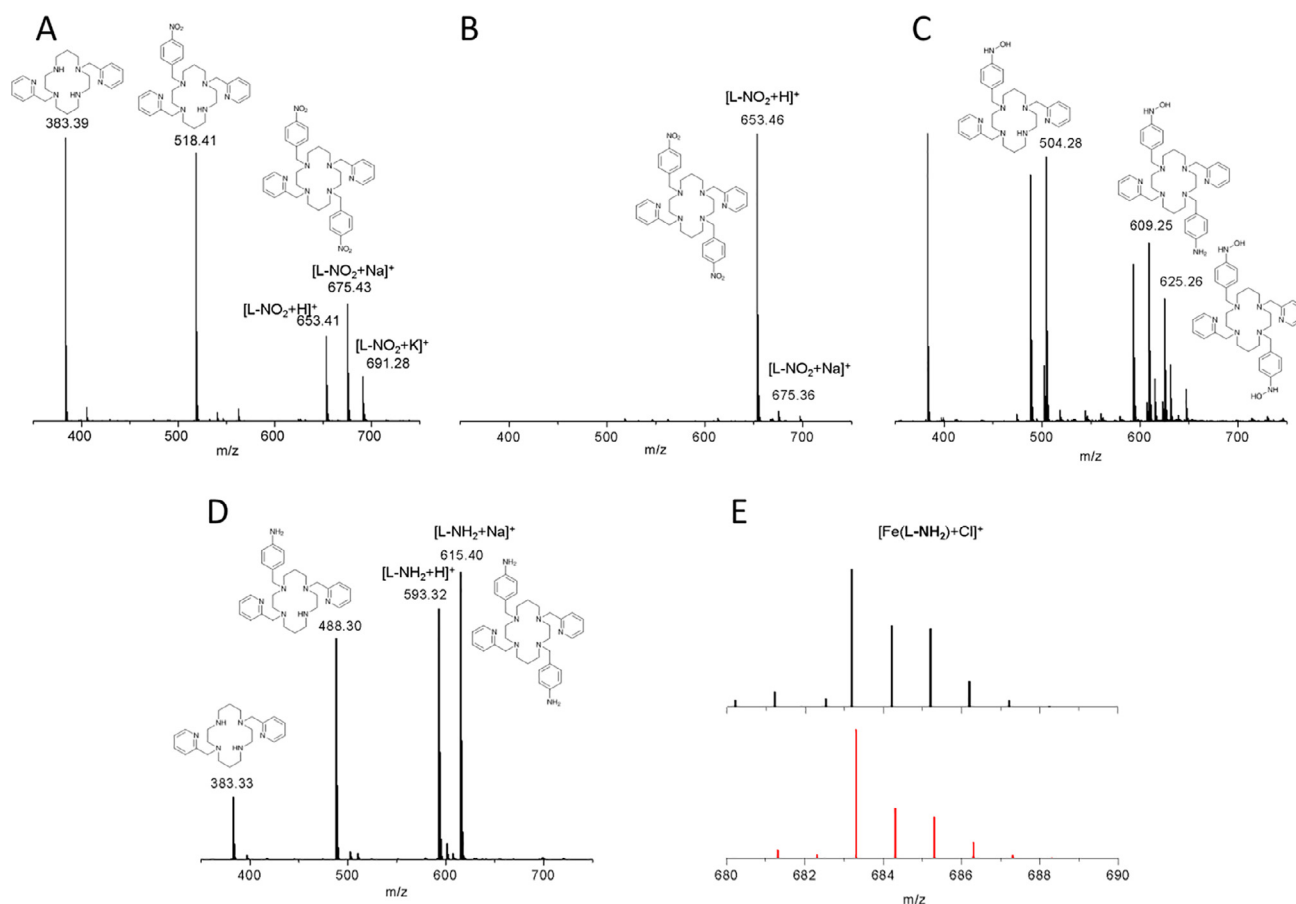
Fig. 3. Progress of the synthesis of **L-NH₂** and its Fe(II) complex monitored by mass spectrometry. A) Reaction mixture after addition of 2.04 eqv. of *p*-nitrobenzylbromide. B) Reaction mixture after addition of additional 0.4 eqv. of *p*-nitrobenzylbromide. C) Reaction mixture after first addition of Ra-Ni. D) Reaction mixture after third addition of Ra-Ni. E) Isotopic pattern of [Fe(**L-NH₂**) + Cl]⁺ species found in the mass spectrum of [Fe(**L-NH₂**)]Cl₂·2.5H₂O in positive mode (*black*) compared with the simulated one (*red*).

mixing of **L-NH₂** with anhydrous FeCl₂ in mixture of dimethylformamide and CH₃OH. Solid product was precipitated by addition of excess of diethyl ether. Formation of the product was confirmed by elemental analysis, mass spectrum (Fig. 3E) and IR spectrum (Fig. S5), which is significantly different from that of free ligand (Fig. S5).

Despite several attempts to prepare single-crystals of the Fe(II) complex by slow diffusion of diethyl ether vapors at low temperature to its solution in dimethylformamide/CH₃OH, we were not successful, because always either yellow–brown oily product or amorphous solid was obtained. Thus, the molecular/crystal structure of [Fe(**L-NH₂**)]Cl₂·2.5H₂O could not be determined.

3.2. Magnetic measurement

The results of dc magnetic measurement are displayed in Fig. 4. The value of $\mu_{\text{eff}}/\mu_{\text{B}} = 5.12$ at room temperature is slightly higher than the theoretical spin only value ($\mu_{\text{eff}}/\mu_{\text{B}} = 4.90$ for $S = 2$ and $g = 2.0$). Upon cooling, the $\mu_{\text{eff}}/\mu_{\text{B}}$ value decreased abruptly below 50 K to a minimum of 3.39 at 1.9 K as a result of the magnetic anisotropy described by the zero-field splitting (ZFS) effects. Also, the isothermal magnetizations measured at 2 and 4.6 K revealed significant magnetic anisotropy, because only value of $M_{\text{mol}}/N_{\text{A}}\mu_{\text{B}} = 2.2$ at $B = 7$ T was reached, which is much smaller than the theoretical saturation value of the isothermal magnetization calculated as $M_{\text{mol}}/N_{\text{A}}\mu_{\text{B}} = g{\cdot}S = 4$ for $g = 2.0$. These theoretical values are much larger than the experimental ones (Fig. 4) pointing to the presence of the large magnetic anisotropy induced by the ligand-field. According to this data it is evident, that no SCO occurred and the Fe(II) complex remained in HS state over the whole

temperature range. This behavior, different from Fe(II) complexes of **Py₂-C** and **Py₂-CB** showing SCO with different counter ions, could be explained by various different reasons: (i) lower ligand field strength caused by substitution of secondary nitrogen atoms with electron-withdrawing benzyl groups, (ii) different coordination mode (*trans*) of pyridine functional groups, (iii) different non-covalent intermolecular interactions and crystal packing, (iv) different morphology of the microcrystalline powder (lower cooperativity). In order to exclude the effect of co-crystallized water molecules, the sample was heated twice up to 400 K during the measurement of magnetic data (see ESI Fig. S6), which were almost identical to those of the parent complex without any indication of SCO occurrence.

Next, the experimental magnetic data were analyzed with spin Hamiltonian for mononuclear complexes including ZFS.[30]

$$\hat{H} = D(\hat{S}_z^2 - \hat{S}^2/3) + E(\hat{S}_x^2 - \hat{S}_y^2) + \mu_B B g \hat{S}_a - zj\langle\hat{S}_a\rangle\hat{S}_a \quad (1)$$

where D and E are the single-ion axial and rhombic ZFS parameters, respectively, and zj is molecular-field correction parameter reflecting intermolecular interactions, and Zeeman term is defined for *a*-direction of magnetic field as $B_a = B(\sin(\theta)\cos(\varphi), \sin(\theta)\sin(\varphi), \cos(\theta))$ with the help of the polar coordinates. Then, the molar magnetization in given direction of magnetic field B_a was calculated as

$$M_a = -N_A \frac{\sum_i \left(\sum_k \sum_l C_{ik}^+ (Z_a)_{kl} C_{li}\right) \exp(-\varepsilon_{a,i}/kT)}{\sum_i \exp(-\varepsilon_{a,i}/kT)} \quad (2)$$

where Z_a is the matrix element of the Zeeman term for the *a*-direction of the magnetic field and C are the eigenvectors resulting from the diagonalization of the complete spin Hamiltonian matrix. The inclusion of *zj*
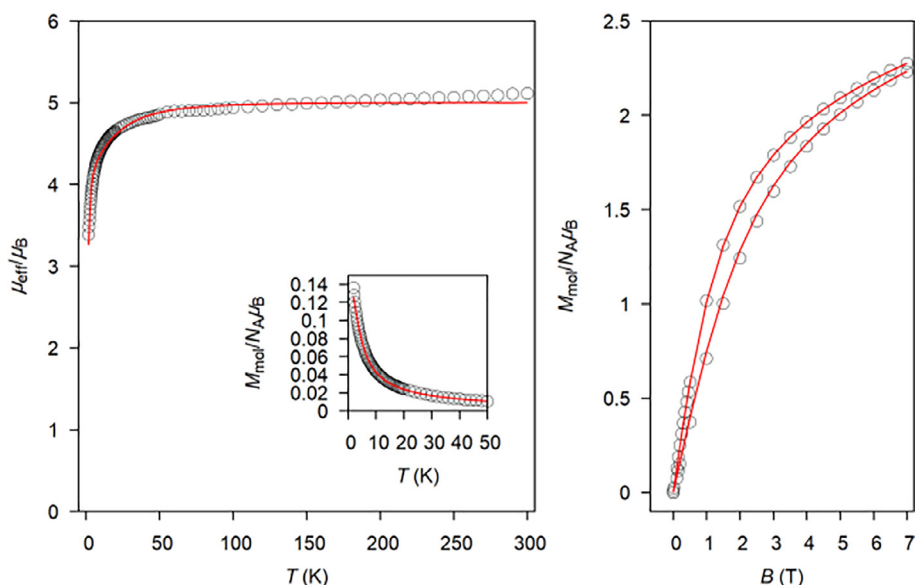
Fig. 4. Temperature dependence of the effective magnetic moment (*left*) and isothermal magnetizations measured at $T = 2$ and 4.6 K (*right*) for [Fe(**L-NH₂**)]Cl₂·2.5H₂O. Empty circles – experimental data, full lines – calculated data with $g = 2.04$, $D = -17.7$ cm^{-1}, $E/D = 0.31$, $zj = 0.21$ cm^{-1}.

means that an iterative procedure was applied. Finally, the integral (orientational) average of molar magnetization was calculated by Eq. (3) in order to properly simulate experimental powder magnetization data as

$$M_{mol} = \frac{1}{4\pi} \int_0^{2\pi} \int_0^{\pi} M_a \sin\theta d\theta d\varphi \qquad (3)$$

The best fit was found for these parameters: $g = 2.04$, $D = -17.7$ cm^{-1}, $E/D = 0.31$, $zj = 0.21$ cm^{-1} (Fig. 4). The fitted *D*-parameter is in the range for HS Fe^{II} octahedral complexes [31].

3.3. Theoretical calculations

With the aim to understand the fact that the modification of **Py₂-C** ligand to **L-NH₂** ligand changed the spin crossover behaviour of [Fe^{II}(**Py₂-C**)]$^{2+}$ or [Fe^{II}(**Py₂-CB**)]$^{2+}$ compounds [15,16,17] to high-spin state compound of [Fe(**L-NH₂**)]Cl₂·2.5H₂O, the DFT calculations were performed. It is well known that choice of the DFT functional for studying SCO compounds can be very tricky, therefore we followed the most recent benchmark study of Ruiz et al. [32], in which the hybrid *meta*-GGA functional TPSSh seems to have the best results for 3d metals. Moreover, the bias introduced by the choice of the DFT functional can be partly eliminated by elucidating the trend in the energy separation of HS and LS states, $\Delta = \varepsilon_{HS} - \varepsilon_{LS}$, for various coordination complexes under study in the comparison with the known SCO complexes. Therefore, first, the molecular geometries of *cis/trans*-[Fe^{II}(**Py₂-C**)]$^{2+}$ and *cis*-[Fe^{II}(**Py₂-CB**)]$^{2+}$ were optimized for LS and HS spin states using ORCA software and TPSSh functional together with def2-TZVP basis set for all atoms. The bond distances for the optimized LS and HS geometries are shown in Fig. 5. The calculations correctly favored LS states with $\Delta = 5$–7 kcal/mol (Fig. 6), which is in the range of SCO complexes [32], regardless the *cis-/trans*-configuration of [Fe^{II}(**Py₂-C**)]$^{2+}$. Then, the molecular geometries of [Fe^{II}(**L-NH₂**)]$^{2+}$ were optimized for LS and HS states in similar way considering both *cis*- and *trans*- isomers, which resulted in $\Delta = -2.7$ and -1.7 kcal/mol, respectively. This clearly shows that Fe(II) complex with modified macrocyclic ligand **L-NH₂** regardless its *cis-/trans*-configuration prefers to be in HS state, which explains the observed magnetic behavior for [Fe(**L-NH₂**)]Cl₂·2.5H₂O. Again, the relevant bond distances for the optimized LS and HS geometries are shown in Fig. 5. It is evident that *p*-aminobenzyl pendant arms reduced the electron density on nitrogen atom of the macrocyclic ligand, which

is manifested by elongated Fe–N bond distances, e.g. in LS states d (Fe–N$_{arm}$) = 2.073 Å in [Fe^{II}(**Py₂-C**)]$^{2+}$ vs. d(Fe-N$_{arm}$) = 2.211 and 2.228 Å in *cis*-[Fe^{II}(**L-NH₂**)]$^{2+}$.

Furthermore, the calculated energies for *trans*-[Fe^{II}(**L-NH₂**)]$^{2+}$ in both HS and LS states are lower than those for *cis*-isomer ($\delta = \varepsilon_{trans} - \varepsilon_{cis} = -3.87$ and -4.87 kcal/mol for HS and LS states, respectively) and thus, formation of *trans*- isomer is more probable – Fig. 7. On contrary, the analogous calculations showed that in case of [Fe^{II}(**Py₂-C**)]$^{2+}$ δ-values are positive both for LS and HS spin states, hence the formation of *cis*-[Fe^{II}(**Py₂-C**)]$^{2+}$ is preferred in agreement with reported strucutures. Nevertheless, in this particular case not the different preferred geometrical configuration (*trans*-[Fe^{II}(**L-NH₂**)]$^{2+}$ vs. *cis*-[Fe^{II}(**Py₂-C**)]$^{2+}$), but rather the electron density on nitrogen atoms plays the crucial role for SCO occurrence (positive Δ values for both *cis/trans*-[Fe^{II}(**Py₂-C**)]$^{2+}$ while negative ones for both *cis/trans*-[Fe^{II}(**L-NH₂**)]$^{2+}$).

4. Conclusions

In order to transform Fe(II) SCO complex to magnetically multi-functional molecular material, specially-designed ligand **L-NH₂** has been synthesized. It contains NH₂ groups allowing easy consequent structural modification (incorporation of e.g. carboxylic acid, o-va-nillin, amines, other macrocycle etc.) important for consequent attachment of other molecule of magnetic interest. According to the dc magnetic data, prepared Fe(II) complex [Fe(**L-NH₂**)]Cl₂·2.5H₂O do not show SCO upon cooling down to 2 K and remains in the high spin state even upon heating to 400 K. This magnetic behavior was rationalized by the DFT computational study, which identified *trans*- configuration and HS state as preferential for [Fe(**L-NH₂**)]$^{2+}$ complex in contrast to SCO complexes [Fe^{II}(**Py₂-C**)]$^{2+}$ and [Fe^{II}(**Py₂-CB**)]$^{2+}$ in which LS state and *cis*- configuration is preferred. Such behavior can be more likely explained by electron-withdrawing effect of *p*-aminobenzyl groups inducing weaker donor properties of macrocyclic nitrogen atoms and thus, weaker ligand field, than by the different preffered *trans*-configuration of [Fe(**L-NH₂**)]$^{2+}$ complex. Thus, in future, the group for substitution has to be chosen more carefully, if SCO should be preserved in Fe(II) complexes of derivatives of parent macrocycle **Py₂-C**. These synthetic strategies could be beneficial: (i) substitution by less electron-withdrawing group, (ii) substitution of only one secondary nitrogen atoms in **Py₂-C**, (iii) substitution of the side-chain rather than the
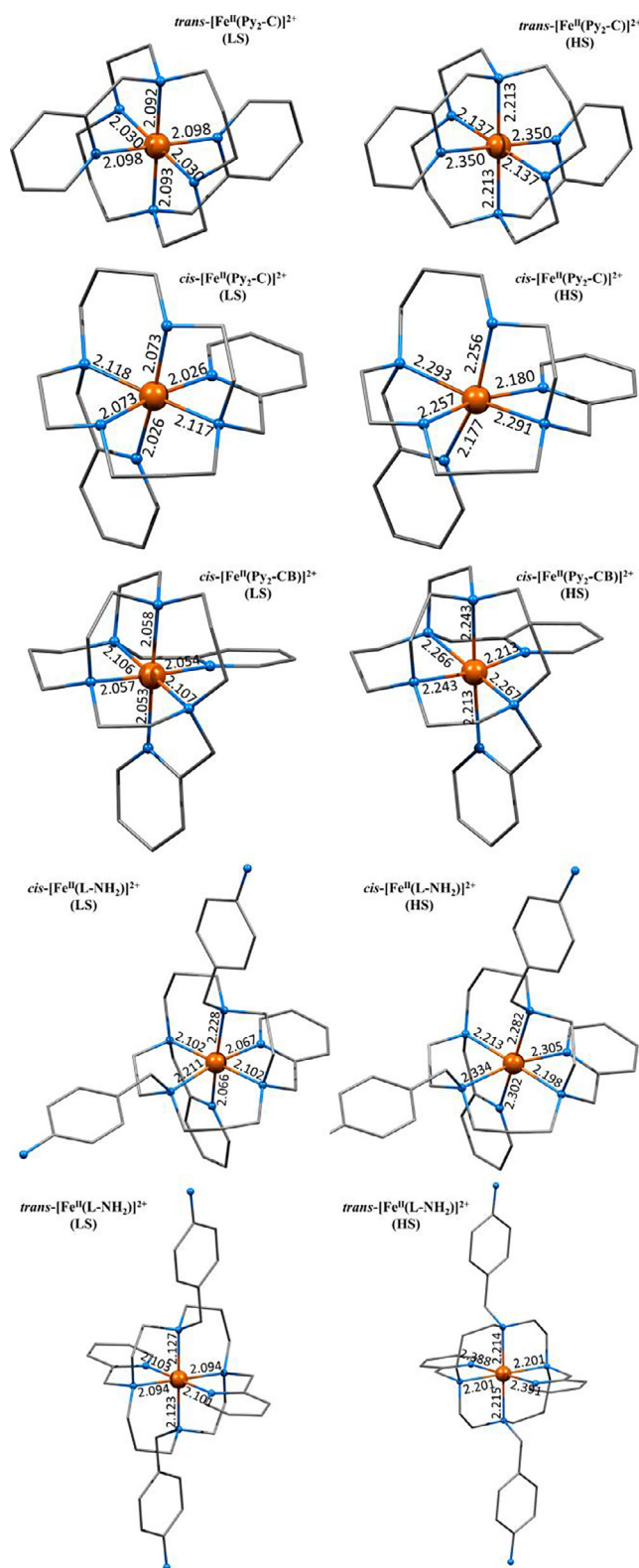
Fig. 5. The DFT optimized LS and HS states molecular geometries of *cis/trans*-[Fe^{II}(**Py$_2$-C**)]$^{2+}$, *cis*-[Fe^{II}(**Py$_2$-CB**)]$^{2+}$, and *cis/trans*-[Fe(**L-NH$_2$**)]$^{2+}$ using TPSSh/def2-TZVP. The hydrogen atoms are not shown for clarity.

secondary nitrogen atoms.
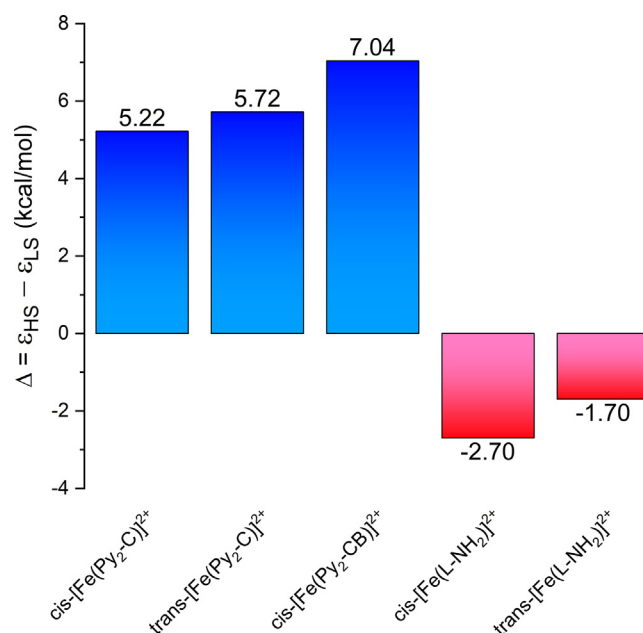
Fig. 6. The energy separation of HS and LS states of *cis/trans*-[Fe^{II}(**Py$_2$-C**)]$^{2+}$, *cis*-[Fe^{II}(**Py$_2$-CB**)]$^{2+}$ and *cis/trans*-[Fe(**L-NH$_2$**)]$^{2+}$ calculated using TPSSh/def2-TZVP.
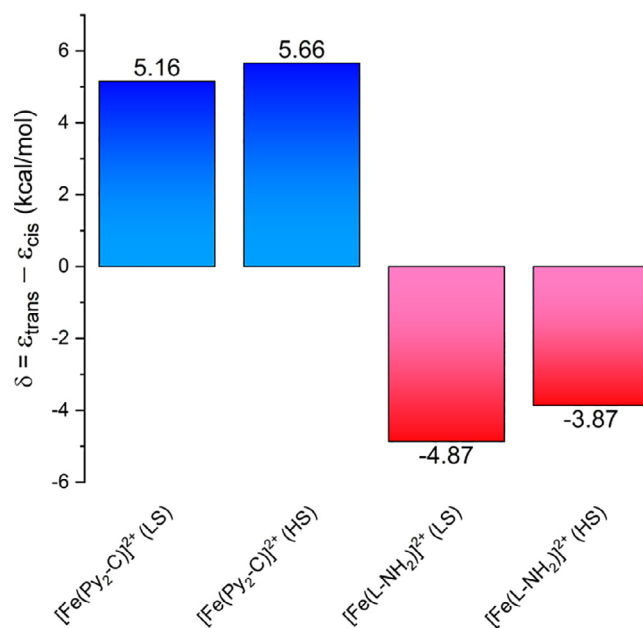
Fig. 7. The energy separation of *trans*- and *cis*- isomers of LS and HS forms of [Fe^{II}(**Py$_2$-C**)]$^{2+}$ and [Fe(**L-NH$_2$**)]$^{2+}$ calculated using TPSSh/def2-TZVP.

Appendix A. Supplementary data

Supplementary data to this article can be found online at https://doi.org/10.1016/j.ica.2019.05.020.

References

[1] P. Gutlich, H.A. Goodwin, Top. Curr. Chem. (2004) 233–235.

[2] Spin-crossover materials – properties and applications, ed. M. A. Halcrow, John Wiley & Sons, Chichester, UK, 2013.

[3] A.B. Gaspar, V. Ksenofontov, M. Seredyuk, P. Gütlich, Coord. Chem. Rev. 249 (2005) 2661–2676.

[4] D. Gatteshi, R. Sessoli, J. Villain, Molecular Nanomegnets, Oxford University Press, New York, 2006.

[5] Molecular Nanomagnets and Related Phenomena; S. Gao, Ed.; Structure and Bonding, Vol. 164; Springer: Berlin, 2015.

[6] J.S. Miller, D. Gatteschi, Molecule-based magnets themed issue No. 6, Chem. Soc. Rev. 40 (2011) 3065–3365.

[7] R. Ababei, C. Pichon, O. Roubeau, Y.-G. Li, N. Bréfuel, L. Buisson, P. Guionneau, C. Mathonière, R. Clérac, J. Am. Chem. Soc. 135 (2013) 14840–14853.

[8] S. Mossin, B.L. Tran, D. Adhikari, M. Pink, F.W. Heinemann, J. Sutter, R.K. Szilagyi, K. Meyer, D.J. Mindiola, J. Am. Chem. Soc. 134 (2012) 13651–13661.

[9] X. Feng, C. Mathoniere, R. Jeon Ie, M. Rouzieres, A. Ozarowski, M.L. Aubrey, M.I. Gonzalez, R. Clerac, J.R. Long, J. Am. Chem. Soc. 135 (2013) 15880–15884.

[10] A. Urtizberea, O. Roubeau, Chem Sci 8 (2017) 2290–2295.

[11] C. Mathoniere, H.J. Lin, D. Siretanu, R. Clerac, J.M. Smith, J. Am. Chem. Soc. 135 (2013) 19083–19086.

[12] L. Chen, J. Song, W. Zhao, G. Yi, Z. Zhou, A. Yuan, Y. Song, Z. Wang, Z.W. Ouyang, Dalton Trans. 47 (2018) 16596–16602.

[13] D. Shao, L. Shi, L. Yin, B.L. Wang, Z.X. Wang, Y.Q. Zhang, X.Y. Wang, Chem. Sci. 9 (2018) 7986–7991.

[14] V. García-López, F.J. Orts-Mula, M. Palacios-Corella, J.M. Clemente-Juan, M. Clemente-León, E. Coronado, Polyhedron 150 (2018) 54–60.

[15] F. El Hajj, G. Sebki, V. Patinec, M. Marchivie, S. Triki, H. Handel, S. Yefsah, R. Tripier, C.J. Gomez-Garcia, E. Coronado, Inorg. Chem. 48 (2009) 10416–10423.

[16] E. Milin, B. Benaicha, F. El Hajj, V. Patinec, S. Triki, M. Marchivie, C.J. Gómez-García, S. Pillet, Eur. J. Inorg. Chem. (2016) 5305–5314.

[17] B. Drahoš, Z. Trávníček, Dalton Trans. 47 (2018) 6134–6145.

[18] G. Royal, V. Dahaoui-Gindrey, S. Dahaoui, A. Tabard, R. Guilard, P. Pullumbi, C. Lecomte, Eur. J. Org. Chem. (1998) 1971–1975.

[19] J. Prousek, Collect. Chem. Czech. Commun. 56 (1991) 1358–1360.

[20] F. Yuste, M. Saldaña, F. Walls, Tetrahedron Lett. 23 (1982) 147–148.

[21] F. Neese, Wiley Interdiscip. Rev.: Comput. Mol. Sci. 8 (2018) e1327.

[22] a) J.P. Perdew, S. Kurth, A. Zupan, P. Blaha, Phys. Rev. Lett. 82 (1999) 2544–2547;
b) J.P. Perdew, J. Tao, V.N. Staroverov, G.E. Scuseria, J. Chem. Phys. 120 (2004) 6898–6911.

[23] F. Weigend, R. Ahlrichs, Phys. Chem. Chem. Phys. 7 (2005) 3297–3305.

[24] F. Weigend, Phys. Chem. Chem. Phys. 8 (2006) 1057–1065.

[25] a) F. Neese, F. Wennmohs, A. Hansen, U. Becker, Chem. Phys. 356 (2009) 98–109;
b) R. Izsak, F. Neese, J. Chem. Phys. 135 (2011) 144105/1–144105/11.

[26] O. Enoki, T. Imaoka, K. Yamamoto, Org. Lett. 5 (2003) 2547–2549.

[27] P.J. Riss, C. Burchardt, M.J. Zimny, J. Peters, F. Roesch, RSC Adv. 2 (2012) 7156–7160.

[28] I. Pogorelić, M. Filipan-Litvić, S. Merkaš, G. Ljubić, I. Cepanec, M. Litvić, J. Mol. Catal. A: Chem. 274 (2007) 202–207.

[29] M. Salavati-Niasari, J. Coord. Chem. 62 (2009) 980–995.

[30] R. Boča, A Handbook of Magnetochemical Formulae, Elsevier, Amsterdam, 2012.

[31] R. Boča, Coord. Chem. Rev. 248 (2004) 757–815.

[32] J. Cirera, M. Via-Nadal, E. Ruiz, Inorg. Chem. 57 (2018) 14097–14105.